

SANDIA REPORT

SAND2019-11095

Printed September 18, 2019



Sandia
National
Laboratories

Library of Advanced Materials for Engineering (LAMÉ) 4.54

LAMÉ Team
Solid Mechanics Department
Engineering Sciences Center

Prepared by
Sandia National Laboratories
Albuquerque, New Mexico 87185
Livermore, California 94550

Issued by Sandia National Laboratories, operated for the United States Department of Energy by National Technology & Engineering Solutions of Sandia, LLC.

NOTICE: This report was prepared as an account of work sponsored by an agency of the United States Government. Neither the United States Government, nor any agency thereof, nor any of their employees, nor any of their contractors, subcontractors, or their employees, make any warranty, express or implied, or assume any legal liability or responsibility for the accuracy, completeness, or usefulness of any information, apparatus, product, or process disclosed, or represent that its use would not infringe privately owned rights. Reference herein to any specific commercial product, process, or service by trade name, trademark, manufacturer, or otherwise, does not necessarily constitute or imply its endorsement, recommendation, or favoring by the United States Government, any agency thereof, or any of their contractors or subcontractors. The views and opinions expressed herein do not necessarily state or reflect those of the United States Government, any agency thereof, or any of their contractors.

Printed in the United States of America. This report has been reproduced directly from the best available copy.

Available to DOE and DOE contractors from

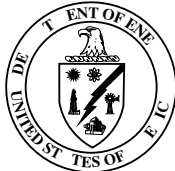
U.S. Department of Energy
Office of Scientific and Technical Information
P.O. Box 62
Oak Ridge, TN 37831

Telephone: (865) 576-8401
Facsimile: (865) 576-5728
E-Mail: reports@osti.gov
Online ordering: <http://www.osti.gov/scitech>

Available to the public from

U.S. Department of Commerce
National Technical Information Service
5301 Shawnee Road
Alexandria, VA 22312

Telephone: (800) 553-6847
Facsimile: (703) 605-6900
E-Mail: orders@ntis.gov
Online order: <https://classic.ntis.gov/help/order-methods>



ABSTRACT

Accurate and efficient constitutive modeling remains a cornerstone issue for solid mechanics analysis. Over the years, the LAMÉ advanced material model library has grown to address this challenge by implementing models capable of describing material systems spanning soft polymers to stiff ceramics including both isotropic and anisotropic responses. Inelastic behaviors including (visco)plasticity, damage, and fracture have all incorporated for use in various analyses. This multitude of options and flexibility, however, comes at the cost of many capabilities, features, and responses and the ensuing complexity in the resulting implementation. Therefore, to enhance confidence and enable the utilization of the LAMÉ library in application, this effort seeks to document and verify the various models in the LAMÉ library. Specifically, the broader strategy, organization, and interface of the library itself is first presented. The physical theory, numerical implementation, and user guide for a large set of models is then discussed. Importantly, a number of verification tests are performed with each model to not only have confidence in the model itself but also highlight some important response characteristics and features that may be of interest to end-users. Finally, in looking ahead to the future, approaches to add material models to this library and further expand the capabilities are presented.

ACKNOWLEDGMENTS

This document, and the models contained with it, are the result of a longstanding commitment to material modeling at Sandia National Laboratories. As such, a number of people representing a wide set of expertise and discipline have all contributed in various forms. While the current LAMÉ manual is maintained by William Scherzinger and Brian Lester, it would not be possible without the contributions of numerous others. The list of people includes, but is not limited to, Lupe Arguello, Arthur Brown, Bob Chambers, Jim Cox, Arlo Fossum, Jay Foulk, Arne Gullerud, Jason Hales, Dan Hammerand, Sam Key, Kevin Long, Jeffery McGuire, Mike Neilsen, Pania Newell, Jake Ostien, Ben Reedlunn, Ben Spencer, Mike Stone, and Jerry Wellman.

Additionally, as LAMÉ is a part of Sierra/SolidMechanics the continued development of this document and the corresponding models would not be possible without the support of core development team for Sierra/SolidMechanics including, Frank Beckwith, Kenneth Noel Belcourt, Gabriel J. de Frias, San Le, Kevin L. Manktelow, Mark T. Merewether, Matthew D. Mosby, Julia A. Plews, Vicki L. Porter, Timothy R. Shelton, Jesse D. Thomas, Michael R. Tupek, Michael G. Veilleux, and Patrick G. Xavier.

CONTENTS

1. Overview	17
2. Strategy	18
2.1. Code Development	19
2.2. Model Implementation	20
2.2.1. Code Standards	20
2.2.2. Testing Standards	20
2.2.3. Documentation Standards	21
3. Interface	22
4. Material Models	24
4.1. Hypoelastic Models	24
4.2. Hyperelastic Models	27
4.3. Elastic Model	30
4.3.1. Theory	30
4.3.2. Implementation	31
4.3.3. Verification	31
4.3.4. User Guide	37
4.4. Elastic Three Dimensional Orthotropic Model	39
4.4.1. Theory	39
4.4.2. Implementation	40
4.4.3. Verification	41
4.4.4. User Guide	45
4.5. Neo-Hookean Model	47
4.5.1. Theory	47
4.5.2. Implementation	47
4.5.3. Verification	48
4.5.4. User Guide	55
4.6. Gent Model	57
4.6.1. Theory	57
4.6.2. Implementation	57
4.6.3. Verification	58
4.6.4. User Guide	62
4.7. Elastic-Plastic Model	64
4.7.1. Theory	64
4.7.2. Implementation	66

4.7.3. Verification	67
4.7.4. User Guide	74
4.8. Elastic-Plastic Power Law Hardening Model	77
4.8.1. Theory	77
4.8.2. Implementation	78
4.8.3. Verification	79
4.8.4. User Guide	84
4.9. Ductile Fracture Model	87
4.9.1. Theory	87
4.9.2. Implementation	87
4.9.3. Verification	89
4.9.4. User Guide	93
4.10. Multilinear Elastic-Plastic Model	96
4.10.1. Theory	96
4.10.2. Implementation	97
4.10.3. Verification	98
4.10.4. User Guide	103
4.11. Multilinear Elastic-Plastic Fail Model	105
4.11.1. Theory	105
4.11.2. Implementation	105
4.11.3. Verification	107
4.11.4. User Guide	110
4.12. Johnson-Cook Model	114
4.12.1. Theory	114
4.12.2. Implementation	115
4.12.3. Verification	116
4.12.4. User Guide	122
4.13. J_2 Plasticity Model	125
4.13.1. Theory	125
4.13.2. Implementation	130
4.13.3. Verification	131
4.13.4. User Guide	140
4.14. Hosford Plasticity Model	145
4.14.1. Theory	145
4.14.2. Implementation	149
4.14.3. Verification	151
4.14.4. User Guide	160
4.15. Hill Plasticity Model	163
4.15.1. Theory	163
4.15.2. Implementation	168
4.15.3. Verification	169
4.15.4. User Guide	185
4.16. Barlat Plasticity Model	188
4.16.1. Theory	188
4.16.2. Implementation	193

4.16.3. Verification	195
4.16.4. User Guide	210
4.17. Plane Stress Rate Plasticity Model	214
4.17.1. Theory	214
4.17.2. Implementation	217
4.17.3. User Guide	220
4.18. Modular Plane Stress Plasticity Model	223
4.18.1. Theory	223
4.18.2. Implementation	229
4.18.3. Verification	232
4.18.4. User Guide	236
4.19. Power Law Creep Model	240
4.19.1. Theory	240
4.19.2. Implementation	240
4.19.3. Verification	241
4.19.4. User Guide	245
4.20. Viscoplastic Model	247
4.20.1. Theory	247
4.20.2. Implementation	249
4.20.3. Verification	250
4.20.4. User Guide	254
4.21. Munson-Dawson Viscoplastic Model	257
4.21.1. Theory	257
4.21.2. Implementation	259
4.21.3. Verification	260
4.21.4. User Guide	267
4.22. Hyperfoam Model	270
4.22.1. Theory	270
4.22.2. Implementation	271
4.22.3. Verification	271
4.22.4. User Guide	284
4.23. Hyperelastic Damage Model	286
4.23.1. Theory	286
4.23.2. Implementation	287
4.23.3. Verification	288
4.23.4. User Guide	291
4.24. Soil and Foam Model	293
4.24.1. Theory	293
4.24.2. Implementation	294
4.24.3. Verification	295
4.24.4. User Guide	297
4.25. Shape Memory Alloy Model	299
4.25.1. Theory	299
4.25.2. Implementation	303
4.25.3. Verification	305

4.25.4. User Guide	309
4.26. Low Density Foam Model	312
4.26.1. Theory	312
4.26.2. Implementation	313
4.26.3. Verification	314
4.26.4. User Guide	317
4.27. Foam Plasticity Model	319
4.27.1. Theory	319
4.27.2. Implementation	320
4.27.3. Verification	321
4.27.4. User Guide	323
4.28. Viscoplastic Foam Model	325
4.28.1. Theory	325
4.28.2. Implementation	327
4.28.3. Verification	328
4.28.4. User Guide	331
4.29. Foam Damage	334
4.29.1. Theory	334
4.29.2. Implementation	337
4.29.3. Verification	340
4.29.4. User Guide	347
4.30. Orthotropic Crush Model	350
4.30.1. Theory	350
4.30.2. Implementation	351
4.30.3. Verification	353
4.30.4. User Guide	355
4.31. Orthotropic Rate Model	357
4.31.1. Theory	357
4.31.2. Implementation	359
4.31.3. Verification	361
4.31.4. User Guide	365
4.32. Universal Polymer Model (UPM)	368
4.32.1. Theory	368
4.32.2. Implementation	371
4.32.3. Verification	373
4.32.4. User Guide	379
4.33. Wire Mesh Model	384
4.33.1. Theory	384
4.33.2. Implementation	385
4.33.3. Verification	386
4.33.4. User Guide	390
A. Common Boundary Value Problems	392
A.1. Uniaxial Stress - Displacement Controlled	392
A.2. Simple Shear	393

A.3. Pure Shear	394
A.4. Hydrostatic Compression	395
A.5. Constant Equivalent Plastic Strain Rate	396
A.5.1. Uniaxial Stress	396
A.5.2. Pure Shear	398

Appendices

392

LIST OF FIGURES

Figure 4-1.	Elastic Verification: Uniaxial Stress - axial stress	32
Figure 4-2.	Elastic Verification: Uniaxial Stress - lateral strain	33
Figure 4-3.	Elastic Verification: Biaxial Stress - out of plane stress	34
Figure 4-4.	Elastic Verification: Biaxial Stress - in plane normal stresses	35
Figure 4-5.	Elastic Verification: Pure Shear - shear stress	36
Figure 4-6.	Elastic 3D Orthotropic Verification: Biaxial Displacement	43
Figure 4-7.	Elastic 3D Orthotropic Verification: Rotated Uniaxial Strain	44
Figure 4-8.	Neo-Hookean Verification: Uniaxial Stress	50
Figure 4-9.	Neo-Hookean Verification: Shear Strain	51
Figure 4-10.	Neo-Hookean Verification: Shear Stress	51
Figure 4-11.	Neo-Hookean Verification: Uniaxial Strain	53
Figure 4-12.	Neo-Hookean Verification: Simple Shear	54
Figure 4-13.	Gent Verification: Uniaxial Strain	59
Figure 4-14.	Gent Verification: Simple Shear	60
Figure 4-15.	Gent Verification: Hydrostatic Compression	61
Figure 4-16.	Elastic-Plastic Theory: Example yield surface, f	65
Figure 4-17.	Elastic-Plastic Verification: Uniaxial Stress - axial stress	70
Figure 4-18.	Elastic-Plastic Verification: Uniaxial Stress - lateral strains	70
Figure 4-19.	Elastic-Plastic Verification: Pure Shear - shear stresses	73
Figure 4-20.	EP Power Law Hardening Theory: Example Response	78
Figure 4-21.	EP Power Law Hardening Verification: Uniaxial Stress - axial stress	81
Figure 4-22.	EP Power Law Hardening Verification: Uniaxial Stress - lateral strain	81
Figure 4-23.	EP Power Law Hardening Verification: Pure Shear - shear stress	83
Figure 4-24.	Ductile Fracture Verification: Uniaxial Stress	90
Figure 4-25.	Ductile Fracture Verification: Pure Shear - tearing parameter	92
Figure 4-26.	Ductile Fracture Verification: Pure Shear - shear stress	92
Figure 4-27.	Multilinear EP Theory: Example Response	97
Figure 4-28.	Multilinear EP Verification: Uniaxial Stress - axial stress	100
Figure 4-29.	Multilinear EP Verification: Uniaxial Stress - lateral strain	100
Figure 4-30.	Multilinear EP Verification: Pure Shear - shear stress	102
Figure 4-31.	Multilinear EP Failure Verification: Uniaxial Stress	108
Figure 4-32.	Multilinear EP Failure Verification: Uniaxial Stress	109
Figure 4-33.	Johnson-Cook Verification: Uniaxial Stress - $\beta = 0.0$	118
Figure 4-34.	Johnson-Cook Verification: Uniaxial Stress - $\beta \neq 0.0$	119
Figure 4-35.	Johnson-Cook Verification: Pure Shear - $\beta = 0.0$	120
Figure 4-36.	Johnson-Cook Verification: Pure Shear - $\beta \neq 0.0$	121
Figure 4-37.	J_2 Plasticity Verification: Rate-Independent Hardening	133

Figure 4-38. J_2 Plasticity Verification: Rate-Dependent Hardening Uniaxial Stress	134
Figure 4-39. J_2 Plasticity Verification: Rate-Dependent Hardening Pure Shear	135
Figure 4-40. J_2 Plasticity Verification: Flow-Stress Hardening Uniaxial Stress	136
Figure 4-41. J_2 Plasticity Verification: Flow-Stress Hardening Pure Shear	137
Figure 4-42. J_2 Plasticity Verification: Decoupled Flow-Stress Hardening Uniaxial Stress $\check{\sigma}_y(\theta)$	138
Figure 4-43. J_2 Plasticity Verification: Decoupled Flow-Stress Hardening Uniaxial Stress $\check{\sigma}_h(\theta)$	139
Figure 4-44. Hosford Plasticity Theory: Hosford yield surface with $a = 4, 8, 100$	146
Figure 4-45. Hosford Plasticity Verification: Uniaxial Stress	151
Figure 4-46. Hosford Plasticity Verification: Pure Shear	152
Figure 4-47. Hosford Plasticity Verification: Linear Hardening	154
Figure 4-48. Hosford Plasticity Verification: Power-Law Hardening	154
Figure 4-49. Hosford Plasticity Verification: Voce Hardening	155
Figure 4-50. Hosford Plasticity Verification: Johnson-Cook Hardening Uniaxial Stress	156
Figure 4-51. Hosford Plasticity Verification: Johnson-Cook Hardening Pure Shear	157
Figure 4-52. Hosford Plasticity Verification: Power-Law Breakdown Hardening Uniaxial Stress	158
Figure 4-53. Hosford Plasticity Verification: Power-Law Breakdown Hardening Pure Shear	159
Figure 4-54. Hill Plasticity Theory: Hill yield surface	164
Figure 4-55. Hill Plasticity Verification: Uniaxial Stress - normal stresses	173
Figure 4-56. Hill Plasticity Verification: Uniaxial Stress - lateral strain (loading in the 1 direction)	173
Figure 4-57. Hill Plasticity Verification: Uniaxial Stress - lateral strain (loading in the 2 direction)	174
Figure 4-58. Hill Plasticity Verification: Uniaxial Stress - lateral strain (loading in the 3 direction)	174
Figure 4-59. Hill Plasticity Verification: Pure Shear - shear stress	177
Figure 4-60. Hill Plasticity Verification: Linear Hardening	178
Figure 4-61. Hill Plasticity Verification: Power-Law Hardening	179
Figure 4-62. Hill Plasticity Verification: Voce Hardening	180
Figure 4-63. Hill Plasticity Verification: Johnson-Cook Hardening Uniaxial Stress	181
Figure 4-64. Hill Plasticity Verification: Johnson-Cook Hardening Pure Shear	182
Figure 4-65. Hill Plasticity Verification: Power-Law Breakdown Hardening Uniaxial Stress	183
Figure 4-66. Hill Plasticity Verification: Power-Law Breakdown Hardening Pure Shear	184
Figure 4-67. Barlat Plasticity Theory: Barlat yield surface	190
Figure 4-68. Barlat Plasticity Verification: Uniaxial Stress - axial stress	197
Figure 4-69. Barlat Plasticity Verification: Uniaxial Stress - lateral strain	199
Figure 4-70. Barlat Plasticity Verification: Uniaxial Stress - loading in the 2 direction	200
Figure 4-71. Barlat Plasticity Verification: Uniaxial Stress - loading in the 3 direction	200
Figure 4-72. Barlat Plasticity Verification: Pure Shear	202
Figure 4-73. Barlat Plasticity Verification: Linear Hardening	203
Figure 4-74. Barlat Plasticity Verification: Power-Law Hardening	204
Figure 4-75. Barlat Plasticity Verification: Voce Hardening	205
Figure 4-76. Barlat Plasticity Verification: Johnson-Cook Hardening Uniaxial Stress	206

Figure 4-77. Barlat Plasticity Verification: Johnson-Cook Hardening Pure Shear	207
Figure 4-78. Barlat Plasticity Verification: Power-Law Breakdown Hardening Uniaxial Stress	208
Figure 4-79. Barlat Plasticity Verification: Power-Law Breakdown Hardening Pure Shear ..	209
Figure 4-80. MPSP Verification: Uniaxial Stress	233
Figure 4-81. MPSP Verification: Balanced Biaxial	234
Figure 4-82. MPSP Verification: Biaxial Shear	235
Figure 4-83. Power Law Creep Verification: Creep	242
Figure 4-84. Power Law Creep Verification: Stress Relaxation	244
Figure 4-85. Viscoplastic Verification: Creep	252
Figure 4-86. Viscoplastic Verification: Stress Relaxation	253
Figure 4-87. Munson-Dawson Viscoplastic Theory: Equivalent stress surface	262
Figure 4-88. Munson-Dawson Viscoplastic Verification: Transient strain limit dependencies	262
Figure 4-89. Munson-Dawson Viscoplastic Verification: Steady-state strain rate dependencies	262
Figure 4-90. Munson-Dawson Viscoplastic Verification: Triaxial Compression	263
Figure 4-91. Munson-Dawson Viscoplastic Verification: Pure Shear	265
Figure 4-92. Munson-Dawson Viscoplastic Verification: Unequal Biaxial Compression ..	266
Figure 4-93. Hyperfoam Verification: Uniaxial Strain - stresses (tension)	273
Figure 4-94. Hyperfoam Verification: Uniaxial Strain - stresses (compression)	274
Figure 4-95. Hyperfoam Verification: Uniaxial Strain - stresses (comparison)	275
Figure 4-96. Hyperfoam Verification: Biaxial Strain - normal stresses (tension)	277
Figure 4-97. Hyperfoam Verification: Biaxial Strain - normal stresses (compression) ..	278
Figure 4-98. Hyperfoam Verification: Biaxial Strain - normal stresses (comparison) ..	279
Figure 4-99. Hyperfoam Verification: Pure Shear - stresses	281
Figure 4-100. Hyperfoam Verification: Simple Shear - stresses	283
Figure 4-101. Hyperelastic Damage Verification: Uniaxial Strain	289
Figure 4-102. Hyperelastic Damage Verification: Simple Shear	290
Figure 4-103. Soil and Foam Verification: Triaxial Compression - lateral strains	296
Figure 4-104. Soil and Foam Verification: Triaxial Compression - axial stress	296
Figure 4-105. Shape Memory Alloy Theory: Phase Diagram	300
Figure 4-106. Shape Memory Alloy Verification: Pseudoelasticity	306
Figure 4-107. Shape Memory Alloy Verification: Actuation	308
Figure 4-108. Low Density Foam Verification: Uniaxial Compression – skeleton	315
Figure 4-109. Low Density Foam Verification: Uniaxial Compression – foam	316
Figure 4-110. Low Density Foam Verification: Hydrostatic Compression - foam pressure ..	316
Figure 4-111. Foam Plasticity Verification: Hydrostatic Compression - pressure	322
Figure 4-112. Viscoplastic Foam Verification: Uniaxial Compression - axial stress	329
Figure 4-113. Viscoplastic Foam Verification: Hydrostatic Compression - pressure	330
Figure 4-114. Foam Damage Verification: Uniaxial Compression	342
Figure 4-115. Foam Damage Verification: Uniaxial Compression – normal strains	343
Figure 4-116. Foam Damage Verification: Uniaxial Tension - axial stress and damage	344
Figure 4-117. Foam Damage Verification: Hydrostatic Compression - pressure	345
Figure 4-118. Foam Damage Verification: Hydrostatic Tension - pressure and damage	346
Figure 4-119. Orthotropic Crush Theory: Example Crush Curve	352

Figure 4-120. Orthotropic Crush Verification: Input Crush Curves	353
Figure 4-121. Orthotropic Crush Verification: Uniaxial Stress - stresses	354
Figure 4-122. Orthotropic Rate Theory: Orientation of Material Coordinate System	357
Figure 4-123. Orthotropic Rate Verification: Input strength functions, f_{β_y}	362
Figure 4-124. Orthotropic Rate Verification: Uniaxial Strain - Isotropic Response	363
Figure 4-125. Orthotropic Rate Verification: Uniaxial Strain - Orthotropic Response	364
Figure 4-126. Universal Polymer Model Verification: Shift Factor During a Thermal Cycle ..	375
Figure 4-127. Universal Polymer Model Verification: Uniaxial Strain – two-stage load and hold	378
Figure 4-128. Wire Mesh Verification: Uniaxial Stress – compression	387
Figure 4-129. Wire Mesh Verification: Uniaxial Strain – tension	388
Figure 4-130. Wire Mesh Verification: Hydrostatic Compression	389

LIST OF TABLES

Table 4-1.	Elastic 3D Orthotropic Verification: Material and Model Parameters	42
Table 4-2.	Elastic 3D Orthotropic Verification: Coordinate System Rotations	43
Table 4-3.	Neo-Hookean Verification: Material and Model Parameters	48
Table 4-4.	Gent Verification: Material and Model Parameters	58
Table 4-5.	State Variables for ELASTIC PLASTIC Model	74
Table 4-6.	State Variables for ELASTIC PLASTIC Model for Shells	75
Table 4-7.	State Variables for EP POWER HARD Model	84
Table 4-8.	State Variables for EP POWER HARD Model for Shells	85
Table 4-9.	State Variables for DUCTILE FRACTURE Model	94
Table 4-10.	State Variables for MULTILINEAR EP Model	103
Table 4-11.	State Variables for MULTILINEAR EP Model for Shells	104
Table 4-12.	State Variables for ML EP FAIL Model	111
Table 4-13.	State Variables for ML EP FAIL Model for Shells	112
Table 4-14.	Johnson-Cook Verification: Material and Model Parameters	116
Table 4-15.	State Variables for JOHNSON COOK Model	123
Table 4-16.	J_2 Verification: Hardening Model Parameters	132
Table 4-17.	State Variables for J_2 PLASTICITY Model	143
Table 4-18.	Hosford Verification: Hardening Model Parameters	153
Table 4-19.	State Variables for HOSFORD PLASTICITY Model	161
Table 4-20.	Hill Verification: Hardening Model Parameters	178
Table 4-21.	State Variables for HILL PLASTICITY Model	186
Table 4-22.	Barlat Plasticity Verification: Material and Model Parameters	195
Table 4-23.	Barlat Verification: Hardening Model Parameters	203
Table 4-24.	State Variables for BARLAT PLASTICITY Model	212
Table 4-25.	State Variables for PLANE STRESS RATE PLASTICITY Model	221
Table 4-26.	MPSP Verification: Model Parameters	232
Table 4-27.	State Variables for MODULAR PLANE STRESS PLASTICITY Model	238
Table 4-28.	Power Law Creep Verification: Material and Model Parameters	242
Table 4-29.	State Variables for POWER LAW CREEP Model	245
Table 4-30.	Viscoplastic Verification: Material and Model Parameters	251
Table 4-31.	State Variables for VISCOPLASTIC Model	255
Table 4-32.	State Variables for MD_VISCOPLASTIC Model	268
Table 4-33.	Hyperfoam Verification: Material and Model Parameters	272
Table 4-34.	Hyperelastic Damage Verification: Material and Model Parameters	288
Table 4-35.	State Variables for HYPERELASTIC DAMAGE Model	291
Table 4-36.	State Variables for SOIL FOAM Model	297
Table 4-37.	Shape Memory Alloy Verification: Material and Model Parameters	305

Table 4-38. State Variables for SHAPE MEMORY ALLOY Model	310
Table 4-39. Low Density Foam Verification: Material and Model Parameters	314
Table 4-40. State Variables for LOW DENSITY FOAM Model	317
Table 4-41. Foam Plasticity Verification: Material and Model Parameters	321
Table 4-42. State Variables for FOAM PLASTICITY Model	323
Table 4-43. Viscoplastic Foam Verification: Material and Model Parameters	329
Table 4-44. State Variables for VISCOPLASTIC FOAM Model	332
Table 4-45. Foam Damage Verification: Material and Model Parameters	340
Table 4-46. State Variables for FOAM DAMAGE Model	348
Table 4-47. Orthotropic Crush Verification: Material and Model Parameters	353
Table 4-48. State Variables for ORTHOTROPIC CRUSH Model	355
Table 4-49. Orthotropic Crush Verification: Material and Model Parameters	362
Table 4-50. State Variables for ORTHOTROPIC RATE Model	366
Table 4-51. Universal Polymer Model Verification: Material and Model Parameters	374
Table 4-52. State Variables for Universal Polymer Model	382
Table 4-53. Wire Mesh Verification: Material and Model Parameters	386
Table 4-54. State Variables for WIRE MESH Model	390

1. OVERVIEW

Constitutive modeling is a fundamental aspect of solid mechanics modeling and simulation. The wide range of behaviors of solid materials requires a vast number of models capable of modeling all (or even some of) the different responses. This is in contrast to fluid mechanics, for example. As such, constitutive modeling is arguably *the* major problem in solid mechanics. A constitutive model is necessary for accurately predicting the state of a material. This determination includes both the stress state whose resolution is essential for many phenomena of interest like fracture and failure as well as capturing inelastic responses like damage or multiphysics couplings.

One aspect of obtaining an accurate resolution of the stress field is, in one sense, easy to understand. It is mesh discretization. More degrees of freedom in a simulation enables better resolution and results in a more accurate stress field if we look just at the mathematics. If all materials followed an elastic law, then mesh resolution on its own would be all that is needed to resolve the stress field. In reality, however, materials do not exhibit elastic responses except in very limited cases.

This leads us to a second aspect of calculating accurate stress fields, which is much harder to understand. This one concerns the physics. The specific behavior of a material depends on the physical processes specific to that material, and this must be included in a constitutive model in some form or another. The main goal of the Library of Advanced Materials for Engineering - LAMÉ - is to provide a simple means to implement the wide variety of models in a library that can be used by our solid mechanics application codes.

2. STRATEGY

As a third party library, the Library of Advanced Materials for Engineering (LAMÉ) is renewing a commitment to accurate, robust, and efficient constitutive modeling for solid mechanics. There are three distinct groups that require services from LAMÉ: constitutive model developers, application code developers, and analysts. Each group has different, but related, requirements on LAMÉ.

Constitutive modelers who develop the mathematical models describing the response of interest and the associated numerical methodologies require a framework for developing and implementing these models. This framework must be well documented so that these developers can easily develop and implement a model that can, when the model is sufficiently robust, be used reliably in production calculations.

Application code developers, on the other hand, require that the library of constitutive models share a common, simple interface. This requires that the conceptual division between a constitutive model and the application code be well understood. The application codes also require verified behavior of the models along with certain performance requirements as these models can be called billions of times in an analysis.

Analysts require constitutive models that are both verified and well documented. The responses of interest can very greatly depending on the material utilized and the conditions under which it is loaded. This accounts for the wide range and sheer volume of constitutive models in the literature. Furthermore, there may be nothing that affects the results of an analysis more than the constitutive model. Therefore, the analyst needs a thorough knowledge of the behavior of the models along with how to use it in an application code. Such an understanding is also essential for the accurate determination and calibration of different material and model parameters. In some cases, even subtle changes in a material specimen's history can lead to large variation in properties and responses. As such, a clear description and understanding of this input data is essential for appropriate utilization of different models.

Due to the varied requirements on LAMÉ, a strategy for supporting these various user groups has been developed. This strategy is described here.

2.1. CODE DEVELOPMENT

There are many strategies that can be employed for a code development process. The choice of such a procedure depends on what the overall project is creating. And even after a development process has been selected, it is often tailored to the needs of the specific code project.

The LAMÉ code development team has spent some time deciding on an appropriate process that reflects the needs of the project and its stakeholders.

Given that LAMÉ has two roles, as an interface to a host code that will supply a material model response and as a repository for constitutive models, this led us to consider two different code development processes: one for the interface and one for the constitutive models.

For the interface an *iterative* process was chosen. The iterative process allows us to plan and generate requirements, perform analysis and design, implement and deploy code changes and finally test and evaluate the code. This process can work well for the interface design where we implement the conceptual changes that we want to the interface. The models beneath the interface should be unaffected by these changes, and where they are affected it will be on the surface.

For the constitutive models a *waterfall* process was chosen. Generally the process of developing and implementing a constitutive model is a linear process that is followed by a single person. That person generates requirements, designs the solution, implements the solution as a piece of code, verifies the code and maintains the code. Much of the constitutive modeler's work involves formulating the model, which is a solid mechanics and applied mathematics problem first and foremost. This can be seen as either the gathering requirements phase or part of the design phase. The design and implementation phases are where the code development occur. All models are verified after they are implemented. However, model verification itself is quite complicated, so this step is not simple. Finally the model is maintained through documentation and user support. Bug fixes are also an aspect of code maintenance in this process.

2.2. MODEL IMPLEMENTATION

The key feature in LAMÉ that allows constitutive models to be implemented easily and application codes to be able to use those models is the interface. *The key concept to understand concerning the interface is that it defines what roles the constitutive models have, what roles the application codes have, and how the models and the codes transfer information.*

From the application code perspective we would like all of the constitutive models to look the same. Of course this is not the case. This is why, if we were to look at our legacy finite element codes, we see information regarding specific constitutive models show up in the application codes. Even a piece of information as simple as a material model ID will show up in the application code in order that the code call the correct model. Modern programming languages/styles allow us to avoid this confusion.

From a constitutive modeling perspective we would like a simple interface for implementing constitutive models. Constitutive modelers are only part-time code developers. They can have strengths in many areas in addition to code development, including physics, chemistry, continuum mechanics, applied mathematics, numerical methods and experimental mechanics. Having a code development environment that is useful for a constitutive model developer is necessary in the design of the constitutive model library.

2.2.1. Code Standards

The need to supply not only robust constitutive models, but also a robust constitutive modeling environment, requires strict adherence to code standards. Some code standards are stylistic. These are necessary to support the code (promoting readability) and to simplify the effort needed by the constitutive modeler to implement a model. Other code standards are necessary to support the code on various platforms and to prevent unintended behavior like memory leaks.

2.2.2. Testing Standards

Ensuring robust and reliable constitutive models also requires testing. There are two main concerns in providing constitutive modeling to an application code: accuracy and speed. Both of these concerns can be addressed to a large degree through testing. Toward this end two testing systems are developed: a verification test suite and a performance test suite.

2.2.2.1. Verification Testing

Constitutive models for the large deformation of materials can be extremely complex. This complexity is added to by the issues associated with implementing the model in the code. There are two questions associated with assessing this complexity. First, what is the expected result of the model, independent of its implementation? Second, does the implementation model that response?

2.2.2.2. *Performance Testing*

In a nonlinear solid mechanics analysis, the constitutive models are called often. For an explicit transient dynamics problem, the model is called once for each time step for each integration point in the finite element model. On the other hand, implicit quasi-static analyses call the model every iteration of every time step for each integration point in the finite element model.

Given the amount of time that a nonlinear solid mechanics finite element analysis spends calculating the stresses in a constitutive model, the performance of the constitutive model can have a large effect on the performance of the host code.

In order to ensure some measure of performance, a procedure for testing the performance of the models is proposed. First, a baseline set of performance data must be generated. Given that the CPU time used by the model can depend on many things, including the current loads on the machine where the test is being run, developing an approach for modeling the performance is not straightforward. If we call the various states of the machine "configurations", then the best approach appears to be to generate a large set of data for the performance of the constitutive model that reflects the performance on a single machine over a large variety of its configurations.

Specifically, since we want to test only the speed of the constitutive model, we run tests that are fully prescribed strain paths. This eliminates any need for the material driver to solve an equilibrium state. We also want to test as many of the features of the constitutive model as possible. This requires a prescribed strain path that pushes the model into regimes of interest. For example, for an elastic-plastic model the performance test has to trigger plasticity, otherwise it will not reflect accurately on how the model performs in an analysis. We also want the strain path to push the plasticity model deep enough into the plastic range.

Determination of an appropriate strain path is not clear cut for all materials. Recognizing this, the performance tests should be documented clearly so that we know exactly what we are testing and we can go back and modify a test if there is some feature of the model that doesn't appear in the performance test.

2.2.3. *Documentation Standards*

In order to disseminate information about the models in LAMÉ, there must be a commitment to documentation. The theory behind the models and their implementation must be documented. Furthermore, much of the success of the verification and performance testing depends on documentation too. Finally, documentation must be generated for analysts that allows them to understand what materials and behavior the model can represent, along with the inputs necessary to use the model and the outputs that come from the model.

3. INTERFACE

LAMÉ is designed to have a simple interface that allows the easy implementation of a wide range of constitutive models. This interface is between the application code (sometimes referred to as the “host code”) and the constitutive model.

The interface has two main aspects: the data that is passed between the application code and the model, and the functions that pass this data. Given that the interface consists of data and functions, the most reasonable way to set up this interface is through a class.

The class that defines this interface is the **Material** class, which is declared in `include/interface/Material.h`.

There are two types of data that are passed between the application code and the model. The first is the material property information. This is done using an object in the **MatProps** class. This is used when constructing a material model at the beginning of an analysis.

The second type of data that is passed between the application code and the material model is the data that the material model uses during an analysis. This data is in the **MatParams** struct. This data consists of the stress, the kinematics, the time and time step, etc.

More detail can be found in [\[1\]](#).

REFERENCES

- [1] W.M. Scherzinger and D.C. Hammerand. Library of advanced materials for engineering (LAMÉ). Technical Report SAND2007-5515, Sandia National Laboratories, Albuquerque, NM, August 2007. [pdf](#).

4. MATERIAL MODELS

This section details the constitutive models that are implemented and supported in LAMÉ. The description of each model has four sections. First, a section discussing the *theory* of the model is found. This is the mathematical description of the model in a continuum mechanics framework, independent of its implementation in a computational code. As these models are intended for solid mechanics analysis, the following section describes the *numerical implementation* of the model. This delves into how the model is implemented in the code and any special numerical techniques that are used to integrate the model. The subsequent section presents the *verification* problems that are run for the model. Through the results of such problems, evidence is provided that, to the best of our understanding, the model is behaving as expected. Finally, documentation of the model *user inputs* and *user outputs* are given for analyst reference.

It is our belief that this collection of documentation is important for the use of our constitutive models, and it provides confidence that our models are implemented correctly for the capabilities that are tested.

What this documentation does not provide is guidance on how to use the models. Different materials behave differently, and it is the responsibility of the user to ensure that the material model chosen can accurately model the behavior of a particular material. Furthermore, even with a single material, many models might be capable of modeling the material depending on the loading in a given analysis. It is the responsibility of the analyst to ensure that the model they choose is the best model for their problem. Across the different models, parameters may also vary in value or have slight changes in interpretation. Care needs to be undertaken to ensure that material and model parameters used accurately reflect the specific material being investigated (some parameters may vary with simple changes in processing route) and capture the behaviors that of interest. If emphasis needs to be placed on initial yield rather than failure, subtle differences in some parameters may be expected.

4.1. HYPOELASTIC MODELS

Many models presented in this report are derived starting with small deformation formulations. These models are implemented in finite deformation codes by substituting the rate of deformation for the strain rate¹, and making the stress rate objective. There are many objective stress rates to choose from, the two most common being the Jaumann and the Green-McInnis.

Models that are implemented using the Jaumann or Green-McInnis stress rate are done so in an unrotated configuration. This means that the incremental constitutive relations are written in this

¹It should be noted that the rate of deformation is *not* the rate of any strain measure.

configuration. The tensor components of the Cauchy stress, σ_{ij} , and the rate of deformation, D_{ij} , are unrotated using some orthogonal tensor, $Q_{ij}^{-1} = Q_{ji}$, such that

$$T_{ij} = Q_{ki}\sigma_{kl}Q_{lj} \quad ; \quad d_{ij} = Q_{ki}D_{kl}Q_{lj} \quad (4.1.1)$$

where T_{ij} and d_{ij} are the components of the unrotated stress and rate of deformation respectively. The choice of orthogonal tensor, Q_{ij} , depends on the objective stress rate. The incremental constitutive relation is then written as

$$T_{ij}^{n+1} = T_{ij}^n + f_{ij}(d_{kl}, \Delta t) \quad (4.1.2)$$

After the stress is updated in the unrotated configuration, it is rotated forward to the current configuration [1].²

If the Green-McInnis stress rate is used, then the unrotated configuration is found using the rotation tensor from the polar decomposition of the deformation gradient

$$dx_i^{n+1} = F_{ij}dX_j \quad ; \quad F_{ij} = R_{ik}U_{kj} = V_{ik}R_{kj} \quad ; \quad Q_{ij} = R_{ij} \quad (4.1.3)$$

If the Jaumann stress rate is used, then the unrotated configuration is found using the rotation tensor from the polar decomposition of the incremental deformation gradient

$$dx_i^{n+1} = \hat{F}_{ij}dx_j^n \quad ; \quad \hat{F}_{ij} = \hat{R}_{ik}\hat{U}_{kj} = \hat{V}_{ik}\hat{R}_{kj} \quad ; \quad Q_{ij} = \hat{R}_{ij} \quad (4.1.4)$$

Without loss of generality we will assume the Green-McInnis stress rate. The algorithm for the Jaumann stress rate can be recovered by substituting \hat{F}_{ij} for F_{ij} and \hat{R}_{ij} for R_{ij} in what follows.

Before updating the stress, the rotation is calculated from the deformation gradient in the *current* configuration, F_{ij} . The unrotated rate of deformation is then

$$d_{ij} = R_{ki}^{n+1}D_{kl}R_{lj}^{n+1} \quad (4.1.5)$$

and the unrotated stress is updated using (4.1.2). Then the stress is rotated to the current configuration, using the same rotation that we used to unrotate the rate of deformation

$$\sigma_{ij}^{n+1} = R_{ik}^{n+1}T_{kl}^{n+1}R_{lj}^{n+1} \quad (4.1.6)$$

The unrotated stress from the previous time step is simply $T_{ij}^n = R_{ki}^n\sigma_{kl}R_{lj}^n$. Furthermore, for the elastic model (Section 4.3) the stress update algorithm can be reduced to

²The terminology used in describing the unrotated configuration with the rotations backward and forward is infinitely confusing. It is simply one of the many difficulties encountered using finite deformation hypoelastic models.

$$\sigma_{ij}^{n+1} = R_{ik}^{n+1} R_{mk}^n \sigma_{mn} R_{nl}^n R_{jl}^{n+1} + \lambda \delta_{ij} \Delta t D_{kk} + 2\mu \Delta t D_{ij} \quad (4.1.7)$$

One final note about this algorithm. While it is convenient to use the rotation tensor R_{ij}^{n+1} , strictly this is not correct. Since the rate of deformation is most often computed at the mid-step configuration, the rotation used to unrotate the rate of deformation should be the rotation from the mid-step deformation gradient, i.e. the deformation gradient that relates the mid-step configuration to the reference configuration. Other consistency considerations should also be considered, but we will not discuss them here. Suffice it to say that the solutions all converge in the limit of infinitesimal time steps. In a future release of LAMÉ other options might be added.

4.2. HYPERELASTIC MODELS

Hyperelastic materials are in many ways easier to understand than hypoelastic materials, and are often considered more thermodynamically consistent. On the other hand, it may be difficult to consistently extend a small deformation model to the finite deformation regime in a hyperelastic framework. Regardless of the pluses and minuses of the two formulations, hyperelastic models are in LAMÉ and will be reviewed here.

Hyperelastic models generally assume a scalar valued strain energy density that is a function of invariants of the deformation through the deformation gradient, F_{ij} . Using the principle of material frame indifference, the strain energy density is written as a function of the symmetric right Cauchy-Green tensor, $C_{ij} = F_{ki}F_{kj}$

$$W = W(C_{ij}) \quad (4.2.1)$$

The stress, in particular the second Piola-Kirchhoff stress, is found by taking the derivative of W with respect to C_{ij} . This relation comes from the stress-power relations. From the second Piola-Kirchhoff stress, we can find the Cauchy stress

$$S_{ij} = 2 \frac{\partial W}{\partial C_{ij}} \quad ; \quad \sigma_{ij} = \frac{1}{J} F_{ik} S_{kl} F_{jl} \quad (4.2.2)$$

Hyperelastic models are generally of two types. The most common are written in terms of the three invariants of C_{ij} : I_1 , I_2 , and I_3

$$I_1 = \text{tr}\mathbf{C} = C_{ii} \quad ; \quad I_2 = \frac{1}{2} (C_{ii}C_{jj} - C_{ij}C_{ij}) \quad ; \quad I_3 = \det\mathbf{C} \quad (4.2.3)$$

The second Piola-Kirchhoff stress is then

$$S_{ij} = 2 \left(\frac{\partial W}{\partial I_1} \frac{\partial I_1}{\partial C_{ij}} + \frac{\partial W}{\partial I_2} \frac{\partial I_2}{\partial C_{ij}} + \frac{\partial W}{\partial I_3} \frac{\partial I_3}{\partial C_{ij}} \right) \quad (4.2.4)$$

Evaluating this expression requires the derivatives of the invariants with respect to the components C_{ij}

$$\frac{\partial I_1}{\partial C_{ij}} = \delta_{ij} \quad ; \quad \frac{\partial I_2}{\partial C_{ij}} = I_1 \delta_{ij} - C_{ij} \quad ; \quad \frac{\partial I_3}{\partial C_{ij}} = I_3 C_{ij}^{-1} \quad (4.2.5)$$

Using this in the expression for the second Piola-Kirchhoff stress, and converting it to the Cauchy stress, we have

$$\sigma_{ij} = \frac{2}{J} \left\{ \frac{\partial W}{\partial I_3} \delta_{ij} + \left(\frac{\partial W}{\partial I_1} + I_1 \frac{\partial W}{\partial I_2} \right) B_{ij} - \frac{\partial W}{\partial I_2} B_{ij}^2 \right\} \quad (4.2.6)$$

The majority of hyperelastic models calculate the stress in this manner.

Some hyperelastic models, however, have their strain energy densities written in terms of the principal stretches [2]. When this is the case the calculation of the stress is more complex. The right stretch can be written as

$$\mathbf{U} = \sum_{i=1}^3 \lambda_i \bar{\mathbf{e}}_i \otimes \bar{\mathbf{e}}_i \quad (4.2.7)$$

where λ_i are the principal stretches, or eigenvalues, and $\bar{\mathbf{e}}_i$ are the principal directions, or eigenvectors. The strain energy density is $W(\lambda_i)$. We calculate the stress components of the second Piola-Kirchhoff stress, \bar{S}_{ij} , with respect to the principal directions

$$\mathbf{S} = \bar{S}_{ij} \bar{\mathbf{e}}_i \otimes \bar{\mathbf{e}}_j \quad (4.2.8)$$

This is done by calculating $\partial W / \partial \mathbf{C}$ in the following manner

$$\delta W = \frac{\partial W}{\partial \lambda_i} \delta \lambda_i = \frac{\partial W}{\partial \mathbf{C}} : \delta \mathbf{C} \quad (4.2.9)$$

Writing the right Cauchy-Green tensor with respect to the principal directions we have

$$\mathbf{C} = \sum_{i=1}^3 \lambda_i^2 \bar{\mathbf{e}}_i \otimes \bar{\mathbf{e}}_i \quad ; \quad \delta \mathbf{C} = \sum_{i=1}^3 2\lambda_i \delta \lambda_i \bar{\mathbf{e}}_i \otimes \bar{\mathbf{e}}_i + \lambda_i^2 \delta \bar{\omega}_{ij} (\bar{\mathbf{e}}_i \otimes \bar{\mathbf{e}}_j + \bar{\mathbf{e}}_j \otimes \bar{\mathbf{e}}_i) \quad (4.2.10)$$

Equating terms on both sides of (4.2.9) we get

$$\bar{S}_{11} = \frac{1}{\lambda_1} \frac{\partial W}{\partial \lambda_1} \quad ; \quad \bar{S}_{22} = \frac{1}{\lambda_2} \frac{\partial W}{\partial \lambda_2} \quad ; \quad \bar{S}_{33} = \frac{1}{\lambda_3} \frac{\partial W}{\partial \lambda_3} \quad ; \quad \bar{S}_{ij} = 0 \quad \text{otherwise} \quad (4.2.11)$$

These calculations can also be checked by writing the invariants in terms of the principal stretches. For a hyperelastic model written in terms of the invariants the results should be the same.

The differences between hypoelastic and hyperelastic models should not matter for the analyst. For the constitutive modeler, however, the benefits and drawbacks of the two formulations must be considered.

REFERENCES

- [1] D.P. Flanagan and L. M. Taylor. An accurate numerical algorithm for stress integration with finite rotations. *Computer Methods in Applied Mechanics and Engineering*, 62:305–320, 1987.
- [2] R. W. Ogden. *Non-Linear Elastic Deformaitons*. Dover, New York, 1984.

4.3. ELASTIC MODEL

4.3.1. Theory

The elastic model is a hypoelastic extension of isotropic, small-strain, linear elasticity [1] [2] [3]. The stress-strain response for an isotropic, elastic material is

$$\sigma_{ij} = \lambda \delta_{ij} \varepsilon_{kk} + 2\mu \varepsilon_{ij} \quad (4.3.1)$$

where the Lamé constants, λ and μ , are given by

$$\lambda = \frac{E\nu}{(1+\nu)(1-2\nu)} \quad ; \quad \mu = \frac{E}{2(1+\nu)} \quad (4.3.2)$$

This model is extended to a finite-deformation, hypoelastic model by first making it a rate equation. Then the stress rate is replaced with an objective stress rate and the strain rate is replaced with the rate of deformation. This gives us

$$\overset{\circ}{\sigma}_{ij} = \lambda \delta_{ij} D_{kk} + 2\mu D_{ij} \quad (4.3.3)$$

The stress rate is arbitrary, as long as it is objective. Two objective stress rates are commonly used: the Jaumann rate and the Green-McInnis rate. For problems with fixed principal axes of deformation, these two rates give the same answers. For problems where the principal axes of deformation rotate during the deformation, the two rates can give different answers. Generally speaking there is no reason to pick one objective rate over another. Sierra/SM uses the Green-McInnis rate.

The fourth-order elastic moduli are used in many constitutive models. There are many equivalent representations for the elastic moduli. In index notation we present the following three representations

$$\begin{aligned} \overset{\circ}{\sigma}_{ij} &= \mathbb{C}_{ijkl} D_{kl} \\ \mathbb{C}_{ijkl} &= \frac{E}{1+\nu} \left[\frac{\nu}{1-2\nu} \delta_{ij} \delta_{kl} + \frac{1}{2} (\delta_{ik} \delta_{jl} + \delta_{il} \delta_{jk}) \right] \end{aligned} \quad (4.3.4)$$

$$\mathbb{C}_{ijkl} = \lambda \delta_{ij} \delta_{kl} + \mu (\delta_{ik} \delta_{jl} + \delta_{il} \delta_{jk}) \quad (4.3.5)$$

$$\mathbb{C}_{ijkl} = K \delta_{ij} \delta_{kl} + \mu \left(\delta_{ik} \delta_{jl} + \delta_{il} \delta_{jk} - \frac{2}{3} \delta_{ij} \delta_{kl} \right) \quad (4.3.6)$$

where K is the elastic bulk modulus and is given by

$$K = \frac{E}{3(1-2\nu)} \quad (4.3.7)$$

4.3.2. Implementation

The elastic model is a hypoelastic model and is implemented using an unrotated configuration in order to preserve objectivity. Given an unrotated rate of deformation, d_{ij} , and the unrotated stress at time t_n , T_{ij}^n , the unrotated stress is updated by integrating the constant unrotated rate of deformation

$$T_{ij}^{n+1} = T_{ij}^n + \lambda \delta_{ij} \Delta t d_{kk} + 2\mu \Delta t d_{ij} \quad (4.3.8)$$

4.3.3. Verification

Three verification problems are run for the elastic model: uniaxial stress, pure shear, and biaxial stress. The results of these test problems serve as verification for the elastic model.

4.3.3.1. Uniaxial Stress

The elastic model was verified in uniaxial stress. The problem was run with a Young's modulus of 200 GPa and a Poisson's ratio of 0.3. The axial stress is simply

$$\sigma_{11} = E \varepsilon_{11} \quad (4.3.9)$$

The axial stress is shown in Figure 4-1. The axial stress is linear with the axial strain and has a slope of $E = 200 \times 10^3$ MPa.

The lateral strains for uniaxial stress are

$$\varepsilon_{22} = \varepsilon_{33} = -\nu \varepsilon_{11} \quad (4.3.10)$$

The lateral strains are shown in Figure 4-2.

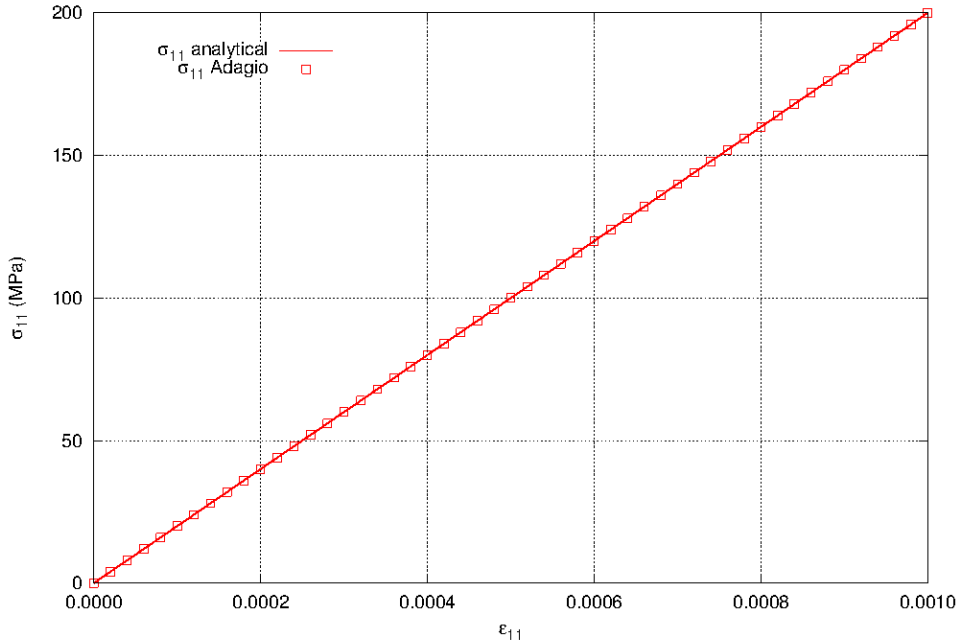


Figure 4-1. The axial stress component σ_{11} in uniaxial stress using the elastic model.

4.3.3.2. Biaxial Stress

The elastic model is verified in biaxial stress. Biaxial stress is a plane stress state where $\sigma_{11} = \sigma_1$, $\sigma_{22} = \sigma_2$, and all other stress components are zero. The problem is displacement controlled in the x_1 and x_2 directions. If the applied strains are $\varepsilon_{11} = \varepsilon$ and $\varepsilon_{22} = \alpha\varepsilon$ where $\alpha \in [0, 1]$, then the applied displacements are

$$\begin{aligned} u_1 &= \lambda_1 - 1 \quad ; \quad \lambda_1 = \exp(\varepsilon) \\ u_2 &= \lambda_2 - 1 \quad ; \quad \lambda_2 = \exp(\alpha\varepsilon). \end{aligned} \tag{4.3.11}$$

In the following results, α will be taken to be 0.45. For the plane stress state, we have $\sigma_{33} = 0$, which allows us to solve for ε_{33}

$$\varepsilon_{33} = -\frac{\nu}{1-\nu}(1+\alpha)\varepsilon. \tag{4.3.12}$$

The component ε_{33} is shown in Figure 4-3. The in-plane stress components are

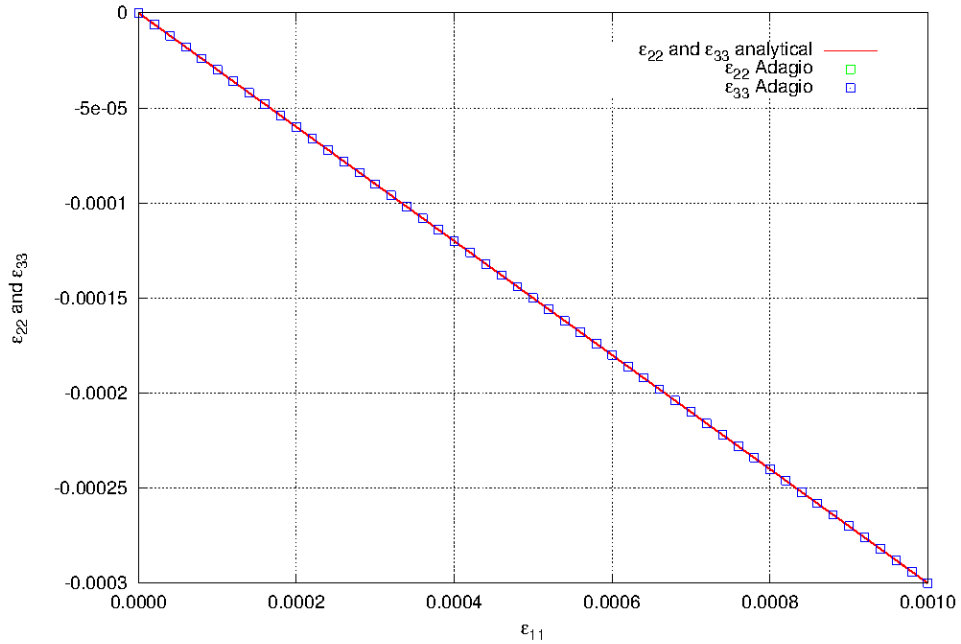


Figure 4-2. The lateral strain components ε_{22} and ε_{33} in uniaxial stress using the elastic model.

$$\sigma_{11} = \frac{E}{1-\nu^2} (1 + \alpha\nu) \varepsilon \quad (4.3.13)$$

$$\sigma_{22} = \frac{E}{1-\nu^2} (\alpha + \nu) \varepsilon.$$

The in-plane stress components are shown in Figure 4-4.

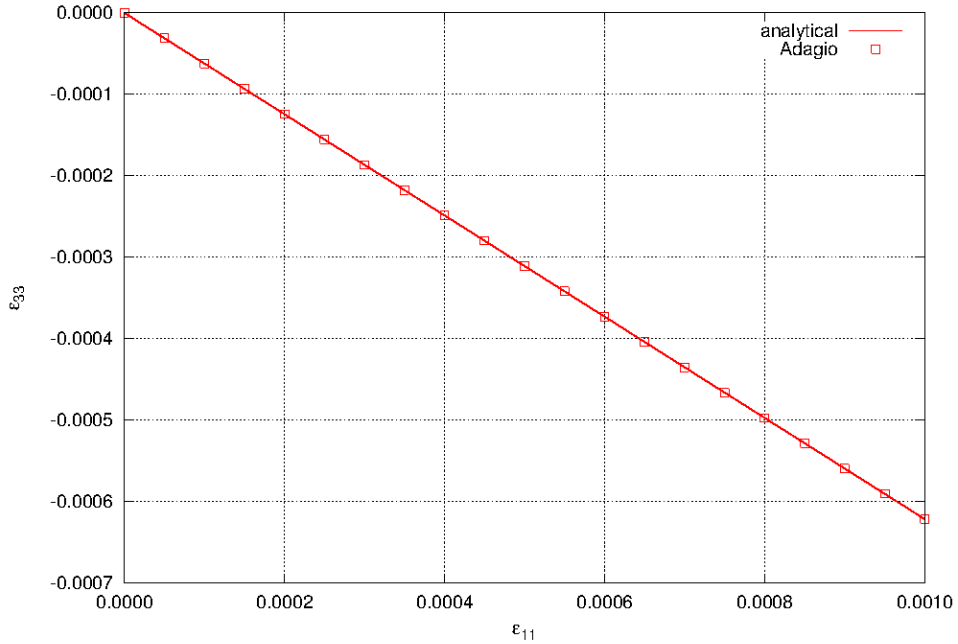


Figure 4-3. The strain component ϵ_{33} in biaxial stress using the elastic model.

4.3.3.3. Pure Shear

The elastic model is verified in pure shear. Pure shear gives a stress state where σ_{12} is the only non-zero stress component. The problem is completely displacement controlled and the applied shear strain is $\epsilon_{12} = \epsilon(t)$.

The shear stress in the problem is

$$\sigma_{12} = 2\mu\epsilon \quad (4.3.14)$$

The shear stress-strain response is shown in Figure 4-5.

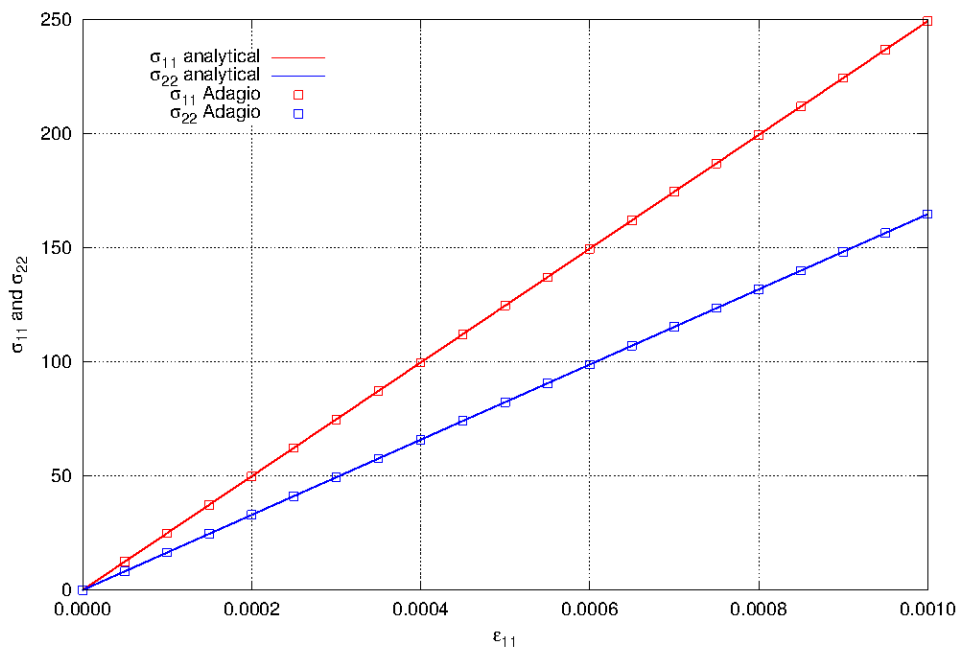


Figure 4-4. The normal stress components σ_{11} and σ_{22} in biaxial stress using the elastic model.

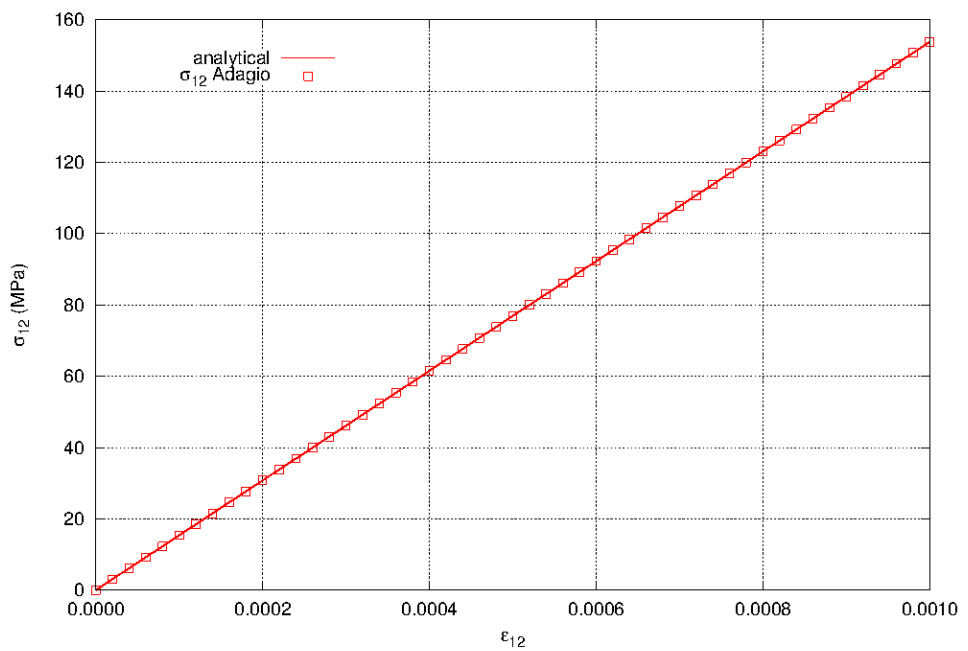


Figure 4-5. The shear stress component σ_{12} in pure shear using the elastic model.

4.3.4. User Guide

```
BEGIN PARAMETERS FOR MODEL ELASTIC
#
# Elastic constants
#
YOUNGS MODULUS = <real> E
POISONS RATIO = <real> ν
SHEAR MODULUS = <real> G
BULK MODULUS = <real> K
LAMBDA = <real> λ
TWO MU = <real> 2μ
END [PARAMETERS FOR MODEL ELASTIC]
```

There are no output variables available for the elastic model. For information about the elastic model, consult [\[4\]](#).

REFERENCES

- [1] A. E. H. Love. *A Treatise on the Mathematical Theory of Elasticity*. Dover, 4th edition, 1944.
- [2] I. S. Sokolnikoff. *Mathematical Theory of Elasticity*. Krieger Publishing Company, 1956.
- [3] S. Timoshenko and J.N. Goodier. *Theory of Elasticity*. McGraw Hill Book Company, 3rd edition, 1970.
- [4] C.M. Stone. SANTOS – a two-dimensional finite element program for the quasistatic, large deformation, inelastic response of solids. Technical Report SAND90-0543, Sandia National Laboratories, Albuquerque, NM, 1996. [pdf](#).

4.4. ELASTIC THREE DIMENSIONAL ORTHOTROPIC MODEL

4.4.1. Theory

The ELASTIC 3D ORTHOTROPIC model is an extension of the previously discussed ELASTIC routine and describes the linear elastic response of a material which exhibits orthotropic symmetry, where the orientation of the principal material directions can be arbitrary with respect to the global Cartesian axes as specified by the user.

First, a rectangular, cylindrical, or spherical reference coordinate system is defined. The material coordinate system can then be defined through two successive rotations about axes in the reference coordinate system. These principal axes are denoted as A, B, and C in the following. Thermal strains are also defined with respect to these principal material axes.

The elastic stiffness for an orthotropic material can be described in terms of the elastic compliance which relates the strain to the stress, $\varepsilon_{ij} = \mathbb{S}_{ijkl}\sigma_{kl}$. For a material with an orthogonal ABC coordinate system, and written in that reference frame, the elastic compliance tensor is given by

$$[\tilde{\mathbb{S}}] = \begin{bmatrix} \frac{1}{E_{AA}} & -\frac{\nu_{BA}}{E_{BB}} & -\frac{\nu_{CA}}{E_{CC}} & 0 & 0 & 0 \\ -\frac{\nu_{AB}}{E_{AA}} & \frac{1}{E_{BB}} & -\frac{\nu_{CB}}{E_{CC}} & 0 & 0 & 0 \\ -\frac{\nu_{AC}}{E_{AA}} & -\frac{\nu_{BC}}{E_{BB}} & \frac{1}{E_{CC}} & 0 & 0 & 0 \\ 0 & 0 & 0 & \frac{1}{2G_{AB}} & 0 & 0 \\ 0 & 0 & 0 & 0 & \frac{1}{2G_{BC}} & 0 \\ 0 & 0 & 0 & 0 & 0 & \frac{1}{2G_{CA}} \end{bmatrix}, \quad (4.4.1)$$

where the “~” is used to denote a variable in the ABC material system.

From the definition (4.4.1), it can be seen that requiring symmetry leads to relations of the form,

$$\nu_{BA} = \nu_{AB} \frac{E_{BB}}{E_{AA}} ; \quad \nu_{CB} = \nu_{BC} \frac{E_{CC}}{E_{BB}} ; \quad \nu_{AC} = \nu_{CA} \frac{E_{AA}}{E_{CC}}. \quad (4.4.2)$$

Therefore, only 9 independent constants are needed to fully define the model behavior.

The orthotropic model is also formulated in a hypoelastic fashion, leading to a constitutive equation (in the ABC material frame) of,

$$\overset{\circ}{\tilde{\sigma}}_{ij} = \tilde{\mathbb{C}}_{ijkl} (\tilde{D}_{kl} - \tilde{D}_{kl}^{th}), \quad (4.4.3)$$

where \tilde{D}_{ij}^{th} is the thermal strain rate.

The elastic stiffness tensor, $\tilde{\mathbb{C}}_{ijkl}$, is the inverse of the compliance, $\tilde{\mathbb{C}}_{ijkl} = \tilde{\mathbb{S}}_{ijkl}^{-1}$, and as such may be determined to be,

$$[\tilde{\mathbb{C}}] = \begin{bmatrix} \mathbb{C}_{AAAA} & \mathbb{C}_{AABB} & \mathbb{C}_{CCAA} & 0 & 0 & 0 \\ \mathbb{C}_{AABB} & \mathbb{C}_{BBBB} & \mathbb{C}_{BBCC} & 0 & 0 & 0 \\ \mathbb{C}_{CCAA} & \mathbb{C}_{BBCC} & \mathbb{C}_{CCCC} & 0 & 0 & 0 \\ 0 & 0 & 0 & 2G_{AB} & 0 & 0 \\ 0 & 0 & 0 & 0 & 2G_{BC} & 0 \\ 0 & 0 & 0 & 0 & 0 & 2G_{CA} \end{bmatrix}. \quad (4.4.4)$$

where

$$\begin{aligned} \mathbb{C}_{AAAA} &= \frac{1 - \nu_{BC}\nu_{CB}}{\Delta} E_{AA} & \mathbb{C}_{BBBB} &= \frac{1 - \nu_{CA}\nu_{AC}}{\Delta} E_{BB} & \mathbb{C}_{CCCC} &= \frac{1 - \nu_{AB}\nu_{BA}}{\Delta} E_{CC} \\ \mathbb{C}_{AABB} &= \frac{\nu_{BA} + \nu_{CA}\nu_{BC}}{\Delta} E_{AA} & \mathbb{C}_{BBCC} &= \frac{\nu_{CB} + \nu_{AB}\nu_{CA}}{\Delta} E_{BB} & \mathbb{C}_{CCAA} &= \frac{\nu_{AC} + \nu_{BC}\nu_{AB}}{\Delta} E_{CC} \end{aligned} \quad (4.4.5)$$

and $\Delta = 1 - \nu_{AB}\nu_{BA} - \nu_{BC}\nu_{CB} - \nu_{CA}\nu_{RT} - 2\nu_{AB}\nu_{BC}\nu_{CA}$.

See [1] for more information about the elastic three-dimensional orthotropic model.

4.4.2. Implementation

Given the similarities in formulation, the 3D orthotropic and elastic models are integrated in a similar fashion. Section 4.3.2 discussed many of these issues in detail for the isotropic elastic formulation. As such, in this section, special attention is paid to the treatment of the complexity associated with the orthotropic model – namely, the multiple coordinate systems.

To implement the elastic 3D orthotropic model, two coordinate systems need to be considered – the local *ABC* material and global *XYZ* coordinate systems. The former is used in defining the material response and the latter refers to the larger boundary value problem being analyzed. To

map between these configurations, a user-defined coordinate system is specified that can be rotated twice about one of its current axes to give the final, desired directions. A corresponding rotation tensor, \tilde{Q}_{ij} , may also be constructed in this way and used to transform various variables. Noting that the elastic stiffness tensor is constant throughout loading enables the transformation

$$\mathbb{C}_{ijkl} = \tilde{Q}_{ai}\tilde{Q}_{bj}\tilde{Q}_{ck}\tilde{Q}_{dl}\tilde{\mathbb{C}}_{abcd} \quad (4.4.6)$$

to be performed during initialization. The “~” is used with the rotation tensor Q_{ij} to emphasize that it does not map between the unrotated and rotated configurations (as defined in (4.1.1)) and is instead associated with transforming between the *ABC* and *XYZ* frames.

In the material coordinate system, the thermal strain tensor may be written as,

$$\tilde{\varepsilon}_{ij}^{th} = \varepsilon_{aa}^{th}(\theta)\delta_{ia}\delta_{ja} + \varepsilon_{bb}^{th}(\theta)\delta_{ib}\delta_{jb} + \varepsilon_{cc}^{th}(\theta)\delta_{ic}\delta_{jc}, \quad (4.4.7)$$

where $\varepsilon_{aa}^{th}(\theta)$, $\varepsilon_{bb}^{th}(\theta)$, and $\varepsilon_{cc}^{th}(\theta)$ are the temperature (θ) dependent thermal strain functions in the *A*, *B*, and *C* principal material directions, respectively, and δ_{ij} is the Kronecker delta. Using the same constant transformation, \tilde{Q}_{ij} , the *XYZ*-system thermal strain tensor is determined to be,

$$\varepsilon_{ij}^{th}(\theta) = \tilde{Q}_{ai}\tilde{\varepsilon}_{ab}^{th}\tilde{Q}_{jb}. \quad (4.4.8)$$

Following (4.1.7), the updated Cauchy stress may then be found to be,

$$\sigma_{ij}^{n+1} = R_{ik}^{n+1}R_{mk}^n\sigma_{mn}^nR_{nl}^nR_{jl}^{n+1} + \mathbb{C}_{ijkl}(\Delta t D_{kl} - (\varepsilon_{kl}^{th}(\theta^{n+1}) - \varepsilon_{kl}^{th}(\theta^n))), \quad (4.4.9)$$

where the time dependency in the thermal strains is accounted for through changes in the temperature field.

4.4.3. Verification

The elastic 3D orthotropic model is verified through both biaxial displacement and uniaxial strain tests. The first is performed with the material and global coordinate systems aligned to investigate anisotropy while the second is done with the material coordinate system misaligned with respect to the global system. The latter also incorporates a thermal loading component to test the thermal strain contributions. In this case, it is assumed that each of the thermal strain input functions have linear slopes of α_{aa} , α_{bb} , and α_{cc} for the *A*, *B*, and *C* principal material axes, respectively. A common zero strain reference temperature, T_0 , is assumed for all three functions. The set of material properties used for these tests are given in Table 4-1.

$E_{AA} = E$	10,000.0 ksi	G_{AB}	100.0 ksi
E_{BB}	200.0 ksi	G_{BC}	1,000.0 ksi
E_{CC}	10.0 ksi	G_{CA}	5.0 ksi
$\nu_{AB} = \nu$	0.25	α_{aa}	$50 \frac{\mu\epsilon}{K}$
ν_{BC}	0.2	α_{bb}	$500 \frac{\mu\epsilon}{K}$
ν_{CA}	0.003	α_{cc}	$5 \frac{\mu\epsilon}{K}$
		θ_0	293 K

Table 4-1. The material properties for the elastic 3D orthotropic model used for the varying temperature, uniaxial stress tests.

4.4.3.1. Biaxial Displacement

First, to investigate anisotropic effects, the case of a biaxial applied displacement of the form,

$$u_i = \lambda_1 \delta_{1i} + \lambda_2 \delta_{2i}, \quad (4.4.10)$$

is considered for a material which has its axes aligned with the global Cartesian system – $\alpha_1 = \alpha_2 = 0$ or the A , B , and C frame is the same as the \hat{e}_1 , \hat{e}_2 , and \hat{e}_3 . To simplify the problem, $\lambda_2 = \frac{1}{2}\lambda_1$ and it can be shown that (noting $\sigma_{33} = 0$ from a corresponding traction free condition),

$$\begin{aligned} \varepsilon_{11} &= \ln(1 + \lambda_1), \\ \varepsilon_{22} &= \ln\left(1 + \frac{1}{2}\lambda_1\right) \\ \varepsilon_{33} &= -\frac{\nu_{AC} + \nu_{BC}\nu_{AB}}{1 - \nu_{AB}\nu_{BA}}\varepsilon_{11} - \frac{\nu_{BC} + \nu_{BA}\nu_{AC}}{1 - \nu_{AB}\nu_{BA}}\varepsilon_{22}. \end{aligned} \quad (4.4.11)$$

With the strain state known, analytical stresses may be found via Hooke's law. The corresponding results of both the numerical and analytical results are presented below in Figure 4-6. Numerical results are found through a single element test. Importantly, by comparing the results of Figures 4-6a and 4-6b the expected and desired anisotropy may be clearly seen in the vast difference of stress magnitudes (as indicated by the figure scaling). Additionally, the matching results serves to verify the model under such conditions.

4.4.3.2. Uniaxial Strain

Secondly, the capabilities of this model under arbitrary rotations are explored. To be able to analytically consider this problem, a uniaxial strain ($\varepsilon_{ij} = \varepsilon_{11}\delta_{i1}\delta_{j1}$) loading is investigated. The material properties are rotated with the specified orientations per Equations (4.4.6) and (4.4.8) using the specified orientations in Table 4-2. A combined thermal-mechanical loading is considered. Specifically, the material is first stretched to the specified strain and that strain is then held fixed during a heating step ($\Delta T = 400$ K) to investigate the ability of the model to accurately incorporate anisotropic coefficients of thermal expansion. The results for both the analytical and

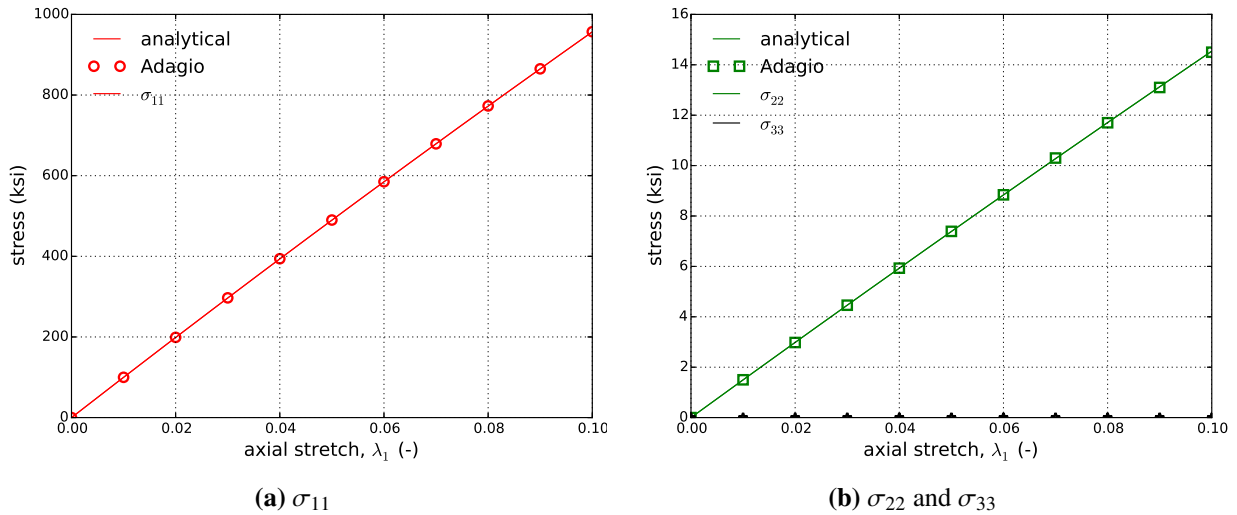


Figure 4-6. Analytical and numerical results of axial σ_{11} and transverse σ_{22} and σ_{33} , as a function of the stretch λ_1 .

numerical (from a corresponding single element simulation) analyses are shown in Figure 4-7 with the normal and shear stresses presented in Figures 4-7a and 4-7b respectively. Clear agreement may be seen during both the thermal and mechanical loading stages including the anisotropic effects further verifying model capabilities.

α_1	30	Direction 1	3
α_2	60	Direction 2	1

Table 4-2. The coordinate system rotations used with the elastic 3D orthotropic model for the uniaxial strain test.

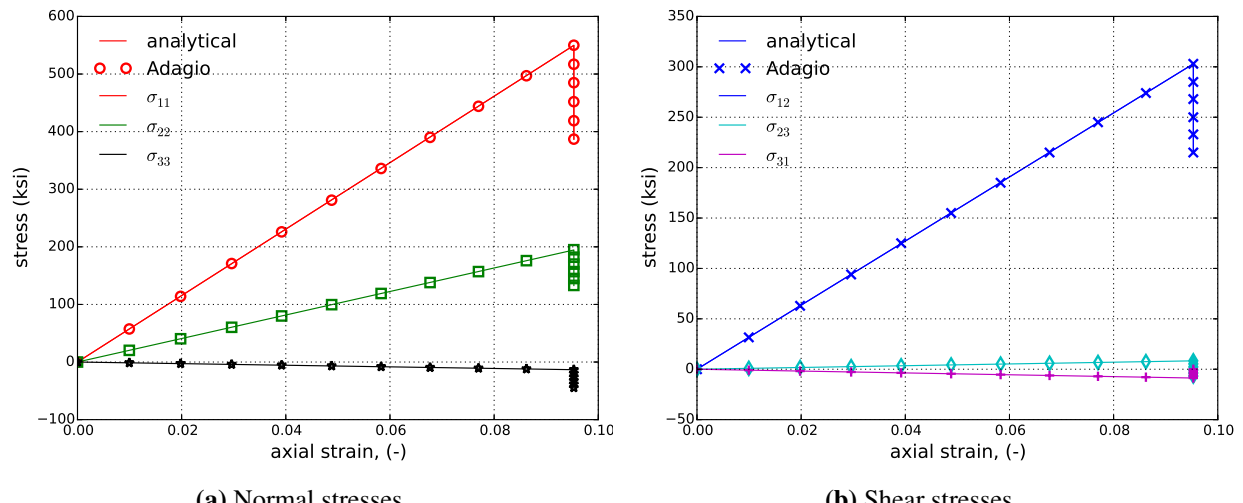


Figure 4-7. Analytical and numerical results of the stress state through a thermomechanical uniaxial strain loading as a function of the axial strain ε_{11} .

4.4.4. User Guide

```

BEGIN PARAMETERS FOR MODEL ELASTIC_3D_ORTHOTROPIC
#
# Elastic constants
#
YOUNGS MODULUS = <real> E
POISSONS RATIO = <real> ν
SHEAR MODULUS = <real> G
BULK MODULUS = <real> K
LAMBDA = <real> λ
TWO MU = <real> 2μ
#
# Material coordinates system definition
#
COORDINATE SYSTEM = <string> coordinate_system_name
DIRECTION FOR ROTATION = <real> 1|2|3
ALPHA = <real> α1 (degrees)
SECOND DIRECTION FOR ROTATION = <real> 1|2|3
SECOND ALPHA = <real> α2 (degrees)
#
# Required parameters
#
YOUNGS MODULUS AA = <real> EAA
YOUNGS MODULUS BB = <real> EBB
YOUNGS MODULUS CC = <real> ECC
POISSONS RATIO AB = <real> νAB
POISSONS RATIO BC = <real> νBC
POISSONS RATIO CA = <real> νCA
SHEAR MODULUS AB = <real> GAB
SHEAR MODULUS BC = <real> GBC
SHEAR MODULUS CA = <real> GCA
#
# Thermal strain functions
#
THERMAL STRAIN AA FUNCTION = <string> εaath(θ)
THERMAL STRAIN BB FUNCTION = <string> εbbth(θ)
THERMAL STRAIN CC FUNCTION = <string> εccth(θ)
#
END [PARAMETERS FOR MODEL ELASTIC_3D_ORTHOTROPIC]

```

There are no output variables available for the Elastic Three-Dimensional Orthotropic material model.

REFERENCES

[1] A.E. Green and W. Zerna. *Theoretical Elasticity, 2nd Edition*. Clarendon Press, Oxford, 1968.

4.5. NEO-HOOKEAN MODEL

4.5.1. Theory

The neo-Hookean model is a hyperelastic generalization of isotropic, small-strain linear elasticity. The stress-strain response for the neo-Hookean model may be determined from a free energy function - in this case the strain energy density, W . The form of the strain energy density ([1]) is

$$W(C_{ij}) = \frac{1}{2}K \left[\frac{1}{2} (J^2 - 1) - \ln J \right] + \frac{1}{2}\mu (\bar{C}_{kk} - 3) , \quad (4.5.1)$$

where K and μ are the bulk and shear moduli, respectively. The deformation measure is given by C_{ij} , the components of the right Cauchy-Green tensor, where $C_{ij} = F_{ki}F_{kj}$. The determinant of the deformation gradient is given by J and is a measure of the volumetric part of the deformation. \bar{C}_{ij} provides the isochoric part of the deformation and is given by

$$\bar{C}_{ij} = \bar{F}_{ki}\bar{F}_{kj}, \quad ; \quad \bar{F}_{ij} = J^{-1/3}F_{ij} . \quad (4.5.2)$$

The second Piola-Kirchoff stress, with components S_{ij} , may be determined by taking a derivative of the strain energy density and the Cauchy stress may be found by mapping from the second Piola-Kirchoff stress. The components of the Cauchy stress are

$$\sigma_{ij} = \frac{1}{2}K \left(J - \frac{1}{J} \right) \delta_{ij} + J^{-5/3}\mu \left(B_{ij} - \frac{1}{3}B_{kk}\delta_{ij} \right) , \quad (4.5.3)$$

where $B_{ij} = F_{ik}F_{jk}$, are the components of the left Cauchy-Green tensor and δ_{ij} is the Kronecker delta.

Linearizing (4.5.3) we recover small strain linear elasticity

$$\begin{aligned} \sigma_{ij} &= \left(K - \frac{2}{3}\mu \right) u_{k,k}\delta_{ij} + \mu (u_{i,j} + u_{j,i}) \\ &= \left(K - \frac{2}{3}\mu \right) \varepsilon_{kk}\delta_{ij} + 2\mu\varepsilon_{ij} . \end{aligned} \quad (4.5.4)$$

The neo-Hookean model is used for the recoverable (elastic) part for a number of inelastic, finite deformation constitutive models.

4.5.2. Implementation

As a hyperelastic model, the current state of the material may be determined by the total deformation. To this end we use the polar decomposition of the deformation gradient,

$$F_{ij} = V_{ik}R_{kj} \quad , \quad (4.5.5)$$

in which V_{ij} are the components of the left stretch tensor and R_{ij} is the corresponding rotation. Noting that,

$$B_{ij} = V_{ik}V_{kj} \quad , \quad (4.5.6)$$

and $J = \det(V_{ij})$, the Cauchy stress (via (4.5.3)) is found. The unrotated stress, T_{ij} , which is needed for internal force calculations in Sierra/SM, is found using the transformation

$$T_{ij} = R_{ki}\sigma_{kl}R_{lj} \quad . \quad (4.5.7)$$

4.5.3. Verification

It is possible to find closed form solutions for a number of loadings. Five problems are described here: uniaxial stress, pure shear strain, pure shear stress, uniaxial strain and simple shear. One set of material properties was used for all tests and they are given in Table 4-3. The elastic modulus and Poisson's ratio are given in addition to the bulk and shear moduli.

K	0.5 MPa	μ	0.375 MPa
E	0.9 MPa	ν	0.2

Table 4-3. The material properties for the neo-Hookean model used for both the uniaxial and simple shear tests.

4.5.3.1. Uniaxial Stress

For uniaxial stress we will assume, without loss of generality, that $\sigma_{11} \neq 0$. The deformation, in terms of the components of the left stretch tensor, for this stress state is

$$V_{11} = \lambda_1 \quad ; \quad V_{22} = V_{33} = \lambda_2 \quad , \quad (4.5.8)$$

with all other components being zero.

The Cauchy stress is given by (4.5.3), however for simplicity we will use the Kirchhoff stress instead

$$\tau_{ij} = J\sigma_{ij} \quad , \quad (4.5.9)$$

where in what follows $\tau_{11} = \tau$. With the lateral stresses being zero we have two equations

$$\begin{aligned}\tau &= \frac{K}{2} (J^2 - 1) + \frac{2}{3} \mu J^{-2/3} (\lambda_1^2 - \lambda_2^2) \\ 0 &= \frac{K}{2} (J^2 - 1) - \frac{1}{3} \mu J^{-2/3} (\lambda_1^2 - \lambda_2^2) .\end{aligned}\quad (4.5.10)$$

First, we solve for J by looking at the trace of the stress tensor. This gives us

$$\tau = \frac{3K}{2} (J^2 - 1) ; \quad J = \sqrt{1 + \frac{2\tau}{3K}} . \quad (4.5.11)$$

Once we have J we can write $\lambda_2^2 = J/\lambda_1$ and solve for λ_1 by looking at the deviatoric part of the Kirchhoff stress. For this we have

$$\tau = \mu J^{-2/3} \left(\lambda_1^2 - \frac{J}{\lambda_1} \right) . \quad (4.5.12)$$

Rearranging we get a cubic equation for λ_1

$$\lambda_1^3 - \left(\frac{\tau}{\mu} J^{2/3} \right) \lambda_1 - J = 0 . \quad (4.5.13)$$

A solution for this can be found with the following substitution

$$\lambda_1 = x + \frac{p}{3x} ; \quad p = \frac{\tau}{\mu} J^{2/3} , \quad (4.5.14)$$

which gives a quadratic equation for x^3

$$x^6 - Jx^3 + \frac{p^3}{27} = 0 . \quad (4.5.15)$$

The one meaningful solution to this polynomial is

$$x = \left[\frac{J}{2} + \sqrt{\left(\frac{J}{2} \right)^2 - \left(\frac{p}{3} \right)^3} \right]^{1/3} , \quad (4.5.16)$$

with which we can substitute into (4.5.14) to get λ_1 . With J and λ_1 we can solve for λ_2 . Note that in this solution the axial Kirchhoff stress, τ , is the independent variable.

This solution is compared to the solution from a single element problem in Sierra/SM in Figures 4-8a and 4-8b. It should be noted that the response of the neo-Hookean model is *slightly* nonlinear. The linear elastic solution is given by the green line in each figure.

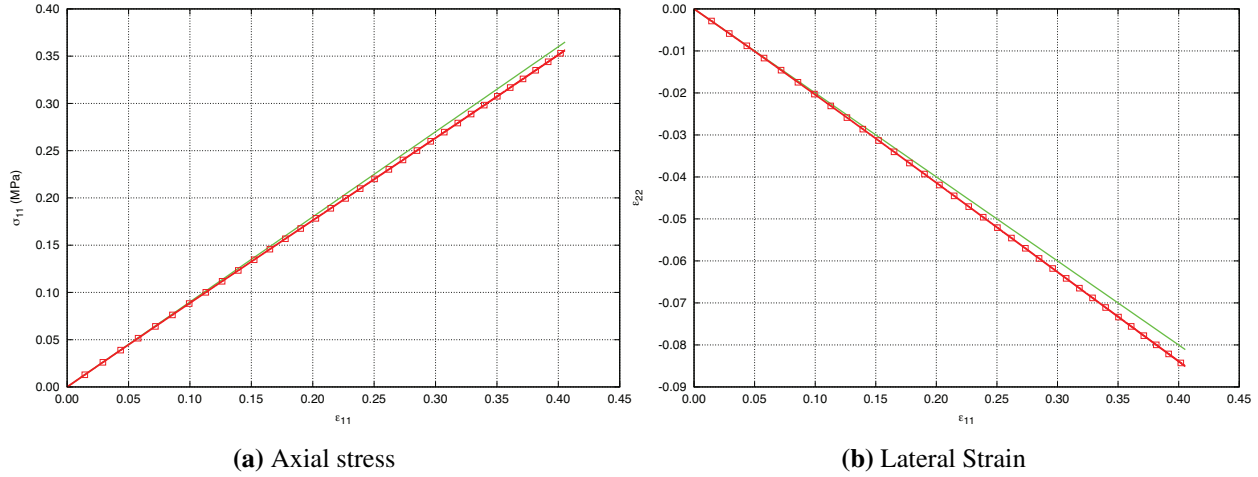


Figure 4-8. Analytical and numerical results for the (a) uniaxial stress and (b) lateral strain. The green line gives the linear elastic response.

4.5.3.2. Pure Shear Strain

For pure shear strain the deformation gradient, which is symmetric, is

$$[F_{ij}] = \frac{1}{2} \begin{bmatrix} (\lambda + \lambda^{-1}) & (\lambda - \lambda^{-1}) & 0 \\ (\lambda - \lambda^{-1}) & (\lambda + \lambda^{-1}) & 0 \\ 0 & 0 & 2 \end{bmatrix} , \quad (4.5.17)$$

which gives no volume change, $J = 1$. Since there is no volume change, the Kirchhoff stress is equal to the Cauchy stress: $\tau = \sigma$. Using (4.5.3), the non-zero stress components are

$$\begin{aligned} \sigma_{12} &= \frac{\mu}{2} (\lambda^2 - \lambda^{-2}) \\ \sigma_{11} = \sigma_{22} &= \frac{\mu}{3} \left[\frac{1}{2} (\lambda^2 + \lambda^{-2}) - 1 \right] \\ \sigma_{33} &= \frac{\mu}{3} (2 - \lambda^2 + \lambda^{-2}) . \end{aligned} \quad (4.5.18)$$

The results of a single element problem in Sierra/SM are compared with the analytical solution in Figure 4-9. It is interesting to note that the normal stresses, σ_{11} , σ_{22} , and σ_{33} are not equal to zero. This is a much different result than what we get for the linear hypoelastic model.

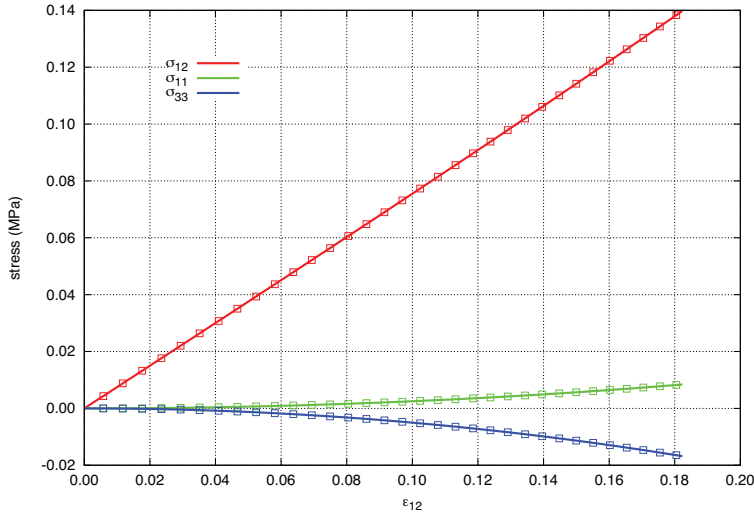


Figure 4-9. Analytical and numerical results for the neo-Hookean model subjected to a pure shear strain. The solid lines are the analytical results and the boxes are results from Sierra/SM.

4.5.3.3. Pure Shear Stress

Since pure shear strain did not result in a pure shear stress state, we do not expect a pure shear stress state to result in a pure shear strain state. For pure shear stress the only non-zero stress component is

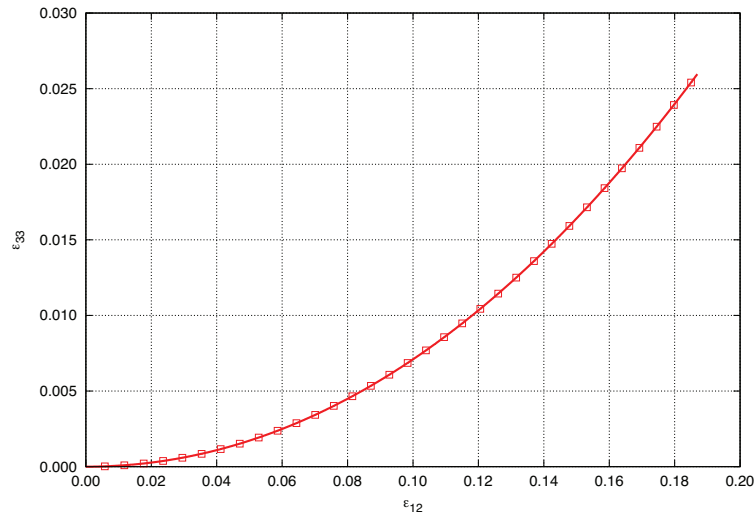


Figure 4-10. Analytical and numerical results for the neo-Hookean model subjected to a pure shear stress. The curve gives the logarithmic strain component, $\varepsilon_{33} = \frac{1}{2} \ln B$. The solid lines are the analytical results and the boxes are results from Sierra/SM.

$$\sigma_{12} = \tau = \mu B_{12} , \quad (4.5.19)$$

and using (4.5.3) it can be shown that $J = 1$. The deformation, in terms of the left Cauchy-Green deformation tensor, is

$$[B_{ij}] = \begin{bmatrix} B & B_{12} & 0 \\ B_{12} & B & 0 \\ 0 & 0 & B \end{bmatrix} . \quad (4.5.20)$$

The equation we need to solve for the deformation is $\det \mathbf{B} = 1$. This gives us the cubic equation

$$B^3 - \left(\frac{\tau}{\mu}\right)^2 B - 1 = 0 . \quad (4.5.21)$$

This is a cubic equation of the same form as that in the uniaxial stress problem. We make the substitution

$$B = x + \frac{p}{3x} ; \quad p = \left(\frac{\tau}{\mu}\right)^2 . \quad (4.5.22)$$

This gives us a quadratic equation in x^3

$$x^6 - x^3 + \frac{p^3}{27} = 0 , \quad (4.5.23)$$

which has the solution

$$x = \left[\frac{1}{2} + \frac{1}{2} \sqrt{1 - \frac{4p^3}{27}} \right]^{1/3} . \quad (4.5.24)$$

Substituting this solution into (4.5.22) gives B .

The results of a single element problem in Sierra/SM are compared with the analytical solution in Figure 4-10. Of interest here is the fact that the normal strains, ε_{11} , ε_{22} , and ε_{33} are not equal to zero. Again, this is a different result than what we get for the linear hypoelastic model.

4.5.3.4. Uniaxial Strain

First, utilizing a displacement condition corresponding to uniaxial strain results in a deformation gradient of the form,

$$F_{ij} = \lambda \delta_{1i} \delta_{1j} + \delta_{2i} \delta_{2j} + \delta_{3i} \delta_{3j}. \quad (4.5.25)$$

By evaluating relation (4.5.3) with this deformation field produces stresses that may be written as

$$\begin{aligned} \sigma_{11} &= \frac{1}{2} K \left(\lambda - \frac{1}{\lambda} \right) + \frac{2}{3} \mu \left(\lambda^2 - 1 \right) \lambda^{-5/3}, \\ \sigma_{22} = \sigma_{33} &= \frac{1}{2} K \left(\lambda - \frac{1}{\lambda} \right) - \frac{1}{3} \mu \left(\lambda^2 - 1 \right) \lambda^{-5/3} \end{aligned} \quad (4.5.26)$$

with the shear stress components equal to zero. Both the corresponding analytical and numerical solutions are presented in Figure 4-11.

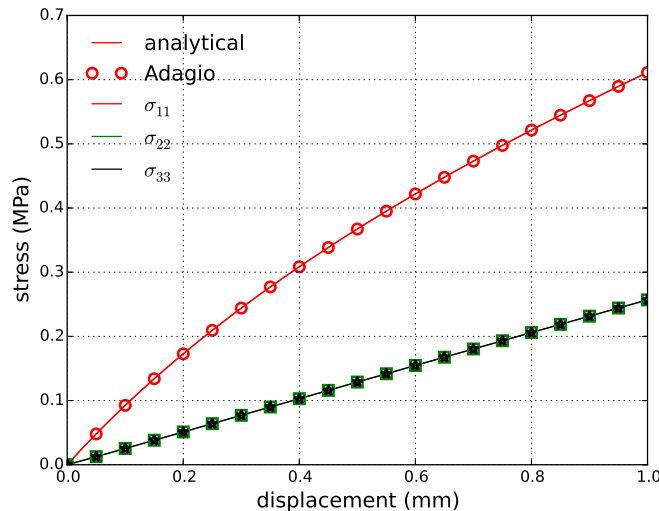


Figure 4-11. Analytical and numerical results for the uniaxial stretch case.

4.5.3.5. Simple Shear

For the simple shear case, a deformation gradient of the form,

$$F_{ij} = \delta_{ij} + \gamma \delta_{1i} \delta_{2j}, \quad (4.5.27)$$

is assumed. Noting this is a volume preserving deformation ($J = 1$) and again evaluating (4.5.3) produces stresses that may be written as,

$$\sigma_{11} = \frac{2}{3}\mu\gamma^2$$

$$\sigma_{22} = \sigma_{33} = -\frac{1}{3}\mu\gamma^2 \quad (4.5.28)$$

$$\sigma_{12} = \mu\gamma \quad (4.5.29)$$

Both the corresponding analytical and numerical solutions are presented in Figure 4-12.

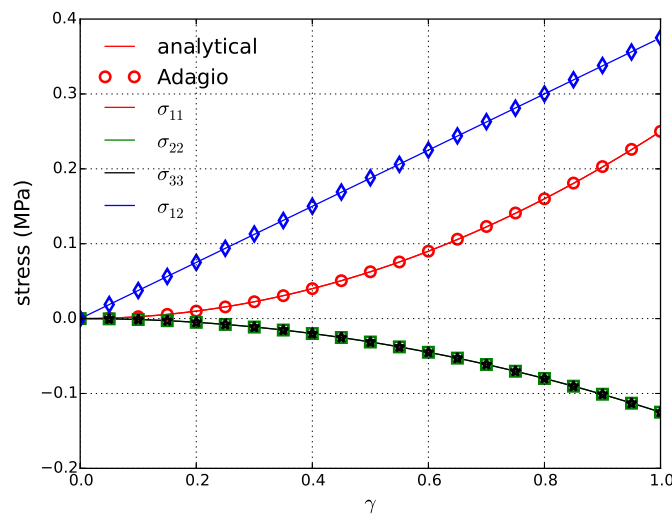


Figure 4-12. Analytical and numerical results for the simple shear case.

4.5.4. User Guide

```
BEGIN PARAMETERS FOR MODEL NEO_HOOKEAN
#
# Elastic constants
#
YOUNGS MODULUS = <real> E
POISSONS RATIO = <real> ν
SHEAR MODULUS = <real> G
BULK MODULUS = <real> K
LAMBDA = <real> λ
TWO MU = <real> 2μ
END [PARAMETERS FOR MODEL NEO_HOOKEAN]
```

There are no output variables available for the neo-Hookean model.

REFERENCES

- [1] J.C. Simo and T.J.R. Hughes. *Computational Inelasticity*. Springer-Verlag, New York, NY, 1998.

4.6. GENT MODEL

4.6.1. Theory

The Gent model is a hyperelastic model of rubber elasticity developed from phenomenological continuum mechanics approaches. Specifically, the model is based on the concept of limiting chain extensibility and is an accurate approximation to the Arruda-Boyce model. To determine the stress-strain response of the Gent model, a strain energy density of the form ([1]),

$$W(B_{ij}) = \frac{1}{2}K \left[\frac{1}{2} (J^2 - 1) - \ln J \right] + \frac{1}{2}\mu J_m \ln \left(1 - \frac{\bar{B}_{kk} - 3}{J_m} \right), \quad (4.6.1)$$

is proposed with K and μ the bulk and shear moduli, J the determinant of the deformation gradient and J_m an input parameter for limiting the value of $\bar{B}_{kk} - 3$. J_m is the parameter effectively accounting for limiting chain extensibility. The deformation measure is given by B_{ij} , the components of the Left Cauchy Green tensor, where $B_{ij} = F_{ik}F_{jk}$. \bar{B}_{kk} provides the isochoric part of the deformation and is given by

$$\bar{B}_{ij} = \bar{F}_{ik}\bar{F}_{jk}; \bar{F}_{ij} = J^{-1/3}F_{ij}. \quad (4.6.2)$$

In the limit where $J_m \rightarrow \infty$ the Gent model reduces to the classical neo-Hookean model (see (4.5.1)). This can be seen by defining x to be $\frac{1}{J_m}$, taking a Taylor series expansion of $\ln(1 - (\bar{B}_{kk} - 3)x)$ about $x = 0$ and taking the limit as $x \rightarrow 0$.

The second Piola-Kirchoff stress, with components S_{ij} , may be determined by taking a derivative of the strain energy density. A mapping of the second Piola-Kirchoff may be used to determine the Cauchy stress. These relations produce components of the Cauchy stress, σ_{ij} , that are

$$\sigma_{ij} = \frac{1}{2}K \left(J - \frac{1}{J} \right) \delta_{ij} + \frac{J^{-5/3}\mu J_m (B_{ij} - \frac{1}{3}\bar{B}_{kk}\delta_{ij})}{J_m - \bar{B}_{kk} + 3}, \quad (4.6.3)$$

where δ_{ij} is the Kronecker delta.

The Gent model is a useful model for rubber elasticity as it is simple and provides similar predictions to comparatively complicated molecular models. It is also a practical model to use since analytic solutions to benchmark problems exist for this model.

4.6.2. Implementation

As a hyperelastic model, the current state of the material may be determined by the total deformation. To this end we use the polar decomposition of the deformation gradient,

$$F_{ij} = V_{ik}R_{kj}, \quad (4.6.4)$$

in which V_{ij} are the components of the left stretch tensor and R_{ij} is the corresponding rotation. Noting that,

$$B_{ij} = V_{ik}V_{kj}, \quad (4.6.5)$$

and $J = \det(V_{ij})$, the Cauchy stress (via (4.6.3)) is found. The unrotated stress, T_{ij} , which is needed for internal force calculations in Sierra/SM, is found using the transformation

$$T_{ij} = R_{ki}\sigma_{kl}R_{lj}. \quad (4.6.6)$$

4.6.3. Verification

It is possible to find closed form solutions for a number of loadings. Three problems are described here: uniaxial strain, simple shear, and hydrostatic compression. One set of material properties was used for all tests and they are given in Table 4-4. The elastic modulus and Poisson's ratio are given in addition to the bulk modulus, shear modulus, and limiting chain extensibility parameter, J_m .

K	0.325 MPa	μ	0.15 MPa	J_m	13.125
E	0.39 MPa	ν	0.33		

Table 4-4. The material properties for the Gent model used for uniaxial strain, simple shear, and hydrostatic compression tests.

4.6.3.1. Uniaxial Strain

First, utilizing a displacement condition corresponding to uniaxial strain results in a deformation gradient of the form,

$$F_{ij} = \lambda\delta_{1i}\delta_{1j} + \delta_{2i}\delta_{2j} + \delta_{3i}\delta_{3j}. \quad (4.6.7)$$

By evaluating relation (4.6.3) with this deformation field, we produce stresses that may be written as,

$$\begin{aligned} \sigma_{11} &= \frac{1}{2}K\left(\lambda - \frac{1}{\lambda}\right) - \frac{2}{3}\frac{J_m\mu(\lambda^2-1)}{\lambda^3-(J_m+3)\lambda^{5/3}+2\lambda} \\ \sigma_{22} = \sigma_{33} &= \frac{1}{2}K\left(\lambda - \frac{1}{\lambda}\right) + \frac{1}{3}\frac{J_m\mu(\lambda^2-1)}{\lambda^3-(J_m+3)\lambda^{5/3}+2\lambda}, \end{aligned} \quad (4.6.8)$$

with the shear stress components equal to zero. Both the corresponding analytical and numerical solutions are presented in Figure 4-13.

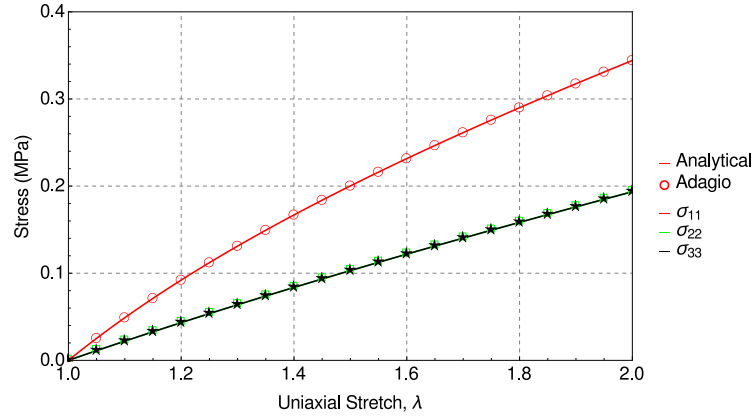


Figure 4-13. Analytical and numerical results for the uniaxial stretch case.

4.6.3.2. Simple Shear

For the simple shear case, a deformation gradient of the form,

$$F_{ij} = \delta_{ij} + \gamma \delta_{1i} \delta_{2j}, \quad (4.6.9)$$

is assumed. Noting this is a volume preserving deformation ($J = 1$) and again evaluating (4.6.3) produces stresses that may be written as,

$$\begin{aligned} \sigma_{11} &= \frac{2}{3} \frac{J_m \mu \gamma^2}{J_m - \gamma^2} \\ \sigma_{22} = \sigma_{33} &= -\frac{1}{3} \frac{J_m \mu \gamma^2}{J_m - \gamma^2} \\ \sigma_{12} &= \frac{J_m \mu \gamma}{J_m - \gamma^2} \end{aligned} \quad (4.6.10)$$

Both the corresponding analytical and numerical solutions are presented in Figure 4-14.

4.6.3.3. Hydrostatic Compression

The volumetric deformation capabilities of the model are also investigated through displacement controlled hydrostatic compression. Specifically, hydrostatic compression results in a

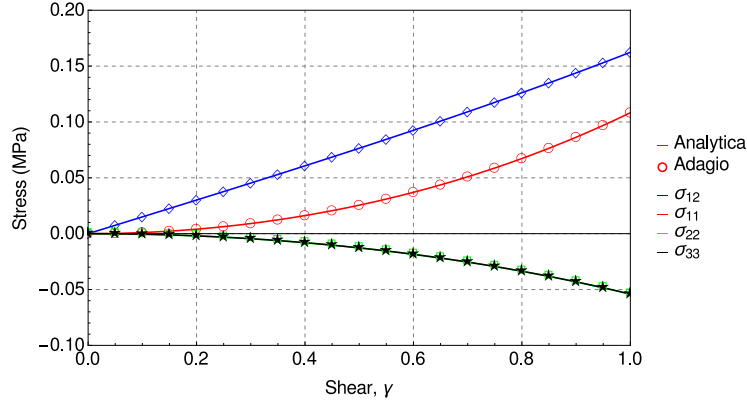


Figure 4-14. Analytical and numerical results for the simple shear case.

deformation gradient of the form,

$$F_{ij} = \lambda \delta_{ij}, \quad (4.6.11)$$

where $0 < \lambda \leq 1$. As there is no deviatoric deformation, evaluation of (4.6.3) produces stresses that may be written as,

$$\sigma_{11} = \sigma_{22} = \sigma_{33} = \frac{1}{2}K \left(\lambda^3 - \frac{1}{\lambda^3} \right), \quad (4.6.12)$$

with the shear stress components equal to zero. Both the corresponding analytical and numerical solutions are presented in Figure 4-15.

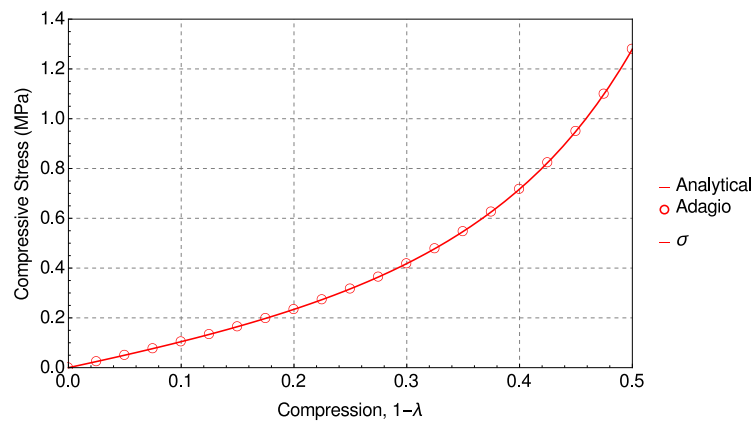


Figure 4-15. Stress determined analytically and numerically for the Gent model during displacement controlled hydrostatic compression.

4.6.4. User Guide

```
BEGIN PARAMETERS FOR MODEL GENT
#
# Elastic constants
#
YOUNGS MODULUS = <real> E
POISSONS RATIO = <real> ν
SHEAR MODULUS = <real> G
BULK MODULUS = <real> K
LAMBDA = <real> λ
TWO MU = <real> 2μ
#
Jm Parameter = <real>  $J_m$ 
END [PARAMETERS FOR MODEL GENT]
```

There are no output variables available for the Gent model.

REFERENCES

[1] A.N. Gent. A new constitutive relation for rubber. *Rubber Chemistry and Technology*, 69(1): 59–61, 1996.

4.7. ELASTIC-PLASTIC MODEL

4.7.1. Theory

The elastic-plastic model is a hypoelastic, rate-independent linear hardening plasticity model. The rate form of the constitutive equation assumes an additive split of the rate of deformation into an elastic and plastic part

$$D_{ij} = D_{ij}^e + D_{ij}^p \quad (4.7.1)$$

The stress rate only depends on the elastic strain rate in the problem

$$\overset{\circ}{\sigma}_{ij} = \mathbb{C}_{ijkl} D_{kl}^e \quad (4.7.2)$$

where \mathbb{C}_{ijkl} are the components of the fourth-order, isotropic elasticity tensor.

The key to the model is finding the plastic rate of deformation. For associated flow the plastic rate of deformation is in a direction normal to the yield surface. The yield surface is given by

$$f(\sigma_{ij}, \alpha_{ij}, \bar{\varepsilon}^p) = \phi(\sigma_{ij}, \alpha_{ij}) - \bar{\sigma}(\bar{\varepsilon}^p) = 0 \quad (4.7.3)$$

where ϕ is the effective stress, α_{ij} are the components of the back stress (used with kinematic hardening), and $\bar{\sigma}$ is the hardening function which is a function of an internal state variable, the equivalent plastic strain $\bar{\varepsilon}^p$. An example of such a yield surface (plotted in the deviatoric π -plane) is presented below in Figure 4-16. The isotropy of the yield surface is clearly evident.

For the elastic plastic model a linear hardening law is assumed

$$\bar{\sigma} = \sigma_y + H' \bar{\varepsilon}^p \quad (4.7.4)$$

where σ_y is the yield stress and H' is the hardening modulus.

If the stress state is such that $f < 0$, the behavior of the material is elastic; if the stress state is such that $f = 0$ and $\dot{f} < 0$, i.e. the strain rate brings the stress inside the yield surface, then the behavior of the material is elastic; if the stress state is such that $f = 0$ and $\dot{f} > 0$, i.e. the strain rate brings the stress outside the yield surface, then plastic deformation occurs.

We assume associated flow in this model, which gives the plastic rate of deformation

$$D_{ij}^p = \dot{\gamma} \frac{\partial \phi}{\partial \sigma_{ij}} \quad (4.7.5)$$

where $\dot{\gamma}$ is the consistency parameter. For the elastic-plastic model the yield surface is assumed to be a von Mises yield surface with a back stress tensor to denote the center of the yield surface. The effective stress for a von Mises yield surface is

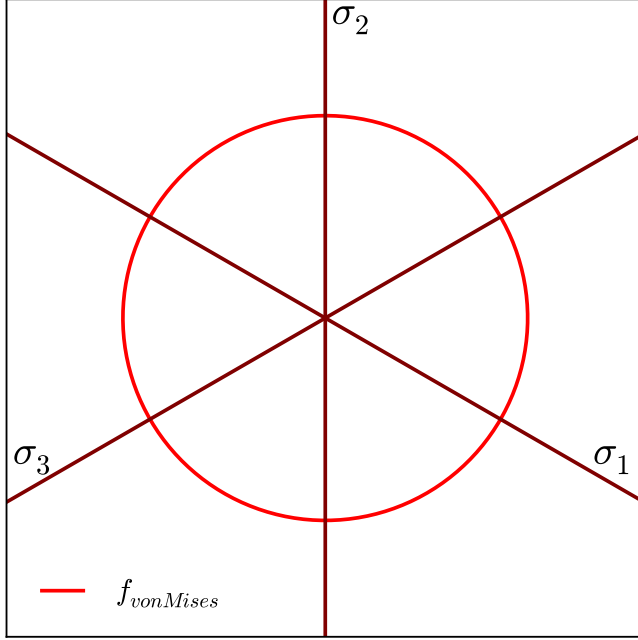


Figure 4-16. Example von Mises yield surface (J_2) used by the elastic-plastic model presented in the deviatoric π -plane. In this case the surface is plotted for $\alpha_{ij} = 0$ and $\bar{\varepsilon}^p = 0$.

$$\phi(\sigma_{ij}) = \sqrt{\frac{3}{2}\xi_{ij}\xi_{ij}} ; \quad \xi_{ij} = s_{ij} - \alpha_{ij} \quad (4.7.6)$$

where s_{ij} are the components of the deviatoric stress tensor

$$s_{ij} = \sigma_{ij} - \frac{1}{3}\delta_{ij}\sigma_{kk} \quad (4.7.7)$$

and α_{ij} are the components of the back stress tensor, another internal state variable.

The equivalent plastic strain is found through equating the rate of plastic work

$$\dot{W}^p = \sigma_{ij}D_{ij}^p = \bar{\sigma}\dot{\varepsilon}^p \rightarrow \dot{\varepsilon}^p = \dot{\gamma} \quad (4.7.8)$$

$$\bar{\varepsilon}^p = \int_0^t \dot{\gamma} dt$$

Finally, the model allows for kinematic hardening through the back stress. The back stress is a symmetric, deviatoric rank two tensor that evolves in the following manner

$$\dot{\alpha}_{ij} = \frac{2}{3}(1-\beta)H'D_{ij}^p \quad (4.7.9)$$

The radius of the yield surface can be defined, $R = \sqrt{\xi_{ij}\xi_{ij}}$. The evolution of the radius of the yield surface is given by

$$\dot{R} = \sqrt{\frac{2}{3}\beta H'\dot{\varepsilon}^p} \quad (4.7.10)$$

In (4.7.9) and (4.7.10) the parameter $\beta \in [0, 1]$ distributes the hardening between isotropic and kinematic hardening. If $\beta = 1$ the hardening is isotropic, if $\beta = 0$ the hardening is kinematic, and if β is between 0 and 1 the hardening is a combination of isotropic and kinematic.

4.7.2. Implementation

The elastic-plastic linear hardening model is implemented using a predictor-corrector algorithm. First, an elastic trial stress state is calculated. This is done by assuming that the rate of deformation is completely elastic

$$T_{ij}^{tr} = T_{ij}^n + \Delta t (\lambda \delta_{ij} d_{kk} + 2\mu d_{ij}) \quad (4.7.11)$$

The trial stress state can be decomposed into a pressure and a deviatoric stress

$$p^{tr} = \frac{1}{3}T_{kk}^{tr} \quad ; \quad s_{ij}^{tr} = T_{ij}^{tr} - p^{tr}\delta_{ij} \quad (4.7.12)$$

The difference between the deviatoric trial stress state and the back stress is compared to the current radius of the yield surface

$$\xi_{ij}^{tr} = s_{ij}^{tr} - \alpha_{ij}^n \quad ; \quad \xi_{tr}^2 = \xi_{ij}^{tr}\xi_{ij}^{tr} \quad (4.7.13)$$

If $\xi_{tr}^2 < R^2$ then the strain rate is elastic and the stress update is finished. If $\xi_{tr}^2 > R^2$ then plastic deformation has occurred. The algorithm then needs to determine the extent of plastic deformation.

The normal to the yield surface, N_{ij} is assumed to lie in the direction of the trial stress state. This gives us the following expression for N_{ij}

$$N_{ij} = \frac{\xi_{ij}^{tr}}{\|\xi_{ij}^{tr}\|} \quad (4.7.14)$$

In what follows the change in the yield surface is assumed to be a linear combination of isotropic and kinematic hardening, i.e. the yield surface grows and or moves. Using a backward Euler algorithm the final deviatoric stress state is

$$s_{ij}^{n+1} = s_{ij}^{tr} - \Delta t 2\mu d_{ij}^p \quad (4.7.15)$$

where the plastic strain increment is

$$\Delta t d_{ij}^p = \sqrt{\frac{3}{2}} \Delta \bar{\varepsilon}^p N_{ij} \quad (4.7.16)$$

The updated back stress is

$$\alpha_{ij}^{n+1} = \alpha_{ij}^n + \sqrt{\frac{2}{3}} (1 - \beta) (H' \Delta \bar{\varepsilon}^p) N_{ij} \quad (4.7.17)$$

and the updated radius of the yield surface is

$$R^{n+1} = R^n + \beta \sqrt{\frac{2}{3}} (H' \Delta \bar{\varepsilon}^p) \quad (4.7.18)$$

Combining these expressions we get an equation for the change in the equivalent plastic strain over the load step

$$(3\mu + H') \Delta \bar{\varepsilon}^p = \sqrt{\frac{3}{2}} (\|\xi_{ij}^{tr}\| - R^n) \quad ; \quad \xi_{ij}^{tr} = s_{ij}^{tr} - \alpha_{ij}^n \quad (4.7.19)$$

With $\Delta \bar{\varepsilon}^p$ we can update the stress and the internal state variables.

4.7.3. Verification

The elastic-plastic material model is verified for a number of loading conditions. The elastic properties used in these analyses are $E = 70$ GPa and $\nu = 0.25$. The hardening parameters are $\sigma_y = 200$ MPa, $H' = 500$ MPa, and $\beta = 1$. By setting $\beta = 1$ the hardening is isotropic.

4.7.3.1. Uniaxial Stress

The elastic-plastic model is tested in uniaxial tension. The test looks at the stress, strain, and equivalent plastic strain and compares these values against analytical results for the same problem. The model is tested in uniaxial stress in the x (x_1) directions.

For the uniaxial stress problem, the only non-zero stress component is σ_{11} . In the analysis that follows $\sigma_{11} = \sigma$. There are three non-zero strain components, ε_{11} , ε_{22} , and ε_{33} . In the analysis that follows $\varepsilon_{11} = \varepsilon$. Furthermore, the axial elastic stress, $\varepsilon_{11}^e = \sigma/E$ will be denoted by ε^e .

Axial Stresses

The uniaxial stress calculated by the model in Adagio is compared to an analytical solution. For uniaxial loading in the x_1 direction, the effective stress is

$$\phi = \sigma \quad (4.7.20)$$

If the stress state is on the yield surface, then $\phi = \bar{\sigma}(\bar{\varepsilon}^p)$, so the axial stress, as a function of the hardening function, is

$$\sigma = \bar{\sigma}(\bar{\varepsilon}^p) = \sigma_y + H' \bar{\varepsilon}^p \quad (4.7.21)$$

The stress state can be calculated from the hardening law and the anisotropy parameters.

To evaluate the axial stress we need the equivalent plastic strain as a function of the axial strain. If we equate the rate of plastic work we get

$$\bar{\sigma} \dot{\bar{\varepsilon}}^p = \sigma (\dot{\varepsilon} - \dot{\varepsilon}^e) \rightarrow \dot{\bar{\varepsilon}}^p = \dot{\varepsilon} - \dot{\varepsilon}^e \quad (4.7.22)$$

which, when integrated, gives us an equation for the equivalent plastic strain

$$\bar{\varepsilon}^p = \frac{E\varepsilon - \sigma_y}{E + H'} \quad (4.7.23)$$

The equivalent plastic strain can then be used in (4.15.25) to find the axial stress, σ

$$\sigma = \frac{\sigma_y + H' \varepsilon}{1 + H'/E} \quad (4.7.24)$$

The axial stresses is shown in Figure 4-17.

Lateral Strains

For the lateral strains we need the plastic strains and therefore the normal to the yield surface. The components of the normal to the yield surface are

$$\frac{\partial\phi}{\partial\sigma_{11}} = 1 \quad ; \quad \frac{\partial\phi}{\partial\sigma_{22}} = \frac{\partial\phi}{\partial\sigma_{33}} = -\frac{1}{2} \quad (4.7.25)$$

The elastic axial and lateral strain components are

$$\varepsilon_{11}^e = \frac{\sigma}{E} = \varepsilon^e \quad ; \quad \varepsilon_{22}^e = \varepsilon_{33}^e = -\nu \frac{\sigma}{E} = -\nu \varepsilon^e \quad (4.7.26)$$

The plastic axial strain component is

$$\varepsilon_{11}^p = \varepsilon_{11} - \frac{\sigma}{E} = \varepsilon - \varepsilon^e \quad (4.7.27)$$

which comes from the additive decomposition of the strain rates. Using the equivalent plastic strain (4.15.27) we can find the lateral plastic strain components

$$\varepsilon_{22}^p = \varepsilon_{33}^p = -\frac{1}{2}(\varepsilon - \varepsilon^e) \quad (4.7.28)$$

The lateral *total* strain components prior to yield are $\varepsilon_{22} = \varepsilon_{33} = -\nu\varepsilon$. After yield they are

$$\varepsilon_{22} = \varepsilon_{33} = -\nu\varepsilon^e - \frac{1}{2}\bar{\varepsilon}^p \quad (4.7.29)$$

where $\varepsilon^e = \sigma/E$.

Results are shown in Figure 4-18.

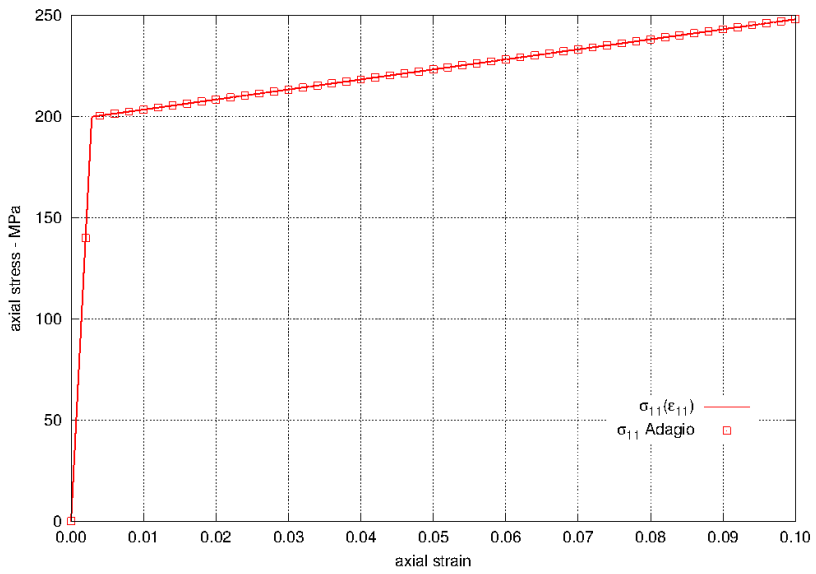


Figure 4-17. Axial stress for loading in the x_1 direction for the elastic-plastic model with linear hardening.

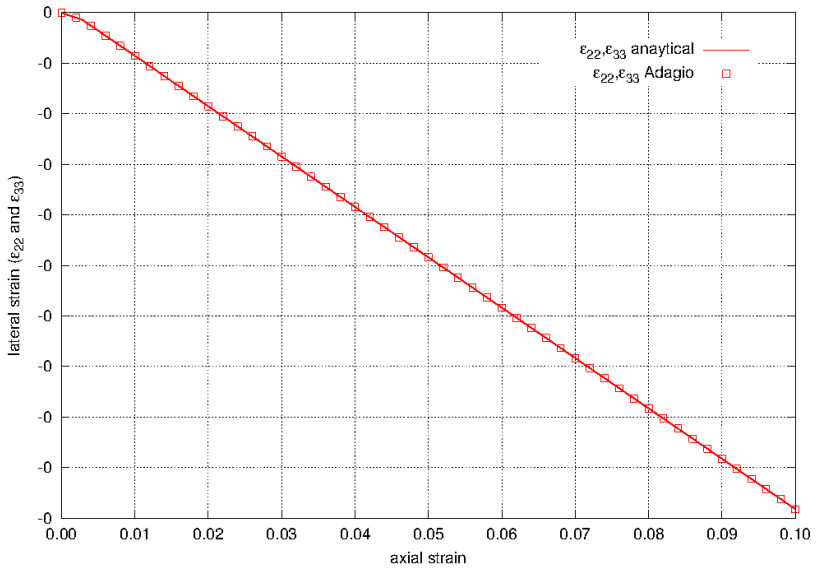


Figure 4-18. Lateral strains for uniaxial stress loading in the x_1 direction for the elastic-plastic model with linear hardening.

4.7.3.2. Pure Shear

The shear stress calculated by the elastic-plastic model in Adagio is compared to analytical solutions. Considering pure shear with respect to the x_1 - x_2 axes, the only non-zero shear stress is σ_{12} , and the only non-zero shear strain will be ε_{12} . For pure shear with respect to the x_1 - x_2 axes, the effective stress is

$$\phi = \sqrt{3} \sigma_{12} \quad (4.7.30)$$

If the stress state is on the yield surface, then $\phi = \bar{\sigma}(\bar{\varepsilon}^p)$, so the shear stress is

$$\sigma_{12} = \frac{\bar{\sigma}(\bar{\varepsilon}^p)}{\sqrt{3}} \quad (4.7.31)$$

Using this, the pure shear stress state can be calculated from the hardening law and the anisotropy parameters.

To evaluate the shear stress we need the equivalent plastic strain as a function of the shear strain. If we equate the rate of plastic work we get

$$\bar{\sigma} \dot{\varepsilon}^p = 2\sigma_{12} (\dot{\varepsilon}_{12} - \dot{\varepsilon}_{12}^e) \rightarrow \dot{\varepsilon}^p = \frac{2}{\sqrt{3}} (\dot{\varepsilon}_{12} - \dot{\varepsilon}_{12}^e) \quad (4.7.32)$$

which, when integrated, gives us an implicit equation for the equivalent plastic strain

$$\bar{\varepsilon}^p = \frac{2}{\sqrt{3}} \left(\varepsilon_{12} - \frac{\bar{\sigma}(\bar{\varepsilon}^p)}{\sqrt{3}G} \right) \quad (4.7.33)$$

The equivalent plastic strain can now be used to find the shear stress.

Boundary Conditions for Pure Shear

The deformation gradient that gives pure shear for loading relative to the x_1 - x_2 axes is

$$[\mathbf{F}] = \begin{bmatrix} \frac{1}{2}(\lambda + \lambda^{-1}) & \frac{1}{2}(\lambda - \lambda^{-1}) & 0 \\ \frac{1}{2}(\lambda - \lambda^{-1}) & \frac{1}{2}(\lambda + \lambda^{-1}) & 0 \\ 0 & 0 & 1 \end{bmatrix} \rightarrow [\boldsymbol{\varepsilon}] = \begin{bmatrix} 0 & \varepsilon & 0 \\ \varepsilon & 0 & 0 \\ 0 & 0 & 0 \end{bmatrix} ; \quad \varepsilon = \ln \lambda \quad (4.7.34)$$

For loading relative to the x_2 - x_3 axes and the x_3 - x_1 axes the boundary conditions are modified appropriately.

Results

The results for the elastic-plastic model loaded in pure shear are shown in Figure 4-18. We see that the stress strain curves in pure shear as calculated by Adagio follow the expected stress strain curves. All other stress and strain components for the three problems are zero.

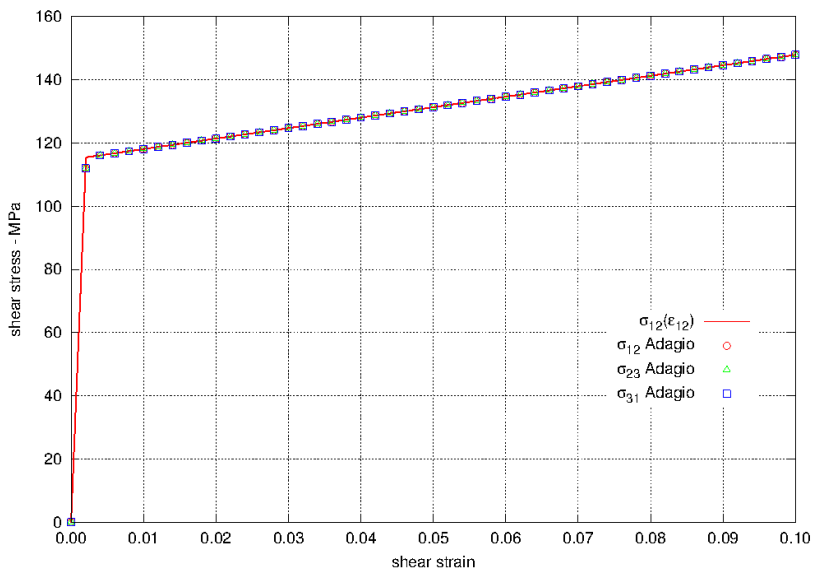


Figure 4-19. Shear stress versus shear strain using the elastic-plastic model. Results are for shear in the x_1 - x_2 plane, x_2 - x_3 plane, and x_3 - x_1 plane.

4.7.4. User Guide

```
BEGIN PARAMETERS FOR MODEL ELASTIC_PLASTIC
#
# Elastic constants
#
YOUNGS MODULUS = <real> E
POISSONS RATIO = <real> ν
SHEAR MODULUS = <real> G
BULK MODULUS = <real> K
LAMBDA = <real> λ
TWO MU = <real> 2μ
#
# Hardening Behavior
#
YIELD STRESS = <real> σy
BETA = <real> β (1.0)
HARDENING MODULUS = <real> H'
END [PARAMETERS FOR MODEL ELASTIC_PLASTIC]
```

Output variables available for this model are listed in Table 4-5 and Table 4-6. For information about the elastic-plastic model, consult [1].

Table 4-5. State Variables for ELASTIC PLASTIC Model

Name	Description
EQPS	equivalent plastic strain, $\bar{\epsilon}^p$
RADIUS	radius of the yield surface, R
BACK_STRESS	back stress (symmetric tensor), α_{ij}

Table 4-6. State Variables for ELASTIC PLASTIC Model for Shells

Name	Description
EQPS	equivalent plastic strain, $\bar{\epsilon}^P$
TENSILE_EQPS	equivalent plastic strain only accumulated when the material is in tension (trace of stress tensor is positive)
RADIUS	radius of the yield surface, R
BACK_STRESS	back stress (symmetric tensor), α_{ij}
ITERATIONS	radial return iterations
ERROR	error in plane stress iterations
PS_ITER	plane stress iterations
TSTRAIN	integrated thickness strain

REFERENCES

- [1] C.M. Stone. SANTOS – a two-dimensional finite element program for the quasistatic, large deformation, inelastic response of solids. Technical Report SAND90-0543, Sandia National Laboratories, Albuquerque, NM, 1996. [pdf](#).

4.8. ELASTIC-PLASTIC POWER LAW HARDENING MODEL

4.8.1. Theory

The elastic-plastic power law hardening model is a hypoelastic, rate-independent plasticity model with power law hardening [1]. The rate form of the constitutive equation assumes an additive split of the rate of deformation into an elastic and plastic part

$$D_{ij} = D_{ij}^e + D_{ij}^p \quad (4.8.1)$$

The stress rate only depends on the elastic strain rate in the problem

$$\overset{\circ}{\sigma}_{ij} = \mathbb{C}_{ijkl} D_{kl}^e \quad (4.8.2)$$

where \mathbb{C}_{ijkl} are the components of the fourth-order, isotropic elasticity tensor.

The key to integrating the model is finding the plastic rate of deformation. For associated flow the plastic rate of deformation is in a direction normal to the yield surface. The yield surface is given by

$$f(\sigma_{ij}, \bar{\varepsilon}^p) = \phi(\sigma_{ij}) - \bar{\sigma}(\bar{\varepsilon}^p) = 0 \quad (4.8.3)$$

where ϕ is the equivalent stress and $\bar{\sigma}$ is the hardening function which is a function of the equivalent plastic strain $\bar{\varepsilon}^p$. For this model the hardening function uses a power law

$$\bar{\sigma}(\bar{\varepsilon}^p) = \sigma_y + A \langle \bar{\varepsilon}^p - \varepsilon_L \rangle^n \quad (4.8.4)$$

which is shown in Figure 4-20. The yield stress is σ_y , the hardening constant is A , the hardening exponent is n , and the Lüders strain is ε_L . The bracket $\langle \cdot \rangle$ is the Macaulay bracket defined as

$$\langle x \rangle = \begin{cases} 0, & \text{if } x \leq 0 \\ x, & \text{if } x > 0. \end{cases} \quad (4.8.5)$$

By assuming associated plastic flow, the plastic rate of deformation can be written as

$$D_{ij}^p = \dot{\gamma} \frac{\partial \phi}{\partial \sigma_{ij}}. \quad (4.8.6)$$

For this model the yield surface is chosen to be a von Mises yield surface, so

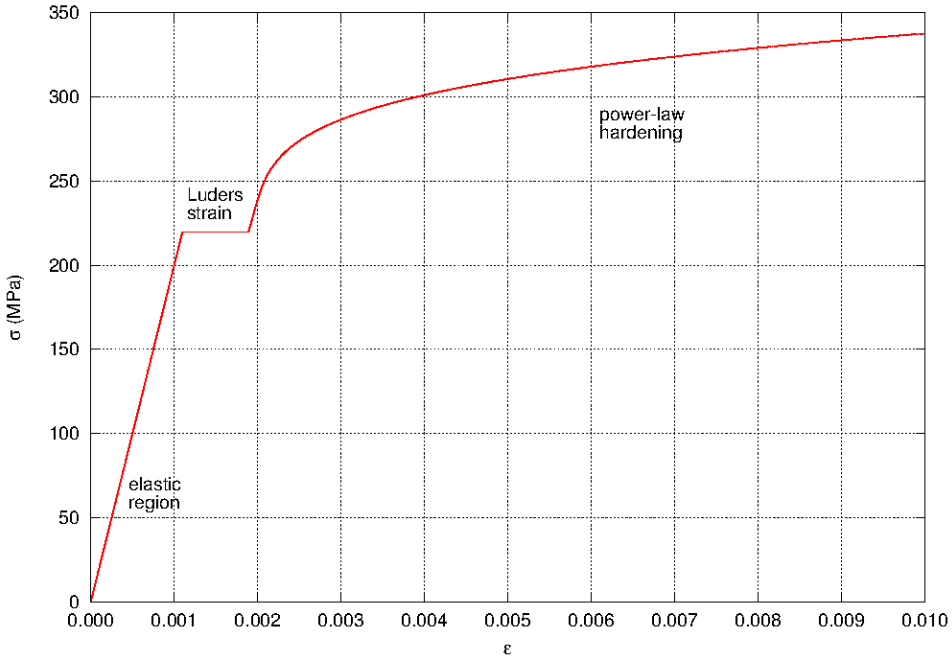


Figure 4-20. Typical stress-strain response for the power-law hardening model.

$$\phi(\sigma_{ij}) = \sqrt{\frac{3}{2}s_{ij}s_{ij}} \quad (4.8.7)$$

where s_{ij} are the components of the deviatoric stress

$$s_{ij} = \sigma_{ij} - \frac{1}{3}\delta_{ij}\sigma_{kk} \quad (4.8.8)$$

Unlike the elastic-plastic model 4.7, the power-law hardening model does not allow for kinematic hardening, so there is no back stress.

4.8.2. Implementation

The elastic-plastic power-law hardening model is implemented using a predictor-corrector algorithm. First, an elastic trial stress state is calculated. This is done by assuming that the rate of deformation is completely elastic

$$T_{ij}^{tr} = T_{ij}^n + \Delta t (\lambda\delta_{ij}d_{kk} + 2\mu d_{ij}) \quad (4.8.9)$$

The trial stress state is decomposed into a pressure and a deviatoric stress

$$p^{tr} = \frac{1}{3} T_{kk}^{tr} \quad ; \quad s_{ij}^{tr} = T_{ij}^{tr} - p^{tr} \delta_{ij} \quad (4.8.10)$$

The effective trial stress is calculated and used in the yield function (4.8.3).

$$f(s_{ij}^{tr}, \bar{\varepsilon}^p) = \phi(s_{ij}^{tr}) - \bar{\sigma}(\bar{\varepsilon}^p) \quad (4.8.11)$$

If $f \leq 0$ then the strain rate is elastic and the stress update is finished. If $f > 0$ then plastic deformation has occurred and a radial return algorithm determines the extent of plastic deformation.

The normal to the yield surface is assumed to lie in the direction of the trial stress state. This gives us the following expression for N_{ij}

$$N_{ij} = \frac{s_{ij}^{tr}}{\|s_{ij}^{tr}\|} \quad (4.8.12)$$

Using a backward Euler algorithm, the final deviatoric stress state is

$$s_{ij}^{n+1} = s_{ij}^{tr} - \Delta t 2\mu d_{ij}^p \quad (4.8.13)$$

where the plastic strain increment is

$$\Delta d_{ij}^p = \sqrt{\frac{3}{2}} \Delta \bar{\varepsilon}^p N_{ij} \quad (4.8.14)$$

The equation for the change in the equivalent plastic strain over the load step is found as the solution to

$$3\mu \Delta \bar{\varepsilon}^p + \bar{\sigma}(\bar{\varepsilon}_n + \Delta \bar{\varepsilon}^p) - \phi^{tr} + f_n = 0 \quad (4.8.15)$$

4.8.3. Verification

The elastic-plastic power-law hardening model is verified for uniaxial stress and pure shear. The elastic properties used in these analyses are $E = 70$ GPa and $\nu = 0.25$. The hardening law used for the model is

$$\bar{\sigma}(\bar{\varepsilon}^p) = \sigma_y + A \langle \bar{\varepsilon}^p - \varepsilon_L \rangle^n \quad (4.8.16)$$

For these calculations $\sigma_y = 200$ MPa, $A = 400$ MPa, $n = 0.25$, and $\varepsilon_L = 0.008$.

4.8.3.1. Uniaxial Stress

The elastic-plastic power-law hardening model is tested in uniaxial tension. The test looks at the axial stress and the lateral strain and compares these values against analytical results for the same problem. In this verification problem only the normal strains/stresses are needed, and the shear terms are not exercised.

For the uniaxial stress problem, the only non-zero stress component is σ_{11} . In the analysis that follows $\sigma_{11} = \sigma$. There are three non-zero strain components, ε_{11} , ε_{22} , and ε_{33} . In the analysis that follows $\varepsilon_{11} = \varepsilon$ and $\varepsilon_{22} = \varepsilon_{33}$. Furthermore, the axial elastic strain, $\varepsilon_{11}^e = \sigma/E$ will be denoted by ε^e .

The equivalent plastic strain, $\bar{\varepsilon}^p$, for this model is equivalent to ε_{11}^p , and is

$$\bar{\varepsilon}^p = \varepsilon - \frac{\bar{\sigma}(\bar{\varepsilon}^p)}{E} \quad (4.8.17)$$

This allows us, after yield, to parameterize the problem with the equivalent plastic strain.

For the lateral strains we need the lateral plastic strain. Plastic incompressibility ($\varepsilon_{kk}^p = 0$) gives us

$$\varepsilon_{22}^p = -\frac{1}{2}\bar{\varepsilon}^p \quad (4.8.18)$$

Combined with the lateral elastic strains we have the lateral strain as a function of the equivalent plastic strain

$$\varepsilon_{22} = -\nu \frac{\bar{\sigma}(\bar{\varepsilon}^p)}{E} - \frac{1}{2}\bar{\varepsilon}^p \quad (4.8.19)$$

The results are shown in Figures 4-21 and 4-22 and show agreement between the model in Adagio and the analytical results.

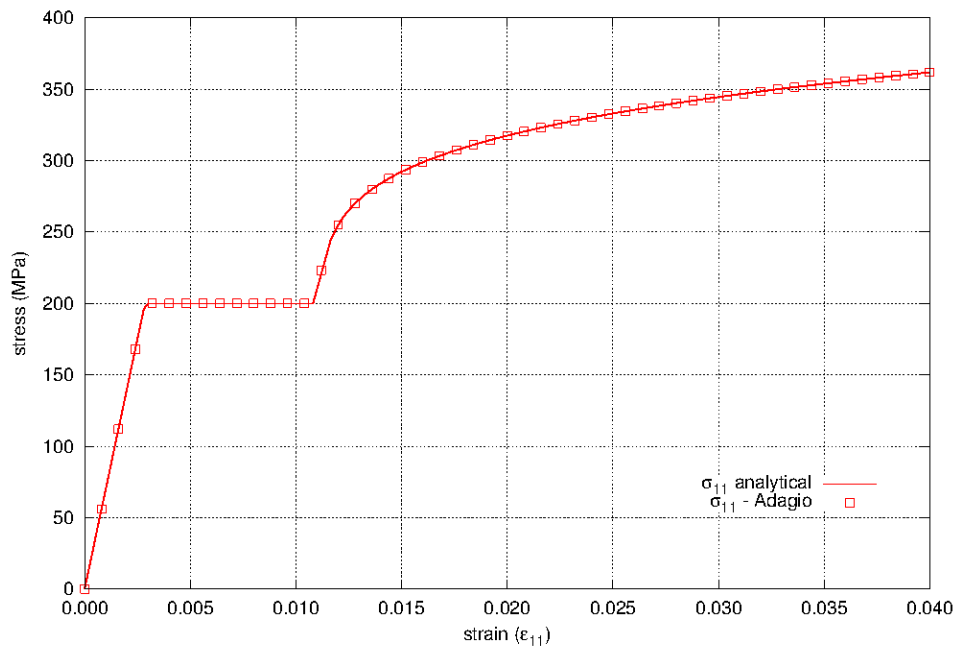


Figure 4-21. The axial stress as a function of axial strain for the elastic-plastic power-law hardening model.

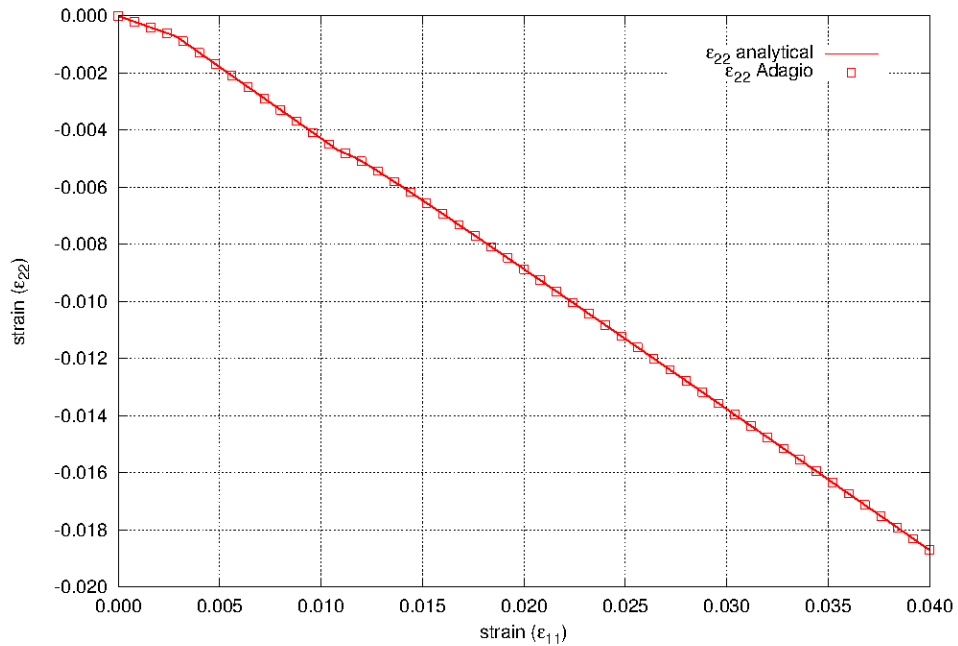


Figure 4-22. The lateral strain as a function of axial strain for the elastic-plastic power-law hardening model.

4.8.3.2. Pure Shear

The elastic-plastic power-law hardening model is tested in pure shear. The test looks at the shear stress as a function of the shear strain and compares these values against analytical results for the same problem. For the pure shear problem, the only non-zero strain component is ε_{12} and the only non-zero stress component is σ_{12} .

After yield, the shear stress as a function of the hardening curve is $\sigma_{12} = \bar{\sigma}(\bar{\varepsilon}^p) / \sqrt{3}$. The elastic shear strain is $\varepsilon_{12}^e = \sigma_{12}/2G$; the plastic shear strain is $\varepsilon_{12}^p = \sqrt{3}\bar{\varepsilon}^p/2$. Using this, the shear stress and strain are given as functions of the equivalent plastic strain

$$\sigma_{12} = \frac{\bar{\sigma}(\bar{\varepsilon}^p)}{\sqrt{3}} \quad ; \quad \varepsilon_{12} = \frac{\sqrt{3}}{2} \bar{\varepsilon}^p + \frac{1}{\sqrt{3}} \frac{\bar{\sigma}(\bar{\varepsilon}^p)}{2\mu} \quad (4.8.20)$$

This allows us, after yield, to parameterize the problem with $\bar{\varepsilon}^p$.

The results are shown in Figure 4-23 and show agreement between the model in Adagio and the analytical results.

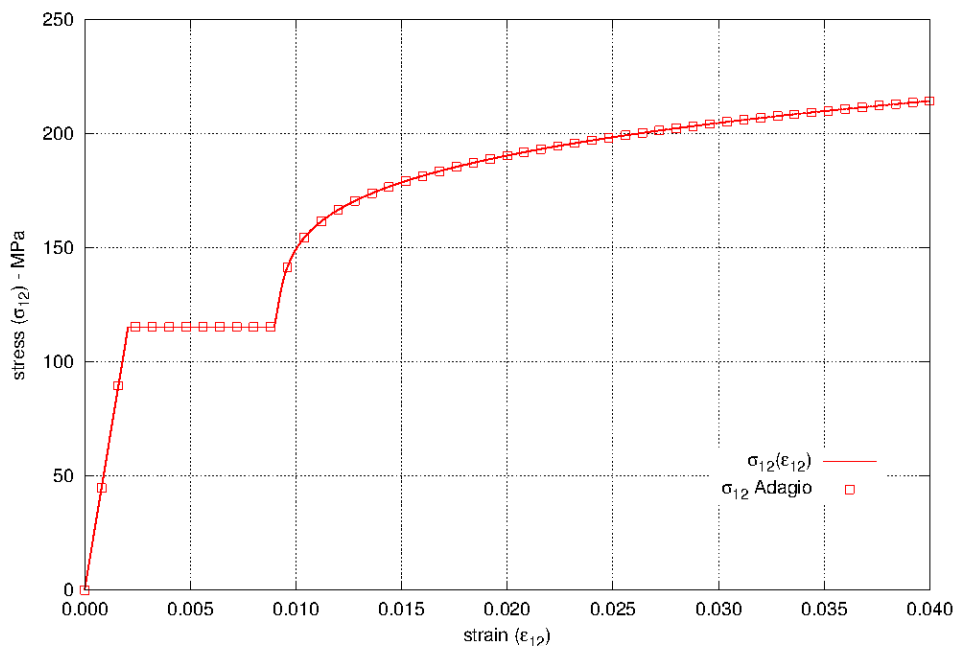


Figure 4-23. The shear stress as a function of shear strain for the elastic-plastic power-law hardening model.

4.8.4. User Guide

```

BEGIN PARAMETERS FOR MODEL EP_POWER_HARD
#
# Elastic constants
#
YOUNGS MODULUS = <real> E
POISSONS RATIO = <real> ν
SHEAR MODULUS = <real> G
BULK MODULUS = <real> K
LAMBDA = <real> λ
TWO MU = <real> 2μ
#
# Hardening behavior
#
YIELD STRESS = <real> σy
HARDENING CONSTANT = <real> A
HARDENING EXPONENT = <real> n
LUDERS STRAIN = <real> εL
END [PARAMETERS FOR MODEL EP_POWER_HARD]

```

Output variables available for this model are listed in Table 4-7 and Table 4-8. For information about the elastic-plastic power-law hardening model, consult [2].

Table 4-7. State Variables for EP POWER HARD Model

Name	Description
EQPS	equivalent plastic strain, $\bar{\epsilon}^p$
TENSILE_EQPS	equivalent plastic strain only accumulated when the material is in tension (trace of stress tensor is positive)
RADIUS	radius of yield surface, R
ITERATIONS	number of radial return iterations

Table 4-8. State Variables for EP POWER HARD Model for Shells

Name	Description
EQPS	equivalent plastic strain, $\bar{\varepsilon}^p$
TENSILE_EQPS	equivalent plastic strain only accumulated when the material is in tension (trace of stress tensor is positive)
RADIUS	radius of yield surface, R
ITERATIONS	number of radial return iterations
ERROR	error in plane stress iterations
PS_ITER	plane stress iterations

REFERENCES

- [1] C. M. Stone, G. W. Wellman, and R. D. Krieg. A vectorized elastic/plastic power law hardening material model including Lüders strains. Technical Report SAND90-0153, Sandia National Laboratories, Albuquerque, NM, March 1990. [pdf](#).
- [2] C.M. Stone. SANTOS – a two-dimensional finite element program for the quasistatic, large deformation, inelastic response of solids. Technical Report SAND90-0543, Sandia National Laboratories, Albuquerque, NM, 1996. [pdf](#).

4.9. DUCTILE FRACTURE MODEL

4.9.1. Theory

The ductile fracture model is identical to the elastic-plastic power-law hardening model with the addition of a failure criterion and an isotropic decay of the stress to zero during the failure process within the constitutive model. To accomplish this task, the tearing parameter, t_p , proposed by Wellman [1] is introduced and the functional form as given as

$$t_p = \int_0^{\varepsilon} \left\langle \frac{2\sigma_{\max}}{3(\sigma_{\max} - \sigma_m)} \right\rangle^4 d\bar{\varepsilon}^p \quad (4.9.1)$$

where σ_{\max} is the maximum principal stress, and σ_m is the mean stress. It can also be noted that the tearing parameter evolves during the plastic deformation regime as indicated by integrating over the effective plastic strain, $\bar{\varepsilon}^p$. The angle brackets denoting the Macaulay brackets, where

$$\langle x \rangle = \begin{cases} 0 & \text{if } x \leq 0 \\ x & \text{if } x > 0 \end{cases}, \quad (4.9.2)$$

are used to ensure that the failure process occurs only with tensile stress states and prevent “damage healing”. The failure process then initiates at a critical tearing parameter, t_p^{crit} , and the corresponding stress decay occurs over a strain interval corresponding to the *critical crack opening strain*, $\varepsilon_{\text{ccos}}$. Importantly, the $\varepsilon_{\text{ccos}}$ serves a dual role in that it may also be used to control the energy dissipated during failure. With respect to the latter point, careful selection of the critical crack opening strain may be used to ensure consistent energy is dissipated through different meshes. This decay process is isotropic and linear with the current damage value being equivalent to the ratio of crack opening strain in the direction of the maximum principal stress to the critical value.

4.9.2. Implementation

The ductile fracture model seeks to capture both the nonlinear elastic-plastic and fracture responses of a ductile metal. Independently, each of these requirements necessitates the use of a nonlinear solution algorithm and the combination of the two is even more complex. This consideration is compounded by the relaxation and softening observed during the failure process that introduces additional complications for the global finite element solver. For this discussion, however, the focus is solely on the underlying numerical treatment of the failure process at the constitutive level. The solution of the elastic-plastic constitutive problem was discussed in detail in Section 4.8.2 while details of the implications at the global finite element problem are found in the Sierra/SM User’s Guide [2]. With respect to the latter, it is important to note that in quasistatic cases the ductile fracture model is tightly integrated with the multilevel CONTROL FAILURE capabilities although details of this coupling are left to [1, 2].

Prior to fracture initiation – while $t_p^{n+1} < t_p^{\text{crit}}$ – the ductile fracture model is exactly that of the elastic-plastic power law. Through this process the tearing parameter is continually calculated at the plastically converged state. When fracture initiation is first detected – $t_p^{n+1} \geq t_p^{\text{crit}}$ – the direction of the maximum principal stress, denoted by the normalized vector n_i^{cr} , is determined and stored. Regardless of loading path, this vector does not change during the unloading process. Additionally, for this first initial failure step, the unrotated stress tensor, T_{ij} must be set equal to its maximum value, T_{ij}^{crit} before any unloading may be performed. This maximum value is simply given by,

$$T_{ij}^{\text{crit}} = T_{ij}^n + (T_{ij}^{tr} - T_{ij}^n) \frac{t_p^{\text{crit}} - t_p^n}{t_p^{n+1} - t_p^n} \quad (4.9.3)$$

with T_{ij}^{tr} being the elastic trial stress. As alluded to in the prior section, a linear decay based on the crack opening strain in the direction of maximum stress, ε_{cos} , is utilized. To determine this decay value, the crack opening strain increment is first found via

$$d\varepsilon_{\text{cos}}^{n+1} = \langle \beta n_i^{cr} d_{ij}^{n+1} n_j^{cr} \rangle, \quad (4.9.4)$$

where d_{ij}^{n+1} is the total unrotated rate of deformation and β is a partitioning factor between plastic and crack opening strains and takes the value of 1 for all loading steps *except* the initiation step. The “ $\langle \cdot \rangle$ ” are the Macaulay brackets. During the first fracture step,

$$\beta = \frac{t_p^{n+1} - t_p^{\text{crit}}}{t_p^{n+1} - t_p^n}. \quad (4.9.5)$$

The current crack opening strain is then simply,

$$\varepsilon_{\text{cos}}^{n+1} = \varepsilon_{\text{cos}}^n + d\varepsilon_{\text{cos}}^{n+1} \Delta t \quad (4.9.6)$$

and the decay value, α^{n+1} , is then found as,

$$\alpha^{n+1} = \max \left[0, \frac{\varepsilon_{\text{ccos}} - \varepsilon_{\text{cos}}^{n+1}}{\varepsilon_{\text{ccos}}} \right]. \quad (4.9.7)$$

To perform the actual stress decay, the hardening and yield values are proportionally decayed via,

$$\bar{\sigma}^{n+1}(\bar{\varepsilon}^p) = \alpha^{n+1} \bar{\sigma}^f; \quad \beta_{ij}^{n+1} = \alpha^{n+1} \beta_{ij}^n, \quad (4.9.8)$$

with $\bar{\sigma}^f = \phi(T_{ij}^{\text{crit}})$ being the critical yield stress associated with the yield surface, ϕ , and β_{ij} is the backstress tensor used with kinematic hardening. The decayed stress is then found by radially

returning to the reduced yield stress, $\bar{\sigma}^{n+1}(\bar{\varepsilon})$. As a J_2 deviatoric yield stress is used for the plastic response, the hydrostatic component of the stress tensor is similarly decayed.

4.9.3. Verification

The ductile fracture model is tested in uniaxial stress and pure shear. For these test problems, the Young's modulus and Poisson's ratio are $E = 70$ GPa and $\nu = 0.25$. The yield stress is taken to be $\sigma_y = 200$ MPa while the hardening constant and exponent are $A = 400$ MPa and $n = 0.25$, respectively, and the Lüders strain is 0.008. To describe failure, the critical tearing parameter is $t_p^{\text{crit}} = 0.025$ and the critical crack opening strain is $\varepsilon_{\text{ccos}} = 0.001$.

4.9.3.1. Uniaxial Stress

For loading in uniaxial stress the only non-zero stress component is σ_{11} . All other stress components are zero. If the stress state is on the yield surface then this stress is

$$\sigma_{11} = \bar{\sigma}(\bar{\varepsilon}^p), \quad (4.9.9)$$

with $\bar{\sigma}$ being the yield stress including any hardening effects associated with the evolution of the effective plastic strain, $\bar{\varepsilon}^p$. To evaluate the axial stress we need the equivalent plastic strain as a function of the axial strain, ε_{11} . If we equate the rate of plastic work we get

$$\bar{\sigma} \dot{\bar{\varepsilon}}^p = \sigma_{11} (\dot{\varepsilon}_{11} - \dot{\varepsilon}_{11}^e) \rightarrow \dot{\bar{\varepsilon}}^p = \dot{\varepsilon}_{11} - \dot{\varepsilon}_{11}^e = \dot{\varepsilon}_{11}^p \quad (4.9.10)$$

which, when integrated, gives us an implicit equation for the equivalent plastic strain

$$\bar{\varepsilon}^p = \left(\varepsilon_{11} - \frac{\bar{\sigma}(\bar{\varepsilon}^p)}{E} \right). \quad (4.9.11)$$

Alternatively, we write the axial strain as a function of the equivalent plastic strain, which allows us to parameterize the problem with $\bar{\varepsilon}^p$

$$\varepsilon_{11} = \bar{\varepsilon}^p + \frac{\bar{\sigma}(\bar{\varepsilon}^p)}{E}. \quad (4.9.12)$$

In uniaxial stress the pressure is $\sigma_{11}/3$ and the maximum principal stress is $\sigma_{\text{max}} = \sigma_{11}$. Using this in (4.9.1) we get

$$t_p = \bar{\varepsilon}^p \quad (4.9.13)$$

i.e. the tearing parameter is equal to the equivalent plastic strain. This result is shown in Figure 4-24a. The final value for the tearing parameter is a function of the number of steps, or the step size. The smaller the step size the closer the final value is to t_p^{crit} .

The axial stress as a function of axial strain is shown in Figure 4-24b. The axial stress depends on the elastic-plastic response until the critical tearing parameter is reached. As with the tearing parameter results, this point is time step dependent. Once the critical tearing parameter is reached the stress decay occurs over the critical crack opening strain.

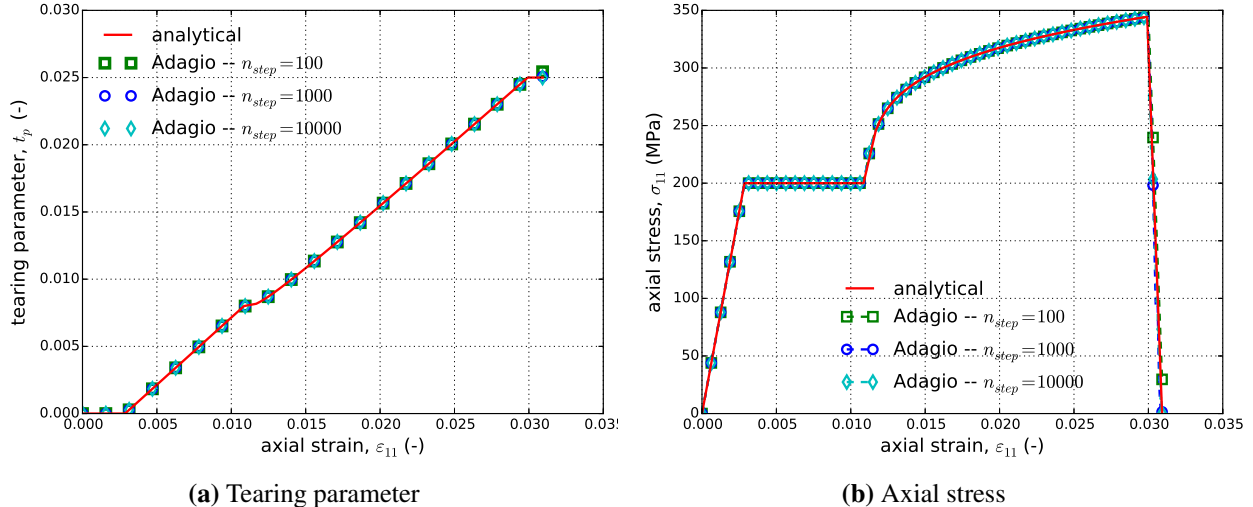


Figure 4-24. The (a) tearing parameter, t_p , and (b) axial stress-strain response for the ductile fracture model in uniaxial stress. The post failure reduction in stress depends on the time discretization or step size.

4.9.3.2. Pure Shear

For loading in pure shear the only non-zero stress component is σ_{12} . All other stress components are zero. If the stress state is on the yield surface then the shear stress is

$$\sigma_{12} = \frac{\bar{\sigma}(\bar{\varepsilon}^p)}{\sqrt{3}}. \quad (4.9.14)$$

To evaluate the shear stress we need the equivalent plastic strain as a function of the shear strain. If we equate the rate of plastic work we get

$$\bar{\sigma} \dot{\varepsilon}^p = 2\sigma_{12} (\dot{\varepsilon}_{12} - \dot{\varepsilon}_{12}^e) \rightarrow \dot{\varepsilon}^p = \frac{2}{\sqrt{3}} (\dot{\varepsilon}_{12} - \dot{\varepsilon}_{12}^e) \quad (4.9.15)$$

which, when integrated, gives us an implicit equation for the equivalent plastic strain

$$\bar{\varepsilon}^p = \frac{2}{\sqrt{3}} \left(\varepsilon_{12} - \frac{\bar{\sigma}(\bar{\varepsilon}^p)}{\sqrt{3}G} \right). \quad (4.9.16)$$

Alternatively, we write the shear strain, ε_{12} as a function of the equivalent plastic strain, which allows us to parameterize the problem with $\bar{\varepsilon}^p$

$$\varepsilon_{12} = \frac{\sqrt{3}}{2} \bar{\varepsilon}^p + \frac{\bar{\sigma}(\bar{\varepsilon}^p)}{\sqrt{3}G}. \quad (4.9.17)$$

In pure shear the pressure is zero, and the maximum principal stress is $\sigma_{\max} = \sigma_{12}$. Using this in (4.9.1) we get

$$t_p = \left(\frac{2}{3} \right)^4 \bar{\varepsilon}^p. \quad (4.9.18)$$

This result is shown in Figure 4-25, where the tearing parameter is a function of the shear strain. The final value for the tearing parameter is a function of the number of steps, or the step size. The smaller the step size the closer the final value is to t_p^{crit} .

The shear stress as a function of shear strain is shown in Figure 4-26. The shear stress depends on the elastic-plastic response until the critical tearing parameter is reached. As with the tearing parameter results, this point is time step dependent. Once the critical tearing parameter is reached the stress decay occurs over the critical crack opening strain.

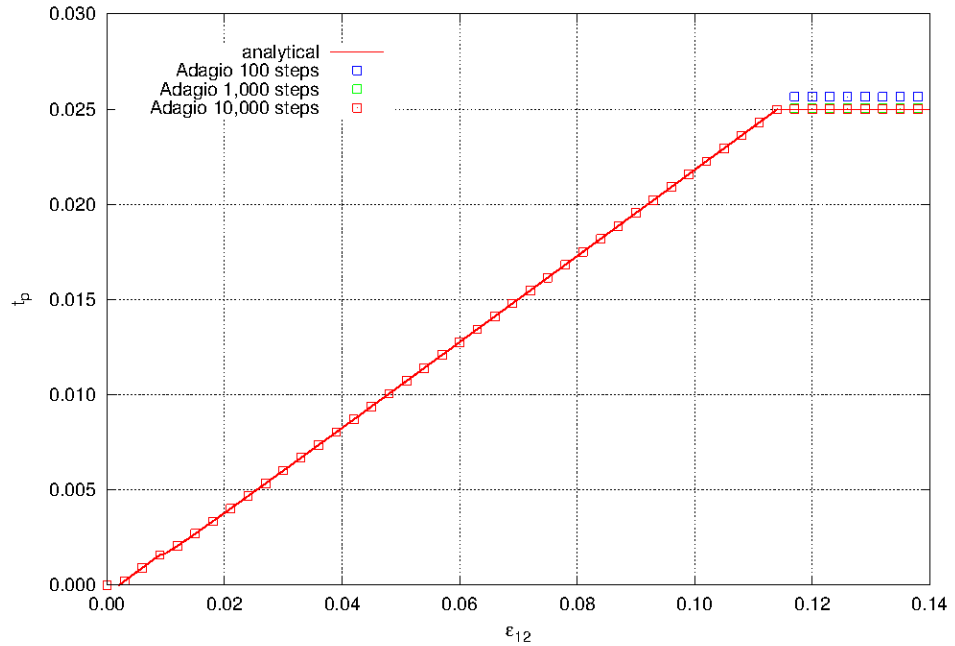


Figure 4-25. The tearing parameter, t_p , in pure shear. The maximum tearing parameter depends on the time discretization or step size.

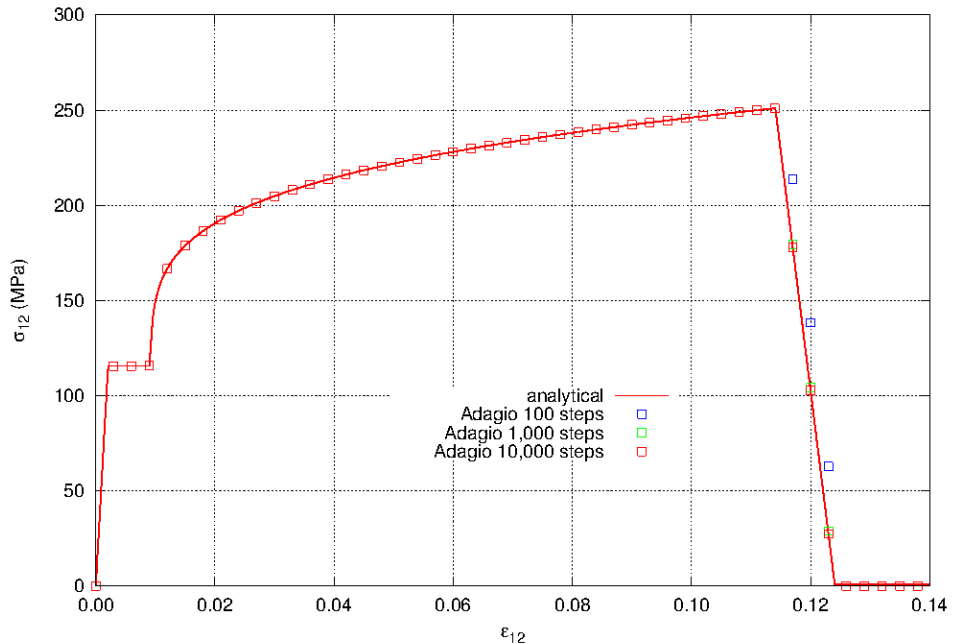


Figure 4-26. Shear stress vs. shear strain for the ductile fracture model in pure shear. The post failure reduction in stress depends on the time discretization or step size.

4.9.4. User Guide

```
BEGIN PARAMETERS FOR MODEL DUCTILE_FRACTURE
#
# Elastic constants
#
YOUNGS MODULUS = <real> E
POISSONS RATIO = <real> ν
SHEAR MODULUS = <real> G
BULK MODULUS = <real> K
LAMBDA = <real> λ
TWO MU = <real> 2μ
#
# Yield surface parameters
#
YIELD STRESS = <real> σy
HARDENING CONSTANT = <real> A
HARDENING EXPONENT = <real> n
LUDERS STRAIN = <real> εL
#
# Failure parameters
#
CRITICAL TEARING PARAMETER = <real> tpcrit
CRITICAL CRACK OPENING STRAIN = <real> εccos
END [PARAMETERS FOR MODEL DUCTILE_FRACTURE]
```

Output variables available for this model are listed in Table 4-9. For information about the ductile fracture material model, consult [1].

Table 4-9. State Variables for DUCTILE FRACTURE Model

Name	Description
EQPS	equivalent plastic strain, $\bar{\epsilon}^p$
RADIUS	radius of yield surface, R
BACK_STRESS	back stress - tensor α_{ij}
TEARING_PARAMETER	Current value of the integrated tearing parameter
CRACK_OPENING_STRAIN	Current value of the crack opening strain. Will be zero prior to reaching the maximum tearing parameter.
FAILURE_DIRECTION	Crack opening direction (maximum principal stress direction at failure) - vector
DF_STRAIN_XX	XX component of current strain
DF_STRAIN_YY	YY component of current strain
DF_STRAIN_ZZ	ZZ component of current strain
DF_STRAIN_XY	XY component of current strain
DF_STRAIN_YZ	YZ component of current strain
DF_STRAIN_ZX	ZX component of current strain
MAX_RADIUS	Yield surface radius at failure
MAX_PRESS	Stress pressure norm at failure

REFERENCES

- [1] G. W. Wellman. A simple approach to modeling ductile failure. Technical Report SAND2012-1343, Sandia National Laboratories, Albuquerque, NM, June 2012. [pdf](#).
- [2] Sierra/SolidMechanics Team. Sierra/SolidMechanics VOTD User's Guide. Technical Report In draft, Sandia National Laboratories, Albuquerque, NM, 2019.

4.10. MULTILINEAR ELASTIC-PLASTIC MODEL

4.10.1. Theory

The multilinear elastic-plastic model is a generalization of the standard rate independent plasticity models already presented - the linear and power law hardening models. However, rather than having a specific functional form, the multilinear hardening model allows the user to input a piecewise linear function for the hardening curve. The rate form of the constitutive equation assumes an additive split of the rate of deformation into an elastic and plastic part such that

$$D_{ij} = D_{ij}^e + D_{ij}^p. \quad (4.10.1)$$

The stress rate only depends on the elastic strain rate so that,

$$\dot{\sigma}_{ij} = \mathbb{C}_{ijkl} D_{kl}^e, \quad (4.10.2)$$

where \mathbb{C}_{ijkl} are the components of the fourth-order, isotropic elasticity tensor.

The key to the model is finding the plastic rate of deformation. For associated flow, the plastic rate of deformation is in the direction normal to the yield surface. With a yield surface given by

$$\phi(\sigma_{ij}) - \bar{\sigma}(\bar{\varepsilon}^p) = 0 \quad (4.10.3)$$

then the plastic rate of deformation can be written as

$$D_{ij}^p = \dot{\gamma} \frac{\partial \phi}{\partial \sigma_{ij}}. \quad (4.10.4)$$

For this model the yield surface is taken to be a von Mises yield surface, such that

$$\phi(\sigma_{ij}) = \sqrt{\frac{3}{2} s_{ij} s_{ij}} \quad (4.10.5)$$

where s_{ij} are the components of the deviatoric stress

$$s_{ij} = \sigma_{ij} - \frac{1}{3} \delta_{ij} \sigma_{kk}. \quad (4.10.6)$$

For simplicity it is easier to write (4.10.4) in terms of the normal to the yield surface

$$D_{ij}^p = \dot{\gamma} N_{ij} \quad ; \quad N_{ij} = \frac{\partial \phi}{\partial \sigma_{ij}} / \left\| \frac{\partial \phi}{\partial \sigma_{ij}} \right\| \quad (4.10.7)$$

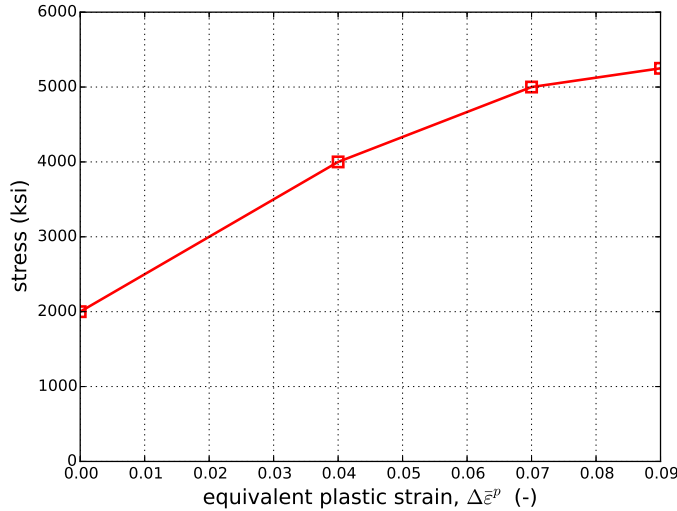


Figure 4-27. An example of a multilinear elastic-plastic stress-strain curve.

The model also incorporates temperature dependence in that the elastic properties and the yield stress can be functions of temperature. This is not as general as having the yield curves depend on temperature. For that behavior the thermoelastic-plastic model can be used.

An example stress vs. plastic strain hardening curve is shown in Figure 4-27. This curve was generated for a loading case of uniaxial strain. In this case, the effective stress is the same as the uniaxial. Therefore, for use with the multilinear elastic-plastic model this curve would simply have to be discretized and used as input.

4.10.2. Implementation

The multilinear elastic-plastic model is implemented using a predictor-corrector algorithm. First, an elastic trial stress state is calculated. This is done in the unrotated configuration (see Section 4.1) by assuming that the rate of deformation is completely elastic

$$T_{ij}^{tr} = T_{ij}^n + \Delta t (\lambda \delta_{ij} d_{kk} + 2\mu d_{ij}) . \quad (4.10.8)$$

The trial stress state is decomposed into a pressure and a deviatoric stress

$$p^{tr} = \frac{1}{3} T_{kk}^{tr} ; \quad s_{ij}^{tr} = T_{ij}^{tr} - p^{tr} \delta_{ij} \quad (4.10.9)$$

The effective trial stress is calculated and used with the yield function (4.8.3),

$$f(s_{ij}^{tr}, \bar{\varepsilon}^p) = \phi(s_{ij}^{tr}) - \bar{\sigma}(\bar{\varepsilon}^p). \quad (4.10.10)$$

If $f \leq 0$ then the response is elastic and the stress update is finished. If $f > 0$ then plastic deformation has occurred and a radial return algorithm is used to determine the extent of this behavior.

The model assumes associated flow such that the normal to the yield surface lies in the direction of the trial stress state. This leads to the following expression for the normal, N_{ij} ,

$$N_{ij} = \frac{s_{ij}^{tr}}{\|s_{ij}^{tr}\|}. \quad (4.10.11)$$

Using a backward Euler algorithm, the final deviatoric stress state may be written as

$$s_{ij}^{n+1} = s_{ij}^{tr} - \Delta t 2\mu d_{ij}^p \quad (4.10.12)$$

where the plastic strain increment, Δd_{ij}^p , is

$$\Delta d_{ij}^p = \sqrt{\frac{3}{2}} \Delta \bar{\varepsilon}^p N_{ij}. \quad (4.10.13)$$

Thus, to determine the response of the material the increment of the effective plastic strain, $\Delta \bar{\varepsilon}^p$, needs to be determined. This may be done by solving the linearized consistency equation over the load step that is written as,

$$3\mu \Delta \bar{\varepsilon}^p + \bar{\sigma}(\bar{\varepsilon}_n + \Delta \bar{\varepsilon}^p) - \phi^{tr} + f_n = 0. \quad (4.10.14)$$

4.10.3. Verification

The multilinear elastic-plastic material model is verified for uniaxial stress and pure shear. The elastic properties used in these analyses are $E = 70$ GPa and $\nu = 0.25$. In order to appropriately verify this model, the hardening curve must have a functional form to appropriately determine an analytical solution. Here, the hardening law used for the model is a Voce law with the following form

$$\bar{\sigma}(\bar{\varepsilon}^p) = \sigma_y + A(1 - \exp(-n\bar{\varepsilon}^p)). \quad (4.10.15)$$

In the numerical analyses, this expression is discretized at a series of plastic strain values and used as input. For these calculations $\sigma_y = 200$ MPa, $A = 200$ MPa, and $n = 20$.

4.10.3.1. Uniaxial Stress

The multilinear elastic-plastic model is tested in uniaxial tension. The test looks at the axial stress and the lateral strain and compares these values against analytical results for the same problem. In this verification problem only the normal strains/stresses are needed, and the shear terms are not exercised.

For the uniaxial stress problem, the only non-zero stress component is σ_{11} . In the analysis that follows $\sigma_{11} = \sigma$. There are three non-zero strain components, ε_{11} , ε_{22} , and ε_{33} . In the analysis that follows $\varepsilon_{11} = \varepsilon$ and $\varepsilon_{22} = \varepsilon_{33}$. Furthermore, the axial elastic strain, $\varepsilon_{11}^e = \sigma/E$ will be denoted by ε^e .

The equivalent plastic strain, $\bar{\varepsilon}^p$, for this model is equivalent to ε_{11}^p , and is

$$\bar{\varepsilon}^p = \varepsilon - \frac{\bar{\sigma}(\bar{\varepsilon}^p)}{E} \quad (4.10.16)$$

This allows us, after yield, to parameterize the problem with the equivalent plastic strain.

For the lateral strains we need the lateral plastic strain. Incompressibility gives us

$$\bar{\varepsilon}_{22}^p = -\frac{1}{2}\bar{\varepsilon}^p \quad (4.10.17)$$

Combined with the lateral elastic strains we have the lateral strain as a function of the equivalent plastic strain

$$\varepsilon_{22} = -\nu \frac{\bar{\sigma}(\bar{\varepsilon}^p)}{E} - \frac{1}{2}\bar{\varepsilon}^p \quad (4.10.18)$$

The results are shown in Figures 4-28 and 4-29 and show agreement between the model in Adagio and the analytical results.

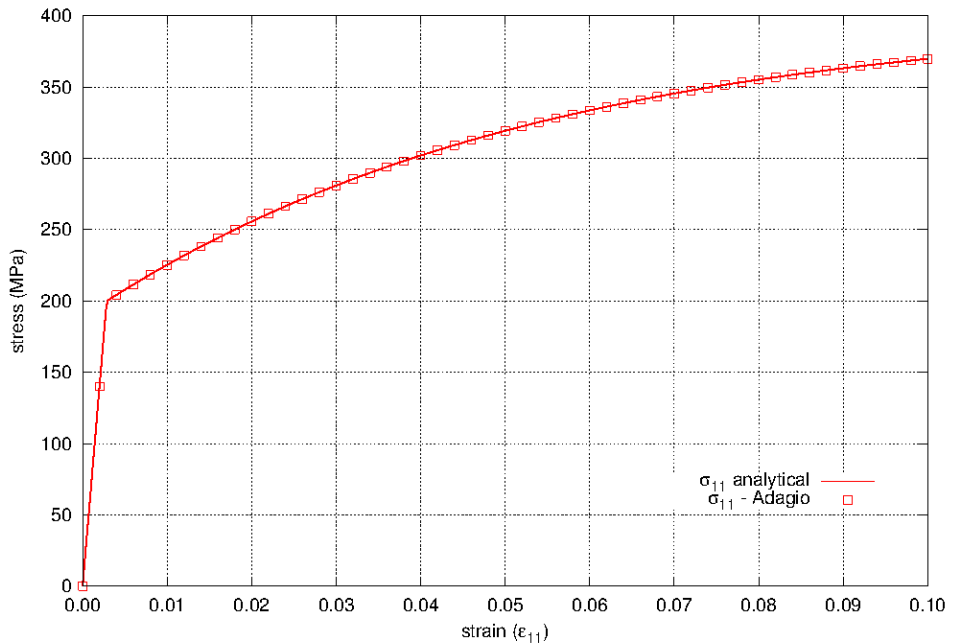


Figure 4-28. The axial stress as a function of axial strain for the multilinear elastic-plastic model with an analytical Voce law for the hardening model.

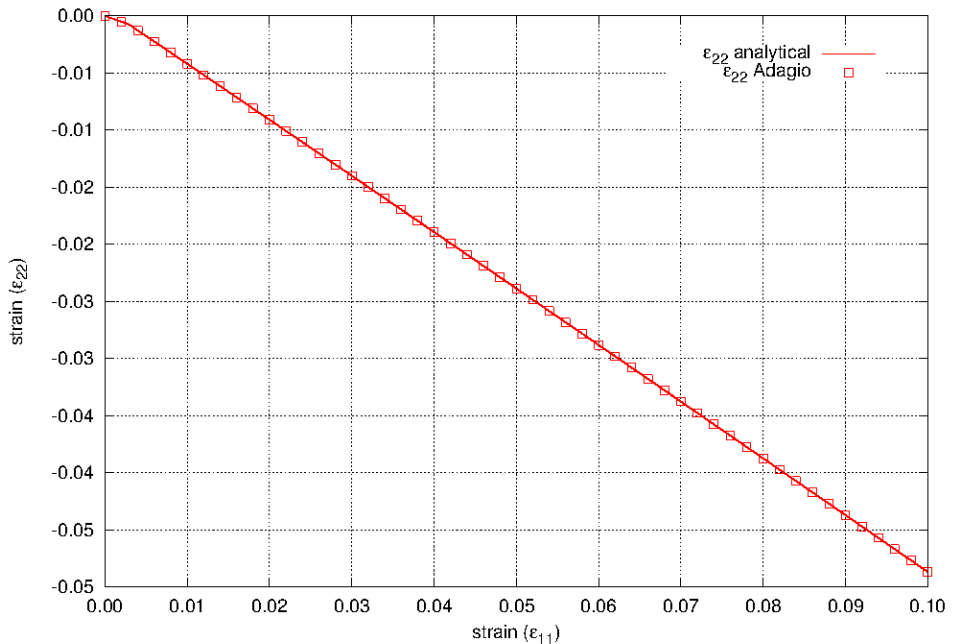


Figure 4-29. The lateral strain as a function of axial strain for the multilinear elastic-plastic model with an analytical Voce law for the hardening model.

4.10.3.2. Pure Shear

The multilinear elastic-plastic model is tested in pure shear. The test looks at the shear stress as a function of the shear strain and compares these values against analytical results for the same problem. For the pure shear problem, the only non-zero strain component is ε_{12} and the only non-zero stress component is σ_{12} .

After yield, the shear stress as a function of the hardening curve is $\sigma_{12} = \bar{\sigma}(\bar{\varepsilon}^p) / \sqrt{3}$. The elastic shear strain is $\varepsilon_{12}^e = \sigma_{12}/2G$; the plastic shear strain is $\varepsilon_{12}^p = \sqrt{3}\bar{\varepsilon}^p/2$. Using this, the shear stress and strain are given as functions of the equivalent plastic strain

$$\sigma_{12} = \frac{\bar{\sigma}(\bar{\varepsilon}^p)}{\sqrt{3}} \quad ; \quad \varepsilon_{12} = \frac{\sqrt{3}}{2} \bar{\varepsilon}^p + \frac{1}{\sqrt{3}} \frac{\bar{\sigma}(\bar{\varepsilon}^p)}{2G} \quad (4.10.19)$$

This allows us, after yield, to parameterize the problem with $\bar{\varepsilon}^p$.

The results are shown in Figure 4-30 and show agreement between the model in Adagio and the analytical results.

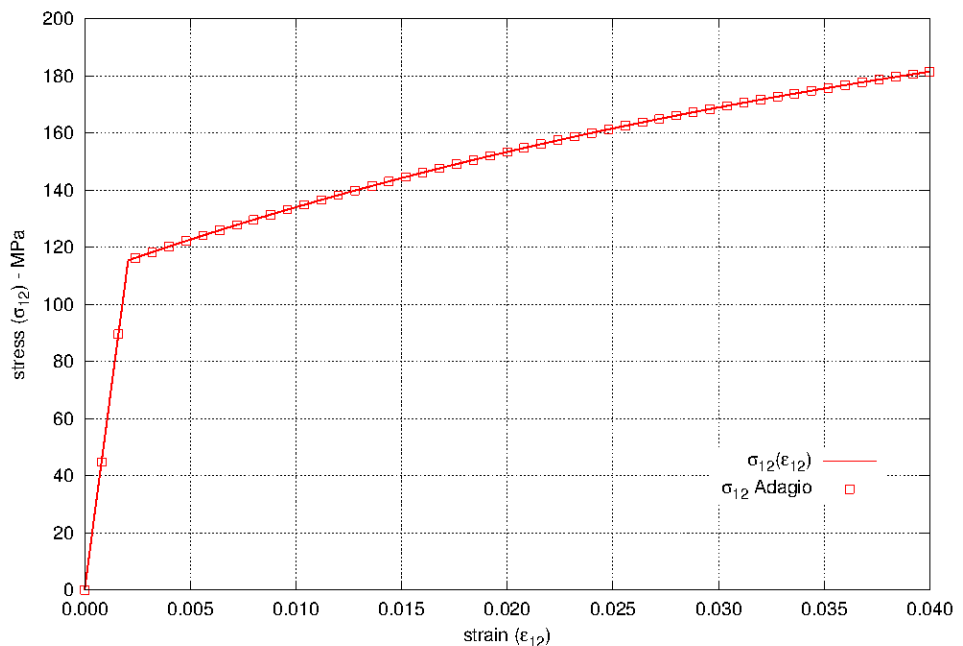


Figure 4-30. The shear stress as a function of shear strain for the multilinear elastic-plastic model with an analytical Voce law for the hardening model.

4.10.4. User Guide

```

BEGIN PARAMETERS FOR MODEL MULTILINEAR_EP
#
# Elastic constants
#
YOUNGS MODULUS = <real> E
POISONS RATIO = <real> ν
SHEAR MODULUS = <real> G
BULK MODULUS = <real> K
LAMBDA = <real> λ
TWO MU = <real> 2μ
#
# Hardening behavior
#
YIELD STRESS = <real> σy
BETA = <real> β (1.0)
HARDENING FUNCTION = <string> hardening_function_name
#
# Functions
#
YOUNGS MODULUS FUNCTION = <string> ym_function_name
POISONS RATIO FUNCTION = <string> pr_function_name
YIELD STRESS FUNCTION = <string> yield_stress_function_name
END [PARAMETERS FOR MODEL MULTILINEAR_EP]

```

Output variables available for this model are listed in Table 4-10 and Table 4-11.

Table 4-10. State Variables for MULTILINEAR EP Model

Name	Description
EQPS	equivalent plastic strain
TENSILE_EQPS	equivalent plastic strain only accumulated when the material is in tension (trace of stress tensor is positive)
RADIUS	radius of yield surface
BACK_STRESS	back stress (symmetric tensor)
YOUNGS_MODULUS	the current Young's modulus as a function of temperature
POISONS_RATIO	the current Poisson's ratio as a function of temperature
YIELD_STRESS	the current yield stress as a function of temperature
ITERATIONS	radial return iterations
YIELD_FLAG	inside (0) or on (1) the yield surface

Table 4-11. State Variables for MULTILINEAR EP Model for Shells

Name	Description
EQPS	equivalent plastic strain
TENSILE_EQPS	equivalent plastic strain only accumulated when the material is in tension (trace of stress tensor is positive)
RADIUS	radius of yield surface
BACK_STRESS	back stress (symmetric tensor)
YOUNGS_MODULUS	the current Young's modulus as a function of temperature
POISSONS_RATIO	the current Poisson's ratio as a function of temperature
YIELD_STRESS	the current yield stress as a function of temperature
ITERATIONS	radial return iterations
ERROR	error in plane stress iterations
PS_ITER	plane stress iterations

4.11. MULTILINEAR ELASTIC-PLASTIC FAIL MODEL

4.11.1. Theory

Like the ductile fracture model, the multilinear elastic-plastic fail model is an extension of an existing plasticity model (multilinear elastic-plastic) to include a ductile failure criteria. Again, the tearing parameter criterion and failure propagation model of Wellman [1] is selected. Specifically, this approach uses a failure criterion (the tearing parameter, t_p) that is based on the history of the plastic strain and stress states. Most failure criteria for ductile failure involve some form of the stress triaxiality, or the ratio of the pressure and the effective (shear) stress. The tearing parameter, however, is slightly different in that it depends on the pressure and the maximum principal stress and is given as,

$$t_p = \int_0^{\varepsilon} \left\langle \frac{2\sigma_{\max}}{3(\sigma_{\max} - \sigma_m)} \right\rangle^m d\varepsilon_p, \quad (4.11.1)$$

with σ_{\max} and σ_m being the maximum principal and mean stresses, respectively. The exponent m is typically taken to be 4 while the $\langle \cdot \rangle$ are Macaulay brackets defined as,

$$\langle x \rangle = \begin{cases} 0 & x \leq 0 \\ x & x > 0 \end{cases}, \quad (4.11.2)$$

and introduced so that failure only occurs and propagates under tensile stress states. Failure then initiates when the tearing parameter, t_p , reaches a critical value, t_p^{crit} . After this point, the stress decays (to 0) in a linear fashion according to the ratio of the crack opening strain in the maximum principal stress direction to its critical value, $\varepsilon_{\text{ccos}}$. Modification and control of this latter parameter is important as it may be used to ensure consistent energy is dissipated through different meshes.

4.11.2. Implementation

The multilinear elastic-plastic fail model seeks to capture both the nonlinear elastic-plastic and fracture responses of a ductile metal. Independently, each of these requirements necessitates the use of a nonlinear solution algorithm and the combination of the two is even more complex. This consideration is compounded by the relaxation and softening observed during the failure process that introduces additional complications for the global finite element solver. For this discussion, however, the focus is solely on the underlying numerical treatment of the failure process at the constitutive level. The solution of the elastic-plastic constitutive problem was discussed in detail in Section 4.10.2 while details of the implications at the global finite element problem are found in the Sierra/SM User's Guide [2]. With respect to the latter, it is important to note that the ductile fracture model is tightly integrated with the multilevel CONTROL FAILURE capabilities although details of this coupling are left to [1, 2].

Prior to fracture initiation – while $t_p^{n+1} < t_p^{\text{crit}}$ – the multilinear elastic-plastic fail model is the same as the “normal” multilinear elastic-plastic model. Through this process the tearing parameter is continually calculated at the plastically converged state. When fracture initiation is first detected – $t_p^{n+1} \geq t_p^{\text{crit}}$ – the crack direction (assumed aligned with the maximum principal stress), denoted by the normalized vector n_i^{cr} , is determined and stored. Regardless of loading path, this vector does not change during the unloading process. Additionally, for this first initial failure step, the unrotated stress tensor, T_{ij} must be updated to its maximum value, T_{ij}^{crit} before any unloading may be performed. This is done simply by,

$$T_{ij}^{\text{crit}} = T_{ij}^n + (T_{ij}^{tr} - T_{ij}^n) \frac{t_p^{\text{crit}} - t_p^n}{t_p^{n+1} - t_p^n}, \quad (4.11.3)$$

with T_{ij}^{tr} being the elastic trial stress. As alluded to in the prior section, a linear decay based on the crack opening strain in the direction of maximum stress, ε_{cos} , is utilized. To determine this decay value, the crack opening strain increment is first found via

$$d\varepsilon_{\text{cos}}^{n+1} = \langle \gamma n_i^{cr} d_{ij}^{n+1} n_j^{cr} \rangle, \quad (4.11.4)$$

where d_{ij}^{n+1} is the unrotated rate of deformation and γ is a partitioning factor between plastic and crack opening strains and takes the value of 1 for all loading steps *except* the initiation step and the “ $\langle \cdot \rangle$ ” are the Macaulay brackets. During the first fracture step,

$$\gamma = \frac{t_p^{n+1} - t_p^{\text{crit}}}{t_p^{n+1} - t_p^n}. \quad (4.11.5)$$

The current crack opening strain is then simply,

$$\varepsilon_{\text{cos}}^{n+1} = \varepsilon_{\text{cos}}^n + d\varepsilon_{\text{cos}}^{n+1} \Delta t. \quad (4.11.6)$$

and the decay factor, α , may be written as

$$\alpha^{n+1} = \max \left[0, \frac{\varepsilon_{\text{ccos}} - \varepsilon_{\text{cos}}^{n+1}}{\varepsilon_{\text{ccos}}} \right]. \quad (4.11.7)$$

Given the temperature dependence, stress decay is slightly more complicated than in the ductile fracture case. This task is primarily accomplished by decreasing the yield stress (radius) proportionally with the decay factor,

$$\bar{\sigma}^{n+1}(\bar{\varepsilon}^p) = \alpha^{n+1} \bar{\sigma}^f, \quad (4.11.8)$$

where $\bar{\sigma}^f = \phi(T^{\text{crit}})$ is the yield stress at failure. The decayed stress is then found by radially returning to this reduced yield stress. Similarly, the hydrostatic and von Mises effective stress at

failure (σ_m^f and $\bar{\sigma}_{vM}^f$, respectively) are also calculated and stored to appropriately constrain the stress state. An additional check is then performed to ensure (and if necessary modify) the decayed stress to ensure that,

$$\sigma_m \leq \alpha \sigma_m^f; \quad \bar{\sigma}_{vM} \leq \alpha \bar{\sigma}_{vM}^f. \quad (4.11.9)$$

4.11.3. Verification

The multilinear elastic-plastic model with failure has been tested with a number of verification tests. Specifically, uniaxial stress and uniaxial strain loadings are considered. For the elastic-plastic response, the same material properties as those in Section 4.10.3 are again considered. To this end, the Young's modulus and Poisson ratio are $E = 70$ GPa and $\nu = 0.25$, respectively, and a Voce hardening model of the form,

$$\bar{\sigma}(\bar{\varepsilon}^p) = \sigma_y + A(1 - \exp(-n\bar{\varepsilon}^p)), \quad (4.11.10)$$

is discretized and used. In this case, $\sigma_y = 200$ MPa, $A = 200$ MPa, and $n = 20$.

In terms of failure, the critical tearing parameter, t_p^{crit} is taken to be .04, the critical crack opening strain, $\varepsilon_{\text{ccos}}$, is .005 and $m = 4.0$.

4.11.3.1. Uniaxial Stress

To consider the uniaxial response, displacement controlled deformations are applied such that the only non-zero stress is the axial component, σ_{11} . Through such a loading path, three distinct regimes result. The first is the elastic domain with $t_p = 0$. Second is the plastic domain. During this stage,

$$\sigma_{11} = \bar{\sigma}(\bar{\varepsilon}^p), \quad (4.11.11)$$

and by considering the rate of plastic work and integrating yields the implicit (in terms of equivalent plastic strain) relation,

$$\bar{\varepsilon}^p = \left(\varepsilon_{11} - \frac{\bar{\sigma}(\bar{\varepsilon}^p)}{E} \right). \quad (4.11.12)$$

By rearranging, the axial strain may be found in terms of the plastic strain as,

$$\varepsilon_{11} = \bar{\varepsilon}^p + \frac{\bar{\sigma}(\bar{\varepsilon}^p)}{E}. \quad (4.11.13)$$

With this stress state ($\sigma_{ij} = \sigma_{11}\delta_{i1}\delta_{j1}$), the pressure is simply $\sigma_{11}/3$ and the maximum principal stress is $\sigma_{\text{max}} = \sigma_{11}$. From (4.11.1), the tearing parameter is then

$$t_p = \bar{\varepsilon}^p. \quad (4.11.14)$$

The final stage of deformation corresponds to the failure process in which the axial stress is,

$$\sigma_{11} = \alpha \sigma_{\text{peak}}, \quad (4.11.15)$$

and

$$\alpha = \frac{\varepsilon_{\text{ccos}} - (\varepsilon_{11} - \varepsilon_{\text{peak}})}{\varepsilon_{\text{ccos}}}. \quad (4.11.16)$$

In the preceding relations, σ_{peak} and $\varepsilon_{\text{peak}}$ are the axial stress and strain, respectively, at failure initiation. The former is simply $\sigma_{\text{peak}} = \bar{\sigma}(t_p^{\text{crit}})$ and $\varepsilon_{\text{peak}} = t_p^{\text{crit}} + \sigma_{\text{peak}}/E$.

The tearing parameter and axial stress evolution as a function of axial strain are presented in Figures 4-31a and 4-31b, respectively. Good agreement is observed between the results verifying the model capability under such a loading. Three different numerical load increments were considered in this analysis and some dependence on load step is noted in the post-failure response of Figure 4-31b. Even with this observation, the resulting agreement between the different responses is still quite good.

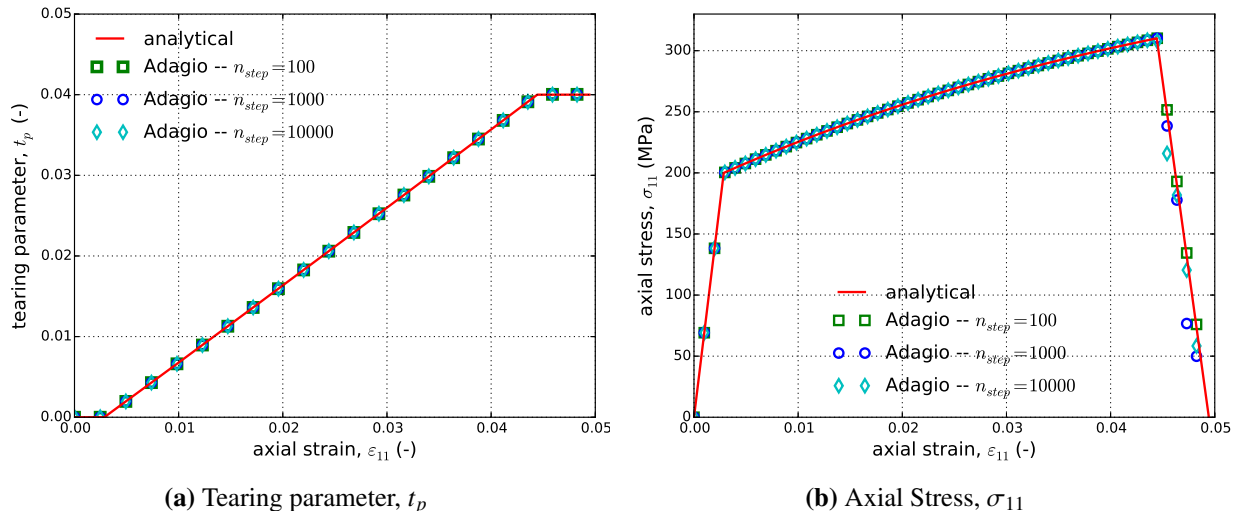


Figure 4-31. Analytical and numerical results of the tearing parameter and axial stress evolution through a uniaxial tension loading path as a function of the axial strain, ε_{11} .

4.11.3.2. Pure Shear

The analysis of the pure shear loading path follows closely with that of the ductile fracture model (Section 4.9.3.2). In this case, pure shear deformations are applied such that the only non-zero

stress and strain are σ_{12} and ε_{12} , respectively. Therefore, during plastic loading

$$\sigma_{12} = \frac{\bar{\sigma}}{\sqrt{3}}, \quad (4.11.17)$$

and by comparing the plastic rate of work,

$$\varepsilon_{12} = \frac{\sqrt{3}}{2} \bar{\varepsilon}^p + \frac{\bar{\sigma}(\bar{\varepsilon}^p)}{\sqrt{3}\mu}. \quad (4.11.18)$$

Additionally, as the stress state is purely in shear there is no hydrostatic stress and the maximum principal stress is simply $\sigma_{\max} = \sigma_{12}$ leading to an expression for the tearing parameter of the form,

$$t_p = \left(\frac{2}{3}\right)^4 \bar{\varepsilon}^p. \quad (4.11.19)$$

The stress then simply decays after the critical tearing parameter is reached. Numerical (from Adagio) and analytical results are presented in Figure 4-32. Specifically, the tearing parameter and shear stress evolutions are presented in Figures 4-32a and 4-32b, respectively. Clear agreement is noted indicating the ability of the model to capture the response over a variety of loading paths.

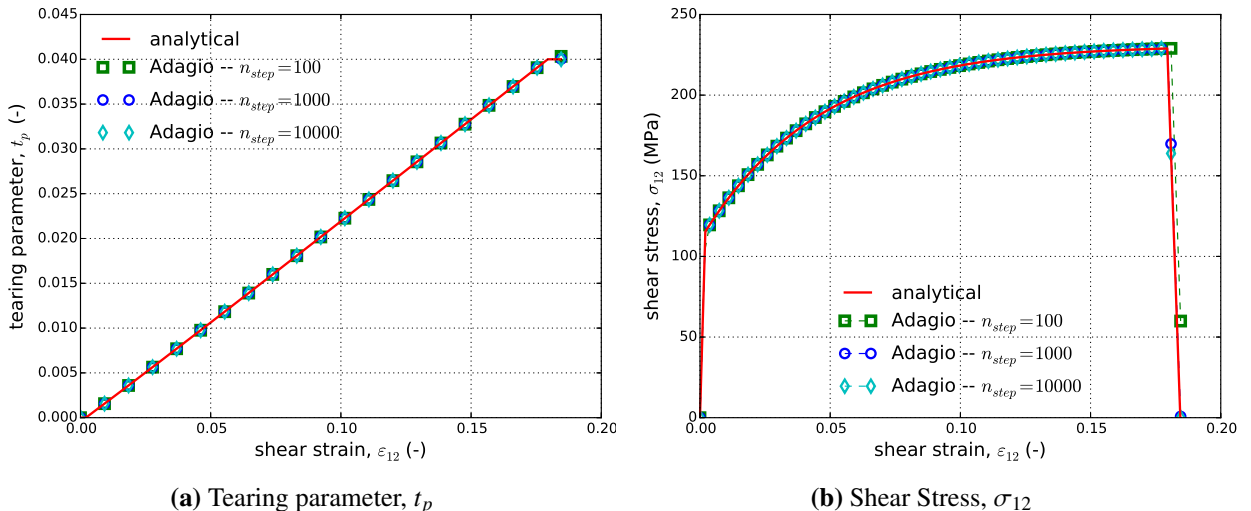


Figure 4-32. Analytical and numerical results of the tearing parameter and shear stress evolution through a pure shear loading path as a function of the shear strain, ε_{12} .

4.11.4. User Guide

```
BEGIN PARAMETERS FOR MODEL ML_EP_FAIL
#
# Elastic constants
#
YOUNGS MODULUS = <real> E
POISSONS RATIO = <real> ν
SHEAR MODULUS = <real> G
BULK MODULUS = <real> K
LAMBDA = <real> λ
TWO MU = <real> 2μ
#
# Hardening behavior
#
YIELD STRESS = <real> σy
BETA = <real> β (1.0)
HARDENING FUNCTION = <string> hardening_function_name
#
# Functions
#
YOUNGS MODULUS FUNCTION = <string> ym_function_name
POISSONS RATIO FUNCTION = <string> pr_function_name
YIELD STRESS FUNCTION = <string> yield_stress_function_name
#
# Failure parameters
#
CRITICAL TEARING PARAMETER = <real>  $t_p^{\text{crit}}$ 
CRITICAL CRACK OPENING STRAIN = <real> εccos
CRITICAL BIAXIALITY RATIO = <real> critical_ratio(0.0)
FAILURE EXPONENT = <real> m (4.0)
END [PARAMETERS FOR MODEL ML_EP_FAIL]
```

Output variables available for this model are listed in Table 4-12 and Table 4-13.

Table 4-12. State Variables for ML EP FAIL Model

Name	Variable Description
EQPS	Equivalent plastic strain
RADIUS	Radius of yield surface
BACK_STRESS	back stress - tensor
BACK_STRESS_XX	back stress - xx component
BACK_STRESS_YY	back stress - yy component
BACK_STRESS_ZZ	back stress - zz component
BACK_STRESS_XY	back stress - xy component
BACK_STRESS_YZ	back stress - yz component
BACK_STRESS_ZX	back stress - zx component
YOUNGS_MODULUS	Current Young's modulus as a function of temperature
POISSONS_RATIO	Current Poisson's ratio as a function of temperature
YIELD_STRESS	Current Yield stress as a function of temperature
TENSILE_EQPS	equivalent plastic strain only accumulated when the material is in tension (trace of stress tensor is positive)
ITERATIONS	radial return iterations
YIELD_FLAG	inside(0) or on(1) yield surface
TEARING_PARAMETER	Current integrated value of the tearing parameter. Zero until yield is reached
CRACK_OPENING_STRAIN	Current value of the crack opening strain. Zero until the critical tearing parameter is reached
FAILURE_DIRECTION	crack opening direction at failure - vector
FAILURE_DIRECTION_X	crack opening direction at failure - x component
FAILURE_DIRECTION_Y	crack opening direction at failure - y component
FAILURE_DIRECTION_Z	crack opening direction at failure - z component
MAX_RADIUS	maximum radius at initial failure
MAX_PRESSURE	maximum stress pressure norm at initial failure
CRITICAL_CRACK_OPENING_STRAIN	
CRITICAL_TEARING_PARAMETER	

Table 4-13. State Variables for ML EP FAIL Model for Shells

Name	Variable Description
EQPS	equivalent plastic strain
RADIUS	radius of yield surface
BACK_STRESS	back stress - tensor
BACK_STRESS_XX	back stress - xx component
BACK_STRESS_YY	back stress - yy component
BACK_STRESS_ZZ	back stress - zz component
BACK_STRESS_XY	back stress - xy component
BACK_STRESS_YZ	back stress - yz component
BACK_STRESS_ZX	back stress - zx component
YOUNGS_MODULUS	Current Young's modulus as a function of temperature
POISSONS_RATIO	Current Poisson's ratio as a function of temperature
YIELD_STRESS	Current Yield stress as a function of temperature
ITER	radial return iterations
ERROR	Error in plane stress iterations
PS_ITER	Plane stress iterations
TEARING_PARAMETER	Current integrated value of the tearing parameter. Zero until yield is reached
CRACK_OPENING_STRAIN	Current value of the crack opening strain. Zero until the critical tearing parameter is reached
FAILURE_DIRECTION	crack opening direction at failure - vector
FAILURE_DIRECTION_X	crack opening direction at failure - x component
FAILURE_DIRECTION_Y	crack opening direction at failure - y component
FAILURE_DIRECTION_Z	crack opening direction at failure - z component
RADIUS_MAX	maximum radius at initial failure
TENSILE_EQPS	equivalent plastic strain only accumulated when the material is in tension (trace of stress tensor is positive)

REFERENCES

- [1] G. W. Wellman. A simple approach to modeling ductile failure. Technical Report SAND2012-1343, Sandia National Laboratories, Albuquerque, NM, June 2012. [pdf](#).
- [2] Sierra/SolidMechanics Team. Sierra/SolidMechanics VOTD User's Guide. Technical Report In draft, Sandia National Laboratories, Albuquerque, NM, 2019.

4.12. JOHNSON-COOK MODEL

4.12.1. Theory

The Johnson-Cook model [1, 2] is an isotropic, hypoelastic plasticity model. Unlike the previously discussed models, the Johnson-Cook formulation is rate-*dependent* and as such is often considered for high-rate, finite strain simulations like those for impact. The viscoplastic response is phenomenological in that the form of the model is not derived from any physical mechanisms like other viscoplastic models, e.g. Zerilli-Armstrong [3], Steinberg-Guinan-Lund [4, 5], BCJ [6], and the MTS model [7, 8] to name a few. Like most other rate-dependent models, the current formulation utilizes an effective plastic strain rate, $\dot{\bar{\varepsilon}}^p$, to capture rate dependence.

As with other hypoelastic plasticity models, an additive decomposition of the total rate of deformation such that,

$$D_{ij} = D_{ij}^e + D_{ij}^p, \quad (4.12.1)$$

is used such that an objective stress rate of the form,

$$\dot{\bar{\sigma}}_{ij} = \mathbb{C}_{ijkl} D_{kl}^e, \quad (4.12.2)$$

with \mathbb{C}_{ijkl} being the fourth-order, isotropic elasticity tensor, may be used.

With respect to the yield behavior, the Johnson-Cook model incorporates both strain rate and temperature, θ , dependence. This leads to a yield function of the form,

$$f(\sigma_{ij}, \bar{\varepsilon}^p, \dot{\bar{\varepsilon}}^p, \theta) = \phi(\sigma_{ij}) - \bar{\sigma}(\bar{\varepsilon}^p, \dot{\bar{\varepsilon}}^p, \theta), \quad (4.12.3)$$

in which $\phi(\sigma_{ij})$ is the effective stress – the von Mises effective stress is used – and $\bar{\sigma}$ is the isotropic hardening function. Incorporating the temperature and rate dependency, the hardening function is written as,

$$\bar{\sigma}(\bar{\varepsilon}^p, \dot{\bar{\varepsilon}}^p, \theta) = [A + B(\bar{\varepsilon}^p)^N] [1 + C \langle \ln \dot{\bar{\varepsilon}}^{p*} \rangle] [1 - \theta^{*M}] \quad (4.12.4)$$

where $\bar{\varepsilon}^p$ is the equivalent plastic strain, $\dot{\bar{\varepsilon}}^{p*} = \dot{\bar{\varepsilon}}^p / \dot{\bar{\varepsilon}}_0$ is a dimensionless plastic strain rate, and θ^* is the homologous temperature. The quantities A , B , C , $\dot{\bar{\varepsilon}}_0$, N , and M are material parameters.

The Macaulay brackets in (4.12.4) ensure that $\bar{\sigma}$ is equal to the static flow stress

$\bar{\sigma}_s = [A + B(\bar{\varepsilon}^p)^N] [1 - \theta^{*M}]$ when $\dot{\bar{\varepsilon}}^p < \dot{\bar{\varepsilon}}_0$. The homologous temperature is defined as,

$$\theta^* = \frac{\theta - \theta_{\text{ref}}}{\theta_{\text{melt}} - \theta_{\text{ref}}}, \quad (4.12.5)$$

with θ , θ_{ref} , and θ_{melt} being the current, reference, and melt temperatures. Note, the temperature used internal to the Johnson-Cook model is NOT the standard prescribed “temperature” field.

Instead, the material temperature is initialized by a model input as θ_0 . By assuming adiabatic thermal conditions, subsequent plastic work raises the material temperature via,

$$\Delta\theta = \frac{\beta}{\rho C_v} \bar{\sigma} \dot{\bar{\varepsilon}}^p, \quad (4.12.6)$$

where ρ is the materials density, C_v is the specific heat, and β ($0 \leq \beta \leq 1$) is the fraction of plastic work that is converted to heat.

The Johnson-Cook model also has a failure criterion. The Johnson-Cook damage model [2] has a failure strain that is given by:

$$\varepsilon^f = (D_1 + D_2 \exp(D_3 \eta)) (1 + D_4 \ln \dot{\bar{\varepsilon}}^{p*}) (1 + D_5 \theta^*) \quad (4.12.7)$$

with D_1 , D_2 , D_3 , D_4 , and D_5 being material parameters and η is the triaxiality ($\eta = (1/3)\sigma_{kk}/\bar{\sigma}_{vM}$). The damage in the model is accumulated over time using:

$$D = \int_0^t \frac{\dot{\bar{\varepsilon}}^p}{\varepsilon^f} dt. \quad (4.12.8)$$

When $D = 1$, the material has failed. For the default behavior of the Johnson-Cook model, the fracture behavior is not active.

4.12.2. Implementation

The implementation of the Johnson-Cook model requires the effective strain rate to be used for calculating the rate effects on yield. This is done through a predictor-corrector return mapping algorithm. In what follows the temperature dependence is not included; this will be addressed later.

The initial response is assumed to be elastic and a trial stress state is calculated

$$T_{ij}^{\text{tr}} = T_{ij}^n + \mathbb{C}_{ijkl} \Delta t d_{kl} \quad (4.12.9)$$

Since the plastic response is independent of pressure we can use the deviatoric stress

$$\begin{aligned} s_{ij} &= T_{ij} - \frac{1}{3} \delta_{ij} T_{kk} \\ s_{ij}^{\text{tr}} &= s_{ij}^n + 2\mu \Delta t d'_{ij}, \end{aligned} \quad (4.12.10)$$

with d'_{ij} being the total deviatoric rate of deformation – $d'_{ij} = d_{ij} - (1/3) \delta_{ij} d_{kk}$.

If this gives a von Mises stress that is greater than the effective stress, i.e.

$$\phi^{\text{tr}} = \sqrt{\frac{3}{2} s_{ij}^{\text{tr}} s_{ij}^{\text{tr}}} > A + B (\bar{\varepsilon}^{p(n)})^N, \quad (4.12.11)$$

then plastic deformation occurs and we solve the following nonlinear equation for $\dot{\bar{\varepsilon}}^p$,

$$\left[A + B (\bar{\varepsilon}_{p(n)} + \Delta t \dot{\bar{\varepsilon}}^p)^N \right] \left[1 + C \ln \left(\max \left(1, \dot{\bar{\varepsilon}}^p / \dot{\bar{\varepsilon}}_0 \right) \right) \right] = \phi^{\text{tr}} - 3\mu \Delta t \dot{\bar{\varepsilon}}^p. \quad (4.12.12)$$

This simple equation comes from the radial return algorithm

$$s_{ij}^{n+1} = s_{ij}^{\text{tr}} - 3\mu \Delta t \dot{\bar{\varepsilon}}^p \frac{s_{ij}^{\text{tr}}}{\phi^{\text{tr}}} \rightarrow s_{ij}^{n+1} = (\phi^{\text{tr}} - 3\mu \Delta t \dot{\bar{\varepsilon}}^p) \frac{s_{ij}^{\text{tr}}}{\phi^{\text{tr}}} \quad (4.12.13)$$

Taking the inner product of both sides gives (4.12.12).

4.12.3. Verification

The Johnson-Cook model is verified through a series of uniaxial stress and pure shear tests. Given the emphasis on the strain-rate and temperature dependent nature of the model a series of these tests are performed at different loading conditions. The material properties and model parameters used for these tests are given in Table 4-14 and come from the work of Corona and Orient [9]. Note, in this case a modified reference plastic strain rate is used ($\dot{\bar{\varepsilon}}_0 = 1 \times 10^{-4} \text{ s}^{-1}$) as the one reported in [9] was selected based on calibration conditions. Here the value is selected to better investigate and highlight strain rate dependency.

E	71.7 GPa	ν	0.33
A	217 MPa	B	405 MPa
C	0.0075	$\dot{\bar{\varepsilon}}_0$	$1 \times 10^{-4} \text{ s}^{-1}$
θ_{ref}	293 K	θ_{melt}	750 K
N	0.41	M	1.1
ρ	2810 kg/m ³	C_v	960 J/(kg-K)
D_1	0.015	D_2	0.24
D_3	-1.5	D_4	-0.039
D_5	8.0		

Table 4-14. The material properties and model parameters of the Johnson-Cook model used for verification testing

4.12.3.1. Uniaxial Stress

To determine a (semi)-analytical expression of the Johnson-Cook model, the equivalency of plastic work for uniaxial loading is recalled such that,

$$\bar{\sigma} \dot{\varepsilon}^p = \sigma (\dot{\varepsilon} - \dot{\varepsilon}^e), \quad (4.12.14)$$

with σ , $\dot{\varepsilon}$, and $\dot{\varepsilon}^e$ being the uniaxial stress, total strain rate, and elastic strain rate, respectively. Assuming $\dot{\varepsilon}^p \geq \dot{\varepsilon}_0$, and noting that $\dot{\varepsilon}^p = \dot{\varepsilon} - \dot{\varepsilon}^e$, the expression for the flow stress (4.12.4), the definition of the homologous temperature (4.12.5), and the dimensionless strain rate, the plastic work expression (4.12.14) may be rearranged as

$$\dot{\varepsilon}^p = \dot{\varepsilon}_0 \exp \left[\frac{\sigma}{C [A + B(\bar{\varepsilon}^p)^N] [1 - \theta^{*M}]} - \frac{1}{C} \right]. \quad (4.12.15)$$

Given the implicit nature (in terms of effective plastic strain) of (4.12.15), a semi-analytical approach is used to evaluate the Johnson-Cook model. Specifically, a simple forward Euler integration scheme is adopted to solve (4.12.15) and then update the remaining state variables. Using such an approach, Figure 4-33 presents the stress-strain and corresponding damage evolution of the Johnson-Cook determined at three strain rates. A constant total logarithmic strain rate is applied by utilizing an applied displacement of the form,

$$u_i(t) = (e^{\omega t} - 1) \delta_{i1}, \quad (4.12.16)$$

where ω is the considered strain rate. Here rates corresponding to a slow quasistatic ($\omega = 1 \times 10^{-3} \text{ s}^{-1}$), medium ($\omega = 1 \text{ s}^{-1}$), and high rate ($\omega = 1 \times 10^3 \text{ s}^{-1}$) loading are considered to explore a variety of regimes. Temperature effects are not addressed in Figure 4-33 ($\beta = 0$) to first investigate the purely mechanical response. The damage evolution is evaluated by simply integrating expression (4.12.8) and noting that for a uniaxial loading $\eta = 1/3$. In this case, as the constitutive behavior is being probed the material does not degrade when $D \geq 1$.

From the results of Figure 4-33 clear agreement is observed between the numerical and semi-analytical response verifying the model behavior in a variety of conditions. Next, to explore the thermomechanical coupling, three different plastic work conversion ratios ($\beta = 0.00$, 0.50 and 1.0) are considered for the medium strain rate ($\omega = 1 \text{ s}^{-1}$). The stress, damage, and temperature evolutions are all presented in Figure 4-34 as a function of axial strains.

From Figure 4-34 the influence of the thermomechanical coupling may be clearly observed. For instance, a roughly 50 K increase in material temperature over the loading range may be seen in the $\beta = 1$ case leading to a roughly 25% decrease in the damage metric and approximately 10% drop in final stress. Additionally, clear agreement between the semi-analytical and numerical responses providing additional verification of the coupled capabilities of the model.

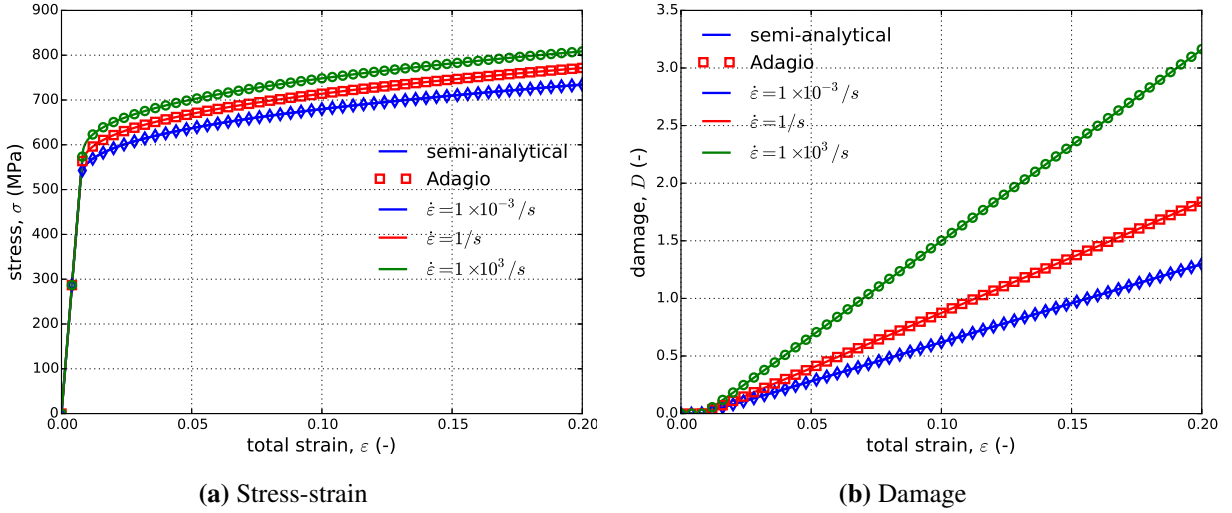


Figure 4-33. Semi-analytical and numerical (a) stress-strain and (b) damage evolutions of the Johnson-Cook model subjected to a uniaxial loading at three different applied strain rates. In these results, $\beta = 0$.

4.12.3.2. Pure Shear

For the pure shear case, a loading like that described in Appendix A.3 is utilized. Specifically, displacements producing a deformation gradient of,

$$F_{ij} = \frac{1}{2} (\lambda + \lambda^{-1}) (\delta_{i1}\delta_{j1} + \delta_{i2}\delta_{j2}) + \frac{1}{2} (\lambda - \lambda^{-1}) (\delta_{i1}\delta_{j2} + \delta_{i2}\delta_{j1}) + \delta_{i3}\delta_{j3}, \quad (4.12.17)$$

are considered with $\lambda = \lambda(t) = e^{\omega t}$. This loading leads to a logarithmic shear strain rate of $\dot{\varepsilon}_{12} = \omega$ that is constant in time enabling the study of strain rate effects.

In the shear stress case, the plastic work equivalency is written as,

$$\bar{\sigma} \dot{\varepsilon}^p = 2\sigma_{12} \dot{\varepsilon}_{12}^p. \quad (4.12.18)$$

Like the uniaxial stress case, the definition of the effective stress may be used with the fact that $\dot{\varepsilon}_{12}^p = \frac{\sqrt{3}}{2} \dot{\varepsilon}^p$ to find the following form of the effective plastic strain rate when $\dot{\varepsilon}^p > \dot{\varepsilon}_0$,

$$\dot{\varepsilon}^p = \dot{\varepsilon}_0 \exp \left[\frac{\sqrt{3}\sigma_{12}}{C [A + B(\bar{\varepsilon}^p)^N] [1 - \theta^{*M}]} - \frac{1}{C} \right]. \quad (4.12.19)$$

A simple forward Euler scheme is then used to integrate the model at three different strain rates – $\omega = .001\text{s}^{-1}$, 1s^{-1} and 1000s^{-1} . The stress-strain and damage evolution responses of these cases

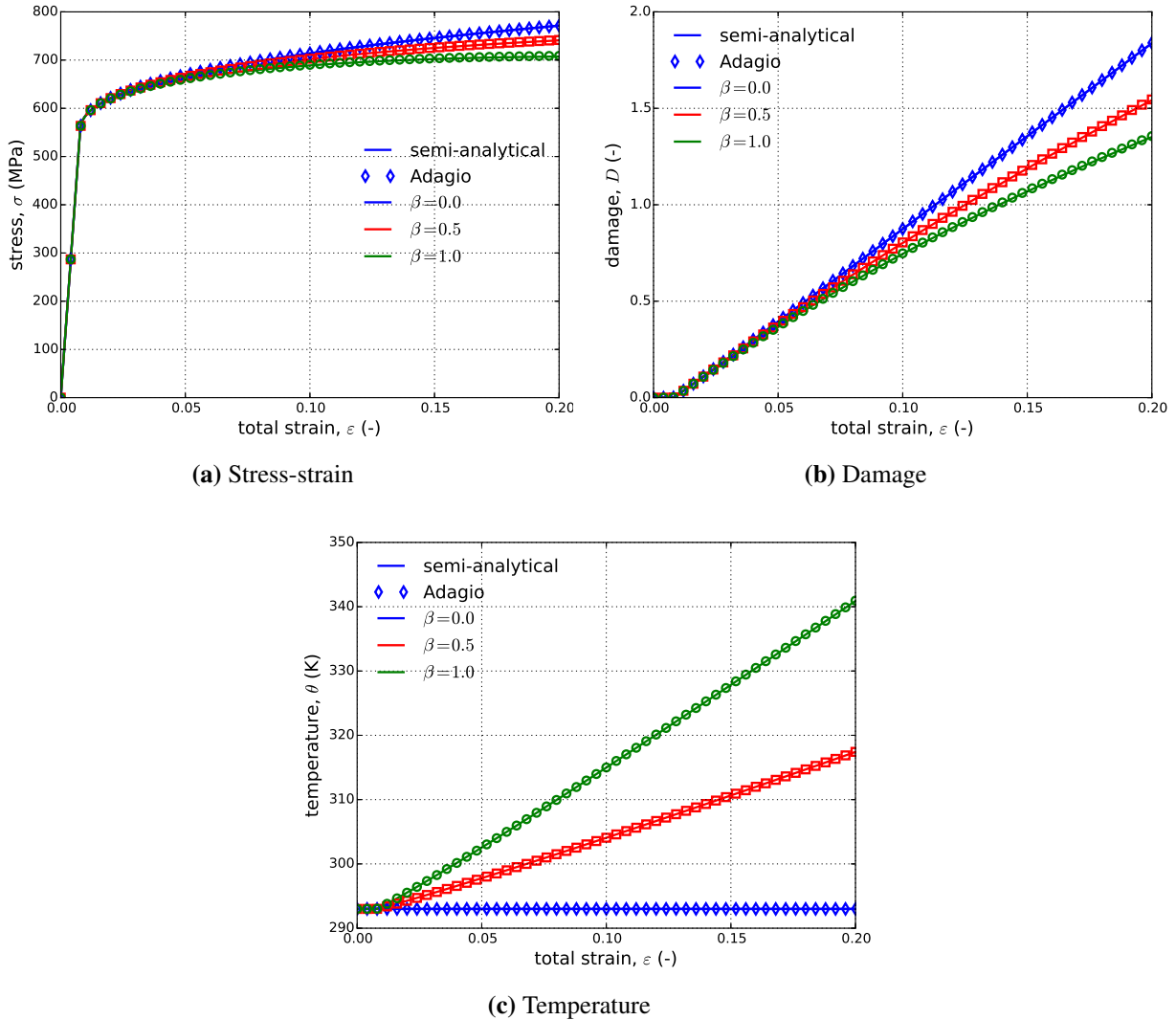


Figure 4-34. Semi-analytical and numerical (a) stress-strain (b) damage and (c) temperature evolutions of the Johnson-Cook model subjected to a uniaxial loading with three different plastic work conversion ratios, β . The strain rate for all three cases is $\dot{\varepsilon} = 1\text{s}^{-1}$.

are presented in Figure 4-35 for the purely mechanical case ($\beta = 0$). With respect to the damage evolution, it is noted that for pure shear responses $\eta = 0$.

The effect of plastic work is considered for $\omega = 1\text{s}^{-1}$ in Figure 4-36. Similar influences like those reported in the uniaxial stress case are observed. A larger increase in temperature through plastic loading is noted however. Regardless in both the results of Figures 4-35 and 4-36 clear agreement between numerical and semi-analytical is observed further verifying the current implementation of the Johnson-Cook model.

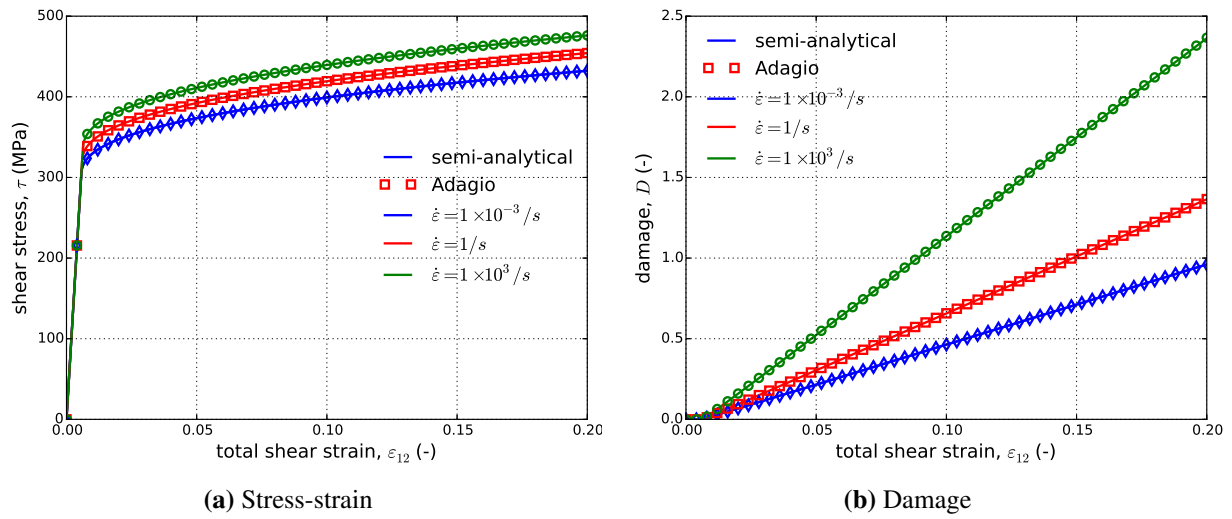


Figure 4-35. Semi-analytical and numerical (a) stress-strain and (b) damage evolutions of the Johnson-Cook model subjected to a pure shear loading at three different applied strain rates. In these results, $\beta = 0$.

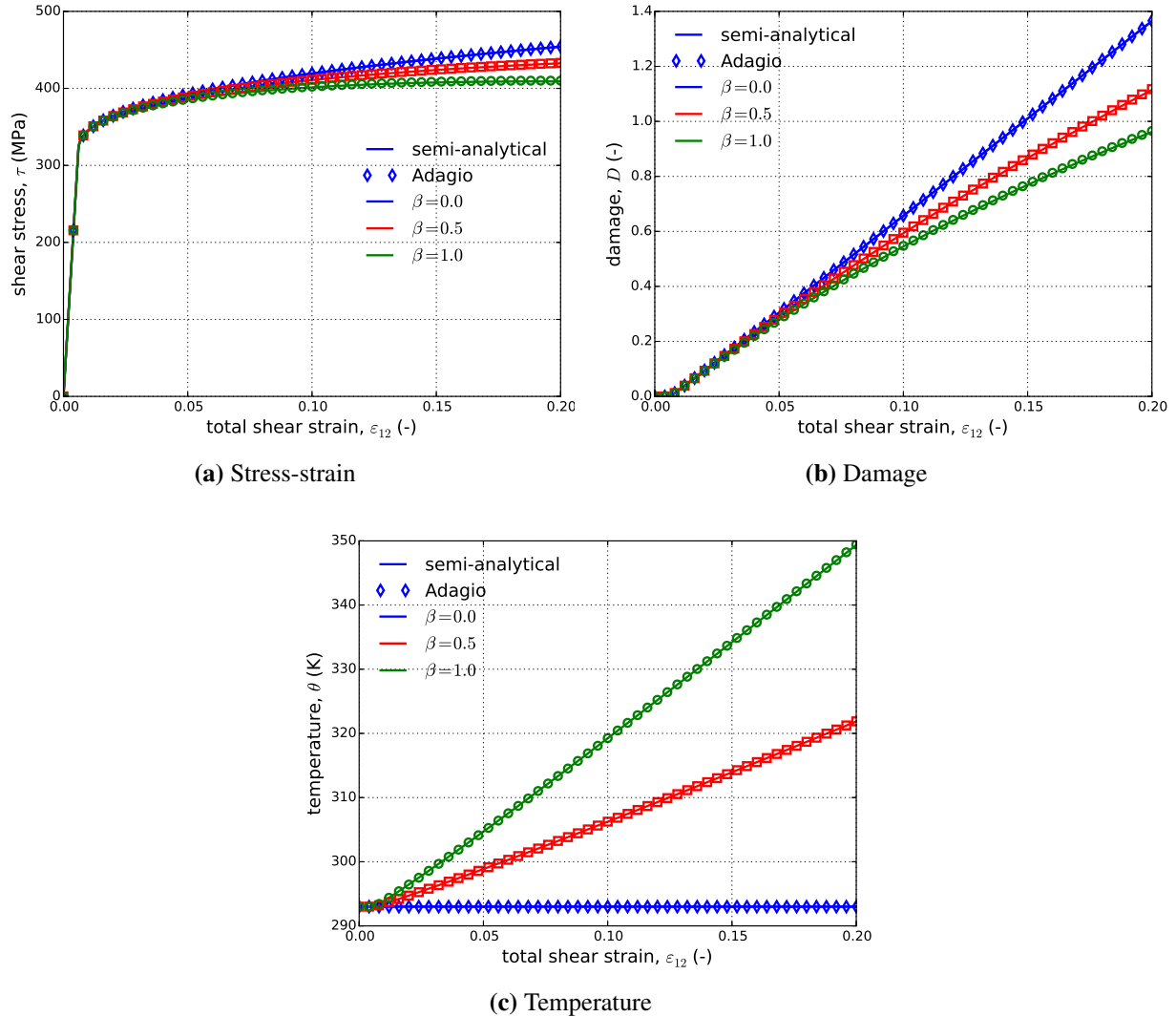


Figure 4-36. Semi-analytical and numerical (a) stress-strain (b) damage and (c) temperature evolutions of the Johnson-Cook model subjected to a pure shear loading with three different plastic work conversion ratios, β . The strain rate for all three cases is $\dot{\varepsilon} = 1\text{s}^{-1}$.

4.12.4. User Guide

```
BEGIN PARAMETERS FOR MODEL JOHNSON_COOK
#
# Elastic constants
#
YOUNGS MODULUS = <real> E
POISSONS RATIO = <real> ν
SHEAR MODULUS = <real> G
BULK MODULUS = <real> K
LAMBDA = <real> λ
TWO MU = <real> 2μ
#
# Yield surface parameters
#
YIELD STRESS = <real> A
HARDENING CONSTANT = <real> B
HARDENING EXPONENT = <real> N
RATE CONSTANT = <real> C
REFERENCE RATE = <real>  $\dot{\varepsilon}_0$  (0.001)
EDOT_REF = <real> (0.0)
#
# Failure strain parameters
#
D1 = <real> D1 (0.0)
D2 = <real> D2 (0.0)
D3 = <real> D3 (0.0)
D4 = <real> D4 (0.0)
D5 = <real> D5 (0.0)
#
# Temperature softening commands
#
RHOCV = <real>  $\rho C_v$ 
BETA = <real>  $\beta$  (0.95)
THERMAL EXPONENT = <real> M
REFERENCE TEMPERATURE = <real>  $\theta_{ref}$ 
MELT TEMPERATURE = <real>  $\theta_{melt}$ 
INITIAL TEMPERATURE = <real>  $\theta_0$ 
#
FORMULATION = <int> (0)
#
END [PARAMETERS FOR MODEL JOHNSON_COOK]
```

Output variables available for this model are listed in Table 4-15.

Table 4-15. State Variables for JOHNSON COOK Model

Name	Variable Description
RADIUS	radius of yield surface
EQPS	equivalent plastic strain
THETA	temperature
EQDOT	effective total strain rate
ITER	
EFAIL	failure strain, ϵ^f
DAMAGE	damage, D
YIELD_STRESS	yield stress

REFERENCES

- [1] G.R. Johnson and W.H. Cook. A constitutive model and data for metals subjected to large strains, high strain rates and high temperatures. In *Proc. 7th. Int. Symp. on Ballistics*, pages 541–547, The Hague, The Netherlands, 1983.
- [2] G.R. Johnson and W.H. Cook. Fracture characteristics of three metals subjected to various strains, strain rates, temperatures and pressures. *Engineering Fracture Mechanics*, 21(1): 31–48, 1985.
- [3] F.J. Zerilli and R.W. Armstrong. Dislocation-mechanics-based constitutive relations for material dynamics calculations. *Journal of Applied Physics*, 61:1816–1825, 1987.
- [4] D.J. Steinberg, S.G. Cochran, and M.W. Guinan. A constitutive model for metals applicable at high-strain rate. *Journal of Applied Physics*, 51:1498–1504, 1980.
- [5] D.J. Steinberg and C.M. Lund. A constitutive model for strain rates from 10^{-4} to 10^6 s $^{-1}$. *Journal of Applied Physics*, 65:1528–1533, 1989.
- [6] A.A. Brown and D.J. Bammann. Validation of a model for static and dynamic recrystallization in metals. *International Journal of Plasticity*, 32–33:17–35, 2012.
- [7] P.S. Follansbee and U.F. Kocks. A constitutive description of the deformation of copper based on the use of the mechanical threshold stress and an internal state variable. *Acta Metallurgica*, 36(1):81–93, 1988.
- [8] P.S. Follansbee and G.T. Gray III. An analysis of the low temperature, low and high strain-rate deformation of Ti-6Al-4V. *Metallurgical Transactions A*, 20A:863–874, 1989.
- [9] E. Corona and G. E. Orient. An evaluation of the Johnson-Cook model to simulate puncture of 7075 aluminum plates. Technical Report SAND2014-1550, Sandia National Laboratories, Albuquerque, NM, 2014. [pdf](#).

4.13. J_2 PLASTICITY MODEL

4.13.1. Theory

The J_2 plasticity model is a generic implementation of a von Mises yield surface with kinematic and isotropic hardening features. Unlike other models (*e.g.* Elastic-Plastic, Elastic-Plastic Power Law) more flexible, general hardening forms are implemented enabling different isotropic hardening descriptions and some rate and/or temperature dependence.

As is common to other plasticity models in LAMÉ, the J_2 plasticity model uses a hypoelastic formulation. As such, the total rate of deformation is additively decomposed into an elastic and plastic part such that

$$D_{ij} = D_{ij}^e + D_{ij}^p \quad (4.13.1)$$

The objective stress rate, depending only on the elastic deformation, may then be written as,

$$\overset{\circ}{\sigma}_{ij} = \mathbb{C}_{ijkl} D_{kl}^e, \quad (4.13.2)$$

where \mathbb{C}_{ijkl} is the fourth-order elastic, isotropic stiffness tensor.

The yield surface for the J_2 plasticity model, f , may be written,

$$f(\sigma_{ij}, \alpha_{ij}, \bar{\varepsilon}^p, \dot{\bar{\varepsilon}}^p, \theta) = \phi(\sigma_{ij}, \alpha_{ij}) - \bar{\sigma}(\bar{\varepsilon}^p, \dot{\bar{\varepsilon}}^p, \theta), \quad (4.13.3)$$

in which α_{ij} , $\bar{\varepsilon}^p$, $\dot{\bar{\varepsilon}}^p$, and θ are the kinematic backstress, equivalent plastic strain, equivalent plastic strain rate, and absolute temperature, respectively, while ϕ and $\bar{\sigma}$ are generically the effective stress and flow stress. Broadly speaking, the effective stress describes the shape of the yield surface and kinematic effects while the flow stress gives the size of the current yield surface. It should also be noted that writing the yield surface in this way splits the dependence on the state variables between the effective stress and flow stress functions.

As the current model is for J_2 plasticity, the effective stress is given as,

$$\phi^2(\sigma_{ij}, \alpha_{ij}) = \frac{3}{2} (s_{ij} - \alpha_{ij}) (s_{ij} - \alpha_{ij}), \quad (4.13.4)$$

with s_{ij} being the deviatoric stress defined as $s_{ij} = \sigma_{ij} - (1/3)\sigma_{kk}\delta_{ij}$. For the flow stress, a general representation of the form,

$$\bar{\sigma}(\bar{\varepsilon}^p, \dot{\bar{\varepsilon}}^p, \theta) = \sigma_y \hat{\sigma}_y(\dot{\bar{\varepsilon}}^p) \check{\sigma}_y(\theta) + K(\bar{\varepsilon}^p) \hat{\sigma}_h(\dot{\bar{\varepsilon}}^p) \check{\sigma}_h(\theta), \quad (4.13.5)$$

is allowed. In this fashion, the effects of isotropic hardening ($K(\bar{\varepsilon}^p)$), rate ($\hat{\sigma}_{y,h}$), and temperature ($\check{\sigma}_{y,h}$) are decomposed although separate temperature and rate dependencies may be specified for

yield (subscript “y”) and hardening (“h”). Such an assumption is an extension of the multiplicative decomposition of the Johnson-Cook model [1, 2]. It should be noted that not all effects need to be included and the default assumption of the hardening classes is that the response is rate and temperature independent. The following section on plastic hardening will go into more detail on possible choices for functional representations.

An associated flow rule is utilized such that the plastic rate of deformation is normal to the yield surface and is given by,

$$\dot{D}_{ij}^p = \dot{\gamma} \frac{\partial \phi}{\partial \sigma_{ij}} = \dot{\gamma} \frac{3}{2\phi} s_{ij}, \quad (4.13.6)$$

where $\dot{\gamma}$ is the consistency multiplier enforcing $f = 0$ during plastic deformation. Given the form of f , it can also be shown that $\dot{\gamma} = \dot{\varepsilon}^p$.

4.13.1.1. Plastic Hardening

Plastic hardening refers to increases in the flow stress, $\bar{\sigma}$, with plastic deformation. As such, hardening is described via the functional relationship between the flow stress and isotropic hardening variable (effective plastic strain), $\bar{\sigma}(\bar{\varepsilon}^p)$. Over the course of nearly a century of work in metal plasticity, a variety of relationships have been proposed to describe the interactions associated with different physical interpretations, deformation mechanisms, and materials. To enable the utilization of the same plasticity models for different material systems, a modular implementation of plastic hardening has been adopted such that the analyst may select different hardening models from the input deck thereby avoiding any code changes or user subroutines. In this section, additional details are given to the different models to enable the user to select the appropriate choice of model. Note, the models being discussed here are only for *isotropic* hardening in which the yield surface expands. *Kinematic* hardening in which the yield surface translates in stress-space with deformation and *distortional* hardening where the shape of the yield surface changes shape with deformation are not treated. For a larger discussion of the phenomenology and history of different hardening types, the reader is referred to [3, 4, 5].

Given the ubiquitous nature of these hardening laws in computational plasticity, some (if not most) of this material may be found elsewhere in this manual. Nonetheless, the discussion is repeated here for the convenience of the reader.

Linear

Linear hardening is conceptually the simplest model available in LAMÉ. As the name implies, a linear relationship is assumed between the hardening variable, $\bar{\varepsilon}^p$, and flow stress. The constant giving the degree of increase of yield stress with plastic flow is termed the hardening modulus and is given as, H' , while the expression for the flow stress may be written,

$$\bar{\sigma} = \sigma_y + H' \bar{\varepsilon}^p. \quad (4.13.7)$$

The simplicity of the model is its main feature as the constant slope,

$$\frac{d\bar{\sigma}}{d\bar{\varepsilon}^p} = H', \quad (4.13.8)$$

makes the model attractive for analytical models and cheap for computational implementations (e.g. radial return algorithms require only a single correction step). Unfortunately, the simplicity of the representation also means that it has limited predictive capabilities and can lead to overly stiff responses.

Power Law

Another common expression for isotropic hardening is the power-law hardening model. Due to its prevalence, a dedicated ELASTIC-PLASTIC POWER LAW HARDENING model may be found in LAMÉ (see Section 4.8.1). This expression is given as,

$$\bar{\sigma} = \sigma_y + A < \bar{\varepsilon}^p - \varepsilon_L >^n, \quad (4.13.9)$$

in which $< \cdot >$ are Macaulay brackets, ε_L is the Lüders strain, A is a fitting constant, and n is an exponent typically taken such that $0 < n \leq 1$. The Lüders strain is a positive, constant strain value (default to zero) giving an initial plastic deformation domain in which the response is perfectly plastic (see Fig. 4-20). The derivative is then simply,

$$\frac{d\bar{\sigma}}{d\bar{\varepsilon}^p} = nA < \bar{\varepsilon}^p - \varepsilon_L >^{(n-1)}. \quad (4.13.10)$$

Note, one difficulty in such an implementation is that when the effective equivalent plastic strain is zero, numerical difficulties may arise in evaluating the derivative necessitating special treatment of the case.

Voce

The Voce hardening model (sometimes referred to as a saturation model) uses a decaying exponential in terms of the equivalent plastic strain such that the hardening eventually saturates to a specified value (thus the name). Such a relationship has been observed in some structural metals giving rise to the popularity of the model. The hardening response is given as,

$$\bar{\sigma} = \sigma_y + A (1 - \exp(-n\bar{\varepsilon}^p)), \quad (4.13.11)$$

in which A is a fitting constant and n is a fitting exponent describing how quickly the hardening saturates. Importantly, the derivative is written as,

$$\frac{d\bar{\sigma}}{d\bar{\varepsilon}^p} = nA \exp(-n\bar{\varepsilon}^p), \quad (4.13.12)$$

and is well defined everywhere giving the selected form an advantage over the aforementioned power law model.

Johnson-Cook

The Johnson-Cook [1, 2] hardening type is a *rate-dependent* formulation utilizing the assumption that rate-independent and rate-dependent contributions may be multiplicatively separated. Specifically, use of this option requires specifying a user-defined hardening function to capture rate-independent contributions and Johnson-Cook type rate dependent coefficients. The flow stress may be written in this fashion as,

$$\bar{\sigma} = \tilde{\sigma}_y(\bar{\varepsilon}^p) \left[1 + C \left\langle \ln \left(\frac{\dot{\varepsilon}^p}{\dot{\varepsilon}_0} \right) \right\rangle \right], \quad (4.13.13)$$

in which $\tilde{\sigma}_y(\bar{\varepsilon}^p)$ is the user-specified rate-independent hardening function, C is a fitting constant and $\dot{\varepsilon}_0$ is a reference strain rate. The Macaulay brackets ensure the material behaves in a rate independent fashion when $\dot{\varepsilon}^p < \dot{\varepsilon}_0$.

Power Law Breakdown

Like the Johnson-Cook formulation, the power-law breakdown model is also rate-dependent. Again, a multiplicative decomposition between rate-independent and dependent hardening contributions. In this case, however, the functional form is derived from the analysis of Frost and Ashby [6] in which power-law relationships like those of the Johnson-Cook and cease to appropriately capture the physical response. The form used here is similar to the expression used by Brown and Bammann [7] and is written as,

$$\bar{\sigma} = \tilde{\sigma}_y(\bar{\varepsilon}^p) \left[1 + \operatorname{asinh} \left(\left(\frac{\dot{\varepsilon}^p}{g} \right)^{(1/m)} \right) \right], \quad (4.13.14)$$

with $\tilde{\sigma}_y(\bar{\varepsilon}^p)$ being the user supplied rate independent expression, g is a model parameter related to the activation energy in going from climb to glide-controlled deformation, and m dictates the strength of the dependence.

Flow Stress

Unlike the previously described models, the flow-stress hardening method is less a specific physical representation and more a generalization of the hardening behaviors to allow greater

flexibility in separately describing isotropic hardening, rate-dependence, and temperature dependence. As such, the generic flow-stress definition of

$$\bar{\sigma}(\bar{\varepsilon}^p, \dot{\bar{\varepsilon}}^p, \theta) = \tilde{\sigma}_y(\bar{\varepsilon}^p) \hat{\sigma}(\dot{\bar{\varepsilon}}^p) \check{\sigma}(\theta), \quad (4.13.15)$$

is used in which $\hat{\sigma}$ and $\check{\sigma}$ are rate and temperature multipliers, respectively, that by default are unity (such that the response is rate and temperature independent) and $\tilde{\sigma}_y$ is the isotropic hardening component that may also be specified as,

$$\tilde{\sigma}_y = \sigma_y + K(\bar{\varepsilon}^p), \quad (4.13.16)$$

with σ_y being the constant yield stress and K is the isotropic hardening that is initially zero and a function of the equivalent plastic strain. A multiplicative decomposition such as this mirrors the general structure used by Johnson and Cook [1, 2] although greater flexibility is allowed in terms of the specific form of the rate and temperature multipliers.

Given the aforementioned defaults for rate and temperature dependence, the corresponding multipliers need not be specified. A representation for the isotropic hardening, however, *must* be specified and can be defined via linear, power-law, Voce, or user-defined representations. For the user-defined case, an *isotropic* hardening function is required and it must be highlighted that the interpretation differs from the general user-defined hardening model. *In this case, as the specified function represents the isotropic hardening, it should start from zero – not yield.*

Although the flow-stress hardening model defaults to rate and temperature independent, a multiplier may be defined for either (or both) of the terms. For rate-dependence, either the previously discussed Johnson-Cook or power-law breakdown models or a user-defined multiplier may be used. For the user-defined capability, the multiplier should be input as a strictly positive function of the equivalent plastic strain rate with a value of one in the rate-independent limit.

In terms of temperature dependence, the multiplier may be specified given a Johnson-Cook dependency [1, 2],

$$\check{\sigma}(\theta) = 1 - \left(\frac{\theta - \theta_{\text{ref}}}{\theta_{\text{melt}} - \theta_{\text{ref}}} \right)^M, \quad (4.13.17)$$

with θ_{ref} , θ_{melt} and M being the reference temperature, melting temperature, and temperature exponent. The temperature multiplier may also be specified via a user defined function.

Decoupled Flow Stress

Like the flow-stress hardening method, the decoupled flow-stress hardening implementation is a generalization of the hardening behaviors to allow greater flexibility. In differentiating the two, for the decoupled model the rate and temperature dependence may be separately specified for the yield and hardening portions of the flow stress. As such, the generic flow-stress definition of

$$\bar{\sigma}(\bar{\varepsilon}^p, \dot{\bar{\varepsilon}}^p, \theta) = \sigma_y \hat{\sigma}_y(\dot{\bar{\varepsilon}}^p) \check{\sigma}_y(\theta) + K(\bar{\varepsilon}^p) \hat{\sigma}_h(\dot{\bar{\varepsilon}}^p) \check{\sigma}_h(\theta), \quad (4.13.18)$$

is used in which $\hat{\sigma}$ and $\check{\sigma}$ are rate and temperature multipliers, respectively, that by default are unity (such that the response is rate and temperature independent) with subscripts “y” and “h” denoting functions associated with yield and hardening. The isotropic hardening is described by $K(\bar{\varepsilon}^p)$ and σ_y is the constant initial yield stress. It may also be seen that if the yield and hardening dependencies are the same ($\hat{\sigma}_y = \hat{\sigma}_h$ and $\check{\sigma}_y = \check{\sigma}_h$) the decoupled flow stress model reduces to that of the flow stress case and mirrors the general structure of the Johnson-Cook model [1, 2].

Given the aforementioned defaults for rate and temperature dependence, the corresponding multipliers need not be specified. A representation for the isotropic hardening, however, *must* be specified and can be defined via linear, power-law, Voce, or user-defined representations. For the user-defined case, an *isotropic* hardening function should be used and it must be highlighted that the interpretation differs from the general user-defined hardening model. *In this case, as the specified function represents the isotropic hardening, it should start from zero – not yield.*

Although the decoupled flow-stress hardening model defaults to rate and temperature independent, a multiplier may be defined for any of the terms. For rate-dependence, either the previously discussed Johnson-Cook or power-law breakdown models or a user-defined multiplier may be used. For the user-defined capability, the multiplier should be input as a strictly positive function of the equivalent plastic strain rate with a value of one in the rate-independent limit.

In terms of temperature dependence, the multiplier may be specified given a Johnson-Cook dependency [1, 2],

$$\check{\sigma}(\theta) = 1 - \left(\frac{\theta - \theta_{\text{ref}}}{\theta_{\text{melt}} - \theta_{\text{ref}}} \right)^M, \quad (4.13.19)$$

where θ_{ref} , θ_{melt} , and M are the reference temperature, melting temperature, and temperature exponent. A temperature multiplier may also be specified via a user defined function.

4.13.2. Implementation

The J_2 plasticity model is implemented using a radial return predictor-corrector algorithm. First, an elastic trial stress state is calculated. This is done by assuming that the rate of deformation is completely elastic,

$$T_{ij}^{tr} = T_{ij}^n + \Delta t (\lambda \delta_{ij} d_{kk} + 2\mu d_{ij}). \quad (4.13.20)$$

The trial stress state is decomposed into a pressure and a deviatoric stress

$$p^{tr} = \frac{1}{3} T_{kk}^{tr} ; \quad s_{ij}^{tr} = T_{ij}^{tr} - p^{tr} \delta_{ij}. \quad (4.13.21)$$

A trial yield function value, f^{tr} , is calculated by assuming purely thermoelastic deformations ($\dot{\varepsilon}^p = 0, \bar{\varepsilon}_{tr}^p = \bar{\varepsilon}_n^p$) such that,

$$f^{tr} (s_{ij}^{tr}, \alpha_{ij}^n, \bar{\varepsilon}_n^p, \dot{\varepsilon}_{tr}^p = 0, \theta_{n+1}) = \phi^{tr} (s_{ij}^{tr}, \alpha_{ij}^n) - \bar{\sigma} (\bar{\varepsilon}_n^p, \dot{\varepsilon}_{tr}^p = 0, \theta_{n+1}). \quad (4.13.22)$$

If $f^{tr} \leq 0$ then the strain rate is elastic and the stress update is finished. If $f^{tr} > 0$ then plastic deformation has occurred and a radial return algorithm determines the extent of plastic deformation.

The normal to the yield surface is assumed to lie in the direction of the trial stress state. This gives the following expression for N_{ij} ,

$$N_{ij} = \frac{(s_{ij}^{tr} - \alpha_{ij}^n)}{\| (s_{ij}^{tr} - \alpha_{ij}^n) \|}. \quad (4.13.23)$$

Using a backward Euler algorithm, the final deviatoric stress state is

$$s_{ij}^{n+1} = s_{ij}^{tr} - \Delta t 2\mu d_{ij}^p, \quad (4.13.24)$$

where the plastic strain increment is

$$\Delta d_{ij}^p = \sqrt{\frac{3}{2}} \Delta \bar{\varepsilon}^p N_{ij}. \quad (4.13.25)$$

The equation for the change in the equivalent plastic strain over the load step is found as the solution to

$$3\mu \Delta \bar{\varepsilon}^p + \bar{\sigma} (\bar{\varepsilon}_n + \Delta \bar{\varepsilon}^p, \Delta t, \theta_{n+1}) - \phi^{tr} + f_n = 0, \quad (4.13.26)$$

in which the plastic strain rate is approximated as, $\dot{\varepsilon}^p = \Delta \bar{\varepsilon}^p / \Delta t$.

4.13.3. Verification

The J_2 plasticity model is verified through a series of uniaxial and pure shear tests considering a variety of hardening models. Specifically, the boundary value problems of Appendix A.5 are used. Throughout these tests, the elastic properties are maintained as $E = 70$ GPa and $\nu = 0.25$.

4.13.3.1. Plastic Hardening

For the verification of the J_2 model, a series of tests using different rate-*independent*, rate-*dependent*, and combinations of these hardening models are investigated for both uniaxial

stress and pure shear. For these cases, by imposing a constant plastic strain rate as described in Appendix A.5 the model response may be analytically determined as a function of time. For the rate-*independent* cases, a constant plastic $\dot{\varepsilon}^p = 1 \times 10^{-4} \text{ s}^{-1}$ is used to replicate quasi-static conditions.

The various rate-*dependent* and rate-*independent* hardening coefficients are found in Table 4-16 while the remaining model parameters are unchanged from the previous verification exercises. For the current verification exercises, the rate-*independent* hardening models (linear, Voce, and power-law) and rate-*dependent* forms (Johnson-Cook, power-law breakdown) are examined.

C	0.1	$\dot{\varepsilon}_0$	$1 \times 10^{-4} \text{ s}^{-1}$
g	0.21 s^{-1}	m	16.4
$\tilde{H}_{\text{Linear}}$	200 MPa	-	-
\tilde{A}_{PL}	400 MPa	\tilde{n}_{PL}	0.25
\tilde{A}_{Voce}	200 MPa	\tilde{n}_{Voce}	20

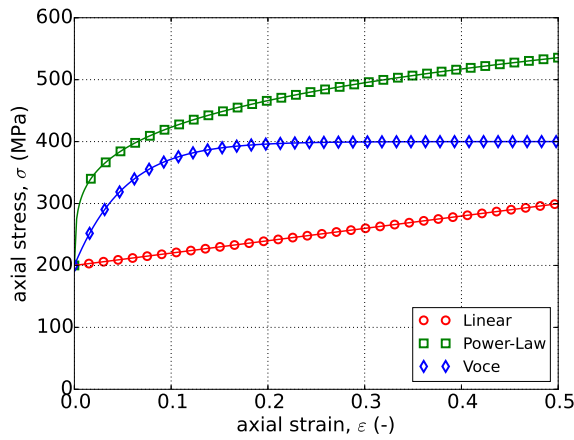
Table 4-16. The model parameters for the hardening verification tests used with the J_2 plasticity model during verification tests. Parameters for the rate-*independent* hardening functions, $\tilde{\sigma}_y$, are also given and denoted with a $\tilde{\cdot}$ while the subscript refers to the functional form.

Rate-Independent

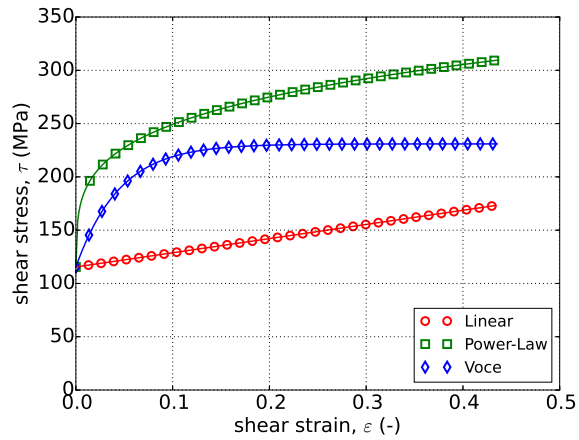
First, the ability of the built-in rate-*independent* hardening models is assessed in both uniaxial stress and pure shear. Specifically, the linear, power-law, and Voce hardening models are considered and the results determined analytically and numerically are presented in Figure 4-37. As expected, excellent agreement is noted between the two sets of results. Importantly, as the responses of all three rate-*independent* isotropic hardening models are presented in the same figures, the corresponding behaviors can be seen. Note, the given parameterizations are not selected for any form of equivalency. Nonetheless, the linear post-yielding behavior of the corresponding model can be seen and compared to the non-linear responses of the Voce and power-law implementations. The critical difference of the latter two being that the Voce response saturates at a stress level while the power-law continues to grow.

Rate-Dependent

With the performance of the model under rate-*independent* conditions established, next the capabilities of the rate-*dependent* (Johnson-Cook and power-law breakdown) formulations are considered. Note, the flow-stress and decoupled flow-stress models that incorporate temperature dependence are left to later sections. As such, in these cases user-defined analytic functions are used for each of the specified rate-*independent* hardening models rather than particular implementations.



(a) Uniaxial Stress



(b) Pure Shear

Figure 4-37. Analytical and numerical (a) uniaxial stress-strain and (b) pure shear responses of the J_2 plasticity model with linear, power-law, and Voce rate-independent isotropic hardening. Solid lines are analytical while open symbols are numerical.

The uniaxial stress-strain responses are interrogated for the Johnson-Cook and Power-law breakdown rate-*dependent* hardening models considering linear, power-law, and Voce isotropic hardening in Figure 4-38. Five decades of plastic strain rates $\dot{\varepsilon}^p = 1 \times 10^{-3} \rightarrow 1 \times 10^1 \text{ s}^{-1}$ are considered. In comparing the analytical and numerical results between all of the cases exceptional agreement is noted between every case.

Similarly, the pure shear responses of the six hardening combinations over the five plastic strain rates are given in Figure 4-39 for both analytical and numerical approaches. As with the normal cases, outstanding agreement is noted between the various results. Thus, between the plethora of problems presented in Figures 4-38 and 4-39 the performance of the rate-dependent models may be considered verified.

Flow Stress

Decoupled Flow Stress

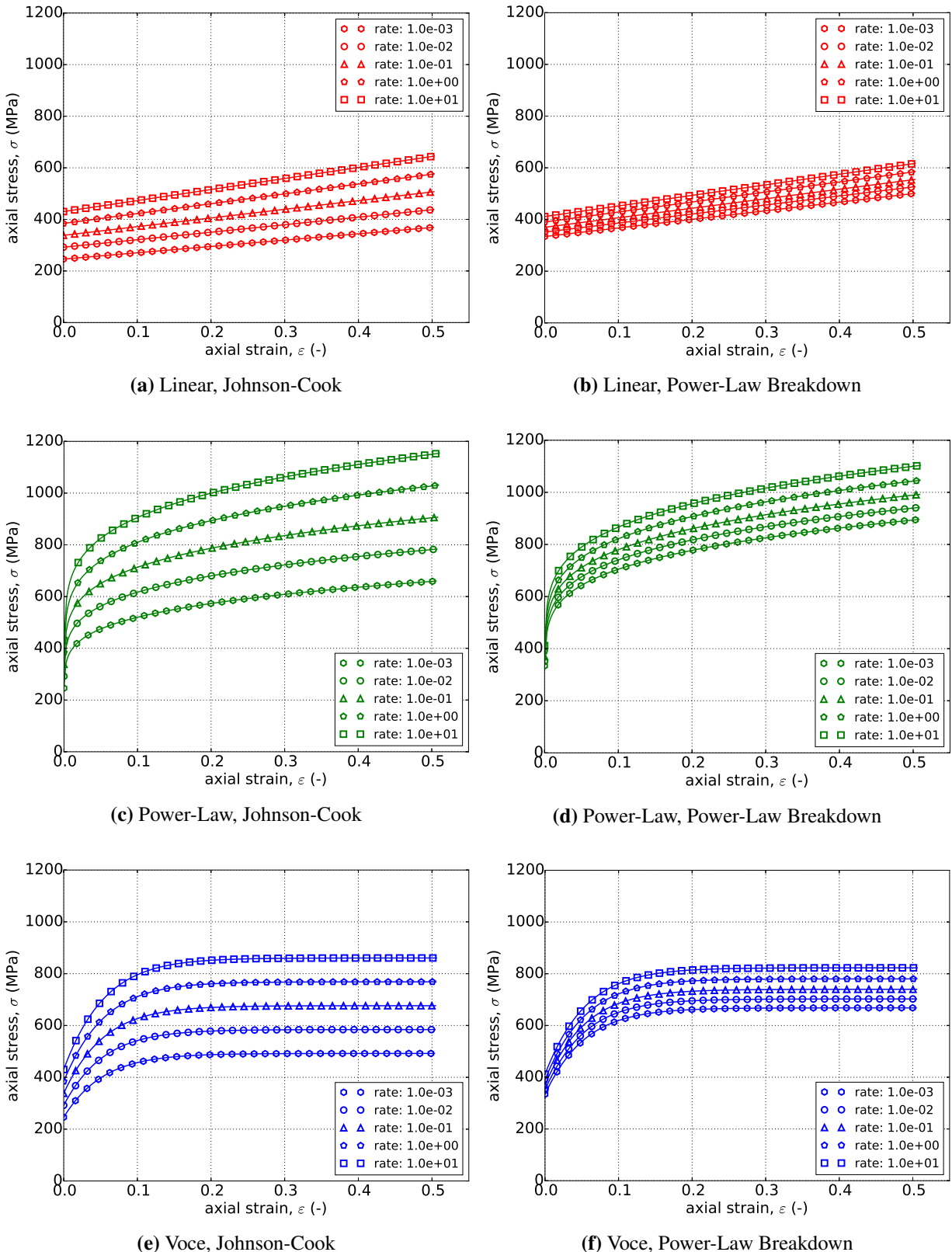


Figure 4-38. Uniaxial stress-strain responses of the J_2 plasticity model with (a,b) linear, (c,d) power-law, and (e,f) Voce isotropic hardening with the (a,c,e) Johnson-Cook and (b,d,f) Power-law breakdown rate-dependent hardening models. Solid lines are analytical while open symbols are numerical.

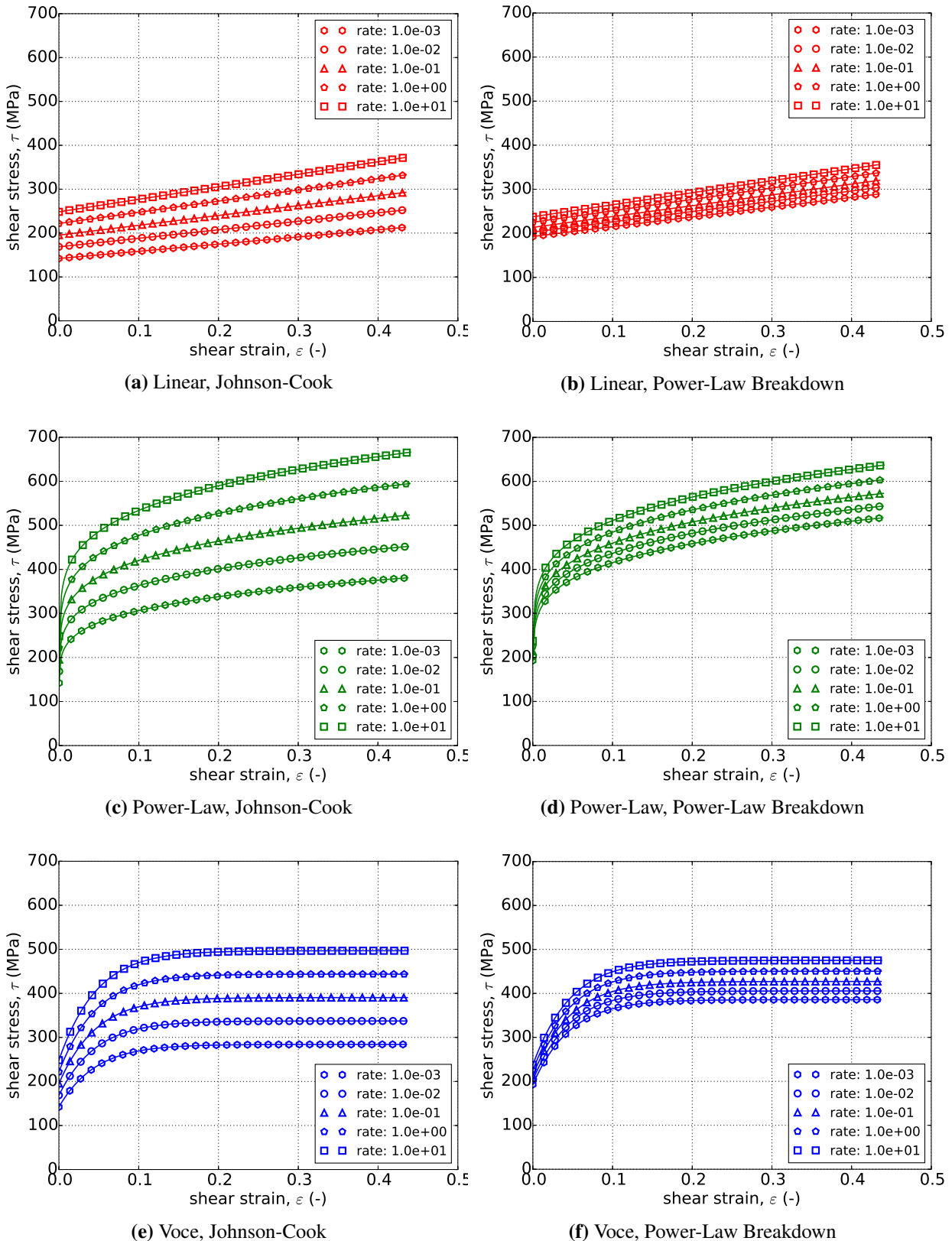


Figure 4-39. Pure shear responses of the J_2 plasticity model with (a,b) linear, (c,d) power-law, and (e,f) Voce isotropic hardening with the (a,c,e) Johnson-Cook and (b,d,f) Power-law breakdown rate-dependent hardening models. Solid lines are analytical while open symbols are numerical.

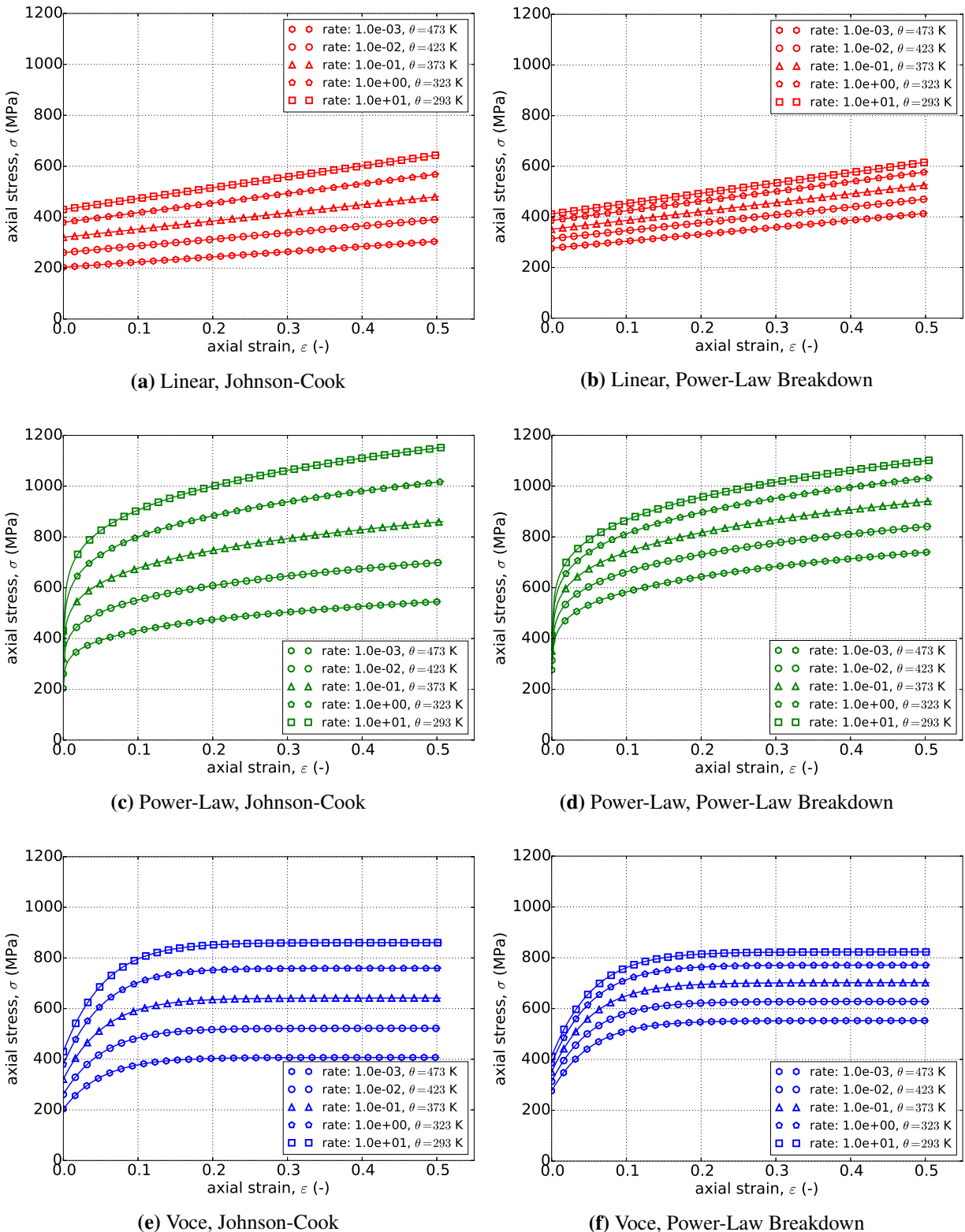


Figure 4-40. Uniaxial stress-strain responses of the J_2 plasticity model using the flow-stress hardening model comprised of (a,b) linear, (c,d) power-law, and (e,f) Voce isotropic hardening, (a,c,e) Johnson-Cook and (b,d,f) power-law breakdown rate multipliers, and (a-f) Johnson-Cook temperature multipliers. Solid lines are analytical while open symbols are numerical.

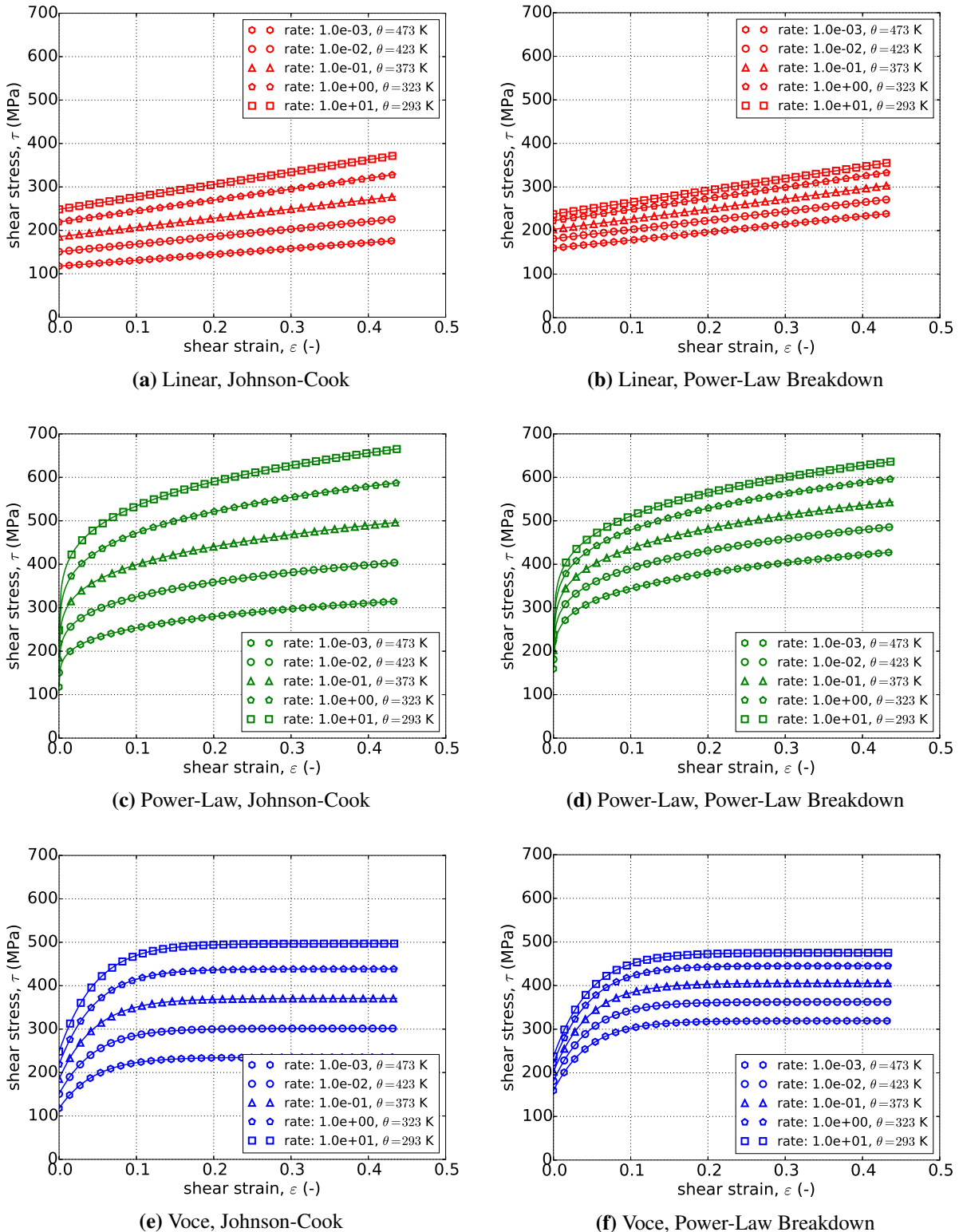


Figure 4-41. Pure shear responses of the J_2 plasticity model using the flow-stress hardening model comprised of (a,b) linear, (c,d) power-law, and (e,f) Voce isotropic hardening, (a,c,e) Johnson-Cook and (b,d,f) Power-law breakdown rate multipliers and (a-f) Johnson-Cook temperature multipliers. Solid lines are analytical while open symbols are numerical.

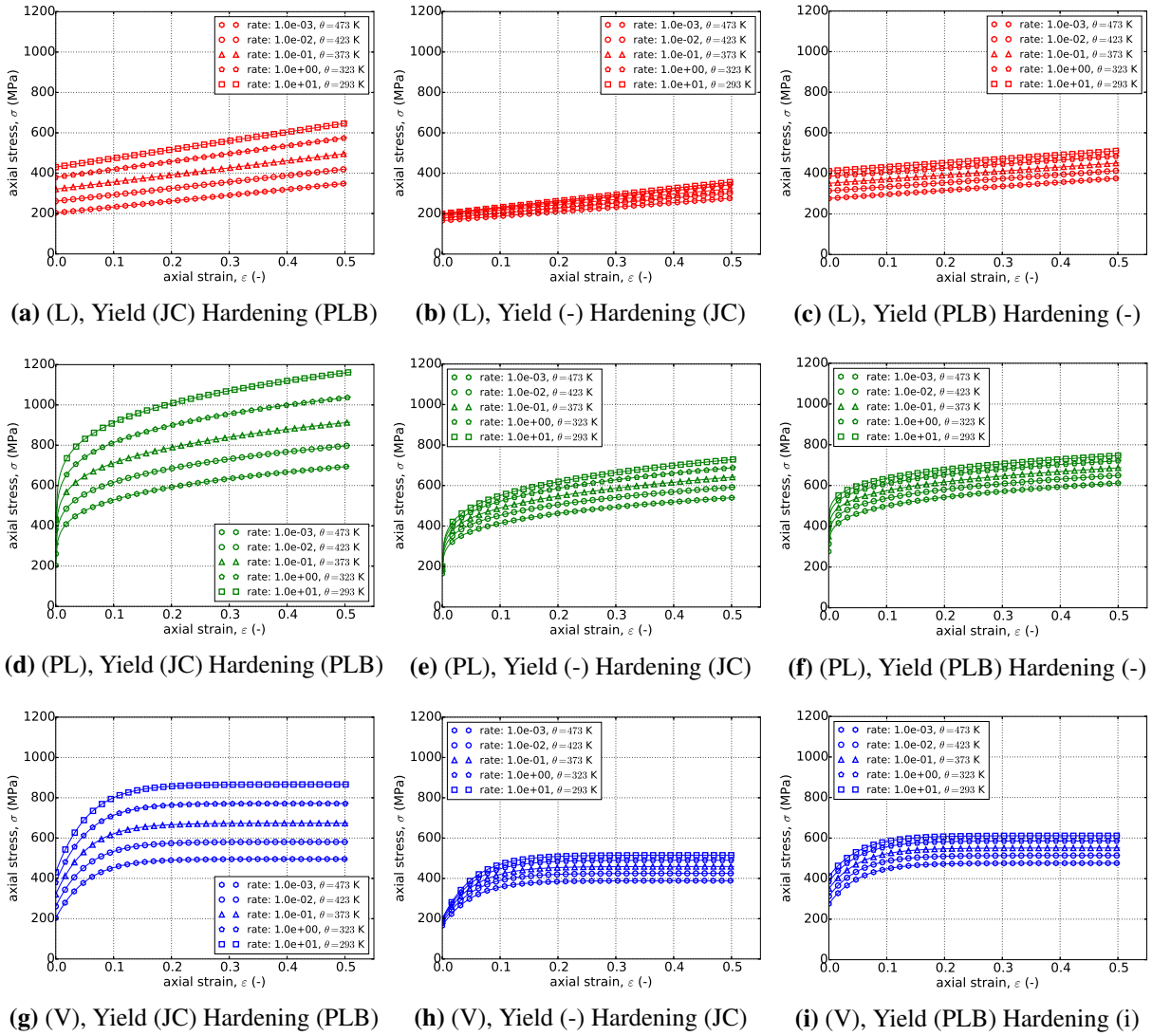


Figure 4-42. Uniaxial stress-strain responses of the J_2 plasticity model using the decoupled flow-stress hardening model comprised of (a-c) linear ("L"), (d-f) power-law ("PL"), and (g-i) Voce isotropic hardening ("V"), (a-i) temperature independent hardening, (a-i) Johnson-Cook type temperature multiplier for yield, (a,d,g) Johnson-Cook ("JC") and power-law breakdown ("PLB") type yield and hardening rate multipliers, respectively, (b,e,h) rate-independent (-) yield with Johnson-Cook type hardening rate dependence, and (c,f,i) power-law breakdown yield rate dependence with rate-independent hardening. Solid lines are analytical while open symbols are numerical.

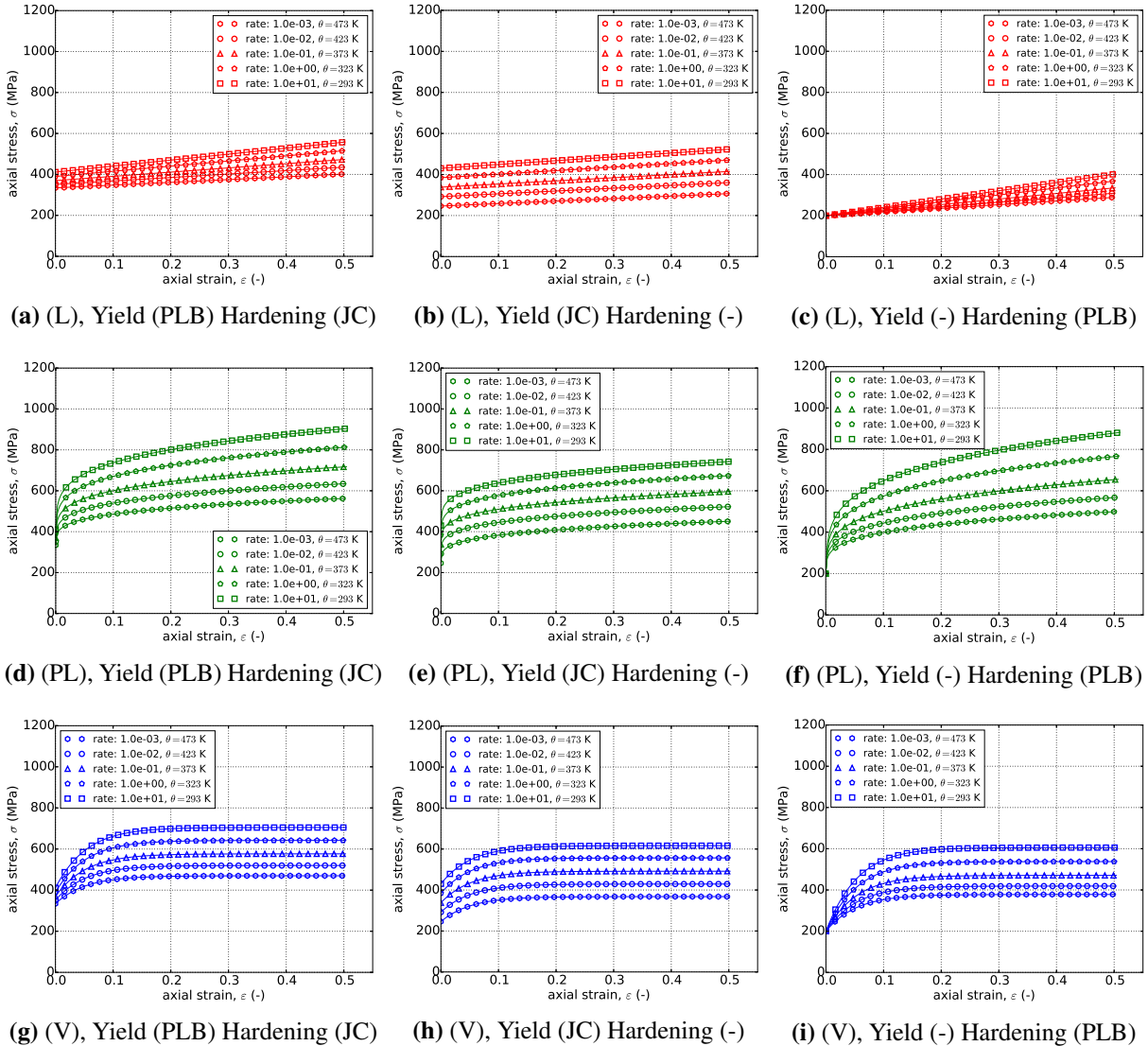


Figure 4-43. Uniaxial stress-strain responses of the J_2 plasticity model using the decoupled flow-stress hardening model comprised of (a-c) linear ("L"), (d-f) power-law ("PL"), and (g-i) Voce ("V") isotropic hardening, (a-i) temperature independent yield, (a-i) Johnson-Cook type temperature multiplier for hardening, (a,d,g) power-law breakdown ("PLB") and Johnson-Cook ("JC") rate multipliers for yield and hardening, respectively (b,e,h) rate-independent (-)hardening with Johnson-Cook type yield rate dependence, and (c,f,i) power-law breakdown hardening rate dependence with rate-independent yield. Solid lines are analytical while open symbols are numerical.

4.13.4. User Guide

```
BEGIN PARAMETERS FOR MODEL J2_PLASTICITY
#
# Elastic constants
#
YOUNGS MODULUS = <real> E
POISSONS RATIO = <real> v
SHEAR MODULUS = <real> G
BULK MODULUS = <real> K
LAMBDA = <real> λ
TWO MU = <real>  $2\mu$ 
#
# Yield surface parameters
#
YIELD STRESS = <real>  $\sigma_y$ 
BETA = <real>  $\beta$  (1.0)
#
# Hardening model
#
HARDENING MODEL = LINEAR | POWER_LAW | VOCE | USER_DEFINED |
    FLOW_STRESS | DECOUPLED_FLOW_STRESS | CUBIC_HERMITE_SPLINE |
    JOHNSON_COOK | POWER_LAW_BREAKDOWN
#
# Linear hardening
#
HARDENING MODULUS = <real> H'
#
# Power-law hardening
#
HARDENING CONSTANT = <real> A
HARDENING EXPONENT = <real> n (0.5)
LUDERS STRAIN = <real>  $\epsilon_L$  (0.0)
#
# Voce hardening
#
HARDENING MODULUS = <real> A
EXPONENTIAL COEFFICIENT = <real> n
#
# Johnson-Cook hardening
#
HARDENING FUNCTION = <string>hardening_function_name
RATE CONSTANT = <real> C
REFERENCE RATE = <real>  $\dot{\epsilon}_0$ 
#
# Power law breakdown hardening
#
```

```

HARDENING FUNCTION = <string>hardening_function_name
RATE COEFFICIENT    = <real> g
RATE EXPONENT       = <real> m
#
# User defined hardening
#
HARDENING FUNCTION = <string>hardening_function_name
#
# Spline based hardening curve
#
CUBIC SPLINE TYPE  = <string>
CARDINAL PARAMETER = <real> val
KNOT EQPS          = <real_list> vals
KNOT STRESS         = <real_list> vals
#
#
# Following Commands Pertain to Flow_Stress Hardening Model
#
#      - Isotropic Hardening model
#
ISOTROPIC HARDENING MODEL = LINEAR | POWER_LAW | VOCE |
                           USER_DEFINED
#
# Specifications for Linear, Power-law, and Voce same as above
#
# User defined hardening
#
ISOTROPIC HARDENING FUNCTION = <string>iso_hardening_fun_name
#
#      - Rate dependence
#
RATE MULTIPLIER = JOHNSON_COOK | POWER_LAW_BREAKDOWN |
                  USER_DEFINED | RATE_INDEPENDENT (RATE_INDEPENDENT)
#
# Specifications for Johnson-Cook, Power-law-breakdown
#      same as before EXCEPT no need to specify a
#      hardening function
#
# User defined rate multiplier
#
RATE MULTIPLIER FUNCTION = <string> rate_mult_function_name
#
#      - Temperature dependence
#
TEMPERATURE MULTIPLIER = JOHNSON_COOK | USER_DEFINED |
                           TEMPERATURE_INDEPENDENT (TEMPERATURE_INDEPENDENT)
#

```

```

# Johnson-Cook temperature dependence
#
# MELTING TEMPERATURE = <real>  $\theta_{melt}$ 
# REFERENCE TEMPERATURE = <real>  $\theta_{ref}$ 
# TEMPERATURE EXPONENT = <real>  $M$ 
#
# User-defined temperature dependence
# TEMPERATURE MULTIPLIER FUNCTION = <string>temp_mult_function_name
#
#
# Following Commands Pertain to Decoupled_Flow_Stress Hardening Model
#
# - Isotropic Hardening model
#
# ISOTROPIC HARDENING MODEL = LINEAR | POWER_LAW | VOCE | USER_DEFINED
#
# Specifications for Linear, Power-law, and Voce same as above
#
# User defined hardening
#
# ISOTROPIC HARDENING FUNCTION = <string>isotropic_hardening_function_name
#
# - Rate dependence
#
# YIELD RATE MULTIPLIER = JOHNSON_COOK | POWER_LAW_BREAKDOWN |
#                         USER_DEFINED | RATE_INDEPENDENT (RATE_INDEPENDENT)
#
# Specifications for Johnson-Cook, Power-law-breakdown same as before
# EXCEPT no need to specify a hardening function
# AND should be preceded by YIELD
#
# As an example for Johnson-Cook yield rate dependence,
#
# YIELD RATE CONSTANT = <real>  $C^y$ 
# YIELD REFERENCE RATE = <real>  $\dot{\epsilon}_0^y$ 
#
# User defined rate multiplier
#
# YIELD RATE MULTIPLIER FUNCTION = <string>yield_rate_mult_function_name
#
# HARDENING_RATE MULTIPLIER = JOHNSON_COOK | POWER_LAW_BREAKDOWN |
#                             USER_DEFINED | RATE_INDEPENDENT (RATE_INDEPENDENT)
#
# Syntax same as for yield parameters but with a HARDENING prefix
#
# - Temperature dependence
#

```

```

YIELD TEMPERATURE MULTIPLIER = JOHNSON_COOK | USER_DEFINED |
    TEMPERATURE_INDEPENDENT (TEMPERATURE_INDEPENDENT)
#
#  Johnson-Cook temperature dependence
#
YIELD MELTING TEMPERATURE = <real>  $\theta_m^Y$ 
YIELD REFERENCE TEMPERATURE = <real>  $\theta_{ref}^Y$ 
YIELD TEMPERATURE EXPONENT = <real>  $M^Y$ 
#
#  User-defined temperature dependence
YIELD TEMPERATURE MULTIPLIER FUNCTION = <string>yield_temp_mult_fun_name
#
HARDENING TEMPERATURE MULTIPLIER = JOHNSON_COOK | USER_DEFINED |
    TEMPERATURE_INDEPENDENT (TEMPERATURE_INDEPENDENT)
#
#  Syntax for hardening constants same as for yield but
#      with HARDENING prefix
#
END [PARAMETERS FOR MODEL J2_PLASTICITY]

```

Output variables available for this model are listed in Table 4-17.

Table 4-17. State Variables for J2 PLASTICITY Model

Name	Description
EQPS	equivalent plastic strain, $\bar{\epsilon}^P$
EQDOT	equivalent plastic strain rate, $\dot{\bar{\epsilon}}^P$
SEFF	effective stress, ϕ

REFERENCES

- [1] G.R. Johnson and W.H. Cook. A constitutive model and data for metals subjected to large strains, high strain rates and high temperatures. In *Proc. 7th. Int. Symp. on Ballistics*, pages 541–547, The Hague, The Netherlands, 1983.
- [2] G.R. Johnson and W.H. Cook. Fracture characteristics of three metals subjected to various strains, strain rates, temperatures and pressures. *Engineering Fracture Mechanics*, 21(1): 31–48, 1985.
- [3] R. Hill. *The Mathematical Theory of Plasticity*. Oxford University Press, 1950.
- [4] J. Lemaître and J.-L. Chaboche. *Mechanics of Solid Materials*. Cambridge University Press, 1990.
- [5] J. Lubliner. *Plasticity Theory*. Dover, 2008.
- [6] H. J. Frost and M. F. Ashby. *Deformation mechanism maps: the plasticity and creep of metals and ceramics*. Pergamon press, 1982.
- [7] A.A. Brown and D.J. Bammann. Validation of a model for static and dynamic recrystallization in metals. *International Journal of Plasticity*, 32–33:17–35, 2012.

4.14. HOSFORD PLASTICITY MODEL

4.14.1. Theory

Like other elastic-plastic models in Lamé, the Hosford plasticity model is a rate-independent hypoelastic formulation. Unlike the Hill and other more complex plasticity models, it is isotropic. In a similar fashion to those models, the total rate of deformation is additively decomposed into an elastic and plastic part such that

$$D_{ij} = D_{ij}^e + D_{ij}^p. \quad (4.14.1)$$

The objective stress rate, depending only on the elastic deformation, may then be written as,

$$\dot{\sigma}_{ij} = \mathbb{C}_{ijkl} D_{kl}^e. \quad (4.14.2)$$

The Hosford plasticity model utilizes a yield surface first put forth by W. F. Hosford in the 1970's [1] that is isotropic but non-quadratic. This specific form was proposed due to experimental observations of biaxial stretching in which neither the Tresca or J_2 yield surfaces could describe the results. In contrast to many of the yield surfaces proposed for similar purposes, only two parameters are utilized. Even with these limited terms, the developed model is quite versatile and can be reduced to von Mises or Tresca conditions as well as capturing responses in between. This yield surface is given as,

$$f(\sigma_{ij}, \bar{\varepsilon}^p) = \phi(\sigma_{ij}) - \bar{\sigma}(\bar{\varepsilon}^p) = 0, \quad (4.14.3)$$

in which $\phi(\sigma_{ij})$ is the Hosford effective stress and $\bar{\sigma}(\bar{\varepsilon}^p)$ is the isotropic hardening function. The Hosford effective stress is a non-quadratic function of the principal stresses (σ_i , $i = 1, 2, 3$) and is given as

$$\phi(\sigma_{ij}) = \left[\frac{|\sigma_1 - \sigma_2|^a + |\sigma_2 - \sigma_3|^a + |\sigma_1 - \sigma_3|^a}{2} \right]^{1/a} \quad (4.14.4)$$

in which a is the yield surface exponent. Interestingly, if $a = 2$ or 4 the yield surface reduces to that of a J_2 von Mises surface while $a = 1$ or as $a \rightarrow \infty$ produces a Tresca like shape. If the value of a is above 4 the yield surface takes a position between the Tresca and J_2 limits. Typical values are $a = 6$ or $a = 8$ for *bcc* and *fcc* metals, respectively [2]. To highlight this variability the yield surface is plotted below in Figure 4-44 for three values of a – $a = 4, 8$, and 100 .

For the hardening function, $\bar{\sigma}(\bar{\varepsilon}^p)$, a variety of forms including linear, power law, or a more general user defined function may be used.

An associated flow rule is utilized such that the plastic rate of deformation is normal to the yield surface and is given by,

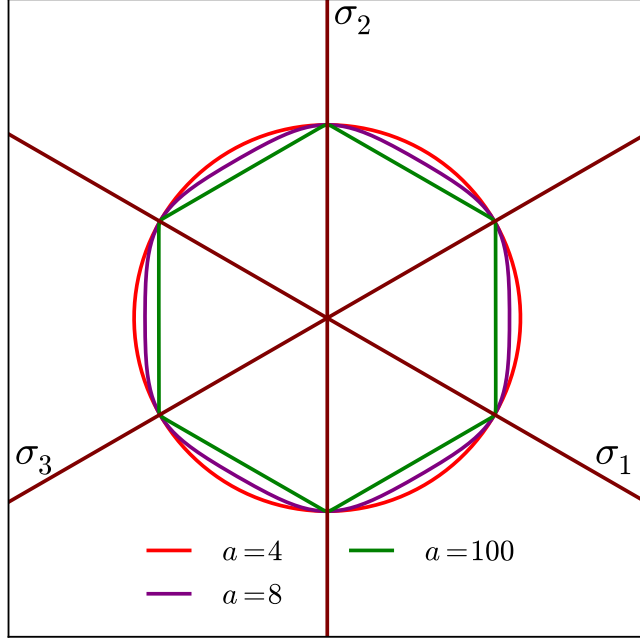


Figure 4-44. Example Hosford yield surfaces, $f(\sigma_{ij}, \bar{\varepsilon}^p = 0; a)$, presented in the deviatoric π -plane. The presented surfaces correspond to the different yield exponents $a = 4, 8$, and 100 .

$$\dot{D}_{ij}^p = \dot{\gamma} \frac{\partial \phi}{\partial \sigma_{ij}}, \quad (4.14.5)$$

where $\dot{\gamma}$ is the consistency multiplier enforcing $f = 0$ during plastic deformation. Given the form of f , it can also be shown that $\dot{\gamma} = \dot{\varepsilon}^p$.

For details, please see [3].

4.14.1.1. Plastic Hardening

Plastic hardening refers to increases in the flow stress, $\bar{\sigma}$, with plastic deformation. As such, hardening is described via the functional relationship between the flow stress and isotropic hardening variable (effective plastic strain), $\bar{\sigma}(\bar{\varepsilon}^p)$. Over the course of nearly a century of work in metal plasticity, a variety of relationships have been proposed to describe the interactions associated with different physical interpretations, deformation mechanisms, and materials. To enable the utilization of the same plasticity models for different material systems, a modular implementation of plastic hardening has been adopted such that the analyst may select different hardening models from the input deck thereby avoiding any code changes or user subroutines. In this section, additional details are given to the different models to enable the user to select the appropriate choice of model. Note, the models being discussed here are only for *isotropic* hardening in which the yield surface expands. *Kinematic* hardening in which the yield surface translates in stress-space with deformation and *distortional* hardening where the shape of the

yield surface changes shape with deformation are not treated. For a larger discussion of the phenomenology and history of different hardening types, the reader is referred to [4, 5, 6].

Given the ubiquitous nature of these hardening laws in computational plasticity, some (if not most) of this material may be found elsewhere in this manual. Nonetheless, the discussion is repeated here for the convenience of the reader.

Linear

Linear hardening is conceptually the simplest model available in LAMÉ. As the name implies, a linear relationship is assumed between the hardening variable, $\bar{\varepsilon}^p$, and flow stress. The constant giving the degree of increase of yield stress with plastic flow is termed the hardening modulus and is given as, H' , while the expression for the flow stress may be written,

$$\bar{\sigma} = \sigma_y + H' \bar{\varepsilon}^p. \quad (4.14.6)$$

The simplicity of the model is its main feature as the constant slope,

$$\frac{d\bar{\sigma}}{d\bar{\varepsilon}^p} = H', \quad (4.14.7)$$

makes the model attractive for analytical models and cheap for computational implementations (*e.g.* radial return algorithms require only a single correction step). Unfortunately, the simplicity of the representation also means that it has limited predictive capabilities and can lead to overly stiff responses.

Power Law

Another common expression for isotropic hardening is the power-law hardening model. Due to its prevalence, a dedicated ELASTIC-PLASTIC POWER LAW HARDENING model may be found in LAMÉ (see Section 4.8.1). This expression is given as,

$$\bar{\sigma} = \sigma_y + A < \bar{\varepsilon}^p - \varepsilon_L >^n, \quad (4.14.8)$$

in which $< \cdot >$ are Macaulay brackets, ε_L is the Lüders strain, A is a fitting constant, and n is an exponent typically taken such that $0 < n \leq 1$. The Lüders strain is a positive, constant strain value (default to zero) giving an initial plastic deformation domain in which the response is perfectly plastic (see Fig. 4-20). The derivative is then simply,

$$\frac{d\bar{\sigma}}{d\bar{\varepsilon}^p} = nA < \bar{\varepsilon}^p - \varepsilon_L >^{(n-1)}. \quad (4.14.9)$$

Note, one difficulty in such an implementation is that when the effective equivalent plastic strain is zero, numerical difficulties may arise in evaluating the derivative necessitating special treatment of the case.

Voce

The Voce hardening model (sometimes referred to as a saturation model) uses a decaying exponential in terms of the equivalent plastic strain such that the hardening eventually saturates to a specified value (thus the name). Such a relationship has been observed in some structural metals giving rise to the popularity of the model. The hardening response is given as,

$$\bar{\sigma} = \sigma_y + A (1 - \exp(-n\bar{\varepsilon}^p)), \quad (4.14.10)$$

in which A is a fitting constant and n is a fitting exponent describing how quickly the hardening saturates. Importantly, the derivative is written as,

$$\frac{d\bar{\sigma}}{d\bar{\varepsilon}^p} = nA \exp(-n\bar{\varepsilon}^p), \quad (4.14.11)$$

and is well defined everywhere giving the selected form an advantage over the aforementioned power law model.

Johnson-Cook

The Johnson-Cook [7, 8] hardening type is a *rate-dependent* formulation utilizing the assumption that rate-independent and rate-dependent contributions may be multiplicatively separated. Specifically, use of this option requires specifying a user-defined hardening function to capture rate-independent contributions and Johnson-Cook type rate dependent coefficients. The flow stress may be written in this fashion as,

$$\bar{\sigma} = \tilde{\sigma}_y(\bar{\varepsilon}^p) \left[1 + C \left\langle \ln \left(\frac{\dot{\varepsilon}^p}{\dot{\varepsilon}_0} \right) \right\rangle \right], \quad (4.14.12)$$

in which $\tilde{\sigma}_y(\bar{\varepsilon}^p)$ is the user-specified rate-independent hardening function, C is a fitting constant and $\dot{\varepsilon}_0$ is a reference strain rate. The Macaulay brackets ensure the material behaves in a rate independent fashion when $\dot{\varepsilon}^p < \dot{\varepsilon}_0$.

Power Law Breakdown

Like the Johnson-Cook formulation, the power-law breakdown model is also rate-dependent. Again, a multiplicative decomposition between rate-independent and dependent hardening contributions. In this case, however, the functional form is derived from the analysis of Frost and

Ashby [9] in which power-law relationships like those of the Johnson-Cook and cease to appropriately capture the physical response. The form used here is similar to the expression used by Brown and Bammann [10] and is written as,

$$\bar{\sigma} = \tilde{\sigma}_y(\bar{\varepsilon}^p) \left[1 + \operatorname{asinh} \left(\left(\frac{\dot{\varepsilon}^p}{g} \right)^{(1/m)} \right) \right], \quad (4.14.13)$$

with $\tilde{\sigma}_y(\bar{\varepsilon}^p)$ being the user supplied rate independent expression, g is a model parameter related to the activation energy in going from climb to glide-controlled deformation, and m dictates the strength of the dependence.

4.14.2. Implementation

The Hosford plasticity model is implicitly integrated using a closest point projection (CPP) return mapping algorithm (RMA). The resulting nonlinear equations are solved via a line search augmented Newton-Raphson method and the stress update routine is very similar to that of the Hill plasticity model. The key difference between the two is the isotropy. Specifically, given that the Hosford yield surface is isotropic and the functional form is given in terms of principal stresses, the stress update routine is performed in *principal stress* space and then converted to global Cartesian values.

For a loading step, a trial stress state, T_{ij}^{tr} , may be computed by knowing the rate of deformation, d_{ij} , and time step as,

$$T_{ij}^{tr} = T_{ij}^n + \Delta t \mathbb{C}_{ijkl} d_{kl}. \quad (4.14.14)$$

The principal stresses, T_i^{tr} , may then be used to determine the trial yield function value, $\phi^{tr} = \phi(T_i^{tr}, \bar{\varepsilon}^{p(n)})$. If $\phi^{tr} < 0$, the elastic trial solution is acceptable. On the other hand, if the trial solution is inadmissible, the aforementioned CPP-RMA problem is solved in principal stress space. The crux of this algorithm is the simultaneous solution of two nonlinear equations – (i) the flow rule and (ii) consistency condition. The former leads to a residual, R_i , of the form (again in principal stress space),

$$R_i = \Delta d_i^p - \Delta \gamma \frac{\partial \phi}{\partial T_i} = 0, \quad (4.14.15)$$

while the latter is enforced by the yield function,

$$f = \phi(T_i) - \bar{\sigma}(\bar{\varepsilon}^p) = 0, \quad (4.14.16)$$

and its derivative (\dot{f}) being zero. This system is solved via a Newton-Raphson type approach in which the state variables (stress, T_i , and consistency multiplier, γ) are iteratively corrected until the residuals are satisfied. Using $(k+1)$ and (k) to denote the next and current iterations, this updating takes the form,

$$\begin{aligned}\Delta\gamma^{(k+1)} &= \Delta\gamma^{(k)} + \Delta(\Delta\gamma), \\ T_i^{(k+1)} &= T_i^{(k)} + \Delta T_i,\end{aligned}\quad (4.14.17)$$

in which $T^{(0)} = T_i^{tr}$ and $\Delta\gamma^{(0)} = 0$. Consistent linearization of the two equations can be solved to give correction increments of the form,

$$\begin{aligned}\Delta(\Delta\gamma) &= \frac{f^{(k)} - R_i^{(k)} \mathcal{L}_{ij}^{(k)} \frac{\partial\phi^{(k)}}{\partial T_j}}{\frac{\partial\phi^{(k)}}{\partial T_i} \mathcal{L}_{ij}^{(k)} \frac{\partial\phi^{(k)}}{\partial T_j} + H'^{(k)}}, \\ \Delta T_i &= -\mathcal{L}_{ij}^{(k)} \left(R_j^{(k)} + \Delta(\Delta\gamma) \frac{\partial\phi^{(k)}}{\partial T_j} \right),\end{aligned}\quad (4.14.18)$$

with $\mathcal{L}_{ij}^{(k)}$ being the Hessian of the CPP-RMA problem and $H'^{(k)}$ is the slope of the hardening curve.

Previous studies have indicated that the Newton-Raphson method alone may be insufficient to guarantee convergence with arbitrary stress states in the case of non-quadratic yield surfaces [11, 12, 3]. To address this, a *line search* method is adopted. In such an approach, the incrementation rule (4.14.17) is modified such that,

$$\begin{aligned}\Delta\gamma^{(k+1)} &= \Delta\gamma^{(k)} + \alpha\Delta(\Delta\gamma), \\ T_i^{(k+1)} &= T_i^{(k)} + \alpha\Delta T_i,\end{aligned}\quad (4.14.19)$$

where $\alpha \in (0, 1]$ is the step magnitude. This parameter enforces that the solution be converging and is determined via various convergence criteria. The $\alpha = 1$ case corresponds to the Newton-Raphson method. Utilization of this approach has been shown to greatly increase the robustness of this algorithm under large trial stresses [3].

Finally, upon convergence of the algorithm, the Cartesian stress are found from the principal stresses via,

$$T_{ij}^{n+1} = \sum_{k=1}^3 T_k^{n+1} \hat{e}_i^k \hat{e}_j^k, \quad (4.14.20)$$

in which \hat{e}_i^k is the eigenvector of the k^{th} principal stress.

Details of this implementation and the line search algorithm may be found in the work of Scherzinger [3].

4.14.3. Verification

The Hosford plasticity material model is verified through a variety of loading and material conditions. For these cases, the elastic properties corresponding to 2090-T3 aluminum [13] given in Section 4.15.3 are utilized. The elastic properties are $E = 70$ GPa and $\nu = 0.25$ while a linear hardening law of the form,

$$\bar{\sigma}(\bar{\varepsilon}^p) = \sigma_y + K\bar{\varepsilon}^p, \quad (4.14.21)$$

with $\sigma_y = 200$ MPa and $K = E/200$ is assumed. For these studies, two different yield surface exponents will be used, $a = 4, 8$. The former corresponds to the J_2 surface while the latter is a common value for aluminum.

4.14.3.1. Uniaxial Stress

In the case of uniaxial stress (σ), it is trivial to note that the corresponding principal stress state is simply $\sigma_1 = \sigma$, $\sigma_2 = \sigma_3 = 0$. As such, regardless of a ,

$$\phi = |\sigma_1|. \quad (4.14.22)$$

With the aforementioned linear hardening, this case reduces to that discussed in Section 4.7.3.1. Corresponding analytical and numerical results (both with $a = 4$ and 8) of the axial stress and lateral strain are presented in Figures 4-45a and 4-45b, respectively. In these figures, the invariance of response on yield surface exponent through this loading is clearly observed.

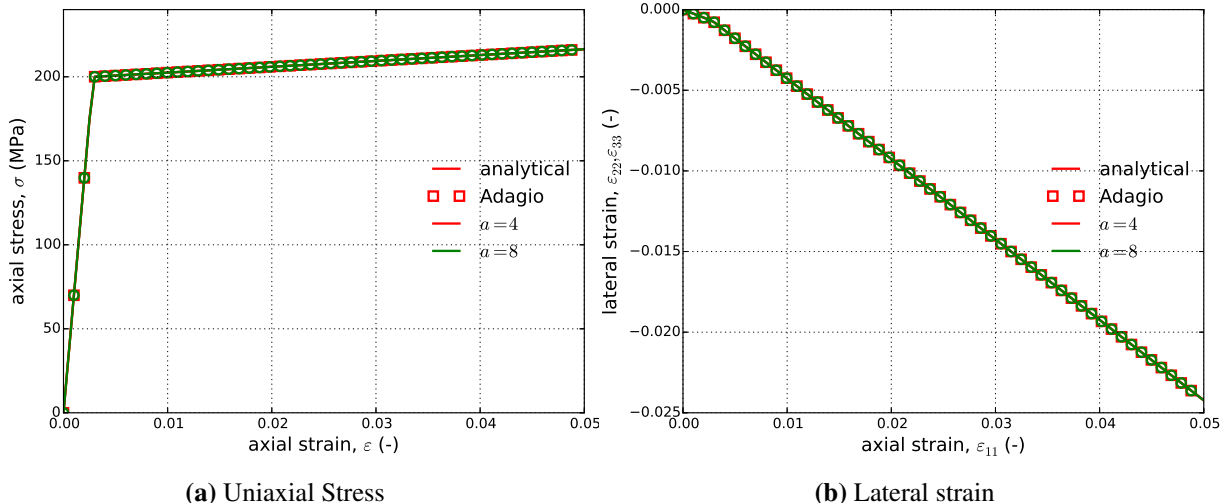


Figure 4-45. (a) Axial stress-strain and (b) lateral strain results of the Hosford plasticity model determined analytically and numerically for the case of yield surface exponents $a = 4, 8$.

4.14.3.2. Pure Shear

To explore the impact of the yield exponent a , the case of pure shear is considered. Specifically, the only shear component shall be in the Cartesian $e_1 - e_2$ direction such that $\sigma_{12} = \tau$ and ε_{12} are the only non-zero components. Noting that the three principal stresses are $\tau, 0, -\tau$, the yield condition simplifies to

$$\phi = [1 + 2^{a-1}]^{1/a} \tau. \quad (4.14.23)$$

The equivalent plastic strain may then be found as a function of ε_{12} in the same way as presented in Section 4.15.3.2. Shear stress-strain results for both $a = 4, 8$ are presented in Figure 4-46 as determined both by adagio and analytically. The boundary conditions for this loading are given in Appendix A.3. In these results, the effect of the yield surface exponent, a , may clearly be seen.

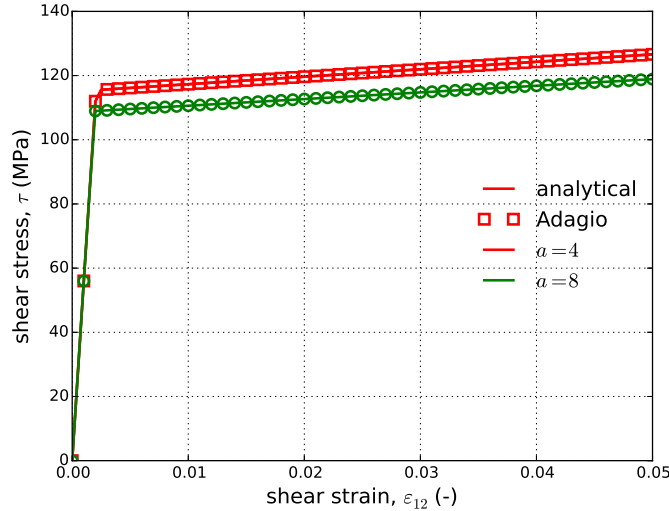


Figure 4-46. Shear stress-strain results of the Hosford plasticity model determined analytically and numerically for the case of yield surface exponents $a = 4, 8$.

4.14.3.3. Plastic Hardening

To verify the capabilities of the hardening models, rate-*independent* and rate-*dependent* alike, the constant equivalent plastic strain rate, $\dot{\varepsilon}^p$, uniaxial stress and pure shear verification tests described in Appendix A.5 are utilized. In these simplified loading cases, the material state may be found explicitly as a function of time knowing the prescribed equivalent strain rate. For the rate-*independent* cases, a strain rate of $\dot{\varepsilon}^p = 1 \times 10^{-4} \text{ s}^{-1}$ is used for ease in simulations although the selected rate does not affect the results. Through this testing protocol, the hardening models are not only tested at different rates but also different yield surface shapes. In the current Hosford

case, multiple yield surface exponents, a , are considered to probe this effect. Additionally, the rate-*dependent* models are tested for a wide range of strain rates (over five decades) and with all three rate-*independent* hardening functions ($\tilde{\sigma}_y$ in the previous theory section). Although linear, Voce, and power-law rate-*independent* representations are utilized in the rate-*dependent* tests, in those cases the hardening models are prescribed via user-defined analytic functions. The rate-*independent* verification exercises, on the other hand, examine the built-in hardening models. This distinction necessitates the different considerations and treatments.

The various rate-*dependent* and rate-*independent* hardening coefficients are found in Table 4-18 while the remaining model parameters are unchanged from the previous verification exercises. For the current verification exercises, the rate-*independent* hardening models (linear, Voce, and power-law) will first be considered and then the rate-*dependent* forms (Johnson-Cook, power-law breakdown).

C	0.1	$\dot{\varepsilon}_0$	$1 \times 10^{-4} \text{ s}^{-1}$
g	0.21 s^{-1}	m	16.4
$\tilde{H}_{\text{Linear}}$	200 MPa	-	-
\tilde{A}_{PL}	400 MPa	\tilde{n}_{PL}	0.25
\tilde{A}_{Voce}	200 MPa	\tilde{n}_{Voce}	20

Table 4-18. The model parameters for the hardening verification tests used with the Hosford plasticity model during verification tests. Parameters for the rate-*independent* hardening functions, $\tilde{\sigma}_y$, are also given and denoted with a $\tilde{\cdot}$ while the subscript refers to the functional form.

Linear

The aforementioned verification exercises from Appendix A.5 are used to investigate the numerical implementation of the rate-*independent* linear hardening model. Results from uniaxial stress and pure shear exercises determined analytically and numerically are given in Figure 4-47 for three different exponents $a = 4, 8$, and 20 . The first exponent produces a J_2 like response with the latter increasing the curvature of the yield surface. As discussed in Section 4.14.3.1, a purely uniaxial response is independent of exponent thus producing the collapsed results in Figure 4-47a. In both the uniaxial stress and pure shear cases, clear agreement is noted between the two sets of results. The linear slope (tangent modulus) giving the model its name is also observable in the results of Figure 4-47.

Power-Law

To consider the performance of the common power-law hardening model with the Hosford yield surface, the uniaxial stress and pure shear exercises of Appendix A.5 are solved analytically and numerically. These results are presented in Figure 4-48 for three different Hosford exponents – $a = 4, 8$ and 20 . As expected from previous discussions the uniaxial stress results in Figure 4-48a

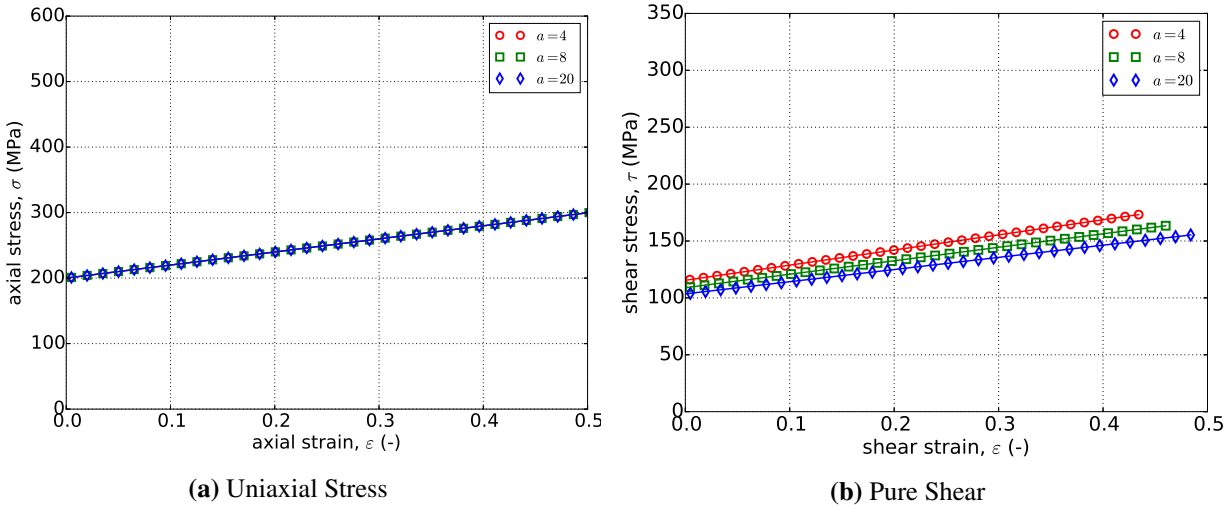


Figure 4-47. (a) Uniaxial stress-strain and (b) pure shear responses of the Hosford plasticity model with rate-*independent*, linear hardening. Solid line are analytical while open symbols are numerical.

are independent of a . For both the uniaxial stress and pure shear results, the desired agreement between analytical and numerical solutions is apparent. These results also highlight the initial curved response during plastic-deformation eventually transitioning into a more linear type response.

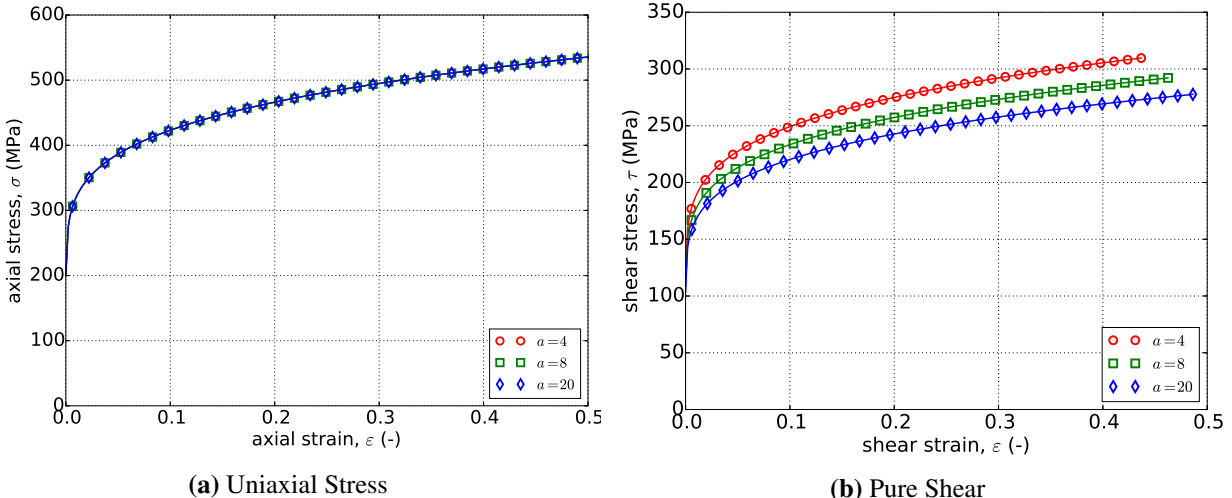


Figure 4-48. (a) Uniaxial stress-strain and (b) pure shear responses of the Hosford plasticity model with rate-*independent*, power-law hardening. Solid line are analytical while open symbols are numerical.

Voce

For the rate-*independent* Voce hardening model, the problems of Appendix A.5 are used to verify the model response. Specifically, results for the uniaxial stress and pure shear analyses are presented in Figure 4-49 as determined analytically and numerically for three different values of a – $a = 4, 8$, and 20 . From these results, clear agreement is noted between the two sets of results; including the invariance of the uniaxial stress case to a (Figure 4-49a). Additionally, the results of Figure 4-49 also exemplify the saturation nature of the Voce hardening model as the stress-strain response eventually asymptotes.

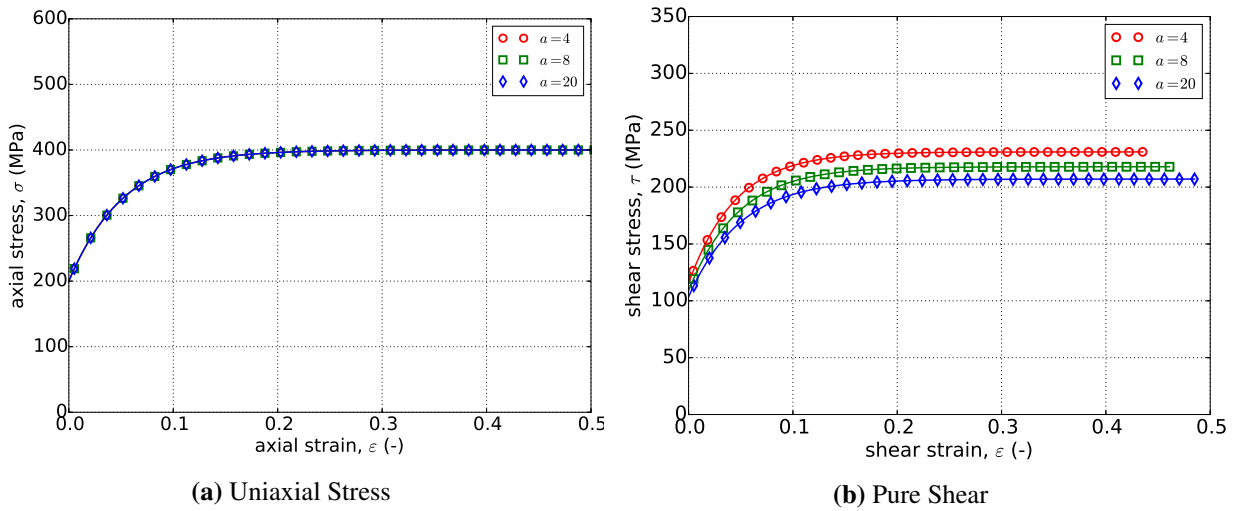


Figure 4-49. (a) Uniaxial stress-strain and (b) pure shear responses of the Hosford plasticity model with rate-*independent*, Voce hardening. Solid line are analytical while open symbols are numerical.

Johnson-Cook

As noted in Section 4.14.3.1, the uniaxial stress response is independent of a . This is also reflected Appendix A.5.1 in which the stress weighting coefficients (Γ) for the Hosford uniaxial case are one. As such in Figure 4-50 the results of the constant equivalent plastic strain rate uniaxial stress test are presented with $a = 8$ and using the linear (4-50a), power-law (4-50b), and Voce (4-50c) rate-*independent* hardening models for five different rates – $\dot{\varepsilon}^p = 1 \times 10^{-3}, 1 \times 10^{-2}, 1 \times 10^{-1}, 1 \times 10^0$ and $1 \times 10^1 \text{ s}^{-1}$. In all cases in Figure 4-50 excellent agreement is observed between the results.

Unlike the uniaxial stress case, for pure shear the response depends on the exponent a . Therefore, in addition to the three hardening models, results are also presented for three different exponent values – $a = 4, 8$, and 20 . The results for all nine cases are presented in Figure 4-51 and again excellent agreement is noted in all instances.

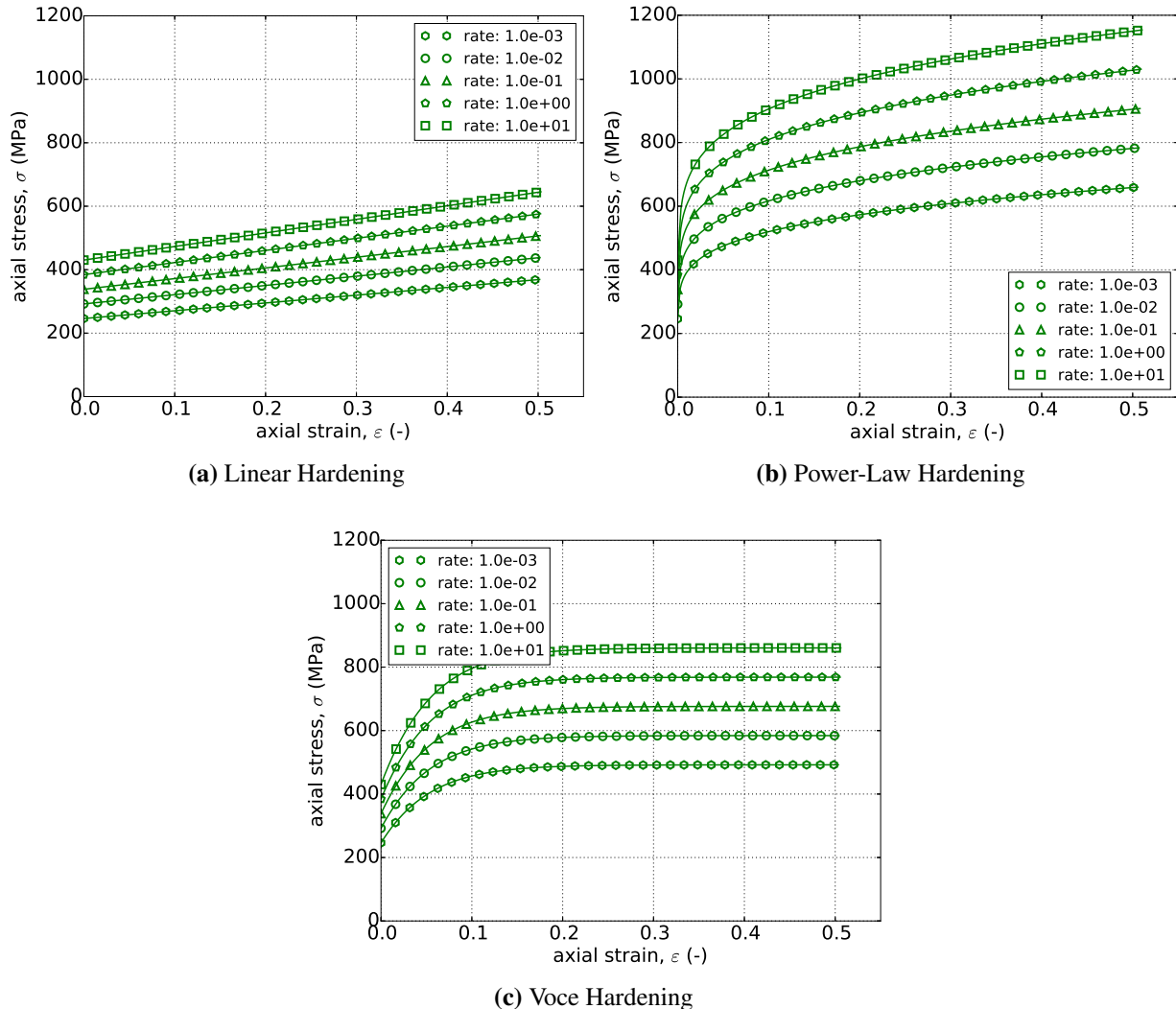


Figure 4-50. Uniaxial stress-strain response of the Hosford plasticity model ($a = 8$) with rate-dependent, Johnson-Cook type hardening with (a) linear (b) power-law and (c) Voce rate-independent hardening. Solid lines are analytical results while open symbols are numerical.

Power-Law Breakdown

As mentioned in the previous Johnson-Cook section, for the Hosford model under uniaxial stress the response is independent of yield surface exponent, a . Therefore, Figure 4-52 presents the results of the constant equivalent plastic strain rate verification test of Appendix A.5.1 for strain rates spanning five decades $-\dot{\varepsilon}^p = 1 \times 10^{-3}, 1 \times 10^{-2}, 1 \times 10^{-1}, 1 \times 10^0$ and $1 \times 10^1 \text{ s}^{-1}$. The tests are performed for each rate-independent hardening model. In all fifteen cases excellent agreement is noted between numerical and analytical results.

Similarly, Figure 4-53 gives the results of the pure shear variant of the constant equivalent plastic

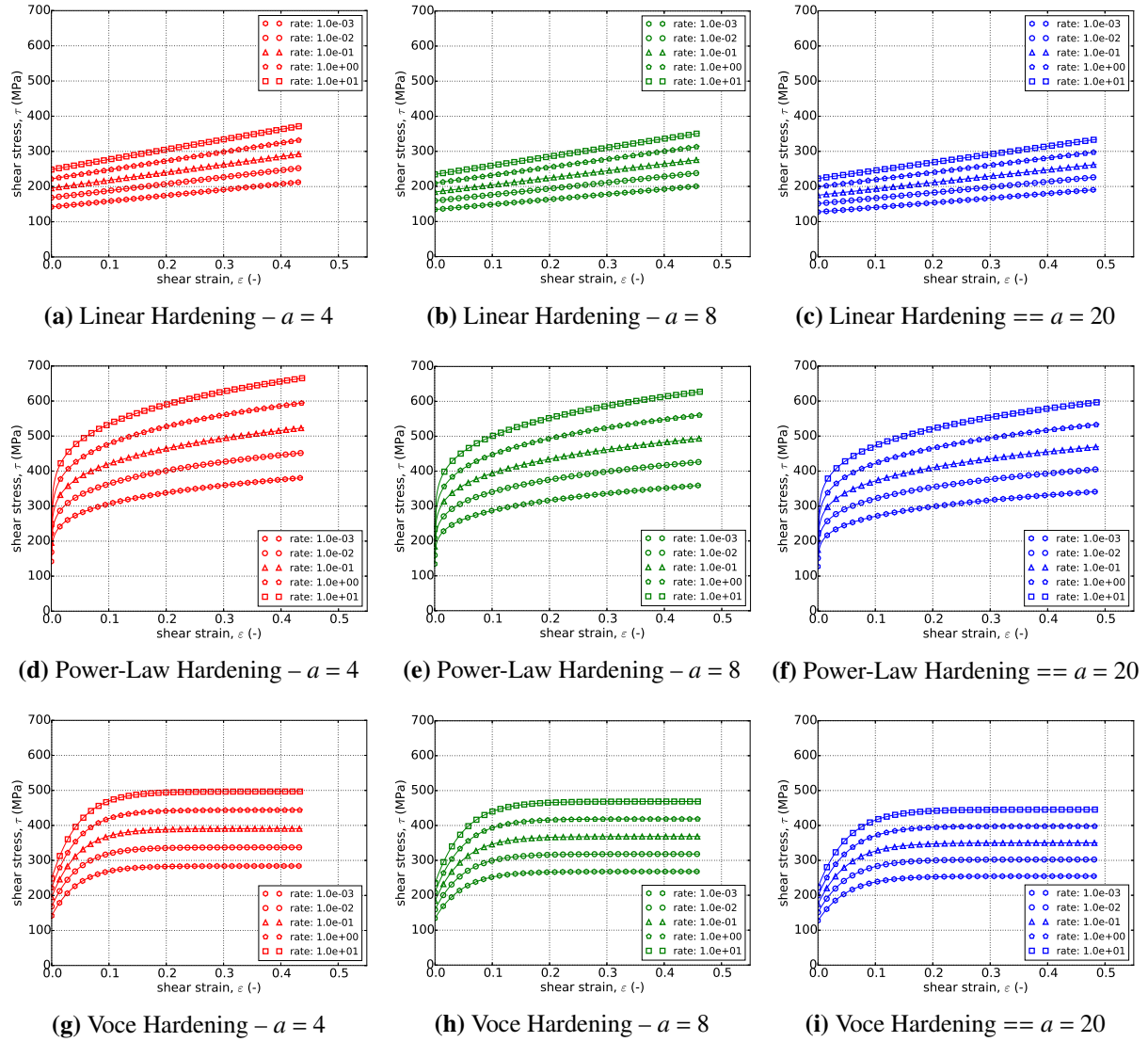


Figure 4-51. Stress-strain response of the Hosford plasticity model with rate-dependent, Johnson-Cook type hardening in pure shear with (a-c) linear (d-f) power-law and (g-i) Voce rate-independent hardening. Solid lines are analytical results while open symbols are numerical.

strain rate verification test of Appendix A.5.2. The same five rates used in the uniaxial stress case are again utilized although in this instance as the pure shear response does depend on a the results are given for three yield surface exponents – $a = 4, 8$ and 20 . In the forty-five cases shown in Figure 4-53 quite acceptable agreement is noted verifying the capabilities of the rate-dependent Hosford implementation.

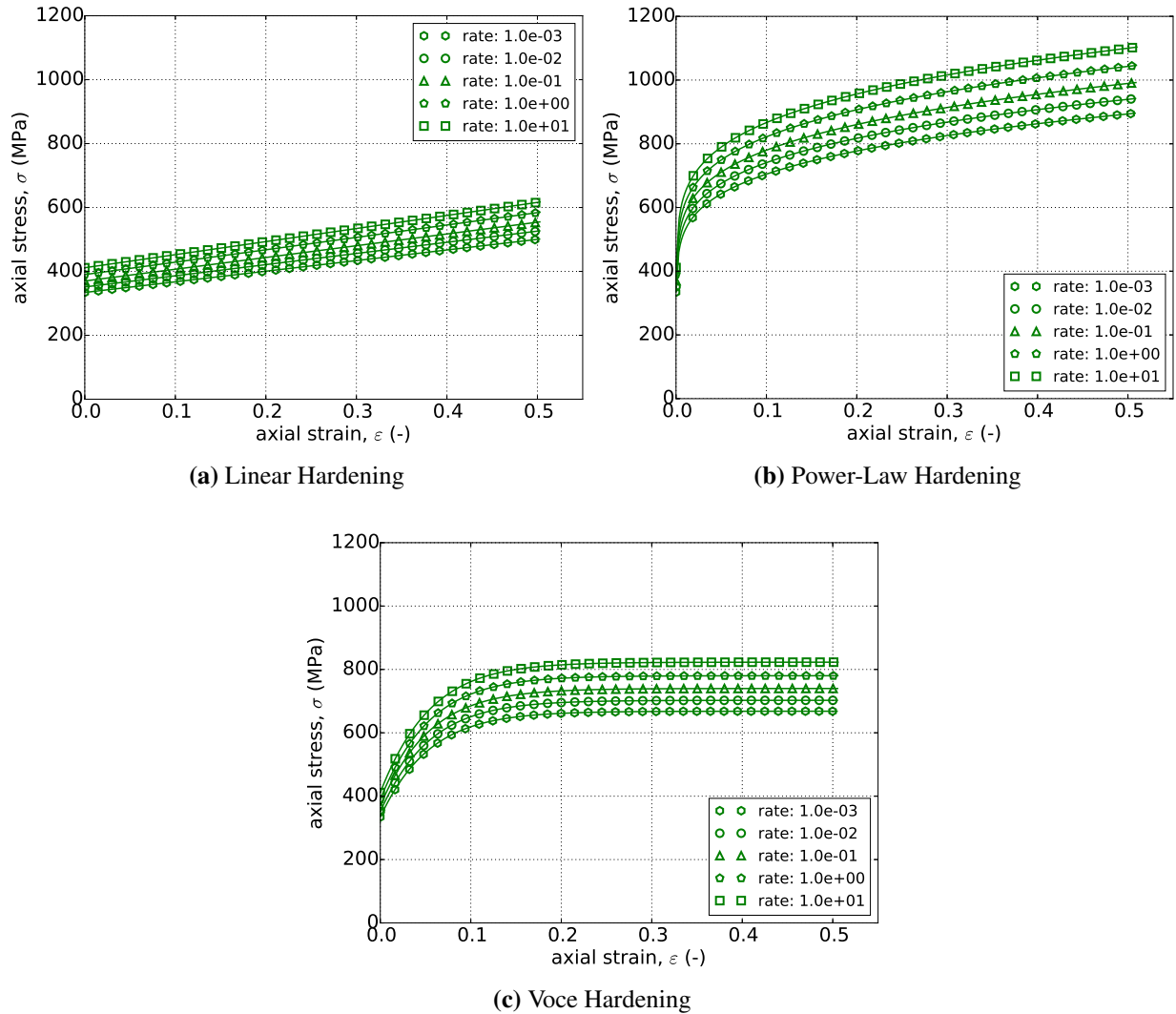


Figure 4-52. Uniaxial stress-strain response of the Hosford plasticity model ($a = 8$) with rate-dependent, power-law breakdown type hardening with (a) linear (b) power-law and (c) Voce rate-independent hardening. Solid lines are analytical results while open symbols are numerical.

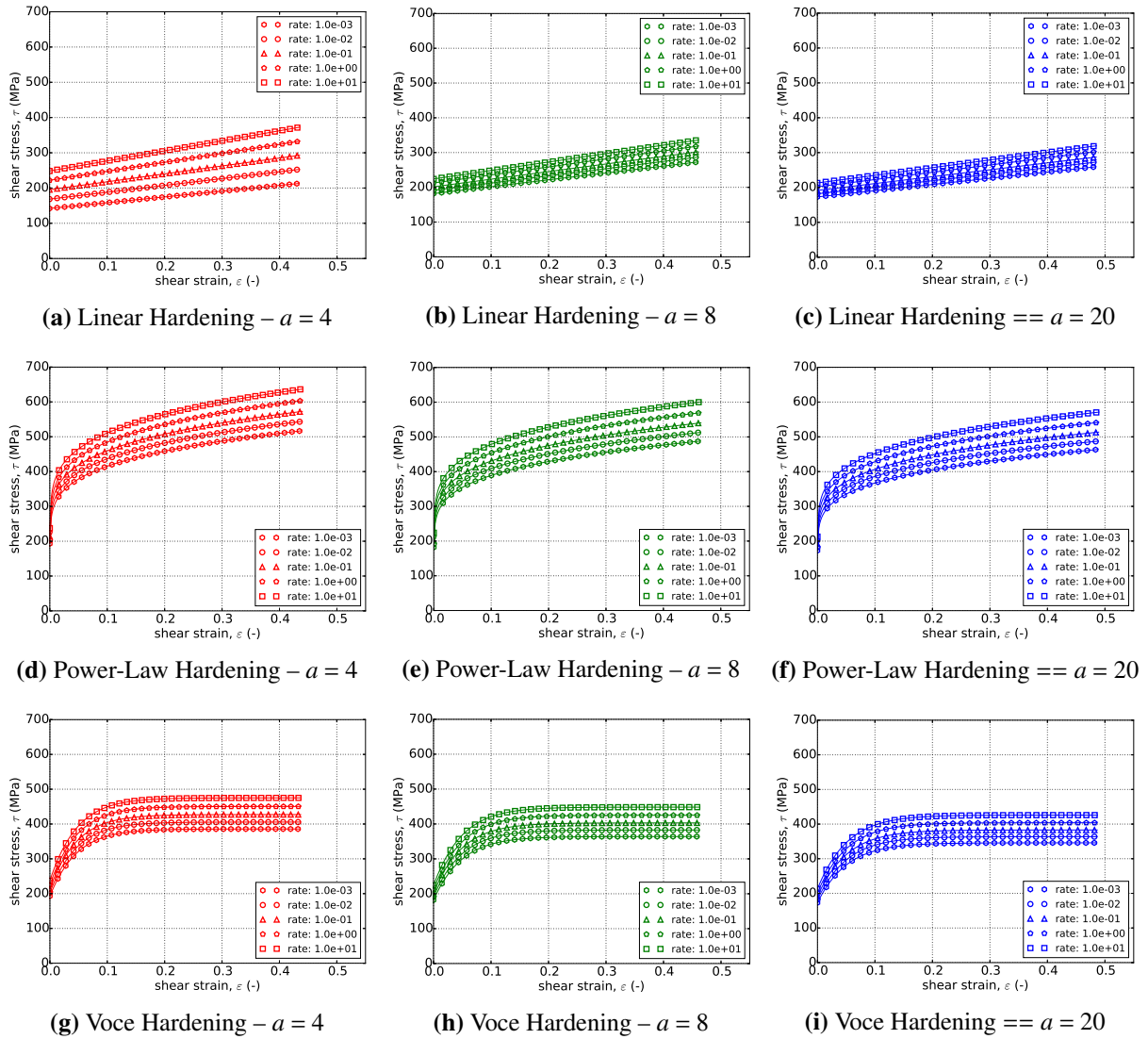


Figure 4-53. Stress-strain response of the Hosford plasticity model with rate-dependent, power-law breakdown type hardening in pure shear with (a-c) linear (d-f) power-law and (g-i) Voce rate-independent hardening. Solid lines are analytical results while open symbols are numerical.

4.14.4. User Guide

```
BEGIN PARAMETERS FOR MODEL HOSFORD_PLASTICITY
#
# Elastic constants
#
YOUNGS MODULUS = <real> E
POISSONS RATIO = <real> ν
SHEAR MODULUS = <real> G
BULK MODULUS = <real> K
LAMBDA = <real> λ
TWO MU = <real> 2μ
#
# Yield surface parameters
#
YIELD STRESS = <real> σy
A = <real> a (1.0)
#
# Hardening model
#
HARDENING MODEL = LINEAR | POWER_LAW | VOCE | USER_DEFINED |
    CUBIC_HERMITE_SPLIT | JOHNSON_COOK | POWER_LAW_BREAKDOWN
#
# Linear hardening
#
HARDENING MODULUS = <real> H'
#
# Power-law hardening
#
HARDENING CONSTANT = <real> A
HARDENING EXPONENT = <real> n (0.5)
LUDERS STRAIN = <real> εL (0.0)
#
# Voce hardening
#
HARDENING MODULUS = <real> A
EXPONENTIAL COEFFICIENT = <real> n
#
# Johnson-Cook hardening
#
HARDENING FUNCTION = <string>hardening_function_name
RATE CONSTANT = <real> C
REFERENCE RATE = <real> ε̇0
#
# Power law breakdown hardening
#
HARDENING FUNCTION = <string>hardening_function_name
```

```

RATE COEFFICIENT      = <real> g
RATE EXPONENT        = <real> m
#
# User defined hardening
#
HARDENING FUNCTION = <string>hardening_function_name
#
# Spline based hardening curve
#
CUBIC SPLINE TYPE   = <string>
CARDINAL PARAMETER  = <real> val
KNOT EQPS            = <real_list> vals
KNOT STRESS          = <real_list> vals
END [PARAMETERS FOR MODEL HOSFORD_PLASTICITY]

```

Output variables available for this model are listed in Table 4-19.

Table 4-19. State Variables for HOSFORD PLASTICITY Model

Name	Description
EQPS	equivalent plastic strain, $\bar{\epsilon}^p$
EQDOT	equivalent plastic strain rate, $\dot{\bar{\epsilon}}^p$
SEFF	effective stress, ϕ

REFERENCES

- [1] W.F. Hosford. A generalized isotropic yield criterion. *Journal of Applied Mechanics*, 39: 607–609, 1972.
- [2] A. Graf and W. Hosford. Calculations of forming limit diagrams. *Metallurgical Transactions A*, 21A:87–94, 1990.
- [3] W. M. Scherzinger. A return mapping algorithm for isotropic and anisotropic plasticity models using a line search method. *Computer Methods in Applied Mechanics and Engineering*, 317:526–553, 2017.
- [4] R. Hill. *The Mathematical Theory of Plasticity*. Oxford University Press, 1950.
- [5] J. Lemaitre and J.-L. Chaboche. *Mechanics of Solid Materials*. Cambridge University Press, 1990.
- [6] J. Lubliner. *Plasticity Theory*. Dover, 2008.
- [7] G.R. Johnson and W.H. Cook. A constitutive model and data for metals subjected to large strains, high strain rates and high temperatures. In *Proc. 7th. Int. Symp. on Ballistics*, pages 541–547, The Hague, The Netherlands, 1983.
- [8] G.R. Johnson and W.H. Cook. Fracture characteristics of three metals subjected to various strains, strain rates, temperatures and pressures. *Engineering Fracture Mechanics*, 21(1): 31–48, 1985.
- [9] H. J. Frost and M. F. Ashby. *Deformation mechanism maps: the plasticity and creep of metals and ceramics*. Pergamon press, 1982.
- [10] A.A. Brown and D.J. Bammann. Validation of a model for static and dynamic recrystallization in metals. *International Journal of Plasticity*, 32–33:17–35, 2012.
- [11] F. Armero and A. Pèrez-Foguet. On the formulation of closest-point projection algorithms in elastoplasticity – part I: The variational structure. *International Journal for Numerical Methods in Engineering*, 53:297–329, 2002.
- [12] A. Pèrez-Foguet and F. Armero. On the formulation of closest-point projection algorithms in elastoplasticity – part II: Globally convergent schemes. *International Journal for Numerical Methods in Engineering*, 53:331–374, 2002.
- [13] F. Barlat, H. Aretz, J. W. Yoon, J. C. Brem, and R. E. Dick. Linear transformation-based anisotropic yield functions. *International Journal of Plasticity*, 21:1009–1039, 2005.

4.15. HILL PLASTICITY MODEL

4.15.1. Theory

The Hill plasticity model is similar to other plasticity models except that it is not isotropic. It is a hypoelastic, rate-independent plasticity model. The rate form of the equation assumes an additive split of the rate of deformation into an elastic and plastic part

$$D_{ij} = D_{ij}^e + D_{ij}^p \quad (4.15.1)$$

The stress rate only depends on the elastic rate of deformation

$$\dot{\sigma}_{ij} = \mathbb{C}_{ijkl} D_{kl}^e \quad (4.15.2)$$

where \mathbb{C}_{ijkl} are the components of the fourth-order, isotropic elasticity tensor.

The Hill plasticity model has an orthotropic yield surface that assumes orthogonal principal material directions. An example of this yield surface is presented below in Figure 4-54 along with examples of two isotropic surfaces – the von Mises (J_2) and Hosford (with $a = 8$). The various surface parameters correspond to 2090-T3 aluminum and the specific Hill strengths are found in [1]. By comparing the Hill surface to the two isotropic surfaces, the impact of the anisotropy is clear. Additionally, substantial differences to the normals of the yield surfaces at points of intersection highlight the impact of the yield function selection on the resulting flow directions.

In functional form, the Hill yield surface looks like a von Mises yield surface except that there are 6 yield stresses: σ_{11}^y , σ_{22}^y , σ_{33}^y , τ_{12}^y , τ_{23}^y , and τ_{31}^y . These yield stresses correspond to 3 normal and 3 shear yield stresses. The yield function takes the form

$$\begin{aligned} \phi^2(\sigma_{ij}) = & F(\hat{\sigma}_{22} - \hat{\sigma}_{33})^2 + G(\hat{\sigma}_{33} - \hat{\sigma}_{11})^2 + H(\hat{\sigma}_{11} - \hat{\sigma}_{22})^2 \\ & + 2L\hat{\sigma}_{23}^2 + 2M\hat{\sigma}_{31}^2 + 2N\hat{\sigma}_{12}^2 = \bar{\sigma}^2(\bar{\varepsilon}^p) \end{aligned} \quad (4.15.3)$$

The coefficients F , G , H , L , M , and N were introduced by Hill. In terms of the yield stresses they are:

$$\begin{aligned} F &= \frac{(\bar{\sigma})^2}{2} \left[\frac{1}{(\sigma_{22}^y)^2} + \frac{1}{(\sigma_{33}^y)^2} - \frac{1}{(\sigma_{11}^y)^2} \right] ; \quad L = \frac{(\bar{\sigma})^2}{2} \left[\frac{1}{(\tau_{23}^y)^2} \right] \\ G &= \frac{(\bar{\sigma})^2}{2} \left[\frac{1}{(\sigma_{33}^y)^2} + \frac{1}{(\sigma_{11}^y)^2} - \frac{1}{(\sigma_{22}^y)^2} \right] ; \quad M = \frac{(\bar{\sigma})^2}{2} \left[\frac{1}{(\tau_{31}^y)^2} \right] \end{aligned} \quad (4.15.4)$$

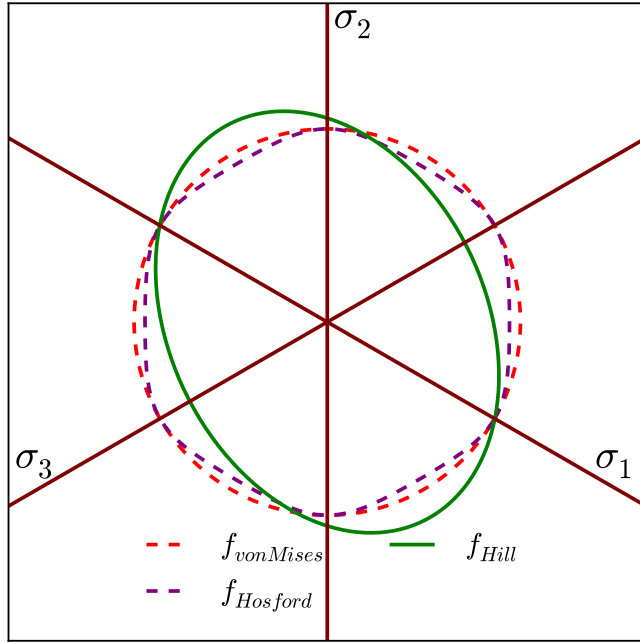


Figure 4-54. Example anisotropic Hill yield surface, $f_{Hill}(\sigma_{ij}, \bar{\epsilon}^p = 0)$, presented in the deviatoric π -plane fit to 2090-T3 aluminum. Comparison von Mises (J_2) and Hosford (with $a = 8$) surfaces are also presented.

$$H = \frac{(\bar{\sigma})^2}{2} \left[\frac{1}{(\sigma_{11}^y)^2} + \frac{1}{(\sigma_{22}^y)^2} - \frac{1}{(\sigma_{33}^y)^2} \right] ; \quad N = \frac{(\bar{\sigma})^2}{2} \left[\frac{1}{(\tau_{12}^y)^2} \right]$$

where $\bar{\sigma}$ is a reference yield stress.

Rather than input the six independent yield stresses, the ratios of the yield stresses to some reference yield stress are generally used as input. These ratios are

$$\begin{aligned}
 R_{11} &= \frac{\sigma_{11}^y}{\bar{\sigma}} ; \quad R_{12} = \sqrt{3} \frac{\tau_{12}^y}{\bar{\sigma}} \\
 R_{22} &= \frac{\sigma_{22}^y}{\bar{\sigma}} ; \quad R_{23} = \sqrt{3} \frac{\tau_{23}^y}{\bar{\sigma}} \\
 R_{33} &= \frac{\sigma_{33}^y}{\bar{\sigma}} ; \quad R_{31} = \sqrt{3} \frac{\tau_{31}^y}{\bar{\sigma}}
 \end{aligned} \tag{4.15.5}$$

These ratios are set up so that if $R_{ij} = 1$ then the yield surface is isotropic.

The orientation of the principal material axes with respect to the global Cartesian axes may be specified by the user. First, a rectangular or cylindrical reference coordinate system is defined. *Spherical coordinate systems are not currently implemented for the Hill model.* The material coordinate system can then be defined through two successive rotations about axes in the reference rectangular or cylindrical coordinate system. In the case of the cylindrical coordinate system this allows the principal material axes to vary point-wise in a given element block.

The plastic rate of deformation, as with the isotropic models, assumes associated flow

$$D_{ij}^p = \dot{\gamma} \frac{\partial \phi}{\partial \sigma_{ij}} \quad (4.15.6)$$

Given the form for ϕ , the consistency parameter, $\dot{\gamma}$ is equal to the rate of the equivalent plastic strain, $\dot{\varepsilon}^p$.

The hardening behavior is given by $\bar{\sigma}(\bar{\varepsilon}^p)$. This hardening function can be a linear hardening function, a power law hardening function, or a user defined hardening function.

For more information about the Hill plasticity model, consult [2].

4.15.1.1. Plastic Hardening

Plastic hardening refers to increases in the flow stress, $\bar{\sigma}$, with plastic deformation. As such, hardening is described via the functional relationship between the flow stress and isotropic hardening variable (effective plastic strain), $\bar{\sigma}(\bar{\varepsilon}^p)$. Over the course of nearly a century of work in metal plasticity, a variety of relationships have been proposed to describe the interactions associated with different physical interpretations, deformation mechanisms, and materials. To enable the utilization of the same plasticity models for different material systems, a modular implementation of plastic hardening has been adopted such that the analyst may select different hardening models from the input deck thereby avoiding any code changes or user subroutines. In this section, additional details are given to the different models to enable the user to select the appropriate choice of model. Note, the models being discussed here are only for *isotropic* hardening in which the yield surface expands. *Kinematic* hardening in which the yield surface translates in stress-space with deformation and *distortional* hardening where the shape of the yield surface changes shape with deformation are not treated. For a larger discussion of the phenomenology and history of different hardening types, the reader is referred to [3, 4, 5].

Given the ubiquitous nature of these hardening laws in computational plasticity, some (if not most) of this material may be found elsewhere in this manual. Nonetheless, the discussion is repeated here for the convenience of the reader.

Linear

Linear hardening is conceptually the simplest model available in LAMÉ. As the name implies, a linear relationship is assumed between the hardening variable, $\bar{\varepsilon}^p$, and flow stress. The constant

giving the degree of increase of yield stress with plastic flow is termed the hardening modulus and is given as, H' , while the expression for the flow stress may be written,

$$\bar{\sigma} = \sigma_y + H' \bar{\varepsilon}^p. \quad (4.15.7)$$

The simplicity of the model is its main feature as the constant slope,

$$\frac{d\bar{\sigma}}{d\bar{\varepsilon}^p} = H', \quad (4.15.8)$$

makes the model attractive for analytical models and cheap for computational implementations (*e.g.* radial return algorithms require only a single correction step). Unfortunately, the simplicity of the representation also means that it has limited predictive capabilities and can lead to overly stiff responses.

Power Law

Another common expression for isotropic hardening is the power-law hardening model. Due to its prevalence, a dedicated ELASTIC-PLASTIC POWER LAW HARDENING model may be found in LAMÉ (see Section 4.8.1). This expression is given as,

$$\bar{\sigma} = \sigma_y + A < \bar{\varepsilon}^p - \varepsilon_L >^n, \quad (4.15.9)$$

in which $< \cdot >$ are Macaulay brackets, ε_L is the Lüders strain, A is a fitting constant, and n is an exponent typically taken such that $0 < n \leq 1$. The Lüders strain is a positive, constant strain value (default to zero) giving an initial plastic deformation domain in which the response is perfectly plastic (see Fig. 4-20). The derivative is then simply,

$$\frac{d\bar{\sigma}}{d\bar{\varepsilon}^p} = nA < \bar{\varepsilon}^p - \varepsilon_L >^{(n-1)}. \quad (4.15.10)$$

Note, one difficulty in such an implementation is that when the effective equivalent plastic strain is zero, numerical difficulties may arise in evaluating the derivative necessitating special treatment of the case.

Voce

The Voce hardening model (sometimes referred to as a saturation model) uses a decaying exponential in terms of the equivalent plastic strain such that the hardening eventually saturates to a specified value (thus the name). Such a relationship has been observed in some structural metals giving rise to the popularity of the model. The hardening response is given as,

$$\bar{\sigma} = \sigma_y + A (1 - \exp(-n\bar{\varepsilon}^p)), \quad (4.15.11)$$

in which A is a fitting constant and n is a fitting exponent describing how quickly the hardening saturates. Importantly, the derivative is written as,

$$\frac{d\bar{\sigma}}{d\bar{\varepsilon}^p} = nA \exp(-n\bar{\varepsilon}^p), \quad (4.15.12)$$

and is well defined everywhere giving the selected form an advantage over the aforementioned power law model.

Johnson-Cook

The Johnson-Cook [6, 7] hardening type is a *rate-dependent* formulation utilizing the assumption that rate-independent and rate-dependent contributions may be multiplicatively separated. Specifically, use of this option requires specifying a user-defined hardening function to capture rate-independent contributions and Johnson-Cook type rate dependent coefficients. The flow stress may be written in this fashion as,

$$\bar{\sigma} = \tilde{\sigma}_y(\bar{\varepsilon}^p) \left[1 + C \left\langle \ln \left(\frac{\dot{\varepsilon}^p}{\dot{\varepsilon}_0} \right) \right\rangle \right], \quad (4.15.13)$$

in which $\tilde{\sigma}_y(\bar{\varepsilon}^p)$ is the user-specified rate-independent hardening function, C is a fitting constant and $\dot{\varepsilon}_0$ is a reference strain rate. The Macaulay brackets ensure the material behaves in a rate independent fashion when $\dot{\varepsilon}^p < \dot{\varepsilon}_0$.

Power Law Breakdown

Like the Johnson-Cook formulation, the power-law breakdown model is also rate-dependent. Again, a multiplicative decomposition between rate-independent and dependent hardening contributions. In this case, however, the functional form is derived from the analysis of Frost and Ashby [8] in which power-law relationships like those of the Johnson-Cook and cease to appropriately capture the physical response. The form used here is similar to the expression used by Brown and Bammann [9] and is written as,

$$\bar{\sigma} = \tilde{\sigma}_y(\bar{\varepsilon}^p) \left[1 + \operatorname{asinh} \left(\left(\frac{\dot{\varepsilon}^p}{g} \right)^{(1/m)} \right) \right], \quad (4.15.14)$$

with $\tilde{\sigma}_y(\bar{\varepsilon}^p)$ being the user supplied rate independent expression, g is a model parameter related to the activation energy in going from climb to glide-controlled deformation, and m dictates the strength of the dependence.

4.15.2. Implementation

The Hill plasticity model uses a predictor-corrector algorithm for integrating the constitutive model. Given a rate of deformation, d_{ij} , and a time step, Δt , a trial stress state is calculated based on an elastic response

$$T_{ij}^{tr} = T_{ij}^n + \Delta t \mathbb{C}_{ijkl} d_{kl} \quad (4.15.15)$$

If the trial stress state lies outside the yield surface, i.e. if $\phi(T_{ij}^{tr}) > \bar{\sigma}$, then the model uses a backward Euler algorithm to return the stress to the yield surface. There are two equations that need to be solved. To ensure that the plastic strain increment is in the correct direction we have

$$R_{ij}^p = \Delta t d_{ij}^p - \Delta \gamma \frac{\partial \phi}{\partial T_{ij}} = 0 \quad (4.15.16)$$

while to ensure that the stress state is on the yield surface we require

$$f = \phi(T_{ij}) - \bar{\sigma}(\bar{\varepsilon}^p) = 0 \quad (4.15.17)$$

The primary algorithm for solving these equations is a Newton-Raphson algorithm. Using $\Delta \gamma$ (which is equal to $\Delta \bar{\varepsilon}^p$) and T_{ij} as the solution variables, we set up an iterative algorithm where

$$\begin{aligned} \Delta \gamma^{(k+1)} &= \Delta \gamma^{(k)} + \Delta(\Delta \gamma) \\ T_{ij}^{(k+1)} &= T_{ij}^{(k)} + \Delta T_{ij} \end{aligned} \quad (4.15.18)$$

where $\Delta \gamma^{(0)} = 0$ and $T_{ij}^{(0)} = T_{ij}^{tr}$ and

$$\Delta t d_{ij}^p = \mathbb{C}_{ijkl}^{-1} (T_{kl}^{tr} - T_{kl}) \quad (4.15.19)$$

The Newton-Raphson algorithm gives

$$\begin{aligned} \Delta(\Delta \gamma) &= \frac{f^{(k)} - R_{ij}^{(k)} \mathcal{L}_{ijkl}^{(k)} \frac{\partial \phi^{(k)}}{\partial T_{kl}}}{\frac{\partial \phi^{(k)}}{\partial T_{ij}} \mathcal{L}_{ijkl}^{(k)} \frac{\partial \phi^{(k)}}{\partial T_{kl}} + H'^{(k)}} \\ \Delta T_{ij} &= -\mathcal{L}_{ijkl}^{(k)} \left(R_{kl}^{(k)} + \Delta(\Delta \gamma) \frac{\partial \phi^{(k)}}{\partial T_{kl}} \right) \end{aligned} \quad (4.15.20)$$

A straightforward Newton-Raphson algorithm does not always converge, so the return mapping algorithm is augmented with a line search algorithm

$$\begin{aligned}\Delta\gamma^{(k+1)} &= \Delta\gamma^{(k)} + \alpha\Delta(\Delta\gamma) \\ T_{ij}^{(k+1)} &= T_{ij}^{(k)} + \alpha\Delta T_{ij}\end{aligned}\tag{4.15.21}$$

where $\alpha \in (0, 1]$ is the line search parameter which is determined from certain convergence considerations. If $\alpha = 1$ then the Newton-Raphson algorithm is recovered. The line search algorithm greatly increases the reliability of the return mapping algorithm.

4.15.3. Verification

The Hill plasticity material model is verified for a number of loading conditions. The elastic properties used in these analyses are $E = 70$ GPa and $\nu = 0.25$. The parameters that are used to define the yield surface are

$$\begin{aligned}R_{11} &= 1.000680 & R_{12} &= 0.909194 \\ R_{22} &= 0.906397 & R_{23} &= 0.851434 \\ R_{33} &= 1.027380 & R_{31} &= 0.799066\end{aligned}\tag{4.15.22}$$

These parameters correspond to a parameterization of the Barlat model for 2090-T3 aluminum [10] that is fit to the Hill model. The hardening law used for the model is a Voce law with the following form

$$\bar{\sigma}(\bar{\varepsilon}^p) = \sigma_y + A(1 - \exp(-n\bar{\varepsilon}^p))\tag{4.15.23}$$

For these calculations $\sigma_y = 200$ MPa, $A = 200$ MPa, and $n = 20$. Finally, the coordinate system used in these calculations is a rectangular coordinate system with the e_1, e_2, e_3 axes aligned with the x, y, z axes.

4.15.3.1. Uniaxial Stress

The Hill plasticity model is tested in uniaxial tension along the three orthogonal principal material directions. The tests looks at the stress, the strain, and the equivalent plastic strain and compares

these values against analytical results for the same problem. In this verification problem only the normal stresses are needed, and the shear terms are not exercised. Therefore, the parameters R_{12} , R_{23} , and R_{31} are not used in the problem and a separate verification test will be needed for shear response.

The model is tested in uniaxial stress in the x , y , and z directions, giving three test problems. Each problem can be formulated exactly the same. For the description of the test we will only look at loading in the x direction (x_1 direction).

For the uniaxial stress problem, the only non-zero stress component is σ_{11} . In the analysis that follows $\sigma_{11} = \sigma$. There are three non-zero strain components, ε_{11} , ε_{22} , and ε_{33} . In the analysis that follows $\varepsilon_{11} = \varepsilon$. Furthermore, the axial elastic strain, $\varepsilon_{11}^e = \sigma/E$ will be denoted by ε^e .

Axial Stresses

The uniaxial stress calculated by the model in Adagio is compared to analytical solutions. For uniaxial loading in the e_1 direction, the effective stress is

$$\phi = \frac{\sigma}{R_{11}} \quad (4.15.24)$$

If the stress state is on the yield surface, then $\phi = \bar{\sigma}(\bar{\varepsilon}^p)$, so the axial stress, as a function of the hardening function, is

$$\sigma = R_{kk} \bar{\sigma}(\bar{\varepsilon}^p) \quad (4.15.25)$$

This shows that the stress state can be calculated from the hardening law and the anisotropy parameters.

To evaluate the axial stress we need the equivalent plastic strain as a function of the axial strain. If we equate the rate of plastic work we get

$$\bar{\sigma} \dot{\varepsilon}^p = \sigma (\dot{\varepsilon} - \dot{\varepsilon}^e) \rightarrow \dot{\varepsilon}^p = R_{11} (\dot{\varepsilon} - \dot{\varepsilon}^e) \quad (4.15.26)$$

which, when integrated, gives us an implicit equation for the equivalent plastic strain

$$\bar{\varepsilon}^p = R_{11} \left(\varepsilon - R_{11} \frac{\bar{\sigma}(\bar{\varepsilon}^p)}{E} \right) \quad (4.15.27)$$

The equivalent plastic strain can then be used in (4.15.25) to find the axial stress, σ .

The axial stresses for loading in the other directions can be found the same way. The axial stresses for loading in the e_1 , e_2 , and e_3 directions are shown in Figure 4-55.

Lateral Strains

For the lateral strains we need the plastic strains and therefore the normal to the yield surface. The components of the normal to the yield surface are

$$\frac{\partial\phi}{\partial\sigma_{11}} = \frac{1}{R_{11}} \quad ; \quad \frac{\partial\phi}{\partial\sigma_{22}} = -HR_{11} \quad ; \quad \frac{\partial\phi}{\partial\sigma_{33}} = -GR_{11} \quad (4.15.28)$$

The elastic axial and lateral strain components are

$$\varepsilon_{11}^e = \frac{\sigma}{E} = \varepsilon^e \quad ; \quad \varepsilon_{22}^e = \varepsilon_{33}^e = -\nu \frac{\sigma}{E} = -\nu \varepsilon^e \quad (4.15.29)$$

The plastic axial strain component is

$$\varepsilon_{11}^p = \varepsilon_{11} - \frac{\sigma}{E} = \varepsilon - \varepsilon^e \quad (4.15.30)$$

which comes from the additive decomposition of the strain rates. Using the equivalent plastic strain (4.15.27) we can find the lateral plastic strain components

$$\varepsilon_{22}^p = -(\varepsilon - \varepsilon^e) HR_{11}^2 \quad ; \quad \varepsilon_{33}^p = -(\varepsilon - \varepsilon^e) GR_{11}^2 \quad (4.15.31)$$

The lateral *total* strain components prior to yield are $\varepsilon_{22} = \varepsilon_{33} = -\nu\varepsilon$. After yield they are

$$\begin{aligned} \varepsilon_{22} &= -\nu\varepsilon^e - HR_{11}\bar{\varepsilon}^p \\ \varepsilon_{33} &= -\nu\varepsilon^e - GR_{11}\bar{\varepsilon}^p \end{aligned} \quad (4.15.32)$$

where $\varepsilon^e = \sigma/E$.

For loading in the y direction, a similar analysis leads to the lateral strains, after yield

$$\begin{aligned} \varepsilon_{33} &= -\nu\varepsilon^e - FR_{22}\bar{\varepsilon}^p \\ \varepsilon_{11} &= -\nu\varepsilon^e - HR_{22}\bar{\varepsilon}^p \end{aligned} \quad (4.15.33)$$

For loading in the z direction, a similar analysis leads to the lateral strains, after yield

$$\begin{aligned}\varepsilon_{11} &= -\nu \varepsilon^e - GR_{33} \bar{\varepsilon}^p \\ \varepsilon_{22} &= -\nu \varepsilon^e - FR_{33} \bar{\varepsilon}^p\end{aligned}\tag{4.15.34}$$

Results for all three loadings are shown in Figures 4-56, 4-57, and 4-58.

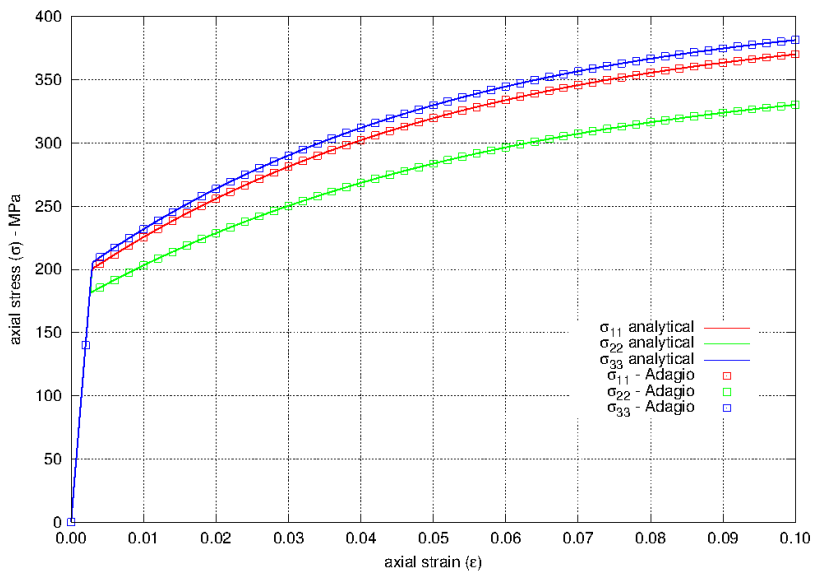


Figure 4-55. Stresses when loading in the e_1 , e_2 , and e_3 -directions using the Hill model with a Voce hardening law.

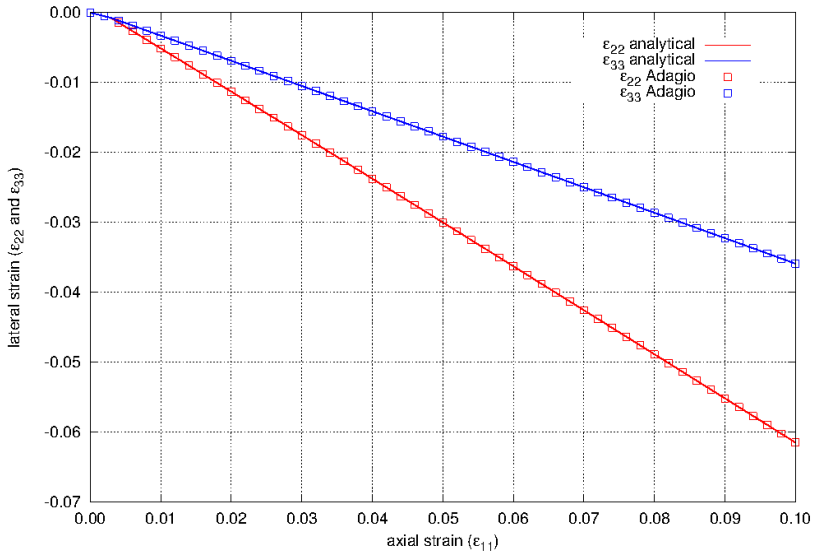


Figure 4-56. Lateral strain as a function of axial strain for the Hill model of 2090-T3 aluminum. Loading is in the e_1 -direction and the hardening law is a Voce law.

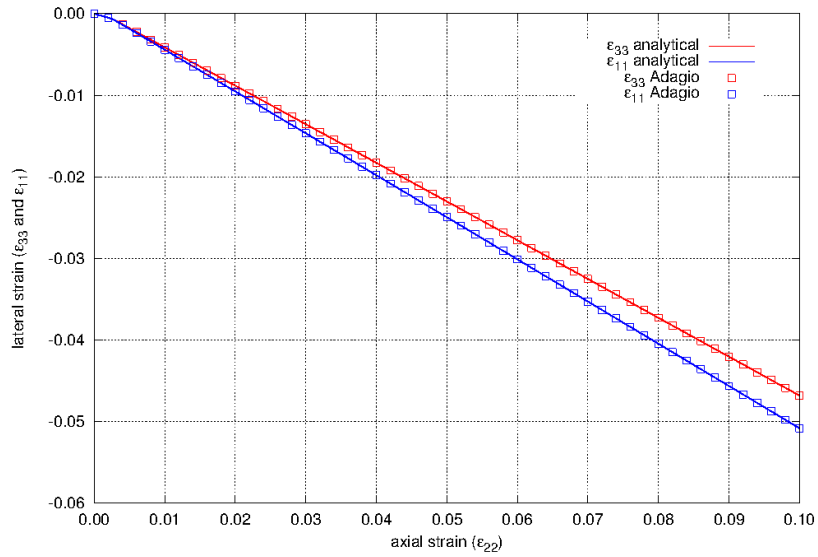


Figure 4-57. Lateral strain as a function of axial strain for the Hill model of 2090-T3 aluminum. Loading is in the e_2 -direction and the hardening law is a Voce law.

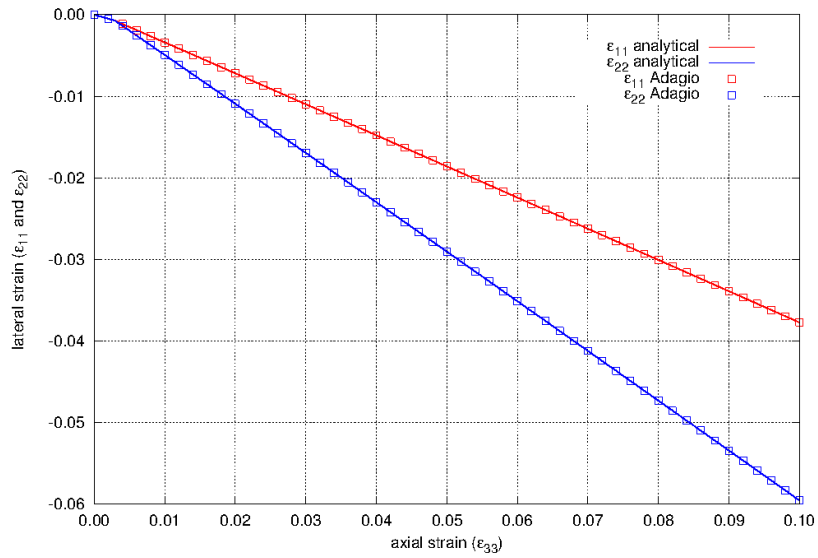


Figure 4-58. Lateral strain as a function of axial strain for the Hill model of 2090-T3 aluminum. Loading is in the e_3 -direction and the hardening law is a Voce law.

4.15.3.2. Pure Shear

The shear stress calculated by the Hill plasticity model in Adagio is compared to analytical solutions. Without loss of generality we will look at solutions for pure shear with respect to the e_1 - e_2 axes. Solutions for shear with respect to the other axes will be similar. In what follows, the only non-zero shear stress will be σ_{12} , and the only non-zero shear strain will be ε_{12} . In general, for pure shear with respect to the e_1 - e_2 axes, the effective stress is

$$\phi = \sqrt{3} \frac{\sigma_{12}}{R_{12}} \quad (4.15.35)$$

If the stress state is on the yield surface, then $\phi = \bar{\sigma}(\bar{\varepsilon}^p)$, so the shear stress is

$$\sigma_{12} = \frac{R_{12}}{\sqrt{3}} \bar{\sigma}(\bar{\varepsilon}^p) \quad (4.15.36)$$

This shows that the pure shear stress state can be calculated from the hardening law and the anisotropy parameters.

To evaluate the shear stress we need the equivalent plastic strain as a function of the shear strain. If we equate the rate of plastic work we get

$$\bar{\sigma} \dot{\bar{\varepsilon}}^p = 2\sigma_{12} (\dot{\varepsilon}_{12} - \dot{\varepsilon}_{12}^e) \rightarrow \dot{\bar{\varepsilon}}^p = \frac{2R_{12}}{\sqrt{3}} (\dot{\varepsilon}_{12} - \dot{\varepsilon}_{12}^e) \quad (4.15.37)$$

which, when integrated, gives us an implicit equation for the equivalent plastic strain

$$\bar{\varepsilon}^p = \frac{2R_{12}}{\sqrt{3}} \left(\varepsilon_{12} - \frac{R_{12}}{\sqrt{3}} \frac{\bar{\sigma}(\bar{\varepsilon}^p)}{2G} \right) \quad (4.15.38)$$

If we define $\hat{R}_{12} = R_{12}/\sqrt{3}$ then we get a form similar to what we had for uniaxial stress

$$\bar{\varepsilon}^p = 2\hat{R}_{12} \left(\varepsilon_{12} - \hat{R}_{12} \frac{\bar{\sigma}(\bar{\varepsilon}^p)}{2G} \right) \quad (4.15.39)$$

The equivalent plastic strain can now be used to find the shear stress.

Boundary Conditions for Pure Shear

The deformation gradient that gives pure shear for loading relative to the e_1 - e_2 axes is

$$[\mathbf{F}] = \begin{bmatrix} \frac{1}{2}(\lambda + \lambda^{-1}) & \frac{1}{2}(\lambda - \lambda^{-1}) & 0 \\ \frac{1}{2}(\lambda - \lambda^{-1}) & \frac{1}{2}(\lambda + \lambda^{-1}) & 0 \\ 0 & 0 & 1 \end{bmatrix} \rightarrow [\boldsymbol{\varepsilon}] = \begin{bmatrix} 0 & \varepsilon & 0 \\ \varepsilon & 0 & 0 \\ 0 & 0 & 0 \end{bmatrix} ; \quad \varepsilon = \ln \lambda \quad (4.15.40)$$

For loading relative to the e_2 - e_3 axes and the e_3 - e_1 axes the boundary conditions are modified appropriately.

Results

The results for the Hill plasticity model loaded in pure shear are shown in Figure 4-59. We see that the stress strain curves in pure shear as calculated by Adagio follow the expected stress strain curves. All other stress and strain components for the three problems are zero.

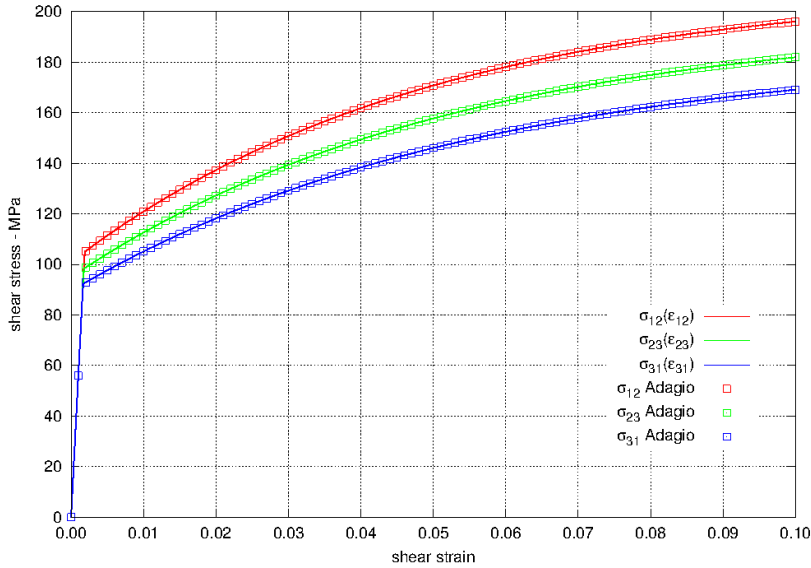


Figure 4-59. Shear stress versus shear strain using the Hill model with a Voce hardening law. Results are for shear in the three orthogonal planes of the material coordinate system.

4.15.3.3. Plastic Hardening

To verify the capabilities of the hardening models, rate-*independent* and rate-*dependent* alike, the constant equivalent plastic strain rate, $\dot{\varepsilon}^p$, uniaxial stress and pure shear verification tests described in Appendix A.5 are utilized. In these simplified loading cases, the material state may be found explicitly as a function of time knowing the prescribed equivalent strain rate. For the rate-*independent* cases, a strain rate of $\dot{\varepsilon}^p = 1 \times 10^{-4} \text{ s}^{-1}$ is used for ease in simulations although the selected rate does not affect the results. Through this testing protocol, the hardening models are not only tested at different rates but also in different principal material directions to consider the anisotropy of the Hill yield surface. Additionally, the rate-*dependent* models are tested for a wide range of strain rates (over five decades) and with all three rate-*independent* hardening functions ($\tilde{\sigma}_y$ in the previous theory section). Although linear, Voce, and power-law rate-*independent* representations are utilized in the rate-*dependent* tests, in those cases the hardening models are prescribed via user-defined analytic functions. The rate-*independent* verification exercises, on the other hand, examine the built in hardening models. This distinction necessitates the different considerations and treatments.

The various rate-*dependent* and rate-*independent* hardening coefficients are found in Table 4-20 while the remaining model parameters are unchanged from the previous verification exercises. For the current verification exercises, the rate-*independent* hardening models (linear, Voce, and power-law) will first be considered and then the rate-*dependent* forms (Johnson-Cook, power-law breakdown).

C	0.1	$\dot{\varepsilon}_0$	$1 \times 10^{-4} \text{ s}^{-1}$
g	0.21 s^{-1}	m	16.4
$\tilde{H}_{\text{Linear}}$	200 MPa	-	-
\tilde{A}_{PL}	400 MPa	\tilde{n}_{PL}	0.25
\tilde{A}_{Voce}	200 MPa	\tilde{n}_{Voce}	20

Table 4-20. The model parameters for the hardening verification tests used with the Hill plasticity model during verification tests. Parameters for the rate-*independent* hardening functions, $\tilde{\sigma}_y$, are also given and denoted with a $\tilde{\cdot}$ while the subscript refers to the functional form.

Linear

To examine the performance of the rate-*independent* linear hardening model, the verification exercises from Appendix A.5 are used. In this case, as the Hill yield surface is being considered, the responses are determined numerically and analytically in the uniaxial stress case with loading in three different principal material directions and three different shear planes for the pure shear case. These results are presented in Figure 4-60. From these responses, superb agreement between the analytical and numerical results is noted. Additionally, the constant linear stress-strain response during plastic deformations clearly demonstrates the behavior giving this model its name.

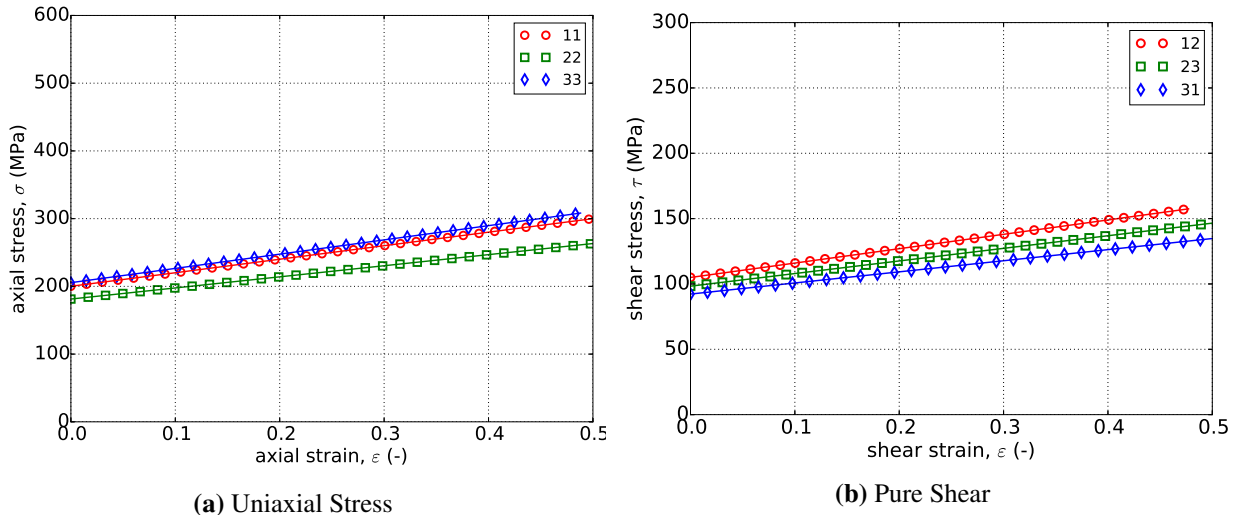


Figure 4-60. (a) Uniaxial stress-strain and (b) pure shear responses of the Hill plasticity model with rate-*independent*, linear hardening. Solid lines are analytical while open symbols are numerical.

Power-Law

The rate-*independent* power-law hardening model is verified by using the uniaxial stress and pure shear problems of Appendix A.5. Results of these endeavors determined analytically and numerically are presented in Figure 4-61 in which the uniaxial stress problem is presented for loading aligned with the three different principal material directions and three different shear planes for the pure shear case. From these results, outstanding agreement is noted between both numerical and analytical results sets verifying the model. Also, the initially stiff hardening decreasing to a lower linear tangent modulus characteristic of power-law hardening models is clearly evident in the various result sets of Figure 4-61.

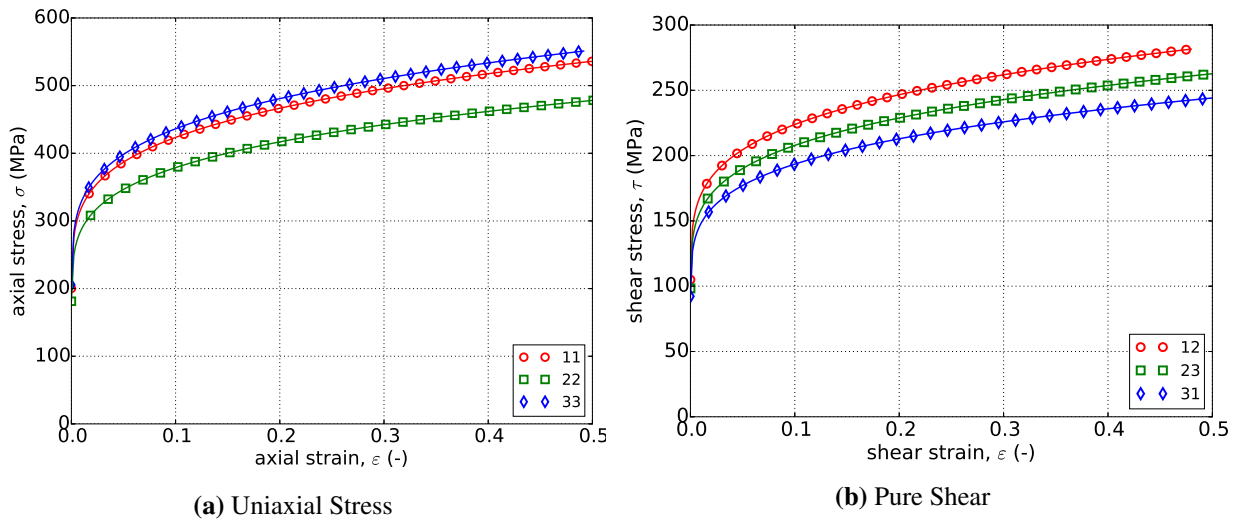


Figure 4-61. (a) Uniaxial stress-strain and (b) pure shear responses of the Hill plasticity model with rate-*independent*, power-law hardening. Solid lines are analytical while open symbols are numerical.

Voce

Verification of the rate-*independent* Voce hardening model is pursued by considering both the uniaxial stress and pure shear approaches of Appendix A.5. The results of these investigations determined analytically and numerically are shown in Figure 4-62. For the uniaxial stress cases, loadings in each of the three principal material directions is presented while complementary results from the three shear planes are shown for the pure shear case. In each of these six instances, exemplary agreement is observed between the different results sets. Additionally, such stress-strain results also show the ‘‘saturation’’ behavior associated with Voce models in which at some equivalent plastic strain the material no longer hardens.

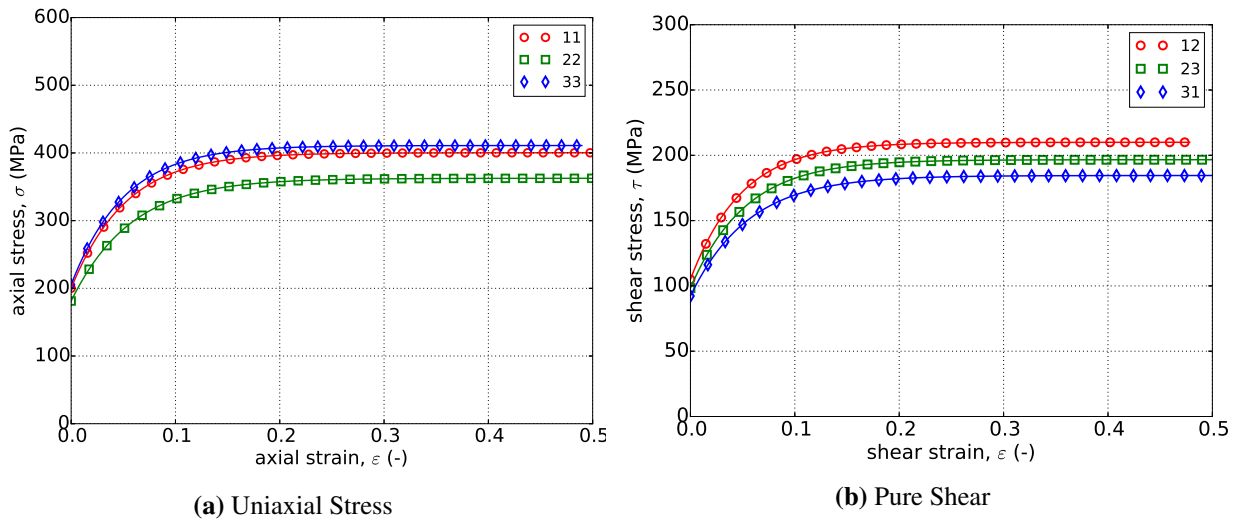


Figure 4-62. (a) Uniaxial stress-strain and (b) pure shear responses of the Hill plasticity model with rate-independent, Voce hardening. Solid lines are analytical while open symbols are numerical.

Johnson-Cook

As noted in Appendix A.5.1, the uniaxial stress response depends on the yield surface anisotropy coefficients (for the Hill model the R 's). The respective coefficients are given in the aforementioned appendix while Figure 4-63 presents the results of forty-five different verification exercises corresponding to different combinations of the three material principal directions (\hat{e}_1 , \hat{e}_2 , and \hat{e}_3), five equivalent plastic strain rates (1×10^{-3} , 1×10^{-2} , 1×10^{-1} , 1×10^0 and $1 \times 10^1 \text{ s}^{-1}$), and three rate-independent hardening models (linear, power-law, and Voce). For each combination, the analytical and numerical results match to within acceptably small numerical differences.

For the pure shear case, the problem discussed in Appendix A.5.2 is considered. The results still depend on the Hill R coefficients and forty-five different loadings are presented in Fig. 4-64. In this instance, three different shearing planes are used in lieu of the principal directions. Nonetheless, for these results the key result remains the same – analytical matches numerical further verifying rate dependent capabilities.

Power-Law Breakdown

For the power-law breakdown model, the same forty-five cases discussed in the previous section (three directions, five rates, three hardening models) are again solved via the approach of Appendix A.5.1 in Figure 4-65. Although the impact of rate on the responses differs due to the assumed representation of the rate-dependent hardening, excellent agreement is still noted between analytical and numerical results.

To expand on the uniaxial stress results, the response through pure shear is also probed via the

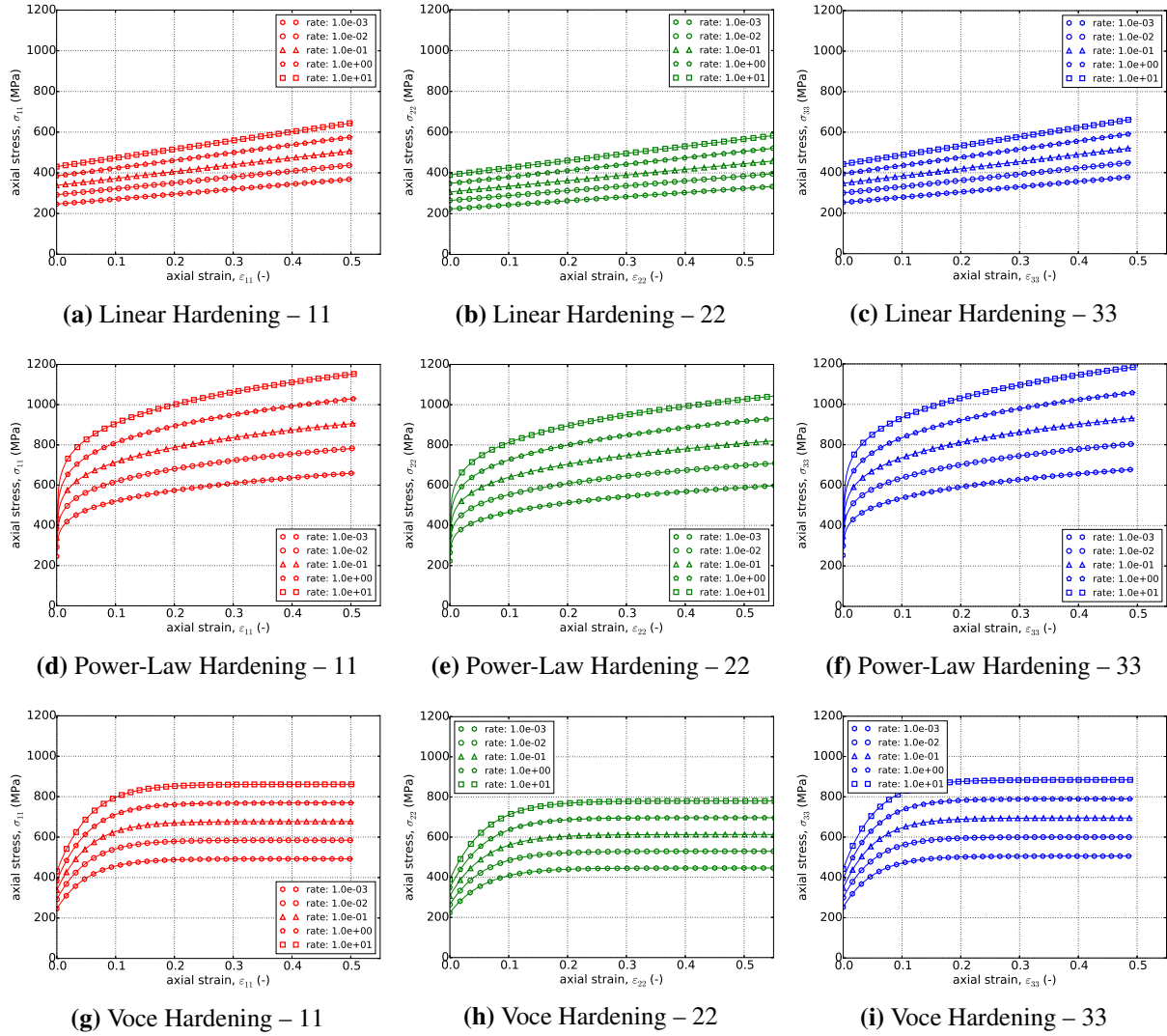


Figure 4-63. Uniaxial stress-strain response of the Hill plasticity model with rate-dependent, Johnson-Cook type hardening with (a-c) linear (d-f) power-law and (g-i) Voce rate-independent hardening. Solid lines are analytical results while open symbols are numerical.

method of Appendix A.5.2. Again forty-five different cases are investigated and their results are presented in Figure 4-66. Once again, the results aligning thereby verifying the capability of the model and producing additional credibility.

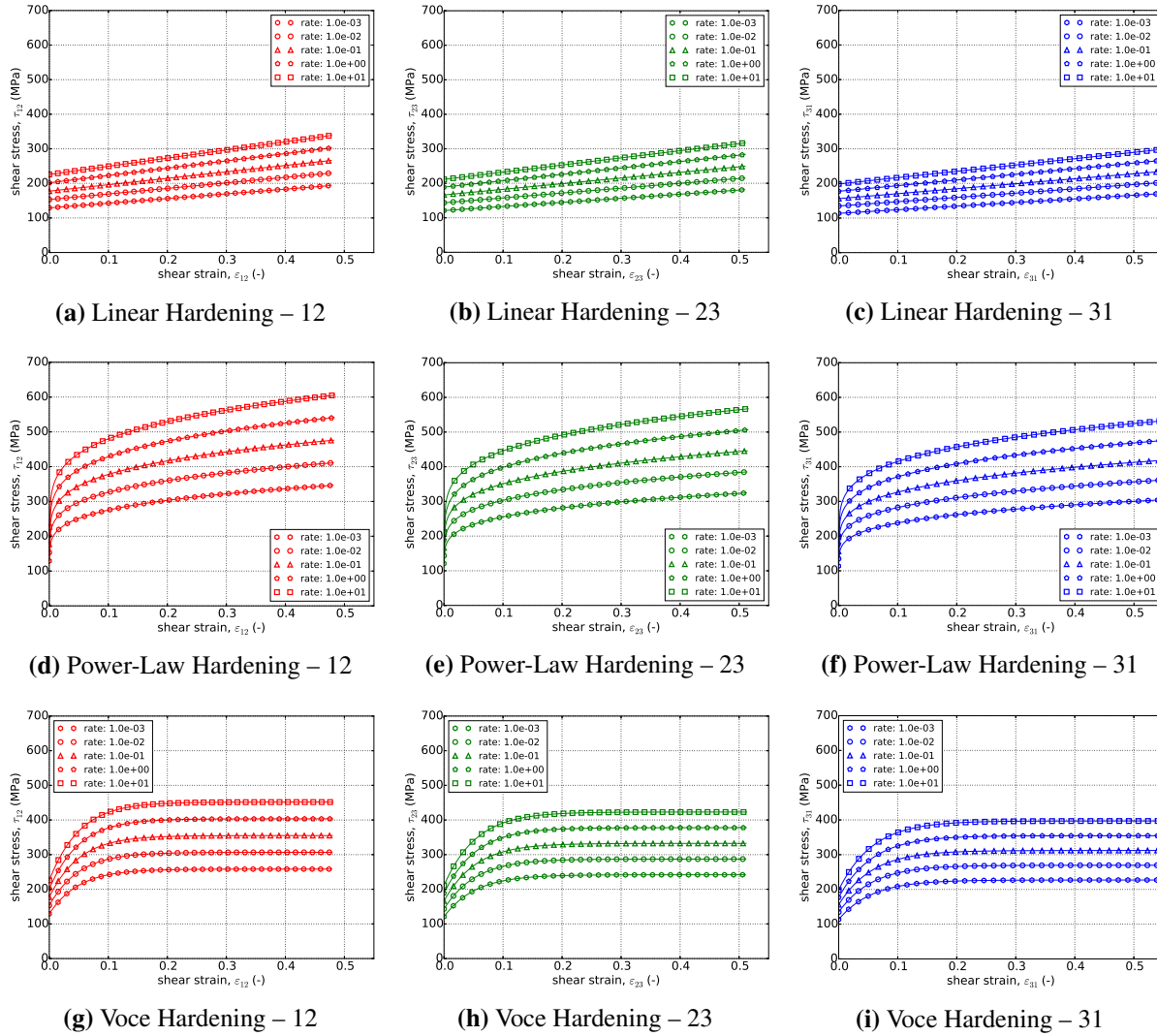


Figure 4-64. Stress-strain response of the Hill plasticity model with rate-dependent, Johnson-Cook type hardening in pure shear with (a-c) linear (d-f) power-law and (g-i) Voce rate-independent hardening. Solid lines are analytical results while open symbols are numerical.

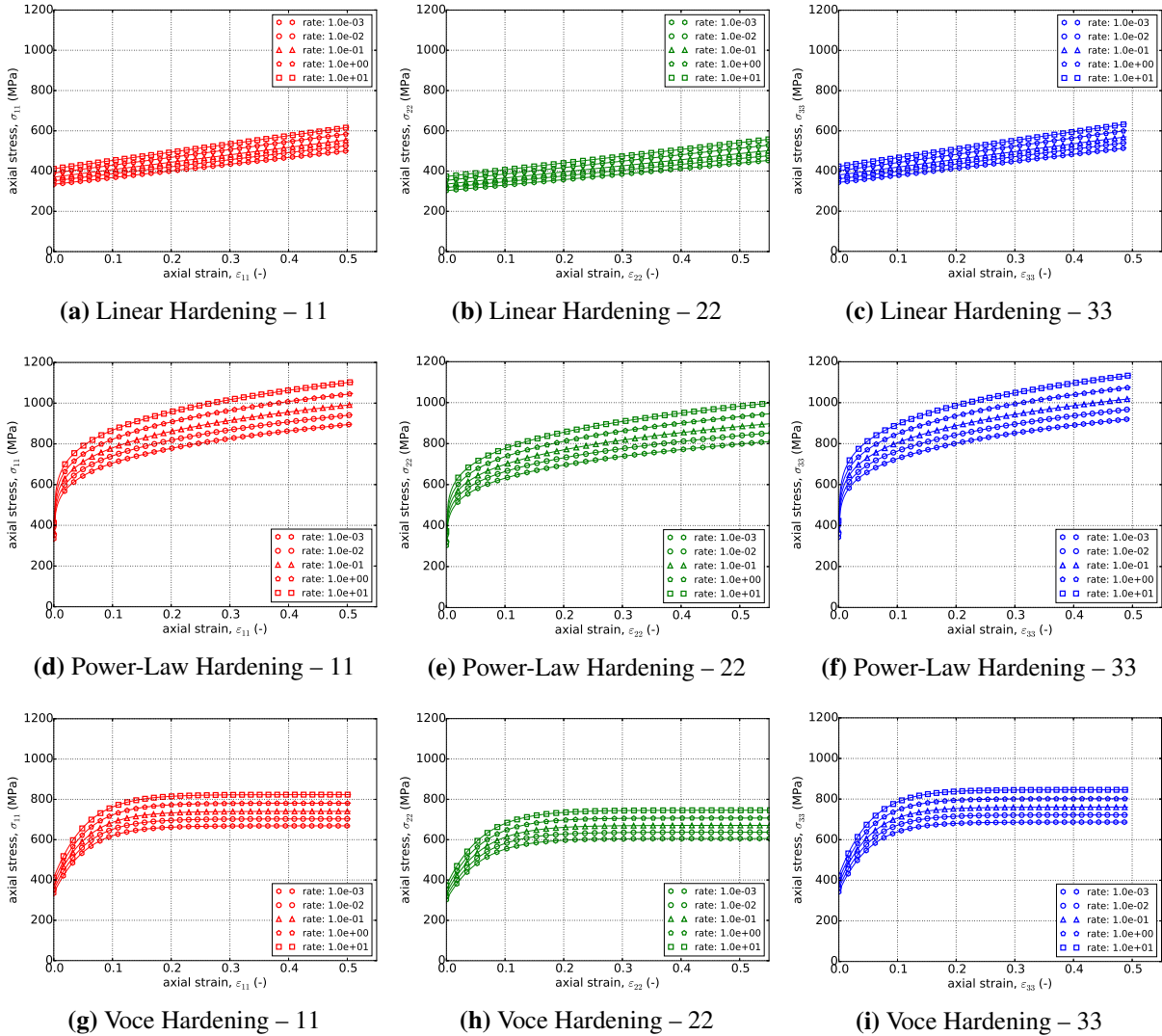


Figure 4-65. Uniaxial stress-strain response of the Hill plasticity model with rate-dependent, power-law breakdown type hardening in with (a-c) linear (d-f) power-law and (g-i) Voce rate-independent hardening. Solid lines are analytical results while open symbols are numerical.

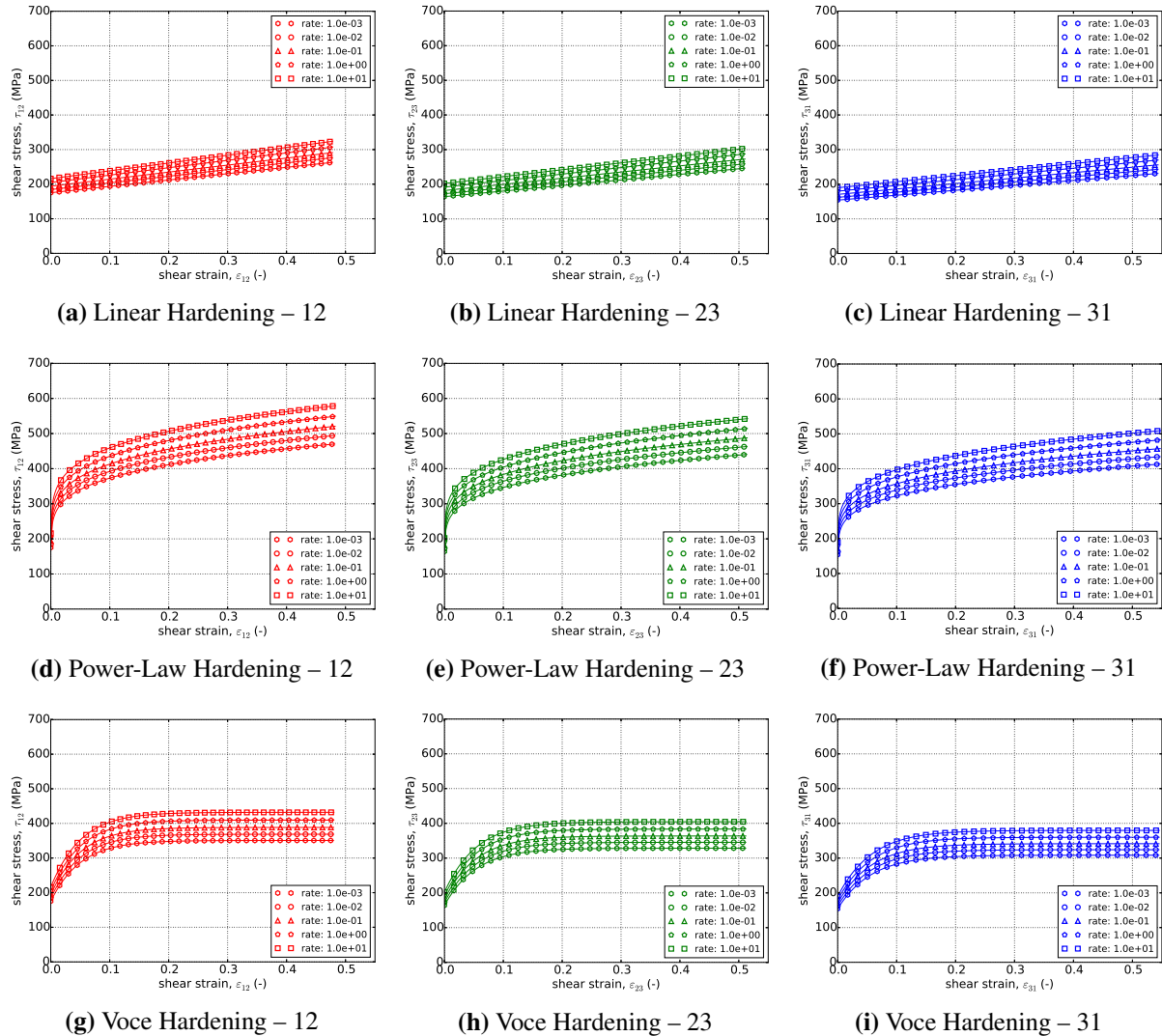


Figure 4-66. Stress-strain response of the Hill plasticity model with rate-dependent, power-law breakdown type hardening in pure shear with (a-c) linear (d-f) power-law and (g-i) Voce rate-independent hardening. Solid lines are analytical results while open symbols are numerical.

4.15.4. User Guide

```
BEGIN PARAMETERS FOR MODEL HILL_PLASTICITY
#
# Elastic constants
#
YOUNGS MODULUS = <real>  $E$ 
POISSONS RATIO = <real>  $\nu$ 
SHEAR MODULUS = <real>  $G$ 
BULK MODULUS = <real>  $K$ 
LAMBDA = <real>  $\lambda$ 
TWO MU = <real>  $2\mu$ 
#
# Material coordinates system definition
#
COORDINATE SYSTEM = <string> coordinate_system_name
DIRECTION FOR ROTATION = <real> 1|2|3
ALPHA = <real>  $\alpha_1$  (degrees)
SECOND DIRECTION FOR ROTATION = <real> 1|2|3
SECOND ALPHA = <real>  $\alpha_2$  (degrees)
#
# Yield surface parameters
#
YIELD STRESS = <real>  $\sigma_y$ 
R11 = <real>  $R_{11}$  (1.0)
R22 = <real>  $R_{22}$  (1.0)
R33 = <real>  $R_{33}$  (1.0)
R12 = <real>  $R_{12}$  (1.0)
R23 = <real>  $R_{23}$  (1.0)
R31 = <real>  $R_{31}$  (1.0)
#
# Hardening model
#
HARDENING MODEL = LINEAR | POWER_LAW | VOCE | USER_DEFINED |
    CUBIC_HERMITE_SPLIT | JOHNSON_COOK | POWER_LAW_BREAKDOWN
#
# Linear hardening
#
HARDENING MODULUS = <real>  $H'$ 
#
# Power-law hardening
#
HARDENING CONSTANT = <real>  $A$ 
HARDENING EXPONENT = <real>  $n$  (0.5)
LUDERS STRAIN = <real>  $\varepsilon_L$  (0.0)
#
# Voce hardening
```

```

#
HARDENING MODULUS      = <real> A
EXPONENTIAL COEFFICIENT = <real> n
#
# Johnson-Cook hardening
#
HARDENING FUNCTION = <string>hardening_function_name
RATE CONSTANT        = <real> C
REFERENCE RATE        = <real>  $\dot{\epsilon}_0$ 
#
# Power law breakdown hardening
#
HARDENING FUNCTION = <string>hardening_function_name
RATE COEFFICIENT     = <real> g
RATE EXPONENT        = <real> m
#
# User defined hardening
#
HARDENING FUNCTION = <string>hardening_function_name
#
# Spline based hardening curve
#
CUBIC SPLINE TYPE   = <string>
CARDINAL PARAMETER  = <real> val
KNOT EQPS            = <real_list> vals
KNOT STRESS          = <real_list> vals
END [PARAMETERS FOR MODEL HILL_PLASTICITY]

```

Output variables available for this model are listed in Table 4-21.

Table 4-21. State Variables for HILL PLASTICITY Model

Name	Description
EQPS	equivalent plastic strain, $\bar{\epsilon}^p$
EQDOT	equivalent plastic strain rate, $\dot{\bar{\epsilon}}^p$
SEFF	effective stress, ϕ

REFERENCES

- [1] W. M. Scherzinger. A return mapping algorithm for isotropic and anisotropic plasticity models using a line search method. *Computer Methods in Applied Mechanics and Engineering*, 317:526–553, 2017.
- [2] R. Hill. *The Mathematical Theory of Plasticity*. Clarendon Press, Oxford, 1950.
- [3] R. Hill. *The Mathematical Theory of Plasticity*. Oxford University Press, 1950.
- [4] J. Lemaitre and J.-L. Chaboche. *Mechanics of Solid Materials*. Cambridge University Press, 1990.
- [5] J. Lubliner. *Plasticity Theory*. Dover, 2008.
- [6] G.R. Johnson and W.H. Cook. A constitutive model and data for metals subjected to large strains, high strain rates and high temperatures. In *Proc. 7th. Int. Symp. on Ballistics*, pages 541–547, The Hague, The Netherlands, 1983.
- [7] G.R. Johnson and W.H. Cook. Fracture characteristics of three metals subjected to various strains, strain rates, temperatures and pressures. *Engineering Fracture Mechanics*, 21(1): 31–48, 1985.
- [8] H. J. Frost and M. F. Ashby. *Deformation mechanism maps: the plasticity and creep of metals and ceramics*. Pergamon press, 1982.
- [9] A.A. Brown and D.J. Bammann. Validation of a model for static and dynamic recrystallization in metals. *International Journal of Plasticity*, 32–33:17–35, 2012.
- [10] F. Barlat, H. Aretz, J. W. Yoon, J. C. Brem, and R. E. Dick. Linear transformation-based anisotropic yield functions. *International Journal of Plasticity*, 21:1009–1039, 2005.

4.16. BARLAT PLASTICITY MODEL

4.16.1. Theory

The Barlat plasticity model is a hypoelastic, rate-independent plasticity model. The underlying yield surface is both anisotropic and non-quadratic [1]. With respect to the former, linear transformations of the deviatoric stress are used to capture texture and anisotropy effects. The rate form of this model assumes an additive split of the rate of deformation into an elastic and plastic part

$$D_{ij} = D_{ij}^e + D_{ij}^p. \quad (4.16.1)$$

The stress rate only depends on the elastic rate of deformation

$$\dot{\sigma}_{ij} = \mathbb{C}_{ijkl} D_{kl}^e \quad (4.16.2)$$

where \mathbb{C}_{ijkl} are the components of the fourth-order, isotropic elasticity tensor.

To describe anisotropy in the yield-behavior, two linear transformation tensors, C'_{ijkl} and C''_{ijkl} , are introduced such that,

$$s'_{ij} = C'_{ijkl} s_{kl} \quad ; \quad s''_{ij} = C''_{ijkl} s_{kl}, \quad (4.16.3)$$

with s_{ij} being the deviatoric stress tensor ($s_{ij} = \sigma_{ij} - 1/3\sigma_{kk}\delta_{ij}$) and s'_{ij} and s''_{ij} being transformed stresses. Two transformations are used to capture both the anisotropy of the yield surface and flow rule. In Voigt notation the two transformation tensors are given as,

$$[C'] = \begin{bmatrix} 0 & -c'_{12} & -c'_{13} & 0 & 0 & 0 \\ -c'_{21} & 0 & -c'_{23} & 0 & 0 & 0 \\ -c'_{31} & -c'_{32} & 0 & 0 & 0 & 0 \\ 0 & 0 & 0 & c'_{44} & 0 & 0 \\ 0 & 0 & 0 & 0 & c'_{55} & 0 \\ 0 & 0 & 0 & 0 & 0 & c'_{66} \end{bmatrix} \quad (4.16.4)$$

$$[C''] = \begin{bmatrix} 0 & -c''_{12} & -c''_{13} & 0 & 0 & 0 \\ -c''_{21} & 0 & -c''_{23} & 0 & 0 & 0 \\ -c''_{31} & -c''_{32} & 0 & 0 & 0 & 0 \\ 0 & 0 & 0 & c''_{44} & 0 & 0 \\ 0 & 0 & 0 & 0 & c''_{55} & 0 \\ 0 & 0 & 0 & 0 & 0 & c''_{66} \end{bmatrix}. \quad (4.16.5)$$

Alternatively, the transformed stresses may be written in terms of the Cauchy stress tensor as,

$$s'_{ij} = L'_{ijkl} \sigma_{kl} \quad ; \quad s''_{ij} = L''_{ijkl} \sigma_{kl}, \quad (4.16.6)$$

where $L'_{ijkl} = C'_{ijmn} H_{mnkl}$ and $L''_{ijkl} = C''_{ijmn} H_{mnkl}$. In this case, H_{ijkl} is the symmetric deviatoric projection tensor and takes the form of,

$$H_{ijkl} = \frac{1}{2} (\delta_{ik}\delta_{jl} + \delta_{il}\delta_{jk}) - \frac{1}{3} \delta_{ij}\delta_{kl}. \quad (4.16.7)$$

In reduced form,

$$[L'] = \frac{1}{3} \begin{bmatrix} c'_{12} + c'_{13} & -2c'_{12} + c'_{13} & c'_{12} - 2c'_{13} & 0 & 0 & 0 \\ -2c'_{21} + c'_{23} & c'_{21} + c'_{23} & c'_{21} - 2c'_{23} & 0 & 0 & 0 \\ -2c'_{31} + c'_{32} & c'_{31} - 2c'_{32} & c'_{31} + c'_{32} & 0 & 0 & 0 \\ 0 & 0 & 0 & 3c'_{44} & 0 & 0 \\ 0 & 0 & 0 & 0 & 3c'_{55} & 0 \\ 0 & 0 & 0 & 0 & 0 & 3c'_{66} \end{bmatrix}, \quad (4.16.8)$$

and an analogous expression may be written for L''_{ijkl} .

The yield surface, f , is given as,

$$f(\sigma_{ij}, \bar{\varepsilon}^p) = \phi(\sigma_{ij}) - \bar{\sigma}(\bar{\varepsilon}^p) = 0, \quad (4.16.9)$$

in which $\phi(\sigma_{ij})$ is the effective stress and $\bar{\sigma}(\bar{\varepsilon}^p)$ is the (isotropic) hardening function. The effective stress is written in terms of the principal transformed stresses (s'_i and s''_i , respectively) and the yield surface exponent, a , as,

$$\begin{aligned} \phi(\sigma_{ij}) = & \left\{ \frac{1}{4} \left[|s'_1 - s''_1|^a + |s'_1 - s''_2|^a + |s'_1 - s''_3|^a \right. \right. \\ & + |s'_2 - s''_1|^a + |s'_2 - s''_2|^a + |s'_2 - s''_3|^a \\ & \left. \left. + |s'_3 - s''_1|^a + |s'_3 - s''_2|^a + |s'_3 - s''_3|^a \right] \right\}^{1/a}. \end{aligned} \quad (4.16.10)$$

An example of such a yield surface is given in Figure 4-67 along with examples of previously presented (von Mises, Hosford, Hill) surfaces. The presented Barlat surface corresponds to that of 2090-T3 aluminum first characterized by Barlat *et al.* [1]. In Figure 4-67, both the anisotropy and non-quadratic nature of the yield surface is evident leading to differing strengths and flow directions at various stresses from any of the other models.

The orientation of the principal material axes with respect to the global Cartesian axes may be specified by the user. First, a rectangular or cylindrical reference coordinate system is defined.

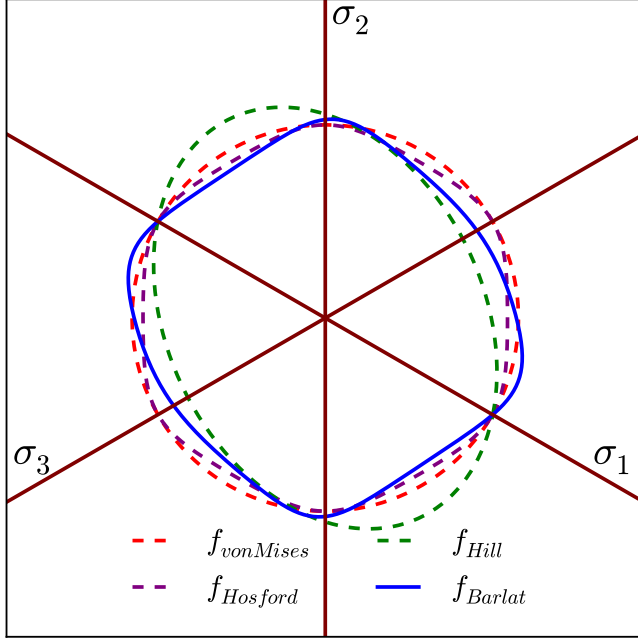


Figure 4-67. Example Barlat yield surface, $f_{Barlat}(\sigma_{ij}, \bar{\varepsilon}^p = 0)$, of 2090-T3 aluminum presented in the deviatoric π -plane. Comparison von Mises (J_2), Hosford (with $a = 8$), and Hill surfaces are also presented for comparison.

Spherical coordinate systems are not currently implemented for the Barlat model. The material coordinate system can then be defined through two successive rotations about axes in the reference rectangular or cylindrical coordinate system. In the case of the cylindrical coordinate system this allows the principal material axes to vary point-wise in a given element block.

The plastic rate of deformation, as with the isotropic models, assumes associated flow

$$D_{ij}^p = \dot{\gamma} \frac{\partial \phi}{\partial \sigma_{ij}}, \quad (4.16.11)$$

in which $\dot{\gamma}$ is the consistency multiplier. Given the form for ϕ , $\dot{\gamma}$ is equal to the rate of the equivalent plastic strain, $\dot{\varepsilon}^p$. As the yield surface is cast in transformed stress space, determining the flow direction in Cartesian space may be done via the chain rule (details may be found in [2]) leading to an expression of the form,

$$\frac{\partial \phi}{\partial \sigma_{ij}} = \sum_{k=1}^3 \left(\frac{\partial \phi}{\partial s'_k} \frac{\partial s'_k}{\partial s'_{mn}} L'_{mnij} + \frac{\partial \phi}{\partial s''_k} \frac{\partial s''_k}{\partial s''_{mn}} L''_{mnij} \right). \quad (4.16.12)$$

The hardening behavior is given by $\bar{\sigma}(\bar{\varepsilon}^p)$. This hardening function can be a linear hardening function, a power law hardening function, or a user defined hardening function.

For more information about the Barlat plasticity model, consult [1, 2].

4.16.1.1. Plastic Hardening

Plastic hardening refers to increases in the flow stress, $\bar{\sigma}$, with plastic deformation. As such, hardening is described via the functional relationship between the flow stress and isotropic hardening variable (effective plastic strain), $\bar{\sigma}(\bar{\varepsilon}^p)$. Over the course of nearly a century of work in metal plasticity, a variety of relationships have been proposed to describe the interactions associated with different physical interpretations, deformation mechanisms, and materials. To enable the utilization of the same plasticity models for different material systems, a modular implementation of plastic hardening has been adopted such that the analyst may select different hardening models from the input deck thereby avoiding any code changes or user subroutines. In this section, additional details are given to the different models to enable the user to select the appropriate choice of model. Note, the models being discussed here are only for *isotropic* hardening in which the yield surface expands. *Kinematic* hardening in which the yield surface translates in stress-space with deformation and *distortional* hardening where the shape of the yield surface changes shape with deformation are not treated. For a larger discussion of the phenomenology and history of different hardening types, the reader is referred to [3, 4, 5].

Given the ubiquitous nature of these hardening laws in computational plasticity, some (if not most) of this material may be found elsewhere in this manual. Nonetheless, the discussion is repeated here for the convenience of the reader.

Linear

Linear hardening is conceptually the simplest model available in LAMÉ. As the name implies, a linear relationship is assumed between the hardening variable, $\bar{\varepsilon}^p$, and flow stress. The constant giving the degree of increase of yield stress with plastic flow is termed the hardening modulus and is given as, H' , while the expression for the flow stress may be written,

$$\bar{\sigma} = \sigma_y + H' \bar{\varepsilon}^p. \quad (4.16.13)$$

The simplicity of the model is its main feature as the constant slope,

$$\frac{d\bar{\sigma}}{d\bar{\varepsilon}^p} = H', \quad (4.16.14)$$

makes the model attractive for analytical models and cheap for computational implementations (*e.g.* radial return algorithms require only a single correction step). Unfortunately, the simplicity of the representation also means that it has limited predictive capabilities and can lead to overly stiff responses.

Power Law

Another common expression for isotropic hardening is the power-law hardening model. Due to its prevalence, a dedicated ELASTIC-PLASTIC POWER LAW HARDENING model may be found in

LAMÉ (see Section 4.8.1). This expression is given as,

$$\bar{\sigma} = \sigma_y + A < \bar{\varepsilon}^p - \varepsilon_L >^n, \quad (4.16.15)$$

in which $< \cdot >$ are Macaulay brackets, ε_L is the Lüders strain, A is a fitting constant, and n is an exponent typically taken such that $0 < n \leq 1$. The Lüders strain is a positive, constant strain value (default to zero) giving an initial plastic deformation domain in which the response is perfectly plastic (see Fig. 4-20). The derivative is then simply,

$$\frac{d\bar{\sigma}}{d\bar{\varepsilon}^p} = nA < \bar{\varepsilon}^p - \varepsilon_L >^{(n-1)}. \quad (4.16.16)$$

Note, one difficulty in such an implementation is that when the effective equivalent plastic strain is zero, numerical difficulties may arise in evaluating the derivative necessitating special treatment of the case.

Voce

The Voce hardening model (sometimes referred to as a saturation model) uses a decaying exponential in terms of the equivalent plastic strain such that the hardening eventually saturates to a specified value (thus the name). Such a relationship has been observed in some structural metals giving rise to the popularity of the model. The hardening response is given as,

$$\bar{\sigma} = \sigma_y + A (1 - \exp(-n\bar{\varepsilon}^p)), \quad (4.16.17)$$

in which A is a fitting constant and n is a fitting exponent describing how quickly the hardening saturates. Importantly, the derivative is written as,

$$\frac{d\bar{\sigma}}{d\bar{\varepsilon}^p} = nA \exp(-n\bar{\varepsilon}^p), \quad (4.16.18)$$

and is well defined everywhere giving the selected form an advantage over the aforementioned power law model.

Johnson-Cook

The Johnson-Cook [6, 7] hardening type is a *rate-dependent* formulation utilizing the assumption that rate-independent and rate-dependent contributions may be multiplicatively separated. Specifically, use of this option requires specifying a user-defined hardening function to capture rate-independent contributions and Johnson-Cook type rate dependent coefficients. The flow stress may be written in this fashion as,

$$\bar{\sigma} = \tilde{\sigma}_y(\bar{\varepsilon}^p) \left[1 + C \left\langle \ln \left(\frac{\dot{\varepsilon}^p}{\dot{\varepsilon}_0} \right) \right\rangle \right], \quad (4.16.19)$$

in which $\tilde{\sigma}_y(\bar{\varepsilon}^p)$ is the user-specified rate-independent hardening function, C is a fitting constant and $\dot{\varepsilon}_0$ is a reference strain rate. The Macaulay brackets ensure the material behaves in a rate independent fashion when $\dot{\varepsilon}^p < \dot{\varepsilon}_0$.

Power Law Breakdown

Like the Johnson-Cook formulation, the power-law breakdown model is also rate-dependent. Again, a multiplicative decomposition between rate-independent and dependent hardening contributions. In this case, however, the functional form is derived from the analysis of Frost and Ashby [8] in which power-law relationships like those of the Johnson-Cook and cease to appropriately capture the physical response. The form used here is similar to the expression used by Brown and Bammann [9] and is written as,

$$\bar{\sigma} = \tilde{\sigma}_y(\bar{\varepsilon}^p) \left[1 + \operatorname{asinh} \left(\left(\frac{\dot{\varepsilon}^p}{g} \right)^{(1/m)} \right) \right], \quad (4.16.20)$$

with $\tilde{\sigma}_y(\bar{\varepsilon}^p)$ being the user supplied rate independent expression, g is a model parameter related to the activation energy in going from climb to glide-controlled deformation, and m dictates the strength of the dependence.

4.16.2. Implementation

Like the Hill and Hosford models, the Barlat plasticity model uses a elastic predictor-inelastic corrector closest point projection (CPP) return mapping algorithm (RMA) for integration. Details of the numerical scheme and forms of the necessary derivatives may be found in the work of Scherzinger [2]. For this approach, given a rate of deformation, d_{ij} , and a time step, Δt , a trial stress state is calculated based on an elastic response

$$T_{ij}^{tr} = T_{ij}^n + \Delta t \mathbb{C}_{ijkl} d_{kl}. \quad (4.16.21)$$

If the trial stress state lies outside the yield surface, i.e. if $\phi(T_{ij}^{tr}) > \bar{\sigma}$, then the model uses an implicit, backward Euler algorithm to return the stress to the yield surface. To perform this task, two nonlinear equations need to be solved. The first is associated with the satisfaction of the flow-rule and ensures that the plastic strain increment is in the correct direction. Such a relation leads to a residual of the form,

$$R_{ij} = \Delta d_{ij}^p - \Delta \gamma \frac{\partial \phi}{\partial T_{ij}} = 0. \quad (4.16.22)$$

while the second equation to be addressed enforces that the converged stress state is on the yield surface and is written as,

$$f = \phi(T_{ij}) - \bar{\sigma}(\bar{\varepsilon}^p) = 0. \quad (4.16.23)$$

The primary method for solving these equations is a Newton-Raphson algorithm. With $\Delta\gamma$ (which is equal to $\Delta\bar{\varepsilon}^p$) and T_{ij} being the solution variables, an iterative algorithm is utilized such that

$$\begin{aligned} \Delta\gamma^{(k+1)} &= \Delta\gamma^{(k)} + \Delta(\Delta\gamma) \\ T_{ij}^{(k+1)} &= T_{ij}^{(k)} + \Delta T_{ij}, \end{aligned} \quad (4.16.24)$$

with $\Delta\gamma^{(0)} = 0$ and $T_{ij}^{(0)} = T_{ij}^{tr}$. The plastic rate of deformation correction is then simply

$$\Delta d_{ij}^p = \mathbb{C}_{ijkl}^{-1} (T_{kl}^{tr} - T_{kl}). \quad (4.16.25)$$

After linearizing the residual and consistency equations (Equations (4.16.22) and (4.16.23)), the set of nonlinear equations may be solved for the correction increments leading to expressions of the form,

$$\begin{aligned} \Delta(\Delta\gamma) &= \frac{f^{(k)} - R_{ij}^{(k)} \mathcal{L}_{ijkl}^{(k)} \frac{\partial\phi^{(k)}}{\partial T_{kl}}}{\frac{\partial\phi^{(k)}}{\partial T_{ij}} \mathcal{L}_{ijkl}^{(k)} \frac{\partial\phi^{(k)}}{\partial T_{kl}} + H'^{(k)}} \\ \Delta T_{ij} &= -\mathcal{L}_{ijkl}^{(k)} \left(R_{kl}^{(k)} + \Delta(\Delta\gamma) \frac{\partial\phi^{(k)}}{\partial T_{kl}} \right), \end{aligned} \quad (4.16.26)$$

and $\mathcal{L}_{ijkl}^{(k)}$ is the Hessian of the RMA problem (*not* the yield surface) and is given as,

$$\mathcal{L}_{ijkl}^{(k)} = \left(\mathbb{S}_{ijkl} + \Delta\gamma^{(k)} \frac{\partial^2\phi^{(k)}}{\partial\sigma_{ij}\partial\sigma_{kl}} \right)^{-1}, \quad (4.16.27)$$

and $\mathbb{S}_{ijkl} = \mathbb{C}_{ijkl}^{-1}$.

Unfortunately, a straightforward Newton-Raphson algorithm does not always converge, so the RMA is augmented with a line search algorithm producing modified incrementation relations with

$$\begin{aligned}\Delta\gamma^{(k+1)} &= \Delta\gamma^{(k)} + \alpha\Delta(\Delta\gamma), \\ T_{ij}^{(k+1)} &= T_{ij}^{(k)} + \alpha\Delta T_{ij},\end{aligned}\tag{4.16.28}$$

where $\alpha \in (0, 1]$ is the line search parameter which is determined from certain convergence considerations. If $\alpha = 1$ then the Newton-Raphson algorithm is recovered. The line search algorithm greatly increases the reliability of the return mapping algorithm.

4.16.3. Verification

To verify the Barlat plasticity model a similar approach to that used for the Hill plasticity model (Section 4.15.3) is utilized. Specifically, both uniaxial stress and pure shear loadings are considered. To this end, the response of a 2090-T3 aluminum with Voce hardening of the form,

$$\bar{\sigma}(\bar{\varepsilon}^p) = \sigma_y + A(1 - \exp(-b\bar{\varepsilon}^p)),\tag{4.16.29}$$

is used. The corresponding elastic, plastic, and anisotropy model parameters are given in Table 4-22.

E	70 GPa	ν	0.25
a	8	σ_y	200 MPa
A	200 MPa	b	20
c'_{12}	-0.069888	c''_{12}	0.981171
c'_{13}	0.936408	c''_{13}	0.476741
c'_{21}	0.079143	c''_{21}	0.575316
c'_{23}	1.003060	c''_{23}	0.866827
c'_{31}	0.524741	c''_{31}	1.145010
c'_{32}	1.363180	c''_{32}	-0.079294
c'_{44}	1.023770	c''_{44}	1.051660
c'_{55}	1.069060	c''_{55}	1.147100
c'_{66}	0.954322	c''_{66}	1.404620

Table 4-22. The material and model parameters for the Barlat plasticity model used for verification testing. The anisotropy coefficients correspond to 2090-T3 aluminum and are from [1].

Finally, the coordinate system used in these calculations is a rectangular coordinate system with the e_i^1, e_i^2, e_i^3 axes aligned with the x, y, z axes.

4.16.3.1. Uniaxial Stress

First, the response of the material subject to a uniaxial stress is considered. As such, the Cauchy stress tensor takes the form $\sigma_{ij} = \sigma\delta_{i1}\delta_{j1}$. In the transformed stress space, this uniaxial tensor becomes,

$$s'_{ij} = \frac{1}{3}\sigma \begin{bmatrix} c'_{12} + c'_{13} & 0 & 0 \\ 0 & -2c'_{21} + c'_{23} & 0 \\ 0 & 0 & -2c'_{31} + c'_{32} \end{bmatrix} \quad (4.16.30)$$

$$s''_{ij} = \frac{1}{3}\sigma \begin{bmatrix} c''_{12} + c''_{13} & 0 & 0 \\ 0 & -2c''_{21} + c''_{23} & 0 \\ 0 & 0 & -2c''_{31} + c''_{32} \end{bmatrix}.$$

It is noted from (4.16.30) that the two transformed stress tensors are purely diagonal and therefore in a principal state. The actual ordering of the components into the corresponding principal stresses depends on the anisotropy coefficients. By inspection of Table 4-22 it is clear in this instance that tensors are already ordered ($s'_1 = s'_{11}$, $s''_1 = s''_{11}$ etc.). With this observation, the effective stress may be reduced to,

$$\phi(\sigma_{ij}) = \omega|\sigma|, \quad (4.16.31)$$

where ω is a constant dependent on model parameters and is written as,

$$\omega = \frac{1}{3} \left\{ \frac{1}{4} \left[|c'_{12} + c'_{13} - c''_{12} - c''_{13}|^a + |c'_{12} + c'_{13} + 2c''_{21} - c''_{23}|^a + |c'_{12} + c'_{13} + 2c''_{31} - c''_{32}|^a \right. \right. \\ \left. \left. + |c'_{23} - 2c'_{21} - c''_{12} - c''_{13}|^a + |c'_{23} - 2c'_{21} + 2c''_{21} - c''_{23}|^a + |c'_{23} - 2c'_{21} + 2c''_{31} - c''_{32}|^a \right. \right. \\ \left. \left. + |c'_{32} - 2c'_{31} - c''_{12} - c''_{13}|^a + |c'_{32} - 2c'_{31} + 2c''_{21} - c''_{23}|^a + |c'_{32} - 2c'_{31} + 2c''_{31} - c''_{32}|^a \right] \right\}^{1/a}. \quad (4.16.32)$$

Axial Stresses

To determine the axial stress, it is first noted that during plastic deformation,

$$\phi(\sigma_{ij}) = \omega\sigma = \bar{\sigma}(\bar{\varepsilon}^p), \quad (4.16.33)$$

where the fact that a tensile loading will be investigated ($\sigma > 0$) is leveraged. The stress is then simply,

$$\sigma = \frac{\bar{\sigma}(\bar{\varepsilon}^p)}{\omega}. \quad (4.16.34)$$

This shows that during plastic deformation the stress state can be calculated from the hardening law and anisotropy parameters.

To evaluate the axial stress, a relationship between the equivalent plastic strain and axial strain is needed. By noting the uniaxial stress state and equating the rate of plastic work, it is evident that,

$$\bar{\sigma} \dot{\varepsilon}^p = \sigma (\dot{\varepsilon} - \dot{\varepsilon}^e) \rightarrow \dot{\varepsilon}^p = \frac{1}{\omega} (\dot{\varepsilon} - \dot{\varepsilon}^e) \quad (4.16.35)$$

which, when integrated, gives an implicit equation for the equivalent plastic strain that is written as

$$\bar{\varepsilon}^p = \frac{1}{\omega} \left(\varepsilon - \frac{\bar{\sigma}(\bar{\varepsilon}^p)}{\omega E} \right). \quad (4.16.36)$$

The equivalent plastic strain can then be used in (4.16.34) to find the axial stress, σ .

Corresponding stress-strain results determined analytically in this fashion and numerically via Adagio are presented below in Figure 4-68.

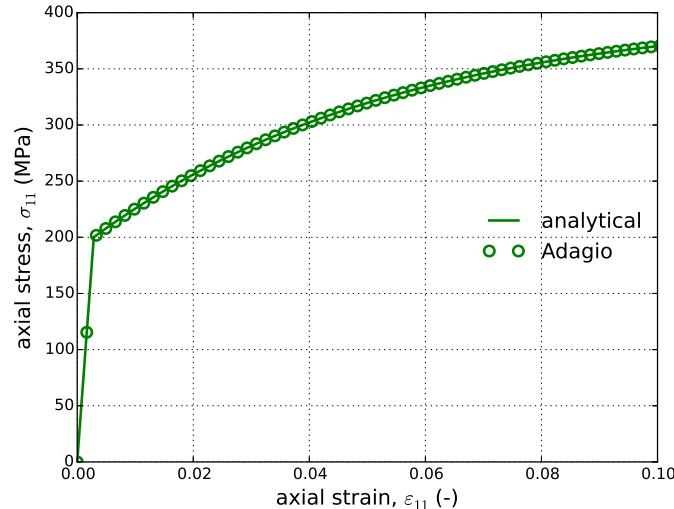


Figure 4-68. Axial stress-strain response determined analytically and numerically for 2090-T3 aluminum using the Barlat plasticity model with Voce hardening.

Lateral Strains

To determine the plastic strain, the derivatives of the yield surface with respect to the Cauchy stress ($\partial\phi/\partial\sigma_{ij}$) are needed. From (4.16.12) it can be seen that these relations are quite complex

and the reader is referred to [2] for a detailed discussion of how to rigorously evaluate these derivatives under arbitrary conditions. In this effort, the fact that the principal directions of the transformed stresses ($\hat{e}_i^{k'}$ and $\hat{e}_i^{k''}$) are aligned with the global coordinate system ($\hat{e}_i^{1'} = e_i^1$ etc.) simplifies the problem sufficiently to allow for an analytical treatments. In this case,

$$\frac{\partial s'_k}{\partial s'_{ij}} = e_i^k e_j^k. \quad (4.16.37)$$

With this observation, the lateral flow directions may be written as,

$$\begin{aligned} \frac{\partial \phi}{\partial \sigma_{22}} = & \frac{1}{3} \left[\frac{\partial \phi}{\partial s'_1} (c'_{13} - 2c'_{12}) + \frac{\partial \phi}{\partial s'_2} (c'_{21} + c'_{23}) + \frac{\partial \phi}{\partial s'_3} (c'_{31} - 2c'_{32}) \right. \\ & \left. + \frac{\partial \phi}{\partial s''_1} (c''_{13} - 2c''_{12}) + \frac{\partial \phi}{\partial s''_2} (c''_{21} + c''_{23}) + \frac{\partial \phi}{\partial s''_3} (c''_{31} - 2c''_{32}) \right] \end{aligned} \quad (4.16.38)$$

$$\begin{aligned} \frac{\partial \phi}{\partial \sigma_{33}} = & \frac{1}{3} \left[\frac{\partial \phi}{\partial s'_1} (c'_{12} - 2c'_{13}) + \frac{\partial \phi}{\partial s'_2} (c'_{21} - 2c'_{23}) + \frac{\partial \phi}{\partial s'_3} (c'_{31} + c'_{32}) \right. \\ & \left. + \frac{\partial \phi}{\partial s''_1} (c''_{12} - 2c''_{13}) + \frac{\partial \phi}{\partial s''_2} (c''_{21} - 2c''_{23}) + \frac{\partial \phi}{\partial s''_3} (c''_{31} + c''_{32}) \right], \end{aligned} \quad (4.16.39)$$

in which the various $\partial \phi / \partial s'_i$ derivatives are functions of the anisotropy coefficients and explicit forms may be found in [2].

The total strain is written simply as,

$$\varepsilon_{ij} = \varepsilon_{ij}^e + \varepsilon_{ij}^p, \quad (4.16.40)$$

with the elastic strain being

$$\varepsilon_{22}^e = \varepsilon_{33}^e = -\nu \frac{\sigma}{E}, \quad (4.16.41)$$

and the plastic strains found via the flow rules as,

$$\varepsilon_{22}^p = \bar{\varepsilon}^p \frac{\partial \phi}{\partial \sigma_{22}} \quad ; \quad \varepsilon_{33}^p = \bar{\varepsilon}^p \frac{\partial \phi}{\partial \sigma_{33}}. \quad (4.16.42)$$

The flow directions were given previously in (4.16.38) and (4.16.39) while the equivalent plastic strain may be found via (4.16.36). Figure 4-69 presents the lateral strains as a function of the axial. Clear agreement may be observed both in Figure 4-68 and 4-69 verifying the model. Additionally, the effect of the anisotropy is plainly evident in Figure 4-69 in which the two lateral strains differ by approximately a factor of four.

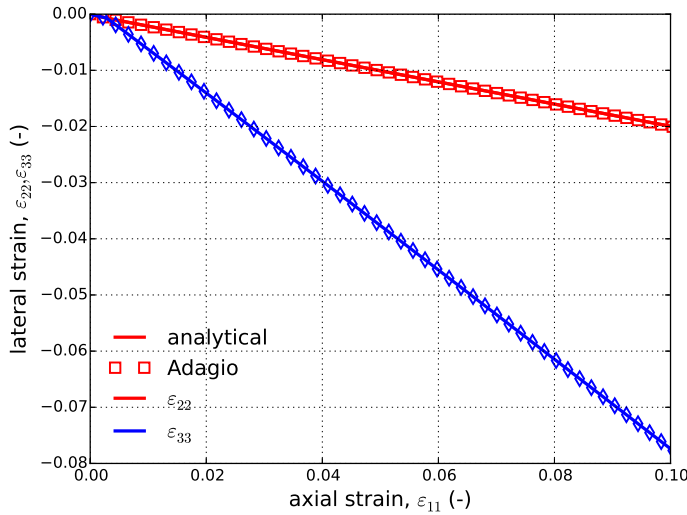


Figure 4-69. Lateral strain as a function of axial strain of 2090-T3 aluminum with Voce hardening as determined by the Barlat plasticity model both analytically and numerically.

To test the other directions and further examine the anisotropic character of the model, the coordinate system rotation input options are used to align the “2” and “3” directions of the material with the applied load. Analytical expressions may be determined by similarly rotating the coefficients in the previous expressions, although these are not repeated here for brevity. The corresponding results for the loading aligned with the “2” and “3” directions are presented in Figures 4-70 and 4-71, respectively. All of the results are given with respect to the original coordinate system to avoid confusion. Clear agreement between analytical and simulation results is noted in both cases further verifying the capabilities of the model. Importantly, by comparing the various stress-strain and lateral strain curves, the influence of the material and model anisotropy on the responses may readily be observed.

4.16.3.2. Pure Shear

In this section, the pure shear response of the Barlat model is interrogated to assess its performance under such conditions. Before proceeding, it is important to recall the ordering of the shear stresses in Sierra/SM. Specifically, the σ_{12} , σ_{23} , and σ_{31} stresses are associated with the 44, 55, and 66, respectively, anisotropy coefficients.

To explore the shear performance of the Barlat plasticity model, a stress tensor of the form $\sigma_{ij} = \tau (\delta_{i1}\delta_{j2} + \delta_{i2}\delta_{j1})$ is considered. The ordered principal stresses of the transformed stress tensors are,

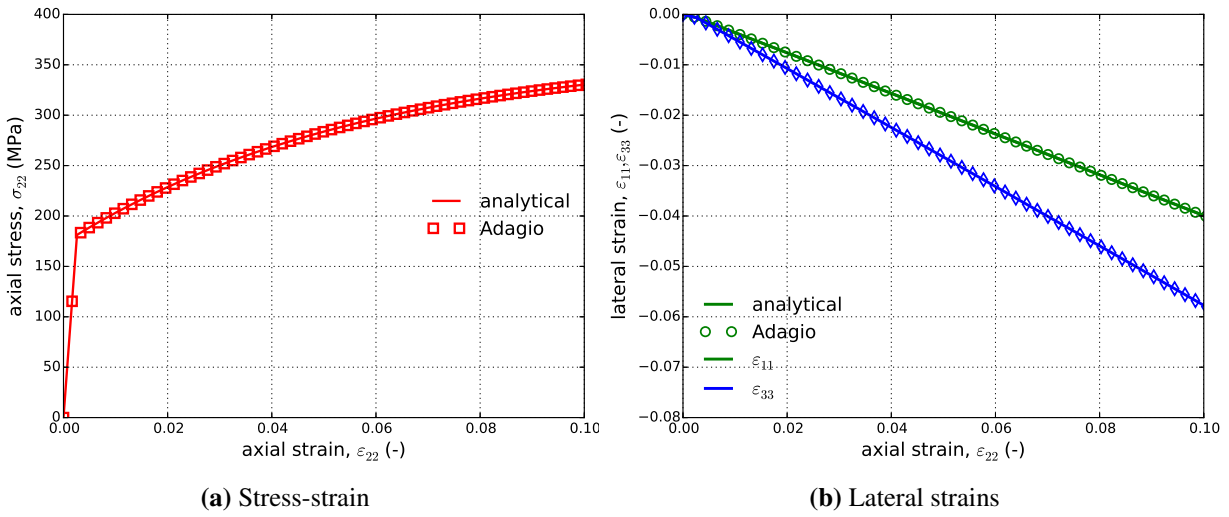


Figure 4-70. (a) Stress-strain and (b) lateral strain responses of 2090-T3 aluminum with Voce hardening and the Barlat plasticity model. The material is rotated such that the loading is aligned with the “2” direction.

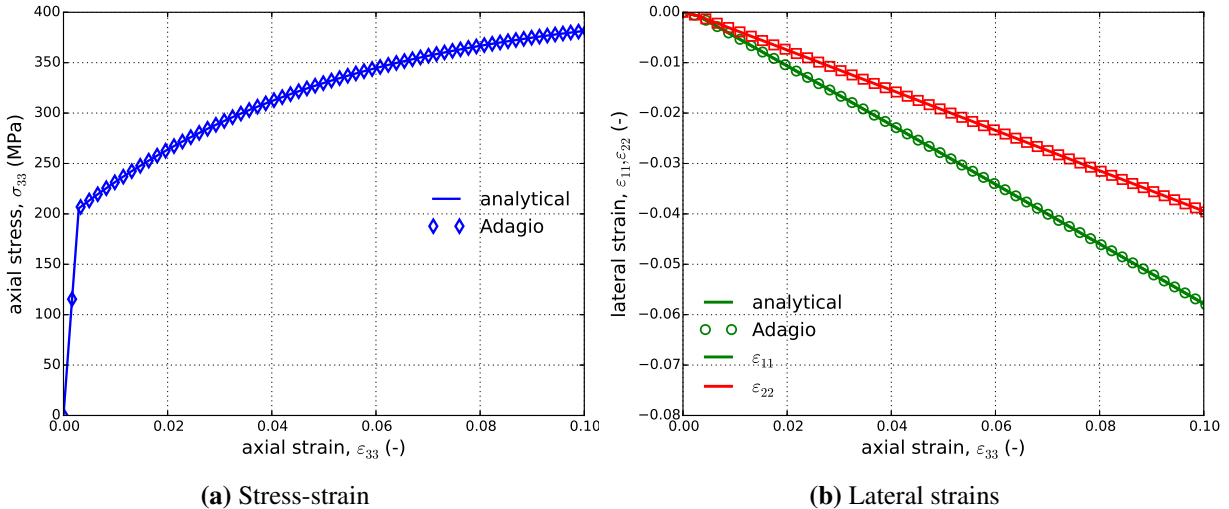


Figure 4-71. (a) Stress-strain and (b) lateral strain responses of 2090-T3 aluminum with Voce hardening and the Barlat plasticity model. The material is rotated such that the loading is aligned with the “3” direction.

$$s'_i = \begin{bmatrix} c'_{44}\tau \\ 0 \\ -c'_{44}\tau \end{bmatrix} \quad ; \quad s''_i = \begin{bmatrix} c''_{44}\tau \\ 0 \\ -c''_{44}\tau \end{bmatrix}, \quad (4.16.43)$$

thereby simplifying the effective stress to,

$$\phi(\sigma_{ij}) = \tau\zeta, \quad (4.16.44)$$

with

$$\zeta = \left\{ \frac{1}{2} \left[|c'_{44} - c''_{44}|^a + |c'_{44} + c''_{44}|^a + |c'_{44}|^a + |c''_{44}|^a \right] \right\}^{1/a}. \quad (4.16.45)$$

During plastic flow,

$$\phi = \tau\zeta = \bar{\sigma}(\bar{\varepsilon}^p), \quad (4.16.46)$$

producing an expression for the stress in terms of equivalent plastic strain as,

$$\tau = \frac{1}{\zeta} \bar{\sigma}(\bar{\varepsilon}^p). \quad (4.16.47)$$

A relationship between the equivalent plastic and axial strains may be determined by first considering the equivalency of plastic work,

$$\bar{\sigma} \dot{\bar{\varepsilon}}^p = 2\tau (\dot{\varepsilon}_{12} - \dot{\varepsilon}_{12}^e) \quad \rightarrow \quad \dot{\bar{\varepsilon}}^p = \frac{2}{\zeta} (\dot{\varepsilon}_{12} - \dot{\varepsilon}_{12}^e). \quad (4.16.48)$$

Integrating leads to an implicit expression of the form,

$$\bar{\varepsilon}^p = \frac{2}{\zeta} \left(\varepsilon_{12} - \frac{\bar{\sigma}(\bar{\varepsilon}^p)}{\zeta G} \right). \quad (4.16.49)$$

The preceding relations may be used to analytically determine the shear stress-strain response. Corresponding results, along with those produced by Adagio, are presented in Figure 4-72. Shear responses are also presented for stress tensors of the form $\sigma_{ij} = \tau(\delta_{2i}\delta_{3j} + \delta_{3i}\delta_{2j})$ ("23") and $\sigma_{ij} = \tau(\delta_{1i}\delta_{3j} + \delta_{3i}\delta_{1j})$ ("31"). Analytically, these results were determined by substituting the relevant anisotropy coefficients in (4.16.43)-(4.16.49). For the results from Adagio, the coordinate system input commands were used to rotate the material coordinate system accordingly.

In all the cases presented in Figure 4-72 excellent agreement is noted. This not only verifies the performance of the current model under pure shear loadings but also demonstrates the impact of the anisotropy and exercises the coordinate system rotation capabilities.

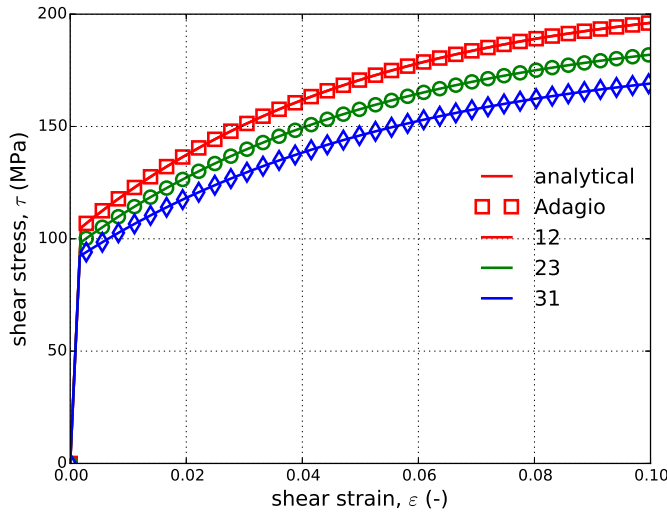


Figure 4-72. Shear stress-strain results for 2090-T3 aluminum determined analytically and numerically by the Barlat plasticity model with Voce Hardening

4.16.3.3. Plastic Hardening

To verify the capabilities of the hardening models, rate-*independent* and rate-*dependent* alike, the constant equivalent plastic strain rate, $\dot{\varepsilon}^p$, uniaxial stress and pure shear verification tests described in Appendix A.5 are utilized. In these simplified loading cases, the material state may be found explicitly as a function of time knowing the prescribed equivalent strain rate. For the rate-*independent* cases, a strain rate of $\dot{\varepsilon}^p = 1 \times 10^{-4} \text{ s}^{-1}$ is used for ease in simulations although the selected rate does not affect the results. Through this testing protocol, the hardening models are not only tested at different rates but also in different principal material directions to consider the anisotropy of the Barlat yield surface. Additionally, the rate-*dependent* models are tested for a wide range of strain rates (over five decades) with all three rate-*independent* hardening functions ($\tilde{\sigma}_y$ in the previous theory section). Although linear, Voce, and power-law rate-*independent* representations are utilized in the rate-*dependent* tests, in those cases the hardening models are prescribed via user-defined analytic functions. The rate-*independent* verification exercises, on the other hand, examine the built-in hardening models. This distinction necessitates the different considerations and treatments.

The rate-*dependent* and rate-*independent* hardening coefficients are found in Table 4-20 while the remaining model parameters are unchanged from the previous verification exercises. For the current verification exercise, the rate-*independent* hardening models (linear, Voce, and power-law) will first be considered and then the rate-*dependent* forms (Johnson-Cook, power-law breakdown).

C	0.1	$\dot{\varepsilon}_0$	$1 \times 10^{-4} \text{ s}^{-1}$
g	0.21 s^{-1}	m	16.4
$\tilde{H}_{\text{Linear}}$	200 MPa	-	-
\tilde{A}_{PL}	400 MPa	\tilde{n}_{PL}	0.25
\tilde{A}_{Voce}	200 MPa	\tilde{n}_{Voce}	20

Table 4-23. The model parameters for the hardening verification tests used with the Barlat plasticity model during verification tests. Parameters for the rate-independent hardening functions, $\tilde{\sigma}_y$, are also given and denoted with a $\tilde{\cdot}$ while the subscript refers to the functional form.

Linear

For the rate-*independent* linear hardening model, verification is considered via the uniaxial stress and pure shear exercises of Appendix A.5. As the anisotropic Barlat yield surface is being used for this examination, the uniaxial stress response is determined for loading in three different principal material planes while the pure shear response is found along three shear planes. Results determined analytically and numerically are presented in Figure 4-73. Clear agreement is evident between the dual solution approaches. Additionally, the linear response and constant tangent modulus during plastic deformation highlights the characteristic feature of the current model.

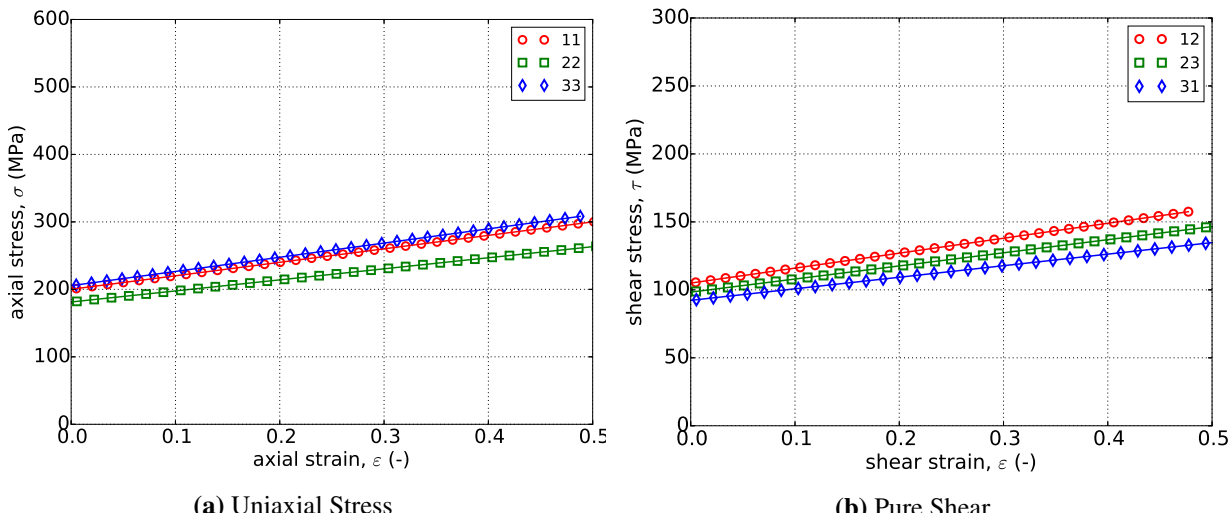


Figure 4-73. (a) Uniaxial stress-strain and (b) pure shear responses of the Barlat plasticity model with rate-independent, linear hardening. Solid lines are analytical while open symbols are numerical.

Power-Law

To probe the power-law rate-*independent* hardening model, analytical and numerical results to the uniaxial stress and pure shear problems of Appendix A.5 are determined. Given the anisotropic nature of the current model, responses are determined along the three principal and three shearing planes for the uniaxial stress and pure shear cases and all six cases are shown in Figure 4-74. In considering Figure 4-74, it is apparent that the numerical and analytical responses agree quite well verifying this specific response. These cases also highlight the initially stiff plastic response that eventually evolves into a more compliant linear like response that is associated with a power-law hardening model.

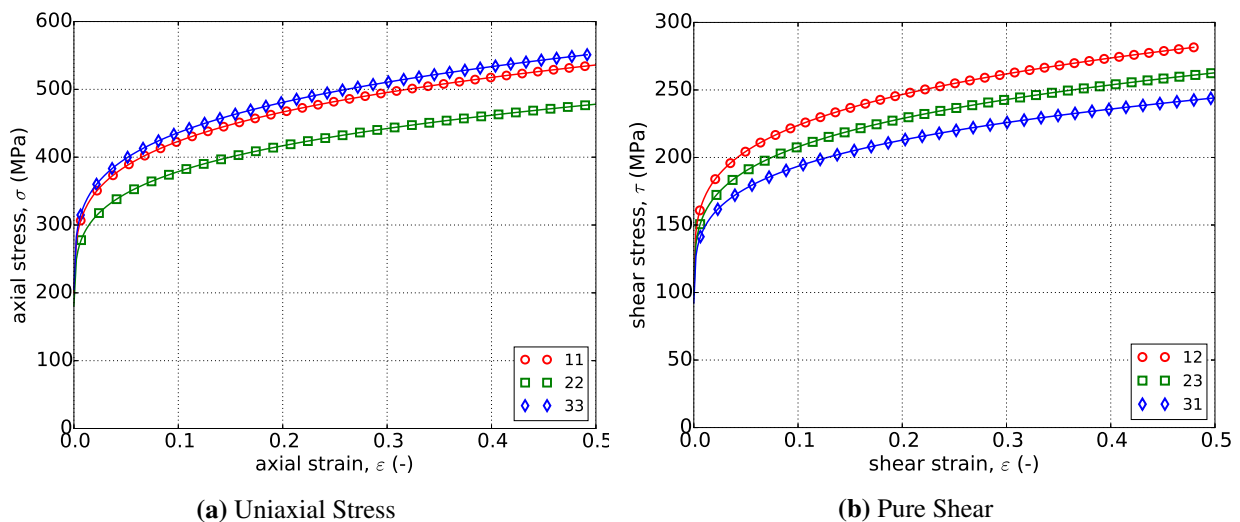


Figure 4-74. (a) Uniaxial stress-strain and (b) pure shear responses of the Barlat plasticity model with rate-*independent*, power-law hardening. Solid lines are analytical while open symbols are numerical.

Voce

Verifying the Voce model is addressed through the methods of Appendix A.5. To this end, analytical and numerical uniaxial stress and pure shear responses are determined along three different principal directions and shear planes, respectively. The results for these various cases are presented in Figure 4-75 and unambiguous agreement is readily seen between the analytical and numerical results providing further credence to hardening model capabilities. Responses in Figure 4-75 also exhibit the clear saturation of hardening with sufficient plastic strain that is usually associated with the Voce model.

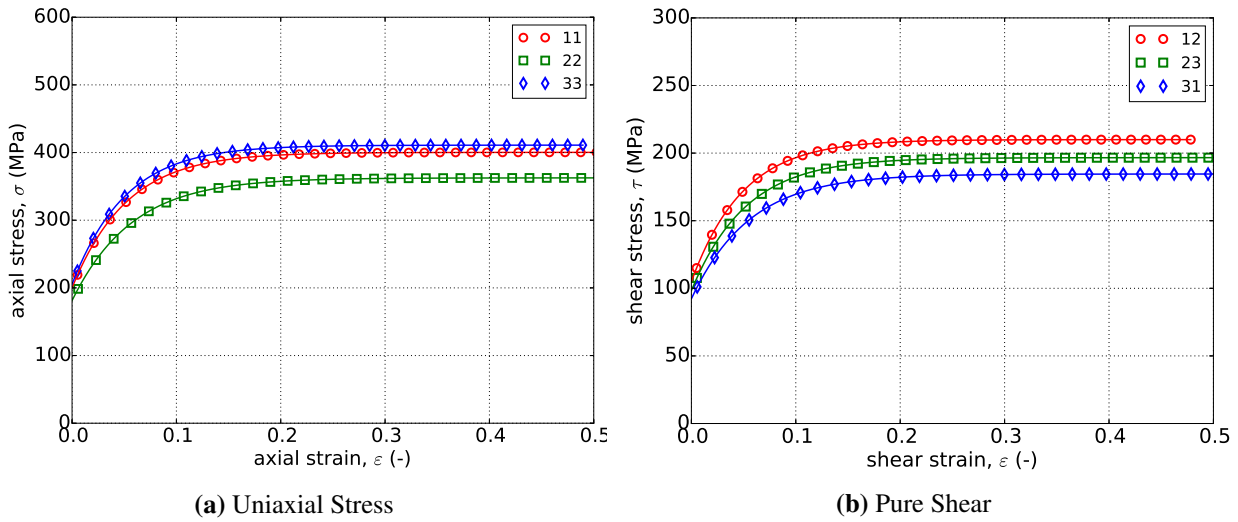


Figure 4-75. (a) Uniaxial stress-strain and (b) pure shear responses of the Barlat plasticity model with rate-independent, Voce hardening. Solid lines are analytical while open symbols are numerical.

Johnson-Cook

To investigate the uniaxial response of the Johnson-Cook rate-*dependent* hardening model, the problem discussed in Appendix A.5.1 is considered. In this analysis, the response depends only on time and the various c'_i and c''_i Barlat yield surface coefficients. For a full-spectrum verification, forty-five different cases are evaluated using three different material principal directions (\hat{e}_1 , \hat{e}_2 , and \hat{e}_3), five different rates ($\dot{\varepsilon}^p = 1 \times 10^{-3}$, 1×10^{-2} , 1×10^{-1} , 1×10^0 and $1 \times 10^1 \text{ s}^{-1}$), and three different rate-*independent* hardening models (linear, Voce, and power-law). All forty-five analytical and numerical results are presented in Figure 4-76 and quite notable agreement is observed in each instance.

For the pure shear case, the forty-five different permutations are again explored. The same five rates and three hardening models are used although three different shearing planes are used instead of the three principal directions. The solution of the pure shear problem is described in Appendix A.5.2 and the analytical and numerical results are presented in Figure 4-77. As with the uniaxial stress response excellent correspondence is noted between the two sets of results.

Power-Law Breakdown

In the case of the power-law Breakdown model, verification is again pursued through the problem of Appendix A.5.1 and using the same forty-five cases discussed with the Johnson-Cook model. Corresponding results are given in Figure 4-78 and as with the preceding results substantial convergence is noted between the analytical and numerical results giving further credence to the hardening models.

As with the uniaxial stress case, the pure shear capabilities are interrogated through the procedure

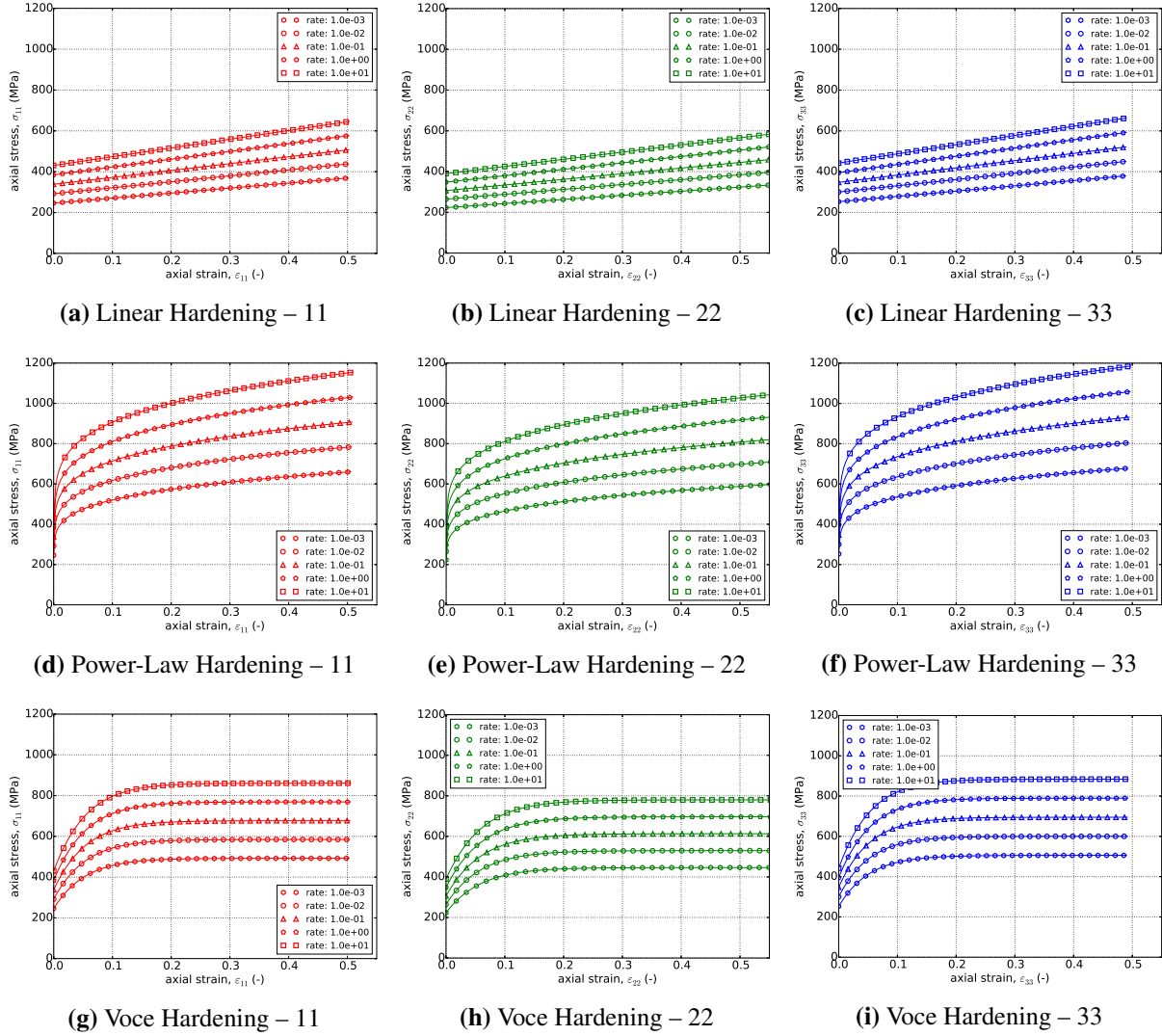


Figure 4-76. Uniaxial stress-strain response of the Barlat plasticity model ($a = 8$) with rate-dependent, Johnson-Cook type hardening with (a-c) linear (d-f) power-law and (g-i) Voce rate-independent hardening. Solid lines are analytical results while open symbols are numerical.

of Appendix A.5.2 using the same forty-five cases outlined in the Johnson-Cook discussion. The analytical and numerical results are presented in Figure 4-79. Again, the two result sets align beautifully enabling further capability credibility.

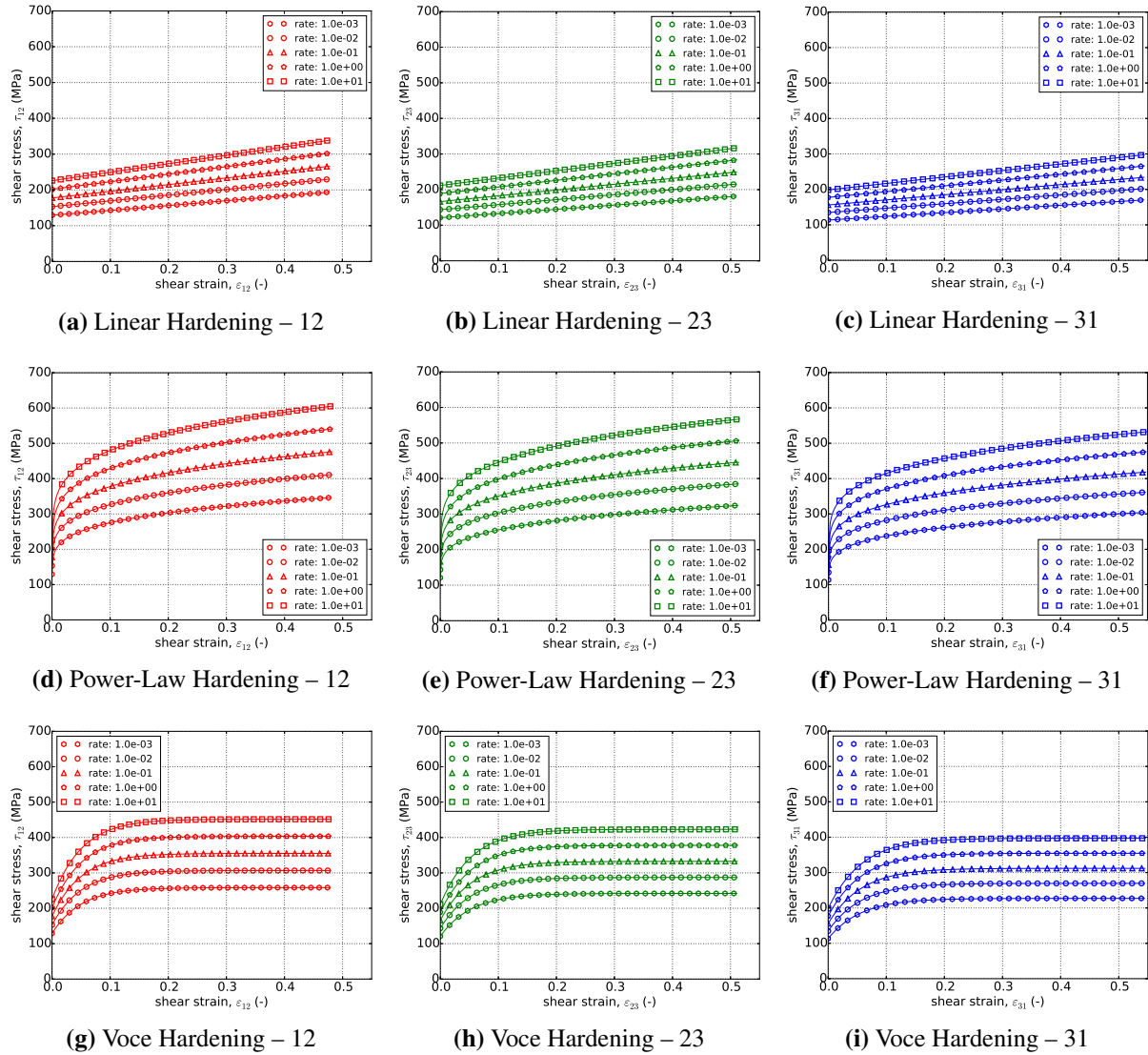


Figure 4-77. Stress-strain response of the Barlat plasticity model

($a = 8$) with rate-dependent, Johnson-Cook type hardening in pure shear with (a-c) linear (d-f) power-law and (g-i) Voce rate-independent hardening. Solid lines are analytical results while open symbols are numerical.

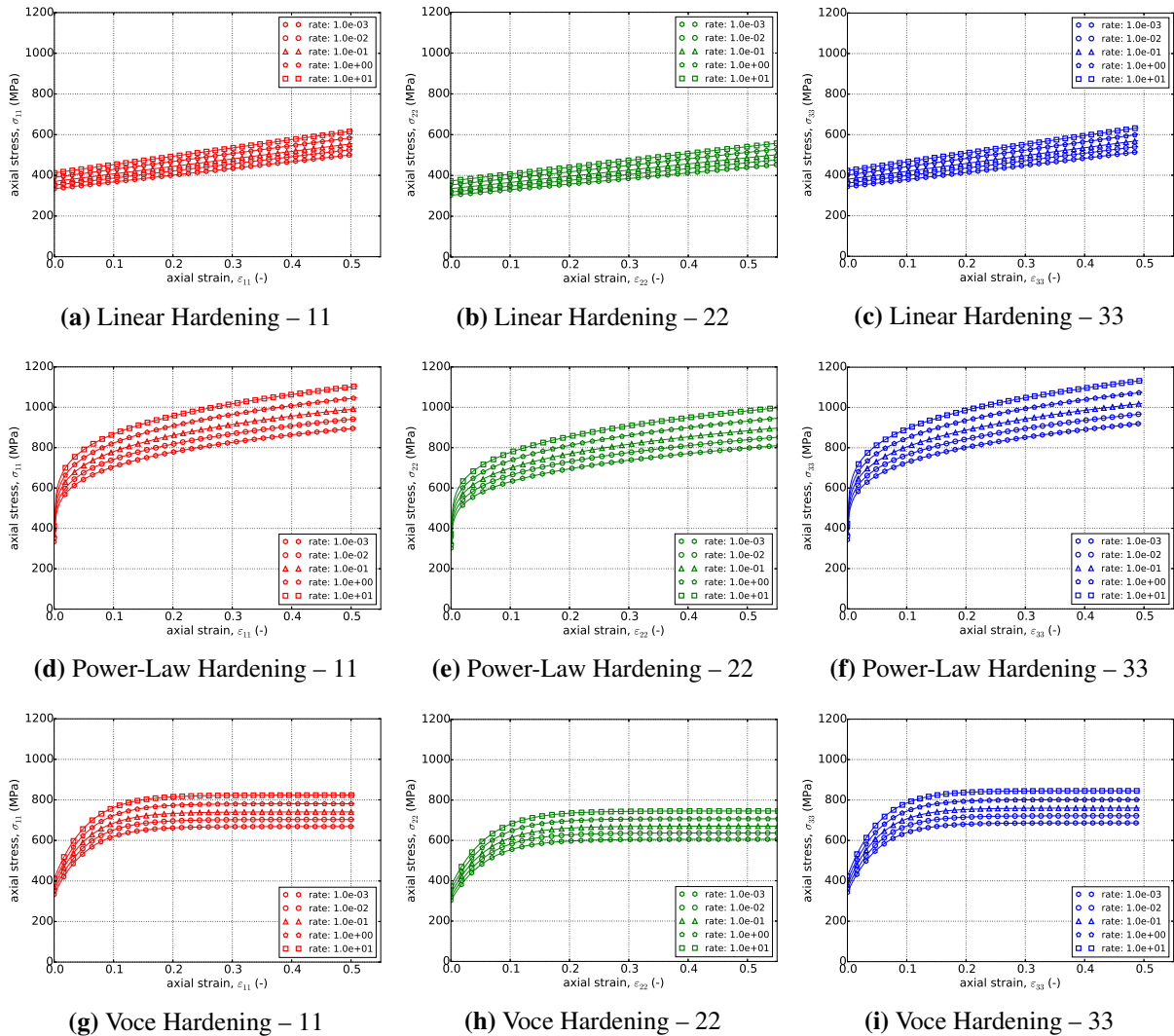


Figure 4-78. Uniaxial stress-strain response of the Barlat plasticity model ($a = 8$) with rate-dependent, power-law breakdown type hardening with (a-c) linear (d-f) power-law and (g-i) Voce rate-independent hardening. Solid lines are analytical while open symbols are numerical.

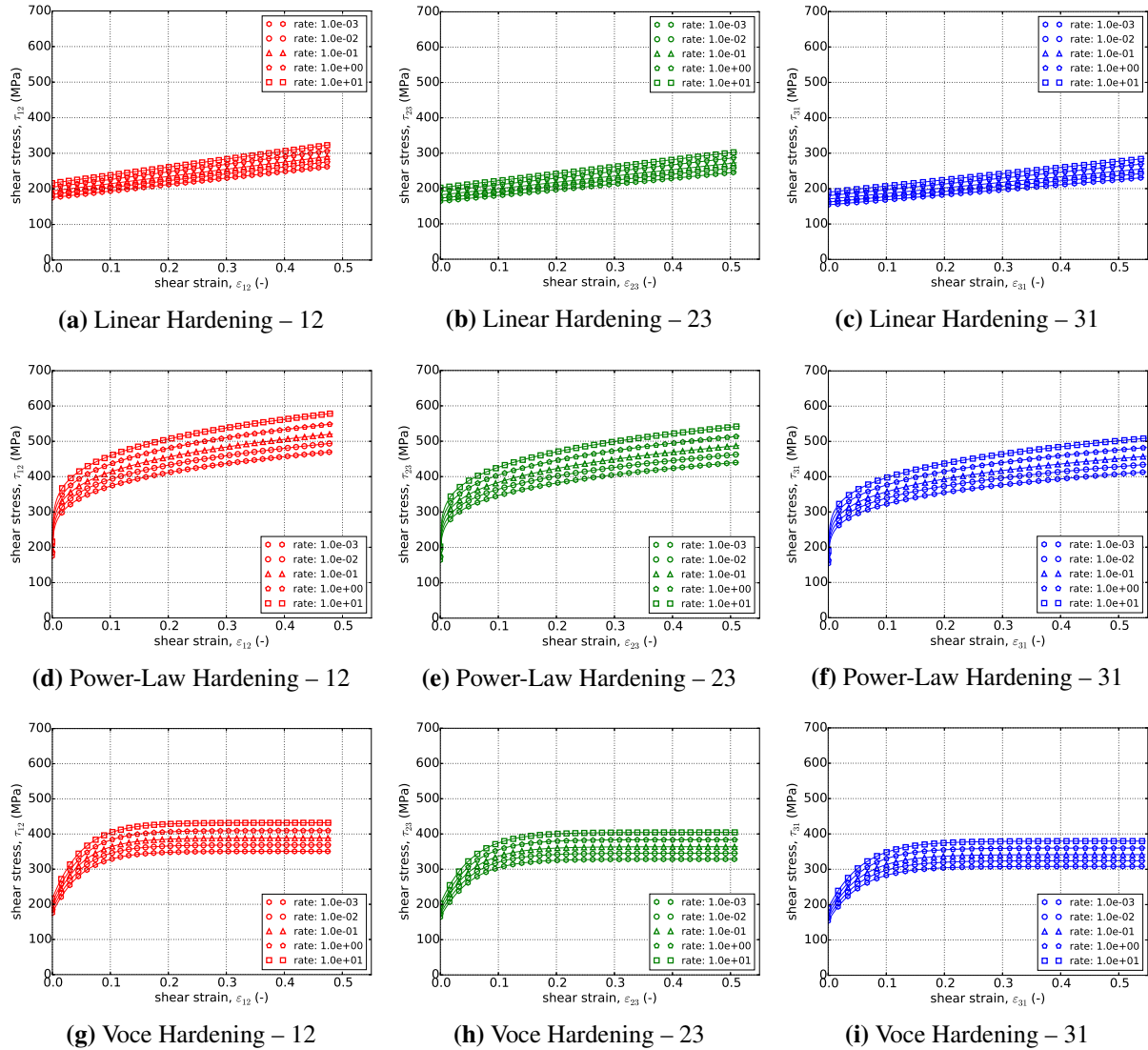


Figure 4-79. Stress-strain response of the Barlat plasticity model ($a = 8$) with rate-dependent, power-law breakdown type hardening in pure shear with (a-c) linear (d-f) power-law and (g-i) Voce rate-independent hardening. Solid lines are analytical results while open symbols are numerical.

4.16.4. User Guide

```
BEGIN PARAMETERS FOR MODEL BARLAT_PLASTICITY
#
# Elastic constants
#
YOUNGS MODULUS = <real> E
POISSONS RATIO = <real> ν
SHEAR MODULUS = <real> G
BULK MODULUS = <real> K
LAMBDA = <real> λ
TWO MU = <real> 2μ
#
# Material coordinates system definition
#
COORDINATE SYSTEM = <string> coordinate_system_name
DIRECTION FOR ROTATION = <real> 1|2|3
ALPHA = <real> α1 (degrees)
SECOND DIRECTION FOR ROTATION = <real> 1|2|3
SECOND ALPHA = <real> α2 (degrees)
#
# Yield surface parameters
#
YIELD STRESS = <real> σy
A = <real> a (4.0)
CP12 = <real> c12' (1.0)
CP13 = <real> c13' (1.0)
CP21 = <real> c21' (1.0)
CP23 = <real> c23' (1.0)
CP31 = <real> c31' (1.0)
CP32 = <real> c32' (1.0)
CP44 = <real> c44' (1.0)
CP55 = <real> c55' (1.0)
CP66 = <real> c66' (1.0)
CPP12 = <real> c12'' (1.0)
CPP13 = <real> c13'' (1.0)
CPP21 = <real> c21'' (1.0)
CPP23 = <real> c23'' (1.0)
CPP31 = <real> c31'' (1.0)
CPP32 = <real> c32'' (1.0)
CPP44 = <real> c44'' (1.0)
CPP55 = <real> c55'' (1.0)
CPP66 = <real> c66'' (1.0)
#
# Hardening model
#
HARDENING MODEL = LINEAR | POWER_LAW | VOCE | USER_DEFINED |
```

```

CUBIC_HERMITE_SPLIT | JOHNSON_COOK | POWER_LAW_BREAKDOWN
#
# Linear hardening
#
HARDENING MODULUS = <real>  $H'$ 
#
# Power-law hardening
#
HARDENING CONSTANT = <real>  $A$ 
HARDENING EXPONENT = <real>  $n$  (0.5)
LUDERS STRAIN      = <real>  $\epsilon_L$  (0.0)
#
# Voce hardening
#
HARDENING MODULUS      = <real>  $A$ 
EXPONENTIAL COEFFICIENT = <real>  $n$ 
#
# Johnson-Cook hardening
#
HARDENING FUNCTION = <string>hardening_function_name
RATE CONSTANT        = <real>  $C$ 
REFERENCE RATE       = <real>  $\dot{\epsilon}_0$ 
#
# Power law breakdown hardening
#
HARDENING FUNCTION = <string>hardening_function_name
RATE COEFFICIENT    = <real>  $g$ 
RATE EXPONENT        = <real>  $m$ 
#
# User defined hardening
#
HARDENING FUNCTION = <string>hardening_function_name
#
# Spline based hardening curve
#
CUBIC SPLINE TYPE   = <string>
CARDINAL PARAMETER = <real> val
KNOT EQPS          = <real_list> vals
KNOT STRESS         = <real_list> vals
END [PARAMETERS FOR MODEL BARLAT_PLASTICITY]

```

Output variables available for this model are listed in Table 4-24.

Table 4-24. State Variables for BARLAT PLASTICITY Model

Name	Description
EQPS	equivalent plastic strain, $\bar{\epsilon}^p$
EQDOT	equivalent plastic strain rate, $\dot{\bar{\epsilon}}^p$
SEFF	effective stress, ϕ

REFERENCES

- [1] F. Barlat, H. Aretz, J. W. Yoon, J. C. Brem, and R. E. Dick. Linear transformation-based anisotropic yield functions. *International Journal of Plasticity*, 21:1009–1039, 2005.
- [2] W. M. Scherzinger. A return mapping algorithm for isotropic and anisotropic plasticity models using a line search method. *Computer Methods in Applied Mechanics and Engineering*, 317:526–553, 2017.
- [3] R. Hill. *The Mathematical Theory of Plasticity*. Oxford University Press, 1950.
- [4] J. Lemaître and J.-L. Chaboche. *Mechanics of Solid Materials*. Cambridge University Press, 1990.
- [5] J. Lubliner. *Plasticity Theory*. Dover, 2008.
- [6] G.R. Johnson and W.H. Cook. A constitutive model and data for metals subjected to large strains, high strain rates and high temperatures. In *Proc. 7th. Int. Symp. on Ballistics*, pages 541–547, The Hague, The Netherlands, 1983.
- [7] G.R. Johnson and W.H. Cook. Fracture characteristics of three metals subjected to various strains, strain rates, temperatures and pressures. *Engineering Fracture Mechanics*, 21(1): 31–48, 1985.
- [8] H. J. Frost and M. F. Ashby. *Deformation mechanism maps: the plasticity and creep of metals and ceramics*. Pergamon press, 1982.
- [9] A.A. Brown and D.J. Bammann. Validation of a model for static and dynamic recrystallization in metals. *International Journal of Plasticity*, 32–33:17–35, 2012.

4.17. PLANE STRESS RATE PLASTICITY MODEL

4.17.1. Theory

The plane stress rate plasticity model is the plane stress formulation of a J_2 plasticity model given by Simo and Taylor [1] (and described again in Simo and Hughes [2]) extended to include rate-dependent hardening and a failure model for use with shell elements.

Like other plasticity models, the components of the objective stress rate, $\overset{\circ}{\sigma}_{ij}$, are written as,

$$\overset{\circ}{\sigma}_{ij} = \mathbb{C}_{ijkl} D_{kl}^e \quad (4.17.1)$$

where \mathbb{C}_{ijkl} are the components of the fourth-order, isotropic elasticity tensor and D_{ij}^e are the components of the elastic part of the total rate of deformation tensor. An additive split of the total rate of deformation tensor into elastic and plastic contributions is assumed such that,

$$D_{ij} = D_{ij}^e + D_{ij}^p. \quad (4.17.2)$$

The plane stress formulation recasts the three-dimensional problem into a constrained subspace with plane stress conditions acting as the constraints. To do this, the plane stress rate plasticity model follows the approach of Simo and Taylor [1] to enforce $\sigma_{13} = \sigma_{23} = \sigma_{33} = 0$ and related conditions.

For the plasticity portion of the model, the formulation of Simo and Taylor [1] is used³ in which a traditional three-dimensional J_2 plasticity model is recast in reduced subspace. To do this, it is recalled that in three-dimensions the von Mises effective stress, ϕ , is written,

$$\phi^2 = \frac{3}{2} s_{ij} s_{ij}, \quad (4.17.3)$$

with $s_{ij} = \sigma_{ij} - (1/3)\sigma_{kk}\delta_{ij}$ the deviatoric stress. To write an equivalent expression in the reduced subspace, the vector, $\underline{\sigma}$, and matrix, $\underline{\underline{P}}$, are introduced as⁴,

$$\underline{\sigma} = \begin{bmatrix} \sigma_{11} \\ \sigma_{22} \\ \sigma_{12} \end{bmatrix}, \quad ; \quad \underline{\underline{P}} = \frac{1}{3} \begin{bmatrix} 2 & -1 & 0 \\ -1 & 2 & 0 \\ 0 & 0 & 3 \end{bmatrix}, \quad (4.17.4)$$

such that,

³In the work of Simo and Taylor [1] (and later Simo and Hughes [2]) hardening is assumed to be rate and temperature independent. Here, such terms are included but do not materially change the formulation. Similarly, the earlier works also introduce kinematic hardening which is not used in the current model.

⁴Note, here the \underline{x} and $\underline{\underline{X}}$ notations are introduced for vector and matrix objects, respectively, to clearly distinguish that these variables are *not* tensors. This results from operating in the constrained stress subspace and means that these terms do not have properties of a tensor and act on each other as traditional matrices and vectors.

$$\underline{s} = \begin{bmatrix} s_{11} \\ s_{22} \\ s_{12} \end{bmatrix} = \underline{\underline{P}} \underline{\sigma}. \quad (4.17.5)$$

In the reduced plane-stress subspace, an alternative effective stress, $\bar{\phi}$, is given as,

$$\bar{\phi}^2 = \underline{\sigma}^T \underline{\underline{P}} \underline{\sigma} = \frac{2}{3} \phi^2, \quad (4.17.6)$$

where

$$\underline{\underline{P}} = \frac{1}{3} \begin{bmatrix} 2 & -1 & 0 \\ -1 & 2 & 0 \\ 0 & 0 & 6 \end{bmatrix}, \quad (4.17.7)$$

in which $\underline{\underline{P}}$ and $\underline{\underline{P}}$ differ by a two in the shear term to reflect Voigt corrections.

A yield function, f , is introduced as,

$$f = \bar{\phi}^2 - R^2, \quad (4.17.8)$$

with,

$$R = \sqrt{\frac{2}{3}} \bar{\sigma}(\bar{\varepsilon}^p, \dot{\bar{\varepsilon}}^p, \theta), \quad (4.17.9)$$

where $\bar{\varepsilon}^p$ and $\dot{\bar{\varepsilon}}^p$ are the equivalent plastic strain (isotropic hardening variable) and its rate, respectively. Various hardening options may be used with this model. In general, the current flow stress is written as,

$$\bar{\sigma}(\bar{\varepsilon}^p, \dot{\bar{\varepsilon}}^p, \theta) = (\sigma_y + K(\bar{\varepsilon}^p)) \hat{\sigma}(\dot{\bar{\varepsilon}}^p) \left(1 - \left(\frac{\theta - \theta_{\text{ref}}}{\theta_{\text{melt}} - \theta_{\text{ref}}} \right)^M \right), \quad (4.17.10)$$

in which σ_y is the original yield stress, K is the isotropic hardening function that may take linear, power-law, or multilinear form, $\hat{\sigma}$ the rate multiplier whose specification will be defined later, and the right-most term is the Johnson-Cook temperature dependence term that may be optionally used to give temperature dependence of the flow-stress.

To complete the theoretical formulation, the flow rules are specified as,

$$d\underline{\varepsilon}^p = \lambda \underline{\underline{P}} \underline{\sigma}, \quad (4.17.11)$$

$$d\bar{\varepsilon}^p = \dot{\bar{\varepsilon}}^p \Delta t = \lambda \sqrt{\frac{2}{3}} \phi, \quad (4.17.12)$$

where λ is the consistency multiplier enforcing $f = 0$ during plastic deformation and $d\bar{\varepsilon}^p$ is the plastic strain increment in the constrained subspace. It is emphasized here that the yield surface described in (4.17.8) is *not* homogeneous of degree one like in other three-dimensional formulations presented in this manual. As such, the consistency multiplier and equivalent plastic strain increment are not equivalent. As an example of this, by consideration of the preceding relations, it is apparent that λ has units of one over stress.

The specification of the rate dependence, $\hat{\sigma}$, is important as it enables the consideration of two different model responses. These behaviors are controlled via the `USER RATE DEPENDENCE` command. If this input parameter is zero, then either an analytical or user-defined rate-dependence may be given. Importantly, in this case failure is *not* modeled. For the analytical case, the Johnson-Cook [3, 4] rate-multiplier is used such that,

$$\hat{\sigma}(\dot{\bar{\varepsilon}}^p) = \begin{cases} 1 + C \ln\left(\frac{\dot{\bar{\varepsilon}}^p}{\dot{\bar{\varepsilon}}_0}\right) & \dot{\bar{\varepsilon}}^p > \dot{\bar{\varepsilon}}_0 \\ 1 & \dot{\bar{\varepsilon}}^p \leq \dot{\bar{\varepsilon}}_0 \end{cases}, \quad (4.17.13)$$

with C being the rate dependence multiplier and $\dot{\bar{\varepsilon}}_0$ is a reference rate. Note, while other models allow user specification of the reference rate, the plane stress rate plasticity model uses the value set in the original work of Johnson-Cook [3] such that $\dot{\bar{\varepsilon}}_0 = 1\text{s}^{-1}$. Alternatively, a user function may be specified for the rate multiplier, $\hat{\sigma}$.

If `USER RATE DEPENDENCE` is set to one, both rate dependence and failure may be modeled. With respect to the rate dependence, (4.17.10) is rewritten,

$$\bar{\sigma}(\bar{\varepsilon}^p, \dot{\bar{\varepsilon}}^p, \theta) = \tilde{\sigma}(\bar{\varepsilon}^p, \dot{\bar{\varepsilon}}^p) \left(1 - \left(\frac{\theta - \theta_{\text{ref}}}{\theta_{\text{melt}} - \theta_{\text{ref}}}\right)^M\right), \quad (4.17.14)$$

in which both isotropic hardening and rate dependence are described via definition of $\tilde{\sigma}$. In this case, $\tilde{\sigma}$ *cannot* be specified through analytical expressions and must instead be given as a series of isotropic hardening curves; each at a different strain rate. For rates not explicitly given, interpolation is performed between relevant curves. Note, no extrapolation is performed with respect to the rates. If a rate is determined outside any specified curves, the hardening is calculated with respect to the bounding curve.

For failure, a failure parameter, α , is calculated as

$$\alpha = \int_0^t \frac{1}{\varepsilon_f(\eta, \dot{\bar{\varepsilon}}^p)} \dot{\bar{\varepsilon}}^p dt = \sum_{t_0}^t \frac{d\bar{\varepsilon}^p}{\varepsilon_f(\eta, \dot{\bar{\varepsilon}}^p)}, \quad (4.17.15)$$

in which the summation is used to imply the discrete calculation of the damage variable over a series of loadsteps and ε_f is the rate and triaxiality, η , dependent failure strain. The failure strain, ε_f , is specified in a fashion similar to $\tilde{\sigma}$. Specifically, a series of triaxiality dependent functions are defined each at a given strain rate. Interpolation is used at rates between those specified. Extrapolation outside the defined bounds is not done and the extremum curves are instead used.

The onset of damage is assumed to occur when $\alpha = 1$ and the current failure strain is taken to be the critical one such that $\varepsilon_f^{cr} = \varepsilon_f(t = t_{cr})$ with t_{cr} being the time at which $\alpha = 1$. Subsequent damage calculation is performed via,

$$\alpha(t > t_{cr}) = \int_0^{t_{cr}} \frac{1}{\varepsilon_f(\eta, \dot{\varepsilon}^p)} \dot{\varepsilon}^p dt + \int_{t_{cr}}^t \frac{1}{\varepsilon_f^{cr}} \dot{\varepsilon}^p dt. \quad (4.17.16)$$

After the critical failure parameter has been reached, an exponential decay relation is used to decrease the strength of the material. In this fashion, a decay relation of the form,

$$\bar{\sigma} = \bar{\sigma} e^{C_1(1-\alpha)}, \quad (4.17.17)$$

is used in which C_1 is the decay coefficient.

For more information about the plane stress rate plasticity model, consult [1, 2].

4.17.2. Implementation

The plane stress rate plasticity model encapsulates both a plasticity and failure model. These features are implemented in a decoupled, sequential sense. As such, the implementation of these features will also be presented and discussed in a sequential fashion.

For the plasticity portion, the approach of Simo and Taylor [1] (and Simo and Hughes [2]) in developing a single scalar equation to solve is adopted. As will be discussed, a slightly different approach will be used to solve this equation versus that used previously. To get to this single scalar equation, an elastic-predictor inelastic corrector scheme is adopted. In this scheme, an elastic predictor is calculated by assuming all deformation is elastic such that,

$$\underline{\sigma}^{tr} = \underline{\sigma}^n + \Delta t \underline{\underline{C}} d\underline{\varepsilon}^{n+1}, \quad (4.17.18)$$

in which “ n ” and “ $n + 1$ ” denote the material states at $t = t_n$ and $t = t_{n+1}$, respectively, with $\Delta t = t_{n+1} - t_n$. The plane stress stiffness matrix, $\underline{\underline{C}}$, is given as,

$$\underline{\underline{C}} = \frac{E}{1-\nu^2} \begin{bmatrix} 1 & \nu & 0 \\ \nu & 1 & 0 \\ 0 & 0 & \frac{1-\nu}{2} \end{bmatrix}, \quad (4.17.19)$$

with E and ν being the Youngs Modulus and Poisson’s ratio, respectively, and $d\underline{\varepsilon}^{n+1}$ is the plane stress total strain increment that is written,

$$d\underline{\varepsilon} = \Delta t \begin{bmatrix} d_{11} \\ d_{22} \\ 2d_{12} \end{bmatrix}, \quad (4.17.20)$$

where d_{ij} are the components of the rate of deformation tensor.

The stress at time $t = t_{n+1}$ may be given as,

$$\underline{\sigma}_{n+1} = \underline{\underline{C}} \left[\underline{\varepsilon}^{n+1} - \underline{\varepsilon}^p \right], \quad (4.17.21)$$

which noting the definition of the trial stress in (4.17.18) may be implicitly rewritten,

$$\underline{\sigma}^{n+1} = \underline{\sigma}^{tr} - \lambda \underline{\underline{C}} \underline{\underline{P}} \underline{\sigma}^{n+1}. \quad (4.17.22)$$

Rearranging yields,

$$\left[\underline{\underline{I}} + \lambda \underline{\underline{C}} \underline{\underline{P}} \right] \underline{\sigma}^{n+1} = \underline{\sigma}^{tr}, \quad (4.17.23)$$

with $\underline{\underline{I}}$ the identity matrix. Importantly, by noting that $\underline{\sigma}^{tr}$ is known it is clear that (4.17.23) is an equation for the updated stress vector in terms of only the unknown scalar consistency parameter, λ . To further simplify the problem, it can be shown that $\underline{\underline{C}}$ and $\underline{\underline{P}}$ share the same principal subspaces such that (see Simo and Hughes [2] for details),

$$\underline{\underline{P}} = \underline{\underline{Q}} \underline{\underline{\Lambda}}^P \underline{\underline{Q}}^T, \quad ; \quad \underline{\underline{C}} = \underline{\underline{Q}} \underline{\underline{\Lambda}}^C \underline{\underline{Q}}^T, \quad (4.17.24)$$

where $\underline{\underline{Q}}^T$ is an orthogonal matrix such that $\underline{\underline{Q}}^T = \underline{\underline{Q}}^{-1}$ and the matrices $\underline{\underline{Q}}$, $\underline{\underline{\Lambda}}^P$ and $\underline{\underline{\Lambda}}^C$ are given as,

$$\underline{\underline{\Lambda}}^P = \begin{bmatrix} 1/3 & 0 & 0 \\ 0 & 1 & 0 \\ 0 & 0 & 2 \end{bmatrix}, \quad ; \quad \underline{\underline{\Lambda}}^C = \begin{bmatrix} E/(1-\nu) & 0 & 0 \\ 0 & 2\mu & 0 \\ 0 & 0 & 2\mu \end{bmatrix} \quad (4.17.25)$$

$$\underline{\underline{Q}} = \frac{1}{\sqrt{2}} \begin{bmatrix} 1 & -1 & 0 \\ 1 & 1 & 0 \\ 0 & 0 & \sqrt{2} \end{bmatrix}. \quad (4.17.26)$$

By introducing a transformed stress vector in the principal space of $\underline{\underline{C}}$ and $\underline{\underline{P}}$, $\underline{\eta}$, such that,

$$\underline{\eta} = \begin{bmatrix} \eta_{11} \\ \eta_{12} \\ \eta_{12} \end{bmatrix} = \underline{\underline{Q}}^T \underline{\sigma}, \quad (4.17.27)$$

the effective stress may be rewritten,

$$\bar{\phi}^2 = \underline{\eta}^T \underline{\underline{\Lambda}}^P \underline{\eta}. \quad (4.17.28)$$

By rewriting (4.17.23) in the transformed space the premultiplying matrix on the left-hand side can be analytically inverted such that,

$$\underline{\eta}^{n+1} = \begin{bmatrix} \frac{\eta_{11}^{tr}}{1+\lambda \frac{E}{3(1-\nu)}} \\ \frac{\eta_{22}^{tr}}{1+\lambda 2\mu} \\ \frac{\eta_{12}^{tr}}{1+\lambda 2\mu} \end{bmatrix}, \quad (4.17.29)$$

and the effective stress may be written as a scalar function of λ ,

$$\bar{\phi}^2(\lambda) = \frac{\frac{1}{3}(\eta_{11}^{tr})^2}{\left[1+\lambda \frac{E}{2(1-\nu)}\right]^2} \frac{(\eta_{22}^{tr})^2 + 2(\eta_{12}^{tr})^2}{\left[1+\lambda 2\mu\right]^2}. \quad (4.17.30)$$

Noting that the equivalent plastic strain and rate may be written,

$$\bar{\varepsilon}^{p(n+1)} = \bar{\varepsilon}^{p(n)} + \lambda \sqrt{\frac{2}{3}}\phi, \quad ; \quad \dot{\bar{\varepsilon}}^p = \frac{\lambda}{\Delta t} \sqrt{\frac{2}{3}}\phi, \quad (4.17.31)$$

means determining the updated states reduces to solving the scalar consistency equation,

$$f(\lambda) = \bar{\phi}^2(\lambda) - \bar{\sigma}(\lambda), \quad (4.17.32)$$

for λ . This is done iteratively by using a line-search augmented Newton-Raphson method like that described in [5].

Failure is handled separately from plasticity and in a straight-forward fashion. Specifically, if $\alpha^n > 1$ (above the critical value) then a decay coefficient, β^{n+1} , is calculated via

$$\beta^{n+1} = e^{C_1(1-\alpha^n)}, \quad (4.17.33)$$

and the yield stress is scaled accordingly such that,

$$\bar{\sigma} = \beta \bar{\sigma}. \quad (4.17.34)$$

Such corrections are done *prior* to performing the plasticity calculation. Updating the damage variable, α^{n+1} , is done via relations (4.17.15) (or (4.17.16)) *after* convergence is achieved for the inelastic correction.

4.17.3. User Guide

```
BEGIN PARAMETERS FOR MODEL PLANE_STRESS_RATE_PLASTICITY
#
# Elastic constants
#
YOUNGS MODULUS = <real> E
POISSONS RATIO = <real> v
SHEAR MODULUS = <real> G
BULK MODULUS = <real> K
LAMBDA = <real> λ
TWO MU = <real> 2μ
#
# Optional parameters related to inelastic correction criteria
#
TOLERANCE = <real> tolerance (1.0e-10)
MAX_INEL_CORR_ITER = <int> maximum_correction_iterations (100)
MAX_LS_CORR_ITER = <int> maximum_line_search_cutbacks (20)
#
USER RATE DEPENDENCE = 0|1(0)
YIELD STRESS = <real> σy
#
FORMULATION = <int> formulation (1)
#
# Input Options for USER RATE DEPENDENCE = 0
#
# linear hardening
HARDENING MODULUS = <real> hardening_modulus
# power law hardening
HARDENING CONSTANT = <real> hardening_constant
HARDENING EXPONENT = <real> hardening_exponent (0.5)
# multilinear hardening
HARDENING FUNCTION = <string> K(̄εp)
#
# Rate dependence
#
# Johnson-Cook rate dependence
RATE CONSTANT = <real> C
# multilinear rate dependence
RATE FUNCTION = <string> rate_function_name
#
# Input Options for USER RATE DEPENDENCE = 1
#
# rate-dependent yield
YIELD STRAIN RATES = <real_list> yield_strain_rates
YIELD CURVES = <string_list> yield_function_names
# rate-dependent damage
```

```

FRACTURE STRAIN RATES = <real_list> fracture_strain_rates
FRACTURE CURVES      = <string_list> fracture_function_names
DECAY COEFFICIENT     = <real> C1 (1.0)
#
# Thermal softening commands (Johnson-Cook)
INITIAL TEMPERATURE   = <real> θ(t=0)
MELT TEMPERATURE       = <real> θmelt
REFERENCE TEMPERATURE = <real> θref
THERMAL EXPONENT      = <real> M
#
END [PARAMETERS FOR MODEL PLANE_STRESS_RATE_PLASTICITY]

```

Output variables available for this model are listed in Table 4-25.

Table 4-25. State Variables for PLANE STRESS RATE PLASTICITY Model

Name	Description
EQPS	equivalent plastic strain, $\bar{\epsilon}^p$
EQDOT	equivalent plastic strain rate, $\dot{\bar{\epsilon}}^p$
SEFF	effective stress, ϕ

REFERENCES

- [1] J. C. Simo and R. L. Taylor. A return mapping algorithm for plane stress elastoplasticity. *International Journal for Numerical Methods in Engineering*, 22:649–670, 1986.
- [2] J.C. Simo and T.J.R. Hughes. *Computational Inelasticity*. Springer-Verlag, New York, NY, 1998.
- [3] G.R. Johnson and W.H. Cook. A constitutive model and data for metals subjected to large strains, high strain rates and high temperatures. In *Proc. 7th. Int. Symp. on Ballistics*, pages 541–547, The Hague, The Netherlands, 1983.
- [4] G.R. Johnson and W.H. Cook. Fracture characteristics of three metals subjected to various strains, strain rates, temperatures and pressures. *Engineering Fracture Mechanics*, 21(1): 31–48, 1985.
- [5] W. M. Scherzinger. A return mapping algorithm for isotropic and anisotropic plasticity models using a line search method. *Computer Methods in Applied Mechanics and Engineering*, 317:526–553, 2017.

4.18. MODULAR PLANE STRESS PLASTICITY MODEL

4.18.1. Theory

Like the plane stress plasticity model of Section 4.17, the modular plane stress plasticity (MPSP) model is a plane stress implementation of a J_2 plasticity formulation largely following and motivated by the works of Simo and Taylor [1] and Simo and Hughes [2]. However, the modular plane stress plasticity model differs from those prior works and the aforementioned plane stress plasticity formulation via its specification of the hardening. Specifically, in the current case kinematic hardening is neglected and expanded isotropic hardening and rate-dependence are considered by leveraging various modular hardening capabilities used with a variety of solid plasticity models (*i.e.* the J_2 plasticity model in Section 4.13).

Like other plasticity models, the components of the objective stress rate, $\overset{\circ}{\sigma}_{ij}$, are written as,

$$\overset{\circ}{\sigma}_{ij} = \mathbb{C}_{ijkl} D_{kl}^e \quad (4.18.1)$$

where \mathbb{C}_{ijkl} are the components of the fourth-order, isotropic elasticity tensor and D_{ij}^e are the components of the elastic part of the total rate of deformation tensor. An additive split of the total rate of deformation tensor into elastic and plastic contributions is assumed such that,

$$D_{ij} = D_{ij}^e + D_{ij}^p. \quad (4.18.2)$$

With a J_2 plasticity model, the effective stress measure, ϕ , may be written,

$$\phi^2 = \frac{3}{2} s_{ij} s_{ij} \quad ; \quad s_{ij} = \sigma_{ij} - \frac{1}{3} \sigma_{kk} \delta_{ij}, \quad (4.18.3)$$

with s_{ij} begin the deviatoric stress tensor. After enforcing the plane-stress conditions ($\sigma_{13} = \sigma_{23} = \sigma_{33} = 0$), there are only three non-zero stress components. As such, the problem may be simplified by introducing the projection matrix, $\underline{\underline{P}}$, of Simo and Taylor [1],

$$\underline{\underline{P}} = \frac{1}{3} \begin{bmatrix} 2 & -1 & 0 \\ -1 & 2 & 0 \\ 0 & 0 & 3 \end{bmatrix}, \quad (4.18.4)$$

so that,

$$\underline{\underline{s}} = \underline{\underline{P}} \underline{\underline{\sigma}} \quad (4.18.5)$$

where,

$$\underline{\underline{\sigma}} = \begin{bmatrix} \sigma_{11} \\ \sigma_{22} \\ \sigma_{12} \end{bmatrix} \quad ; \quad \underline{\underline{s}} = \begin{bmatrix} s_{11} \\ s_{22} \\ s_{12} \end{bmatrix}. \quad (4.18.6)$$

Note, in the previous and following relations an explicit matrix notation is used to denote variables in the projected stress space to reinforce that these terms are not tensors. To this end, a single underline (\underline{x}) is used for a vector while a twice underlined variable ($\underline{\underline{X}}$) is a matrix.

The projected effective stress measure, $\bar{\phi}$, may then be taken to be,

$$\bar{\phi}^2 = \underline{\underline{P}} \underline{\underline{\sigma}}, \quad (4.18.7)$$

in which a superscript “ T ” denotes transpose and,

$$\underline{\underline{P}} = \frac{1}{3} \begin{bmatrix} 2 & -1 & 0 \\ -1 & 2 & 0 \\ 0 & 0 & 6 \end{bmatrix}. \quad (4.18.8)$$

Written in this fashion, there is a small difference between the projected effective stress ($\bar{\phi}$) and the traditional 3D form (ϕ) associated with a constant premultiplier. This is due to subtle differences in notation used by the plane-stress references [1, 2] and is accounted for in the definition of the yield surface radius, R , ensuring equivalence in forms.

A corresponding yield function, f , is introduced such that,

$$f = \bar{\phi}(\underline{\underline{\sigma}}) - R^2 (\bar{\varepsilon}^p, \dot{\bar{\varepsilon}}^p), \quad (4.18.9)$$

where R is the yield surface radius in the deviatoric π -plane that isotropically hardens via dependencies on the equivalent plastic strain (isotropic hardening variable) and its rate that are denoted $\bar{\varepsilon}^p$ and $\dot{\bar{\varepsilon}}^p$, respectively. The radius may be related to the current yield stress, $\bar{\sigma}$, via,

$$R = \sqrt{\frac{2}{3}} \bar{\sigma} (\bar{\varepsilon}^p, \dot{\bar{\varepsilon}}^p). \quad (4.18.10)$$

The distinguishing feature of the modular plane stress plasticity model is a flexible defintion of the isotropic hardening in which the current yield stress is generically written,

$$\bar{\sigma} = \sigma_y \hat{\sigma}_y (\dot{\bar{\varepsilon}}^p) + K (\bar{\varepsilon}^p) \hat{\sigma}_h (\dot{\bar{\varepsilon}}^p), \quad (4.18.11)$$

with σ_y , K , and $\hat{\sigma}_{y,h}$ being the constant initial yield stress, isotropic hardening, and separate rate multipliers for yield and hardening, respectively. A variety of different forms may be assumed as described below.

To complete the theoretical formulation, the flow rules are specified as,

$$d\underline{\varepsilon}^p = \lambda \underline{\underline{P}} \underline{\underline{\sigma}}, \quad (4.18.12)$$

$$d\bar{\varepsilon}^p = \lambda \sqrt{\frac{2}{3}} \bar{\phi}, \quad (4.18.13)$$

where λ is the consistency multiplier enforcing $f = 0$ during plastic deformation and $d\bar{\varepsilon}^p$ is the plastic strain increment in the constrained subspace. It is emphasized here that the current yield function described in is *not* homogeneous of degree one like in other three-dimensional formulations presented in this manual. As such, the consistency multiplier and equivalent plastic strain increment are not equivalent. As an example of this, by consideration of the preceding relations, it is apparent that λ has units of one over stress.

For more information about the modular plane stress plasticity model, consult [1, 2].

4.18.1.1. Plastic Hardening

Plastic hardening refers to increases in the flow stress, $\bar{\sigma}$, with plastic deformation. As such, hardening is described via the functional relationship between the flow stress and isotropic hardening variable (effective plastic strain), $\bar{\sigma}(\bar{\varepsilon}^p)$. Over the course of nearly a century of work in metal plasticity, a variety of relationships have been proposed to describe the interactions associated with different physical interpretations, deformation mechanisms, and materials. To enable the utilization of the same plasticity models for different material systems, a modular implementation of plastic hardening has been adopted such that the analyst may select different hardening models from the input deck thereby avoiding any code changes or user subroutines. In this section, additional details are given to the different models to enable the user to select the appropriate choice of model. Note, the models being discussed here are only for *isotropic* hardening in which the yield surface expands. *Kinematic* hardening in which the yield surface translates in stress-space with deformation and *distortional* hardening where the shape of the yield surface changes shape with deformation are not treated. For a larger discussion of the phenomenology and history of different hardening types, the reader is referred to [3, 4, 5].

Given the ubiquitous nature of these hardening laws in computational plasticity, some (if not most) of this material may be found elsewhere in this manual. Nonetheless, the discussion is repeated here for the convenience of the reader.

Linear

Linear hardening is conceptually the simplest model available in LAMÉ. As the name implies, a linear relationship is assumed between the hardening variable, $\bar{\varepsilon}^p$, and flow stress. The constant giving the degree of increase of yield stress with plastic flow is termed the hardening modulus and is given as, H' , while the expression for the flow stress may be written,

$$\bar{\sigma} = \sigma_y + H' \bar{\varepsilon}^p. \quad (4.18.14)$$

The simplicity of the model is its main feature as the constant slope,

$$\frac{d\bar{\sigma}}{d\bar{\varepsilon}^p} = H', \quad (4.18.15)$$

makes the model attractive for analytical models and cheap for computational implementations (e.g. radial return algorithms require only a single correction step). Unfortunately, the simplicity of the representation also means that it has limited predictive capabilities and can lead to overly stiff responses.

Power Law

Another common expression for isotropic hardening is the power-law hardening model. Due to its prevalence, a dedicated ELASTIC-PLASTIC POWER LAW HARDENING model may be found in LAMÉ (see Section 4.8.1). This expression is given as,

$$\bar{\sigma} = \sigma_y + A \langle \bar{\varepsilon}^p - \varepsilon_L \rangle^n, \quad (4.18.16)$$

in which $\langle \cdot \rangle$ are Macaulay brackets, ε_L is the Lüders strain, A is a fitting constant, and n is an exponent typically taken such that $0 < n \leq 1$. The Lüders strain is a positive, constant strain value (default to zero) giving an initial plastic deformation domain in which the response is perfectly plastic (see Fig. 4-20). The derivative is then simply,

$$\frac{d\bar{\sigma}}{d\bar{\varepsilon}^p} = nA \langle \bar{\varepsilon}^p - \varepsilon_L \rangle^{(n-1)}. \quad (4.18.17)$$

Note, one difficulty in such an implementation is that when the effective equivalent plastic strain is zero, numerical difficulties may arise in evaluating the derivative necessitating special treatment of the case.

Voce

The Voce hardening model (sometimes referred to as a saturation model) uses a decaying exponential in terms of the equivalent plastic strain such that the hardening eventually saturates to a specified value (thus the name). Such a relationship has been observed in some structural metals giving rise to the popularity of the model. The hardening response is given as,

$$\bar{\sigma} = \sigma_y + A (1 - \exp(-n\bar{\varepsilon}^p)), \quad (4.18.18)$$

in which A is a fitting constant and n is a fitting exponent describing how quickly the hardening saturates. Importantly, the derivative is written as,

$$\frac{d\bar{\sigma}}{d\bar{\varepsilon}^p} = nA \exp(-n\bar{\varepsilon}^p), \quad (4.18.19)$$

and is well defined everywhere giving the selected form an advantage over the aforementioned power law model.

Johnson-Cook

The Johnson-Cook [6, 7] hardening type is a *rate-dependent* formulation utilizing the assumption that rate-independent and rate-dependent contributions may be multiplicatively separated. Specifically, use of this option requires specifying a user-defined hardening function to capture rate-independent contributions and Johnson-Cook type rate dependent coefficients. The flow stress may be written in this fashion as,

$$\bar{\sigma} = \tilde{\sigma}_y(\bar{\varepsilon}^p) \left[1 + C \left\langle \ln \left(\frac{\dot{\varepsilon}^p}{\dot{\varepsilon}_0} \right) \right\rangle \right], \quad (4.18.20)$$

in which $\tilde{\sigma}_y(\bar{\varepsilon}^p)$ is the user-specified rate-independent hardening function, C is a fitting constant and $\dot{\varepsilon}_0$ is a reference strain rate. The Macaulay brackets ensure the material behaves in a rate independent fashion when $\dot{\varepsilon}^p < \dot{\varepsilon}_0$.

Power Law Breakdown

Like the Johnson-Cook formulation, the power-law breakdown model is also rate-dependent. Again, a multiplicative decomposition between rate-independent and dependent hardening contributions. In this case, however, the functional form is derived from the analysis of Frost and Ashby [8] in which power-law relationships like those of the Johnson-Cook and cease to appropriately capture the physical response. The form used here is similar to the expression used by Brown and Bammann [9] and is written as,

$$\bar{\sigma} = \tilde{\sigma}_y(\bar{\varepsilon}^p) \left[1 + \operatorname{asinh} \left(\left(\frac{\dot{\varepsilon}^p}{g} \right)^{(1/m)} \right) \right], \quad (4.18.21)$$

with $\tilde{\sigma}_y(\bar{\varepsilon}^p)$ being the user supplied rate independent expression, g is a model parameter related to the activation energy in going from climb to glide-controlled deformation, and m dictates the strength of the dependence.

Flow Stress

Unlike the previously described models, the flow-stress hardening method is less a specific physical representation and more a generalization of the hardening behaviors to allow greater flexibility in separately describing isotropic hardening and rate-dependence. As such, the generic flow-stress definition of

$$\bar{\sigma}(\bar{\varepsilon}^p, \dot{\bar{\varepsilon}}^p) = \tilde{\sigma}_y(\bar{\varepsilon}^p) \hat{\sigma}(\dot{\bar{\varepsilon}}^p), \quad (4.18.22)$$

is used in which $\hat{\sigma}$ is the rate multiplier that by default is unity (such that the response is rate independent) and $\tilde{\sigma}_y$ is the isotropic hardening component that may also be specified as,

$$\tilde{\sigma}_y = \sigma_y + K(\bar{\varepsilon}^p), \quad (4.18.23)$$

with σ_y being the constant yield stress and K is the isotropic hardening that is initially zero and a function of the equivalent plastic strain. A multiplicative decomposition such as this mirrors the general structure used by Johnson and Cook [6, 7] although greater flexibility is allowed in terms of the specific form of the rate multiplier.

Given the aforementioned default for rate-dependence, the corresponding multiplier need not be specified. A representation for the isotropic hardening, however, *must* be specified and can be defined via linear, power-law, Voce, or user-defined representations. For the user-defined case, an *isotropic* hardening function is required and it must be highlighted that the interpretation differs from the general user-defined hardening model. *In this case, as the specified function represents the isotropic hardening, it should start from zero – not yield.*

Although the flow-stress hardening model defaults to rate independent, a multiplier may be defined. For rate-dependence, either the previously discussed Johnson-Cook or power-law breakdown models or a user-defined multiplier may be used. For the user-defined capability, the multiplier should be input as a strictly positive function of the equivalent plastic strain rate with a value of one in the rate-independent limit.

Decoupled Flow Stress

Like the flow-stress hardening method, the decoupled flow-stress hardening implementation is a generalization of the hardening behaviors to allow greater flexibility. In differentiating the two, for the decoupled model the rate dependence may be separately specified for the yield and hardening portions of the flow stress. As such, the generic flow-stress definition of

$$\tilde{\sigma}(\bar{\varepsilon}^p, \dot{\bar{\varepsilon}}^p) = \sigma_y \hat{\sigma}_y(\dot{\bar{\varepsilon}}^p) + K(\bar{\varepsilon}^p) \hat{\sigma}_h(\dot{\bar{\varepsilon}}^p), \quad (4.18.24)$$

is used in which $\hat{\sigma}$ are rate multipliers that by default are unity (such that the response is rate independent) with subscripts “y” and “h” denoting functions associated with yield and hardening. The isotropic hardening is described by $K(\bar{\varepsilon}^p)$ and σ_y is the constant initial yield stress. It may also be seen that if the yield and hardening dependencies are the same ($\hat{\sigma}_y = \hat{\sigma}_h$) the decoupled flow stress model reduces to that of the flow stress case and mirrors the general structure of the Johnson-Cook model [6, 7].

Given the aforementioned default to rate dependence, the corresponding multiplier need not be specified. A representation for the isotropic hardening, however, *must* be specified and can be defined via linear, power-law, Voce, or user-defined representations. For the user-defined case, an *isotropic* hardening function should be used and it must be highlighted that the interpretation differs from the general user-defined hardening model. *In this case, as the specified function represents the isotropic hardening, it should start from zero – not yield.*

Although the decoupled flow-stress hardening model defaults to rate independent, a multiplier may be defined. For rate-dependence, either the previously discussed Johnson-Cook or power-law

breakdown models or a user-defined multiplier may be used. For the user-defined capability, the multiplier should be input as a strictly positive function of the equivalent plastic strain rate with a value of one in the rate-independent limit.

4.18.2. Implementation

The integration approach for the modular plane stress plasticity model follows largely from the elastic-predictor/inelastic-corrector radial return approaches of Simo and Taylor [1] (and Simo and Hughes [2]) with the exception of an extra line-search step and slightly modified treatment for the hardening. To this end, the total strain increment $\underline{d}\varepsilon = \dot{\varepsilon}\Delta t$ is given as,

$$\underline{d}\varepsilon = \Delta t \begin{bmatrix} d_{11} \\ d_{22} \\ 2d_{12} \end{bmatrix} \quad (4.18.25)$$

where $\Delta t = t_{n+1} - t_n$ in which $t = t_n$ and $t = t_{n+1}$ are a completely known state and the state to be determined. The trial stress may then be written,

$$\underline{\sigma}^{tr} = \underline{\underline{C}} \left[\underline{\varepsilon}_n + \underline{d}\varepsilon - \underline{\varepsilon}_n^p \right] \quad (4.18.26)$$

with

$$\underline{\underline{C}} = \frac{E}{1-\nu^2} \begin{bmatrix} 1 & \nu & 0 \\ \nu & 1 & 0 \\ 0 & 0 & \frac{1-\nu}{2} \end{bmatrix} \quad (4.18.27)$$

and E and ν being the elastic modulus and Poisson's ratio, respectively. The trial yield function is then simply,

$$f^{tr} = \bar{\phi}^2(\underline{\sigma}^{tr}) - R^2(\bar{\varepsilon}_n^p, 0). \quad (4.18.28)$$

For the case of plastic loading, if a fully implicit backward Euler scheme is adopted the plastic strain flow rules are,

$$\underline{\varepsilon}_{n+1}^p = \underline{\varepsilon}_n^p + \lambda \underline{\underline{P}} \underline{\sigma}_{n+1}, \quad (4.18.29)$$

$$\bar{\varepsilon}_{n+1}^p = \bar{\varepsilon}_n^p + \lambda \sqrt{\frac{2}{3}} \bar{\phi}_{n+1}. \quad (4.18.30)$$

By introducing,

$$\underline{\sigma}_{n+1} = \underline{\underline{C}} (\underline{\varepsilon}_{n+1} - \underline{\varepsilon}_{n+1}^p), \quad (4.18.31)$$

and using relations (4.18.26) and (4.18.29), the updated stress may be shown to be,

$$\left[\underline{\underline{I}} + \lambda \underline{\underline{\bar{C}}} \underline{\underline{P}} \right] \underline{\underline{\sigma}}_{n+1} = \underline{\underline{\sigma}}^{tr}, \quad (4.18.32)$$

with $\underline{\underline{I}}$ being the identity matrix.

As noted by Simo and Taylor [1], $\underline{\underline{\bar{C}}}$ and $\underline{\underline{P}}$ share characteristic subspaces $\underline{\underline{Q}}$ enabling a principle decomposition such that,

$$\underline{\underline{P}} = \underline{\underline{Q}} \underline{\underline{\Lambda}}^P \underline{\underline{Q}}^T, \quad ; \quad \underline{\underline{\bar{C}}} = \underline{\underline{Q}} \underline{\underline{\Lambda}}^C \underline{\underline{Q}}^T, \quad (4.18.33)$$

in which,

$$\underline{\underline{Q}}^T = \frac{1}{\sqrt{2}} \begin{bmatrix} 1 & 1 & 0 \\ -1 & 1 & 0 \\ 0 & 0 & \sqrt{2} \end{bmatrix} ; \quad \underline{\underline{\Lambda}}^P = \begin{bmatrix} \frac{1}{3} & 0 & 0 \\ 0 & 1 & 0 \\ 0 & 0 & 2 \end{bmatrix} ; \quad \underline{\underline{\Lambda}}^C = \begin{bmatrix} \frac{E}{1-\nu} & 0 & 0 \\ 0 & 2\mu & 0 \\ 0 & 0 & \mu \end{bmatrix}. \quad (4.18.34)$$

In this space, a transformed stress, $\underline{\underline{\eta}}$, may be given as,

$$\underline{\underline{\eta}} = \underline{\underline{Q}}^T \underline{\underline{\sigma}}, \quad (4.18.35)$$

which, when substituted into (4.18.32) yields,

$$\left[\underline{\underline{I}} + \lambda \underline{\underline{\Lambda}}^C \underline{\underline{\Lambda}}^P \right] \underline{\underline{\eta}}_{n+1} = \underline{\underline{\eta}}^{tr}. \quad (4.18.36)$$

Importantly, in (4.18.36) the matrix on the left-hand side is diagonal and easily inverted. The updated transformed stress is thus a function of the consistency multiplier alone. Substituting the corresponding evaluation of the stress into the definition of the effective stress produces a scalar function of λ such that,

$$\bar{\phi}^2 = \frac{\frac{1}{3} (\eta_{11}^{tr})^2}{\left[1 + \lambda \frac{E}{3(1-\nu)} \right]^2} + \frac{(\eta_{22}^{tr})^2 + 2(\eta_{12}^{tr})^2}{\left[1 + \lambda 2\mu \right]^2}. \quad (4.18.37)$$

With the effective stress written as a function of λ alone and the flow rules in (4.18.29) and (4.18.30) only an appropriate approximation for the effective plastic strain rate is needed to arrive at the single scalar consistency equation to be solve. To that end, using (4.18.30), the effective plastic strain rate is taken to be,

$$\dot{\underline{\underline{\varepsilon}}}^p(\lambda) \approx \frac{\bar{\underline{\underline{\varepsilon}}}^p_{n+1} - \bar{\underline{\underline{\varepsilon}}}^p_n}{\Delta t} = \frac{\lambda}{\Delta t} \sqrt{\frac{2}{3}} \bar{\phi}_{n+1}(\lambda). \quad (4.18.38)$$

The updated yield function is now written as,

$$f_{n+1}(\lambda) = \bar{\phi}_{n+1}^2(\lambda) - R^2(\lambda) = 0. \quad (4.18.39)$$

This non-linear equation may be readily solved via a line-search augmented Newton-Raphson approach (see [10]) by recasting the consistency condition as a residual,

$$r^f(\lambda) = f(\lambda) = 0. \quad (4.18.40)$$

Which, when linearized as,

$$r_{k+1}^f = r_k^f + \frac{df}{d\lambda} \Delta\lambda, \quad (4.18.41)$$

with “ k ” being the non-linear correction iteration and $\Delta\lambda$ is the consistency increment yields the solution (with $r_{k+1}^f = 0$),

$$\Delta\lambda = \frac{-r_k^f}{\frac{df}{d\lambda}}. \quad (4.18.42)$$

The derivative is simply given as,

$$\frac{df}{d\lambda} = \frac{d}{d\lambda}(\bar{\phi}^2) - \frac{d}{d\lambda}(R^2), \quad (4.18.43)$$

where

$$\frac{d}{d\lambda}(\bar{\phi}^2) = -2 \left[\frac{E}{3(1-\nu)} \frac{\frac{1}{3}(\eta_{11}^{tr})^2}{\left[1 + \lambda \frac{E}{3(1-\nu)}\right]^3} + 2\mu \frac{(\eta_{22}^{tr})^2 + 2(\eta_{12}^{tr})^2}{\left[1 + \lambda 2\mu\right]^3} \right], \quad (4.18.44)$$

and

$$\frac{d}{d\lambda}(R^2) = \frac{4}{3} (\sigma_y \hat{\sigma}_y + K \hat{\sigma}_h) \left[\hat{\sigma}_h \frac{dK}{d\bar{\varepsilon}^p} \frac{d\bar{\varepsilon}^p}{d\lambda} + \frac{d\dot{\bar{\varepsilon}}^p}{d\lambda} \left(\sigma_y \frac{d\hat{\sigma}_y}{d\dot{\bar{\varepsilon}}^p} + K \frac{d\hat{\sigma}_h}{d\dot{\bar{\varepsilon}}^p} \right) \right], \quad (4.18.45)$$

in which

$$\frac{d\bar{\varepsilon}^p}{d\lambda} = \sqrt{\frac{2}{3}} \left(\phi + \lambda \frac{d\phi}{d\lambda} \right), \quad (4.18.46)$$

$$\frac{d\dot{\bar{\varepsilon}}^p}{d\lambda} = \frac{1}{\Delta t} \sqrt{\frac{2}{3}} \left(\phi + \lambda \frac{d\phi}{d\lambda} \right). \quad (4.18.47)$$

As only a single equation needs to be solved, a merit function, ψ , is simply given as,

$$\psi(\lambda) = \frac{1}{2} \left(\frac{r^f}{\sigma_y^2} \right)^2 \quad (4.18.48)$$

which may be solved via the quadratic approximation line-search scheme of [10].

4.18.3. Verification

Given the modular nature of the modular plane stress plasticity (MPSP) model, a variety of tests are constructed to ascertain performance under different loadings and combinations of hardening models. The model parameters needed for such tests are given below in Table 4-26. While a large number of combinations of the hardening and/or rate multipliers have been tested under different conditions (>100 tests), here, for brevity only a sampling of these tests are presented.

E	70 GPa	ν	0.33 (-)
σ_y	200 MPa	H'	500 MPa
A_{PL}	400 MPa	n_{PL}	0.25 (-)
A_{Voce}	200 MPa	n_{Voce}	20 (-)
C	0.1 (-)	$\dot{\varepsilon}_0$	$1 \times 10^{-4} \text{ s}^{-1}$
g	0.21 s^{-1}	m	16.4 (-)

Table 4-26. Model parameters for verification tests used with the modular plane stress plasticity (MPSP) model.

4.18.3.1. Uniaxial Stress

For the uniaxial stress tests, the constant equivalent plastic strain boundary value problem of Appendix A.5 is used. Although that discussion is for 3D formulations, the plane stress assumptions agree with the assumed boundary conditions (*e.g.* traction free out-of-plane stress) enabling the same results to be used here. Results for such tests and their corresponding analytical solutions are shown in Figure 4-80 for constant strain rates of $\dot{\varepsilon}^p = 1 \times 10^{-3} \text{ s}^{-1}$ (4-80a) and $\dot{\varepsilon}^p = 1 \text{ s}^{-1}$ (4-80b).

4.18.3.2. Balanced Biaxial

To assess performance of the model with multiple stress components, a constant equivalent plastic strain rate balanced biaxial test is considered. For this test, a stress-state (in the projected plane stress space) of

$$\underline{\sigma}(t) = \begin{bmatrix} \sigma(t) \\ -\sigma(t) \\ 0 \end{bmatrix} \quad (4.18.49)$$

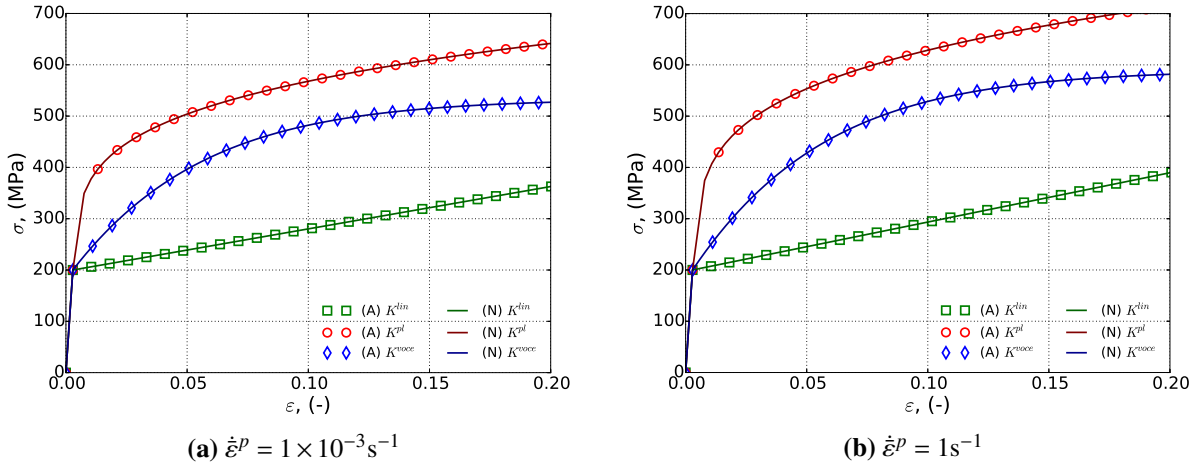


Figure 4-80. Analytical and numerical constant equivalent plastic strain rate verification tests of the modular plane stress plasticity models with a uniaxial stress state and strain rates of (a) $\dot{\varepsilon}^p = 1 \times 10^{-3} \text{ s}^{-1}$ and (b) $\dot{\varepsilon}^p = 1 \text{ s}^{-1}$ with linear, power-law, and voce isotropic hardening and power-law breakdown rate-dependence. Solid lines are analytical and open symbols are from finite element calculations.

is assumed. Note, such a loading is equivalent to a pure shear loading in a rotated frame of reference. As such, many of the pure shear results of Appendix A.5 may be leveraged. To that end, if elasticity effects are included the total strain, $\varepsilon(t)$, may be found to be

$$\varepsilon(t) = \frac{1}{\sqrt{3}} \frac{\sigma_y + \hat{\sigma}_h K(\dot{\varepsilon}^p(t - t^{\text{el}}))}{2\mu} + \frac{\sqrt{3}}{2} \dot{\varepsilon}^p(t - t^{\text{el}}), \quad (4.18.50)$$

with t^{el} being the time at yield (elastic limit). To produce the desired stress state, the corresponding displacements are $u_1(t) = \exp(\varepsilon(t)) - 1$ and $u_2(t) = \exp(-\varepsilon(t)) - 1$. Results of such tests and their corresponding analytical solutions are presented below in Figure 4-82 with constant strain rates of $\dot{\varepsilon}^p = 1 \times 10^{-3} \text{ s}^{-1}$ (4-81a) and $\dot{\varepsilon}^p = 1 \text{ s}^{-1}$ (4-81b).

4.18.3.3. Biaxial Shear

As a final set of tests, the pure shear response is probed. To accomplish this loading, the previous balanced biaxial test is reconsidered with the geometry rotated 45° about the out of plane direction producing a stress state of,

$$\underline{\sigma}(t) = \begin{bmatrix} 0 \\ 0 \\ \sigma_{xy}(t) \end{bmatrix}. \quad (4.18.51)$$

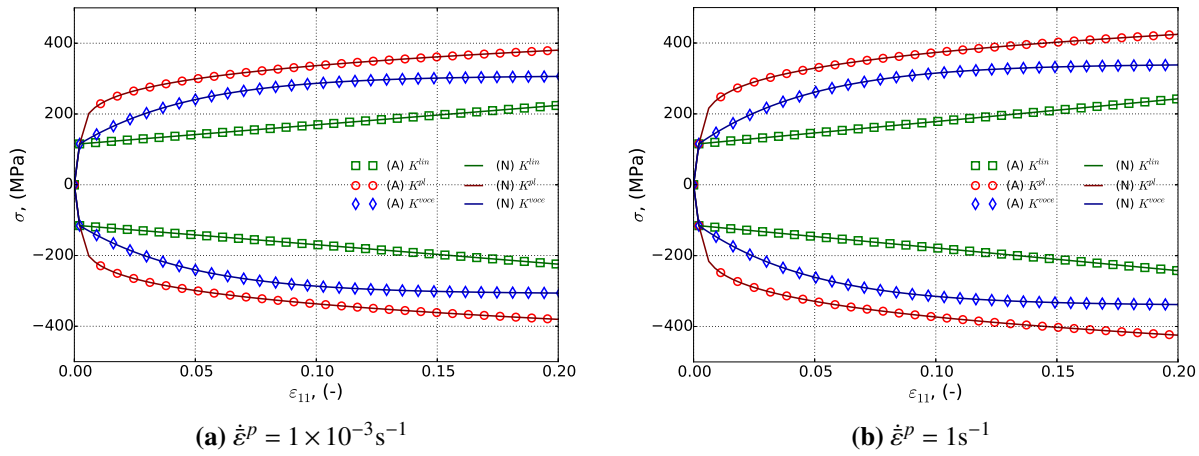


Figure 4-81. Analytical and numerical constant equivalent plastic strain rate verification tests of the modular plane stress plasticity models with a balanced biaxial stress state and strain rates of (a) $\dot{\varepsilon}^p = 1 \times 10^{-3} \text{ s}^{-1}$ and (b) $\dot{\varepsilon}^p = 1 \text{ s}^{-1}$ with linear, power-law, and voce isotropic hardening and power-law breakdown rate-dependence. Solid lines are analytical and open symbols are from finite element calculations. Positive valued stresses correspond to σ_{11} while negative values are σ_{22} .

The previous results from Section 4.18.3.2 regarding the solution for the balanced biaxial problem may again be used with $\sigma_{xy}(t) = \sigma(t)$. Result for this case, both analytical and finite element, are given in Figure 4-82 with constant applied strain rates of $\dot{\varepsilon}^p = 1 \times 10^{-3} \text{ s}^{-1}$ and $\dot{\varepsilon}^p = 1 \text{ s}^{-1}$ in Figures 4-82a and 4-82b, respectively.

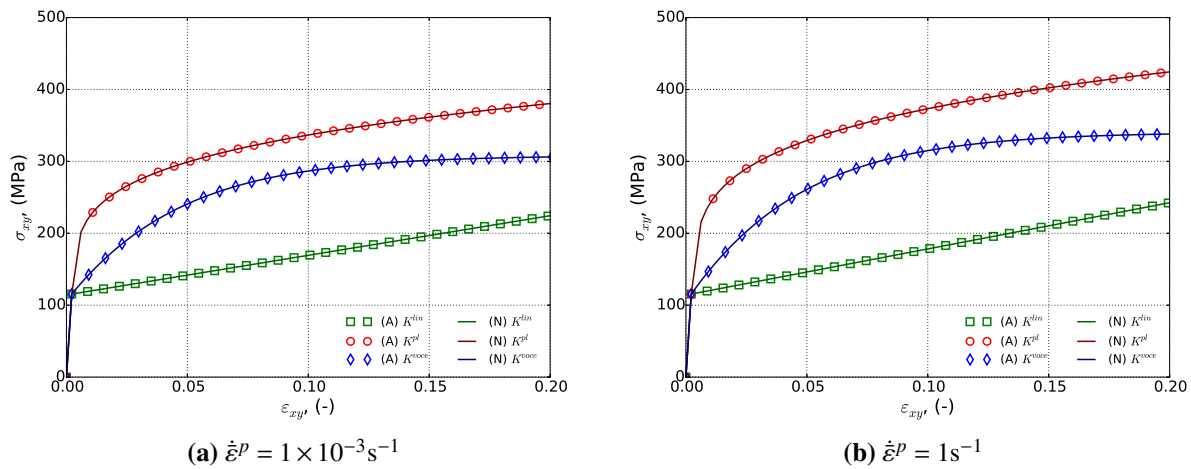


Figure 4-82. Analytical and numerical constant equivalent plastic strain rate verification tests of the modular plane stress plasticity models with a pure shear stress state and strain rates of (a) $\dot{\varepsilon}^p = 1 \times 10^{-3} \text{s}^{-1}$ and (b) $\dot{\varepsilon}^p = 1 \text{s}^{-1}$ with linear, power-law, and voce isotropic hardening and power-law breakdown rate-dependence. Solid lines are analytical and open symbols are from finite element calculations.

4.18.4. User Guide

```
BEGIN PARAMETERS FOR MODEL MODULAR_PLANE_STRESS_PLASTICITY
#
# Elastic constants
#
YOUNGS MODULUS = <real> E
POISONS RATIO = <real> ν
SHEAR MODULUS = <real> G
BULK MODULUS = <real> K
LAMBDA = <real> λ
TWO MU = <real> 2μ
#
YIELD STRESS = <real> σy
#
#
# Hardening model
#
HARDENING MODEL = LINEAR | POWER_LAW | VOCE | USER_DEFINED |
FLOW_STRESS | DECOUPLED_FLOW_STRESS | CUBIC_HERMITE_SPLINE |
JOHNSON_COOK | POWER_LAW_BREAKDOWN
#
# Linear hardening
#
HARDENING MODULUS = <real> H'
#
# Power-law hardening
#
HARDENING CONSTANT = <real> A
HARDENING EXPONENT = <real> n (0.5)
LUDERS STRAIN = <real> εL (0.0)
#
# Voce hardening
#
HARDENING MODULUS = <real> A
EXPONENTIAL COEFFICIENT = <real> n
#
# Johnson-Cook hardening
#
HARDENING FUNCTION = <string>hardening_function_name
RATE CONSTANT = <real> C
REFERENCE RATE = <real> ̇ε0
#
# Power law breakdown hardening
#
HARDENING FUNCTION = <string>hardening_function_name
RATE COEFFICIENT = <real> g
```

```

RATE EXPONENT      = <real> m
#
# User defined hardening
#
HARDENING FUNCTION = <string>hardening_function_name
#
#
# Following Commands Pertain to Flow_Stress Hardening Model
#
#      - Isotropic Hardening model
#
ISOTROPIC HARDENING MODEL = LINEAR | POWER_LAW | VOCE |
                           USER_DEFINED
#
# Specifications for Linear, Power-law, and Voce same as above
#
# User defined hardening
#
ISOTROPIC HARDENING FUNCTION = <string>iso_hardening_fun_name
#
#      - Rate dependence
#
RATE MULTIPLIER = JOHNSON_COOK | POWER_LAW_BREAKDOWN |
                  RATE_INDEPENDENT (RATE_INDEPENDENT)
#
# Specifications for Johnson-Cook, Power-law-breakdown
#      same as before EXCEPT no need to specify a
#      hardening function
#
# User defined rate multiplier
#
RATE MULTIPLIER FUNCTION = <string> rate_mult_function_name
#
#
#
# Following Commands Pertain to Decoupled_Flow_Stress Hardening Model
#
#      - Isotropic Hardening model
#
ISOTROPIC HARDENING MODEL = LINEAR | POWER_LAW | VOCE | USER_DEFINED
#
# Specifications for Linear, Power-law, and Voce same as above
#
# User defined hardening
#
ISOTROPIC HARDENING FUNCTION = <string>isotropic_hardening_function_name
#

```

```

#      - Rate dependence
#
YIELD RATE MULTIPLIER = JOHNSON_COOK | POWER_LAW_BREAKDOWN |
    RATE_INDEPENDENT (RATE_INDEPENDENT)
#
# Specifications for Johnson-Cook, Power-law-breakdown same as before
#     EXCEPT no need to specify a hardening function
#     AND should be preceded by YIELD
#
#     As an example for Johnson-Cook yield rate dependence,
#
YIELD RATE CONSTANT  = <real> Cy
YIELD REFERENCE RATE = <real>  $\dot{\epsilon}_0^y$ 
#
# User defined rate multiplier
#
YIELD RATE MULTIPLIER FUNCTION = <string>yield_rate_mult_function_name
#
HARDENING_RATE MULTIPLIER = JOHNSON_COOK | POWER_LAW_BREAKDOWN |
    RATE_INDEPENDENT (RATE_INDEPENDENT)
#
#     Syntax same as for yield parameters but with a HARDENING prefix
#
#
END [PARAMETERS FOR MODEL MODULAR_PLANE_STRESS_PLASTICITY]

```

Output variables available for this model are listed in Table 4-27.

Table 4-27. State Variables for MODULAR PLANE STRESS PLASTICITY Model

Name	Description
RADIUS	yield surface radius in deviatoric π -plane, R
EQPS	equivalent plastic strain, $\bar{\epsilon}^p$
EQDOT	equivalent plastic strain rate, $\dot{\bar{\epsilon}}^p$

REFERENCES

- [1] J. C. Simo and R. L. Taylor. A return mapping algorithm for plane stress elastoplasticity. *International Journal for Numerical Methods in Engineering*, 22:649–670, 1986.
- [2] J.C. Simo and T.J.R. Hughes. *Computational Inelasticity*. Springer-Verlag, New York, NY, 1998.
- [3] R. Hill. *The Mathematical Theory of Plasticity*. Oxford University Press, 1950.
- [4] J. Lemaitre and J.-L. Chaboche. *Mechanics of Solid Materials*. Cambridge University Press, 1990.
- [5] J. Lubliner. *Plasticity Theory*. Dover, 2008.
- [6] G.R. Johnson and W.H. Cook. A constitutive model and data for metals subjected to large strains, high strain rates and high temperatures. In *Proc. 7th. Int. Symp. on Ballistics*, pages 541–547, The Hague, The Netherlands, 1983.
- [7] G.R. Johnson and W.H. Cook. Fracture characteristics of three metals subjected to various strains, strain rates, temperatures and pressures. *Engineering Fracture Mechanics*, 21(1): 31–48, 1985.
- [8] H. J. Frost and M. F. Ashby. *Deformation mechanism maps: the plasticity and creep of metals and ceramics*. Pergamon press, 1982.
- [9] A.A. Brown and D.J. Bammann. Validation of a model for static and dynamic recrystallization in metals. *International Journal of Plasticity*, 32–33:17–35, 2012.
- [10] W. M. Scherzinger. A return mapping algorithm for isotropic and anisotropic plasticity models using a line search method. *Computer Methods in Applied Mechanics and Engineering*, 317:526–553, 2017.

4.19. POWER LAW CREEP MODEL

4.19.1. Theory

The power law creep model describes the secondary (or steady-state) creep and is useful in capturing the time-dependent behavior of metals, brazes, or solder at high homologous temperatures. It may also be used as a simple model for the time-dependent behavior of geologic materials such as salt. A general discussion of such creep behaviors and the associated modeling may be found in the texts of [1, 2] while the specific implementation used here is discussed in [3].

In the power law creep model, the effective creep strain rate is taken to be explicitly a function of stress and temperature. A power law relation is used for the stress dependence while an Arrhenius like expression is used to capture thermal effects. As such, the effective creep strain rate is written as,

$$\dot{\varepsilon}^c = A \bar{\sigma}_{vM}^m \exp\left(\frac{-Q}{R\theta}\right), \quad (4.19.1)$$

where $\dot{\varepsilon}^c$ is the effective creep strain rate, $\bar{\sigma}_{vM}$ is the von Mises stress, A is the creep constant, m is the creep exponent, Q is the activation energy, R is the universal gas constant (1.987 cal/mole K), and θ is the absolute temperature. As a slip based mechanism, it is assumed that the creep strains are deviatoric leading to a 3D evolution law of the form,

$$D_{ij}^c = \dot{\varepsilon}^c \frac{3}{2} \frac{s_{ij}}{\bar{\sigma}_{vM}}, \quad (4.19.2)$$

with s_{ij} being the deviatoric stress. The corresponding incremental constitutive equation for this model is then given as,

$$\dot{\sigma}_{ij} = \mathbb{C}_{ijkl} (D_{kl} - D_{kl}^c). \quad (4.19.3)$$

4.19.2. Implementation

Given the time-dependent nature of the model response, an explicit, forward Euler scheme is used to integrate the routine. Prior analysis [3] has shown that this implementation is conditionally stable and found an expression of the form

$$\Delta t_{st} < \frac{4(1+\nu)}{3EA \exp\left(\frac{-Q}{R\theta}\right) m \bar{\sigma}_{vM}^{m-1}} \quad (4.19.4)$$

for the critical time step for stability, Δt_{st} . This time step is calculated using the previously determined material state (state n) and compared to the input time step. If necessary, the time step is cut back to meet this critical limit.

To determine the updated material state (state $n + 1$) it is first noted that the creep process is purely deviatoric. Therefore, the stress may be decomposed as,

$$T_{ij}^n = -p^n \delta_{ij} + s_{ij}^n \quad (4.19.5)$$

where p is the pressure ($p^n = -(1/3)T_{kk}^n$) and T_{ij} is the unrotated stress. Given the decoupled nature of the hydrostatic and deviatoric components, the updated pressure may be found as,

$$p^{n+1} = p^n - Kd_{kk}\Delta t, \quad (4.19.6)$$

with d_{ij} being the unrotated rate of deformation. By similarly decomposing the rate of deformation,

$$d_{ij} = \frac{1}{3}d_{kk}\delta_{ij} + \hat{d}_{ij}, \quad (4.19.7)$$

with \hat{d}_{ij} being the deviatoric part of the rate of deformation, the updated deviatoric stress is

$$s_{ij}^{n+1} = s_{ij}^n + 2\mu \left(\hat{d}_{ij} - \frac{3}{2}A \exp \left(\frac{-Q}{R\theta^n} \right) (\bar{\sigma}_{vM}^n)^{m-1} s_{ij}^n \right). \quad (4.19.8)$$

The updated stress is then simply,

$$T_{ij}^{n+1} = -p^{n+1} \delta_{ij} + s_{ij}^{n+1}. \quad (4.19.9)$$

4.19.3. Verification

The power law creep model is verified through two, time-dependent tests – creep and stress relaxation. It is noted that given the strong time dependency and form of the differential constitutive equations, a closed form analytical expression for the response is not readily available. Semi-analytical approaches in which simple numerical integration is used to solve the underlying differential equation, however, are well suited to such efforts and are used here to verify the numerical responses. The set of material properties and model parameters used for these tests are taken from [4] and are given in Table 4-28 and it is assumed that there are no thermal strains.

4.19.3.1. Creep

To consider the creep response, the model response is determined both numerically and semi-analytically. Through such a response, the stress tensor is $\sigma_{ij} = \sigma(t) \delta_{i1} \delta_{j1}$ where $\sigma(t)$ is a prescribed boundary condition. For this investigation, $\sigma(t)$ ramps linearly from 0 to σ_{max} over the

interval $t = [0, 100 \text{ s}]$ and $\sigma_{max} = 300 \text{ MPa}$. The stress is then held constant ($\dot{\sigma} = 0$) for the next 900 s. Inverting the constitutive law (4.19.3) for the strain rate yields,

$$D_{ij} = \mathbb{S}_{ijkl}\dot{\sigma}_{kl} + D_{ij}^c. \quad (4.19.10)$$

Furthermore, given the stress tensor form above, the creep deformation rate is,

$$D_{ij}^c = A\bar{\sigma}_{vM}^m \exp\left(\frac{-Q}{R\theta}\right) \left[\delta_{i1}\delta_{j1} - \frac{1}{2} (\delta_{i2}\delta_{j2} + \delta_{i3}\delta_{j3}) \right], \quad (4.19.11)$$

and

$$\mathbb{S}_{ijkl}\dot{\sigma}_{kl} = \dot{\sigma}\mathbb{S}_{ij11}. \quad (4.19.12)$$

The total deformation rate may then be determined and easily integrated to find an analytical response for the strain. To this end, both the semi-analytical and numerical strain and stress responses (as a function of time) are presented in Figures 4-83a and 4-83b, respectively.

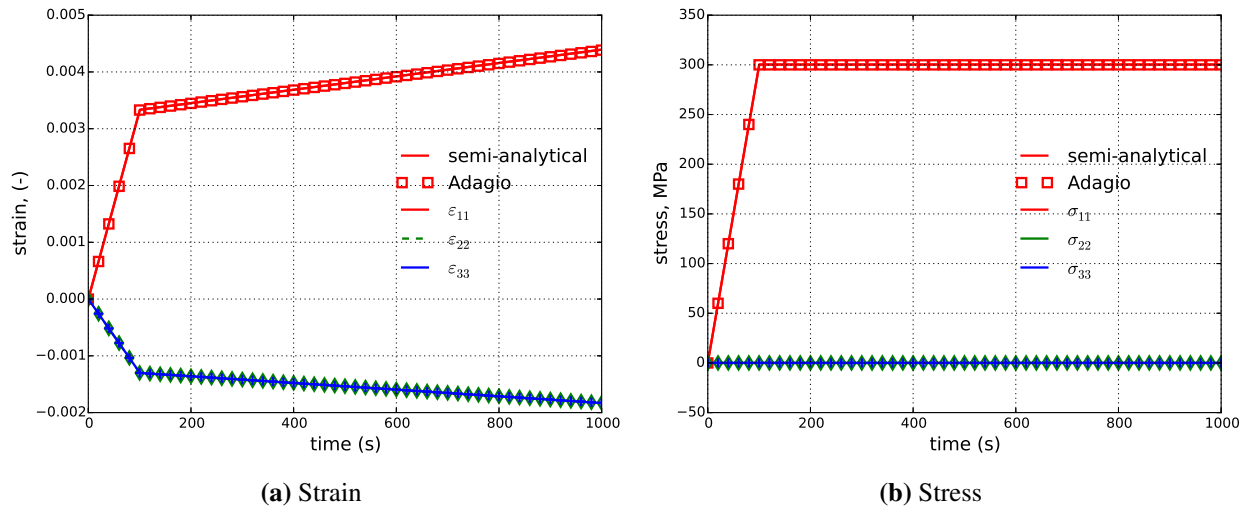


Figure 4-83. Semi-analytical and numerical results of (a) strain and (b) stress evolution during a creep test.

E	90.68 MPa	ν	0.39
A	5.12×10^{-5}	m	4.51
Q/R	19,853.50 K	θ	673.00 K

Table 4-28. The material properties and model parameters for the power law creep model used for the verification testing.

4.19.3.2. Stress Relaxation

The stress relaxation response of the considered model is evaluated both numerically and semi-analytically. Specifically, a displacement controlled loading of $u_1 = \lambda(t)$ is investigated. The other displacement degrees of freedom are not constrained so that a uniaxial stress state results – $\sigma_{ij}(t) = \sigma(t)\delta_{i1}\delta_{j1}$. The displacement is prescribed such that it scales linearly from $u_1 = 0$ at $t = 0$ to $u_1 = .01$ at $t = 100$ s and then held fixed for 900 s. Initially the considered element is of unit length.

To determine the material response, it is noted that: (i) $\sigma_{22} = \sigma_{33} = 0$; (ii) $D_{22}^e = D_{33}^e$ due to isotropy; and (iii) the creep deformation rate takes the form (4.19.11). With these observations, the elastic deformation rate in the direction of loading (D_{11}^e) becomes,

$$D_{11}^e = \frac{\dot{\lambda}(t)}{1 + \lambda(t)} - A\bar{\sigma}_{vM}^m \exp\left(\frac{-Q}{R\theta}\right). \quad (4.19.13)$$

Additionally, from (i) and (ii) above, it may be found that,

$$D_{22}^e = D_{33}^e = -\nu D_{11}^e, \quad (4.19.14)$$

leading to an equation for the stress in the direction of loading of,

$$\dot{\sigma}_{11} = (\mathbb{C}_{1111} - 2\nu\mathbb{C}_{1122})D_{11}^e. \quad (4.19.15)$$

Additionally, as $D_{ij} = D_{ij}^e + D_{ij}^c$ the strains may easily integrated by using relations (4.19.11), (4.19.13), and (4.19.14). The resultant numerical and semi-analytical strain and stress responses are shown in Figures 4-84a and 4-84b, respectively.

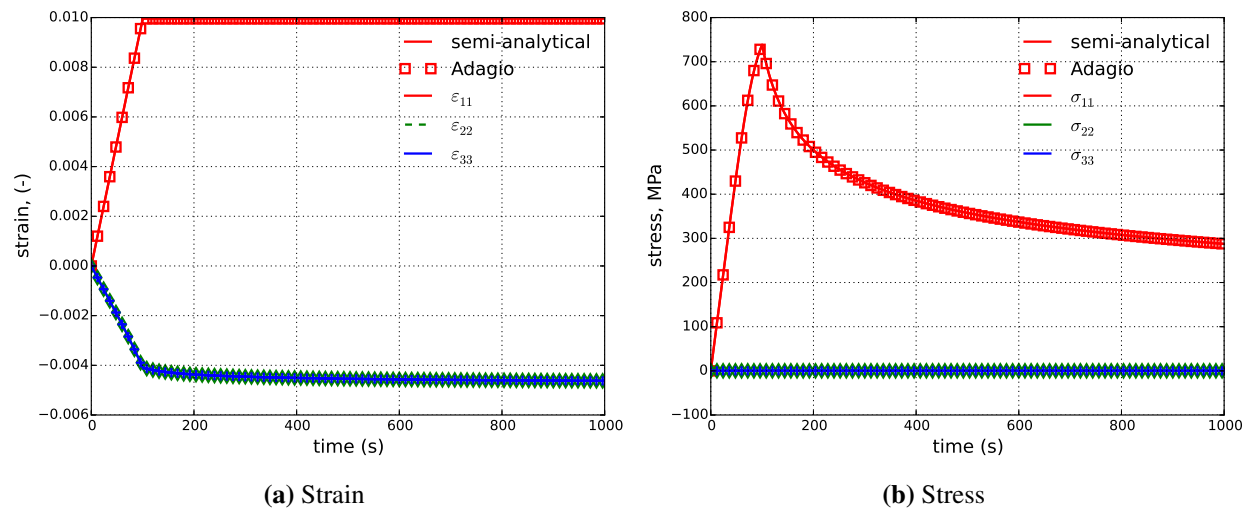


Figure 4-84. Semi-analytical and numerical results of the (a) strain and (b) stress evolution during a stress relaxation test.

4.19.4. User Guide

```
BEGIN PARAMETERS FOR MODEL POWER_LAW_CREEP
#
# Elastic constants
#
YOUNGS MODULUS = <real> E
POISSONS RATIO = <real> ν
SHEAR MODULUS = <real> G
BULK MODULUS = <real> K
LAMBDA = <real> λ
TWO MU = <real> 2μ
#
# Viscoplastic parameters
#
CREEP CONSTANT = <real> A
CREEP EXPONENT = <real> m
THERMAL CONSTANT = <real> Q/R
MAX SUBINCREMENTS = <integer> max_subincrements(100)
END [PARAMETERS FOR MODEL POWER_LAW_CREEP]
```

Output variables available for this model are listed in Table 4-29.

Table 4-29. State Variables for POWER LAW CREEP Model

Name	Description
ECREEP	equivalent creep strain
SEQDOT	equivalent stress rate

REFERENCES

- [1] J. Lemaître and J.-L. Chaboche. *Mechanics of Solid Materials*. Cambridge University Press, 1990.
- [2] F.K.G. Odqvist. *Mathematical theory of creep and creep rupture*. Clarendon Press, Oxford, 1966.
- [3] C.M. Stone. SANTOS – a two-dimensional finite element program for the quasistatic, large deformation, inelastic response of solids. Technical Report SAND90-0543, Sandia National Laboratories, Albuquerque, NM, 1996. [pdf](#).
- [4] W.M. Scherzinger and D.C. Hammerand. Testing of constitutive models in LAME. Technical Report SAND2007-5872, Sandia National Laboratories, Albuquerque, NM, September 2007. [pdf](#).

4.20. VISCOPLASTIC MODEL

4.20.1. Theory

The viscoplastic model is a rate dependent plasticity model that is useful for modeling solders and brazes and was developed by Neilsen et al. [1]. This model is formulated in terms of the stress rate for the material. Like many inelastic models, the rate of deformation, D_{ij} , is additively decomposed into an elastic, D_{ij}^e , and an inelastic, D_{ij}^{in} part such that,

$$D_{ij} = D_{ij}^e + D_{ij}^{\text{in}}. \quad (4.20.1)$$

The elastic rate of deformation is the only part that contributes to the stress rate and it does so through the elastic moduli, \mathbb{C}_{ijkl} , in a linear fashion leading to the relation,

$$\dot{\sigma}_{ij} = \mathbb{C}_{ijkl} D_{kl}^e, \quad (4.20.2)$$

where \mathbb{C}_{ijkl} are the components of the fourth-order, isotropic elasticity tensor. The stress rate is arbitrary, as long as it is objective. Two objective stress rates are commonly used: the Jaumann rate and the Green-McInnis rate. For problems with fixed principal axes of deformation, these two rates give the same answers. For problems where the principal axes of deformation rotate during the deformation, the two rates can give different answers. Generally speaking there is no reason to pick one objective rate over another.

The inelastic strain rate is a function of the stress state, σ_{ij} , the temperature, θ , and a number of internal state variables including both scalar isotropic, D , and tensorial kinematic, B_{ij} , hardening variables. With these dependencies defined, a general form for the evolution of the inelastic deformation may be given by,

$$D_{ij}^{\text{in}} = \frac{3}{2} \gamma (\sigma_{ij}, \theta; D, B_{ij}) n_{ij}, \quad (4.20.3)$$

where n_{ij} is the direction of inelastic deformation and is defined as,

$$n_{ij} = \frac{1}{\tau} \left(s_{ij} - \frac{2}{3} B_{ij} \right), \quad (4.20.4)$$

and

$$\tau = \sqrt{\frac{3}{2} \left(s_{ij} - \frac{2}{3} B_{ij} \right) \left(s_{ij} - \frac{2}{3} B_{ij} \right)}, \quad (4.20.5)$$

with s_{ij} being the deviatoric stress tensor. The inelastic strain rate, γ , is defined via a hyperbolic sin law,

$$\gamma = f(\theta) \left[\sinh \left(\frac{\tau}{\alpha(\theta)D} \right) \right]^{p(\theta)}, \quad (4.20.6)$$

where $f(\theta) = \exp(g(\theta))$. The expressions $g(\theta)$, $\alpha(\theta)$, and $p(\theta)$ are model parameters that are functions of temperature.

The evolution laws for the state variables D and B_{ij} are,

$$\dot{D} = \frac{A_1}{(D - D_0)^{A_3}} \gamma - A_2 (D - D_0)^2, \quad (4.20.7)$$

and

$$\dot{B}_{ij} = \frac{A_4}{b^{A_6}} D_{ij}^{\text{in}} - A_5 b B_{ij}, \quad (4.20.8)$$

where

$$b = \sqrt{\frac{2}{3} B_{ij} B_{ij}}. \quad (4.20.9)$$

The parameters D_0 , A_1 , A_2 , A_3 , A_4 , A_5 and A_6 are model parameters. The parameters A_1 , A_2 , A_4 and A_5 are also functions of temperature. The model can be simplified with the appropriate choice of these parameters.

The following material parameters are functions of temperature and have the following form

$$\begin{aligned} G(\theta) &= G_0 h_G(\theta) \quad ; \quad K(\theta) = K_0 h_K(\theta) \\ g(\theta) &= g_0 h_g(\theta) \quad ; \quad p(\theta) = p_0 h_p(\theta) \quad ; \quad \alpha(\theta) = \alpha_0 h_\alpha(\theta) \\ A_1(\theta) &= A_1^0 h_1(\theta) \quad ; \quad A_2(\theta) = A_2^0 h_2(\theta) \\ A_4(\theta) &= A_4^0 h_4(\theta) \quad ; \quad A_5(\theta) = A_5^0 h_5(\theta) \end{aligned} \quad (4.20.10)$$

where the functions $h_*(\theta)$ are normalized functions of temperature and the values $(*)_0$ or $(*)^0$ are the reference values that are input in the command block.

4.20.2. Implementation

An explicit, forward Euler scheme is used to integrate the viscoplastic model. First, during initialization, the isotropic hardening variable D is set to $1.001D_0$. This is done to avoid a singularity in (4.20.7). Additionally, the kinematic variable is set to zero ($B_{ij} = 0$).

Like the power law creep model that is integrated in a similar fashion, the chosen numerical scheme is conditionally stable. As detailed in [1], a critical stability time step of,

$$\Delta t_{n+1} \leq \frac{2\alpha(\theta)D}{3Gf(\theta)p(\theta)\sinh^{p(\theta)-1}\left(\frac{\tau}{\alpha(\theta)D}\right)\cosh\left(\frac{\tau}{\alpha(\theta)D}\right)}, \quad (4.20.11)$$

may be determined. For convenience, in the following the dependence of f , p , and α will be assumed and not explicitly written. Instead, f^{n+1} will be used to refer to $f(\theta^{n+1})$. Two additional limits are also imposed to ensure accurate integration of the state variables. Specifically,

$$\Delta t_{n+1} \leq \sqrt{\frac{2\delta D_0 \Delta t_n}{|\dot{D}_n - \dot{D}_{n-1}|}}, \quad (4.20.12)$$

and

$$\Delta t_{n+1} \leq \sqrt{\frac{2\delta D_0 \Delta t_n}{|\dot{b}_n - \dot{b}_{n-1}|}}, \quad (4.20.13)$$

where δ is an allowable error measure (here, 1.0×10^{-3}) and \dot{x}_n refers to the time rate of change of variable x at time step n . The current time step is checked to ensure it meets those criteria or else it is scaled back to ensure accurate integration.

After assessing the acceptability of the time step, the new material state at time $t = t_{n+1}$ is determined. If the time step needs to be cut back, multiple sub-increments are used. To elaborate, let k denote a specific sub-increment and N represent the total number of sub-increments. Each k^{th} interval evaluates the numerical routine over a step size Δt^k where $\Delta t = \sum_{k=0}^N \Delta t^k$. In such cases, temperature dependent variables are linearly interpolated between their values at t_n and t_{n+1} . For example,

$$G^k = G_n + \frac{\Delta t^k}{\Delta t} (G_{n+1} - G_n), \quad (4.20.14)$$

where Δt^k is the current sub-increment time, $\Delta t^k = \sum_{r=0}^k \delta t^r$. For simplicity and clarity of presentation, in the discussion below it is assumed that the input time step is acceptable and only a single increment is needed. If additional sub-increments were needed, the below steps would be repeated N times with time intervals of Δt^k .

It is first noted that the unrotated stress, T_{ij} , and deformation rate, d_{ij} , may be decomposed as,

$$T_{ij}^n = -p^n \delta_{ij} + s_{ij}^n, \quad (4.20.15)$$

$$d_{ij}^n = \frac{1}{3} d_{kk}^n \delta_{ij} + \hat{d}_{ij}^n, \quad (4.20.16)$$

with p being the pressure ($p = -\frac{1}{3}T_{kk}$) and \hat{d}_{ij} being the rate of deviatoric deformation. As the inelastic deformation flows in a deviatoric direction, the hydrostatic and deviatoric components may be evaluated separately. With this in mind, the pressure may be easily integrated via,

$$p^{n+1} = p^n \frac{K^{n+1}}{K^n} + \frac{1}{2} (K^n + K^{n+1}) d_{kk} \Delta t, \quad (4.20.17)$$

where K^n is abbreviated notation for $K(\theta^n)$. The inelastic deformation rate is then determined as,

$$D_{ij}^{\text{in}} = \frac{3}{2} \gamma (\sigma_{ij}^n, \theta^n; D^n, B_{ij}^n) n_{ij}^n, \quad (4.20.18)$$

by evaluating expressions (4.20.4)-(4.20.6) at $t = t_n$ and $\theta = \theta^n$. The internal state variables may then be similarly evolved via (4.20.7) and (4.20.8). With the inelastic state determined, the updated deviatoric stress may be found via,

$$s_{ij}^{n+1} = \frac{G^{n+1}}{G^n} s_{ij}^n + 2\Delta t G^n (\hat{d}_{ij} - D_{ij}^{\text{in}}), \quad (4.20.19)$$

with the updated stress being,

$$T_{ij}^{n+1} = -p^{n+1} \delta_{ij} + s_{ij}^{n+1}. \quad (4.20.20)$$

4.20.3. Verification

The viscoplastic model is verified through two, time-dependent tests – creep and stress relaxation. To simplify the problem for verification purposes, the isothermal response only considering isotropic hardening and recovery is investigated. It is noted, however, that given the stress dependence and evolving internal state variable in the inelastic strain rate, a closed-form analytical solution may not be found. Semi-analytical approaches numerically integrating the differential equations are easily obtainable and used for comparison purposes. The considered test temperature is 450°C (723 K) and material properties and model parameters are those of CusilABA taken from Table 3 of [1] and are reproduced for convenience below in Table 4-30.

4.20.3.1. Creep

The creep response of the viscoplastic model is investigated both numerically and semi-analytically. For such a loading, the stress tensor is $\sigma_{ij} = \sigma(t) \delta_{i1} \delta_{j1}$ with $\sigma(t)$ being a

prescribed quantity. For this study, $\sigma(t)$ ramps linearly from 0 to σ_{max} over the interval $t = [0, 100 \text{ s}]$ with $\sigma_{max} = 300 \text{ MPa}$. That magnitude is then maintained for the next 900 s.

To analytically determine the model response, the constitutive law (4.20.2) is inverted to yield

$$D_{ij} = \mathbb{S}_{ijkl}\dot{\sigma}_{kl} + D_{ij}^{\text{in}}, \quad (4.20.21)$$

and it is trivial to determine that

$$\mathbb{S}_{ijkl}\dot{\sigma}_{kl} = \dot{\sigma}\mathbb{S}_{11kl}. \quad (4.20.22)$$

For the inelastic response, for the purely isotropic case it is noted that $\tau = \sigma(t)$ and therefore $n_{ij} = \frac{2}{3} [\delta_{i1}\delta_{j1} - \frac{1}{2} (\delta_{i2}\delta_{j2} + \delta_{i3}\delta_{j3})]$. Additionally, the inelastic strain rate reduces to,

$$\gamma = f \left[\sinh \left(\frac{\sigma(t)}{\alpha D} \right) \right]^p \quad (4.20.23)$$

producing a rate of inelastic deformation of,

$$D_{ij}^{\text{in}} = \gamma \left[\delta_{i1}\delta_{j1} - \frac{1}{2} (\delta_{i2}\delta_{j2} + \delta_{i3}\delta_{j3}) \right]. \quad (4.20.24)$$

Expressions (4.20.21), (4.20.22), (4.20.24), and (4.20.7) can be easily integrated (via forward Euler or Runge-Kutta) to determine a semi-analytical response. Both the numerical and semi-analytical responses of the strain and stress (including flow stress, D) are presented below in Figures 4-85a and 4-85b, respectively.

4.20.3.2. Stress Relaxation

The model response through a stress relaxation type loading is considered here both numerically and semi-analytically. For this purpose, a displacement controlled loading, $u_1 = \lambda(t)$, is employed. The other displacement degrees of freedom are not prescribed to ensure that a uniaxial stress state ($\sigma_{ij} = \sigma(t)\delta_{i1}\delta_{j1}$) develops. Specifically, the displacement is set to scale linearly over

E	77.8 GPa	ν	0.375
g	-13.88	p	2.589
A_1	$3 \times 10^4 \text{ MPa}^{A_3+1}$	A_2	$2.07 \times 10^{-5} \frac{1}{\text{MPa s}}$
A_3	1.746	D_0	50.0 MPa
A_4	0 MPa^{A_6+1}	A_5	$0.0 \frac{1}{\text{MPa s}}$
A_6	0.0	α	1.0

Table 4-30. Material properties and model parameters used for isothermal, isotropic hardening/recovery creep and stress relaxation tests of the viscoplastic model.

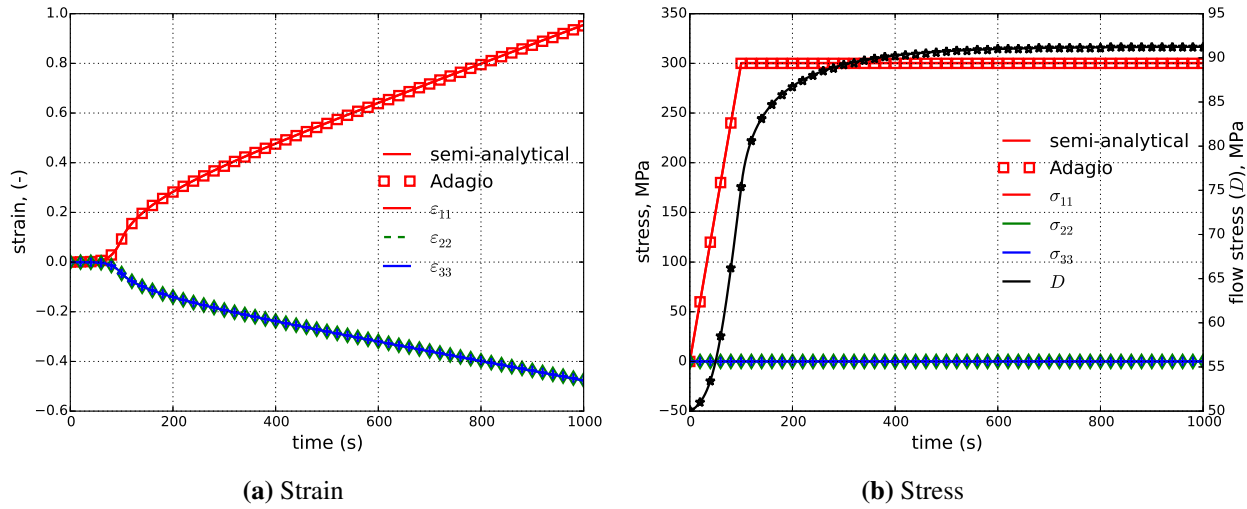


Figure 4-85. Semi-analytical and numerical results of (a) strain and (b) external and internal, (D), stress evolution during a creep test with the viscoplastic model.

100 s (from $t = 0$ to $t = 100$ s) obtaining a maximum of $u_1 = 0.01$ at $t = 100$ s. Initially, a unit length is assumed. This displacement is held fixed over the next 900 s to investigate the stress relaxation characteristics of the model.

A similar procedure to the power law creep model (Section 4.19.3.2) is employed here. Specifically, by noting the elastic isotropy, uniaxial stress state, and (4.20.24) the elastic deformation rate in the direction of loading (D_{11}^e) is found to be,

$$D_{11}^e = \frac{\lambda(t)}{1 + \lambda(t)} - \gamma, \quad (4.20.25)$$

where an expression for γ is given in (4.20.23). By noting $\dot{\sigma}_{ij} = \mathbb{C}_{ijkl}D_{kl}^e$ and $D_{ij} = D_{ij}^e + D_{ij}^{\text{in}}$, the material state may easily be found via numerical integration. The result strain and stress evolutions are given in Figures 4-86a and 4-86b, respectively.

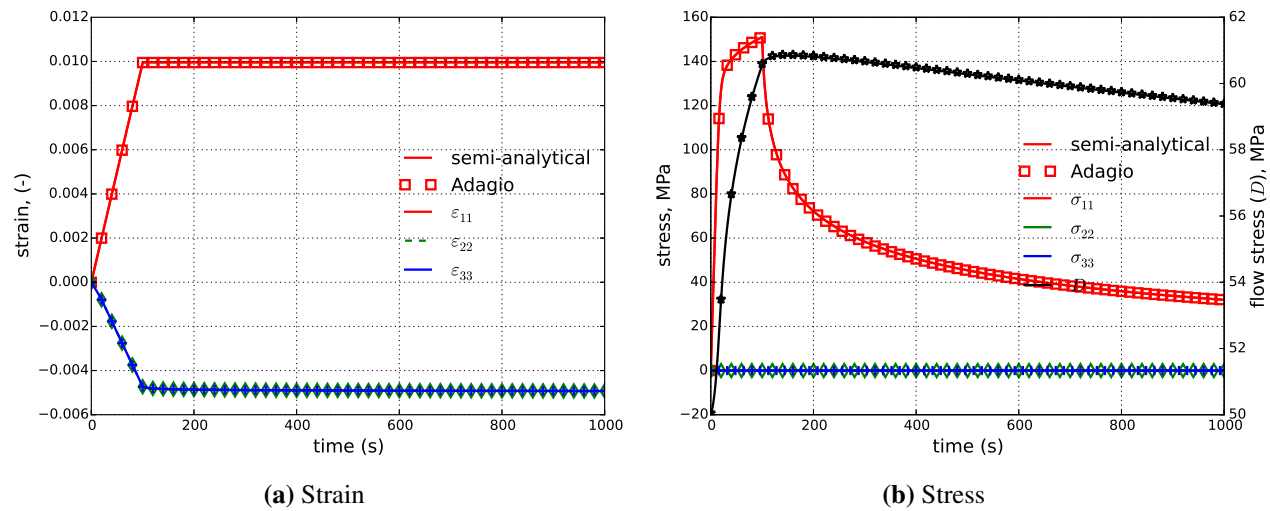


Figure 4-86. Semi-analytical and numerical results of (a) strain and (b) external and internal (D) stress evolution during a stress relaxation test with the viscoplastic model.

4.20.4. User Guide

```
BEGIN PARAMETERS FOR MODEL VISCOPLASTIC
#
# Elastic constants
#
YOUNGS MODULUS = <real> E
POISONS RATIO = <real> ν
SHEAR MODULUS = <real> G
BULK MODULUS = <real> K
LAMBDA = <real> λ
TWO MU = <real> 2μ

FLOW RATE = <real> g₀
SINH EXPONENT = <real> p₀
ALPHA = <real> α₀
ISO HARDENING = <real> A₁⁰
ISO RECOVERY = <real> A₂⁰
ISO EXPONENT = <real> A₃
KIN HARDENING = <real> A₄⁰
KIN RECOVERY = <real> A₅⁰
KIN EXPONENT = <real> A₆
FLOW STRESS = <real> D₀

SHEAR FUNCTION = <string> h_G(θ)
BULK FUNCTION = <string> h_K(θ)
RATE FUNCTION = <string> h_g(θ)
EXPONENT FUNCTION = <string> h_p(θ)
ALPHA FUNCTION = <string> h_α(θ)
IHARD FUNCTION = <string> h₁(θ)
IREC FUNCTION = <string> h₂(θ)
KHARD FUNCTION = <string> h₄(θ)
KREC FUNCTION = <string> h₅(θ)
MAX SUBINCREMENTS = <int> itmax (2000)
END [PARAMETERS FOR MODEL VISCOPLASTIC]
```

Output variables available for this model are listed in Table 4-31.

More information on the model can be found in the report by Neilsen, et. al. [1].

Table 4-31. State Variables for VISCOPLASTIC Model

Name	Description
EQPS	equivalent plastic strain
SVB	kinematic hardening variable, \mathbf{B}
SVB_XX	kinematic hardening variable - xx component, B_{xx}
SVB_YY	kinematic hardening variable - yy component, B_{yy}
SVB_ZZ	kinematic hardening variable - zz component, B_{zz}
SVB_XY	kinematic hardening variable - xy component, B_{xy}
SVB_YZ	kinematic hardening variable - yz component, B_{yz}
SVB_ZX	kinematic hardening variable - zx component, B_{zx}
SVD	isotropic hardening variable, D
EQDOT	inelastic strain rate, γ
COUNT	number of sub-increments
SHEAR	shear modulus, $G(\theta)$
BULK	bulk modulus, $K(\theta)$
RATE	$g(\theta)$ (see (4.20.6))
EXP	$p(\theta)$ (see (4.20.6))
ALPHA	$\alpha(\theta)$ (see (4.20.6))
A1	isotropic hardening parameter, $A_1(\theta)$
A2	isotropic recovery parameter, $A_2(\theta)$
A4	kinematic hardening parameter, $A_4(\theta)$
A5	kinematic recovery parameter, $A_5(\theta)$

REFERENCES

- [1] M.K. Neilsen, S. N. Burchett, C. M. Stone, and J. J. Stephens. A viscoplastic theory for braze alloys. Technical Report SAND96-0984, Sandia National Laboratories, Albuquerque, NM, 1996. [pdf](#).

4.21. MUNSON-DAWSON VISCOPLASTIC MODEL

4.21.1. Theory

The Munson-Dawson (MD) model was originally defined in [1, 2, 3], but several changes were made in [4]. This section presents the current model in a small strain setting. (Section 4.21.2 briefly mentions how the model is extended into the finite deformation realm.) Note that compressive stresses and strains are treated as positive in this section, as is common in the geomechanics literature.

The MD model is an isotropic, unified viscoplastic, material model. The total strain rate $\dot{\varepsilon}_{ij}$ is decomposed into an elastic strain rate $\dot{\varepsilon}_{ij}^{\text{el}}$, a thermal strain rate $\dot{\varepsilon}_{ij}^{\text{th}}$, and a viscoplastic strain rate $\dot{\varepsilon}_{ij}^{\text{vp}}$:

$$\dot{\varepsilon}_{ij} = \dot{\varepsilon}_{ij}^{\text{el}} + \dot{\varepsilon}_{ij}^{\text{th}} + \dot{\varepsilon}_{ij}^{\text{vp}}. \quad (4.21.1)$$

The elastic portion of the MD model utilizes the following simple linear relationship between $\dot{\varepsilon}_{kl}^{\text{el}}$ and the stress rate $\dot{\sigma}_{ij}$,

$$\dot{\sigma}_{ij} = \mathbb{C}_{ijkl} \dot{\varepsilon}_{kl}^{\text{el}} = \mathbb{C}_{ijkl} (\dot{\varepsilon}_{kl} - \dot{\varepsilon}_{kl}^{\text{th}} - \dot{\varepsilon}_{kl}^{\text{vp}}) \quad (4.21.2)$$

$$\mathbb{C}_{ijkl} = (B - 2/3\mu) \delta_{ij} \delta_{kl} + \mu (\delta_{ik} \delta_{jl} + \delta_{il} \delta_{jk}), \quad (4.21.3)$$

where \mathbb{C}_{ijkl} is the elastic stiffness, which is composed of the bulk modulus B , the shear modulus μ , and the Kronecker Delta δ_{ij} . The thermal strain portion of the model is simply

$$\dot{\varepsilon}_{ij}^{\text{th}} = -\alpha \dot{\theta} \delta_{ij} \quad (4.21.4)$$

where α is the coefficient of thermal expansion, and θ is the temperature. Sierra/SM also offers thermal strain functions for adding thermal strain effects to any given model. If $\alpha \neq 0$, then MD model users should not specify a thermal strain function, otherwise thermal strains will be applied twice.

Plastic deformation is assumed to be isochoric and only occurs in the presence of shear stress. The MD model utilizes the Hosford stress as its equivalent shear stress measure $\bar{\sigma}$. The Hosford stress is

$$\bar{\sigma} = \left\{ \frac{1}{2} [|\sigma_1 - \sigma_2|^a + |\sigma_2 - \sigma_3|^a + |\sigma_1 - \sigma_3|^a] \right\}^{1/a}, \quad (4.21.5)$$

where σ_i are the principal stresses and a is a material parameter. This definition for $\bar{\sigma}$ was proposed in [5] because it encompasses the Tresca stress ($a = 1$), the von Mises stress ($a = 2$), and a range of behaviors in-between ($1 < a < 2$). One can also reproduce the Tresca stress with $a = \infty$, the von Mises stress with $a = 4$, and behaviors in-between with $4 < a < \infty$. This second range avoids potential singularities in the first and second derivatives of (4.21.5), so the exponent is restricted to $a \geq 4$.

The viscoplastic strain evolves according to an associated flow rule

$$\dot{\varepsilon}_{ij}^{\text{vp}} = \dot{\varepsilon}^{\text{vp}} \frac{\partial \bar{\sigma}}{\partial \sigma_{ij}}, \quad (4.21.6)$$

where $\dot{\bar{\varepsilon}}^{\text{vp}}$ is the equivalent viscoplastic strain rate. It can be decomposed into two components

$$\dot{\bar{\varepsilon}}^{\text{vp}} = \dot{\bar{\varepsilon}}^{\text{tr}} + \dot{\bar{\varepsilon}}^{\text{ss}}, \quad (4.21.7)$$

where $\dot{\bar{\varepsilon}}^{\text{tr}}$ is the transient equivalent viscoplastic strain rate and $\dot{\bar{\varepsilon}}^{\text{ss}}$ is the steady state equivalent viscoplastic strain rate.

The MD model decomposes the steady state behavior into four “mechanisms”:

$$\begin{aligned} \dot{\bar{\varepsilon}}^{\text{ss}} &= \sum_{i=0}^3 \dot{\bar{\varepsilon}}_i^{\text{ss}} \\ \dot{\bar{\varepsilon}}_i^{\text{ss}} &= A_i \exp\left(-\frac{Q_i}{R\theta}\right) \left(\frac{\bar{\sigma}}{\mu}\right)^{n_i} \quad \text{for } i = 0, 1, \text{ and } 2 \\ \dot{\bar{\varepsilon}}_3^{\text{ss}} &= H(\bar{\sigma} - \bar{\sigma}_g) \sum_{i=0}^2 B_i \exp\left(-\frac{Q_i}{R\theta}\right) \sinh\left(q \frac{(\bar{\sigma} - \bar{\sigma}_g)}{\mu}\right), \end{aligned} \quad (4.21.8)$$

The variables A_i , B_i , Q_i , n_i , $\bar{\sigma}_g$, and q are all model parameters. All four mechanisms have an Arrhenius temperature dependence, where Q_i is an activation energy and $R = 8.314 \text{ J/(K mol)}$ is the universal gas constant. Mechanism 3 is only activated when $\bar{\sigma}$ exceeds $\bar{\sigma}_g$, as reflected in the heaviside function $H(\bar{\sigma} - \bar{\sigma}_g)$. Typically, the parameters B_i are chosen to produce a smooth transition to mechanism 3 at $\bar{\sigma}_g$.

The simple functional forms of (4.21.8) suffice for the steady-state behavior, but the transient behavior is somewhat more complex. During work hardening under constant stress, $\dot{\bar{\varepsilon}}^{\text{tr}}$ approaches the transient strain limit $\bar{\varepsilon}^{\text{tr}*}$ from below, and the total viscoplastic strain rate slows down over time. During recovery under constant stress, $\dot{\bar{\varepsilon}}^{\text{tr}}$ approaches $\bar{\varepsilon}^{\text{tr}*}$ from above, and the total viscoplastic strain rate speeds up over time. The rate that $\dot{\bar{\varepsilon}}^{\text{tr}}$ approaches $\bar{\varepsilon}^{\text{tr}*}$ is governed by

$$\dot{\bar{\varepsilon}}^{\text{tr}} = (F - 1) \dot{\bar{\varepsilon}}^{\text{ss}}, \quad (4.21.9)$$

where

$$F = \exp\left[\text{sign}(\bar{\varepsilon}^{\text{tr}*} - \dot{\bar{\varepsilon}}^{\text{tr}}) \kappa \left(1 - \frac{\dot{\bar{\varepsilon}}^{\text{tr}}}{\bar{\varepsilon}^{\text{tr}*}}\right)^2\right]. \quad (4.21.10)$$

and κ is a quantity that depends on whether the material is work hardening or recovering. These two behaviors are captured in the following equations

$$\kappa = \begin{cases} \alpha_h + \beta_h \log_{10}\left(\frac{\bar{\sigma}}{\mu}\right) & \dot{\bar{\varepsilon}}^{\text{tr}} \leq \bar{\varepsilon}^{\text{tr}*} \\ \alpha_r + \beta_r \log_{10}\left(\frac{\bar{\sigma}}{\mu}\right) & \dot{\bar{\varepsilon}}^{\text{tr}} > \bar{\varepsilon}^{\text{tr}*}. \end{cases} \quad (4.21.11)$$

where α_j and β_j are model parameters. Note that the parameter κ must be non-negative, otherwise (4.21.9) produces a negative/positive $\dot{\bar{\varepsilon}}^{\text{tr}}$ when $\dot{\bar{\varepsilon}}^{\text{tr}}$ is below/above $\bar{\varepsilon}^{\text{tr}*}$. (Such behavior occurs during reverse creep, but the MD model is only designed to model forward creep.) To enforce this, (4.21.11) is calculated first, and then

$$\kappa \leftarrow \max(\kappa, 0) \quad (4.21.12)$$

is applied.

The MD model uses two mechanisms to endow $\bar{\varepsilon}^{\text{tr}*}$ with stress and temperature dependence:

$$\begin{aligned}\bar{\varepsilon}^{\text{tr}*} &= \sum_{i=0}^1 \bar{\varepsilon}_i^{\text{tr}*} \\ \bar{\varepsilon}_i^{\text{tr}*} &= K_i \exp(c_i \theta) \left(\frac{\bar{\sigma}}{\mu} \right)^{m_i},\end{aligned}\quad (4.21.13)$$

where K_i , c_i , and m_i are parameters to be calibrated against experimental results.

4.21.2. Implementation

The full details of the MD model's numerical implementation are published in [4]. This section discusses several salient points for the typical MD model user and to define all the input parameters in Section 4.21.4.

- As discussed in Section 4.21.3, one can obtain an analytical solution to the MD model's ordinary differential equations if the exponent in (4.21.10) is changed from 2 to 1, and $\text{sign}(\bar{\varepsilon}^{\text{tr}*} - \bar{\varepsilon}^{\text{tr}}) = 1$. To accommodate this possibility, (4.21.10) is numerically implemented as

$$F = \exp \left[\text{sign}(\bar{\varepsilon}^{\text{tr}*} - \bar{\varepsilon}^{\text{tr}}) \chi^{-1} \kappa \left(1 - \frac{\bar{\varepsilon}^{\text{tr}}}{\bar{\varepsilon}^{\text{tr}*}} \right)^\chi \right] \quad (4.21.14)$$

where χ is a user specified integer that is equal to 2 by default, but one can set $\chi = 1$ for verification testing.

- Each steady state creep mechanism is implemented with a viscoplastic rate scale factor s , such that (4.21.8) becomes

$$\begin{aligned}\dot{\varepsilon}^{\text{ss}} &= \sum_{i=0}^3 \dot{\varepsilon}_i^{\text{ss}} \\ \dot{\varepsilon}_i^{\text{ss}} &= s A_i \exp \left(-\frac{Q_i}{R\theta} \right) \left(\frac{\bar{\sigma}}{\mu} \right)^{n_i} \quad \text{for } i = 0, 1, \text{ and } 2 \\ \dot{\varepsilon}_3^{\text{ss}} &= s H(\bar{\sigma} - \bar{\sigma}_g) \sum_{i=0}^2 B_i \exp \left(-\frac{Q_i}{R\theta} \right) \sinh \left(q \frac{(\bar{\sigma} - \bar{\sigma}_g)}{\mu} \right).\end{aligned}\quad (4.21.15)$$

This scale factor can be used to speed up or slow down the equivalent steady-state strain rate and the total equivalent viscoplastic strain rate, because $\dot{\varepsilon}^{\text{vp}} = \dot{\varepsilon}^{\text{tr}} + \dot{\varepsilon}^{\text{ss}} = F \dot{\varepsilon}^{\text{ss}}$. The default value is $s = 1$, but it can be useful to set s to some small value to “freeze” the material's viscoplasticity for a period of time, or increase s to larger values to squeeze hundreds of years into a few seconds. Speeding up the viscoplasticity can allow one to make quasi-static simulations using explicit dynamics, provided inertial effects are kept to a minimum. The variable s is implemented as an internal state variable, rather than a material parameter, so a user can modify it in the middle of a simulation. Internal state variables can

be altered by creating a “user variable” with the same name as the internal state variable (`viscoplastic_rate_scale_factor` in this case) in a Sierra input deck and modifying the user variable with a user function or user subroutine (see Sections 2.3 and A.2.1 in [6]).

- The MD model is extended into the finite-deformation realm using hypoelasticity. Consistent with the Green-McInnis stress rate, the infinitesimal strain rates are replaced with the corresponding unrotated rates of deformation (i.e. $\dot{\epsilon}_{ij} \rightarrow D_{ij}$) and the stress is replaced with the unrotated Cauchy stress ($\sigma_{ij} \rightarrow T_{ij}$).
- Following the lead of Scherzinger [7], the model’s time derivatives are discretized using the backwards Euler method, and the resulting non-linear algebraic equations are solved with a line search augmented Newton-Raphson method.

A typical user of the model should not need to adjust the routine’s default numerical parameters, but the parameters are briefly mentioned here should adjustment become necessary.

- The implementation has some expressions where $\bar{\sigma}$ is in the denominator of a fraction. If an initial calculation of the Hosford stress results in $\bar{\sigma} < \bar{\sigma}_{\min}$, then the initial value is replaced with $\bar{\sigma}_{\min}$. The value of $\bar{\sigma}_{\min}$ should be small enough to have negligible impact, yet still avoid $\bar{\sigma} = 0$.
- Each iteration of the implicit integration routine updates the merit function $\omega^{(k)} = 1/2 \left(\mathcal{R}_{ij}^{(k)} \mathcal{R}_{ij}^{(k)} + r^{(k)2} \right)$ for iteration k , where $\mathcal{R}_{ij}^{(k)}$ and $r^{(k)}$ are the residuals associated with the differential equations in (4.21.6) and (4.21.9), respectively. An iteration is considered converged when $\sqrt{\omega^{(k)}} < \sqrt{\omega_{\max}}$. The value of $\sqrt{\omega_{\max}}$ should be a small positive value close to zero.
- If a Newton iteration (or a line search iteration) does not produce sufficient decrease in $\omega^{(k)}$, a line search iteration is performed. The line search algorithm selects $\zeta^{(j)}$, for each iteration j , to search for a sufficient decrease in $\omega^{(k)}(\zeta^{(j)})$ along the search direction provided by the Newton iteration. The start and end of the last Newton iteration are $\zeta^{(j)} = 0$ and $\zeta^{(j)} = 1$, respectively. A decrease in $\omega^{(k)}(\zeta^{(j)})$ is considered sufficient if $\omega^{(k)}(\zeta^{(j)}) < (1 - 2\xi\zeta^{(j-1)})\omega^{(k)}(0)$, where ξ is a positive value usually set close to zero.
- The minimum allowed value of $\zeta^{(j)}$ is γ .
- The maximum number of Newton iterations is k_{\max} .
- The maximum number of line search iterations is j_{\max} .

See [4] for further discussion of these numerical parameters.

4.21.3. Verification

The MD model contains ordinary differential equations ((4.21.6) and (4.21.9)) that make it non-trivial to verify. A straightforward analytical solution, however, can be constructed to these equations if $\chi = 1$ in (4.21.14) and if the stresses and temperatures remain piecewise constant in time.

Temporally constant stresses and temperatures allow (4.21.2), (4.21.3), (4.21.4), (4.21.5), (4.21.6), (4.21.7), and (4.21.8) to be integrated to

$$\varepsilon_{kl} - \varepsilon_{kl}(t_j) = \mathbb{C}_{klmn}^{-1} (\sigma_{mn} - \sigma_{mn}(t_j)) - \alpha (\theta - \theta(t_j)) \delta_{kl} + \varepsilon_{kl}^{\text{vp}} - \varepsilon_{kl}^{\text{vp}}(t_j) \quad (4.21.16)$$

$$\varepsilon_{kl}^{\text{vp}} - \varepsilon_{kl}^{\text{vp}}(t_j) = [\bar{\varepsilon}^{\text{tr}} - \bar{\varepsilon}^{\text{tr}}(t_j) + \dot{\varepsilon}^{\text{ss}}(t - t_j)] \frac{\partial \bar{\sigma}}{\partial \sigma_{kl}} \quad (4.21.17)$$

where t_j is the time at the end of the previous time period j . The quantities from the previous time period ($\varepsilon_{kl}(t_j)$, $\sigma_{mn}(t_j)$, $\theta(t_j)$, $\varepsilon_{kl}^{\text{vp}}(t_j)$, and $\bar{\varepsilon}^{\text{tr}}(t_j)$) are assumed to be known. Setting $\chi = 1$ in (4.21.14) enables the following general analytical solution to (4.21.9):

$$\bar{\varepsilon}^{\text{tr}} = \frac{\bar{\varepsilon}^{\text{tr}^*}}{\kappa} \ln \left\{ \exp(\kappa) + \exp \left[\frac{\kappa}{\bar{\varepsilon}^{\text{tr}^*}} (C_1 - \dot{\varepsilon}^{\text{ss}} t) \right] \right\}. \quad (4.21.18)$$

One can solve for the integration constant C_1 using the initial condition $\bar{\varepsilon}^{\text{tr}} = \bar{\varepsilon}^{\text{tr}}(t_j)$ at $t = t_j$. After substituting the result back into (4.21.18), one obtains

$$\bar{\varepsilon}^{\text{tr}} = \frac{\bar{\varepsilon}^{\text{tr}^*}}{\kappa} \ln \left\{ \exp(\kappa) + \left[\exp \left(\frac{\bar{\varepsilon}^{\text{tr}}(t_j) \kappa}{\bar{\varepsilon}^{\text{tr}^*}} \right) - \exp(\kappa) \right] \exp \left[-\frac{\kappa}{\bar{\varepsilon}^{\text{tr}^*}} \dot{\varepsilon}^{\text{ss}} (t - t_j) \right] \right\}. \quad (4.21.19)$$

Combining (4.21.16), (4.21.17), and (4.21.19) produces the following closed form expression for the total strain change over a time period

$$\begin{aligned} \varepsilon_{kl} - \varepsilon_{kl}(t_j) &= \mathbb{C}_{klmn}^{-1} (\sigma_{mn} - \sigma_{mn}(t_j)) - \alpha (\theta - \theta(t_j)) \delta_{kl} + \\ &\quad \left[\frac{\bar{\varepsilon}^{\text{tr}^*}}{\kappa} \ln \left\{ \exp(\kappa) + \left[\exp \left(\frac{\bar{\varepsilon}^{\text{tr}}(t_j) \kappa}{\bar{\varepsilon}^{\text{tr}^*}} \right) - \exp(\kappa) \right] \exp \left[-\frac{\kappa}{\bar{\varepsilon}^{\text{tr}^*}} \dot{\varepsilon}^{\text{ss}} (t - t_j) \right] \right\} \right. \\ &\quad \left. - \bar{\varepsilon}^{\text{tr}}(t_j) + \dot{\varepsilon}^{\text{ss}}(t - t_j) \right] \frac{\partial \bar{\sigma}}{\partial \sigma_{kl}}. \end{aligned} \quad (4.21.20)$$

The next three subsections compare numerical solutions against analytical solutions for axisymmetric compression, pure shear, and unequal biaxial compression. In each case, the numerical solution for the total strain is denoted as ε_{ij} , while the analytical solution for the total strain in (4.21.20) is denoted as $\hat{\varepsilon}_{ij}$. All the verification tests only involve principal deformations, so hypoelasticity simply reinterprets the stress and strain in Section 4.21.1 as the Cauchy stress and logarithmic strain, respectively. As a reminder, compressive stresses and strains are treated as positive.

All the verification tests utilize Calibration 3B of the MD model. The full parameter set can be found in [4], but Fig. 4-87, 4-88 and 4-89 depict much of the calibration graphically. Figure 4-87 shows the shape of the Hosford equivalent stress surface for $a = 16$. The Hosford surface and the angle ϕ of its normal n_{ij} depend on the Lode angle ψ of the deviatoric stress $\sigma_{ij}^{\text{dev}} = \sigma_{ij} - 1/3\sigma_{kk}\delta_{ij}$. Figures 4-88 and 4-89 show the individual mechanisms $\bar{\varepsilon}_i^{\text{tr}^*}$ and $\dot{\varepsilon}_i^{\text{ss}}$, as well as the sums $\bar{\varepsilon}^{\text{tr}^*} = \sum_{i=0}^1 \bar{\varepsilon}_i^{\text{tr}^*}$ and $\dot{\varepsilon}^{\text{ss}} = \sum_{i=0}^3 \dot{\varepsilon}_i^{\text{ss}}$, so that one can visualize where each mechanism dominates the total behavior.

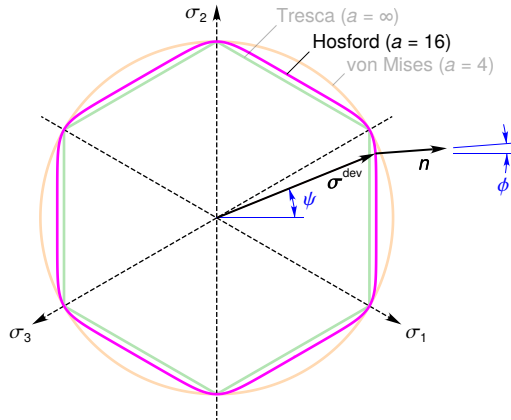


Figure 4-87. Hosford equivalent stress surface in the π -plane.

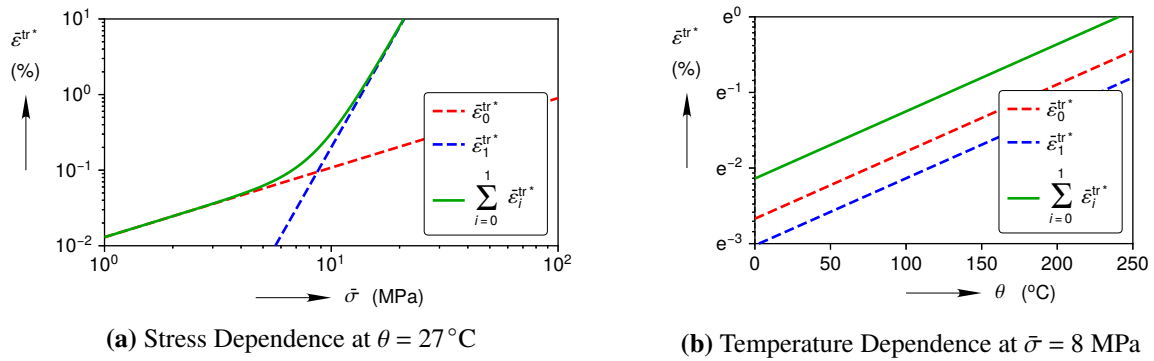


Figure 4-88. Stress and temperature dependence of the transient strain limit for Calibration 3B.

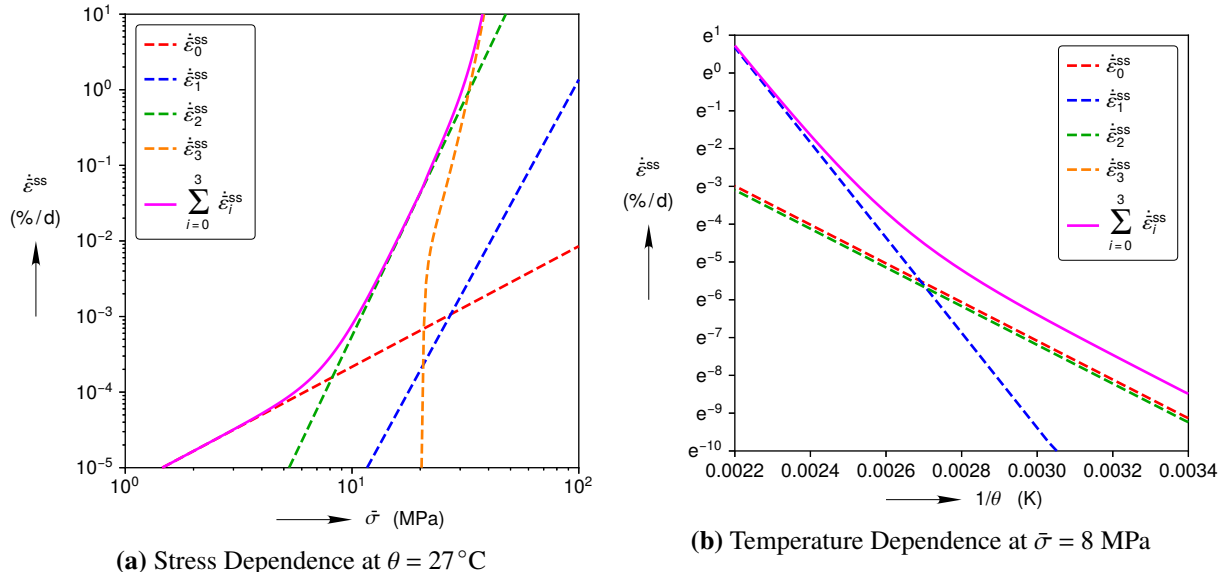


Figure 4-89. Stress and temperature dependence of the steady-state strain rate for Calibration 3B.

4.21.3.1. Triaxial Compression

Triaxial compression tests are frequently used to characterize the creep and strength behavior of geomaterials, such as rock salt. Cylindrical specimens are subjected to a radial confining pressure σ_{rr} and an axial stress σ_{zz} . Axisymmetric compression is perhaps a more appropriate name for these tests, because the hoop stress $\sigma_{\theta\theta}$ is equal to σ_{rr} , but triaxial compression is the common name.

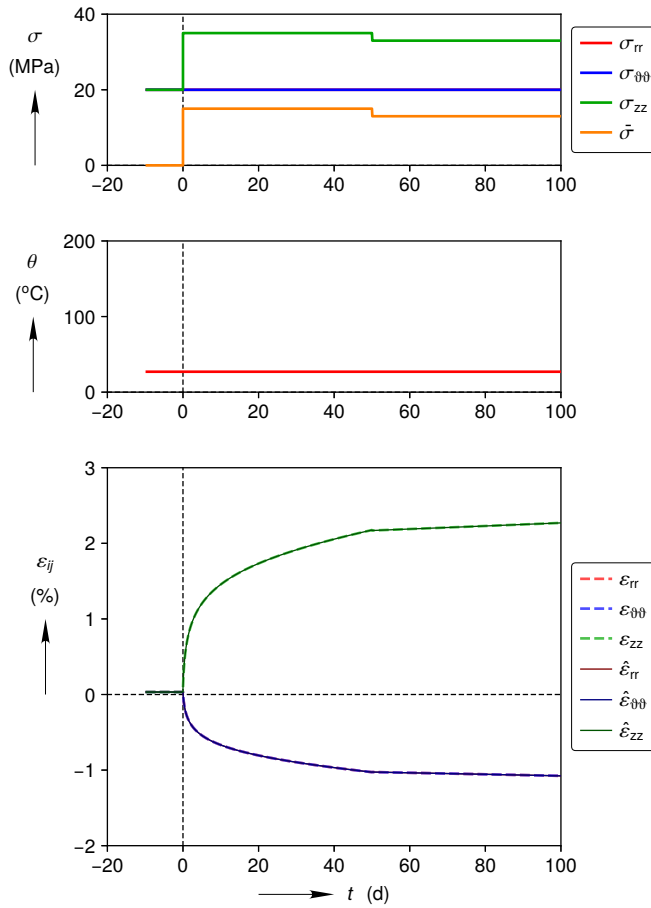


Figure 4-90. Triaxial Compression Verification Test

The applied stress and temperature histories for the test are shown in the top two plots in Fig. 4-90. The test begins with an isothermal, 20 MPa hydrostatic, hold period for 10 days, where the strain is purely elastic. At $t = 0$ d, σ_{zz} is increased to 35 MPa, while the other stresses are held fixed, causing a 15 MPa equivalent stress. This stress state is held for the next 50 days. The strain evolves quickly at first, but slows down to the steady-state rate as the material work hardens. At $t = 50$ d, σ_{zz} is decreased to 33 MPa, while the other stresses are held fixed. The 2 MPa drop in $\bar{\sigma}$ causes the strain rate to slow down markedly, but it gradually builds to a new steady-state rate as the material recovers over the next 50 days.

In summary, the numerical and analytical solutions for the total strain match very well throughout

the test, which verifies:

- Linear elasticity under triaxial compression
- Zero viscoplastic strain evolution under hydrostatic loading
- Viscoplastic strain evolution for $\psi = -30^\circ$
- Work hardening ($\bar{\varepsilon}^{\text{tr}} < \bar{\varepsilon}^{\text{tr}*}$) dominated by transient strain limit mechanism 1
- Recovery ($\bar{\varepsilon}^{\text{tr}} > \bar{\varepsilon}^{\text{tr}*}$) dominated by transient strain limit mechanism 1
- Steady-state strain accumulation dominated by transient strain limit mechanism 2.

4.21.3.2. Pure shear

The Hosford equivalent stress depends on a for $-30^\circ < \psi < 30^\circ$, but it is independent of a for $\psi = -30^\circ$ (triaxial compression) and $\psi = 30^\circ$ (triaxial extension). Pure shear is a simple stress state that exercises the Hosford stress at a Lode angle other than $\psi = \pm 30^\circ$. Pure shear can be expressed in the principal frame as $\sigma_3 = -\sigma_1$ and $\sigma_2 = 0$. In addition to exercising the model under pure shear, this test also varies the temperature to verify thermal expansion and creep at elevated temperatures.

The applied stress and temperature histories for the test are shown in the top two plots in Fig. 4-91. The test begins with a 0 MPa hydrostatic hold period for 10 days while the temperature is linearly ramped from 27°C to 57°C. Some thermal strains develop during this time. At $t = 0$ d, the temperature ramp stops, σ_1 is increased to 5 MPa, σ_2 is held at zero, and σ_3 is reduced to -5 MPa. This state is held for the next 50 days, while the material creeps. At $t = 50$ d, θ is increased to 112°C, but the stresses remain fixed. The sharp increase in θ causes a step change in thermal strain, and then accelerated creep is observed over the next 50 days.

In summary, the numerical and analytical solutions for the total strain match very well throughout the test, which verifies:

- Linear elasticity under pure shear
- Thermal expansion
- Viscoplastic strain evolution for $\psi = 0^\circ$
- Temperature dependence of transient strain limit mechanism 1
- Steady-state strain accumulation dominated by mechanism 1
- Steady-state strain accumulation dominated by mechanism 2.

4.21.3.3. Unequal Biaxial Compression

Unequal biaxial compression is another stress state that exercises the Hosford stress at a Lode angle other than $\psi = \pm 30^\circ$. Unequal compressive stresses σ_{xx} and σ_{yy} are applied to two faces of a cube, while $\sigma_{zz} = 0$. This stress state is slightly more complex than triaxial compression or pure shear because all three stress magnitudes are unequal. This test also alters the stress component

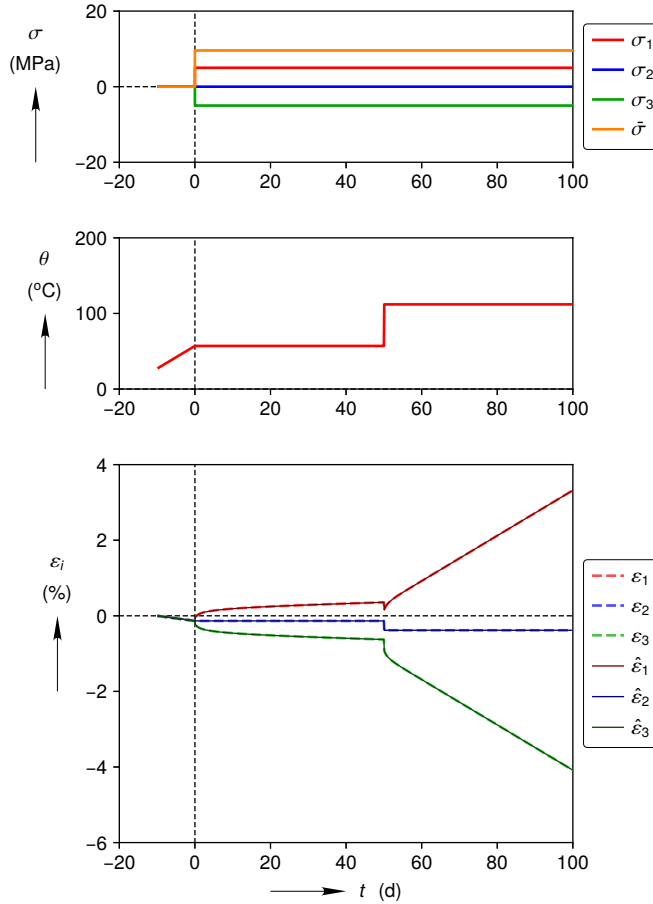


Figure 4-91. Pure Shear Verification Test

ratios after 50 days of creep to verify the model's ability to change Lode angle.

The applied stress and temperature histories for the test are shown in the top two plots in Fig. 4-92. The test begins with a stress free hold period for 10 days. At $t = 0$ d, σ_{xx} is increased to 3.5 MPa, σ_{yy} is increased to 5 MPa, and σ_{zz} is held at zero. In this stress state, $\psi = 13.0^\circ$ and the intermediate principal stress is σ_{xx} . The intermediate principal strain rate $\dot{\varepsilon}_{xx} \approx 0$ and $\dot{\varepsilon}_{yy} \approx -\dot{\varepsilon}_{zz}$ because the flow rule (4.21.6) causes $\dot{\varepsilon}^{vp}$ to be coaxial with the flow potential normal n_{ij} , and n_{ij} is nearly horizontal at $\psi = 13.0^\circ$ in Calibration 3B (see Fig. 4-87). At $t = 50$ d, σ_{xx} is increased to 6.0 MPa, while the other stresses remain fixed. The sharp increase in σ_{xx} causes a step change in elastic strain that is visible because the viscoplastic strains are small at these low values of $\bar{\sigma}$. In this stress state, $\psi = 21.1^\circ$ and the intermediate principal stress is σ_{yy} . Accordingly, $\dot{\varepsilon}_{yy} \approx 0$ and $\dot{\varepsilon}_{xx} \approx -\dot{\varepsilon}_{zz}$. If one looks more closely, however, $\dot{\varepsilon}_{yy}$ is slightly positive and $\dot{\varepsilon}_{xx} > -\dot{\varepsilon}_{zz}$ because $\psi = 21.1^\circ$ is beginning to approach the corner of the Tresca hexagon (see again Fig. 4-87).

In summary, the numerical and analytical solutions for the total strain match very well throughout the test, which verifies:

- Linear elasticity under unequal biaxial compression

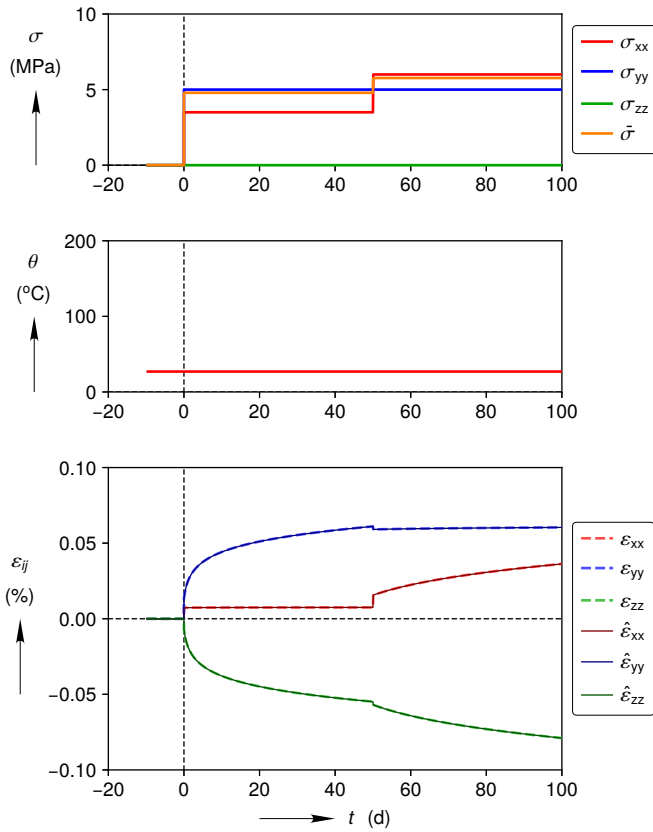


Figure 4-92. Unequal Biaxial Compression Verification Test

- Viscoplastic strain evolution for $\psi = 13.0^\circ$ and a subsequent change to $\psi = 21.1^\circ$
- Transient strain accumulation dominated by transient strain limit mechanism 0
- Steady-state strain accumulation dominated by mechanism 0.

4.21.4. User Guide

```

BEGIN PARAMETERS FOR MODEL MD_VISCOPLASTIC
  # Elastic constants
  YOUNGS MODULUS = <real> E
  POISSONS RATIO = <real> ν
  SHEAR MODULUS = <real> G
  BULK MODULUS = <real> K
  LAMBDA = <real> λ
  TWO MU = <real> 2μ
  # Steady-state creep parameters
  A0 = <real> A₀ (0.0)
  A1 = <real> A₁ (0.0)
  A2 = <real> A₂ (0.0)
  Q₀oR = <real> Q₀/R (0.0)
  Q₁oR = <real> Q₁/R (0.0)
  Q₂oR = <real> Q₂/R (0.0)
  n₀ = <real> n₀ (0.0)
  n₁ = <real> n₁ (0.0)
  n₂ = <real> n₂ (0.0)
  sigma_g = <real> σ_g
  B₀ = <real> B₀ (0.0)
  B₁ = <real> B₁ (0.0)
  B₂ = <real> B₂ (0.0)
  q = <real> q (0.0)
  # Transient creep parameters
  K₀ = <real> K₀ (0.0)
  K₁ = <real> K₁ (0.0)
  c₀ = <real> c₀ (0.0)
  c₁ = <real> c₁ (0.0)
  m₀ = <real> m₀ (0.0)
  m₁ = <real> m₁ (0.0)
  alpha_h = <real> α_h (0.0)
  alpha_r = <real> α_r (0.0)
  beta_h = <real> β_h (0.0)
  beta_r = <real> β_r (0.0)
  # Other parameters
  alpha = <real> α (0.0)
  a = <real> a (1000.0)
  # Numerical implementation parameters
  _chi = <real> χ (2.0)
  _sigma_min = <real> σ_min (μ × 10⁻¹⁰)
  _sqrt_omega_max = <real> √ω_max (10⁻¹¹)
  _xi = <real> ξ (10⁻⁴)
  _gamma = <real> γ (0.1)
  _k_max = <real> k_max (100)
  _j_max = <real> j_max (10)

```

```
END [PARAMETERS FOR MODEL MD_VISCOPLASTIC]
```

Output variables available for this model are listed in Table 4-32.

Table 4-32. State Variables for MD_VISCOPLASTIC Model

Name	Description
EQ_TR_STRAIN	equivalent transient viscoplastic strain, $\bar{\varepsilon}^{\text{tr}}$
EQ_VP_STRAIN	equivalent viscoplastic strain, $\bar{\varepsilon}^{\text{vp}}$
EQ_STRESS	equivalent stress, $\bar{\sigma}$
VP_RATE_SCALE_FACTOR	viscoplastic rate scale factor, s

REFERENCES

- [1] Darrell E Munson and PR Dawson. Constitutive model for the low temperature creep of salt (with application to WIPP). Technical Report SAND79-1853, Sandia National Laboratories, Albuquerque, NM, 1979.
- [2] Darrell E Munson and PR Dawson. Transient creep model for salt during stress loading and unloading. Technical Report SAND82-0962, Sandia National Laboratories, Albuquerque, NM, 1982.
- [3] Darrell E Munson, Arlo F Fossum, and Paul E Senseny. Advances in resolution of discrepancies between predicted and measured in situ WIPP room closures. Technical Report SAND88-2948, Sandia National Laboratories, Albuquerque, NM, 1989.
- [4] Benjamin Reedlunn. Enhancements to the munson-dawson model for rock salt. Technical Report SAND2018-12601, Sandia National Laboratories, Albuquerque, NM, 2018.
- [5] W.F. Hosford. A generalized isotropic yield criterion. *Journal of Applied Mechanics*, 39: 607–609, 1972.
- [6] Benjamin Reedlunn, James Bean, John Wilkes, and John Bignell. Simulations of criticality control overpack container compaction at the waste isolation pilot plant. Technical Report SAND2019-3106 O, Sandia National Laboratories, Albuquerque, NM, 2019.
- [7] W. M. Scherzinger. A return mapping algorithm for isotropic and anisotropic plasticity models using a line search method. *Computer Methods in Applied Mechanics and Engineering*, 317:526–553, 2017.

4.22. HYPERFOAM MODEL

4.22.1. Theory

The hyperfoam model is a hyperelastic model that can be used for modeling elastomeric foams. It is based on a strain energy with a form given by Störakers [1] which is similar to a form presented by Ogden [2]. The strain energy depends on the principal stretch ratios of the material and is given by

$$W(\lambda_k) = \sum_{i=1}^N \frac{2\mu_i}{\alpha_i^2} \left[\lambda_1^{\alpha_i} + \lambda_2^{\alpha_i} + \lambda_3^{\alpha_i} - 3 + \frac{1}{\beta_i} (J^{-\alpha_i \beta_i} - 1) \right] \quad (4.22.1)$$

where μ_i and α_i are input parameters and J is the determinant of the deformation gradient. The value of β_i is calculated from the parameters ν_i via

$$\beta_i = \frac{\nu_i}{1 - 2\nu_i}. \quad (4.22.2)$$

The ν_i can be thought of as Poisson's ratios, however in the context of the summation in (4.22.1) it is best to consider them as fitting parameters.

The strain energy (4.22.1) is a sum of N contributions. The principal Kirchoff stresses for the hyperfoam model, τ_k , can be calculated as

$$\tau_k = \lambda_k \frac{\partial W}{\partial \lambda_k} \quad (4.22.3)$$

which can be used to calculate the components of the Kirchoff stress, τ_{ij} , through

$$\tau_{ij} = \sum_{k=1}^3 \tau_k \hat{e}_i^k \hat{e}_j^k. \quad (4.22.4)$$

where \hat{e}_i^k are the components of the k^{th} eigenvector of the left stretch tensor in the global Cartesian coordinate system. The components of the Cauchy stress are then

$$\sigma_{ij} = \frac{1}{J} \tau_{ij}. \quad (4.22.5)$$

Finally, it should be noted that the Hyperfoam model is also capable of reproducing the Blatz-Ko model [3, 4]. If only one term is chosen, $N = 1$, and $\mu_1 = \mu$, $\alpha_1 = -2$, and $\nu_1 = 0.25$ we get the Blatz-Ko strain energy density

$$W = \frac{\mu}{2} \left(\frac{I_2}{I_3} + 2 \sqrt{I_3} - 5 \right) , \quad (4.22.6)$$

where I_2 and I_3 are the second and third invariants of the right Cauchy-Green tensor.

4.22.2. Implementation

The hyperfoam model is evaluated using the left stretch tensor, V_{ij} . Given the left stretch, the eigenvalues, λ_k , and eigenvectors, \hat{e}_i^k , of the stretch are calculated

$$V_{ij} \hat{e}_j^k = \lambda_k \hat{e}_i^k \quad ; \quad V_{ij} = \sum_{k=1}^3 \lambda_k \hat{e}_i^k \hat{e}_j^k. \quad (4.22.7)$$

Next, the determinant of the deformation gradient is calculated

$$J = \lambda_1 \lambda_2 \lambda_3. \quad (4.22.8)$$

Then the contribution of each term in the expansion is added to the Kirchoff stress

$$\tau_{ij}^n = \tau_{ij}^{n-1} + \lambda_1 \frac{\partial W^{(n)}}{\partial \lambda_1} \hat{e}_i^1 \hat{e}_j^1 + \lambda_2 \frac{\partial W^{(n)}}{\partial \lambda_2} \hat{e}_i^2 \hat{e}_j^2 + \lambda_3 \frac{\partial W^{(n)}}{\partial \lambda_3} \hat{e}_i^3 \hat{e}_j^3 \quad (4.22.9)$$

where $\tau_{ij}^0 = 0$ and

$$\lambda_k \frac{\partial W^{(n)}}{\partial \lambda_k} = \frac{2\mu_n}{\alpha_n} (\lambda_k^{\alpha_n} - J^{-\alpha_n \beta_n}). \quad (4.22.10)$$

After summing the terms $n = 1, \dots, N$ the Kirchoff stress is converted to the Cauchy stress using (4.22.5). If necessary the Cauchy stress is transformed back into an unrotated configuration to be returned to the host code.

4.22.3. Verification

The hyperfoam model is verified for four loading paths: uniaxial strain, biaxial strain, pure shear, and simple shear. The material parameters used for the verification tests are shown in Table 4-33. For these problems $N = 3$.

4.22.3.1. Uniaxial Strain

Since the hyperfoam model is formulated in terms of principal stretches, a uniaxial strain problem is a very simple verification problem that can be run.

In uniaxial strain, the stretch ratio in the direction of straining is $\lambda = \exp(\varepsilon)$, where ε is the applied strain. In a direction orthogonal to the direction of straining the stretch ratios are equal to one.

The determinant of the deformation gradient is $J = \lambda$.

Since the deformation is aligned with the global coordinate axes, the eigenvectors of the left stretch are also aligned with the global coordinate axes. Using the derivatives of the strain energy density given in (4.22.10), the non-zero stress components are

$$\sigma_{11} = \frac{1}{\lambda} \sum_{i=1}^N \frac{2\mu_i}{\alpha_i} (\lambda^{\alpha_i} - \lambda^{-\alpha_i\beta_i}) \quad (4.22.11)$$

$$\sigma_{22} = \sigma_{33} = \frac{1}{\lambda} \sum_{i=1}^N \frac{2\mu_i}{\alpha_i} (1 - \lambda^{-\alpha_i\beta_i})$$

The results of the analysis in tension are shown in Figures 4-93 to Figure 4-95.

For the results in Figure 4-93, a single element is strained to $\varepsilon = 0.6$ which, in uniaxial strain in tension, is very large for this model. At some point the stresses begin to increase rapidly. Since the axial stress and the lateral stresses are both very large, the pressure in uniaxial strain in tension is also very large. For this extreme loading the model in Adagio shows agreement with the analytical solution.

The model is also loaded in uniaxial compression. These results are shown in Figure 4-94. The model again shows agreement with the analytical solution. The behavior in compression is very different than tension. The maximum stress is an order of magnitude less at a strain of $\varepsilon = -0.6$, where the axial stress is just over 9 MPa, compared to $\varepsilon = 0.6$ in tension where the axial and lateral stresses are nearly 450 MPa. The lateral stresses reach a plateau while the axial stress increases. The stresses in compression also have a different nonlinear form than the stresses in tension.

Finally, both the tension and compression responses are shown in Figure 4-95. Here the continuity of the behavior at $\varepsilon = 0$ can be seen along with the very different responses in tension and compression.

μ_i	25.8 MPa	-21.9 MPa	0.0814 MPa
α_i	2.536	2.090	-8.807
ν_i	0.5630	0.5507	0.3662

Table 4-33. The material properties for the hyperfoam model tested in uniaxial strain.

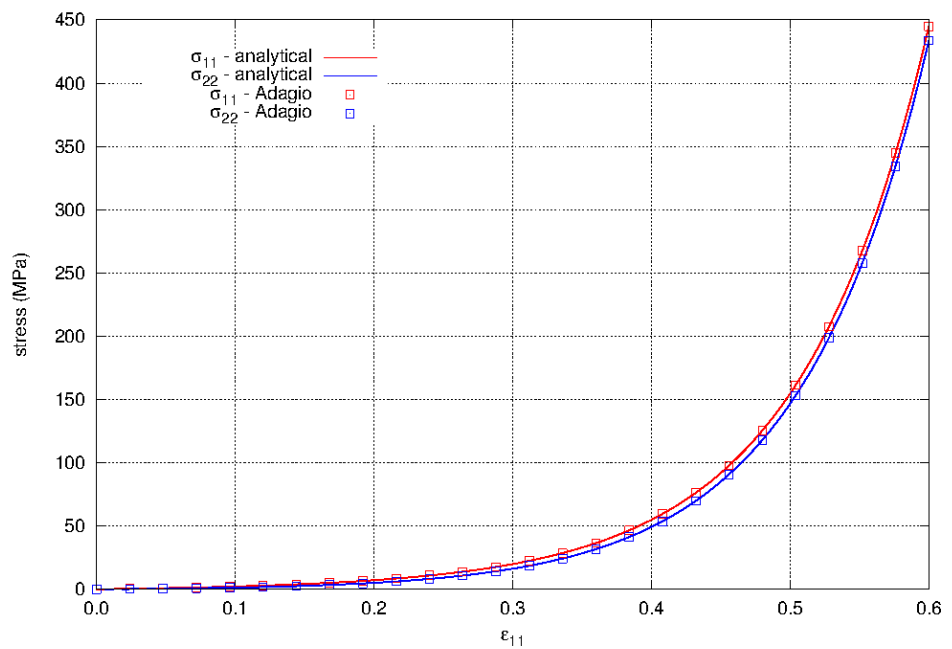


Figure 4-93. The axial and lateral stresses for uniaxial strain in tension using the hyperfoam model. The results show agreement with the analytical results. The material properties for the model are given in Table 4-33.

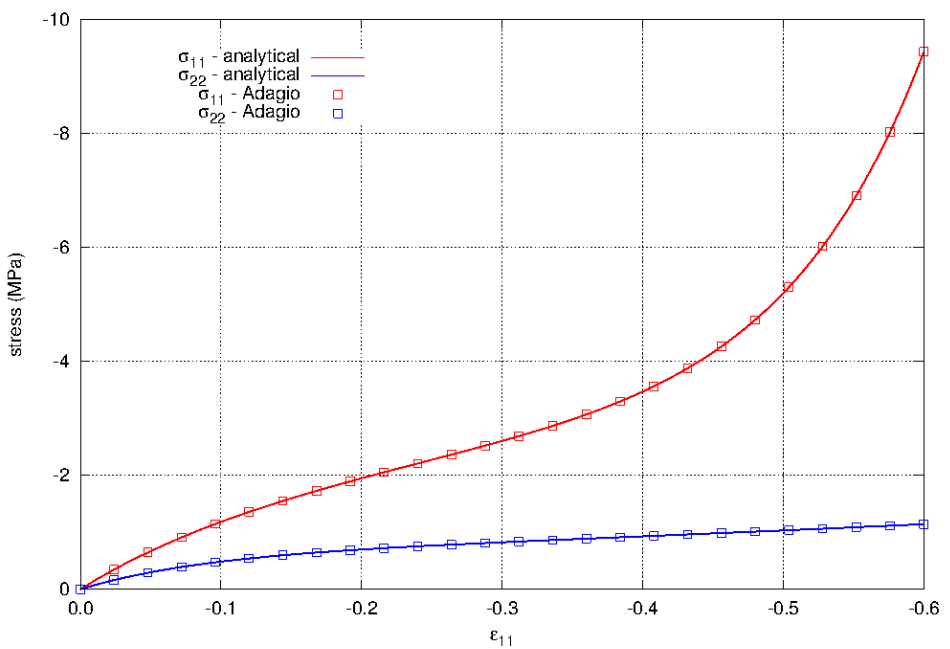


Figure 4-94. The axial and lateral stresses for uniaxial strain in compression using the hyperfoam model. The results show agreement with the analytical results. The material properties for the model are given in Table 4-33.

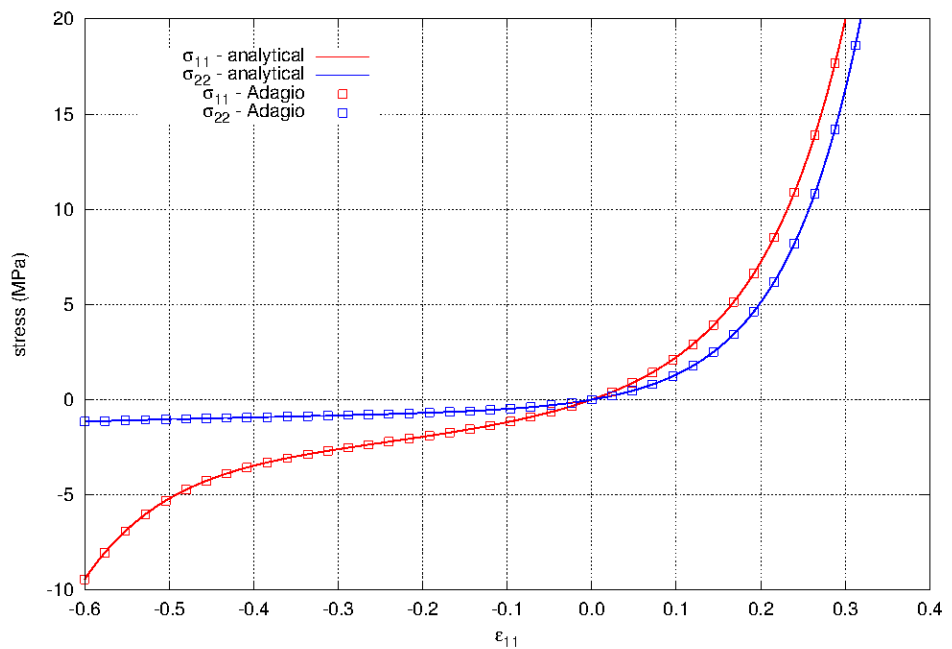


Figure 4-95. The axial and lateral stresses for uniaxial strain in both tension and compression using the hyperfoam model. The results show agreement with the analytical results and that the response of the material is very different in tension and compression. The material properties for the model are given in Table 4-33.

4.22.3.2. Biaxial Strain

Another simple verification problem for the hyperfoam model is biaxial strain.

In biaxial strain, the stretch ratios are prescribed in two orthogonal directions. For this $\lambda_1 = \exp(\varepsilon_1)$ and $\lambda_2 = \exp(\varepsilon_2)$, where ε_i are the applied strains in the x_1 and x_2 directions. In the third direction orthogonal to the first two, the stretch ratio is one. The determinant of the deformation gradient is $J = \lambda_1 \lambda_2$.

$$\begin{aligned}\sigma_{11} &= \frac{1}{\lambda_1 \lambda_2} \sum_{i=1}^N \frac{2\mu_i}{\alpha_i} [\lambda_1^{\alpha_i} - (\lambda_1 \lambda_2)^{-\alpha_i \beta_i}] \quad ; \quad \sigma_{22} = \frac{1}{\lambda_1 \lambda_2} \sum_{i=1}^N \frac{2\mu_i}{\alpha_i} [\lambda_2^{\alpha_i} - (\lambda_1 \lambda_2)^{-\alpha_i \beta_i}] \\ \sigma_{33} &= \frac{1}{\lambda_1 \lambda_2} \sum_{i=1}^N \frac{2\mu_i}{\alpha_i} [1 - (\lambda_1 \lambda_2)^{-\alpha_i \beta_i}]\end{aligned}\quad (4.22.12)$$

The results of the analysis in tension are shown in Figures 4-96 to Figure 4-98.

For the results in Figure 4-96, a single element is strained with $\varepsilon_1 = 0.4$ and $\varepsilon_2 = 0.2$ which, in biaxial strain in tension, is very large for this model. At some point the normal stresses begin to increase rapidly. Since the normal stresses are very large, the hydrostatic pressure is also very large. For this extreme loading the model in Adagio shows agreement with the analytical solution.

The model is also loaded in biaxial compression. These results are shown in Figure 4-97. The model again shows agreement with the analytical solution. The behavior in compression is very different than tension. The maximum stress is orders of magnitude less at a strain of $\varepsilon_1 = -0.4$ and $\varepsilon_2 = -0.3$, where the maximum normal stress is just over 4.5 MPa, compared to $\varepsilon_1 = 0.4$ and $\varepsilon_2 = 0.3$ in tension where the normal stresses from the model are nearly 1.3 GPa. The lateral stress σ_{zz} reaches a plateau while the other two stress increase with increased straining. The stresses in compression also have a different nonlinear form than the stresses in tension.

Finally, both the tension and compression responses are shown in Figure 4-98. Here the continuity of the behavior at $\varepsilon = 0$ can be seen along with the very different responses in tension and compression.

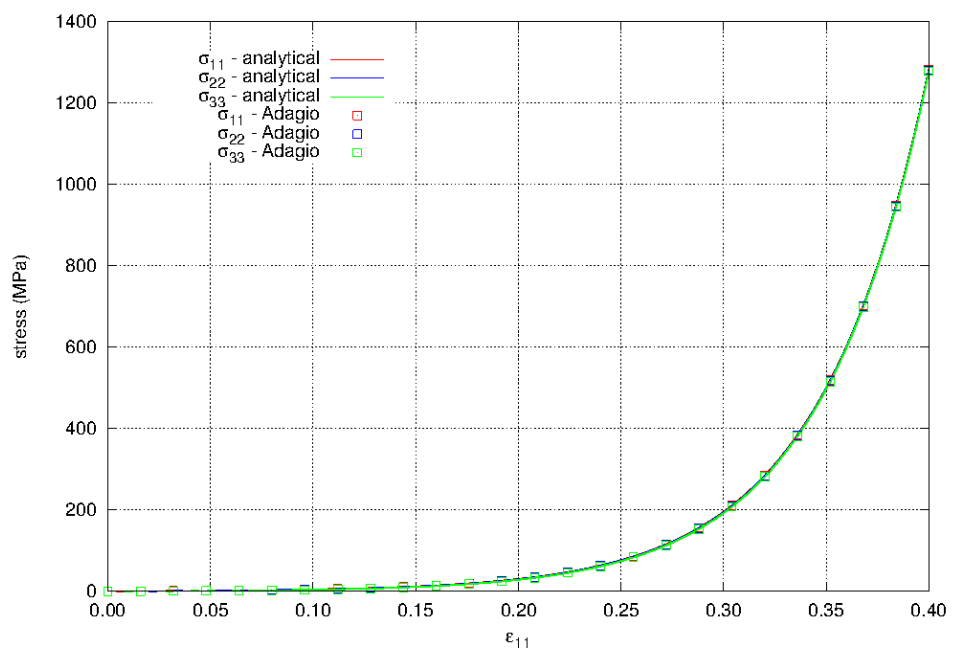


Figure 4-96. The normal stresses for biaxial strain in tension using the hyperfoam model. The results show agreement with the analytical results. The material properties for the model are given in Table 4-33.

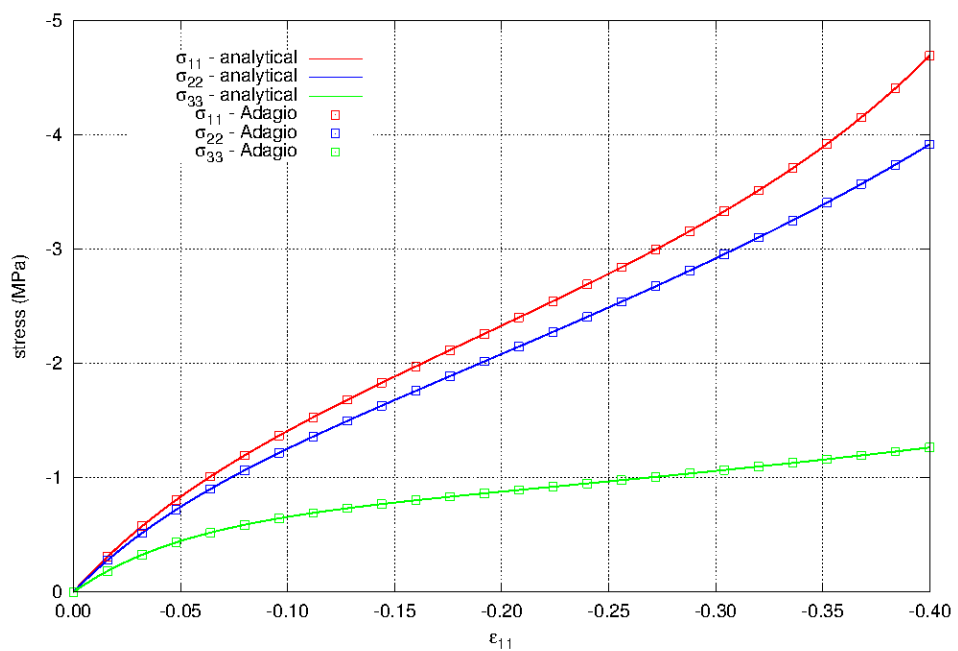


Figure 4-97. The normal stresses for biaxial strain in compression using the hyperfoam model. The results show agreement with the analytical results. The material properties for the model are given in Table 4-33.

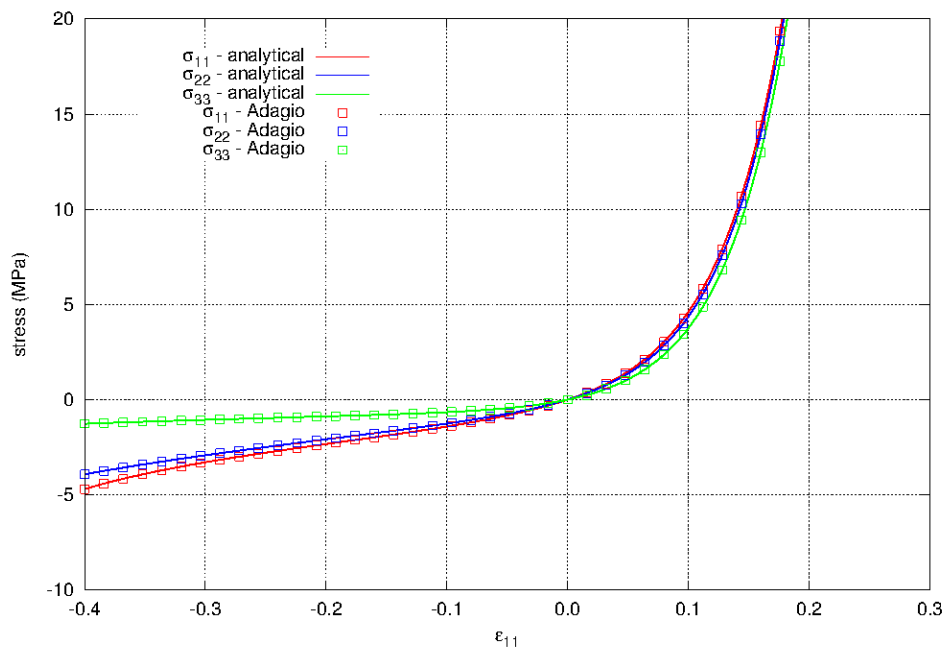


Figure 4-98. The normal stresses for biaxial strain in both tension and compression using the hyperfoam model. The results show agreement with the analytical results and that the response of the material is very different in tension and compression. The material properties for the model are given in Table 4-33.

4.22.3.3. Pure Shear

The hyperfoam model is also tested in pure shear in strain. Note that this is different from pure shear in stress.

In pure shear, the principal stretch ratios are $\lambda_1 = \lambda$, $\lambda_2 = 1$, and $\lambda_3 = \lambda^{-1}$. The determinant of the deformation gradient is $J = 1$, which means the Kirchhoff and Cauchy stress measures are the same.

The principal stresses are

$$\sigma_1 = \sum_{i=1}^N \frac{2\mu_i}{\alpha_i} (\lambda^{\alpha_i} - 1) \quad ; \quad \sigma_2 = 0 \quad ; \quad \sigma_3 = \sum_{i=1}^N \frac{2\mu_i}{\alpha_i} (\lambda^{-\alpha_i} - 1) \quad (4.22.13)$$

The principal axes of deformation are aligned at 45° to the coordinate axes. In the global coordinate system the non-zero stress components are

$$\begin{aligned} \sigma_{11} = \sigma_{22} &= \sum_{i=1}^N \frac{2\mu_i}{\alpha_i} (\lambda^{\alpha_i} + \lambda^{-\alpha_i} - 2) \\ \sigma_{12} &= \sum_{i=1}^N \frac{2\mu_i}{\alpha_i} (\lambda^{\alpha_i} - \lambda^{-\alpha_i}) \end{aligned} \quad (4.22.14)$$

The results of the analysis in pure shear are shown in Figure 4-99. A single element is strained to a shear strain of $\varepsilon = 0.4$. The model in Adagio shows agreement with the analytical solution presented above. It is interesting to note that pure shear strain produces not only normal stresses with the hyperfoam model, but a non-zero pressure. The deviatoric/volumetric split so often used with our constitutive model does not occur with the hyperfoam model.

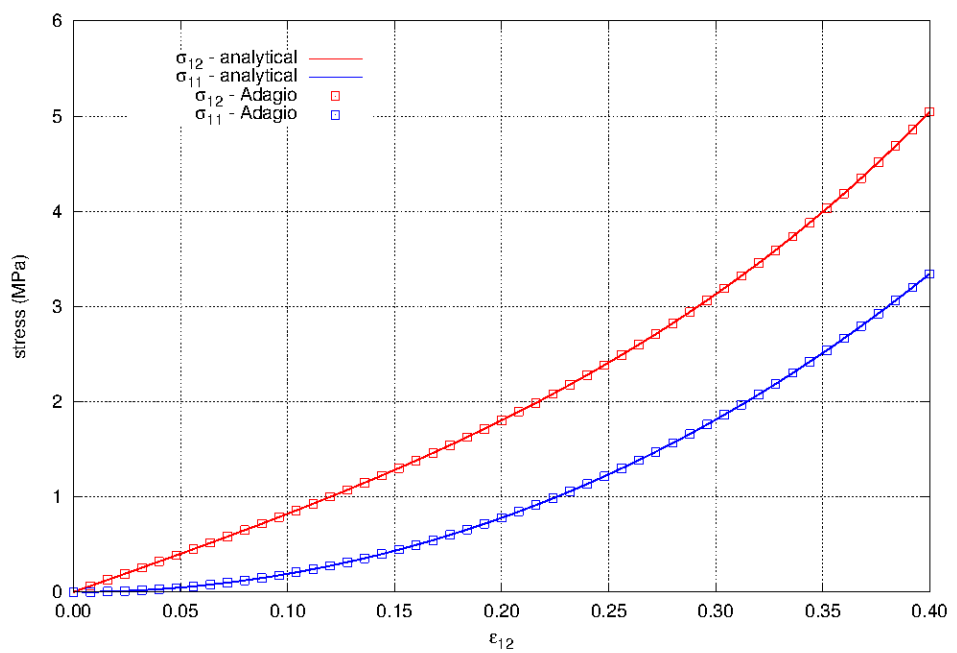


Figure 4-99. The shear and normal stresses for the hyperfoam model in pure shear. The material properties for the model are given in Table 4-33.

4.22.3.4. Simple Shear

The hyperfoam model is also tested in simple shear. Note that this is a different deformation path than pure shear. In simple shear the deformation gradient is

$$[F_{ij}] = \begin{bmatrix} 1 & \gamma & 0 \\ 0 & 1 & 0 \\ 0 & 0 & 1 \end{bmatrix} \quad (4.22.15)$$

The principal stretch ratios are $\lambda_1 = \lambda$, $\lambda_2 = 1$, and $\lambda_3 = \lambda^{-1}$. The determinant of the deformation gradient is $J = 1$, which means the Kirchhoff and Cauchy stress measures are the same. This gives the *same* principal stresses as in pure shear when written in terms of the principal stretch ratio, λ . The principal stresses are

$$\sigma_1 = \sum_{i=1}^N \frac{2\mu_i}{\alpha_i} (\lambda^{\alpha_i} - 1) \quad ; \quad \sigma_2 = 0 \quad ; \quad \sigma_3 = \sum_{i=1}^N \frac{2\mu_i}{\alpha_i} (\lambda^{-\alpha_i} - 1) \quad (4.22.16)$$

The principal stretch ratio is

$$\lambda = \frac{1 + \sin \theta}{\cos \theta} \quad ; \quad \theta = \tan^{-1} \left(\frac{\gamma}{2} \right) \quad (4.22.17)$$

The principal axes of deformation in the current configuration, i.e. the eigenvectors of the left stretch, are given by

$$\hat{e}_i^1 = \cos \phi e_i^1 + \sin \phi e_i^2 \quad ; \quad \hat{e}_i^2 = e_i^3 \quad ; \quad \hat{e}_i^3 = -\sin \phi e_i^1 + \cos \phi e_i^2 \quad (4.22.18)$$

where $\phi = \pi/4 - \theta/2$.

The results of the analysis in simple shear are shown in Figure 4-100. A single element is strained to a shear parameter of $\gamma = 0.4$. The model in Adagio shows agreement with the analytical solution presented above. It is interesting to note that simple shear with the hyperfoam model produces different normal stresses than simple shear, i.e. the two non-zero normal stresses are not equal. The difference arises from the fact that the principal axes of deformation in pure shear are fixed, while in simple shear the principal axes rotate. There is still a non-zero pressure which again shows that the deviatoric/volumetric split does not occur with the hyperfoam model.

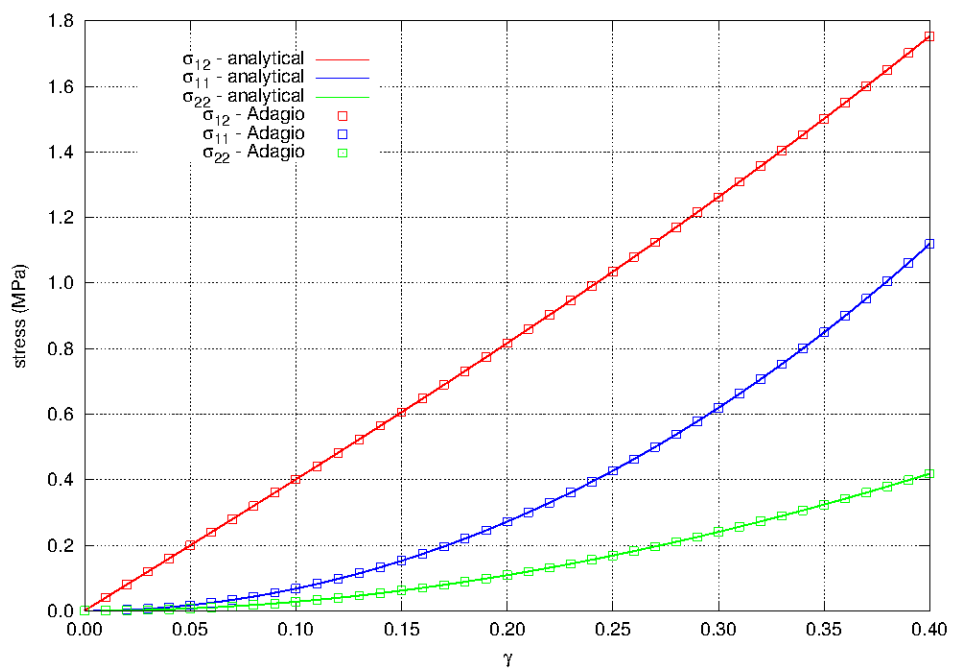


Figure 4-100. The shear and normal stresses for the hyperfoam model in simple shear. The material properties for the model are given in Table 4-33.

4.22.4. User Guide

```
BEGIN PARAMETERS FOR MODEL HYPERFOAM
#
# Elastic constants
#
YOUNGS MODULUS = <real> E
POISSONS RATIO = <real> ν
SHEAR MODULUS = <real> G
BULK MODULUS = <real> K
LAMBDA = <real> λ
TWO MU = <real> 2μ
#
# Strain energy density
#
N = <integer> N
SHEAR = <real_list> μi
ALPHA = <real_list> αi
POISSON = <real_list> νi
END [PARAMETERS FOR HYPERFOAM]
```

There are no output variables available for this model.

REFERENCES

- [1] B. Störakers. On material representation and constitutive branching in finite compressible elasticity. *Journal of the Mechanics and Physics of Solids*, 34:125–145, 1986.
- [2] R. W. Ogden. *Non-Linear Elastic Deformaitons*. Dover, New York, 1984.
- [3] P. J. Blatz and W. L. Ko. Application of finite elasticity theory to the deformation of rubbery materials. *Transactions of the Society of Rheology*, 6:223–251, 1962.
- [4] G. Bolzon and R. Vitaliani. The blatz-ko model and homogenization. *Archive of Applied Mechanics*, 63:228–241, 1993.

4.23. HYPERELASTIC DAMAGE MODEL

4.23.1. Theory

The hyperelastic damage model is an isotropic, strain rate and temperature independent continuum damage formulation. In this case, the specific form is that discussed by Holzapfel [1] and proposed primarily for particulate reinforced (filled) rubber-like materials exhibiting the so called Mullins effect. Specifically, this model utilizes a Kachanov-like effective stress concept to propose an *effective* Helmholtz free energy, W , of the form

$$W = (1 - \zeta) W_0 (C_{ij}), \quad (4.23.1)$$

in which $\zeta = [0, 1]$ is the isotropic damage variable and W_0 is the Helmholtz free energy of the *undamaged* material and C_{ij} is the right Cauchy-Green tensor ($C_{ij} = F_{ki}F_{kj}$ with F_{ij} the deformation gradient). The free energy expression of the neo-Hookean model (Section 4.5) is used to describe the undamaged strain energy and is given as,

$$W_0 (C_{ij}) = \frac{1}{2} K \left[\frac{1}{2} (J^2 - 1) - \ln J \right] + \frac{1}{2} \mu (\bar{C}_{kk} - 3), \quad (4.23.2)$$

with K and μ the bulk and shear moduli, J the determinant of the deformation gradient and \bar{C}_{kk} the isochoric part of the deformation – $\bar{C}_{ij} = \bar{F}_{ki}\bar{F}_{kj}$ and $\bar{F}_{ij} = J^{-1/3}F_{ij}$. In the undamaged configuration, the second Piola-Kirchoff stress, S_{ij}^0 , is the energetic conjugate of the right Cauchy-Green strain such that

$$S_{ij}^0 = 2 \frac{\partial W_0}{\partial C_{ij}}, \quad (4.23.3)$$

leading to a *damaged* stress of the form,

$$S_{ij} = (1 - \zeta) S_{ij}^0. \quad (4.23.4)$$

To describe the softening process, two damage related variables are needed. The first is the previously mentioned smooth, continuous effective damage variable, ζ , while the second is the so-called discontinuous damage variable, α . In essence, this second variable may be considered to be the maximum strain energy in the undamaged material throughout the entire loading history. This statement may be expressed as,

$$\alpha = \max_{s \in [0, t]} W_0(s), \quad (4.23.5)$$

in which s is a history variable representing any time in the loading history and the dependence on s in (4.23.5) is used to indicate the loading history and not an explicit dependence on time or

strain rate. The two damage terms are related by assuming $\zeta = \zeta(\alpha)$. To ascertain this dependence, it is noted that $\zeta(0) = 0$ and $\zeta(\infty) = 1$ the former explicitly stating that the material is initially undamaged and the latter noting in the limit the material is completely damaged the strain energy will go to ∞ . These observations lead to an expression of the form,

$$\zeta(\alpha) = \zeta_\infty [1 - \exp(-\alpha/\tau)], \quad (4.23.6)$$

with τ being a constant referred to as the damage saturation parameter and ζ_∞ being the maximum value of the damage parameter that may be achieved.

The evolution of the damage process is governed by a so-called damage function, $f(C_{ij}, \alpha)$ (analogous to the yield function in plasticity), postulated as,

$$f(C_{ij}, \alpha) = \phi(C_{ij}) - \alpha, \quad (4.23.7)$$

where ϕ is the thermodynamic driving of the damage process. In this case, the thermodynamic conjugate of the damage variable ζ is the undamaged strain energy, W_0 , such that $\phi(C_{ij}) = W_0(C_{ij})$. By enforcing the consistency condition during damage ($\dot{f} = 0$), it can be shown that,

$$\dot{\alpha} = \dot{\phi} = \frac{\partial W_0}{\partial C_{ij}} \dot{C}_{ij} = \frac{1}{2} S_{ij}^0 \dot{C}_{ij}. \quad (4.23.8)$$

4.23.2. Implementation

For the hyperelastic damage model, the first step is to calculate the undamaged second Piola-Kirchoff stress, $S_{ij}^{0(n+1)}$ of the current $(n+1)^{th}$ time step. To this end, the deformation gradient, $F_{ij}^{(n+1)}$, is calculated based on the input stretch, $V_{ij}^{(n+1)}$, and rotation, $R_{ij}^{(n+1)}$, tensors via the polar decomposition. The second Piola-Kirchoff stress may then be determined as,

$$S_{ij}^{0(n+1)} = \left[\frac{1}{2} K \left((J^{(n+1)})^2 - 1 \right) I_{il} + \mu (J^{(n+1)})^{-2/3} \left(C_{il}^{(n+1)} - \frac{1}{3} C_{kk}^{(n+1)} I_{il} \right) \right] \left(C_{jl}^{(n+1)} \right)^{-1}. \quad (4.23.9)$$

To determine the damage state, the undamaged strain energy $W_0^{(n+1)}$, is first calculated as,

$$W_0^{(n+1)} = \frac{1}{2} K \left(\frac{1}{2} \left((J^{(n+1)})^2 - 1 \right) - \ln J^{(n+1)} \right) + \frac{1}{2} \mu \left[(J^{(n+1)})^{-2/3} C_{kk}^{(n+1)} - 3 \right]. \quad (4.23.10)$$

The current discrete damage variable, $\alpha^{(n+1)}$, may then be determined via,

$$\alpha^{(n+1)} = \max \left[\alpha^{(n)}, W_0^{(n+1)} \right], \quad (4.23.11)$$

so that the current continuous damage variable, $\zeta^{(n+1)}$, is,

$$\zeta^{(n+1)} = \zeta_\infty \left[1 - \exp \left(\alpha^{(n+1)} / \tau \right) \right]. \quad (4.23.12)$$

Finally, these expressions lead to an unrotated Cauchy stress of the form,

$$T_{ij}^{(n+1)} = \frac{1}{J^{(n+1)}} (1 - \zeta^{(n+1)}) R_{ki}^{(n+1)} F_{km}^{(n+1)} S_{mn}^{0(n+1)} F_{rn}^{(n+1)} R_{rj}^{(n+1)}. \quad (4.23.13)$$

4.23.3. Verification

Given the hyperelastic formulation of the hyperelastic damage model, it is possible to find closed form solutions for simple loadings. Two such instances (uniaxial strain and simple shear) are considered here to evaluate and verify the response of this implementation. In this case, the results explored here are extensions of the neo-Hookean verification tests previously discussed in Section 4.5.3 and [2]. One set of material properties was used for all tests and they are given in Table 4-34. The damage parameters are taken from [1].

K	0.5 MPa	μ	0.375 MPa
ζ_∞	0.8	τ	0.3 MPa

Table 4-34. The material properties for the hyperelastic damage model used for both the uniaxial and simple shear tests.

4.23.3.1. Uniaxial Strain

First, utilizing a displacement condition corresponding to uniaxial strain results in a deformation gradient of the form,

$$F_{ij} = \lambda \delta_{1i} \delta_{1j} + \delta_{2i} \delta_{2j} + \delta_{3i} \delta_{3j}. \quad (4.23.14)$$

As the undamaged material is neo-Hookean, it is noted that the under these loading conditions the stress field is found by evaluating relation (4.5.3) and may be written as

$$\begin{aligned} \sigma_{11}^0 &= \frac{1}{2} K \left(\lambda - \frac{1}{\lambda} \right) + \frac{2}{3} \mu (\lambda^2 - 1) \lambda^{-5/3}, \\ \sigma_{22}^0 = \sigma_{33}^0 &= \frac{1}{2} K \left(\lambda - \frac{1}{\lambda} \right) - \frac{1}{3} \mu (\lambda^2 - 1) \lambda^{-5/3}, \\ \sigma_{12}^0 = \sigma_{23}^0 = \sigma_{31}^0 &= 0. \end{aligned} \quad (4.23.15)$$

The damaged, effective stresses are then simply $\sigma_{ij} = (1 - \zeta) \sigma_{ij}^0$ and the problem reduces to the determination of ζ . In this case, given the deformation gradient in (4.23.14), $J = \lambda$ and

$$W_0 = \frac{1}{2}K \left[\frac{1}{2} (\lambda^2 - 1) - \ln \lambda \right] + \frac{1}{2}\mu \left[\lambda^{-2/3} (\lambda^2 + 2) - 3 \right]. \quad (4.23.16)$$

During loading, $\alpha = W_0$ while during unloading $\alpha = W_0(\lambda^{\max})$ and ζ can be determined from (4.23.6).

Both the corresponding analytical and numerical solutions are presented in Figure 4-101 for a complete loading and unloading cycle. Note, the damage parameter, ζ , increases during loading but remains constant during unloading verifying the irreversibility of the proposed model.

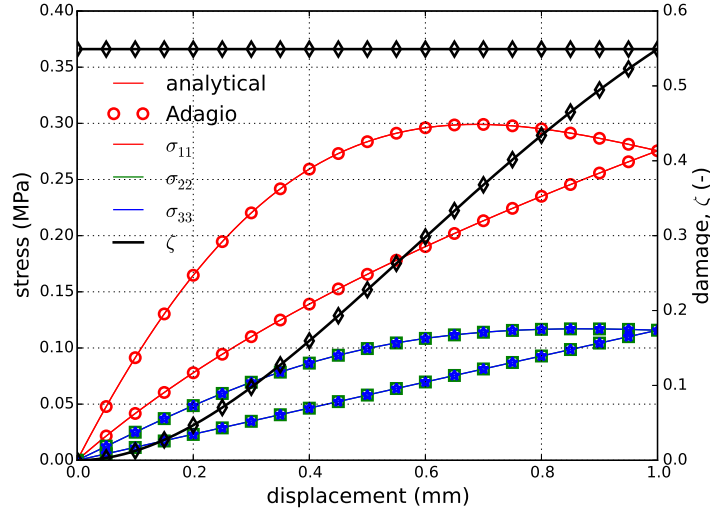


Figure 4-101. Analytical and numerical results of the stress and damage state for the uniaxial stretch case.

4.23.3.2. Simple Shear

For the simple shear case, a deformation gradient of the form,

$$F_{ij} = \delta_{ij} + \gamma \delta_{1i} \delta_{2j}, \quad (4.23.17)$$

is prescribed. Again, from the neo-Hookean model definitions the undamaged stresses may be determined via (4.5.3) and noting this is a volume preserving definition ($J = 1$) leading to expressions of the form,

$$\begin{aligned}
\sigma_{11}^0 &= \frac{2}{3}\mu\gamma^2, \\
\sigma_{22}^0 = \sigma_{33}^0 &= -\frac{1}{3}\mu\gamma^2, \\
\sigma_{12}^0 &= \mu\gamma, \\
\sigma_{23}^0 = \sigma_{31}^0 &= 0.
\end{aligned} \tag{4.23.18}$$

In this case, the undamaged strain energy is simply,

$$W_0 = \frac{1}{2}\mu\gamma^2, \tag{4.23.19}$$

and ζ may be evaluated via (4.23.6). The effective stresses are then $\sigma_{ij} = (1 - \zeta)\sigma_{ij}^0$

Both the corresponding analytical and numerical solutions are presented in Figure. 4-102 for a complete loading and unloading cycle. Note, the damage parameter, ζ , increases during loading but remains constant during unloading given the irreversible form of the damage process.

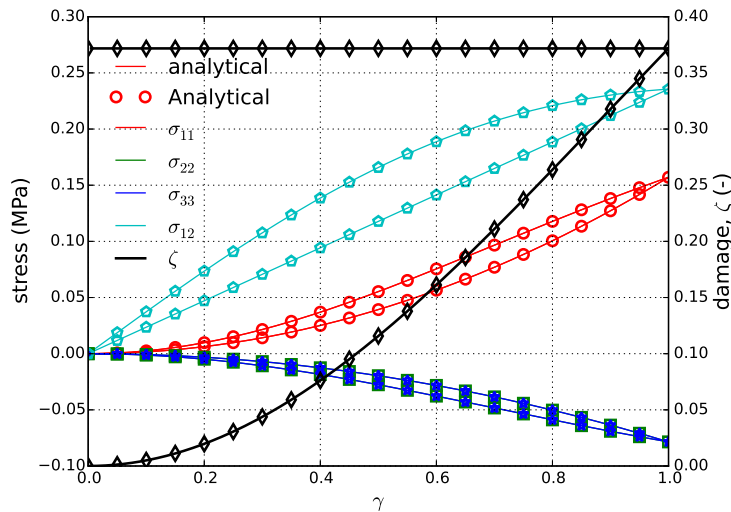


Figure 4-102. Analytical and numerical results of the stress and damage state for the simple shear case.

4.23.4. User Guide

```
BEGIN PARAMETERS FOR MODEL HYPERELASTIC_DAMAGE
#
# Elastic constants
#
YOUNGS MODULUS = <real> E
POISONS RATIO = <real> ν
SHEAR MODULUS = <real> G
BULK MODULUS = <real> K
LAMBDA = <real> λ
TWO MU = <real> 2μ
#
DAMAGE MAX = <real> ζ∞
DAMAGE SATURATION = <real> τ
END [PARAMETERS FOR MODEL HYPERELASTIC_DAMAGE]
```

Output variables available for this model are listed in Table 4-35. For information about the hyperelastic damage model, consult [1].

Table 4-35. State Variables for HYPERELASTIC DAMAGE Model

Name	Description
DAMAGE	continuous isotropic damage variable, ζ
ALPHA	discontinuous damage variable, α
PRESSURE	reference undamaged tensile pressure, $(1/3)(1 - \zeta)S_{kk}$

REFERENCES

- [1] G. A. Holzapfel. *Nonlinear Solid Mechanics: A Continuum Approach For Engineering*. John Wiley & Sons, Ltd, 2000.
- [2] W.M. Scherzinger and D.C. Hammerand. Testing of constitutive models in LAME. Technical Report SAND2007-5872, Sandia National Laboratories, Albuquerque, NM, September 2007. [pdf](#).

4.24. SOIL AND FOAM MODEL

4.24.1. Theory

The soil and crushable foam model is a plasticity model that can be used for modeling soil, crushable foam, or other highly compressible materials. Given the right input, the model is a Drucker-Prager model.

For the soil and crushable foam model, the yield surface is a surface of revolution about the hydrostat in principal stress space. A planar end cap is assumed for the yield surface so that the yield surface is closed. The yield stress σ_{yd} is specified as a polynomial in pressure p . The yield stress is given as:

$$\sigma_{yd} = a_0 + a_1 p + a_2 p^2, \quad (4.24.1)$$

where the pressure p is positive in compression. The determination of the yield stress from Equation (4.24.1) places severe restrictions on the admissible values of a_0 , a_1 , and a_2 . There are three valid cases for the yield surface. In the first case, there is an elastic–perfectly plastic deviatoric response, and the yield surface is a cylinder oriented along the hydrostat in principal stress space. In this case, a_0 is positive, and a_1 and a_2 are zero. In the second case, the yield surface is conical. A conical yield surface is obtained by setting a_2 to zero and using appropriate values for a_0 and a_1 . In the third case, the yield surface has a parabolic shape. For the parabolic yield surface, all three coefficients in Equation (4.24.1) are nonzero. The coefficients are checked to determine that a valid negative tensile-failure pressure can be derived based on the specified coefficients.

For the case of the cylindrical yield surface (e.g., $a_0 > 0$ and $a_1 = a_2 = 0$), there is no tensile-failure pressure. For the other two cases, the computed tensile-failure pressure may be too low. To handle the situations where there is no tensile-failure pressure or the tensile-failure pressure is too low, a pressure cutoff can be defined. If a pressure cutoff is defined, the tensile-failure pressure is the larger of the computed tensile-failure pressure and the defined cutoff pressure.

The plasticity theories for the volumetric and deviatoric parts of the material response are completely uncoupled. The volumetric response is computed first. The mean pressure p is assumed to be positive in compression, and a yield function ϕ_p is written for the volumetric response as:

$$\phi_p = p - f_p(\varepsilon_V), \quad (4.24.2)$$

where $f_p(\varepsilon_V)$ defines the volumetric stress-strain curve for the pressure. The yield function ϕ_p determines the motion of the end cap along the hydrostat.

4.24.2. Implementation

The soil and crushable foam model is a rate-independent, hypoelastic model that splits and sequentially evaluates the volumetric and deviatoric response. To determine the inelastic flow, an elastic predictor-inelastic corrector approach is adopted for each of the aforementioned responses.

For the volumetric response, an updated logarithmic volume strain, ε_v^{n+1} , is computed by,

$$\varepsilon_v^{n+1} = \varepsilon_v^n - \Delta t d_{kk}. \quad (4.24.3)$$

Note, in this case, the volume strain is defined such that it is positive in compression. This strain value is then used to evaluate the volumetric yield function defined in (4.24.2) and determine the appropriate pressure, p , the material is subject to.

To evaluate the deviatoric response, a trial deviatoric stress, s_{ij}^{tr} , is defined as,

$$s_{ij}^{tr} = s_{ij}^n + 2\mu \hat{d}_{ij} \Delta t, \quad (4.24.4)$$

with \hat{d}_{ij} being the deviatoric part of the unrotated rate of deformation. The deviatoric yield function, f , is then used to evaluate if any deviatoric plastic flow is occurring and is written as,

$$f(s_{ij}, p) = \phi(s_{ij}) - \sigma_{yd}(p), \quad (4.24.5)$$

where σ_{yd} is the yield stress given in (4.24.1) and $\phi(s_{ij})$ the effective stress given as,

$$\phi(s_{ij}) = \sqrt{\frac{3}{2} s_{ij} s_{ij}}. \quad (4.24.6)$$

If an elastic response is evident ($f \leq 0$), then the final stress is simply,

$$T_{ij}^{n+1} = s_{ij}^{tr} - p \delta_{ij}. \quad (4.24.7)$$

Otherwise, if a plastic response is observed, a radial return approach like that discussed in Section 4.7.2 is utilized to find the equivalent plastic strain increment, $\Delta \bar{\varepsilon}^p$. Unlike that case, given the decoupling between the volumetric and deviatoric behaviors, the hardening component of the yield surface does not change leading to an expression of the form,

$$\Delta \bar{\varepsilon}^p = \frac{f}{3\mu}, \quad (4.24.8)$$

and the final stress is,

$$T_{ij}^{n+1} = s_{ij}^{tr} - 3\mu\Delta\bar{\varepsilon}^p \frac{s_{ij}^{tr}}{\phi} - p\delta_{ij}. \quad (4.24.9)$$

4.24.3. Verification

The soil and foam model is verified for a triaxial compression load path. First the material is biaxially loaded in plane strain using load control, then the prescribed loads are released while the material is compressed in displacement control.

4.24.3.1. *Triaxial Compression*

The soil and foam model is tested in triaxial compression. For this problem, both lateral stresses, σ_{11} and σ_{33} , are prescribed along with the axial strain, ε_{22} . Furthermore, the lateral stresses are equal, $\sigma_{11} = \sigma_{33}$. For the elastic response, the axial stress is

$$\sigma_{22} = E\varepsilon_{22} + 2\nu\sigma_{11} \quad (4.24.10)$$

where E is the elastic modulus and ν is the Poisson's ratio. The lateral strains are

$$\varepsilon_{11} = -\nu(\varepsilon_{22} - \sigma_{11}/\lambda) \quad (4.24.11)$$

where λ is the Lamé constant.

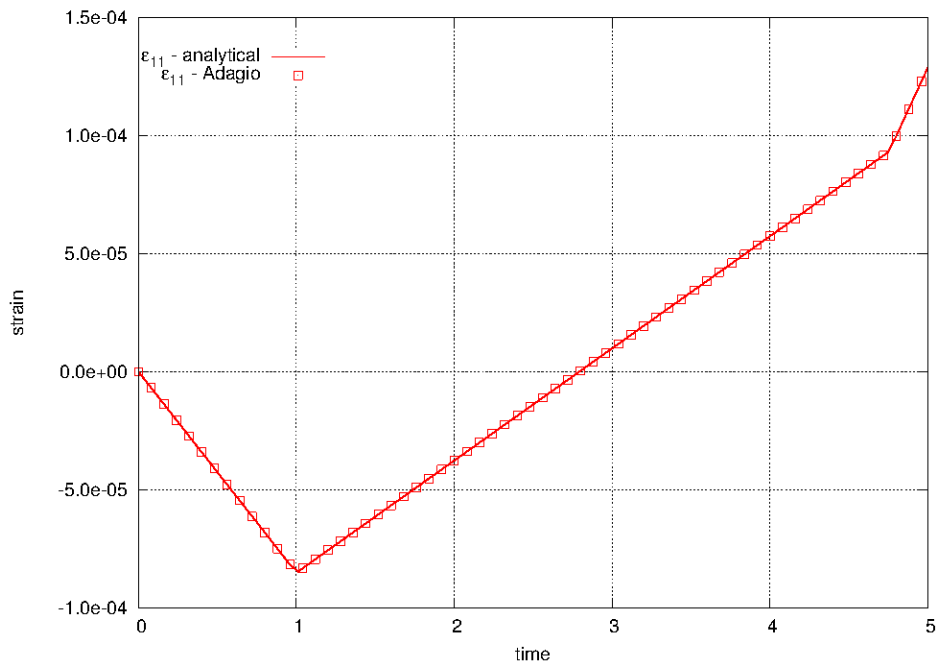


Figure 4-103. Lateral strain, ε_{11} and ε_{33} , over the course of the prescribed triaxial loading path.

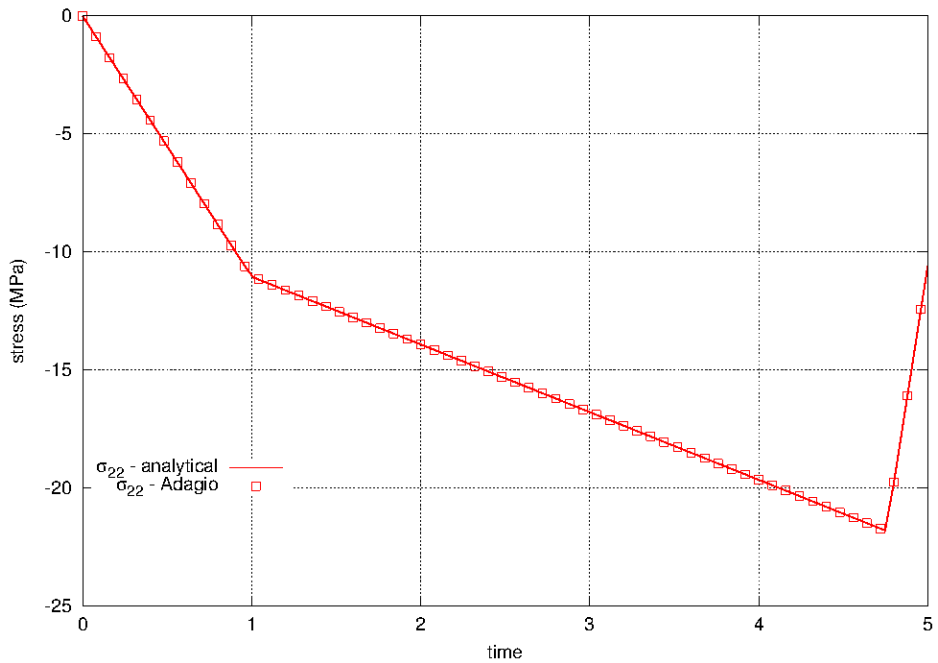


Figure 4-104. Axial stress, σ_{22} , over the course of the prescribed triaxial loading path.

4.24.4. User Guide

```

BEGIN PARAMETERS FOR MODEL SOIL_FOAM
#
# Elastic constants
#
YOUNGS MODULUS = <real> E
POISSONS RATIO = <real> ν
SHEAR MODULUS = <real> G
BULK MODULUS = <real> K
LAMBDA = <real> λ
TWO MU = <real> 2μ
#
# Yield surface parameters
#
A0 = <real> a0
A1 = <real> a1
A2 = <real> a2
PRESSURE CUTOFF = <real> pc
PRESSURE FUNCTION = <string> fp(εV)
END [PARAMETERS FOR MODEL SOIL_FOAM]

```

For information about the soil and crushable foam model, see the PRONTO3D document listed as Reference [1]. The soil and crushable foam model is the same as the soil and crushable foam model in PRONTO3D. The PRONTO3D model is based on a material model developed by Krieg [2]. The Krieg version of the soil and crushable foam model was later modified by Swenson and Taylor [3]. The soil and crushable foam model developed by Swenson and Taylor is the model in PRONTO3D and is also the shared model for Presto and Adagio.

Output variables available for this model are listed in Table 4-36.

Table 4-36. State Variables for SOIL FOAM Model

Name	Description
EVOL_MAX	maximum volumetric strain seen by the material point
EVOL_FRAC	volumetric strain for tensile fracture
EVOL	current volumetric strain
EQPS	equivalent plastic strain

REFERENCES

- [1] L.M. Taylor and D.P. Flanagan. Pronto3D: A three-dimensional transient solid dynamics program. Technical Report SAND87-1912, Sandia National Laboratories, Albuquerque, NM, March 1989. [pdf](#).
- [2] R.D. Krieg. A simple constitutive description for cellular concrete. Technical Report SAND SC-DR-72-0883, Sandia National Laboratories, Albuquerque, NM, 1978. [pdf](#).
- [3] D.V. Swenson and L. M. Taylor. A finite element model for the analysis of tailored pulse stimulation of boreholes. *International Journal for Numerical and Analytical Methods in Geomechanics*, 7:469–484, 1983. [doi](#).

4.25. SHAPE MEMORY ALLOY MODEL

4.25.1. Theory

The shape memory alloy (SMA) model is used to describe the thermomechanical response of intermetallics (e.g. NiTi, NiTiCu, NiTiPd, NiTiPt) that can undergo a reversible, diffusionless, solid-to-solid martensitic transformation. Specifically, the materials have a high-symmetry (typically cubic) austenitic crystallographic structure at high temperature and/or low stress. At lower-temperatures and/or high stress the crystallographic structure is transformed to a lower symmetry (typically orthorhombic or monoclinic) martensitic phase. The change in structure and symmetry may be taken advantage of to produce large inelastic strains of $\approx 1\text{-}8\%$. Importantly, this class of materials differentiates itself from TRIP steels in that the transformation is *reversible* and a variety of thermomechanical loading paths have been conceived of to take advantage of this behavior. A notable application of these materials is as an actuator in smart, morphing structures.

Phenomenologically, the macroscopic behavior of SMAs is typically discussed in effective stress-temperature space via a *phase diagram* like in Figure 4-105. The four lines denoted M_s , M_f , A_s , and A_f indicate the martensitic start, martensitic finish, austenitic start, and austenitic finish transformation surfaces. *Forward transformation* (from an austenitic to a martensitic state) is described by the martensitic start and finish surfaces. Specifically, the former refers to the thermomechanical conditions at which transformation will initiate while the latter corresponds to complete transformation. The difference between the two surfaces is associated with internal hardening effects due to microstructure (i.e. texture, back stresses). Transformation from martensite to austenite is referred to as *reverse* and is characterized by the austenitic start and finish surfaces. Detailed discussion of the crystallography and phenomenology may be found in [1, 2]⁵.

Two responses characteristic of SMAs may also be represented via the phase diagram. These are the *actuation response* and the *pseudoelastic* (often referred to as *superelastic* in the literature) responses. The first (actuation) is indicated by path “A” in Figure 4-105. In this case, a mechanical bias load is applied to the SMA and the material is then thermally cycled through forward and reverse transformation. The resulting transformation first produces and then removes the large transformation strains of SMAs and is commonly used for (surprisingly) actuation applications. At higher temperatures ($T > A_f$), mechanical loading may be used to induce forward and, upon unloading, reverse transformation as indicated in path “B” of Figure 4-105. Through such a cycle, a distinctive flag shape in the stress strain response is observed through which large amounts of energy may be dissipated while producing no permanent deformations. As such, this loading path is often considered for vibration isolation or damping applications.

In LAMÉ, the response of SMAs is described by the phenomenological model of Lagoudas and coworkers [3]. This model was motivated by actuator applications and it describes the inelastic

⁵In the martensitic configuration, the crystallographic structure can either self-accommodate in a *twinned* configuration producing no macroscopic inelastic strain or an internal or external stress field may be used to *detwin* the microstructure thereby producing the desired inelastic strain. For simplicity, this distinction is bypassed in this brief text and the interested reader should consult the referenced works.

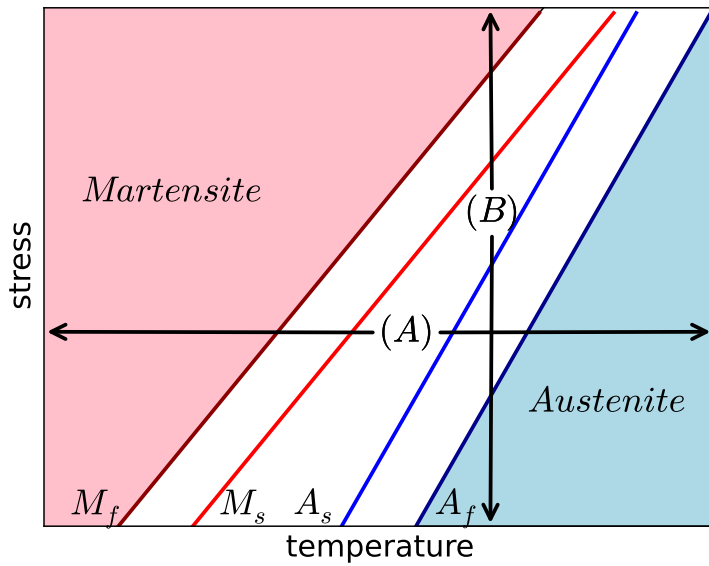


Figure 4-105. Representative phase diagram of shape memory alloys highlighting characteristic loading paths ((A) and (B)), transformation surfaces, and phases.

deformation associated with martensitic transformation through two internal state variables – the scalar martensitic volume fraction, ξ , and tensorial transformation strain tensor, $\varepsilon_{ij}^{\text{tr}}$. Before proceeding it should be noted that the *structural* response of SMA specimens and components exhibit a rate dependency associated with the strong thermomechanical coupling of SMAs. Specifically, the transformation process gives off/absorbs large amounts of energy via the *latent heat of transformation*. The rate dependence observed is a result of the characteristic time scale associated with thermal transport of this heat. In pure mechanical analyses (like Sierra/SM), this means quasistatics loadings are typically considered (a strain rate of $\approx 1 \times 10^{-4}$ and/or heating/cooling rate of $\approx 2^\circ\text{C}/\text{min}$). Formulations accounting for the full coupling have been developed but require more complex implementations.

To begin, the model assumes an additive decomposition of the total, elastic, thermal, and transformation deformation (strain) rates respectively denoted by D_{ij} , D_{ij}^e , D_{ij}^{th} and D_{ij}^{tr} producing a total deformation rate of the form,

$$D_{ij} = D_{ij}^e + D_{ij}^{\text{th}} + D_{ij}^{\text{tr}}. \quad (4.25.1)$$

With respect to the thermoelastic deformations, it is noted that the different crystallographic phases have different thermoelastic constants. Previous studies have demonstrated that a rule of mixtures on the compliance and other material properties of the form,

$$\mathbb{S}_{ijkl} = \mathbb{S}_{ijkl}^A + \xi (\mathbb{S}_{ijkl}^M - \mathbb{S}_{ijkl}^A) = \mathbb{S}_{ijkl}^A + \xi \Delta \mathbb{S}_{ijkl}, \quad (4.25.2)$$

$$\alpha_{ij} = \alpha^A \delta_{ij} + \xi (\alpha^M \delta_{ij} - \alpha^A \delta_{ij}) = \alpha^A \delta_{ij} + \xi \Delta \alpha \delta_{ij}, \quad (4.25.3)$$

in which \mathbb{S}_{ijkl} and α_{ij} are the current effective compliance and coefficient of thermal expansion and the superscripts “A” and “M” denote thermoelastic properties in the austenitic and martensitic configuration. The symbol “ Δ ” is used to indicate the difference in a property between the martensitic and austenitic phases while δ_{ij} is the Kronecker delta. Isotropy is assumed for all these properties and the compliances are determined via the definition of elastic moduli and Poisson’s ratio of the two phases – E^A , E^M , ν^M , and ν^A . The two Poisson ratios are often the same and take typical values for metals ($\nu^A \approx \nu^M \approx 0.3$) while the elastic moduli can differ by a factor of more than two. For instance the austenitic modulus of NiTi is typically given as ≈ 70 GPa while the martensitic one is ≈ 30 GPa⁶. Importantly, this difference means that the thermoelastic properties and corresponding deformations vary with transformation. As such, the corresponding rates of deformation are given as,

$$D_{ij}^e = \dot{\xi} \Delta \mathbb{S}_{ijkl} \sigma_{kl} + \mathbb{S}_{ijkl} \dot{\sigma}_{kl}, \quad (4.25.4)$$

$$D_{ij}^{\text{th}} = \dot{\xi} \Delta \alpha \delta_{ij} (\theta - \theta_0) + \alpha \delta_{ij} \dot{\theta}, \quad (4.25.5)$$

where θ and θ_0 are the current and reference temperature and σ_{ij} is the symmetric Cauchy stress. Note, in using the SMA model a temperature field *must* be defined. The stress rate may then be shown to be,

$$\dot{\sigma}_{ij} = \mathbb{C}_{ijkl} (D_{kl} - \alpha \delta_{kl} \dot{\theta}) - \dot{\xi} (\Delta \mathbb{S}_{klmn} \sigma_{mn} + \Delta \alpha \delta_{kl} (\theta - \theta_0)) - D_{kl}^{\text{tr}}, \quad (4.25.6)$$

with \mathbb{C}_{ijkl} being the current stiffness tensor defined as $\mathbb{C}_{ijkl} = \mathbb{S}_{ijkl}^{-1}$.

To describe the transformation strain evolution, it is assumed that these deformations evolve with (and only with) the martensitic volume fraction, ξ . The corresponding flow rule is given as,

$$D_{ij}^{\text{tr}} = \dot{\xi} \Lambda_{ij}, \quad (4.25.7)$$

and Λ_{ij} is the transformation direction tensor assumed to be of the form,

$$\Lambda_{ij} = \begin{cases} H^{\text{cur}} (\bar{\sigma}_{vM}) \frac{3}{2} \frac{s_{ij}}{\bar{\sigma}_{vM}} & \dot{\xi} \geq 0 \\ \frac{\dot{\sigma}_{ij}^{\text{tr-rev}}}{\dot{\xi}^{\text{rev}}} & \dot{\xi} < 0 \end{cases}. \quad (4.25.8)$$

In (4.25.8), H^{cur} is the transformation strain magnitude that is dependent on the von Mises effective stress, $\bar{\sigma}_{vM}$, and s_{ij} is the deviatoric stress. With forward transformation defined in this

⁶Given the lower symmetry of the martensitic phase the determination of an isotropic elastic modulus can vary with characterization methodology. In this case, the apparent elastic modulus measured from macroscopic thermoelastic tests should be used.

way, it is assumed that deformation is shear-based and follows a J_2 like flow direction. For reverse transformation ($\dot{\xi} < 0$), the postulated form is utilized to ensure complete recovery of transformation strains with martensitic volume fraction. In other words, all transformation strain components are zero-valued at $\xi = 0$. Without enforcing this condition in this way, non-proportional loading paths could be constructed producing a non-zero transformation strain when the material is austenitic. The transformation strain at load reversal, $\varepsilon_{ij}^{\text{tr-rev}}$, and martensitic volume fraction at load reversal, ξ^{rev} , are then tracked (via the implementation) and used for this purpose.

The transformation strain magnitude, H^{cur} , is a function of the von Mises effective stress ($\bar{\sigma}_{vM}$) and is introduced to incorporate detwinning effects without introducing an additional internal state variable complicating the model. Specifically, at low stress values, this function returns a minimum value. If the microstructure is self-accommodated this value will be zero. A decaying exponential is used such that as the stress increases the value of the strain magnitude becomes that of the maximum value incorporating both crystallographic and texture effects. The given functional form is,

$$H^{\text{cur}} = \begin{cases} H_{\min} & \bar{\sigma}_{vM} \leq \sigma_{\text{crit}} \\ H_{\min} + (H_{\text{sat}} - H_{\min}) (1 - \exp(-k(\bar{\sigma}_{vM} - \sigma_{\text{crit}}))) & \bar{\sigma}_{vM} > \sigma_{\text{crit}} \end{cases}, \quad (4.25.9)$$

where H_{\min} , H_{sat} , k , and σ_{crit} are model parameters giving the minimum transformation strain magnitude, maximum transformation strain magnitude, exponential fitting parameter governing the transition zone, and critical stress values (in some ways analogous to the detwinning stress).

The evolution of martensitic transformation process is governed by a transformation function serving an analogous role to the yield function in plasticity. This function is given by,

$$f(\sigma_{ij}, \theta, \xi) = \pm\phi(\sigma_{ij}, \theta, \xi) - \bar{\sigma}(\sigma_{ij}), \quad (4.25.10)$$

with ϕ begin the thermodynamic driving force for transformation and $\bar{\sigma}$ the critical value. The \pm is used to denote either forward (+) or reverse (-) transformation. This transformation function and the associated forms are derived from continuum thermodynamic considerations and the details of that process are neglected here for brevity but may be found in [3]. The functional forms of these variables are given as,

$$\begin{aligned} \phi(\sigma_{ij}, \theta, \xi) &= \sigma_{ij}\Lambda_{ij} + \frac{1}{2}\sigma_{ij}\Delta\S_{ijkl}\sigma_{kl} + \sigma_{ij}\Delta\alpha\delta_{ij}(\theta - \theta_0) + \rho\Delta s_0\theta - \rho\Delta u_0 - f^t(\xi), \\ \bar{\sigma}(\sigma_{ij}) &= \sigma_0 + D\sigma_{ij}\Lambda_{ij}, \end{aligned} \quad (4.25.11)$$

in which $\rho\Delta s_0$ and $\rho\Delta u_0$ are the differences in reference entropy and internal energy of the two phases, D is a calibration parameter intended to capture variations in dissipation with stress, and $f^t(\xi)$ is the hardening function. With respect to this latter term, empirical observations were used to arrive at a postulated form of,

$$f^t(\xi) = \begin{cases} \frac{1}{2}a_1(1 + \xi^{n_1} - (1 - \xi)^{n_2}) + a_3 & \dot{\xi} \geq 0 \\ \frac{1}{2}a_2(1 + \xi^{n_3} - (1 - \xi)^{n_4}) - a_3 & \dot{\xi} < 0 \end{cases}, \quad (4.25.12)$$

with a_1 , a_2 , and a_3 being fitting parameters and n_1 , n_2 , n_3 , and n_4 are exponents fit to match the smooth transformation from elastic to inelastic deformations at the start of forward, end of forward, start of reverse, and end of reverse transformation respectively.

Before proceeding, one final note should be given in regards to calibration. Specifically, some of the model parameters just listed (a_1 , a_2 , a_3 , D , σ_0 , $\rho\Delta s_0$ and $\rho\Delta u_0$) are not easily identified or conceptualized in terms of common thermomechanical experiments. Some easily identifiable parameters (M_s , M_f , A_s , and A_f), however, are not evident in the theoretical formulation. Conditions associated with these terms and some physical constraints may be used to determine the model parameters in terms of these more accessible properties. These relations are,

$$\rho\Delta s_0 = \frac{-2(C^M C^A) \left[H^{\text{cur}}(\sigma) + \sigma \frac{\partial H^{\text{cur}}}{\partial \sigma} + \sigma \left(\frac{1}{E^M} - \frac{1}{E^A} \right) \right]}{C^M + C^A} \Big|_{\sigma=\sigma^*}, \quad (4.25.13)$$

$$D = \frac{(C^M - C^A) \left[H^{\text{cur}}(\sigma) + \sigma \frac{\partial H^{\text{cur}}}{\partial \sigma} + \sigma \left(\frac{1}{E^M} - \frac{1}{E^A} \right) \right]}{(C^M + C^A) \left[H^{\text{cur}}(\sigma) + \sigma \frac{\partial H^{\text{cur}}}{\partial \sigma} \right]} \Big|_{\sigma=\sigma^*}, \quad (4.25.14)$$

$$a_1 = \rho\Delta s_0 (M_f - M_s), \quad a_2 = \rho\Delta s_0 (A_s - A_f), \quad (4.25.15)$$

$$a_3 = -\frac{a_1}{4} \left(1 + \frac{1}{n_1 + 1} - \frac{1}{n_2 + 1} \right) + \frac{a_2}{4} \left(1 + \frac{1}{n_3 + 1} - \frac{1}{n_4 + 1} \right), \quad (4.25.16)$$

$$\rho\Delta u_0 = \frac{\rho\Delta s_0}{2} (M_s + A_f), \quad \sigma_0 = \frac{\rho\Delta s_0}{2} (M_s - A_f) - a_3, \quad (4.25.17)$$

in which σ^* is the scalar stress measure in which the calibration is performed at. For additional discussion on the characterization of SMAs and calibration of this model, the user is referred to [4, 5].

4.25.2. Implementation

Similar to the various plasticity models in LAMÉ, an elastic predictor-inelastic corrector approach is used to perform the stress updating routine. Unlike the other models, however, in the shape memory alloy routine a convex cutting plane (CCP) return mapping algorithm (RMA) is used in lieu of the closest point projection. This difference essentially simplifies the integration of flow rule and the corresponding problem at the cost of some algorithmic stability. Prior studies [6] have shown that this implementation is sufficient for convergence in most cases while providing a substantial savings in cost. The specific implementation used here is that of [3].

To compute an elastic trial state, a trial stress is determined assuming purely thermoelastic deformations such that,

$$T_{ij}^{tr} = \mathbb{C}_{ijkl}(\xi^n) (d_{kl}\Delta t - \alpha_{kl}(\xi^n) \Delta\theta), \quad \Delta\theta = \theta^{n+1} - \theta^n. \quad (4.25.18)$$

In this case, it is assumed that the temperature fields are known at t_{n+1} and t_n (denoted θ^{n+1} and θ^n , respectively) and the thermoelastic properties are computed using the martensitic volume

fraction at the previous time step ξ^n . At this stage, a perturbation stress ($T_{ij}^{per} = T_{ij}^n + \beta (T_{ij}^{tr} - T_{ij}^n)$ with $\beta \ll 1$) is computed and used to determine local variations of the thermodynamic driving force, ϕ . This is necessary to determine the direction of transformation (forward or reverse). Using the full trial stress to this end can produce spurious results in some thermally-driven cases. The trial yield function value is then computed as,

$$f^{tr} = f(T_{ij}^{tr}, \theta^{n+1}, \xi^n) = \pm \phi(T_{ij}^{tr}, \theta^{n+1}, \xi^n) - \bar{\sigma}(T_{ij}^{tr}). \quad (4.25.19)$$

If $f^{tr} < 0$, no nonlinear deformation occurs and the trial solution is accepted as the material state at $t = t_{n+1}$. When this condition is not satisfied, the CCP-RMA routine is used to correct the trial state and return it to the yield surface.

To perform the inelastic correction, the Newton-Raphson method is iteratively used to update the material state (T_{ij} and ξ) until convergence is achieved. Denoting the current and next iteration by (k) and $(k+1)$, respectively, produces updating expressions of the form,

$$\begin{aligned} T_{ij}^{(k+1)} &= T_{ij}^{(k)} + \Delta T_{ij}, \\ \xi^{(k+1)} &= \xi^{(k)} + \Delta \xi, \end{aligned} \quad (4.25.20)$$

with $\xi^{(0)}$ and $T_{ij}^{(0)}$ initialized to ξ^n and T_{ij}^{tr} , respectively. The key difference between the CCP and closest point projection (CPP) methods is associated with how the inelastic strain flow rules are integrated. In the former method, an explicit evaluation of the flow direction is utilized while the latter is associated with a fully implicit expression. For the CPP algorithms, this implicit expression means the flow rule must be solved in a nonlinear system of equations with the consistency equation. Relaxing this assumption via the CCP method, however, produces an explicitly evaluated flow rule of,

$$\varepsilon_{ij}^{t(k+1)} = \varepsilon_{ij}^{t(k)} + \Delta \xi \Lambda_{ij}^{(k)}. \quad (4.25.21)$$

Importantly, this means that the only nonlinear equation to be solved is the scalar consistency equation ($f = 0$) which can be linearized such that,

$$\Delta \xi = -\frac{f^{(k)}}{\frac{\partial f^{(k)}}{\partial \xi} - \frac{\partial f^{(k)}}{\partial T_{ij}} \mathbb{C}_{ijkl}(\xi^{(k)}) \left(\Delta \mathbb{S}_{klmn} T_{mn}^{(k)} + \Delta \alpha_{kl} \Delta \theta + \Lambda_{kl}^{(k)} \right)}, \quad (4.25.22)$$

and the stress increment is then found as,

$$\Delta T^{(k)} = -\mathbb{C}_{ijkl}(\xi^{(n)}) \left(\Delta \mathbb{S}_{klmn} T_{mn}^{(k)} + \Delta \alpha_{kl} \Delta \theta + \Lambda_{kl}^{(k)} \right) \Delta \xi. \quad (4.25.23)$$

4.25.3. Verification

The shape memory alloy model is verified through a series of thermomechanical loadings. The material properties and model parameters for these investigations are given in Table 4-37. These properties correspond to those given in Table 3.4 in [1] with all n 's assumed to be 1 and setting $E^M = E^A$.

E^A	55 GPa	E^M	55 GPa
ν^A	0.33	ν^M	0.33
α^A	$22.0 \times 10^{-6} \frac{1}{K}$	α^M	$22.0 \times 10^{-6} \frac{1}{K}$
M_s	245 K	A_s	270 K
M_f	230 K	A_f	280 K
C^M	$7.4 \frac{\text{MPa}}{\text{K}}$	C^A	$7.4 \frac{\text{MPa}}{\text{K}}$
H_{\min}	0.056	H_{sat}	0.056

Table 4-37. The material and model parameters for the shape memory alloy model used during verification test.

It should also be clear that because $H_{\min} = H_{\text{sat}}$ the model response is independent of the values of σ^{crit} and k . For convenience, values of $k = 1.0 \times 10^6$ and $\sigma^{\text{crit}} = 0$ will be used. Additionally, σ^* will be taken to be zero although inspection of Equation (4.25.13) and consideration of the relative magnitudes of the transformation strain and the difference in elastic strain similarly indicates an invariance in the model response to this parameter with constant H^{cur} . The default prestrain values are also utilized such that the SMA is initially austenitic.

4.25.3.1. Uniaxial Stress – Pseudoelasticity

First, the isothermal ($\theta > A_f$) pseudoelastic response through a uniaxial stress loading is explored. Importantly, the simplifications and model parameters described above ($E^A = E^M = E$, $H^{\text{cur}}(\bar{\sigma}_{vM}) = H$, $C^A = C^M = C$, $n_i = 1$) allow for a simple analytical description of the pseudoelastic response (essentially trilinear). For instance, given the constant slopes of the transformation surfaces, the stresses needed to induce or complete transformation are simply given by,

$$\sigma^\beta(\theta) = C(\theta - \beta), \quad \beta = M_s, M_f, A_s, A_f, \quad (4.25.24)$$

where $\sigma^{M_s}(\theta)$ is the stress needed to start forward transformation at temperature, θ . Given a stress value, the strain and material state may be completely determined by knowing the martensitic volume fraction, ξ . Specifically, the axial (here taken to be the 1 direction) strain is simply,

$$\varepsilon_{11} = \frac{\sigma}{E} + \xi H, \quad (4.25.25)$$

and the lateral strains are

$$\varepsilon_{22} = \varepsilon_{33} = -\nu \frac{\sigma}{E} - \frac{1}{2} \xi H, \quad (4.25.26)$$

in which the fact that the transformation strain tensor is deviatoric is being leveraged. The martensitic volume fraction may then simply be found by noting that $f = 0$ during transformation. Therefore, for forward transformation,

$$\xi = \begin{cases} 0 & \sigma \leq \sigma^{M_s} \\ \frac{1}{a_1} (\sigma H + \rho \Delta s_0 \theta - \rho \Delta u_0 - a_3 - \sigma_0) & \sigma^{M_s} < \sigma < \sigma^{M_f} \\ 1 & \sigma \geq \sigma^{M_f} \end{cases} . \quad (4.25.27)$$

A comparable expression is easily determined for reverse transformation.

The results of this simple analytical expression and those determined by Adagio are presented in Figure 4-106 for three different temperatures. Figure 4-106a presents the stress-strain response under these conditions while Figure 4-106b presents the evolution of the martensitic volume fraction.

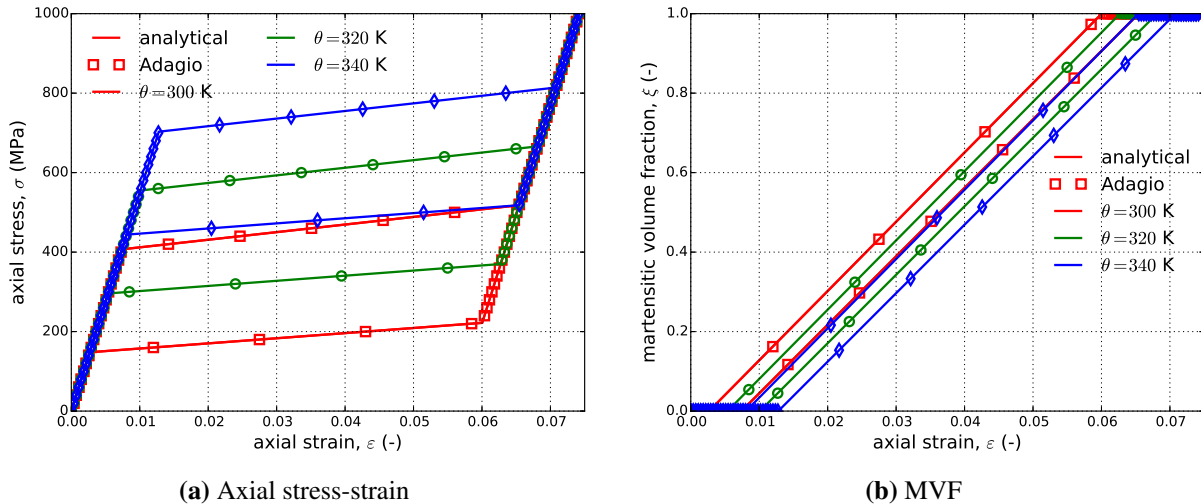


Figure 4-106. (a) Axial stress-strain response and (b) martensitic volume fraction, ξ , evolution determined analytically and via adagio for three different ambient temperatures $\theta = 300, 320$ and 340 K.

4.25.3.2. Constant Stress Actuation

To consider thermally driven transformation, the constant stress actuation response is investigated. In such a loading, a mechanical load is applied at high temperature ($\theta > A_f$) and held constant while the specimen is cooled through forward transformation and then heated back to its initial state. Given the aforementioned simplifications to the model parameters, the analytical response is determined in a very similar fashion to that of pseudoelasticity. In this instance, critical temperatures needed for transformation are first determined by

$$\beta^\sigma = \beta + \frac{\sigma}{C}, \quad \beta = M_s, M_f, A_s, A_f, \quad (4.25.28)$$

with M_s^σ being the temperature needed to start forward transformation at an effective stress, σ . The zero-stress value is M_s . Similarly, the axial and lateral strains may be adjusted as,

$$\varepsilon_{11} = \frac{\sigma}{E} + \xi H + \alpha(\theta - \theta_0), \quad (4.25.29)$$

$$\varepsilon_{22} = \varepsilon_{33} = -\nu \frac{\sigma}{E} - \frac{1}{2} \xi H + \alpha(\theta - \theta_0). \quad (4.25.30)$$

The martensitic volume fraction is found through relations (4.25.27) albeit with the piecewise intervals defined in terms of temperature (e.g $\sigma^{M_s} < \sigma < \sigma^{M_f} \leftrightarrow M_f^\sigma < \theta < M_s^\sigma$). Results for the axial strain-temperature, lateral strain-temperature, and martensitic volume fraction-temperature as determined analytically and via adagio are presented below in Figures 4-107a, 4-107b, and 4-107c, respectively.

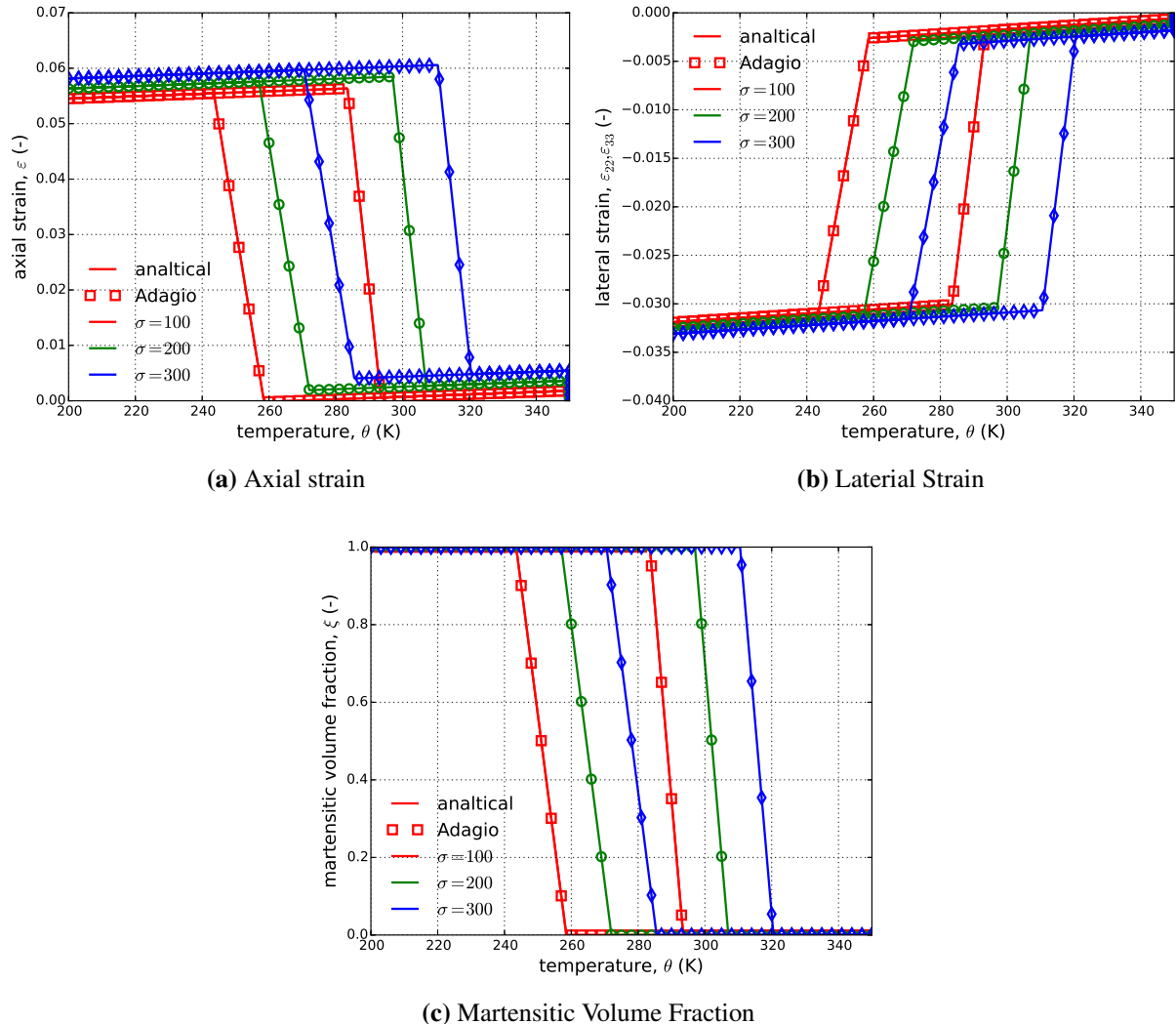


Figure 4-107. (a) Axial strain (b) lateral strain and (c) martensitic volume fraction, ξ , evolution as a function of temperature as determined analytically and numerically (Sierra/SM). Results are presented for three different applied bias stresses $\sigma = 100, 200$ and 300 MPa.

4.25.4. User Guide

```
BEGIN PARAMETERS FOR MODEL SHAPE_MEMORY_ALLOY
#
# Elastic constants
#
YOUNGS MODULUS = <real> E
POISSONS RATIO = <real> ν
SHEAR MODULUS = <real> G
BULK MODULUS = <real> K
LAMBDA = <real> λ
TWO MU = <real> 2μ
#
# Thermoelastic properties of two crystallographic phases
#
ELASTIC MODULUS AUSTENITE = <real> EA
POISSON RATIO AUSTENITE = <real> νA
CTE AUSTENITE = <real> αA
ELASTIC MODULUS MARTENSITE = <real> EM
POISSON RATIO MARTENSITE = <real> νM
CTE MARTENSITE = <real> αM
#
# Phase diagram parameters
#
MARTENSITE START = <real> Ms
MARTENSITE FINISH = <real> Mf
AUSTENITE START = <real> As
AUSTENITE FINISH = <real> Af
STRESS INFLUENCE COEFF MARTENSITE = <real> CM
STRESS INFLUENCE COEFF AUSTENITE = <real> CA
#
# Transformation strain magnitude parameters
#
H_MIN = <real> Hmin
H_SAT = <real> Hsat
KT = <real> k
SIGMA_CRITICAL = <real> σcrit
#
# Calibration parameters
#
N1 = <real> n1
N2 = <real> n2
N3 = <real> n3
N4 = <real> n4
SIGMA STAR = <real> σ*
T0 = <real> θ0
#
```

```

# Initial phase conditions
#
#  

X10           = <real>  $\xi(t=0)$  (0.0)  

PRESTRAIN_DIRECTION = <int>  $n^{ps}$  (0)  

PRESTRAIN_MAGNITUDE = <real>  $\|\varepsilon_{ij}^{tr}(t=0)\|$  (0.0)  

#  

END [PARAMETERS FOR MODEL SHAPE_MEMORY_ALLOY]

```

Output variables available for this model are listed in Table 4-38.

Table 4-38. State Variables for SHAPE MEMORY ALLOY Model

Name	Description
MVF	martensitic volume fraction, ξ
TransStrain	transformation strain tensor, ε_{ij}^{tr}

REFERENCES

- [1] D. C. Lagoudas, editor. *Shape Memory Alloys: Modeling and Engineering Application*. Springer, New York, NY USA, 2008.
- [2] K. Otsuka and X. Ren. Physical metallurgy of Ti-Ni-based shape memory alloys. *Progress in Materials Science*, 50:511–678, 2005.
- [3] D. Lagoudas, D. Hartl, Y. Chemisky, L. Machado, and P. Popov. Constitutive model for the numerical analysis of phase transformation in polycrystalline shape memory alloys. *International Journal of Plasticity*, 32-33:155–183, 2012.
- [4] D. J. Hartl, D. C. Lagoudas, F. T. Calkins, and J. H. Mabe. Use of a Ni60Ti shape memory alloy for active jet engine chevron application: I. thermomechanical characterization. *Smart Materials and Structures*, 19:015020, 2010.
- [5] D. J. Hartl, J. T. Mooney, D. C. Lagoudas, F. T. Calkins, and J. H. Mabe. Use of a Ni60Ti shape memory alloy for active jet engine chevron application: II. experimentally validated numerical analysis. *Smart Materials and Structures*, 19:015021, 2010.
- [6] M. A. Qidwai and D. C. Lagoudas. Numerical implementation of a shape memory alloy thermomechanical constitutive model using return mapping algorithms. *International Journal for Numerical Methods in Engineering*, 47:1123–1168, 2000.

4.26. LOW DENSITY FOAM MODEL

4.26.1. Theory

The low density foam material model is a phenomenological model for rigid, low density polyurethane foams. Development of this model followed extensive characterization efforts at Sandia National Laboratory with special emphasis placed on hydrostatic and triaxial compression tests [1]. A key observation of this investigation was the impact of trapped air inside the foam on the load bearing capabilities of the material.

In constructing a model describing the response of the low-density foams, Neilsen et al. [1] decomposed the response into that of the polymeric skeleton and the air such that,

$$\sigma_{ij} = \sigma_{ij}^{\text{sk}} + \sigma^{\text{air}} \delta_{ij}, \quad (4.26.1)$$

where the super script “sk” is used to refer to variables relating to the skeleton and “air” to the air. The contribution of the air component is only present, however, in constrained cases when the internal gases are trapped and not allowed to escape. If the foam material is not encased or encapsulated in someway, the air may escape and $\sigma^{\text{air}} = 0$. A model parameter, N_{air} , is included to distinguish between these cases. If N_{air} is set to 0, the air pressure term is set to zero. For any other value, it is included.

Using the ideal gas law, it can be found that for an isothermal case,

$$\sigma^{\text{air}} = \frac{p_0 \varepsilon_V}{\varepsilon_V + 1 - \phi}, \quad (4.26.2)$$

where p_0 , ε_V , and ϕ are the initial air pressure, volumetric strain, and the volume fraction of the solid (skeleton) material. Knowing the total stress of the material volume and air contribution, the skeleton stress may be found via (4.26.1). Furthermore, it should be noted that the foam (total) and skeleton strains are the same.

Based on their experimental observations, Neilsen et al. [1] noted a decoupling between the skeleton principal stresses. Therefore, the Poisson’s ratio of the skeleton is zero and that the yielding behavior in each principal direction is independent. A yield function of the form,

$$f_i = \sigma_i^{\text{sk}} - \bar{\sigma}, \quad (4.26.3)$$

where f_i and σ_i^{sk} are the i^{th} yield function and skeleton principal stress, respectively, and

$$\bar{\sigma} = A \langle I'_2 \rangle + B(1.0 + C \varepsilon_V) \quad (4.26.4)$$

with A, B, and C are material parameters, and $\langle \cdot \rangle$ denoting the Heaviside step function where

$$\langle x \rangle = \begin{cases} 0 & \text{if } x \leq 0 \\ 1 & \text{if } x > 0 \end{cases}, \quad (4.26.5)$$

was proposed. Additionally, I'_2 is the second invariant of the deviatoric strain. If a skeleton principal stress indicates yielding, it is set to the effective yield stress value, $\bar{\sigma}$.

4.26.2. Implementation

The low density foam material model is implemented in a hypoelastic fashion. Therefore, a trial material state of,

$$T_{ij}^{\text{sk}-tr} = T_{ij}^{\text{sk}-n} + E\Delta t d_{ij}, \quad (4.26.6)$$

$$\varepsilon_{ij}^{n+1} = \varepsilon_{ij}^n + \Delta t d_{ij}, \quad (4.26.7)$$

with d_{ij} , T_{ij}^{sk} , and ε_{ij} are the unrotated rate of deformation, unrotated skeleton stress, and foam strain, respectively, is calculated. The superscript “*tr*” denotes a trial stress while E is the Young’s Modulus and (4.26.6) leverages the fact that the Poisson’s ratio of the skeleton is zero. The principal stresses of the trial skeleton stress state, $T_i^{\text{sk}-tr}$, are then computed via the algorithm of Scherzinger and Dohrmann [2].

To check the yielding behavior, the (logarithmic) volumetric strain, ε_V^{n+1} , and second invariant of the deviatoric strain, I'_2 , are needed. These values are simply calculated as,

$$\varepsilon_V^{n+1} = \exp(\varepsilon_{kk}^{n+1}) - 1, \quad (4.26.8)$$

$$I_2^{n+1} = \hat{\varepsilon}_{11}^{n+1} \hat{\varepsilon}_{22}^{n+1} + \hat{\varepsilon}_{11}^{n+1} \hat{\varepsilon}_{33}^{n+1} + \hat{\varepsilon}_{22}^{n+1} \hat{\varepsilon}_{33}^{n+1} - \left[(\hat{\varepsilon}_{12}^{n+1})^2 + (\hat{\varepsilon}_{23}^{n+1})^2 + (\hat{\varepsilon}_{31}^{n+1})^2 \right], \quad (4.26.9)$$

with $\hat{\varepsilon}_{ij}^{n+1}$ being the deviatoric strain tensor. The effective yield stress, $\bar{\sigma}^{n+1}$, may be written as,

$$\bar{\sigma}^{n+1} = A \langle I_2^{n+1} \rangle + B (1 + C \varepsilon_V^{n+1}). \quad (4.26.10)$$

It should also be noted that a steep sinusoidal approximation of the Heaviside step function to alleviate numerical issues associated with the sharp discontinuity inherit to the use of the Heaviside function. The updated principal stresses may then be determined as,

$$T_i^{\text{sk}-n+1} = \begin{cases} T_i^{\text{sk}-tr}, & |T_i^{\text{sk}-tr}| \leq |\bar{\sigma}| \\ \text{sgn}(T_i^{\text{sk}-tr}) \bar{\sigma}, & |T_i^{\text{sk}-tr}| > |\bar{\sigma}| \end{cases}, \quad (4.26.11)$$

where $\text{sgn}(x)$ denotes the sign of x . An updated air pressure is then computed from (4.26.2) and the current stress is found to be,

$$T_{ij}^{n+1} = \sum_{k=1}^3 T_k^{\text{sk}-n+1} \hat{e}_i^k \hat{e}_j^k + \sigma^{\text{air}-n+1} (\varepsilon_{\text{V}}^{n+1}) \delta_{ij}, \quad (4.26.12)$$

where \hat{e}_i^k is the eigenvector associated with the k^{th} principal skeleton stress.

4.26.3. Verification

The low density foam model is implemented through two compression tests – uniaxial and hydrostatic. Cases both including ($N_{\text{air}} = 1.0$) and excluding ($N_{\text{air}} = 0.0$) the contribution of the air are investigated. The rest of the properties and parameters used for these tests are given in Table 4-39 and are originally from [3].

4.26.3.1. Uniaxial Compression

First, a uniaxial compression test under displacement control is considered with and without the contribution of air. In this case, a displacement of the form $u_1 = \lambda$ is applied while the other two directions are left traction free. When air pressure does not play a role, the model response reduces to that of the skeleton and the problem becomes one-dimensional. The deformation rate can be easily integrated to find that $\varepsilon_{11} = \ln(1 + \lambda)$ and $\varepsilon_{\text{V}} = \lambda$. Additionally, the uniaxial compression loading considered here is obviously deviatoric in nature leading to $\langle I'_2 \rangle$ evaluating to 1. Therefore,

$$\bar{\sigma} = A + B(1 + C\lambda), \quad (4.26.13)$$

$$\sigma_{11} = \begin{cases} E\varepsilon_{11} & |\sigma_{11}| \leq |\bar{\sigma}| \\ \text{sgn}(\varepsilon_{11})\bar{\sigma} & |\sigma_{11}| > |\bar{\sigma}| \end{cases}. \quad (4.26.14)$$

The corresponding stress and strain results are presented in Figures 4-108a and 4-108b.

The case of internal air pressure is also considered by setting $N_{\text{air}} = 1$. This, however, complicates the response and turns it into a three-dimensional case given the pressure components in the off-loading directions. Specifically, it can be found trivially that, $\varepsilon_{22} = \varepsilon_{33} = -\sigma^{\text{air}}/E$. The complication arises as the volumetric strain is now,

E	3010 psi	ν	0.0
A	49.2 psi	B	60.8 psi
C	-0.517	p_0	14.7 psi
ϕ	0.09		

Table 4-39. Material properties and model parameters for the low density foam model used during verification testing.

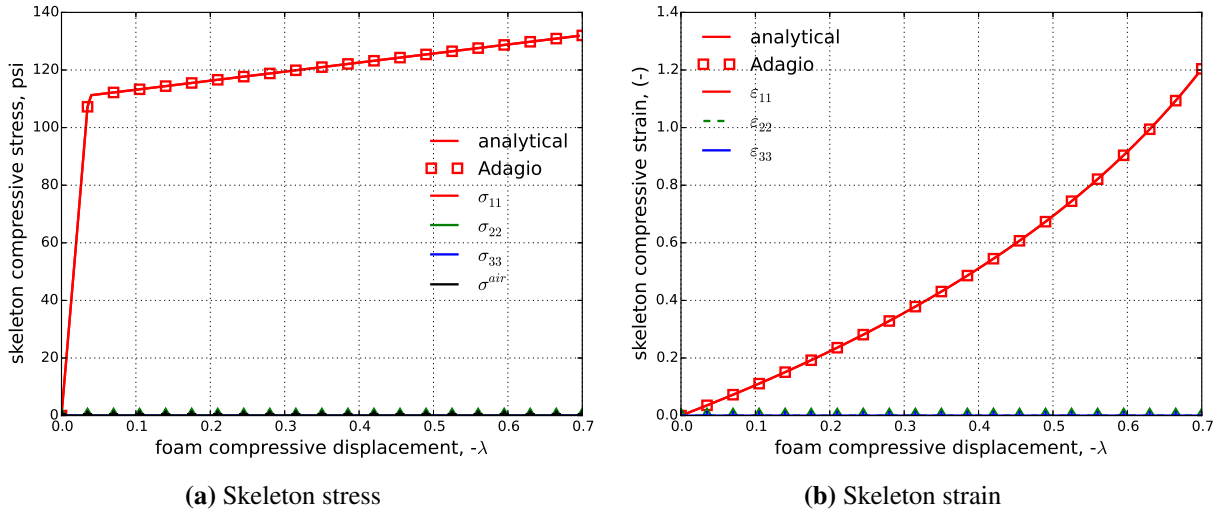


Figure 4-108. Skeleton (a) stress and (b) strain determined analytically and numerically (with $N_{\text{air}} = 0$) with the low density foam model during a displacement controlled uniaxial compression test.

$$\varepsilon_V = (1 + \lambda) \exp(-2\sigma^{\text{air}}/E) - 1, \quad (4.26.15)$$

leading to an implicit expression for σ^{air} . By evaluating σ^{air} in a forward Euler fashion, noting $\bar{\sigma} = A + B(1 + C\varepsilon_V)$, and treating (4.26.14) as an expression for σ_{11}^{sk} the stress and strain responses may be found as given in Figures 4-109a and 4-109b. The impact of the air on the model response is clear by comparing the two sets of figures.

4.26.3.2. Hydrostatic Compression

The volumetric deformation capabilities of the model are also investigated through displacement controlled hydrostatic compression. Specifically, an imposed displacement of the form $u_i = \lambda$ is considered. The resultant strain field is $\varepsilon_{11} = \varepsilon_{22} = \varepsilon_{33} = \ln(1 + \lambda)$ leading to a volumetric strain of the form $\varepsilon_V = (1 + \lambda)^3 - 1$. As there is no deviatoric deformation it is apparent that $\langle I'_2 \rangle = 0$. Therefore, the effective yield stress is $\bar{\sigma} = B(1 + C\varepsilon_V)$. Also noting that $\sigma = \sigma_{11} = \sigma_{22} = \sigma_{33}$, the foam response through such a loading may easily be determined. The foam stress for both the with and without air case is presented in Figure 4-110 along with σ^{air} for the appropriate case.

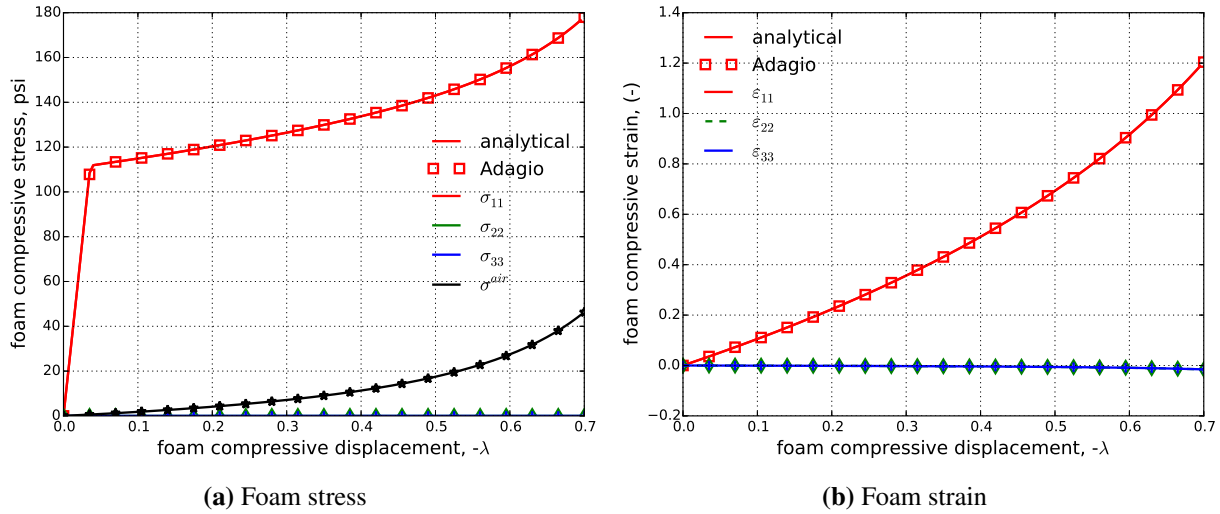


Figure 4-109. Foam (a) stress and (b) strain determined analytically and numerically (with $N_{air} = 1$) with the load density foam model during a displacement controlled uniaxial compression test.

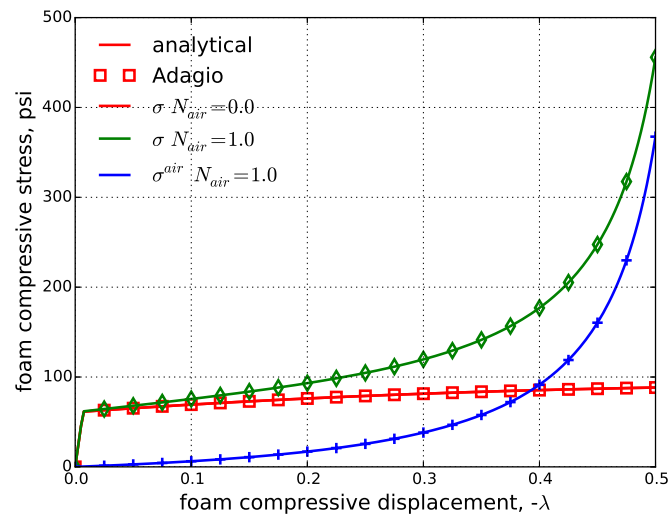


Figure 4-110. Foam stress determined analytically and numerically for both $N_{air} = 0.0$ and $N_{air} = 1.0$ cases for the low density foam model during displacement controlled hydrostatic compression

4.26.4. User Guide

```
BEGIN PARAMETERS FOR MODEL LOW_DENSITY_FOAM
#
# Elastic constants
#
YOUNGS MODULUS = <real> E
POISSONS RATIO = <real> ν
SHEAR MODULUS = <real> G
BULK MODULUS = <real> K
LAMBDA = <real> λ
TWO MU = <real> 2μ
#
A = <real> A
B = <real> B
C = <real> C
NAIR = <real> Nair
P0 = <real> p0
PHI = <real> φ
END [PARAMETERS FOR MODEL LOW_DENSITY_FOAM]
```

State variables for this model are listed in Table 4-40.

For more information on the low density foam material model, see [1].

Table 4-40. State Variables for LOW DENSITY FOAM Model

Name	Description
PAIR	Air pressure

REFERENCES

- [1] M.K. Neilsen, H.S. Morgan, and R.D. Krieg. A phenomenological constitutive model for low density polyurethane foams. Technical Report SAND86-2927, Sandia National Laboratories, Albuquerque, NM, April 1987. [pdf](#).
- [2] W.M. Scherzinger and C.R. Dohrmann. A robust algorithm for finding the eigenvalues and eigenvectors of 3x3 symmetric matrices. *Computer Methods in Applied Mechanics and Engineering*, 197(45-48):4007–4015, 2008.
- [3] W.M. Scherzinger and D.C. Hammerand. Testing of constitutive models in LAME. Technical Report SAND2007-5872, Sandia National Laboratories, Albuquerque, NM, September 2007. [pdf](#).

4.27. FOAM PLASTICITY MODEL

4.27.1. Theory

The foam plasticity model was developed to describe the response of porous materials (like closed-cell polyurethane foams) exhibiting irreversible, elastic-plastic like responses through large deformations. Such foams can exhibit significant plastic deviatoric and volumetric strains leading to permanent shape and volume changes, respectively. The former behavior is quite typical of metals and corresponding theories are well established. The latter response, however, is not typical of metals and a theory combining these two behaviors is needed. Given these responses of interest, the foam plasticity model is well suited to use with metal foams and many closed-cell polymeric foams (e.g. polyurethane, polystyrene bead, etc.) subjected to large deformations. As permanent strains are of interest, this model is not appropriate for use with flexible foams that return to their undeformed shape after loads are removed.

Specifically, the model developed by Neilsen et al. [1] seeks to capture the response associated with three distinct deformation regimes. First, when foams are initially compressed, they typically exhibit an elastic response. After sufficient load is applied, a plateau of nearly constant stress over a large deformation region is noted as pores start to compress and cell walls undergo substantial deformation. Eventually, the various collapsed cells and walls begin to interact and a densification response with substantial hardening is observed. Details of these deformation processes may be found in the text of Gibson and Ashby [2].

Like other plasticity-based models, the incremental constitutive law for the foam plasticity model is written as,

$$\dot{\sigma}_{ij} = \mathbb{C}_{ijkl} D_{kl}^e, \quad (4.27.1)$$

where an additive decomposition of the strain rates such that $D_{ij} = D_{ij}^e + D_{ij}^p$ is assumed. To describe the inelastic response of the foams of interest, Neilsen and coworkers [1] proposed a yield function of the form

$$f = \frac{\bar{\sigma}^2}{a^2} + \frac{p^2}{b^2} - 1, \quad (4.27.2)$$

where $\bar{\sigma}$ is the von Mises effective stress ($\bar{\sigma} = \sqrt{(3/2)s_{ij}s_{ij}}$ with s_{ij} being the deviatoric stress) and p being the hydrostatic pressure that is positive in compression ($p = -(1/3)\sigma_{kk}$). In such a form, the initial yield surface forms an ellipsoid about the hydrostat. The two denominators, a and b , are state variables capturing hardening effects and have the functional form of,

$$a = A_0 + A_1 \phi^{A_2}, \quad (4.27.3)$$

$$b = \begin{cases} B_0 + B_1 \phi^{B_2} & p \geq 0 \\ B_0 & p < 0 \end{cases}, \quad (4.27.4)$$

with A_0 , A_1 , A_2 , B_0 , B_1 , and B_2 being model parameters and ϕ being the maximum volume fraction of solid material obtained through the loading history and is defined as,

$$\phi = \phi_0 \frac{V_0}{V}, \quad (4.27.5)$$

in which ϕ_0 is the initial volume fraction of solid material and V_0 and V are the initial volume and current volume, respectively, of the foam. Put in terms of the deformation,

$$\phi = \phi_0 \frac{1}{1 + \varepsilon_V}, \quad (4.27.6)$$

where ε_V is the engineering volume strain.

To describe the inelastic plastic deformation, a non-associated flow rule is used. Specifically,

$$D_{ij}^p = \dot{\gamma} g_{ij}, \quad (4.27.7)$$

where $\dot{\gamma}$ is the consistency multiplier found by enforcing the corresponding condition and

$$g_{ij} = (1 - \beta) g_{ij}^a + \beta g_{ij}^r, \quad (4.27.8)$$

with the superscripts “a” and “r” being used to denote associated and radial flow directions, respectively. The model parameter β is introduced in (4.27.8) to enable associated ($\beta = 0$), radial ($\beta = 1$), or a linear combination of the two flow rules ($0 < \beta < 1$) to be used. The two direction vectors may be written as,

$$g_{ij}^a = \frac{\frac{\partial f}{\partial \sigma_{ij}}}{\left| \frac{\partial f}{\partial \sigma_{kl}} \right|} = \frac{\frac{3}{a^2} s_{ij} - \frac{2}{3b^2} p \delta_{ij}}{\left| \frac{3}{a^2} s_{ij} - \frac{2}{3b^2} p \delta_{ij} \right|}, \quad (4.27.9)$$

$$g_{ij}^r = \frac{\sigma_{ij}}{|\sigma_{kl}|} = \frac{\sigma_{ij}}{\sqrt{\sigma_{kl} \sigma_{kl}}}. \quad (4.27.10)$$

4.27.2. Implementation

Like other more classical rate-independent plasticity models (e.g. 4.7.2), the foam plasticity model is implemented in a hypoelastic fashion using an elastic predictor-inelastic corrector scheme. As such, a trial material state is calculated by assuming purely elastic deformations. The trial stress is given by,

$$T_{ij}^{tr} = T_{ij}^n + \Delta t (\lambda \delta_{ij} d_{kk} + 2\mu d_{ij}), \quad (4.27.11)$$

and an updated logarithmic volume strain is given by,

$$\varepsilon_{kk}^{n+1} = \varepsilon_{kk}^n + \Delta t d_{kk}. \quad (4.27.12)$$

The engineering volume strain may then be readily computed via $\varepsilon_V^{n+1} = \exp(\varepsilon_{kk}^{n+1}) - 1$. A trial solid volume fraction is then calculated, $\phi^{tr} = \phi_0 \frac{1}{1 + \varepsilon_V^{n+1}}$, and compared to the previous maximum to obtain the maximum solid volume fraction over the loading history,

$$\phi^{n+1} = \max(\phi^n, \phi^{tr}). \quad (4.27.13)$$

Equations (4.27.3) and (4.27.4) are evaluated using the volume fraction found in (4.27.13). Using invariants of the trial stress state, the yield function (4.27.2) is calculated. If $f \leq 0$, the loading is elastic and the trial solution is correct. On the other hand, if $f > 0$ a correction scheme is necessary to iterate and determine the inelastic solution. To that end, by noting

$\Delta T_{ij} = -\mathbb{C}_{ijkl} \Delta d_{kl}^P = -\Delta \gamma \mathbb{C}_{ijkl} g_{kl}$ (with “ Δ ” being a correction increment), the consistency condition may be used to find,

$$\Delta \gamma = \frac{f}{\frac{\partial f}{\partial \sigma_{ij}} \mathbb{C}_{ijkl} g_{kl}}, \quad (4.27.14)$$

where the fact that the strain (and therefore a and b do not change over an increment. The correction is repeated until $f < \text{tol}$.

4.27.3. Verification

The foam plasticity model is verified through a hydrostatic compression tests. Material properties used for this test are presented in Table 4-41 and correspond to room temperature properties of the PMDI20 rigid polyurethane foam characterized in [1].

E	22,600 psi	ν	0.343
A_0	513.3 psi	A_1	4,629 psi
A_2	2.90	ϕ_0	0.238
B_0	971 psi	B_1	7,377.5 psi
B_2	4.89	β	0.95

Table 4-41. Material properties and model parameters for the foam plasticity model used during verification testing.

4.27.3.1. Hydrostatic Compression

The response of the foam plasticity model to hydrostatic compression is investigated here. Specifically, a displacement of the form $u_i = \lambda$ is imposed resulting in a total strain field of $\varepsilon_{11} = \varepsilon_{22} = \varepsilon_{33} = \ln(1 + \lambda)$ and the engineering volume strain is simply $\varepsilon_V = (1 + \lambda)^3 - 1$.

Furthermore, the maximum solid volume fraction monotonically increases and may be found to be $\phi = \phi_0 \frac{1}{(1+\lambda)^3}$. The stress state undergoes a similar reduction and is given to $\sigma_{ij} = -p\delta_{ij}$ and $s_{ij} = 0$. This simplification leads to a reduced yield function of the form,

$$f = \frac{p^2}{b^2} - 1, \quad (4.27.15)$$

where b is evaluated via (4.27.4) and is a function of the strain. The model may then be simply solved as,

$$p = \begin{cases} -3K \ln(1+\lambda) & f \leq 0 \\ b & f > 0 \end{cases}. \quad (4.27.16)$$

The elastic strains then reduce to $\varepsilon_{ij}^e = -\frac{p}{3K}\delta_{ij}$ and the plastic strains computed as $\varepsilon_{ij}^p = \left(\ln(1+\lambda) + \frac{p}{3K}\right)\delta_{ij}$. The resulting engineering strain vs. pressure results determined numerically and analytically are presented in Figure 4-111.

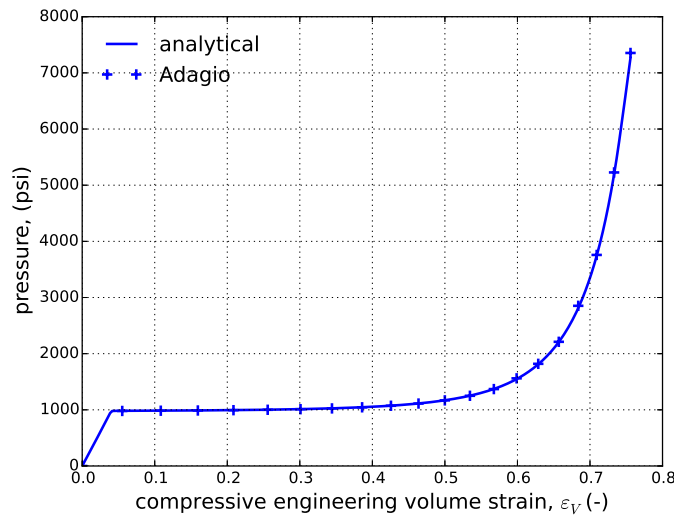


Figure 4-111. Pressure vs. engineering volume strain (ε_V) response of the foam plasticity model through a hydrostatic compression cycle

4.27.4. User Guide

```

BEGIN PARAMETERS FOR MODEL FOAM_PLASTICITY
#
# Elastic constants
#
YOUNGS MODULUS = <real> E
POISONS RATIO = <real> ν
SHEAR MODULUS = <real> G
BULK MODULUS = <real> K
LAMBDA = <real> λ
TWO MU = <real> 2μ
#
#
#
PHI = <real> φ₀
SHEAR STRENGTH = <real> A₀
SHEAR HARDENING = <real> A₁
SHEAR EXPONENT = <real> A₂
HYDRO STRENGTH = <real> B₀
HYDRO HARDENING = <real> B₁
HYDRO EXPONENT = <real> B₂
BETA = <real> β
END [PARAMETERS FOR MODEL FOAM_PLASTICITY]

```

Output variables available for this model are listed in Table 4-42.

Table 4-42. State Variables for FOAM PLASTICITY Model

Name	Description
ITER	iterations
EVOL	volumetric strain
PHI	phi, $φ$
EQPS	equivalent plastic strain, $\bar{ε}^p$
PA	A
PB	B

REFERENCES

- [1] M. K. Neilsen, W. Y. Lu, B. Olsson, and T. Hinnerichs. A viscoplastic constitutive model for polyurethane foams. In *Proceedings ASME 2006 International Mechanical Engineering Congress and Exposition*, Chicago, IL, 2006. ASME.
- [2] L.J. Gibson and M.F. Ashby. *Cellular Solids: Structure and Properties*. Cambridge Solid State Science Series. Cambridge University Press, Cambridge, UK, second edition, 1997.

4.28. VISCOPLASTIC FOAM MODEL

4.28.1. Theory

The viscoplastic foam model is used to model the rate (and temperature) dependent crushing of foams [1]. It is based on an additive split of the rate of deformation into an elastic and plastic portion

$$D_{ij} = D_{ij}^e + D_{ij}^p. \quad (4.28.1)$$

The stress in the material is due strictly to the elastic portion of the rate of deformation so that

$$\overset{\circ}{\sigma}_{ij} = \mathbb{C}_{ijkl} D_{kl}^e, \quad (4.28.2)$$

where \mathbb{C}_{ijkl} are the components of the fourth-order, isotropic elasticity tensor. The stress rate is arbitrary, as long as it is objective. Two objective stress rates are commonly used: the Jaumann rate and the Green-McInnis rate. For problems with fixed principal axes of deformation, these two rates give the same answers. For problems where the principal axes of deformation rotate during deformation, the two rates can give different answers. Generally speaking, there is no reason to pick one objective rate over another.

To describe the rate-dependent response, an over-stress-type yield function is used. Specifically, the rate-independent foam plasticity yield function (4.27.2) is rearranged such that,

$$f = \sigma^* - a, \quad (4.28.3)$$

where σ^* is the effective stress given by

$$\sigma^* = \sqrt{\bar{\sigma}^2 + \frac{a^2}{b^2} p^2}. \quad (4.28.4)$$

In (4.28.4), $\bar{\sigma}$ is the von Mises effective stress ($\bar{\sigma} = \sqrt{\frac{3}{2} s_{ij} s_{ij}}$) and p is the pressure resulting from a stress decomposition of the form,

$$\sigma_{ij} = s_{ij} - p \delta_{ij}. \quad (4.28.5)$$

Furthermore, a and b are state variables that are functions of the absolute temperature, θ , and maximum solid volume fraction, ϕ , and are defined as⁷

⁷In addition to the given analytical expressions, a and b may be optionally specified as user defined functions of the maximum solid volume fraction. In these cases, however, the temperature dependence is neglected.

$$a(\theta, \phi) = A_0(\theta) + A_1(\theta) \phi^{A_2} \quad (4.28.6)$$

$$(4.28.7)$$

$$b(\theta, \phi) = B_0(\theta) + B_1(\theta) \phi^{B_2}. \quad (4.28.8)$$

The temperature dependent material properties in the preceding relations are all defined as, $A_0(\theta) = A_0 h_{A_0}(\theta)$ where A_0 is the reference material parameter and $h_{A_0}(\theta)$ is the relative value as a function of temperature. In addition to the a and b state variables, the Young's modulus and Poisson's ratio are also functions of the absolute temperature. The latter may be written as $\nu(\theta) = \nu h_\nu(\theta)$ while the former is also dependent on the maximum volume fraction of solid material and is given as $E(\theta, \phi) = E h_E(\theta) f_E(\phi)$.

The maximum volume fraction of solid material, ϕ , is given by

$$\phi = \max_{t>0} \tilde{\phi}(t) \quad (4.28.9)$$

where $\tilde{\phi}(t)$ is the current volume fraction of solid material and is defined as,

$$\tilde{\phi}(t) = \frac{\phi_0}{\exp(\varepsilon_\nu^p)} \quad (4.28.10)$$

with ϕ_0 being the initial solid volume fraction and ε_ν^p is

$$\varepsilon_\nu^p = \int_0^t D_{kk}^p dt. \quad (4.28.11)$$

During inelastic deformation ($f > 0$), the corresponding rate of plastic deformation is given in a Perzyna-type form as,

$$D_{ij}^p = \begin{cases} \exp(h(\theta)) \left(\frac{\sigma^*}{a} - 1 \right)^{n(\theta)} g_{ij} & \text{if } f > 0 \\ 0 & \text{if } f < 0 \end{cases} \quad (4.28.12)$$

where $h(\theta)$ and $n(\theta)$ are the flow rate and power exponent respectively. The inelastic flow direction, g_{ij} , is given as a linear combination of the associated (with respect to (4.27.2)), g_{ij}^a , and radial, g_{ij}^r ,

$$g_{ij} = (1 - \beta) g_{ij}^a + \beta g_{ij}^r. \quad (4.28.13)$$

The directions g_{ij}^a and g_{ij}^r are given in Equations (4.27.9) and (4.27.10), respectively. In this model, the flow rule weight, β , may be specified as either a constant value or as a function of the maximum solid volume fraction ($\beta = \beta(\phi)$).

4.28.2. Implementation

As the viscoplastic foam model is a time-dependent, hypoelastic model it is integrated using an explicit, forward Euler scheme. Given this approach, a critical time step for stability is computed based on the shear strength, current modulus, and deviatoric deformation rate. If the input time step is acceptable, the new material state at time $t = t_{n+1}$ is computed. On the other hand, if the time step is too large a series of sub-increments are used. In this case, the total time step Δt is subdivided into N sub-increments. Each such sub-interval (denoted by k) has a time increment δt^k such that $\Delta t = \sum_{k=1}^N \delta t^k$ and the forward Euler time stepping scheme is performed over each sub-interval until the desired material state at time t_{n+1} is determined. For the case of temperature dependent variables (e.g. the Poisson's ratio ν), the value at the start of the sub-increment is determined by linearly interpolating over the total time step,

$$\nu^k = \nu_n + \frac{\Delta t^k}{\Delta t} (\nu_{n+1} - \nu_n), \quad (4.28.14)$$

where Δt^k is the current sub-increment time, $\Delta t^k = \sum_{r=1}^k \delta t^r$. For simplicity, in the remainder of this section it is assumed that the input time step is acceptable and only a single increment is needed. If additional sub-increments are needed, the below steps would be repeated N times with time intervals of δt^k .

Noting the forward Euler approach adopted in this formulation, the first step is to determine the temperature (and solid volume fraction) dependent model parameters (E , ν , A_0 , A_1 , B_0 , B_1 , h and n). With the parameters established, state variables a and b are easily determined through (4.28.6) and (4.28.8), respectively, enabling the calculation of the effective stress via (4.28.4). The effective inelastic (plastic) strain rate, $\dot{\varepsilon}^p$, is then given as,

$$\dot{\varepsilon}^p = \exp(h(\theta_n)) \left\langle \frac{\sigma_n^*}{a_n} - 1 \right\rangle^{n(\theta_n)}, \quad (4.28.15)$$

with $\langle \rangle$ being the Macaulay brackets such that,

$$\langle x \rangle = \begin{cases} x & x \geq 0 \\ 0 & x < 0 \end{cases}. \quad (4.28.16)$$

Knowing the magnitude of the rate of inelastic deformation, the change in deviatoric and hydrostatic stresses is simply,

$$\dot{s}_{ij} = 2\mu(\theta_n, \phi_n) \left(\hat{d}_{ij} - \hat{d}_{ij}^p \right), \quad (4.28.17)$$

$$\dot{p} = K(\theta_n, \phi_n) (d_{kk} - d_{kk}^p), \quad (4.28.18)$$

where d_{ij} is the total unrotated rate of deformation, \hat{x}_{ij} denotes the deviatoric portion of tensor x_{ij} , and d_{ij}^p is the plastic rate of deformation given by,

$$d_{ij}^p = \dot{\varepsilon}^p g_{ij}^n. \quad (4.28.19)$$

In (4.28.19), g_{ij} is the inelastic flow direction and can be calculated via (4.28.13).

An additional comment is needed with respect to accounting for temperature and solid volume fraction dependence in the shear and bulk moduli. This careful consideration is necessary due to the fact that the temperature dependence is only given with respect to the elastic moduli and Poisson's ratio. As such, the shear and bulk moduli inherit the associated dependencies and are calculated for isotropic elastic relations. For the bulk moduli, this leads to an expression of the form,

$$K(\theta, \phi) = \frac{Eh_E(\theta)f_E(\phi)}{3(1-2\nu h_\nu(\theta))}. \quad (4.28.20)$$

The updated stress state is then easily computed by explicitly integrating the established expressions. Specifically,

$$s_{ij}^{n+1} = \frac{\mu_{n+1}}{\mu_n} s_{ij}^n + \dot{s}_{ij} \Delta t, \quad (4.28.21)$$

$$p^{n+1} = \frac{K_{n+1}}{K_n} p^n + \dot{p} \Delta t, \quad (4.28.22)$$

$$T_{ij}^{n+1} = s_{ij}^{n+1} + p^{n+1} \delta_{ij}, \quad (4.28.23)$$

with μ_n and K_n representing $\mu(\theta_n, \phi_n)$ and $K(\theta_n, \phi_n)$, respectively, and T_{ij} being the unrotated stress.

4.28.3. Verification

The viscoplastic foam model was verified in both uniaxial and hydrostatic compression. The material properties and model parameters for both of these investigations are given in Table 4-43. As both loadings are isothermal, temperature dependence is neglected in the relevant model parameters. Furthermore, analytical solutions could not be found directly, so semi-analytical solutions were found.

4.28.3.1. Uniaxial Compression

To obtain a semi-analytical solution for the uniaxial compression test, the model was reduced to a one-dimensional form and then numerically integrated. The results obtained from the implemented model and the semi-analytical solution are shown below in Figure 4-112.

E	4,807 psi	A_0	63.03 psi
ν	0.33	A_1	7000 psi
h	-8.12	A_2	3.7878
n	2	B_0	93 psi
β	0.9	B_1	1483.4 psi
ϕ_0	0.1148	B_2	3.7878

Table 4-43. The material properties for the viscoplastic foam model tested in uniaxial stress.

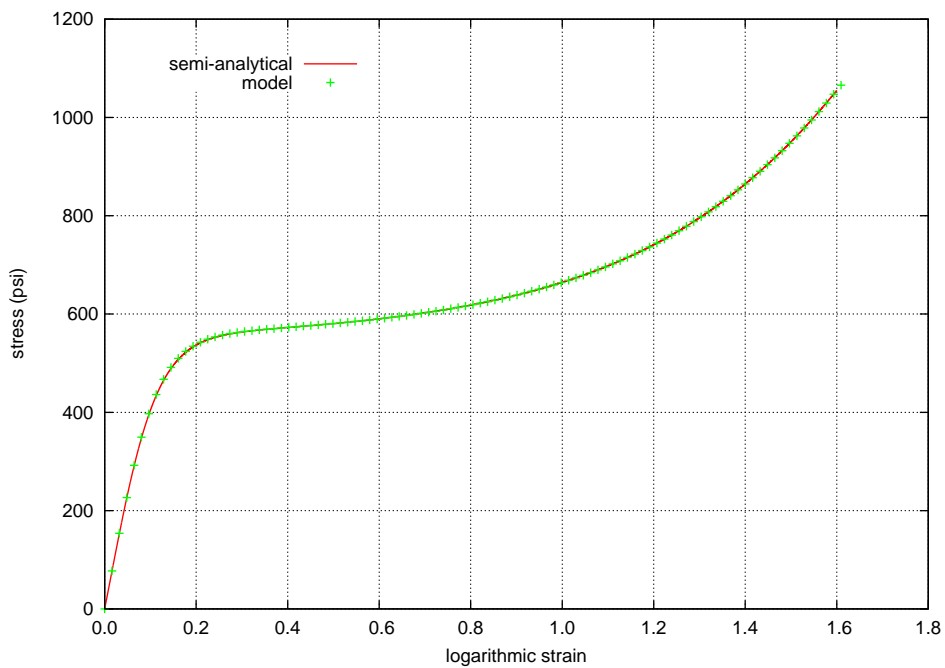


Figure 4-112. Verification of the viscoplastic foam model in uniaxial compression showing the axial stress as a function of the logarithmic strain.

4.28.3.2. Hydrostatic Compression

The response of the model through hydrostatic compression. To this end, a displacement of the form $u_i = \lambda(t)$ is considered. The applied displacement scales linearly from $\lambda = 0$ at $t = 0.0$ to $\lambda = -0.7$ at $t = t_{\max}$. Rate-dependent effects are considered through the use of two cases each with a different t_{\max} . Creatively denoted “Fast” and “Slow”, the two cases correspond to $t_{\max} = 1$ s and $t_{\max} = 100$ s, respectively. With such a displacement field, the engineering volume strain, ε_V , is simply $\varepsilon_V = (1 + \lambda)^3 - 1$. Additionally, the stress state reduces trivially to $\sigma_{ij} = -p\delta_{ij}$.

Given the rate-dependent overstress form of the constitutive model, an analytical solution is not readily available. Therefore, a semi-analytical analysis using a model reduction specialized for hydrostatic loadings is considered. Specifically, noting $s_{ij} = 0$, the overstress reduces to,

$$\sigma^* = \frac{a}{b}|p|. \quad (4.28.24)$$

Furthermore, the associated and radial flow direction vectors simplify to the same form and are given as,

$$g_{ij}^a = g_{ij}^r = -\frac{1}{\sqrt{3}}\text{sgn}(p)\delta_{ij}, \quad (4.28.25)$$

where $\text{sgn}(p)$ is the sign of p . The semi-analytical (integrated in a forward Euler fashion) and numerical results are presented in Figure 4-113.

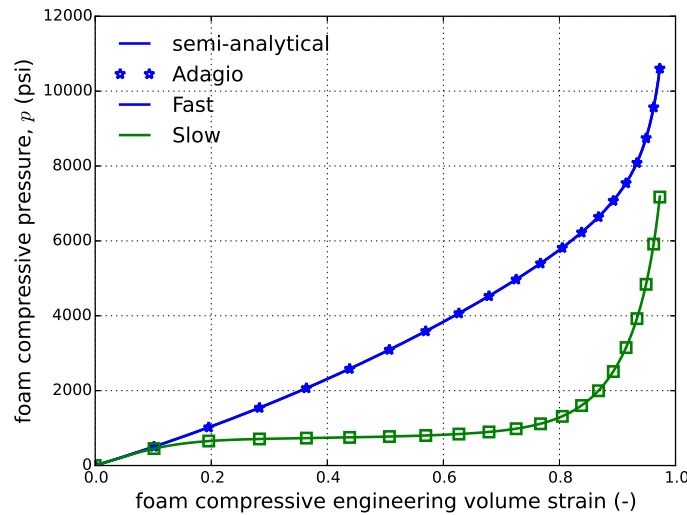


Figure 4-113. Pressure-engineering volume strain results of viscoplastic foam model subjected to a hydrostatic loading at both fast and slow rates determined semi-analytically and numerically.

4.28.4. User Guide

```

BEGIN PARAMETERS FOR MODEL VISCOPLASTIC_FOAM
#
# Elastic constants
#
YOUNGS MODULUS = <real> E
POISSONS RATIO = <real> ν
SHEAR MODULUS = <real> G
BULK MODULUS = <real> K
LAMBDA = <real> λ
TWO MU = <real> 2μ

FLOW RATE = <real> h
POWER EXPONENT = <real> n
BETA = <real> β
PHI = <real> φ₀

SHEAR STRENGTH = <real> A₀
SHEAR HARDENING = <real> A₁
SHEAR EXPONENT = <real> A₂
HYDRO STRENGTH = <real> B₀
HYDRO HARDENING = <real> B₁
HYDRO EXPONENT = <real> B₂

YOUNGS FUNCTION = <string> hE(θ)
POISSONS FUNCTION = <string> hν(θ)
SS FUNCTION = <string> hA₀(θ)
SH FUNCTION = <string> hA₁(θ)
HS FUNCTION = <string> hB₀(θ)
HH FUNCTION = <string> hB₁(θ)
RATE FUNCTION = <string> hh(θ)
EXPONENT FUNCTION = <string> hn(θ)
STIFFNESS FUNCTION = <string> fE(φ)

#Optional user-specified functions
SHEAR HARDENING FUNCTION = <string> a(φ) #Do not specify A₀, A₁, A₂
HYDRO HARDENING FUNCTION = <string> b(φ) #Do not specify B₀, B₁, B₂
BETA FUNCTION = <string> β(φ) #Do not specify β
END [PARAMETERS FOR MODEL VISCOPLASTIC_FOAM]

```

Output variables available for this model are listed in Table 4-44.

Table 4-44. State Variables for VISCOPLASTIC FOAM Model

Name	Description
ITER	number of sub-increments
EPVOL	inelastic volumetric strain, ε_v^p
EDOT	effective inelastic strain rate, $\dot{\varepsilon}^p$
PHI	volume fraction of solid material, ϕ
FA	shear strength, a
FB	hydrostatic strength, b
STIF	elastic stiffness as a function of ϕ

REFERENCES

- [1] M. K. Neilsen, W. Y. Lu, B. Olsson, and T. Hinnerichs. A viscoplastic constitutive model for polyurethane foams. In *Proceedings ASME 2006 International Mechanical Engineering Congress and Exposition*, Chicago, IL, 2006. ASME.

4.29. FOAM DAMAGE

4.29.1. Theory

The foam damage model was developed at Sandia National Laboratories to model the behavior of rigid polyurethane foams under a variety of loading conditions [1]. For instance, temperature, rate, and tension-compression dependencies are all built into this model. This model, leverages previous efforts and experience with other foam models(e.g. low density foam 4.26, foam plasticity 4.27, and viscoplastic foam 4.28). Like those past efforts, this model utilizes an additive decomposition of the strain rates into elastic and inelastic parts,

$$D_{ij} = D_{ij}^e + D_{ij}^{\text{in}}. \quad (4.29.1)$$

It is also assumed that the elastic response is linear and isotropic such that the stress rate for isothermal conditions is given by the following equation

$$\overset{\circ}{\sigma}_{ij} = \mathbb{C}_{ijkl} D_{kl}^e = \mathbb{C}_{ijkl} (D_{kl} - D_{kl}^{\text{in}}), \quad (4.29.2)$$

with \mathbb{C}_{ijkl} being the fourth-order, isotropic elasticity tensor. The specific stress rate considered is arbitrary as long as it is object. Two common rates satisfying that constraint are the Jaumann and Green-McInnis rates.

The initial yield surface is assumed to be an ellipsoid about the hydrostat and is described by the function

$$f = \frac{\bar{\sigma}^2}{a^2} + \frac{p^2}{b^2} - 1 = 0, \quad (4.29.3)$$

where a and b are state variables that define the current deviatoric and volumetric strengths, respectively, of the foam. The von Mises effective stress, $\bar{\sigma}$ is a scalar measure of the deviatoric stress given by

$$\bar{\sigma} = \sqrt{\frac{3}{2} s_{ij} s_{ij}}, \quad (4.29.4)$$

while p is the pressure, or mean stress, and is defined as

$$p = \frac{1}{3} \sigma_{kk}, \quad (4.29.5)$$

with σ_{ij} and s_{ij} being the components of the Cauchy and deviatoric stress. This latter tensor may be written as,

$$s_{ij} = \sigma_{ij} - p\delta_{ij}, \quad (4.29.6)$$

where δ_{ij} are the components of the identity tensor - $\delta_{ij} = 1$ if $i = j$, $\delta_{ij} = 0$ if $i \neq j$.

For this model, the yield function (4.29.3) is re-written as

$$f = \sigma^* - a = 0 \quad (4.29.7)$$

with the effective stress, σ^* , being a function of the von Mises effective stress, $\bar{\sigma}$, and the pressure, p , as follows

$$\sigma^* = \sqrt{\bar{\sigma}^2 + \frac{a^2}{b^2} p^2}. \quad (4.29.8)$$

Next, using a Perzyna-type formulation, the following expression for the inelastic strain rate, D_{ij}^{in} , is developed

$$D_{ij}^{\text{in}} = \begin{cases} \dot{\varepsilon}^p g_{ij} = e^h \left(\frac{\sigma^*}{a} - 1 \right)^n g_{ij} & \text{if } \frac{\sigma^*}{a} - 1 > 0 \\ 0 & \text{if } \frac{\sigma^*}{a} - 1 \leq 0, \end{cases} \quad (4.29.9)$$

where g_{ij} are the components of a symmetric, second-order tensor that defines the orientation of the inelastic flow. This type of model is sometimes referred to as an over-stress model because the inelastic rate is a function of the over-stress - the distance outside the yield surface. For associated flow, g_{ij} is simply normal to the yield surface and is given by

$$g_{ij}^{\text{a}} = \frac{\frac{\partial f}{\partial \sigma_{ij}}}{\left| \frac{\partial f}{\partial \sigma_{kl}} \right|} = \frac{\frac{3}{a^2} s_{ij} + \frac{2}{3b^2} p \delta_{ij}}{\left| \frac{3}{a^2} s_{kl} + \frac{2}{3b^2} p \delta_{kl} \right|}. \quad (4.29.10)$$

When lower density foams are subjected to a simple load path like uniaxial compression, the inelastic flow direction at moderate strains appears nearly uniaxial. In other words, the flow direction is given by the normalized stress tensor as follows

$$g_{ij}^{\text{r}} = \frac{\sigma_{ij}}{|\sigma_{kl}|}. \quad (4.29.11)$$

This type of flow is called radial flow. The foam damage model has another parameter, β , which allows for the flow direction to be prescribed as a linear combination of associated and radial flow such that,

$$g_{ij} = \frac{(1-\beta)g_{ij}^a + \beta g_{ij}^r}{|(1-\beta)g_{kl}^a + \beta g_{kl}^r|}. \quad (4.29.12)$$

Rigid polyurethane foams have little ductility when they are subjected to tensile stress. For this loading case, the materials behave more like brittle materials and even for uniaxial compression the foams often show cracking at large strains.

The damage surfaces for the foam damage model are simply three orthogonal planes with the normals given by the positive principal stress axes. The damage surfaces are given by the following equation

$$f_{\text{dam}}^i = \hat{\sigma}^i - c(1 - w), \quad ; \quad i = 1, 2, 3 \quad (4.29.13)$$

where $\hat{\sigma}^i$ is a principal stress, c is the initial tensile strength which is a material parameter, and w is a scalar measure of the damage. As damage occurs, the damage surface will collapse toward the origin and the foam will lose tensile strength. The foam will, however, still have compressive strength.

Damage is taken to be a positive, monotonically increasing function of the damage strain, ε_{dam} , and the damage strain is a function of the maximum principal strain, ε_{max} , and the plastic volume strain, ε_v^p , such that

$$w = w(\varepsilon_{\text{dam}}) \quad ; \quad \varepsilon_{\text{dam}} = a_{\text{dam}}\varepsilon_{\text{max}} + b_{\text{dam}}\varepsilon_v^p, \quad (4.29.14)$$

with the material parameters a_{dam} and b_{dam} controlling the rate at which damage is generated in tension and compression, respectively. The model does not allow healing, so the damage never decreases even if the damage strain decreases.

To fully capture temperature, strain rate, and lock-up effects, several material parameters are defined as functions of temperature, θ , and/or some measure of the amount of compaction, e.g. the maximum volume fraction of the solid material obtained during any prior loading, ϕ . For instance,

$$\begin{aligned} E(\theta, \phi) &= E h_E(\theta) f_E(\phi), \\ \nu(\theta, \phi) &= \nu h_\nu(\theta) f_\nu(\phi), \end{aligned} \quad (4.29.15)$$

and the natural logarithm of the reference flow rate, h , and the power law exponent, n are also functions of temperature

$$\begin{aligned}
h(\theta) &= h h_h(\theta) \\
n(\theta) &= n h_n(\theta).
\end{aligned} \tag{4.29.16}$$

The current deviatoric and volumetric strengths are hardening functions of the maximum volume fraction of the solid material obtained during any prior loading, ϕ , as is the parameter that defines the fraction of associated and radial flow, β . Therefore,

$$\begin{aligned}
a &= a(\phi) \quad ; \quad b = b(\phi) \\
\beta &= \beta(\phi).
\end{aligned} \tag{4.29.17}$$

Through the loading cycle, the maximum volume fraction of solid material is written as,

$$\phi = \max_{t>0} \tilde{\phi}(t) \tag{4.29.18}$$

where $\tilde{\phi}(t)$ is the current volume fraction of solid material defined as

$$\tilde{\phi}(t) = \frac{\phi_0}{\exp(\varepsilon_v^p)}, \tag{4.29.19}$$

with ϕ_0 and ε_v^p being the initial solid volume fraction and plastic volumetric strain, respectively.

The foam damage model, as presented, provides a phenomenological model with enough flexibility to model the observed deformation and failure of rigid polyurethane foams.

4.29.2. Implementation

Like the other foam models, the foam damage model is integrated using an explicit forward Euler scheme. Essentially, this specific form is a combination of a rate-dependent viscoplastic mechanism and a distinct damage element. At the highest level, these two responses are considered independently and sequentially with the viscoplastic behavior being evaluated first. Initially, the damage parameter is set to 0 and is limited to a maximum value of 0.99 to prevent the tensile strength from going to zero or negative due to numerical round-off. Foam material elements that are completely damaged can be removed using element death based approaches in the case of the damage variable reaching a value close to 1, say 0.99. This topic, however, will not be discussed here as the focus is on the constitutive behavior of the foam model.

To ensure integration stability, an allowable strain increment is first calculated so that a critical time step may be found. Essentially, such a maximum is given by the ratio of shear strength to

elastic modulus. If the input time step is sufficiently small to meet this requirement, the material state at time $t = t_{n+1}$ is calculated directly. For unsuitably large time steps, a series of sub-increments are used such that the integration may proceed in a stable fashion. Specifically, a total time step of Δt is subdivided into N sub-increments with the k^{th} such sub-increment having a time interval of δt^k so that $\Delta t = \sum_{k=1}^N \delta t^k$. In this case, the same forward Euler scheme is used to integrate successively over the sub-increments. For temperature dependent properties (e.g. the power law exponent n), the value at the start of the sub-increment is determined by linearly interpolating over the total time step,

$$n^k = n_n + \frac{\Delta t^k}{\Delta t} (n_{n+1} - n_n), \quad (4.29.20)$$

with Δt^k begin the current sub-increment time step, $\Delta t^k = \sum_{r=1}^k \delta t^r$. For simplicity, in the remainder of this section it is assumed that the input time step is acceptable and only a single increment is needed. If additional sub-increments are needed, the below steps would be repeated N times with time intervals of δt^k .

The rate-dependent plastic response is then calculated in a fashion very similar to that of the viscoplastic foam model (Section 4.28.2). The key differences are primarily the additional, and more complex, dependencies of ν , β , a , and b on the solid volume fraction. As such, first the various material properties and model parameters that are dependent on temperature, θ , or solid volume fraction, ϕ , are determined based on the respective values at $t = t_n$. The effective plastic strain rate, $\dot{\varepsilon}^p$, is readily found as,

$$\dot{\varepsilon}^p = e^{h(\theta_n)} \left\langle \frac{\sigma_n^*}{a(\phi_n)} - 1 \right\rangle^{n(\theta_n)}, \quad (4.29.21)$$

where σ_n^* is given by,

$$\sigma_n^* = \sqrt{\bar{\sigma}_n^2 + \frac{a^2(\phi_n)}{b^2(\phi_n)} p_n^2}, \quad (4.29.22)$$

and $\langle x \rangle$ are the Macaulay brackets evaluated as,

$$\langle x \rangle = \begin{cases} x, & x \geq 0 \\ 0, & x < 0 \end{cases}. \quad (4.29.23)$$

Knowing the effective plastic strain increment, corresponding stress increments may be determined. Specifically, the rates of change of the deviatoric stress, \dot{s}_{ij} , and pressure, \dot{p} , are given for isothermal conditions by

$$\dot{s}_{ij} = 2\mu_n \left(\hat{d}_{ij} - \hat{d}_{ij}^p \right), \quad (4.29.24)$$

$$\dot{p} = K_n \left(d_{kk} - d_{kk}^p \right), \quad (4.29.25)$$

with d_{ij} and d_{ij}^p being the the total and plastic, respectively, rates of deformation, and the symbol “ \hat{x}_{ij} ” denoting the deviatoric part of the tensor x_{ij} . The plastic strain rate is given by,

$$d_{ij}^p = \dot{\hat{\varepsilon}}^p g_{ij}^n, \quad (4.29.26)$$

where g_{ij}^n is evaluated via relation (4.29.10)-(4.29.12) using state variable at time $t = t_n$ and it is noted that $\beta = \beta(\phi_n)$. Elastic constants K_n and μ_n are found through isotropic relations using the values E_n and ν_n so the temperature and solid volume fraction dependencies may be incorporated.

Therefore, after accounting for plastic deformation and any associated temperature changes,

$$\tilde{s}_{ij} = \frac{\mu_{n+1}}{\mu_n} s_{ij}^n + \dot{s}_{ij} \Delta t, \quad (4.29.27)$$

$$\tilde{p}_{ij} = \frac{K_{n+1}}{K_n} p^n + \dot{p} \Delta t, \quad (4.29.28)$$

$$\tilde{T}_{ij} = \tilde{s}_{ij} + \tilde{p} \delta_{ij}, \quad (4.29.29)$$

where the tilde, “ \tilde{x} ”, is used to distinguish the fact that the damage response has not yet been evaluated and these are temporary variables. Updated expressions for the state variables are also given as,

$$\varepsilon_v^{p-n+1} = \varepsilon_v^{p-n} + d_{kk}^p \Delta t, \quad (4.29.30)$$

$$\phi_{n+1} = \max \left[\frac{\phi_0}{\exp(\varepsilon_v^{p-n+1})}, \phi_n \right]. \quad (4.29.31)$$

With the plastic deformations determined, the damage state of the material is evaluated. As a first step, the eigenvalues, $\hat{\sigma}^i$, and vectors, \hat{e}_i^k (where k denotes the corresponding eigenvalue) of the stress state, \tilde{T}_{ij} , and eigenvalues, ε_i of the total strain state are determined. Of particular interest is the maximum eigenvalue of the strain tensor, ε_{\max} . The damage strain, $\varepsilon_{\text{dam}}^{n+1}$, is

$$\varepsilon_{\text{dam}}^{n+1} = \langle a_{\text{dam}} \varepsilon_{\max} + b_{\text{dam}} \varepsilon_v^{p-n+1} \rangle, \quad (4.29.32)$$

with $\langle \rangle$ being Macaulay brackets. This value of the damage strain is then used to evaluate the current value of the damage, w^{n+1} , and a check is also imposed to insure that the damage does not decrease. An effective tensile strength, σ^{dam} , may then be calculated as

$$\sigma^{\text{dam}} = c (1 - w^{n+1}), \quad (4.29.33)$$

leading to a damage surface of the form,

$$f_{\text{dam}}^i = \hat{\sigma}^i - \sigma^{\text{dam}}. \quad (4.29.34)$$

The eigenvalues of the updated stress tensor may be written as,

$$\hat{\sigma}_{n+1}^i = \begin{cases} \hat{\sigma}^i, & f_{\text{dam}}^i \leq 0 \\ \sigma^{\text{dam}}, & f_{\text{dam}}^i > 0 \end{cases}, \quad (4.29.35)$$

producing a final updated stress state of the form,

$$T_{ij}^{n+1} = \sum_{k=1}^3 \hat{\sigma}_{n+1}^k \hat{e}_i^k \hat{e}_j^k. \quad (4.29.36)$$

4.29.3. Verification

Given the complexity and variety of response and features of the foam damage model, a series of verification analyses are performed. Common material properties and model parameters used for these investigations are given in Table 4-45. For these initial studies, isothermal loadings are considered and the solid volume fraction dependence of the elastic properties is neglected ($f_E(\phi) = 1$, $f_V(\phi) = 1$). Properties used correspond to those of a FR3712 foam from [1]. In the case of the elastic modulus, flow rate, and exponent, the values correspond those at a temperature of 18.30°C.

E	9,240 psi	c	280 psi
ν	0.25	a_{dam}	1.0
h	2.60	b_{dam}	0.55
n	14.0	ϕ_0	0.160

Table 4-45. Common material properties and model parameters for the foam damage model used during verification testing.

The shear strength, hydrostatic strength, and damage function all require user defined functional forms. For purposes of these tests, simple linear forms are considered for use in the analytical evaluations. Using the data same FR3712 data as before, simplified expressions of the form,

$$a(\phi) = 160 + 2400\phi, \quad (4.29.37)$$

$$b(\phi) = 160 + 3266.67\phi, \quad (4.29.38)$$

$$w(\varepsilon_{\text{dam}}) = \frac{10}{3}\varepsilon_{\text{dam}}, \quad (4.29.39)$$

are considered.

4.29.3.1. Uniaxial Compression

First, the behavior of the model subject to a uniaxial compression load is considered. As the loading is purely compressive, no tensile stress is generated and the damage surface is not violated. Therefore, only the rate-dependent plasticity is considered in this section. Given the rate-dependent nature, no analytical solution is readily available and a semi-analytical approach is developed by specializing the equations to uniaxial compression. Additionally, it is noted that the flow parameter, β , is not specified above and is enabled in this model to be an user-defined function of the solid volume fraction ϕ . Here, to isolate the impact of this parameter, the two extreme cases are considered – fully associated or radial flow with $\beta = 0, 1$, respectively.

To induce the uniaxial stress state of interest, a displacement of the form $u_1 = \lambda_1$ is applied while the remaining degrees of freedom (2 and 3) are left traction free. The applied displacement scales linearly from $\lambda_1 = 0$ at $t = 0.0$ to $\lambda_1 = -0.7$ at $t = 1.0$. In this case, the stress state is simply

$\sigma_{ij} = \sigma_{11}\delta_{i1}\delta_{j1}$ leading to an overstress of the form $\sigma^* = |\sigma_{11}| \sqrt{1 + \frac{a^2}{9b^2}}$. For both associated and radial flow, the inelastic flow rate simplifies to,

$$D_{ij}^{\text{in}} = e^h \left\langle \frac{|\sigma_{11}|}{3ab} \sqrt{a^2 + 9b^2} - 1 \right\rangle^n g_{ij}, \quad (4.29.40)$$

with $\langle \cdot \rangle$ being Macaulay brackets. The total strains may then be written as,

$$\varepsilon_{11} = \ln(1 + \lambda_1), \quad (4.29.41)$$

$$\varepsilon_{22} = \varepsilon_{33} = -\nu (\ln(1 + \lambda_1) - \varepsilon_{11}^{\text{in}}) + \varepsilon_{22}^{\text{in}}, \quad (4.29.42)$$

where $\varepsilon_{ij}^{\text{in}} = \int_0^t D_{ij}^{\text{in}} d\tau$. The associated and radial flow cases are distinguished by the form of g_{ij} . In the latter case, g_{ij} reduces simply to $g_{ij}^r = \delta_{i1}\delta_{j1}$. The former case, on the other hand, produces a flow direction of the form,

$$\hat{g} = \frac{1}{3 \sqrt{\frac{2}{3} (2a^4 + 81b^4)}}, \quad (4.29.43)$$

$$g_{11}^r = \hat{g} 2 (a^2 + 9b^2), \quad (4.29.44)$$

$$g_{22}^r = g_{33}^r = \hat{g} (2a^2 - 9b^2). \quad (4.29.45)$$

The stress evolution for both of these flow cases determined numerically (adagio) and semi-analytically is presented in Figure 4-114a.

From these results, the impact of the flow direction choice can be observed to have a large impact on the model response. Specifically, in the radial case more substantial hardening is seen throughout the entire plastic domain. As the hardening results from the solid volume fraction (which is a function of volumetric plastic deformation), such a difference may be anticipated.

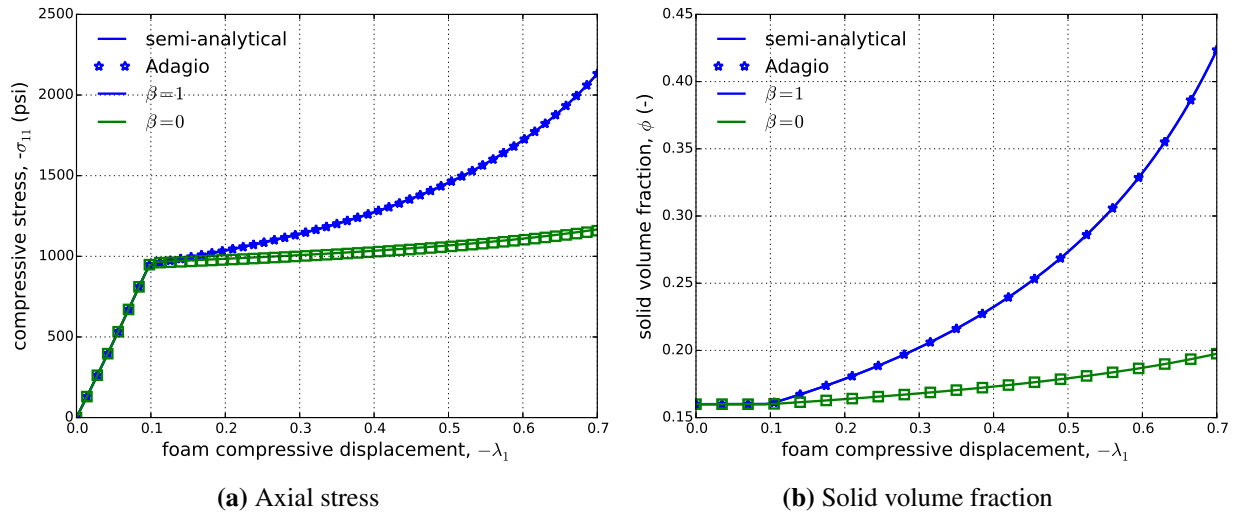


Figure 4-114. (a) Axial stress and (b) maximum solid volume fraction, ϕ , evolution obtained as a function of applied compressive displacement and determined via the foam damage model considering both associated ($\beta = 0$) and radial ($\beta = 1$) flow assumptions semi-analytically and numerically.

Specifically, given the uniaxial plastic flow in the radial case more pronounced volumetric strains are to be expected. The associated case, on the other hand, has a more deviatoric character leading to lower plastic volume strains. This difference may also be more readily observed in the total strain evolutions of the associated and radial cases in Figures 4-115a and 4-115b, respectively.

Specifically, in the radial case, only small off-axis strains are observed while in the associated results much more substantial strains are noted. This difference produces a large impact on the plastic volumetric strain and therefore on the maximum solid volume fraction, ϕ , whose evolution through loading in both cases is presented in Figure 4-114b. To emphasize this point, the radial solid volume fraction is more than double the associated case at the end of loading.

4.29.3.2. Uniaxial Tension

As the compressive and tensile behaviors of the model are different (due to the activation of the damage mechanism), the uniaxial tensile response is also investigated. To this end, a uniaxial displacement is applied, $u_1 = \lambda_1$, while the other off-axis components are kept traction free. For this test, the maximum displacement ($\lambda_1 = 0.2$) is applied linearly from $t = 0.0$ to $t = 1.0$. Use of a displacement condition is essential due to the expected stress degradation. In this case, given the relative values of the strength ($a(\phi_0)$ versus c) it is clear that no plastic deformations will take place and a purely damage driven response is expected. With this simplification, it is also noted that the rate-dependency of the problem is eliminated. As the stress state is uniaxial, it is clear that the only non-zero eigenvalue of the stress tensor is σ_{11} and that

$\varepsilon_{\text{dam}} = a_{\text{dam}} \varepsilon_{11} = a_{\text{dam}} \ln(1 + \lambda_1)$ where the fact that the plastic strain is zero is utilized. Bearing

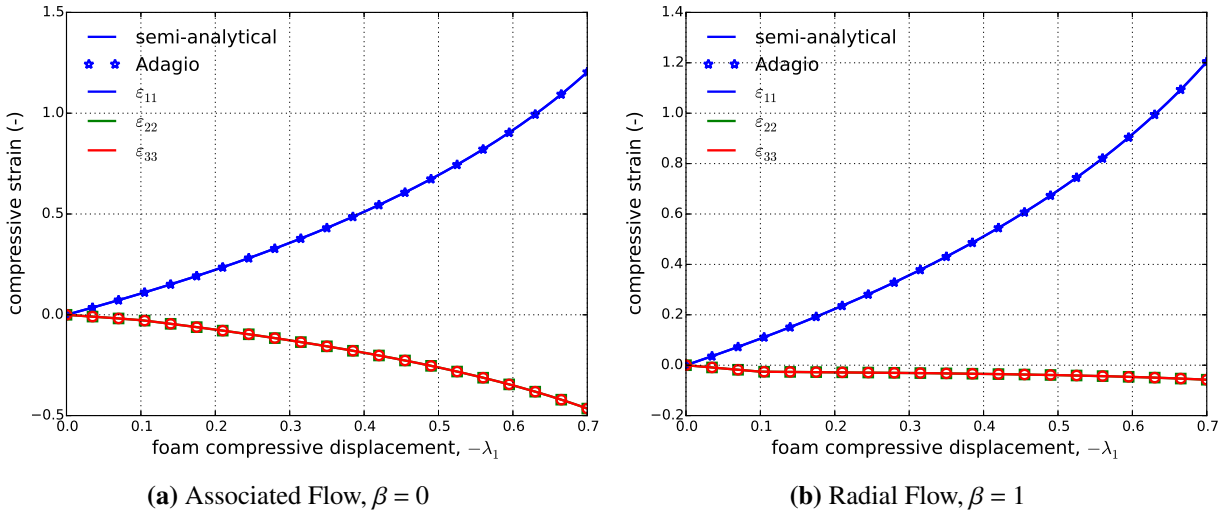


Figure 4-115. Diagon strain evolution through a uniaxial displacement loading of the foam damage model considering (a) associated ($\beta = 0$) and (b) radial ($\beta = 1$) flow determined semi-analytically and numerically.

these simplifications in mind, an analytical expression for the stress and strain may be developed. The stress in the axial direction may be written as,

$$\sigma_{11} = \begin{cases} (\mathbb{C}_{1111} - 2\nu\mathbb{C}_{1122}) \ln(1 + \lambda_1), & \lambda_1 < \lambda_{\text{crit}} \\ c \left(1 - \frac{10}{3}a_{\text{dam}} \ln(1 + \lambda_1)\right), & \lambda_1 \geq \lambda_{\text{crit}} \end{cases}, \quad (4.29.46)$$

where

$$\lambda_{\text{crit}} = \exp\left(\frac{c}{\mathbb{C}_{1111} - 2\nu\mathbb{C}_{1122} + \frac{10}{3}a_{\text{dam}}c}\right) - 1. \quad (4.29.47)$$

The analytical results along with numerical simulations from adagio are given below in Figure 4-116.

4.29.3.3. Hydrostatic Compression

To consider the pressure dependence, the response of this model subject to a hydrostatic compression loading is determined. Specifically, a displacement of the form $u_i = \lambda(t)$ is considered. The applied displacement scales linearly from $\lambda = 0$ at $t = 0.0$ to $\lambda = -0.7$ at $t = t_{\text{max}}$. Two cases are considered to incorporate rate-dependent effects into the analysis. The two tests are denoted “fast” and “slow” and are distinguished via t_{max} values of 1.0 and 100.0, respectively. With this displacement field the engineering volume strain, ε_V , is simply $\varepsilon_V = (1 + \lambda)^3 - 1$. The stress state reduces trivially to $\sigma_{ij} = -p\delta_{ij}$ and the corresponding (repeated) eigenvalue is compressive. Therefore, damage does not play a role in this analysis.

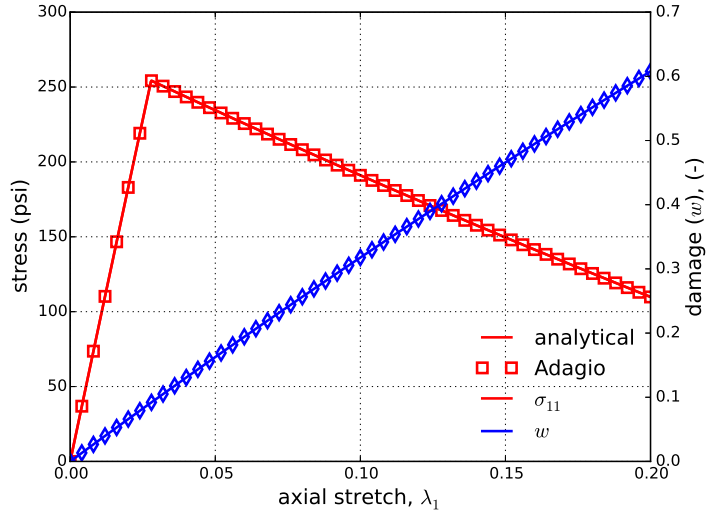


Figure 4-116. Response of the foam damage model through a uniaxial stress, displacement controlled tension simulation. Stress in the loading direction, σ_{11} , and damage measure, w , against the applied displacement, λ_1 , are shown.

No direct analytical solution to this problem is readily obtainable. Therefore, a semi-analytical analysis is used. Reducing the foam damage model for the loading described in this section leads to an expression for the overstress of,

$$\sigma^* = \frac{a}{b}|p|, \quad (4.29.48)$$

where the fact that $s_{ij} = 0$ is leveraged. Additionally, given this stress state, β becomes an unnecessary parameter as,

$$g_{ij} = g_{ij}^a = g_{ij}^r = -\frac{1}{\sqrt{3}}\text{sgn}(p)\delta_{ij}, \quad (4.29.49)$$

with $\text{sgn}(p)$ being the sign of p . Both the numerical (adagio) and semi-analytical (evaluated in a forward Euler fashion) results are presented in Figure 4-117.

4.29.3.4. Hydrostatic Tension

A tensile hydrostatic loading provides an interesting possibility for investigating the damage response. Specifically, with the model parameters defined above the damage tensile strength is always less than the hydrostatic strength - $c < b(\phi_0)$. Additionally, given the tensile loading $\phi(t) = \phi_0$ and no plastic deformation occurs. This also removes the rate-dependency form the model enabling an analytical solution to be obtained.

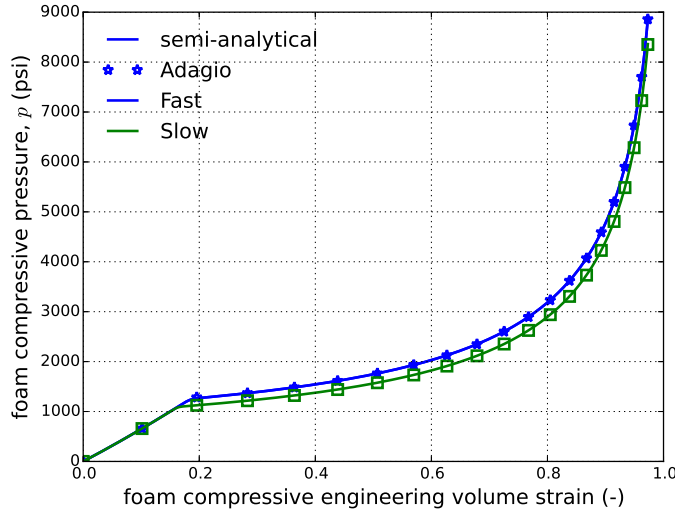


Figure 4-117. Pressure-engineering volume strain results of the foam damage model subjected to a hydrostatic loading at both fast and slow rates determined semi-analytically and numerically.

Through a hydrostatic loading, the only stress eigenvalue is $-p$ (noting the convention of p positive in compression) and the corresponding strain eigenvalue is $\varepsilon_{\max} = \ln(1 + \lambda)$. As no plastic deformation is occurring, the damage is simply a function of the deformation and is given by,

$$w(\varepsilon_{\text{dam}}) = w(\lambda) = \frac{10}{3}a_{\text{dam}} \ln(1 + \lambda). \quad (4.29.50)$$

The pressure is then simply given as,

$$p = \begin{cases} \frac{3K \ln(1 + \lambda)}{c} & \lambda < \lambda_{\text{crit}} \\ c \left(1 - \frac{10}{3}a \ln(1 + \lambda)\right) & \lambda \geq \lambda_{\text{crit}} \end{cases}, \quad (4.29.51)$$

where,

$$\lambda_{\text{crit}} = \exp\left(\frac{3c}{9K + 10c}\right) - 1. \quad (4.29.52)$$

In the preceding relations, the fact that $\varepsilon_{\text{dam}} = a\varepsilon_{\max}$ is used. The analytical and numerical results are given below for a loading of $\lambda = 0$ to $\lambda = 0.2$ through the time period $t = [0, 1]$ in Figure 4-118.

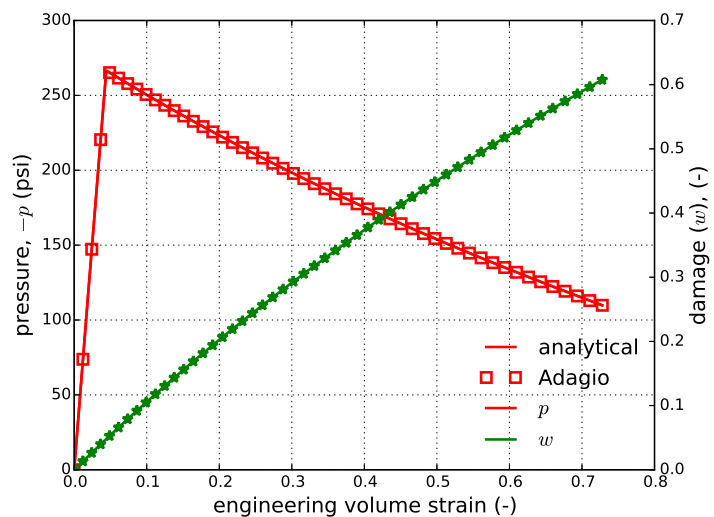


Figure 4-118. Pressure and damage evolutions as function of engineering volume strain results of the foam damage model subject to a tensile hydrostatic loading determined analytically and numerically. Note, conventionally with this model pressure is defined positive in compression.

4.29.4. User Guide

```
BEGIN PARAMETERS FOR MODEL FOAM_DAMAGE
#
# Elastic constants
#
YOUNGS MODULUS = <real> E
POISSONS RATIO = <real> ν
SHEAR MODULUS = <real> G
BULK MODULUS = <real> K
LAMBDA = <real> λ
TWO MU = <real> 2μ
#
# Yield behavior
#
PHI = <real> ϕ₀
FLOW RATE = <real> h
POWER EXPONENT = <real> n
TENSILE STRENGTH = <real> c
ADAM = <real> adam
BDAM = <real> bdam
#
# Functions
#
YOUNGS FUNCTION = <string> hE(θ)
POISSONS FUNCTION = <string> hν(θ)
RATE FUNCTION = <string> hh(θ)
EXPONENT FUNCTION = <string> hn(θ)
SHEAR HARDENING FUNCTION = <string> a(ϕ)
HYDRO HARDENING FUNCTION = <string> b(ϕ)
BETA FUNCTION = <string> β(ϕ)
YOUNGS PHI FUNCTION = <string> fE(ϕ)
POISSONS PHI FUNCTION = <string> fν(ϕ)
DAMAGE FUNCTION = <string> w(εdam)
END [PARAMETERS FOR FOAM_DAMAGE]
```

Output variables available for this model are listed in Table 4-46. For information about the foam damage model, consult [1].

Table 4-46. State Variables for FOAM DAMAGE Model

Name	Variable Description
ITER	number of sub-increments taken in subroutine
EPVOL	plastic volume strain
PHI	maximum volume fraction of solid material
EQPS	equivalent plastic strain
FA	shear strength - a
FB	hydrostatic strength - b
DAMAGE	damage
EMAX	maximum tensile strain
PWORK	plastic work rate

REFERENCES

- [1] M. K. Neilsen, W. Y. Lu, W. M. Scherzinger, T. D. Hinnerichs, and C. S. Lo. Unified creep plasticity damage (UCPD) model for rigid polyurethane foams. Technical Report SAND2015-4352, Sandia National Laboratories, Albuquerque, NM, 2015.

4.30. ORTHOTROPIC CRUSH MODEL

4.30.1. Theory

The orthotropic crush model in LAMÉ is designed to model the energy absorbing capability of crushable orthotropic materials, e.g. aluminum honeycomb, and is empirically based. The formulation follows that used for metallic honeycomb materials in LS-DYNA [1]. Three response regimes are assumed for this material: (i) orthotropic elastic, (ii) crush, and (iii) complete compaction (fully crushed). During the elastic regime, the model exhibits the response of an elastic, orthotropic material with *all Poisson's ratio equal to zero*. After full compaction, the response is taken to be that of an isotropic, perfectly plastic material and the response between these two stages is tailored to smoothly transition between the two extremes. Crushing, incorporating both nonlinear elastic and plastic-like behaviors, is taken to begin as soon as volumetric contraction is noted ($J = \det(F_{ij}) < 1$). As such, the purely elastic response is primarily seen during cyclic loadings in which the material is unloaded. An internal state variable, J_c , is introduced to track the crushed state of the material and is defined as the minimum J over the entire deformation history such that,

$$J_c = \min_{t>0} [J(t)]. \quad (4.30.1)$$

The crushing process manifests through two distinct behaviors: (i) the elastic properties scale linearly with the crush state from the initial orthotropic state to the of the final isotropic completely compacted material; and (ii) a plastic-like response is observed associated with corresponding crush curves (analogous to hardening curves).

Before complete compaction, the incremental constitutive relation may be written in terms of the rate of deformation tensor, D_{ij} , as,

$$\begin{Bmatrix} \overset{\circ}{\sigma}_{11} \\ \overset{\circ}{\sigma}_{22} \\ \overset{\circ}{\sigma}_{33} \\ \overset{\circ}{\sigma}_{12} \\ \overset{\circ}{\sigma}_{23} \\ \overset{\circ}{\sigma}_{31} \end{Bmatrix} = \begin{bmatrix} \hat{E}_{11} & 0 & 0 & 0 & 0 & 0 \\ 0 & \hat{E}_{22} & 0 & 0 & 0 & 0 \\ 0 & 0 & \hat{E}_{33} & 0 & 0 & 0 \\ 0 & 0 & 0 & 2\hat{G}_{12} & 0 & 0 \\ 0 & 0 & 0 & 0 & 2\hat{G}_{23} & 0 \\ 0 & 0 & 0 & 0 & 0 & 2\hat{G}_{31} \end{bmatrix} \begin{Bmatrix} D_{11} \\ D_{22} \\ D_{33} \\ D_{12} \\ D_{23} \\ D_{31} \end{Bmatrix} \quad (4.30.2)$$

where \hat{E}_{11} , \hat{E}_{22} , and \hat{E}_{33} are the normal stiffness and \hat{G}_{12} , \hat{G}_{23} , and \hat{G}_{31} are the shear stiffness. A clear decoupling between the different directional components is evident in (4.30.2). All six stiffness components are assumed to be functions of the current compaction level which may be defined as $1 - J_c$ and the evolution of these terms is responsible for crushing behavior (i) alluded to previously.

The functional forms of the stiffness are given by,

$$\begin{aligned}\hat{E}_\beta &= E_\beta + \alpha (E - E_\beta) & \beta = 11, 22, 33 \\ \hat{G}_\gamma &= G_\gamma + \alpha (G - G_\gamma) & \gamma = 12, 23, 31,\end{aligned}\quad (4.30.3)$$

where E and G are the Young's and shear moduli, respectively, of the fully compacted material while E_β and G_γ are the input orthotropic elastic stiffness components of the virgin, uncompact material. It is assumed that these stiffness vary linearly between the pre- and post-compact material such that,

$$\alpha = \frac{(1 - J_c)}{V_{min}}, \quad (4.30.4)$$

with V_{min} being the minimum relative volume (or maximum compaction).

With respect to the second behavior observed during crushing, a plastic-like response governed by crush curves is observed. Given the decoupling between the different stresses and deformations, a crush curve needs to be defined for each of the six normal and shear stresses. An example of such a curve is presented in Figure 4-119, and three distinct regions are evident. Initially, at low compaction levels, a plateau is observed. This plateau is essentially an initial crush strength and prior to this stress level all nonlinear deformations associated with material compaction manifest through changes in the respective moduli. When the stress reaches the specified levels, however, the curves play a role analogous to the hardening curve and the material stress follows the curve. Physically, the plateau is associated with crushing the internal honeycomb or foam structure of the material. As the material approaches full compaction and microstructural contact effects become important, a sharp rise in the stress is noted (see $\approx 0.6 \leq 1 - J_c \leq 0.7 = V_{min}$ in Figure 4-119). After complete compaction another plateau corresponding to perfect plasticity is evident.

Above some value of compaction ($1 - J_c = V_{min}$), the material will be fully compacted and behave as an elastic, perfectly plastic material. The fully compacted response is given by the Young's modulus, E , Poisson's ratio, ν , and the yield stress, σ_y . Details of this response may be found in previous sections on the various elastic-plastic models (e.g. Section 4.7.1).

4.30.2. Implementation

Implementation of the orthotropic crush model involves addressing two cases: before and after complete compaction. When the material is fully crushed, the model reduces to that of an isotropic perfectly plastic response. As corresponding isotropic elastic-plastic models with various hardenings have been extensively explored in prior sections, this response will not be discussed here and the reader is referred to those sections (e.g. Section 4.7.2). The two cases are distinguished by the previous compaction state variable, J_c^n , where $J_c^{n+1} = \min [J_c^n, J^{n+1}]$ with $J^{n+1} = \det (F_{ij}^{n+1}) = \det (V_{ij}^{n+1})$. If $J_c^n > 1 - V_{min}$, the material has not yet fully crushed and the response is evaluated as discussed in the following.

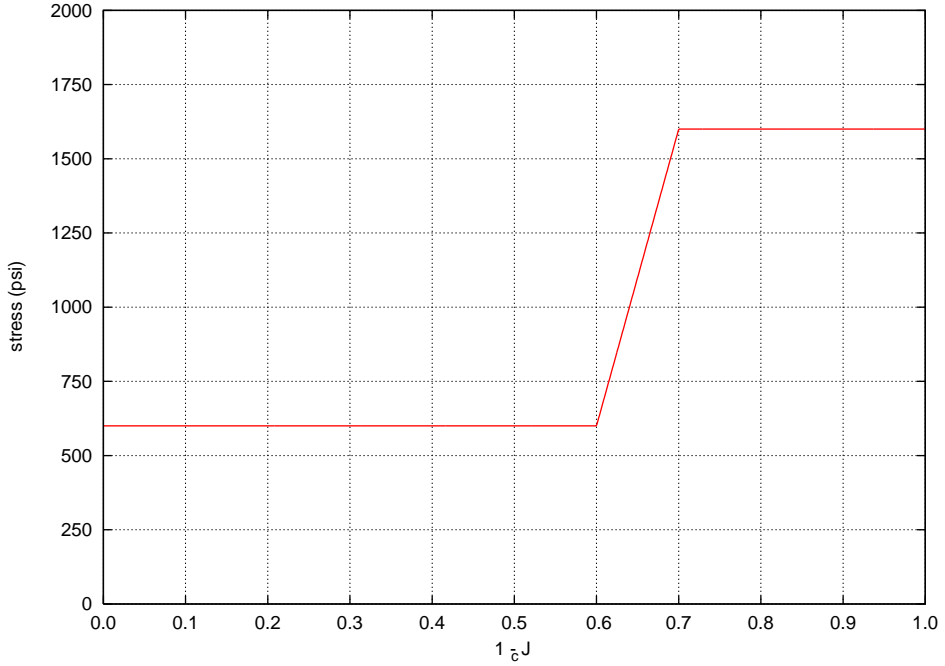


Figure 4-119. An example of an input crush curve for an aluminum honeycomb.

To determine the material state prior to complete compaction, the current values of orthogonal stiffness must be determined via (4.30.3) noting

$$\alpha^{n+1} = \frac{1 - J_c^n}{V_{min}}. \quad (4.30.5)$$

By assuming completely elastic deformation, trial stresses may then be computed as,

$$\begin{aligned} \sigma_{11}^{tr} &= \sigma_{11}^n + \Delta t \hat{E}_{11} (\alpha^{n+1}) d_{11}^{n+1}, \\ \sigma_{22}^{tr} &= \sigma_{22}^n + \Delta t \hat{E}_{22} (\alpha^{n+1}) d_{22}^{n+1}, \\ \sigma_{33}^{tr} &= \sigma_{33}^n + \Delta t \hat{E}_{33} (\alpha^{n+1}) d_{33}^{n+1}, \\ \sigma_{12}^{tr} &= \sigma_{12}^n + 2 \Delta t \hat{G}_{12} (\alpha^{n+1}) d_{12}^{n+1}, \\ \sigma_{23}^{tr} &= \sigma_{23}^n + 2 \Delta t \hat{G}_{23} (\alpha^{n+1}) d_{23}^{n+1}, \\ \sigma_{31}^{tr} &= \sigma_{31}^n + 2 \Delta t \hat{G}_{31} (\alpha^{n+1}) d_{31}^{n+1}, \end{aligned} \quad (4.30.6)$$

with d_{ij}^{n+1} being the unrotated rate of deformation tensor. Given the decoupling between the different stress components, the various trial stresses are considered individually. Specifically, each trial stress must be compared to the crush stress for the current compaction level. Denoting $\sigma_{\beta}^{crush} = \hat{\sigma}_{\beta} (1 - J_c^{n+1})$ (with $\beta = 11, 22, 33, 12, 23$, or 31) to be the current crush stress specified by the crush curve, the current stress of interest is,

$$\sigma_{\beta}^{n+1} = \begin{cases} \sigma_{\beta}^{tr}, & |\sigma_{\beta}^{tr}| \leq \sigma_{\beta}^{crush} \\ \operatorname{sgn}(\sigma_{\beta}^{tr}) \sigma_{\beta}^{crush}, & |\sigma_{\beta}^{tr}| > \sigma_{\beta}^{crush}, \end{cases} \quad (4.30.7)$$

where $\operatorname{sgn}(x)$ returns the sign of the argument and is used as σ_{β}^{crush} is entered as a positive number.

4.30.3. Verification

The orthotropic crush model was verified through a series of uniaxial compression tests. Given the lack of coupling between the different directions, such a variety of tests were performed to test each loading component. One set of material properties was used for all tests and they are given in Table 4-47.

E_{11}	50.0 ksi	E	1000.0 ksi
E_{22}	220.0 ksi	ν	0.25
E_{33}	10.0 ksi	σ_y	2.0 ksi
G_{12}	110.0 ksi		
G_{23}	5.0 ksi	V_{min}	0.7
G_{31}	25.0 ksi		

Table 4-47. The material properties for the orthotropic crush model used for the uniaxial crush tests.

The crush curves used as input for these tests are given in Figure 4-120.

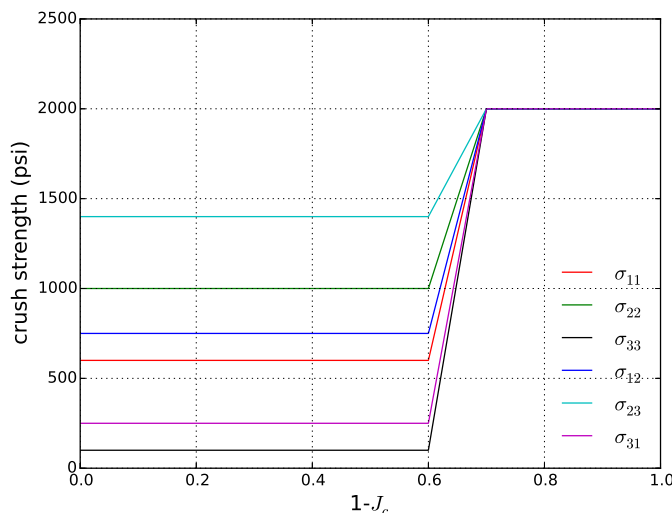


Figure 4-120. Input crush curves used for uniaxial crush analysis.

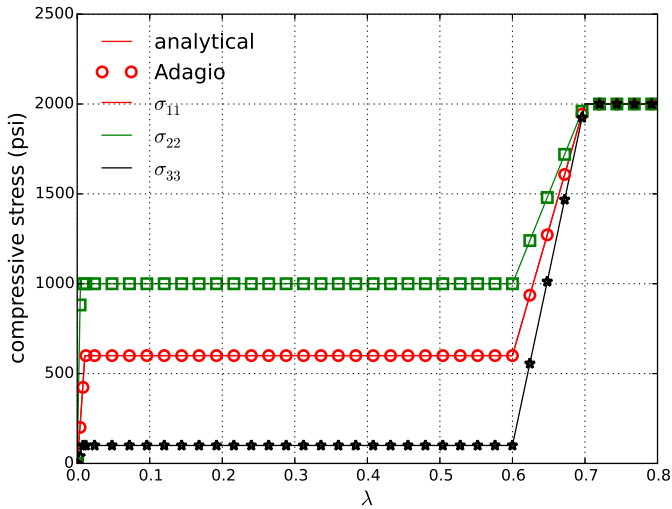


Figure 4-121. Analytical and numerical results for uniaxial crush cases.

To test this model, both the anisotropic nature and different deformation regimes need to be tested. Therefore, given the decoupled directional nature prior to complete compaction, each component will be tested. For the diagonal stress components, a simple uniaxial displacement of the form,

$$u_i = -\lambda \delta_{i\beta}, \quad (4.30.8)$$

where $\beta = 1, 2$, or 3 corresponding to the directional component being tested is applied. In such cases (with a monotonically increasing λ), $J_c = 1 - \lambda$. The model described in the prior to sections can be easily evaluated analytically under such conditions, and the corresponding analytical and numerical results are presented in Figure 4-121.

4.30.4. User Guide

```

BEGIN PARAMETERS FOR MODEL ORTHOTROPIC_CRUSH
#
# Elastic constants - Post lock-up
YOUNGS MODULUS = <real> E
POISSONS RATIO = <real> ν
SHEAR MODULUS = <real> G
BULK MODULUS = <real> K
LAMBDA = <real> λ
TWO MU = <real> 2μ
#
# Orthotropic Elastic properties - Pre-Crush
#
EX = <real> E11
EY = <real> E22
EZ = <real> E33
GXY = <real> G12
GYZ = <real> G23
GZX = <real> G31
#
# Crush properties
#
CRUSH XX = <string>  $\hat{\sigma}_{11}(J_c)$ 
CRUSH YY = <string>  $\hat{\sigma}_{22}(J_c)$ 
CRUSH ZZ = <string>  $\hat{\sigma}_{33}(J_c)$ 
CRUSH XY = <string>  $\hat{\sigma}_{12}(J_c)$ 
CRUSH YZ = <string>  $\hat{\sigma}_{23}(J_c)$ 
CRUSH ZX = <string>  $\hat{\sigma}_{31}(J_c)$ 
VMIN = <real> Vmin
#
# Post lock-up yield properties
#
YIELD STRESS = <real> σy
#
END [PARAMETERS FOR MODEL ORTHOTROPIC_CRUSH]

```

Output variables available for this model are listed in Table 4-48. For information about the orthotropic crush model, consult [1].

Table 4-48. State Variables for ORTHOTROPIC CRUSH Model

Name	Description
CRUSH	current (unrecoverable) compaction/relative volume

REFERENCES

- [1] R.G. Whirley, B.E. Engelmann, and J.O. Halquist. DYNA3D user's manual, 1991.

4.31. ORTHOTROPIC RATE MODEL

4.31.1. Theory

The orthotropic rate model is an improved version of the orthotropic crush model [1] that incorporates anisotropic elasticity, strain-rate dependence, and the ability to define the material coordinate system. The specific form of this model is motivated by metallic honeycombs and the material coordinate system is usually given in terms of T , L , and W directions. These directions correspond to the strong (T) and ribbon (L) axes depicted in Figure 4-122. The third component of the coordinate system, W , is the weak direction and is simply the cross-product of the other two directions.

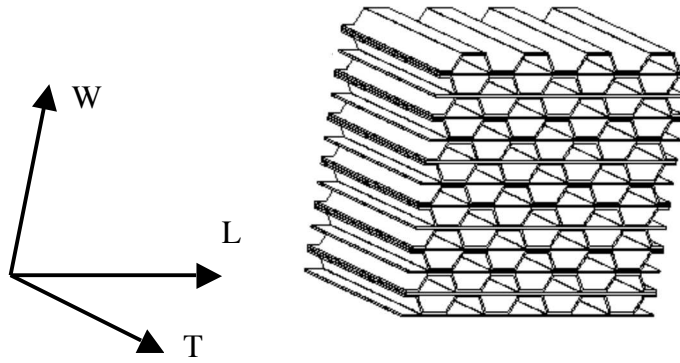


Figure 4-122. Orientation of the T , L and W vectors for 38 pc aluminum honeycomb.

In terms of expected response, and similar to the orthotropic crush model, the deformation is split into two regimes – uncompacted and compacted. Unlike the crush model, the state of compaction is not determined by the determinant of the deformation gradient but is instead a function of the engineering (not logarithmic) volume strain, ε_V . The degree of compaction, α , is therefore defined as,

$$\alpha = \min_{t>0} \left(\frac{V_0 - V(t)}{V_0} \right) = 1 - \frac{\min_{t>0} V(t)}{V_0} = -\min_{t>0} \varepsilon_V(t), \quad (4.31.1)$$

with $V(t)$ and V_0 being the current and original volume of the material. Complete compaction occurs at a user specified value, α_{comp} .

Prior to complete compaction, the elastic stiffness, \mathbb{C}_{ijkl} , is taken to exhibit orthotropic symmetry and depends on the compaction state of the material, $\mathbb{C}_{ijkl} = \mathbb{C}_{ijkl}(\alpha)$. In the material frame and in Voigt notation, this stiffness is represented as,

$$[\mathbb{C}(\alpha)] = \begin{bmatrix} E_{TTTT}(\alpha) & E_{TTLL}(\alpha) & E_{TTWW}(\alpha) & 0 & 0 & 0 \\ E_{TTLL}(\alpha) & E_{LLLL}(\alpha) & E_{LLWW}(\alpha) & 0 & 0 & 0 \\ E_{TTWW}(\alpha) & E_{LLWW}(\alpha) & E_{WWWW}(\alpha) & 0 & 0 & 0 \\ 0 & 0 & 0 & G_{TLTL}(\alpha) & 0 & 0 \\ 0 & 0 & 0 & 0 & G_{LWLW}(\alpha) & 0 \\ 0 & 0 & 0 & 0 & 0 & G_{WTWT}(\alpha) \end{bmatrix}. \quad (4.31.2)$$

Once the material is completely compacted, the elastic stiffness is taken to be isotropic and the evolution of the initially orthotropic components ($E_{TTTT}(\alpha = 0) = E_{TTTT}^0$) to final isotropic, compacted coefficients ($E_{TTTT}(\alpha = \alpha_{\text{comp}}) = \lambda + 2\mu$ with λ and 2μ being Lamé's constant and the shear modulus) is given via a common user-defined scaling function, $f_E(\alpha)$. The mechanical stiffness coefficients then scale as,

$$E_{TTTT}(\alpha) = E_{TTTT}^0 + (\lambda + 2\mu - E_{TTTT}^0) f_E(\alpha), \quad (4.31.3)$$

for the volumetric diagonal terms (E_{TTTT} , E_{LLLL} , E_{WWWW}),

$$E_{TTLL}(\alpha) = E_{TTLL}^0 + (\lambda - E_{TTLL}^0) f_E(\alpha), \quad (4.31.4)$$

for the off-diagonal terms (E_{TTLL} , E_{TTWW} , E_{LLWW}) and

$$G_{TLTL}(\alpha) = G_{TLTL}^0 + (2\mu - G_{TLTL}^0) f_E(\alpha) \quad (4.31.5)$$

for the shear terms. From these relations, it is obvious that $f_E(\alpha)$ should be bounded such that $0 \leq f_E(\alpha) \leq 1$ with $f_E(0) = 0$ and $f_E(\alpha_{\text{comp}}) = 1$.

As was mentioned earlier, the deformation and model response may be readily split between two regimes – the uncompact and compacted. The behavior during the latter regime is simpler and is assumed to be that of an isotropic elastic-perfectly plastic material characterized by the elastic coefficients (λ , 2μ) and yield stress (σ_y). During the uncompact regime the deformation is more complex and typical responses may include elastic bending of cell structures, buckling of cell walls, or densification (see the text of Gibson and Ashby [2] for a complete discussion of these and other mechanisms). In this formulation, however, none of these deformation modes are explicitly modeled. Instead, the response is defined via six independent yield functions (one for each stress component in the material coordinate system), $\phi_{\beta\gamma}$, that are a function of the corresponding stress, the compaction state, and the current strain rate, $\dot{\varepsilon} = \sqrt{d_{ij}d_{ij}}$. Here, d_{ij} is

the unrotated rate of deformation in the global (X, Y, Z) coordinate system and β and γ are being used as subscripts to denote variables in the material coordinate system.

The six yield functions are,

$$\begin{aligned}\phi_{LL} &= \sigma_{LL} - f_{LL}(\alpha)h(\dot{\varepsilon}) \\ \phi_{TT} &= \sigma_{TT} - f_{TT}(\alpha)h(\dot{\varepsilon}) \\ \phi_{WW} &= \sigma_{WW} - f_{WW}(\alpha)h(\dot{\varepsilon}) \\ \phi_{LT} &= \sigma_{LT} - f_{LT}(\alpha)h(\dot{\varepsilon}) \\ \phi_{TW} &= \sigma_{TW} - f_{TW}(\alpha)h(\dot{\varepsilon}) \\ \phi_{WL} &= \sigma_{WL} - f_{WL}(\alpha)h(\dot{\varepsilon})\end{aligned}, \quad (4.31.6)$$

with $\sigma_{\beta\gamma}$ being the current symmetric Cauchy stresses in the material coordinate system, $f_{\beta\gamma}$ are user specified hardening functions defining the maximum stress in that direction for a given compaction state and $h(\dot{\varepsilon})$ is the strain rate sensitivity function that is common to all the yield functions. With these forms, it is evident that the definition of the different hardening functions dictates the model response through the uncompacted regime. All (or none) of the aforementioned deformation mechanisms may be captured by the appropriate definition of those functions. As such, the response is dictated by the desire of the analyst and appropriate selection of the elastic scaling, hardening, and strain rate sensitivity function – $f_E(\alpha)$, $f_{\beta\gamma}(\alpha)$, and $h(\dot{\varepsilon})$.

4.31.2. Implementation

Unlike the orthotropic crush model, the rate variant considered here has couplings between the different directional strains and cannot be evaluate numerically as easily. Therefore, the orthotropic rate model is integrated using a hypoelastic formulation. As was discussed in the preceding section, the model is formulated in the T , L , W coordinate system and not the unrotated frame. Therefore, the first step before proceeding is to map strain and stress values from the unrotated to the material frame. To this end, an orthogonal rotation tensor \tilde{Q}_{ij} is constructed from user input vectors \hat{t}_i and \hat{l}_i defining the strong and ribbon directions, respectively. In this case, the “~” is used to differentiate this tensor from that mapping between the rotated and unrotated configurations defined in (4.1.1). The stress and deformation rates in the material coordinate system, $\tilde{\sigma}_{ij}$ and \tilde{d}_{ij} , are determined via,

$$\tilde{\sigma}_{ij}^n = \tilde{Q}_{ki} T_{kl}^n \tilde{Q}_{lj}, \quad (4.31.7)$$

$$\tilde{d}_{ij}^{n+1} = \tilde{Q}_{kid} d_{kl}^{n+1} \tilde{Q}_{lj}, \quad (4.31.8)$$

where T_{ij}^n and d_{ij}^{n+1} are the unrotated stress and deformation rates, respectively. For convenience, the remainder of this discuss will neglect the “~” notation and all operations will be assumed to be in the material coordinate system unless specifically noted. Additionally, after a converged stress is achieved, the inverse mapping of (4.31.7) is used to determine T_{ij}^{n+1} .

As the strain increment is fixed for a load step, kinematically defined variables such as α^{n+1} and the strain rate, $\dot{\varepsilon}^{n+1}$, may first be determined. The latter term is defined as,

$$\dot{\varepsilon}^{n+1} = \sqrt{d_{ij}^{n+1} d_{ij}^{n+1}}, \quad (4.31.9)$$

with d_{ij}^{n+1} being the strain rate in the global coordinate system. For the former, it must first be noted that the engineering, ε_V , and logarithmic, ε_{kk} , volumetric strains are related via $\varepsilon_V = \exp(\varepsilon_{kk}) - 1$. The current state of compaction is then given as,

$$\alpha^{n+1} = 1 - \hat{\varepsilon}_V^{n+1}, \quad (4.31.10)$$

where $\hat{\varepsilon}_V^{n+1} = \min [\hat{\varepsilon}_V^n, \exp(\varepsilon_{kk}^{n+1})]$.

The material response has two distinct regimes. As discussed in the corresponding theory section, the compacted material behaves as an elastic-plastic material. Such a response and the corresponding numerical analysis has been described in Section 4.7.2. As such, it will not be further presented here and instead the focus is on the behavior during the uncompacted stages.

Earlier, it was mentioned that the response during the compaction process is dictated by three functions – the elastic scaling, hardening, and strain rate sensitivity. These three expressions are dependent on the state of compaction and strain rate. As those kinematic properties have already been calculated, the values of $f_E^{n+1} = f_E(\alpha^{n+1})$, $f_{ij}^{n+1} = f_{ij}(\alpha^{n+1})$, and $h^{n+1} = h(\dot{\varepsilon}^{n+1})$ may easily be calculated. In the remainder of this section, the functional dependencies of these terms will not be explicitly presented for ease and brevity. Similarly, the superscript $n+1$ will be dropped and it should be assumed that unless specifically denoted the variable is evaluated at the $n+1$ step. With f_E (and f_E^n) defined, the elastic stiffness, \mathbb{C}_{ijkl} and \mathbb{C}_{ijk}^n , and compliance, \mathbb{S}_{ijkl} and \mathbb{S}_{ijk}^n , tensors may also be calculated.

To determine the updated material state, the change in elastic stiffness (associated with the change in compaction) must be determined. To this end,

$$\hat{\sigma}_{ij}^n = \mathbb{C}_{ijkl} \varepsilon_{kl}^{e-n} \quad (4.31.11)$$

where

$$\varepsilon_{ij}^{e-n} = \mathbb{S}_{ijkl}^n \sigma_{kl}^n. \quad (4.31.12)$$

In the previous two relations, it is noted that the respective mechanical tensors are determined at different load steps thus leading to the altered stress state. The tensor σ_{ij}^n refers to the stress determined and stored from the previous load step while $\hat{\sigma}_{ij}^n$ incorporates the change in mechanical stiffness. A trial stress state may be calculated as,

$$\sigma_{ij}^{tr} = \hat{\sigma}_{ij}^n + \mathbb{C}_{ijkl} d \varepsilon_{kl}^{e-tr}, \quad (4.31.13)$$

with the trial elastic strain increment, $d\varepsilon_{ij}^{e-tr}$ being that of the total strain increment, $d_{ij}\Delta t$. The flow (yield) functions, f_{ij}^{tr} , are then calculated. If all $f_{ij}^{tr} < 0$, the solution is elastic and the trial state is accepted. On the other hand, if any $f_{ij}^{tr} > 0$ a correction scheme is needed. This poses a more complex problem than in the orthotropic crush model given the multiple (six) yield surfaces.

To perform the plastic correction, an approach similar in principle to the return-mapping schemes heavily used in metal plasticity (e.g. Section 4.7.2). Here, however, there is no internal state variable and associated evolution equations to evolve the state. Instead, in this case the elastic strain is iterated over until all the yield conditions are satisfied. Specifically, for the k -th iteration, the stress is calculated as

$$\sigma_{ij}^k = \hat{\sigma}_{ij}^n + \mathbb{C}_{ijkl}d\varepsilon_{kl}^{e-k}. \quad (4.31.14)$$

Updated yield functions, f_{ij}^k , are then calculated and the active flow directions (those with $f_{ij} > 0$) determined. A tangent modulus is then constructed (essentially by turning off components corresponding to inactive directions) and a plastic flow tensor is determined using the tangent compliance and the value of the yield functions. The updated elastic strain increment, $d\varepsilon_{ij}^{e-k+1}$, is then found by removing the calculated strain. This process is repeated until satisfaction of all the yield functions.

4.31.3. Verification

To verify the orthotropic crush model, a series of uniaxial compression tests are performed. Given the multiple salient features in this model (e.g. strain rate dependence, user-defined coordinate system), the test sequence is constructed to investigate and probe each of the different features to gain confidence in all of the anticipated capabilities. Additionally, the analyzed loading paths correspond to those in which the kinematics are fully prescribed. This is done so that analytical expressions may be found due to the strong coupling between the kinematics and constitutive response through the compaction state, α . The common model parameters used for these tests are given in Table 4-49 and the functional forms of the input strength/hardening curves, $f_{\beta\gamma}$, are presented in Figure 4-123. It is noted, however, that these properties will take various values during the verification tests to activate and deactivate different responses. Additionally, in Figure 4-123, two sets of curves are given – the full, complex set of six distinct functions (4-123a) and a simpler set (4-123b). In the latter, only one curve common to the three diagonal strengths are shown. The other three strength functions are all set artificially high to enable the study of a simpler case.

4.31.3.1. Uniaxial Strain - Isotropic

First, the response of the model with through a uniaxial strain loading is explored. In this case, the prescribed displacement is $u_i = \hat{\lambda}\delta_{i1}$. For this initial study, isotropic elastic constants are assumed leading to $E_L^0 = E_{LLLL}^0 = E_{TTTT}^0 = E_{WWWW}^0 = 5,384.6$ ksi and

E_{TTTT}^0	2,322.0 ksi	E	4000.0 ksi
E_{TTLL}^0	485.8 ksi	ν	0.3
E_{TTWW}^0	68.8 ksi	σ_y	15.0 ksi
E_{LLLL}^0	1,348.0 ksi	\hat{t}_x	1.0
E_{LLWW}^0	121.8 ksi	\hat{t}_y	0.0
E_{WWWW}^0	85.0 ksi	\hat{t}_z	0.0
G_{TLTL}^0	1,345.0 ksi	\hat{l}_x	0.0
G_{LWLW}^0	67.0 ksi	\hat{l}_y	1.0
G_{WTWT}^0	260.0 ksi	\hat{l}_z	0.0
$h(\dot{\varepsilon})$	1.0	$f_E(\alpha)$	α

Table 4-49. Material and model parameters for the orthotropic rate model used during verification testing.

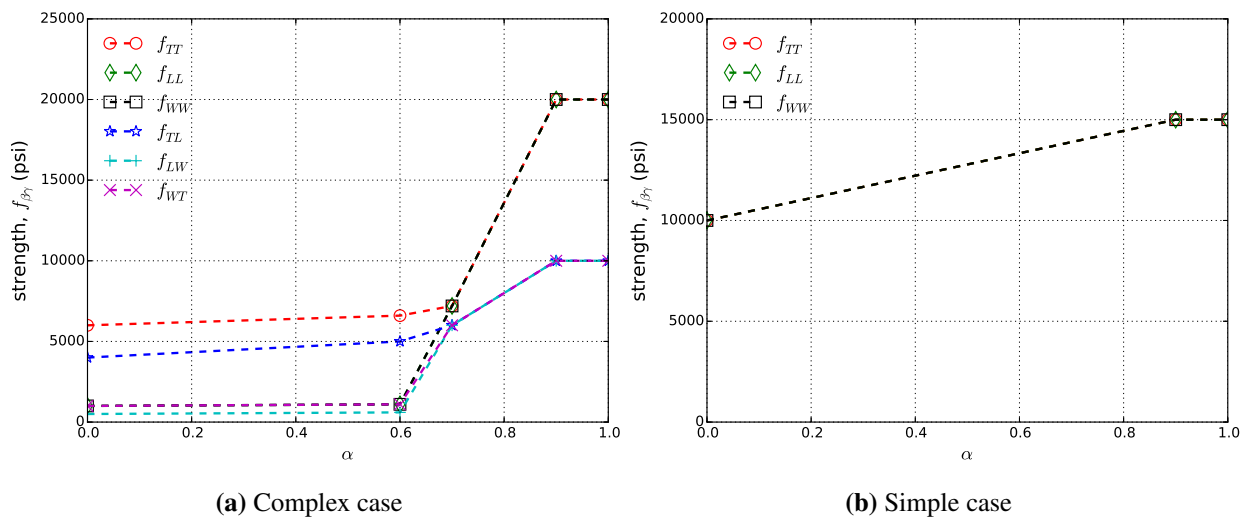


Figure 4-123. Input strength/hardening curves, $f_{\beta\gamma}$, for use in verification tests of the orthotropic rate model.

$E_T^0 = E_{TTLL}^0 = E_{TTWW}^0 = E_{LLWW}^0 = 2,307.7$ ksi. These properties are chosen to match the compacted state and $f_E(\alpha)$ is set to zero. In this way, the elastic properties are constant throughout loading. The shear moduli are scaled accordingly and the remaining properties are left unchanged from Table 4-49. In this case, the model response simplifies to

$$\alpha = -\hat{\lambda}, \quad (4.31.15)$$

and

$$\sigma_{11} = \begin{cases} \hat{\sigma} & \hat{\sigma} \leq f_{TT}(\alpha) \\ f_{TT} & \hat{\sigma} > f_{TT}(\alpha) \end{cases} \quad (4.31.16)$$

$$\sigma_{22} = \sigma_{33} = \begin{cases} \lambda \ln(1 + \hat{\lambda}) & \hat{\sigma} \leq f_{TT}(\alpha) \\ \frac{\lambda}{\lambda + 2\mu} \sigma_{11} & \hat{\sigma} > f_{TT}(\alpha) \end{cases}, \quad (4.31.17)$$

where

$$\hat{\sigma} = (\lambda + 2\mu) \ln(1 + \hat{\lambda}). \quad (4.31.18)$$

The single linear hardening crush curve given in Figure 4-123b is used for this analysis. The resulting stresses as a function of applied displacement, $\hat{\lambda}$, are given in Figure 4-124 and good agreement is noted.

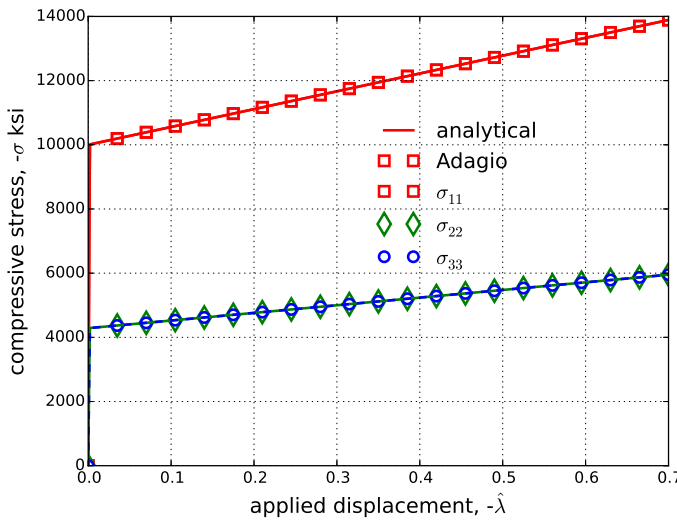


Figure 4-124. Axial and off-axis stresses determined analytically and numerically via the orthotropic rate model with constant, isotropic elastic properties

4.31.3.2. Uniaxial Strain - Orthotropic

The uniaxial problem described in the previous section is again studied – although this time using the orthotropic elastic properties listed in Table 4-49. To test the material coordinate system capabilities two cases are considered – essentially with the x_1 axis aligned with the T and L axes. The first case corresponds to the definition of the \hat{t}_i and \hat{l}_i vectors in Table 4-49. Alternatively, the second case is defined by setting the L direction aligned with the x_1 axis ($\hat{l}_x = 1.0$, $\hat{l}_y = 0.0$, $\hat{l}_z = 0.0$ and $\hat{t}_x = 0.0$, $\hat{t}_y = 0.0$, $\hat{t}_z = 1.0$). The stress state evolutions determined via adagio and analytically for the two considered orientations are shown in Figures 4-125a and 4-125b, respectively. The analytical solutions are found in the same fashion as (4.31.16) with the moduli changed for the orthotropic case. Good agreement is observed.

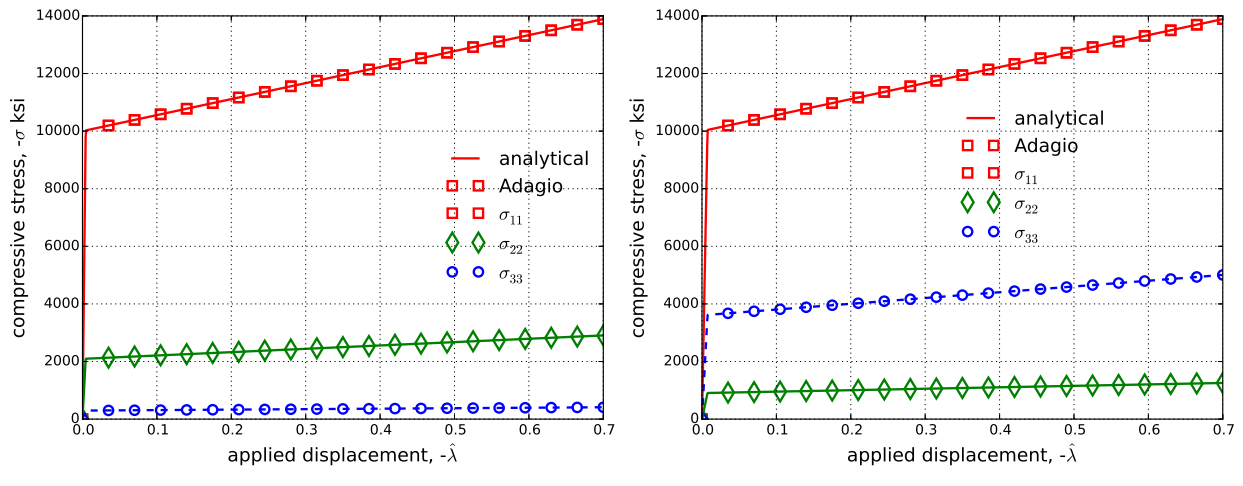


Figure 4-125. Axial and off-axis stresses determined analytically and numerically via the orthotropic rate model with constant, orthotropic elastic constants. The material coordinate systems is rotated in two different directions with the loading direction always aligned with x_1

4.31.4. User Guide

```

BEGIN PARAMETERS FOR MODEL ORTHOTROPIC_RATE
#
# Elastic constants
#
YOUNGS MODULUS = <real> E
POISONS RATIO = <real> ν
SHEAR MODULUS = <real> G
BULK MODULUS = <real> K
LAMBDA = <real> λ
TWO MU = <real> 2μ
#
YIELD STRESS = <real> σy
#
MODULUS TTTT = <real> ETTTT0
MODULUS TTLL = <real> ETTLL0
MODULUS TTWW = <real> ETTWW0
MODULUS LLLL = <real> ELLLL0
MODULUS LLWW = <real> ELLWW0
MODULUS WWWW = <real> EWWWW0
MODULUS TLTL = <real> GTLTL0
MODULUS LWLW = <real> GLWLW0
MODULUS WTWT = <real> GWTWT0
#
TX = <real>  $\hat{t}_x$ 
TY = <real>  $\hat{t}_y$ 
TZ = <real>  $\hat{t}_z$ 
LX = <real>  $\hat{l}_x$ 
LY = <real>  $\hat{l}_y$ 
LZ = <real>  $\hat{l}_z$ 
#
MODULUS FUNCTION = <string> fE(α)
RATE FUNCTION = <string> h( $\dot{\varepsilon}$ )
#
T FUNCTION = <string> fTT(α)
L FUNCTION = <string> fLL(α)
W FUNCTION = <string> fWW(α)
TL FUNCTION = <string> fTL(α)
LW FUNCTION = <string> fLW(α)
WT FUNCTION = <string> fWT(α)
END [PARAMETERS FOR MODEL ORTHOTROPIC_RATE]

```

Output variables for this model are listed in Table 4-50.

Table 4-50. State variables for ORTHOTROPIC RATE Model

Index	Name	Variable Description
1	CRUSH	minimum volume ratio, crush is unrecoverable ($\hat{\epsilon}_V$)

REFERENCES

- [1] S.W. Attaway. Orthotropic crush constitutive relation for PRONTO. Technical Report Memo, Sandia National Laboratories, Albuquerque, NM, September 29, 1992.
- [2] L.J. Gibson and M.F. Ashby. *Cellular Solids: Structure and Properties*. Cambridge Solid State Science Series. Cambridge University Press, Cambridge, UK, second edition, 1997.

4.32. UNIVERSAL POLYMER MODEL (UPM)

4.32.1. Theory

The Universal Polymer Model (UPM) is a phenomenological, non-linear viscoelastic (NLVE) model that is, in the literature, named the Simplified Potential Energy Clock (SPEC) [1]. The UPM model is considerably simpler than the parent model, the Potential Energy Clock (PEC) model, labeled the NLVE polymer model in SIERRA, which itself is not phenomenological but requires extensive data and experience to calibrate [2].

The UPM model is suitable for modeling the finite deformation, thermal-mechanical behavior of glassy materials, both organic and inorganic. Successful usage of the model is widespread. Some examples include the modeling of amorphous, thermosetting polymers across and through the glass transition such as epoxies [3]. It is also suitable for modeling thermoplastics from within the melt state and down into the glass transition from polystyrene to polycarbonate. Finally, it has been used to represent inorganic glasses for glass-to-metal seals. The UPM model was developed for production analyses of encapsulated components. It predicts a full range of behavior including yielding, stress relaxation, volume relaxation, and physical aging.

The key physical principal behind the UPM model is that there exists a material time scale (material clock) separate from the laboratory time scale. If the material time scale is fast, such as in the rubbery state of a polymer, then the UPM model responds instantly to changes in temperature and strain such that the user would observe rate-independent behavior. However, if the material clock is slow relative to the laboratory time scale, viscoelastic memory builds with any process, which causes acute history and thermodynamic path dependent behavior.

The model response is derived from a Helmholtz Free Energy density and takes as an input the unrotated rate of deformation, d_{ij} , the temperature at the start and end of the time step (θ_n and θ_{n+1} , and the time step, Δt . From these inputs, the hereditary integrals within the model are updated, and the unrotated Cauchy stress tensor is returned.

For the UPM model, the strain measure is approximated from the integrated unrotated rate of deformation tensor, which we label ϵ_{ij} ,

$$\epsilon_{ij} = \int_0^\infty (R_{mi} D_{mn} R_{nj}) ds, \quad D_{ij} = \frac{1}{2} (L_{ij} + L_{ji}), \quad F_{ij} = R_{im} U_{mj}. \quad (4.32.1)$$

Here, F_{ij} , R_{ij} , U_{ij} , L_{ij} , and D_{ij} are the deformation gradient, rotation, material stretch, velocity gradient, and rate of deformation tensors standard in Lagrangian continuum mechanics.

The UPM model allows the user to initiate an analysis from a stress-free temperature, θ_{sf} , that is different from the reference temperature, θ_{ref} , at which all material properties are defined. Here we briefly summarize the constitutive equations. The model is derived from a Helmholtz Free Energy, but we begin directly with the (unrotated) Cauchy Stress and refer the reader to reference [1] for more detail:

$$\begin{aligned}
\sigma_{ij} = & (K_G(\theta) - K_\infty(\theta)) \int_0^t f_v(t' - s') \frac{dI_1}{ds} ds \delta_{ij} \\
& - (K_G(\theta) \delta_G(\theta) - K_\infty(\theta) \delta_\infty(\theta)) \int_0^t f_v(t' - s') \frac{d\theta}{ds} ds \delta_{ij} \\
& + 2(G_G(\theta) - G_\infty(\theta)) \int_0^t f_s(t' - s') \frac{d(\text{dev}\epsilon_{ij})}{ds} ds \\
& + (K_\infty(\theta) I_1 - K_\infty(\theta) \delta_\infty(\theta) (\theta - \theta_{sf})) \delta_{ij} + 2G_\infty(\theta) \text{dev}\epsilon_{ij}.
\end{aligned} \tag{4.32.2}$$

The first three lines of terms in Equation 4.32.2 represent the time-dependent and dissipative (non-equilibrium) response of the model to volumetric, thermal, and shear deformation histories. Accordingly, K , δ , and G represent a bulk modulus, volumetric thermal expansion coefficient, and shear modulus while subscripts G or ∞ denote a glassy or rubbery, respectively, properties. The last collection of terms in 4.32.2 furnish the time-independent rubbery (equilibrium) response. The variables in equation 4.32.2 are:

$$I_1 = \delta_{ij}\epsilon_{ij} = \text{tr}\epsilon_{ij}, \quad \text{dev}\epsilon_{ij} = \epsilon_{ij} - \frac{I_1}{3}\delta_{ij}, \tag{4.32.3}$$

$$G_G(\theta) = G_G^{\text{ref}} + \frac{dG_G}{d\theta}(\theta - \theta_{\text{ref}}), \quad G_\infty(\theta) = G_\infty^{\text{ref}} + \frac{dG_\infty}{d\theta}(\theta - \theta_{\text{ref}}), \tag{4.32.4}$$

$$K_G(\theta) = K_G^{\text{ref}} + \frac{dK_G}{d\theta}(\theta - \theta_{\text{ref}}), \quad K_\infty(\theta) = K_\infty^{\text{ref}} + \frac{dK_\infty}{d\theta}(\theta - \theta_{\text{ref}}), \tag{4.32.5}$$

$$\delta_G(\theta) = \delta_G^{\text{ref}} + \frac{d\delta_G}{d\theta}(\theta - \theta_{\text{ref}}), \quad \delta_\infty(\theta) = \delta_\infty^{\text{ref}} + \frac{d\delta_\infty}{d\theta}(\theta - \theta_{\text{ref}}). \tag{4.32.6}$$

The first three terms in Equation 4.32.2 represent the material's viscoelastic response to changes in volume strain, temperature, and shear deformation. Two relaxation functions are used to characterize the thermal/volumetric (f_v) and shear (f_s) relaxation responses. The model assumes the thermal and volumetric relaxation responses are identical. Otherwise, f_v and f_s are typically quite different and are expressed as a Prony series⁸:

$$f_v(x) = \sum_{k=1}^N w^{(k)} \exp\left(-\frac{x}{\tau^{(k)}}\right), \quad f_s(x) = \sum_{l=1}^M w^{(l)} \exp\left(-\frac{x}{\tau^{(l)}}\right). \tag{4.32.7}$$

These relaxation functions describe the material's response to a suddenly applied volumetric/thermal or shear perturbation at the reference temperature where, under certain conditions, the material and laboratory time scales are equivalent. In Equation 4.32.2, the viscous terms (non-rubber) involve hereditary integrals over the difference in material time from $s = 0$ to $s = t$, which is the current laboratory time. An increment in material time, dt' , and the laboratory

⁸Note: to distinguish between indices used with conventional summation convention and those related to Prony series terms, all Prony series summations shall be explicitly written with the relevant index given parenthetically in a superscript.

time, dt , are related through the (highly) history dependent shift factor, a , such that the difference in material time, $t' - s'$, is related to the corresponding difference in laboratory time, $t - s$ through:

$$adt' = dt, \quad t' - s' = \int_{u=s}^{u=t} \frac{du}{a(u)}. \quad (4.32.8)$$

If the material time scale is very slow compared to the laboratory time, then $a \gg 1$, which is often the case inside and below the glass transition for typically glassy materials.

The shift factor is instantaneously defined through:

$$\log_{10} a = \frac{-C_1 N}{C_2 + N}, \quad (4.32.9)$$

$$\begin{aligned} N(t) &= \theta - \theta_{\text{ref}} - \int_0^t f_v(t' - s') \frac{d\theta}{ds} ds \\ &\quad + C_3 \left(I_1 - \int_0^t f_v(t' - s') \frac{dI_1}{ds} ds \right) \\ &\quad + C_4 \int_{u=0}^{u=t} \int_{s=0}^{s=t} \left(f_s(t' - s', t' - u') \frac{d(\text{dev}\epsilon_{ij})}{ds} \frac{d(\text{dev}\epsilon_{ij})}{du} ds du \right). \end{aligned} \quad (4.32.10)$$

The key physics in the model comes from Equation 4.32.9. Temperature rise (generally) causes N to increase, and hence the material shift factor shrinks (the material time scale speeds up).

Shrinking the volume generally causes the shift factor to increase as if the temperature had been decreased. Mechanistically, this feature is the manifestation of the trade-off between between mobility and free volume available to polymer chains. Finally, shear deformation can greatly speed up the material clock through the last term. This phenomenon is a direct manifestation of “deformation induced mobility”, a key mechanism for glassy materials.

Since the shift factor involves hereditary integrals, even at a constant temperature and state of deformation, the material clock will change over time. Under stress-free conditions, the material will creep and densify if the model is out of equilibrium (when any viscous term is non-zero). These phenomena are the model’s manifestations of physical aging, time-dependent material change without a change in composition or microstructure. C_1 , C_2 , C_3 , and C_4 are all material constants. We note that the double relaxation function appearing in the last term takes on a slightly different form from f_s :

$$f_s(x, y) = \sum_{k=1}^N w^{(k)} \exp\left(-\frac{x}{\tau^{(k)}}\right) \exp\left(-\frac{y}{\tau^{(k)}}\right) \quad (4.32.11)$$

It is desirable to relate a special case of the model to the Williams-Landel-Ferry (WLF) form because of how time-temperature superposition fitting is typically performed. Specifically, one can show that the clock parameters, C_1 and C_2 , relate to the WLF parameters, \hat{C}_1 and \hat{C}_2 , through the following relationships: $\hat{C}_1 = C_1$ and $\hat{C}_2 = C_2 / (1 + C_3 \delta_{\infty}^{\text{ref}})$.

For more information about the universal polymer model, consult [1].

4.32.2. Implementation

The hereditary integrals in Equation 4.32.2 and 4.32.9 are difficult to evaluate directly. Instead a rate form is pursued than can be integrated straightforwardly over each time step. Consider a typical hereditary integral after the Prony series for its specific relaxation function has been substituted into it. Differentiate the integral with respect to the current time, t , and use the Leibnitz rule to arrive at:

$$\int_{s=0}^{s=t} f_v(t' - s') \frac{d\theta}{ds} ds = \sum_{k=0}^N w^{(k)} \int_{s=0}^{s=t} \exp\left(-\frac{t' - s'}{\tau^{(k)}}\right) \frac{d\theta}{ds} ds = \sum_{k=0}^N w^{(k)} J^{(k)} \quad (4.32.12)$$

$$\begin{aligned} \frac{dJ^{(k)}}{dt} &= \int_{s=0}^{s=t} \frac{d}{dt} \left(\exp\left(-\frac{t' - s'}{\tau^{(k)}}\right) \frac{d\theta}{ds} \right) ds + \left(\exp\left(-\frac{t' - s'}{\tau^{(k)}}\right) \frac{d\theta}{ds} \right)_{s=t} \frac{d(t)}{dt} \quad (4.32.13) \\ &= \int_{s=0}^{s=t} \exp\left(-\frac{t' - s'}{\tau^{(k)}}\right) \frac{d\theta}{ds} \left(\frac{-1}{\tau^{(k)}} \right) \frac{dt'}{dt} ds + \frac{d\theta}{dt} \\ &= -\frac{1}{a\tau^{(k)}} J^{(k)} + \frac{d\theta}{dt}. \end{aligned}$$

Notice this rate form involves a memory term which decays as well as input from new history, in this case a change in temperature. To integrate this easily, we approximate this rate as constant over the time step in a constitutive equation update and use the mid-step evaluation to determine the rate. Consider a process in which the temperature changes from θ_n at time t_n to θ_{n+1} at t_{n+1} so that $\Delta t = t_{n+1} - t_n$. Then,

$$\frac{dJ^{(k)}}{dt}|_{t_{n+1/2}} \approx \frac{J^{(k)}(t_{n+1}) - J^{(k)}(t_n)}{t_{n+1} - t_n} = -\frac{1}{a_{t_{n+1/2}}\tau^{(k)}} \frac{J^{(k)}|_{n+1} + J^{(k)}|_n}{2} + \frac{\theta_{n+1} - \theta_n}{t_{n+1} - t_n}, \quad (4.32.14)$$

yielding,

$$J^{(k)}|_{n+1} = \left(\frac{2a_{n+1/2}\tau^{(k)} - \Delta t}{2a_{n+1/2}\tau^{(k)} + \Delta t} \right) J^{(k)}|_n + \left(\frac{2a_{n+1/2}\tau^{(k)}}{2a_{n+1/2}\tau^{(k)} + \Delta t} \right) (\theta_{n+1} - \theta_n). \quad (4.32.15)$$

Stability of Equation 4.32.14 requires that the first term to remain positive. Hence, the change in time for the purposes of updating these hereditary integrals is:

$$\Delta t = \text{MIN} (t_{n+1} - t_n, 2a_{n+1/2}\tau^{(k)}). \quad (4.32.16)$$

The collection of $J^{(k)}$ from $k = 1, N$ are internal state variables associated with this particular hereditary integral. Each Prony term for each distinct hereditary integral must be stored as an internal state variable.

Fortunately, changing from a scalar field to a tensor field (θ to ϵ_{ij}) does not alter the above time integration except that for each Prony term, each component of the tensor must be stored and

updated as a state variable. For example, the hereditary integrals associated with deviatoric strain history may be updated by letting,

$$H_{ij} = \int_0^t ds f_s(t' - s') \frac{d(\text{dev}\epsilon_{ij})}{ds} ds = \sum_{k=1}^N w^{(k)} H_{ij}^{(k)}, \quad (4.32.17)$$

and approximating the time rate of change at the midstep as,

$$\frac{dH_{ij}^{(k)}}{dt} \Big|_{t_{n+1/2}} \approx \frac{H_{ij}^{(k)}(t_{n+1}) - H_{ij}^{(k)}(t_n)}{t_{n+1} - t_n} = -\frac{1}{a_{t_{n+1/2}} \tau^{(k)}} \frac{H_{ij}^{(k)}|_{n+1} + H_{ij}^{(k)}|_n}{2} + \frac{H_{ij}^{n+1} - H_{ij}^n}{t_{n+1} - t_n}, \quad (4.32.18)$$

resulting in,

$$H_{ij}^{(k)}|_{n+1} = \left(\frac{2a_{n+1/2} \tau^{(k)} - \Delta t}{2a_{n+1/2} \tau^{(k)} + \Delta t} \right) H_{ij}^{(k)}|_n + \left(\frac{2a_{n+1/2} \tau^{(k)}}{2a_{n+1/2} \tau^{(k)} + \Delta t} \right) (H_{ij}^{n+1} - H_{ij}^n). \quad (4.32.19)$$

Here, $H_{ij}^{(k)}$ is a collection of six state variables that compose the k^{th} Prony term deviatoric strain history hereditary integral as in Equation 4.32.2. The superscripts refer to the Prony term number, and each component of these tensors must be updated and stored.

Because of the double hereditary integral in Equation 4.32.9 associated with shear deformation and shift factor acceleration, a rate form for this kind of term is also needed. Again, differentiate the integral with respect to the current time, t , and use the Leibnitz rule to arrive at:

$$\begin{aligned} & \int_{u=0}^{u=t} \int_{s=0}^{s=t} \left(f_s(t' - s', t' - u') \frac{d(\text{dev}\epsilon_{ij})}{ds} \frac{d(\text{dev}\epsilon_{ij})}{du} ds du \right) \\ &= \sum_{k=1}^N w^{(k)} \int_{u=0}^{u=t} \int_{s=0}^{s=t} \left(\exp\left(-\frac{t' - s'}{\tau^{(k)}}\right) \exp\left(-\frac{t' - u'}{\tau^{(k)}}\right) \frac{d(\text{dev}\epsilon_{ij})}{ds} \frac{d(\text{dev}\epsilon_{ij})}{du} ds du \right) \\ &= \sum_{k=0}^N w^{(k)} Q^{(k)}. \end{aligned} \quad (4.32.20)$$

$$\begin{aligned} \frac{dQ^{(k)}}{dt} &= \frac{-2Q^{(k)}}{a\tau^{(k)}} + 2 \frac{d(\text{dev}\epsilon_{ij})}{dt} \int_{s=0}^{s=t} \left(\exp\left(-\frac{t' - u'}{\tau^{(k)}}\right) \frac{d(\text{dev}\epsilon_{ij})}{du} du \right) \\ &= \frac{-2Q^{(k)}}{a\tau^{(k)}} + 2 \frac{d(\text{dev}\epsilon_{ij})}{dt} H_{ij}^{(k)}. \end{aligned} \quad (4.32.21)$$

The variables $J^{(k)}$, $Q^{(k)}$, and all six components of $H_{ij}^{(k)}$ are state variables that are stored and updated through the midstep algorithm presented above.

The actual update of the constitutive equations involves finding the shift factor at $t_{n+1/2}$, which requires Newton's method on Equation 4.32.9. Using the techniques from Equations 4.32.12 through 4.32.20, it is straightforward to chain rule differentiate the term N in Equation 4.32.9, and that analysis is not reproduced here for brevity.

4.32.3. Verification

Verification for the full non-linear viscoelastic features of the universal polymer model is difficult because analytic solutions are not available. Here we verify that two key parts of the model are working correctly, but at this time not all non-linearities in the material clock are verified. First, we verify that the material clock (shift factor) follows the Williams-Landel-Ferry behavior near and above the glass transition (reference temperature). Then, as the material is cooled below the glass transition, we verify that the thermal hereditary integral in the material clock is working properly. Finally, the specimen is reheated through the glass transition, and the shift factor is again compared between the UPM model and a semi-analytic solution.

Second, with the non-linear portions of the clock turned off and the temperature held fixed, an analytic solution to the uniaxial strain boundary value problem is pursued at three different strain rates. This latter verification exercise demonstrates that the hereditary integrals are updated correctly and that the stress response may be calculated using both the shear and bulk relaxation responses simultaneously even when they have different relaxation functions.

4.32.3.1. Shift Factor During Traction-Free Cooling and Heating

The WLF equation (considering temperature only) provides a simple means of performing time-temperature superposition. It relates the shift factor, a , to the current temperature through,

$$\log_{10} a = -\frac{C_1(\theta - \theta_{\text{ref}})}{C_2 + (\theta - \theta_{\text{ref}})}. \quad (4.32.22)$$

Near and above θ_{ref} , the UPM model limits to the WLF model, and below the glass transition, the hereditary integral in the clock “freezes out” further evolution of the shift factor with temperature.

A single element boundary value problem is analyzed in Sierra/SM with the UPM model. A simple temperature sweep is executed under traction free conditions through the glass transition starting from above it at a constant rate of 1°C per minute. The material is then immediately reheated at 1°C per minute to well above the glass transition. The material properties used for this analysis as well as the uniaxial strain problem below are provided in Table 4-51 and reflect a simplified version of the material properties used to represent 828DGEBA / DEA (often called 828DEA) [1].

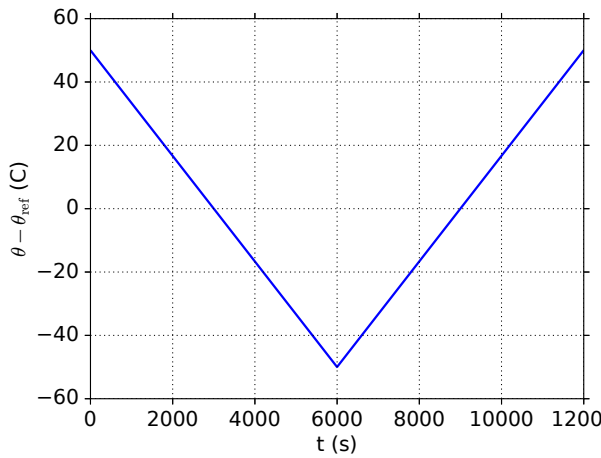
For the verification of the time-temperature shift behavior, the model is expected to exactly match the WLF behavior above θ_{ref} , but as the material is cooled below this point, the temperature hereditary integral in the material shift factor definition (Equation 4.32.9) slows further evolution

θ_{ref}	75°C	θ_{sf}	125°C
\hat{C}_1	16.5	\hat{C}_2	54.5°C
K_G	4.9 GPa	K_∞	3.2 GPa
G_G	0.75 GPa	G_∞	4.5 MPa
$\{f_1\}$	$\{2.99149 \times 10^{-3}, 6.42966 \times 10^{-2}, 6.49783 \times 10^{-1}, 2.82929 \times 10^{-1}\}$		
$\{f_2\}$	$\{1.00305 \times 10^{-2}, 2.11421 \times 10^{-1}, 7.01534 \times 10^{-1}, 7.70145 \times 10^{-2}\}$		
$\{\tau\}$	$\{1.0 \times 10^{-11}, 1.0 \times 10^{-6}, 1.0 \times 10^{-1}, 1.0 \times 10^4\}$ (s)		

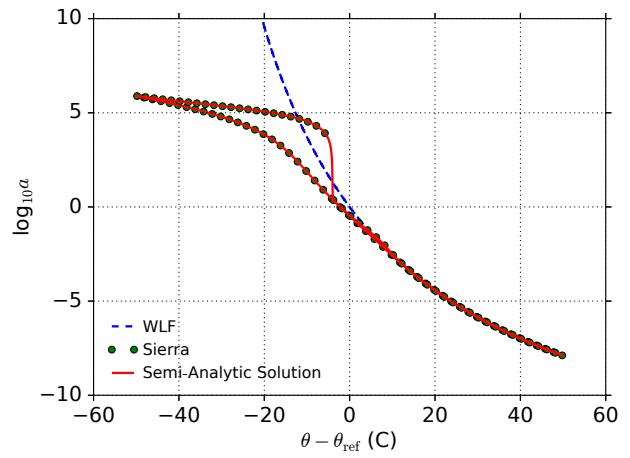
Table 4-51. The material and model parameters for the Universal Polymer Model used for verification testing. Parameters are approximately based on a fit for 828DEA in [1], but they represent a linear thermal-viscoelastic representation of the model. Both the shear and volumetric Prony series weights come from fitting these 4 relaxation times to stretched exponential series as discussed in that paper. The thermal relaxation and volumetric relaxation functions are the same in the UPM model . All other material and model parameters are unused and set to zero.

of the shift factor. WLF behavior is observed in the model, which confirms this elementary behavior of the model in Figure 4-126. Then, as the model is further cooled below the glass transition, the UPM model is compared against a custom Newton-Raphson scheme for this boundary value problem (outside Sierra), and agreement is perfect. During reheat, one sees that the shift factor does not retrace the path through temperature space, and a large hysteresis is observed.

Changing the cooling rate changes the temperature at which the UPM model will depart from WLF behavior with the behavior remaining WLF like at colder temperatures for slower cooling rates and departing at warming temperatures for faster cooling rates.



(a) Applied Temperature History



(b) Shift Factor Vs. Temperature

Figure 4-126. Time-temperature dependence of the shift factor, a , during cooling through the glass transition and then reheating back through it. The cooling/heating rate is 1°C per minute. FEA (circles) show the expected WLF (blue dashed line) behavior for $\theta - \theta_{\text{ref}} > 0$. The UPM model departs from WLF behavior below the reference temperature as expected, and continues to agree with an external to Sierra numerical scheme (solid line) to simulate this boundary value problem.

4.32.3.2. Uniaxial Strain

The second verification problem considered is uniaxial strain under isothermal conditions wherein the non-linear clock terms are set to zero ($C_3 = 0$ and $C_4 = 0$). Here, the temperature is set to the reference temperature, $\theta = \theta_{\text{ref}}$, and a two stage boundary value problem is simulated. A material point (single 8-node hexahedral element with selective deviatoric spatial integration) is loaded at a constant logarithmic strain rate in uniaxial strain up to a prescribed logarithmic strain (characterized by a loading time, t_L). Then, the logarithmic strain rate is fixed to zero. The stress responses in the axial and transverse directions are output over time during this load and hold process. Three logarithmic strain rates are considered: 0.001, 1, and 1000 per second which activate the rubbery, mixed, and glassy responses respectively. For all three cases, the specimen is loaded to 10% axial logarithmic strain, and then the specimen is held for 10 seconds. Uniaxial strain involves finite volume and shape change, and so this boundary value problem tests both relaxation processes simultaneously.

Next we develop the analytic solution for linear thermal-viscoelasticity based on the UPM model. Note that the temperature is fixed to the reference temperature such that the shift factor is 1.0 always. We prescribe the following logarithmic strain rate history on a material point (in a Cartesian frame). Since both the spherical and deviatoric parts of the logarithmic strain history are needed for the model, we derive them too:

$$\text{for } 0 \leq t \leq t_L, \quad \dot{H}_{ij} = \dot{\epsilon} \begin{bmatrix} 1 & 0 & 0 \\ 0 & 0 & 0 \\ 0 & 0 & 0 \end{bmatrix}, \quad \dot{H}_{ij}^{\text{dev}} = \frac{\dot{\epsilon}}{3} \begin{bmatrix} 2 & 0 & 0 \\ 0 & -1 & 0 \\ 0 & 0 & -1 \end{bmatrix}, \quad (4.32.23)$$

$$\text{otherwise} \quad \dot{H}_{ij} = \dot{H}_{ij}^{\text{dev}} = \begin{bmatrix} 0 & 0 & 0 \\ 0 & 0 & 0 \\ 0 & 0 & 0 \end{bmatrix},$$

and the associated strain invariants needed for the model are:

$$I_1, I_2 : \begin{cases} \text{for } 0 \leq t \leq t_L, \\ \quad I_1 = \delta_{ij} H_{ij} = \dot{\epsilon} t \\ \quad \dot{I}_1 = \dot{\epsilon} \\ \quad I_2 = H_{ij}^{\text{dev}} H_{ij}^{\text{dev}} = \frac{2}{3} \dot{\epsilon}^2 t^2 \\ \quad \dot{I}_2 = \frac{4}{3} \dot{\epsilon}^2 t \\ \text{for } t_L \leq t, \\ \quad I_1 = \dot{\epsilon} t_L \\ \quad \dot{I}_1 = 0 \\ \quad I_2 = \frac{2}{3} \dot{\epsilon}^2 t_L^2 \\ \quad \dot{I}_2 = 0 \end{cases} \quad (4.32.24)$$

Now, the motion involves a finite volume change, and the Jacobian of the deformation gradient

will be needed. It is:

$$J = \begin{cases} \text{for } 0 \leq t \leq t_L, \\ \exp(\dot{\epsilon}t) \\ \text{for } t_L \leq t, \\ \exp(\dot{\epsilon}t_L) \end{cases} \quad (4.32.25)$$

The derivation of the linear viscoelastic response proceeds directly with the stress integral from Equation 4.32.2 with equivalent laboratory and material time scales since $\theta = \theta_{\text{ref}}$. Using the prescribed strain history from Equation 4.32.24 and the Jacobian of the deformation gradient (Equation 4.32.25), the Cauchy stress response is given below. Again, there are only two non-zero stress components: the axial stress (σ_{11}) and the transverse stresses ($\sigma_{22} = \sigma_{33}$), which we will label with under score “ σ_A ” and “ σ_T ” respectively. These are:

$$\text{for } 0 \leq t \leq t_L : \begin{cases} J\sigma_A = \exp(-\dot{\epsilon}t) \\ \left\{ \frac{4(G_g - G_\infty)\dot{\epsilon}}{3} \sum_{k=1}^N w^{(k)} \tau^{(k)} \left(1 - \exp\left(-\frac{t}{\tau^{(k)}}\right) \right) \right. \\ \left. + (K_g - K_\infty) \dot{\epsilon} \sum_{l=1}^M q^{(l)} \tau^{(l)} \left(1 - \exp\left(-\frac{t}{\tau^{(l)}}\right) \right) \right\} \\ + (K_\infty + \frac{4}{3}G_\infty) \dot{\epsilon}t, \\ J\sigma_T = \exp(-\dot{\epsilon}t) \\ \left\{ -\frac{2(G_g - G_\infty)\dot{\epsilon}}{3} \sum_{k=1}^N w^{(k)} \tau^{(k)} \left(1 - \exp\left(-\frac{t}{\tau^{(k)}}\right) \right) \right. \\ \left. + (K_g - K_\infty) \dot{\epsilon} \sum_{l=1}^M q^{(l)} \tau^{(l)} \left(1 - \exp\left(-\frac{t}{\tau^{(l)}}\right) \right) \right\} \\ + (K_\infty - \frac{2}{3}G_\infty) \dot{\epsilon}t, \end{cases} \quad (4.32.26)$$

$$\text{for } t_L \leq t : \begin{cases} J\sigma_A = \exp(-\dot{\epsilon}t_L) \\ \left\{ \frac{4(G_g - G_\infty)\dot{\epsilon}}{3} \sum_{k=1}^N w^{(k)} \tau^{(k)} \left(\exp\left(-\frac{t-t_L}{\tau^{(k)}}\right) - \exp\left(-\frac{t}{\tau^{(k)}}\right) \right) \right. \\ \left. + (K_g - K_\infty) \dot{\epsilon} \sum_{l=1}^M q^{(l)} \tau^{(l)} \left(\exp\left(-\frac{t-t_L}{\tau^{(l)}}\right) - \exp\left(-\frac{t}{\tau^{(l)}}\right) \right) \right\} \\ + (K_\infty + \frac{4}{3}G_\infty) \dot{\epsilon}t_L, \\ J\sigma_T = \exp(-\dot{\epsilon}t_L) \\ \left\{ -\frac{2(G_g - G_\infty)\dot{\epsilon}}{3} \sum_{k=1}^N w^{(k)} \tau^{(k)} \left(\exp\left(-\frac{t-t_L}{\tau^{(k)}}\right) - \exp\left(-\frac{t}{\tau^{(k)}}\right) \right) \right. \\ \left. + (K_g - K_\infty) \dot{\epsilon} \sum_{l=1}^M q^{(l)} \tau^{(l)} \left(\exp\left(-\frac{t-t_L}{\tau^{(l)}}\right) - \exp\left(-\frac{t}{\tau^{(l)}}\right) \right) \right\} \\ + (K_\infty - \frac{2}{3}G_\infty) \dot{\epsilon}t_L, \end{cases} \quad (4.32.27)$$

Using the two Prony series in Table 4.51, and the three strain rates (0.1, 1, and 10 per second), the analytic model and UPM are directly compared in Figure 4-127.

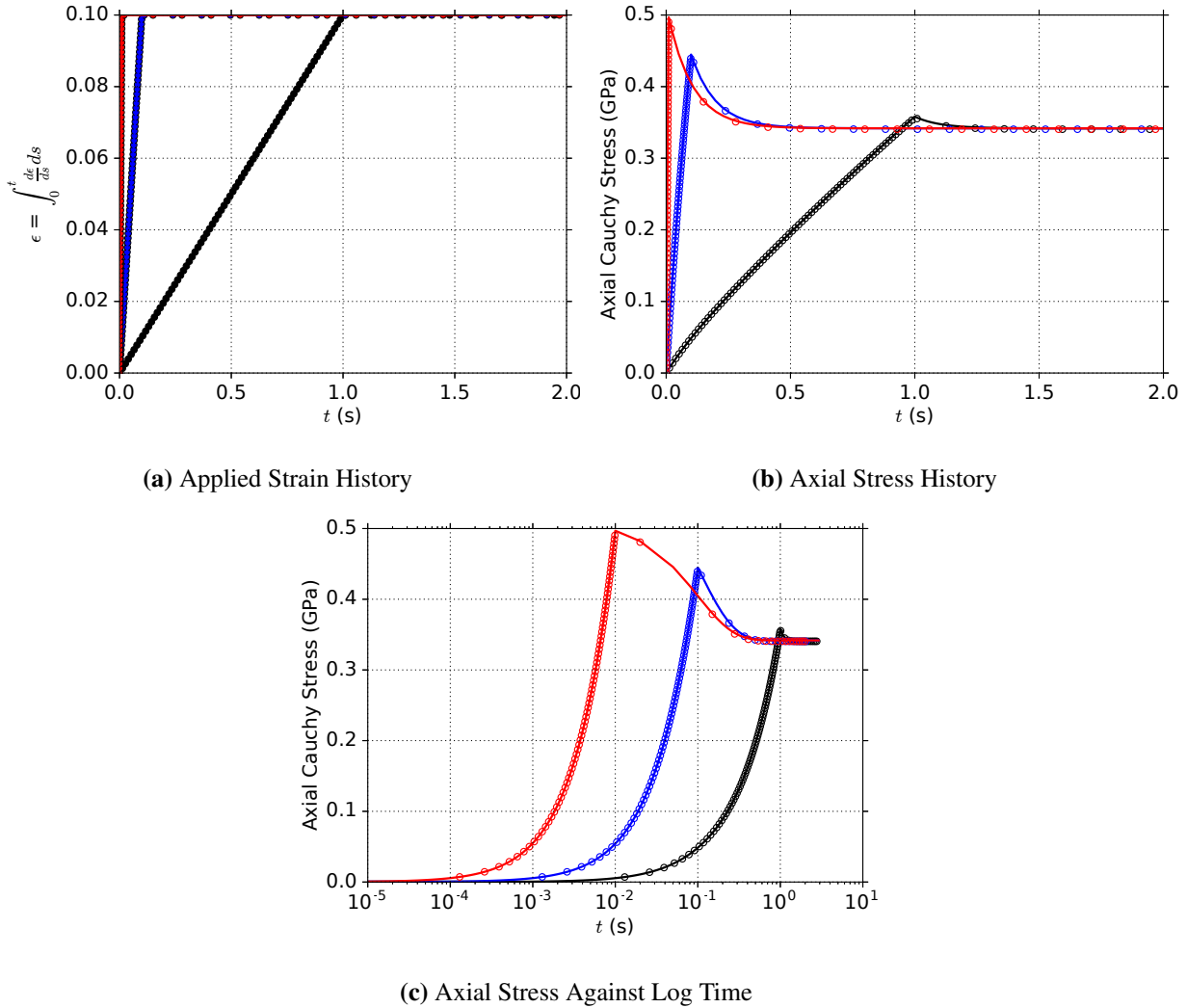


Figure 4-127. Linear viscoelastic response to a two stage uniaxial strain boundary value problem with material and loading properties specified in Table 4-51. Symbols represent FEA simulations with the UPM model while solid lines are the analytic results. The three logarithmic strain rates of 0.1, 1.0, and 10.0 per second are shown, and all cease at 10% strain, and all cases are isothermal at the reference temperature so that the shift factor is unity.

4.32.4. User Guide

The UPM model is commonly used in one of two ways. The most general use case is portrayed in full in the following syntax in which the user specifies both Prony series explicitly. That is, the user specifies all Prony relaxation times (τ) and weights for both the thermal/volumetric (f_v) and shear (f_s) relaxation functions. Note that in the UPM model, only a single set of Prony relaxation times can be specified and acts as the basis for both relaxation spectra. In other words, a single set of relaxation times is specified, and both functions use their own (distinct) weights.

Default parameters are not set. Any system of units can be used with the model. There are no internal units assumptions.

```
BEGIN PARAMETERS FOR MODEL UNIVERSAL_POLYMER
#
# Elastic constants: These Should be Set to the Glassy Moduli
#                     for robustness considerations
#
SHEAR MODULUS    = <real> G
BULK MODULUS     = <real> K
#
## Reference Temperature and Material CLOCK Parameters
#
REFERENCE TEMPERATURE    = <real> θREF # Temperature
STRESS FREE TEMPERATURE = <real> θSF # Temperature
#
WLF C1    = <real>  $\hat{C}_1$ 
WLF C2    = <real>  $\hat{C}_2$  # Temperature
CLOCK C3 = <real> C3 # Temperature
CLOCK C4 = <real> C4 # Temperature
#
## Glassy and Rubbery Moduli
# and CTE Definitions at the Reference Temperature
#
BULK GLASSY 0     = <real> KG # Units of Pressure
BULK RUBBERY 0    = <real> K∞ # Units of Pressure
SHEAR GLASSY 0    = <real> GG # Units of Pressure
SHEAR RUBBERY 0   = <real> G∞ # Units of Pressure
VOLCTE glassy 0   = <real> δG # Units of Inverse Temperature
VOLCTE rubbery 0 = <real> δ∞ # Units of Inverse Temperature
#
FILLER VOL FRACTION = <real>
#
## Relaxation Time Spectra Definitions
#
WWBETA 1 = <real> β1
WWTAU 1  = <real> τ1 # Units of time
WWBETA 2 = <real> β2
WWTAU 2  = <real> τ2 # Units of time
```

```

#
SPECTRUM START TIME = <real>  # Units of time
SPECTRUM END TIME   = <real>  # Units of time
LOG TIME INCREMENT = <real>  # Units of time
#
## Direct Prony Spectra Inputs
#
RELAX TIME 1 = <real>  # Unit of time
RELAX TIME 2 = <real>
.
RELAX TIME 30 = <real>
#
## Thermal/Volumetric Relaxation Spectrum Prony Weights
#
F1 1 = <real>
F1 2 = <real>
.
F1 30 = <real>
#
## Shear Relaxation Spectrum Prony Weights
#
F2 1 = <real>
F2 2 = <real>
.
F2 30 = <real>
END [PARAMETERS FOR MODEL UNIVERSAL_POLYMER]

```

Not all Prony spectra/weight parameter pairs (1-30) need to be specified. Only those specified will be used, and the ones not specified will be set to zero. Prony weights for each relaxation function should sum to 1.0, or the model will rescale the weights so that they do sum to one. This rescaling will change the underlying relaxation response.

When the model is used with both relaxation functions being specified directly, then the parameters: SPECTRUM START TIME, SPECTRUM END TIME, LOG TIME INCREMENT, WW TAU (1,2), and WW BETA (1,2) must be specified as 0 to avoid errors during the model property check. Note (1) is associated with the thermal/volumetric function, and (2) is associated with the shear relaxation function.

Another common usage of the UPM model is to specify the Williams-Watts (KWW) stretched exponential τ, β parameters for either or both relaxation functions (1 and/or 2) corresponding to the function $f = \exp(-(t/\tau)^\beta)$. That is, a set of Prony weights, w_i corresponding to a specific set of Prony times, τ_i , will be found during the model property check routine. If the other relaxation function is directly specified as above, then the Prony times from the directly specified relaxation spectrum are used. In this case, the Prony weights for the relaxation function being fit to the KWW function are found through a Least-Squared Error minimization routine built into the UPM model over a discretely sampled set of times between the minimum and maximum Prony times.

When neither Prony spectrum is directly specified (both will be fit to KWW functions), then the

Prony times (for both relaxation functions) are determined from an evenly logarithmically spaced set of Prony times beginning with the SPECTRUM START TIME and ending with the SPECTRUM END TIME and spaced with the (base 10) LOG TIME INCREMENT. For each relaxation function that is fit with the UPM model to a KWW function, the WW TAU (1,2) and WW BETA (1,2) parameters must be specified. However, if the user specifies both a KWW form and the same Prony series directly, the model will error out during the property check.

There are many useful optional parameters for the UPM model that generally allow for: temperature dependence of moduli, coefficients of thermal expansion, deformation dependence of moduli, and/or alternative material clock parameter specifications. These parameters may optionally be added to the material input block, but are defaulted to 0.0:

```
### OPTIONAL parameters for the universal_polymer model
CLOCK C1      = <real> C1 # CLOCK Coef. 1 instead of "WLF C1"
CLOCK C2      = <real> C2 # CLOCK Coef. 1 instead of "WLF C2"
BULK GLASSY 1  = <real> dKG/dT # Pressure per Temperature
BULK RUBBERY 1 = <real> dK∞/dT # Pressure per Temperature
SHEAR GLASSY 1 = <real> dGG/dT # Pressure per Temperature
SHEAR RUBBERY 1 = <real> dG∞/dT # Pressure per Temperature
VOLCTE GLASSY 1 = <real> dδG/dT # Inverse Temperature Squared
VOLCTE RUBBERY 1 = <real> dδ∞/dT # Inverse Temp. Squared
```

Finally, we note that the UPM model may be reduced to a finite deformation, linear thermoviscoelastic model by choosing $C_3 = 0$ and $C_4 = 0$. Under these conditions the material clock is only temperature (history) dependent but involves no deformation dependence. Moreover, if one wants to fix the laboratory and material time scales to be the same, then one should set WLF $C_1 = 0$.

Output variables available for this model are listed in Table 4-52. The user should always output the shift factor a_{end} or $\log_{10}a$ as this variable is critical for interpreting the material behavior.

Table 4-52. State Variables for Universal Polymer Model

Name	Description
aend	The shift factor relating increments of material to laboratory time, $adt^* = dt_{lab}$
loga	\log_{10} of the shift factor, $\log_{10}a$
epsxx	xx component of the integrated unrotated rate of deformation, ϵ_{xx}
epsyy	yy component of the integrated unrotated rate of deformation, ϵ_{yy}
epszz	zz component of the integrated unrotated rate of deformation, ϵ_{zz}
epsxy	xy component of the integrated unrotated rate of deformation, ϵ_{xy}
epsyz	yz component of the integrated unrotated rate of deformation, ϵ_{yz}
epszx	zx component of the integrated unrotated rate of deformation, ϵ_{zx}
effi2	second (non-Cayley Hamilton) invariant of ϵ providing shear deformation, I_2
if1p1-30	volumetric hereditary integrals 1-30
ikat1-30	thermal hereditary integrals 1-30
igxx1-30	xx component shear hereditary integrals 1-30
igyy1-30	yy component shear hereditary integrals 1-30
igzz1-30	zz component shear hereditary integrals 1-30
igxy1-30	xy component shear hereditary integrals 1-30
igyz1-30	yz component shear hereditary integrals 1-30
igzx1-30	zx component shear hereditary integrals 1-30

REFERENCES

- [1] D. B. Adolf, R. S. Chambers, and M. A. Neidigk. A simplified potential energy clock model for glassy polymers. *Polymer*, 50:4257–4269, 2009.
- [2] J. M. Caruthers, D. B. Adolf, R. S. Chambers, and P. Shrikhande. A thermodynamically consistent, nonlinear viscoelastic approach for modeling glassy polymers. *Polymer*, 45: 4577–4597, 2004.
- [3] D. B. Adolf, R. S. Chambers, and J. M. Caruthers. Extensive validation of a thermodynamically consistent, non-linear viscoelastic model for glassy polymers. *Polymer*, 45:4599–4621, 2004.

4.33. WIRE MESH MODEL

4.33.1. Theory

The wire mesh model was developed at Sandia National Laboratories for use with layered sequences of metallic wire meshes and cloth fabric. Model development was based on an extensive series of experiments performed on these materials (see [1]) and used an existing model for rigid polyurethane foams as a starting point [2].

To be able to analyze the response of this material, the Cauchy stress tensor is first decomposed into its principal components, σ^i . Each principal stress is evaluated independently and two behaviors are considered depending on whether or not the material is in tension or compression. Under a tensile load, the material is taken to be perfectly plastic above a yield stress, τ . For compressive loads, it is assumed that the material hardens functionally with the volumetric engineering strain, ε_V . In this formulation, an arbitrary form of this hardening function, $\bar{\sigma}(\varepsilon_V)$ is assumed although in the original work [1],

$$\bar{\sigma}(\varepsilon_V) = ae^{-b\varepsilon_V}, \quad (4.33.1)$$

with a and b as material constants, was used.

With these assumptions, the yield function of the i^{th} principal stress, f^i , may be written as,

$$f^i = \begin{cases} \sigma^i - \tau, & \sigma^i \geq 0 \\ -\sigma^i - \bar{\sigma}(\varepsilon_V) & \sigma^i < 0 \end{cases} \quad (4.33.2)$$

where τ is the isotropic tensile strength of the material.

Similar to the rigid polyurethane foam model [1], the flow rule is defined as:

$$d_{ij}^p = \dot{\gamma}^1 P_{ijkl}^1 \sigma_{kl} + \dot{\gamma}^2 P_{ijkl}^2 \sigma_{kl} + \dot{\gamma}^3 P_{ijkl}^3 \sigma_{kl} \quad (4.33.3)$$

with $\dot{\gamma}^i$ being the magnitude of the i^{th} plastic strain increment and P_{ijkl}^r is the fourth-order principal projection operator defined as,

$$P_{ijkl}^r = n_i^r n_j^r n_k^r n_l^r \quad (4.33.4)$$

in which n_i^r is the corresponding direction vector of principal stress, σ^r . With this definition,

$$\sigma^r = \sigma_{ij} P_{ijkl}^r \sigma_{kl}. \quad (4.33.5)$$

4.33.2. Implementation

The wire mesh model is implemented in a hypoelastic fashion similar to the previous elastic-plastic models. First, a trial (unrotated) stress is calculated assuming a purely elastic deformation increment,

$$T_{ij}^{tr} = T_{ij}^n + \Delta t (\lambda \delta_{ij} d_{kk} + 2\mu d_{ij}). \quad (4.33.6)$$

Corresponding principal stresses and their complementary directions are then found using the robust, analytical algorithm put forth in [3]. The principal stresses are denoted σ^r and their eigenvectors are symbolically represented by \hat{e}_i^r . Here, $r = 1, 2$, or 3 refer to the respective eigenvalue/vector pair and are not summed unless explicitly indicated. Before evaluating the respective yield functions, the current volumetric engineering strain, ε_V^{n+1} , must be determined. To this end, the current strain tensor, ε_{ij} , is determined via,

$$\varepsilon_{ij}^{n+1} = \varepsilon_{ij}^n + \Delta t d_{ij}, \quad (4.33.7)$$

and the volumetric engineering strain is,

$$\varepsilon_V^{n+1} = \exp(\varepsilon_{kk}^{n+1}) - 1. \quad (4.33.8)$$

The yield function for each principal stress, f^γ , may then be computed as,

$$f^\gamma = \begin{cases} \sigma^\gamma - \tau, & \sigma^\gamma \geq 0 \\ -\sigma^\gamma - \bar{\sigma}(\varepsilon_V^{n+1}), & \sigma^\gamma < 0 \end{cases}. \quad (4.33.9)$$

Principal stresses at the current load increment, σ_{n+1}^γ , are then determined via,

$$\sigma_{n+1}^\gamma = \begin{cases} \sigma^\gamma & f^\gamma < 0 \\ \tau & f^\gamma \geq 0 \end{cases}, \quad (4.33.10)$$

for $\sigma^\gamma > 0$ and,

$$\sigma_{n+1}^\gamma = \begin{cases} \sigma^\gamma & f^\gamma < 0 \\ -\bar{\sigma}(\varepsilon_V^{n+1}) & f^\gamma \geq 0 \end{cases}, \quad (4.33.11)$$

for compressive principal stresses. The final Cartesian stress tensor may be determined via,

$$T_{ij}^{n+1} = \sum_{\gamma=1}^3 \sigma_{n+1}^\gamma \hat{e}_i^\gamma \hat{e}_j^\gamma. \quad (4.33.12)$$

4.33.3. Verification

To investigate the performance of the wire mesh model and verify its capabilities, a series analyses are performed considering both the tensile and compressive behavior. The material properties and model parameters come from [1] and are listed in Table 4-53 with one difference. Specifically, $\nu \neq 0$ to better test the various code interactions. For the numerical simulations the functional hardening form given in (4.33.1) (with a and b given in Table 4-53) is discretized and entered as a piecewise linear function.

E	100,000 psi	ν	0.3
a	120 psi	b	8.68
τ	12,000 psi		

Table 4-53. The material properties and model parameters of the wire mesh model used for verification testing

4.33.3.1. Uniaxial Compression

First, the case of uniaxial compression is treated to investigate the hardening behavior. As a uniaxial compressive stress state is being explored, the principal stresses are simply $\sigma^1 = \sigma^2 = 0$ and $\sigma^3 = \sigma_{11}$ enabling the development of analytical solutions. To this end, $u_1 = \lambda_1$ and the remaining surfaces are left traction free. The corresponding strain state is then,

$$\begin{aligned}\varepsilon_{11} &= \ln(1 + \lambda_1), \\ \varepsilon_{22} = \varepsilon_{33} &= -\nu \ln(1 + \lambda_1),\end{aligned}\tag{4.33.13}$$

producing a engineering volume strain of,

$$\varepsilon_V = (1 + \lambda_1)^{(1-2\nu)} - 1.\tag{4.33.14}$$

Noting the elastic uniaxial stress, $\hat{\sigma}_{11}$, is simply,

$$\hat{\sigma}_{11} = [\lambda(1 - 2\nu) + 2\mu] \ln(1 + \lambda_1),\tag{4.33.15}$$

the final stress state is simply $\sigma_{22} = \sigma_{33} = 0$ and,

$$\sigma_{11} = \begin{cases} \hat{\sigma}_{11} & \hat{\sigma}_{11} \leq -ae^{-b\varepsilon_V} \\ -ae^{-b\varepsilon_V} & \hat{\sigma}_{11} > -ae^{-b\varepsilon_V} \end{cases}.\tag{4.33.16}$$

The analytical and numerical solution (from adagio) of this problem are presented in Figure 4-128 with the stress and strains given in Figures 4-128a and 4-128b, respectively. Excellent agreement is observed verifying the compressive hardening performance.

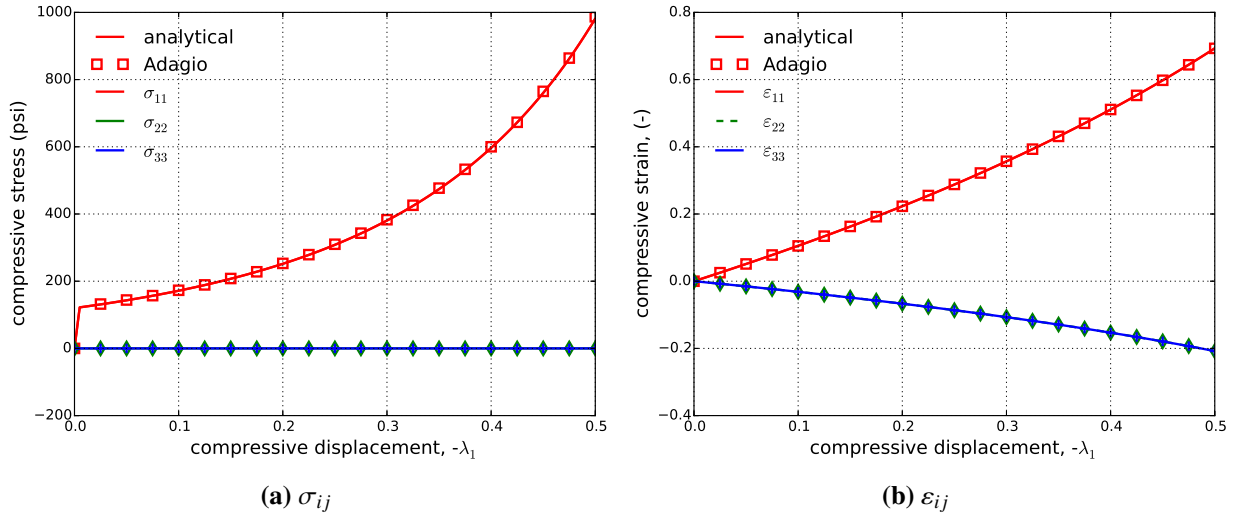


Figure 4-128. Analytical and numerical results of the normal stress and strain components through a compressive uniaxial stress loading path as a function of the applied displacement, λ_1 .

4.33.3.2. Uniaxial Tension

To consider the tensile behavior, the response of the model under a uniaxial tensile *strain* loading is interrogated. In this case the applied displacement is $u_i = \lambda_1 \delta_{i1}$ with the remaining displacements fixed such that $\varepsilon_{22} = \varepsilon_{33} = 0$ and the axial strain is again $\varepsilon_{11} = \ln(1 + \lambda_1)$. Given that the model behavior is perfectly plastic after yield, the axial and off-axis responses both reduce to bilinear forms. As such, the applied deformation necessary to induce the perfectly plastic response in the axial direction, λ_1^{crit} , is simply

$$\lambda_1^{\text{crit}} = e^{\tau/(\lambda+2\mu)} - 1, \quad (4.33.17)$$

leading to an expression for the axial stress as,

$$\sigma_{11} = \begin{cases} (\lambda + 2\mu) \ln(1 + \lambda_1) & \lambda_1 < \lambda_1^{\text{crit}} \\ \tau & \lambda_1 \geq \lambda_1^{\text{crit}} \end{cases}. \quad (4.33.18)$$

For the off-axis behavior, the critical displacement, $\lambda_1^{\text{off-crit}}$, is

$$\lambda_1^{\text{off-crit}} = e^{\tau/\lambda} - 1, \quad (4.33.19)$$

producing stresses of the form,

$$\sigma_{22} = \sigma_{33} = \begin{cases} \lambda \ln(1 + \lambda_1) & \lambda_1 < \lambda_1^{\text{off-crit}} \\ \tau & \lambda_1 \geq \lambda_1^{\text{off-crit}} \end{cases}. \quad (4.33.20)$$

The stress and strain responses (both numerical and analytical) are presented below in Figures 4-129a and 4-129b, respectively, and excellent agreement is observed verifying this behavior in this deformation mode.

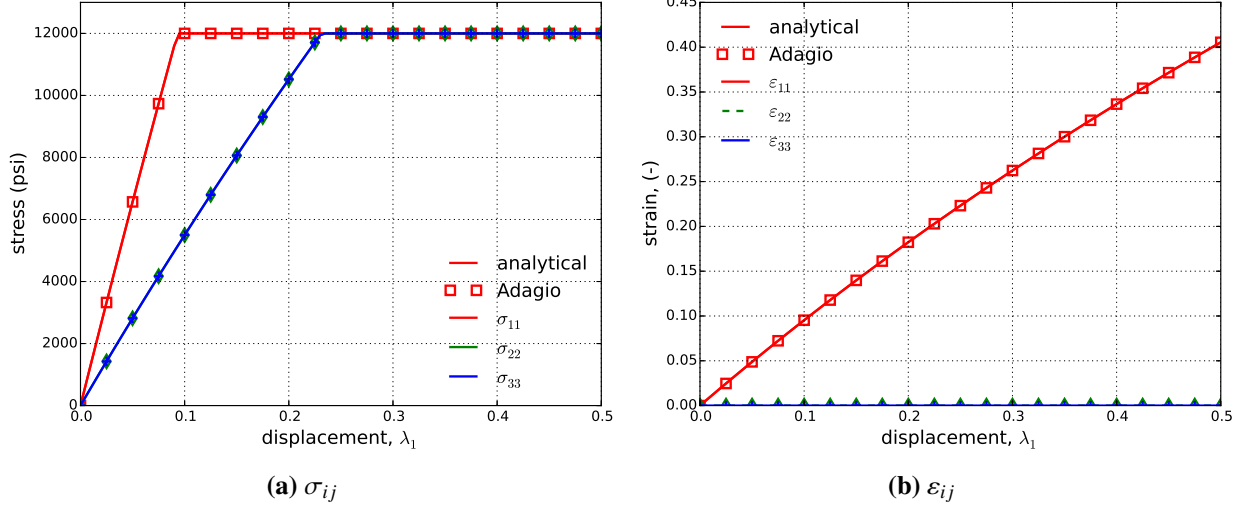


Figure 4-129. Analytical and numerical results of the normal stress and strain components through a tension uniaxial strain loading path as a function of the applied displacement, λ_1 .

4.33.3.3. Hydrostatic Compression

To further explore the compressive response, the models behavior under a hydrostatic (compressive) loading is investigated. In this instance, the corresponding stress state produces a single, repeated, principal stress associated with the pressure, $p = -(1/3)\sigma_{kk}$ (here defined positively in compression). Details of this loading may be found in Section A.4, although in this instance it is important to point out that,

$$\varepsilon_V = (1 + \lambda_1)^3 - 1, \quad (4.33.21)$$

and the stress state reduces to,

$$p = -3K \ln(1 + \lambda_1) \quad (4.33.22)$$

in the elastic limit and

$$p = ae^{-b\varepsilon_V}, \quad (4.33.23)$$

during plastic loading. The numerical and analytical results are presented in Figure 4-130 and excellent agreement is noted.

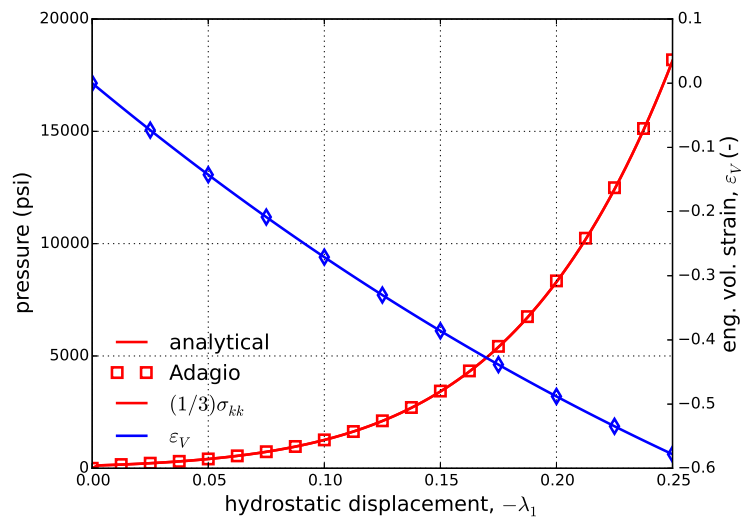


Figure 4-130. Analytical and numerical pressure-volume strain response of the wire mesh model through a hydrostatic compression loading as a function of the applied displacement, λ_1 .

4.33.4. User Guide

```
BEGIN PARAMETERS FOR MODEL WIRE_MESH
#
# Elastic constants
#
YOUNGS MODULUS = <real> E
POISSONS RATIO = <real> ν
SHEAR MODULUS = <real> G
BULK MODULUS = <real> K
LAMBDA = <real> λ
TWO MU = <real> 2μ
#
# Yield surface parameters
#
YIELD FUNCTION = <string>  $\bar{\sigma}(\epsilon_y)$ 
TENSION = <real> τ
END [PARAMETERS FOR MODEL WIRE_MESH]
```

Output variables available for this model are listed in Table 4-54.

More information on the model can be found in the report by Neilsen, et. al. [1].

Table 4-54. State Variables for WIRE MESH Model

Name	Description
EVOL	engineering volumetric strain
YIELD	current yield strength in compression

REFERENCES

- [1] M.K. Neilsen, J.D. Pierce, and R.D. Krieg. A constitutive model for layered wire mesh and aramid cloth fabric. Technical Report SAND91-2850, Sandia National Laboratories, Albuquerque, NM, 1993. [pdf](#).
- [2] M.K. Neilsen, H.S. Morgan, and R.D. Krieg. A phenomenological constitutive model for low density polyurethane foams. Technical Report SAND86-2927, Sandia National Laboratories, Albuquerque, NM, April 1987. [pdf](#).
- [3] W.M. Scherzinger and C.R. Dohrmann. A robust algorithm for finding the eigenvalues and eigenvectors of 3x3 symmetric matrices. *Computer Methods in Applied Mechanics and Engineering*, 197(45-48):4007–4015, 2008.

APPENDIX A. COMMON BOUNDARY VALUE PROBLEMS

Throughout this effort, a wide variety of boundary value problems have been used to verify the various model responses investigated. Although some of these are specially tailored to a model, many of the loading paths and problems are common. As such, these repeated tests are presented and discussed here in this appendix. Emphasis is placed on the boundary conditions and kinematic descriptions that do not depend on the constitutive behavior and are therefore similar for all models. Details on how to produce these paths in a finite element problem are also discussed. For details on the various problems considered, the reader is referred to various texts ([1, 2]) on the subject.

A.1. UNIAXIAL STRESS - DISPLACEMENT CONTROLLED

In all likelihood, the most common test (experimentally or numerically) is that of uniaxial stress. Such a state may be produced via either stress or displacement control. Here, the latter case is discussed as displacement control can be essential when considering model responses that soften through damage or other mechanisms. To produce the uniaxial stress of interest, a displacement of the form $u_1 = \lambda(t)$ is applied along the x_1 edge. In three dimensional finite element cases, it is also essential to leave the x_2 and x_3 surfaces with a traction free condition. With elastically isotropic materials, this produces a strain field of the form,

$$\varepsilon_{ij} = [\delta_{i1}\delta_{j1} - \nu(\delta_{i2}\delta_{j2} + \delta_{i3}\delta_{j3})] \ln(1 + \lambda), \quad (\text{A.1.1})$$

which produces σ_{11} as the only non-zero stress.

A.2. SIMPLE SHEAR

An alternative, and often simpler to implement, shear problem is that of simple shear. With such a deformation field, only one shear stress component is non-zero (like the pure shear case). The difference arises in that given a simple shear loading the diagonal stresses are not necessarily zero. This state may be produced by a motion, $\chi(X_i, t)$ of the form $\chi(X_i, t) = X_i + \gamma(t)X_2\delta_{i1}$. The resultant deformation gradient, F_{ij} , takes the form,

$$F_{ij} = \delta_{ij} + \gamma(t)\delta_{i1}\delta_{j2} \quad (\text{A.2.1})$$

and it is noted that this deformation is volume preserving ($J = \det F_{ij} = 1$). Numerically, such a deformation field results from applying a displacement in the x direction along the y surface.

A.3. PURE SHEAR

To consider shear-based responses and behaviors of a model, uniaxial loadings are often insufficient. One problem, however, that does investigate shear deformations is that of a pure shear problem. In such problems, only a single shear strain and stress component are non-zero. Such a material state results from a deformation gradient of the form,

$$F_{ij} = \frac{1}{2} (\lambda + \lambda^{-1}) (\delta_{i1}\delta_{j1} + \delta_{i2}\delta_{j2}) + \frac{1}{2} (\lambda - \lambda^{-1}) (\delta_{i1}\delta_{j2} + \delta_{i2}\delta_{j1}) + \delta_{i3}\delta_{j3}, \quad (\text{A.3.1})$$

where the shear loading is relative to the $x_1 - x_2$ axis. The logarithmic strain tensor is then simply $\varepsilon_{ij} = \ln \lambda (\delta_{i1}\delta_{j2} + \delta_{i2}\delta_{j1})$. With such a strain tensor, it is trivial to note that σ_{12} is the only non-zero stress.

A.4. HYDROSTATIC COMPRESSION

In many cases, it is preferable to interrogate the pressure-dependent response of various models independently of any deviatoric deformations. To consider such purely volumetric loadings, hydrostatic (almost always compression) problems are invoked. Such loadings are often also referred to as uniform dilation as the volumetric change is the same in all three directions. Specifically, in these cases a purely volumetric response is investigated by applying a deformation of the form $u_i = \lambda(t)$. In a finite element problem, such a deformation field is reproduced by applying the displacement components onto the corresponding edges. With such applied displacement fields, the resulting logarithmic strain tensor is simply,

$$\varepsilon_{ij} = \ln(1 + \lambda(t))\delta_{ij}, \quad (\text{A.4.1})$$

and the corresponding (elastic) stress field is simply $\sigma_{ij} = -p\delta_{ij}$ where,

$$p = -3K\ln(1 + \lambda). \quad (\text{A.4.2})$$

Note, in the preceding relation p is defined as positive in compression.

A.5. CONSTANT EQUIVALENT PLASTIC STRAIN RATE

Typically, for a given boundary value problem it is desirable to know either the stress or deformation (strain) state and solve for the complementary response functions. In the case of rate-dependent hardening, or often rate-independent, it is preferable to prescribe a constant *equivalent plastic strain rate*, $\dot{\bar{\varepsilon}}^p$. Knowing, and controlling, this variable is often essential to finding and solving analytical solutions to verify hardening models.

As the equivalent plastic strain, $\bar{\varepsilon}^p$, is the internal (hidden) state variable corresponding to isotropic hardening, it is counterintuitive to think of prescribing its value. Nonetheless, for many plasticity models such a case is not only possible but relatively simple. Details of this approach may be found in [3], but are repeated here for convenience and completeness. In the following, two cases are treated – uniaxial stress and pure shear. For either problem, it is assumed that the stress state is initially at yield ($\phi(\sigma_{ij}(t=0, \bar{\varepsilon}^p=0)) = \sigma_y^0$) and a constant equivalent plastic strain rate is prescribed such that,

$$\bar{\varepsilon}^p(t) = \dot{\bar{\varepsilon}}^p t. \quad (\text{A.5.1})$$

Furthermore, it is recalled that the yield surface, f , is written as,

$$f(\sigma_{ij}, \bar{\varepsilon}^p, \dot{\bar{\varepsilon}}^p) = \phi(\sigma_{ij}) - \bar{\sigma}(\bar{\varepsilon}^p, \dot{\bar{\varepsilon}}^p), \quad (\text{A.5.2})$$

where,

$$\bar{\sigma}(\bar{\varepsilon}^p, \dot{\bar{\varepsilon}}^p) = \tilde{\sigma}_y(\bar{\varepsilon}^p) \hat{\sigma}_y(\dot{\bar{\varepsilon}}^p). \quad (\text{A.5.3})$$

Note, throughout this section function forms for $\tilde{\sigma}_y$ and $\hat{\sigma}_y$ are not given. For the purposes of the developed problem, the specific forms are unnecessarily as long as $\tilde{\sigma}_y$ depends only on $\bar{\varepsilon}^p$ and $\hat{\sigma}_y$ on the corresponding rate.

A.5.1. Uniaxial Stress

During uniaxial stress, the state of stress reduces to,

$$\sigma_{ij} = \sigma \delta_{i\eta} \delta_{j\eta} \quad (\text{no sum on } \eta) \quad (\text{A.5.4})$$

where η is the direction of loading (taken to align with one of the material principal axes) and

$$\sigma = \Gamma_{\eta\eta} \bar{\sigma}(t), \quad (\text{A.5.5})$$

with $\Gamma_{\eta\eta}$ being a constant associated with and dependent on the model parameters of the plasticity model. Specific forms for the various yield surfaces are given later in this section. Given this stress state, the axial elastic strain is simply,

$$\dot{\varepsilon}_{\eta\eta}^{\text{el}} = \frac{\Gamma_{\eta\eta}\bar{\sigma}(t)}{E}. \quad (\text{A.5.6})$$

To determine the plastic state of the material, the equivalency of plastic work ($\sigma_{ij}\dot{\varepsilon}_{ij}^p = \bar{\sigma}\dot{\varepsilon}^p$) is invoked enabling the axial plastic strain to be given as,

$$\dot{\varepsilon}_{\eta\eta}^p = \frac{\bar{\sigma}}{\sigma}\dot{\varepsilon}^p = \frac{1}{\Gamma_{\eta\eta}}\dot{\varepsilon}^p. \quad (\text{A.5.7})$$

Integrating,

$$\varepsilon_{\eta\eta}^p(t) = \frac{1}{\Gamma_{\eta\eta}}\bar{\varepsilon}^p. \quad (\text{A.5.8})$$

The total strain is found simply as the sum of elastic and plastic components,

$$\varepsilon_{\eta\eta}(t) = \varepsilon_{\eta\eta}^{\text{el}} + \varepsilon_{\eta\eta}^p = \frac{\Gamma_{\eta\eta}\bar{\sigma}(t)}{E} + \frac{1}{\Gamma_{\eta\eta}}\dot{\varepsilon}t. \quad (\text{A.5.9})$$

For this boundary value problem, only the axial displacement need be prescribed as zero traction conditions are required on the remaining surfaces to achieve the uniaxial stress state. As the equivalent plastic strain rate is constant, the flow stress, $\bar{\sigma}(t)$, is known and the total strain of (A.5.9) is only a function of time. Therefore, the desired displacement boundary condition may be prescribed as a function of time alone and is simply,

$$u_{\eta}(t) = \exp(\varepsilon_{\eta\eta}(t)) - 1. \quad (\text{A.5.10})$$

J₂ Plasticity

In the case of an isotropic *J₂* effective stress definition, for a uniaxial state of stress,

$$\Gamma_{\eta\eta} = 1 \quad (\text{no sum on } \eta). \quad (\text{A.5.11})$$

Hosford Plasticity

As the Hosford effective stress definition is isotropic, for a uniaxial state of stress the coefficients $\Gamma_{\eta\eta}$ are simply,

$$\Gamma_{\eta\eta} = 1 \quad (\text{no sum on } \eta). \quad (\text{A.5.12})$$

Hill Plasticity

For a Hill effective stress definition, by inspection of (A.5.5) it is clear that,

$$\Gamma_{\eta\eta} = R_{\eta\eta} \quad (\text{no sum on } \eta). \quad (\text{A.5.13})$$

Barlat Plasticity

With a Barlat effective stress definition, the anisotropy coefficients are,

$$\Gamma_{\eta\eta} = \frac{1}{\omega_\eta} \quad (\text{no sum on } \eta), \quad (\text{A.5.14})$$

where

$$\begin{aligned} \omega_1 = & \frac{1}{3} \left\{ \frac{1}{4} \left[|c'_{12} + c'_{13} - c''_{12} - c''_{13}|^a + |c'_{12} + c'_{13} + 2c''_{21} - c''_{23}|^a + |c'_{12} + c'_{13} + 2c''_{31} - c''_{32}|^a \right. \right. \\ & + |c'_{23} - 2c'_{21} - c''_{12} - c''_{13}|^a + |c'_{23} - 2c'_{21} + 2c''_{21} - c''_{23}|^a + |c'_{23} - 2c'_{21} + 2c''_{31} - c''_{32}|^a \\ & \left. \left. + |c'_{32} - 2c'_{31} - c''_{12} - c''_{13}|^a + |c'_{32} - 2c'_{31} + 2c''_{21} - c''_{23}|^a + |c'_{32} - 2c'_{31} + 2c''_{31} - c''_{32}|^a \right] \right\}^{1/a}, \end{aligned} \quad (\text{A.5.15})$$

$$\begin{aligned} \omega_2 = & \frac{1}{3} \left\{ \frac{1}{4} \left[|c'_{13} - 2c'_{12} - c''_{13} + 2c''_{12}|^a + |c'_{13} - 2c'_{12} - c''_{21} - c''_{23}|^a + |c'_{13} - 2c'_{12} - c''_{31} + 2c''_{32}|^a \right. \right. \\ & + |c'_{21} + c'_{23} - c''_{13} + 2c''_{12}|^a + |c'_{21} + c'_{23} - c''_{21} - c''_{23}|^a + |c'_{21} + c'_{23} - c''_{31} + 2c''_{32}|^a \\ & \left. \left. + |c'_{31} - 2c'_{32} - c''_{13} + 2c''_{12}|^a + |c'_{31} - 2c'_{32} - c''_{21} - c''_{23}|^a + |c'_{31} - 2c'_{32} - c''_{31} + 2c''_{32}|^a \right] \right\}^{1/a}, \end{aligned} \quad (\text{A.5.16})$$

$$\begin{aligned} \omega_3 = & \frac{1}{3} \left\{ \frac{1}{4} \left[|c'_{12} - 2c'_{13} - c''_{12} + 2c''_{13}|^a + |c'_{12} - 2c'_{13} - c''_{21} + 2c''_{23}|^a + |c'_{12} - 2c'_{13} - c''_{31} - c''_{32}|^a \right. \right. \\ & + |c'_{21} - 2c'_{23} - c''_{12} + 2c''_{13}|^a + |c'_{21} - 2c'_{23} - c''_{21} + 2c''_{23}|^a + |c'_{21} - 2c'_{23} - c''_{31} - c''_{32}|^a \\ & \left. \left. + |c'_{31} + c'_{32} - c''_{12} + 2c''_{13}|^a + |c'_{31} + c'_{32} - c''_{21} + 2c''_{23}|^a + |c'_{31} + c'_{32} - c''_{31} - c''_{32}|^a \right] \right\}^{1/a}. \end{aligned} \quad (\text{A.5.17})$$

A.5.2. Pure Shear

To produce a pure shear stress state, the pure shear conditions discussed in Section A.3 are utilized. In this case, for pure shear in the $\hat{e}_\eta - \hat{e}_{zeta}$ plane, a deformation gradient of the form,

$$F_{ij} = \frac{1}{2} (\lambda + \lambda^{-1}) (\delta_{i\eta} \delta_{j\eta} + \delta_{i\zeta} \delta_{j\zeta}) + \frac{1}{2} (\lambda - \lambda^{-1}) (\delta_{i\eta} \delta_{j\zeta} + \delta_{i\zeta} \delta_{j\eta}) + \delta_{i\theta} \delta_{j\theta}, \quad (\text{no sum on } \eta, \zeta, \theta), \quad (\text{A.5.18})$$

with \hat{e}_θ being the cross-product of \hat{e}_η and \hat{e}_ζ . With such a deformation,

$$\varepsilon_{ij} = \ln \lambda (\delta_{i\eta} \delta_{j\zeta} + \delta_{i\zeta} \delta_{j\eta}), \quad (\text{A.5.19})$$

meaning the appropriate displacement boundary conditions may be applied if the total shear strain is known.

For the pure shear strain case, the stress tensor is simply $\sigma_{ij} = \tau (\delta_{i\eta} \delta_{j\zeta} + \delta_{i\zeta} \delta_{j\eta})$ and may be equated to the shear stress as,

$$\tau = \Gamma_{\eta\zeta} \bar{\sigma}(t) \quad (\eta \neq \zeta). \quad (\text{A.5.20})$$

The elastic strain may then simply be written as

$$\varepsilon_{\eta\zeta}^{\text{el}} = \frac{\tau}{2\mu} = \frac{\Gamma_{\eta\zeta}}{2\mu} \bar{\sigma}(t). \quad (\text{A.5.21})$$

To find the plastic strain rate, the plastic work equivalency is recalled such that,

$$\sigma_{ij} \dot{\varepsilon}_{ij}^p = 2\sigma_{\eta\zeta} \dot{\varepsilon}_{\eta\zeta}^p = \bar{\sigma} \dot{\varepsilon}^p, \quad (\eta \neq \zeta) \quad (\text{A.5.22})$$

which produces an expression for the plastic strain rate as,

$$\dot{\varepsilon}_{\eta\zeta}^p = \frac{1}{2\Gamma_{\eta\zeta}} \dot{\varepsilon}^p, \quad (\eta \neq \zeta). \quad (\text{A.5.23})$$

Integrating (A.5.23) yields,

$$\varepsilon_{\eta\zeta}^p(t) = \frac{1}{2\Gamma_{\eta\zeta}} \bar{\varepsilon}^p, \quad (\eta \neq \zeta) \quad (\text{A.5.24})$$

leading to a total strain of the form,

$$\varepsilon_{\eta\zeta}(t) = \frac{\Gamma_{\eta\zeta}}{2\mu} \bar{\sigma}(t) + \frac{1}{2\Gamma_{\eta\zeta}} \dot{\varepsilon}^p t, \quad (\eta \neq \zeta) \quad (\text{A.5.25})$$

and

$$\lambda(t) = \exp(\varepsilon_{\eta\zeta}(t)), \quad (\eta \neq \zeta). \quad (\text{A.5.26})$$

J₂ Plasticity

In the case of a isotropic J_2 effective stress, the pure shear coefficients are,

$$\Gamma_{\eta\zeta} = \frac{1}{\sqrt{3}} \quad (\eta \neq \zeta). \quad (\text{A.5.27})$$

Hosford Plasticity

Although isotropic, the Hosford effective stress definition is non-quadratic leading to a stress multiplier of,

$$\Gamma_{\eta\zeta} = \frac{1}{[1 + 2^{a-1}]^{1/a}} \quad (\eta \neq \zeta). \quad (\text{A.5.28})$$

Hill Plasticity

Like the uniaxial case, for the pure shear response a direct connection may be made between the R stress ratios and $\Gamma_{\eta\zeta}$ such that,

$$\Gamma_{\eta\zeta} = \frac{R_{\eta\zeta}}{\sqrt{3}} \quad (\eta \neq \zeta). \quad (\text{A.5.29})$$

Barlat Plasticity

The Barlat effective stress definition produces stress relationships of the form,

$$\Gamma_{\eta\zeta} = \frac{1}{\xi_{\eta\zeta}} \quad (\eta \neq \zeta), \quad (\text{A.5.30})$$

where,

$$\xi_{12} = \left\{ \frac{1}{2} [|c'_{44} - c''_{44}|^a + |c'_{44} + c''_{44}|^a + |c'_{44}|^a + |c''_{44}|^a] \right\}^{1/a}, \quad (\text{A.5.31})$$

$$\xi_{23} = \left\{ \frac{1}{2} [|c'_{55} - c''_{55}|^a + |c'_{55} + c''_{55}|^a + |c'_{55}|^a + |c''_{55}|^a] \right\}^{1/a}, \quad (\text{A.5.32})$$

$$\xi_{31} = \left\{ \frac{1}{2} [|c'_{66} - c''_{66}|^a + |c'_{66} + c''_{66}|^a + |c'_{66}|^a + |c''_{66}|^a] \right\}^{1/a}. \quad (\text{A.5.33})$$

REFERENCES

- [1] G. A. Holzapfel. *Nonlinear Solid Mechanics: A Continuum Approach For Engineering*. John Wiley & Sons, Ltd, 2000.
- [2] W.M. Lai, D. Rubin, and E. Krempl. *Introduction to Continuum Mechanics*. Pergamon Press, 3rd edition, 1993.
- [3] J. T. Ostien and W. M. Scherzinger. Verification of select rate dependent models coupled to a hill yield surface. Memoraundum, 2017.

DISTRIBUTION

Email—Internal

Name	Org.	Sandia Email Address
Technical Library	01177	libref@sandia.gov



**Sandia
National
Laboratories**

Sandia National Laboratories is a multimission laboratory managed and operated by National Technology & Engineering Solutions of Sandia LLC, a wholly owned subsidiary of Honeywell International Inc., for the U.S. Department of Energy's National Nuclear Security Administration under contract DE-NA0003525.